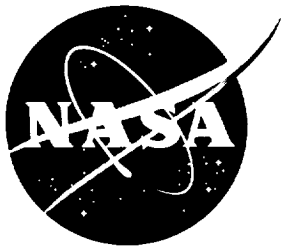

NASA Conference Publication 3350

31st Aerospace Mechanisms Symposium

Compiled by
C.L. Foster and E.A. Boesiger

Proceedings of a symposium held at the Huntsville Marriott, Huntsville, Alabama and hosted by NASA, George C. Marshall Space Flight Center and sponsored by Lockheed Martin Missiles and Space and the Aerospace Mechanisms Symposium Committee
May 14–16, 1997

May 1997

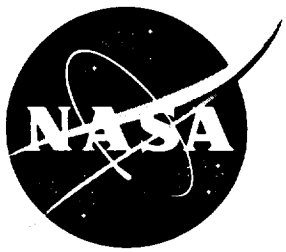

NASA Conference Publication 3350

31st Aerospace Mechanisms Symposium

Compiled by
C.L. Foster
Marshall Space Flight Center • MSFC, Alabama

and

E.A. Boesiger
Lockheed Martin Missiles and Space • Sunnyvale, California

Proceedings of a symposium held at the Huntsville Marriott, Huntsville, Alabama and hosted by NASA, George C. Marshall Space Flight Center and sponsored by Lockheed Martin Missiles and Space and the Aerospace Mechanisms Symposium Committee
May 14–16, 1997

National Aeronautics and Space Administration
Marshall Space Flight Center • MSFC, Alabama 35812

May 1997

PREFACE

The Aerospace Mechanisms Symposium (AMS) provides a unique forum for those active in the design, production and use of aerospace mechanisms. A major focus is the reporting of problems and solutions associated with the development and flight certification of new mechanisms. The National Aeronautics and Space Administration and Lockheed Martin Missiles & Space share responsibility for organizing the AMS. Now in its 31st year, the AMS continues to be well attended, attracting participants from both the US and abroad.

The 31st AMS, hosted by the NASA Marshall Space Flight Center, was held in Huntsville, AL on May 14, 15, and 16, 1997. During these three days, 27 papers were presented. Topics included robotics, deployment mechanisms, bearings, actuators, scanners, boom and antenna release, and test equipment. Hardware displays during the vendor fair gave attendees an opportunity to meet with developers of current and future mechanism components.

The high quality of this symposium is due to the efforts of many people and their efforts are gratefully acknowledged. This extends to the voluntary members of the symposium organizing committee representing the 8 NASA field centers, LMMS, and members from the European Space Agency. Also to be thanked are the session chairs, the authors, and particularly the personnel at NASA MSFC responsible for the symposium arrangements and the publication of these proceedings. Thank you also goes to the symposium executive committee at LMMS who are responsible for the year-to-year management of the AMS, including paper processing and preparation of the program.

CONTENTS

SYMPOSIUM SCHEDULE

TUESDAY, 13 MAY 1997

7:00-9:00 EARLY REGISTRATION AND/OR CHECK-IN
Pre-Function area

WEDNESDAY, 14 MAY 1997

8:00 Wednesday Authors' Breakfast - Season's Cafe

8:30 REGISTRATION AND REFRESHMENTS
Pre-Function area

9:30 INTRODUCTORY REMARKS
Carlton L. Foster, Host Chairman
NASA Marshall Space Flight Center, Huntsville, AL
Stuart H. Loewenthal, General Chairman
Lockheed Martin Missiles & Space, Sunnyvale, CA

CENTER WELCOME
J. Wayne Littles, Center Director
NASA Marshall Space Flight Center, Huntsville, AL

10:00 **SESSION I - INSTRUMENT MECHANISMS**
Derek Binge, Session Chair
TECSTAR Inc., Oxnard, CA

- *The FUSE Mirror Mechanism*
  Paul Nikulla, Swales and Associates, Beltsville, MD
- *Two Unique Methods of Micro-positioning as Implemented in the FUSE Focal Plane Assemblies*
  Jeffrey Lees, Gregg Allison, John Andrews, James Green & James Westfall, University of Colorado, Boulder, CO
- *A Reactionless, Bearingless Linear Shutter Mechanism for the Multispectral Pushbroom Imaging Radiometer*
  Les Krumel, Sandia National Laboratories, Albuquerque, NM
- *Vibration Isolation, Steering, and Suppression Mechanism for Space-Based Sensors*
  Steve Bennett & Torey Davis, Honeywell Satellite Systems Operation, Glendale, AZ; Richard Cobb & Jeanne Sullivan, U.S. Air Force, Kirtland, NM

12:00 LUNCH

1:15 **SESSION II - BEARINGS & TRIBOLOGY**
Dennis Smith, Session Chair
Honeywell Satellite Systems Operation, Glendale, AZ

- *Selection, Preparation and Lubrication of Middle-Size Ball Bearings for Infrared Instruments*
  Jean Lizon, European Southern Observatory, Munich, Germany
- *The Advanced Microwave Sounding Unit-A, Antenna #2 Bearing Life Test*
  Charles Powers, NASA Goddard Space Flight Center, Greenbelt, MD
- *The GSFC Combined Approach of ODC Stockpiling and Tribological Testing to Mitigate the Risks of ODC Elimination*
  Roamer Predmore & Claudia LeBoeuf, NASA Goddard Space Flight Center, Greenbelt, MD; Andrew Hovanec, Unisys, Greenbelt, MD
- *Bearing Assembly, Thermal Radiator Rotary Joint*
  Ed Kibel, Honeywell Satellite Systems Operation, Glendale, AZ
- *The Chemical and Physical Properties of Aerospace Grade Lubricants*
  Paul Bessette, Nye Lubricants, Inc., New Bedford, MA

3:45-5:30 VENDOR DISPLAYS
Invited component and software vendors will display their wares.

6:00-9:00 RECEPTION AT U.S. SPACE & ROCKET CENTER

6:00	Welcome
6:15-7:00	OMNIMAX® Movie
7:00-8:30	Buffet and Self-Guided tour
8:30-9:00	Space Station Presentation "Outpost in Space"

THURSDAY, 15 MAY 1997

7:00 Thursday Authors' Breakfast - Season's Cafe

8:00 **SESSION III - LOW SHOCK**
Scott Tibbitts, Session Chair
Starsys Research Corp., Boulder, CO

- *Development of a New, No-Shock Separation Mechanism for Spacecraft Release Applications*
  Shawn Smith, Starsys Research Corp., Boulder CO; Bill Purdy, Naval Research Laboratory, Washington, D.C.; Bill Nygren, Lockheed Martin Astronautics, Denver, CO

• *Environmental Sensor Boom Experiment Using Shape Memory Alloys for Release, Deployment and Final Lockup*
Steven Robinson, Robert Gammon, John Koch & Jerry Stephenson, Boeing Defense & Space Group, Kent, WA

- *Shape Memory Activated Adaptive Antenna*
  Bernie Carpenter & Duane Grosskrueger, Lockheed Martin Astronautics, Denver, CO
- *The Cassini Magnetospheric Imaging Instrument Ion and Neutral Camera Shutter Door Mechanism Design*
  Douglas Mehoke & Steven Vernon, Johns Hopkins University Applied Physics Laboratory, Laurel, MD

10:00 BREAK

10:15 **SESSION IV - MECHANISMS**
Ernie Schaeffer, Session Chair
Schaeffer Magnetics Inc., Chatsworth, CA

- *SEPTA 14 Gear Development*
  Luc Chatenet & Frederic Canedi, Société Européenne de Propulsion, France
- *The Cassini Main Engine Assembly Cover Mechanism*
  Donald R. Sevilla, Jet Propulsion Laboratory, Pasadena, CA
- *Hexapod Pointing System for Space Applications*
  Luis Genovese & Walter Gallieni, ADS Italia S.r.l., Lecco, Italy; Piero Galione & José Gavira, European Space Agency, Noordwijk, The Netherlands
- *The Galileo Tape Recorder Rewind Operation Anomaly*
  Michael Johnson & Greg Levanas, Jet Propulsion Laboratory, Pasadena, CA

12:15 LUNCH

1:15 **SESSION V - MOTORS & GIMBALS**
Peter Welch, Session Chair
Aerojet Electrosystems, Azusa, CA

- *Design Improvements for a Second Generation Mirror Gimbal*
  Scott Stanley, Ruben Nalbandian & Jeffrey Williams, Schaeffer Magnetics, Inc., Chatsworth, CA
- *Updating Gimbal Actuators for the Long Journey to Saturn*
  Theodore Iskenderian, Benjamin Joffe & Edward Litty, Jet Propulsion Laboratory, Pasadena, CA
- *Design and Qualification of the CRSS Antenna Gimbal*
  G. Cameron Dales & Mark Calassa, Lockheed Martin Missiles & Space, Sunnyvale, CA

2:45 BREAK

3:00 **SESSION VI - TETHERED SATELLITE MISSION AND FAILURE ANALYSIS**

Anthony R. Lavoie, Session Chair & former Chief Engineer of Tethered Satellite Project, NASA Marshall Space Flight Center, Huntsville, AL

- *Re-Flight of the Deployable Retrievable Booms*
  Carlton Foster & Edward Litkenhous, NASA Marshall Space Flight Center, Huntsville, AL
- *TSS-1R Failure Mode Evaluation*
  Jason Vaughn, Matthew McCollum & Rachel Kamenetzky, NASA Marshall Space Flight Center, Huntsville, AL
- Invited speaker: Robert J. Schwinghamer, Associate Director, Technical, NASA Marshall Space Flight Center, Huntsville, AL
  Fault Tree Design
  A unique perspective on the subject of failure investigations drawn from more than 30 years' experience and involvement in numerous investigations, including: Apollo 13, Challenger, Tethered Satellite, TWA 800, and others.

5:15-10:00 COOKOUT AT DITTO LANDING PICNIC PAVILION

5:15	Buses depart Huntsville Marriot
6:00-7:00	Social Hour
7:00-8:30	Dinner
8:30-9:30	Entertainment provided by Pinhook Creek, a local bluegrass band
9:30	Buses leave Ditto Landing and return to hotel

FRIDAY, 16 MAY 1997

7:00 Friday Authors' Breakfast - Season's Cafe

8:00 **SESSION VII - MORE MECHANISMS**

Benjamin E. Goldberg, Session Chair
NASA Marshall Space Flight Center, Huntsville, AL

- *Robotic Materials Handling in Space: Mechanical Design of the Robot Operated Materials Processing System HitchHiker Experiment*
  George Voellmer, NASA Goddard Space Flight Center, Greenbelt, MD
- *3 d.o.f. Robotic Wrist Actuator Redesign*
  Tom Bonner, NASA Kennedy Space Center, FL; Gabor Tamasi, PLD Advanced Automation Systems, Inc., Rockledge, FL
- *NASA Space Shuttle Light Weight Seats - The Final Chapter*

Steven King, Lockheed Martin Engineering & Sciences, Houston, TX

- *Ion Thruster Alignment Mechanism for Artemis: Qualification Test Results and Lessons Learned*
  Manfred Falkner, Christian Schwarzinger & Donald Johnson, Österreichische Raumfahrt-und Systemtechnik, Vienna, Austria
- *Rotary Mechanism for Contactless Data and Power Transfer in Spacecraft*
  Gwyn Roberts & P. Hadfield, Industrial Development Bangor Ltd., Bangor, United Kingdom; M. Humphries, MMS Space Systems Ltd., Filton, United Kingdom; F. Bauder, Mecanex SA, Nyon, Switzerland; J. Gavira Izquierdo, ESA, Noordwijk, The Netherlands

10:30 BREAK

10:45 NASA MARSHALL SPACE FLIGHT CENTER OVERVIEW
G. Sherman Jobe, Director, Science and Engineering Directorate

11:15 PRESENTATION OF THE HERZL AWARD
John W. Redmon, Sr., NASA MSFC (ret)

CLOSING REMARKS
Edward A. Boesiger, Operations Chairman
Lockheed Martin Missiles & Space

11:30 LUNCH AND CHECK-OUT

12:30 BUSES DEPART HOTEL FOR MSFC TOUR

1:00-3:00 NASA MARSHALL SPACE FLIGHT CENTER FACILITY TOUR
Space Station Mockup, Manufacturing Facility, Neutral Buoyancy Simulator, Test Facility

SYMPOSIUM ORGANIZING COMMITTEE

Carlton L. Foster, Host Chairman, NASA MSFC

Stuart H. Loewenthal	General Chairman	Lockheed Martin
Edward A. Boesiger	Operations Chairman	Lockheed Martin
Charles W. Coale	Organizational Chairman	Lockheed Martin (ret)

Obie H. Bradley, Jr.	NASA LaRC
Michael J. Eiden	ESA/ESTeC
David F. Engelbert	NASA ARC
Robert L. Fusaro	NASA LeRC
Claef F. Hakun	NASA GSFC
Alan C. Littlefield	NASA KSC
Edward C. Litty	JPL
Ronald E. Mancini	NASA ARC
Fred G. Martwick	NASA ARC
Stewart C. Meyers	NASA GSFC
Douglas A. Rohn	NASA LeRC
John F. Rogers	NASA LaRC
William C. Schneider	NASA JSC
Donald R. Sevilla	JPL
Sterling W. Walker	NASA KSC
Edward A. Wegner	Lockheed Martin (ret)

SYMPOSIUM ADVISORY COMMITTEE

Aleck C. Bond	NASA JSC (ret)
H. Mervyn Briscoe	ESA/ESTeC (ret)
Otto H. Fedor	Lockheed Martin (ret)
Angelo Giovannetti	NASA ARC (ret)
John E. Harbison	NASA MSFC (ret)
Harvey H. Horiuchi	JPL
Frank T. Martin	NASA GSFC (ret)
John W. Redmon, Sr.	NASA MSFC (ret)
Alfred L. Rinaldo	Lockheed Martin (ret)
Bowden W. Ward, Jr.	NASA GSFC (ret)
Nathan D. Watson	NASA LaRC (ret)

The FUSE Mirror Mechanism

Paul Nikulla

Abstract

A two-tiered mirror mount system and sub-micron actuator assembly with an integral coarse alignment mechanism has been developed by Swales Aerospace Inc.* for the Far Ultraviolet Spectroscopic Explorer (FUSE) instrument. The FUSE instrument is a grating spectrometer that will observe interstellar energy in the ultraviolet spectrum. Observing energy in this spectrum placed extremely stringent requirements on the associated mechanical systems which resulted in many novel and innovative designs.

Novel designs to be presented are a two-tiered mirror mount system, a ball screw used for sub-micron position actuation, a self-reacting over-travel hard stop, a convoluted diaphragm for anti-rotational restraint of the ball screw shaft, and a Coarse Alignment Mechanism. Top-level system requirements, the identification of critical component parameters, and design descriptions with functional and vibration testing results are also reviewed herein.

Introduction

The FUSE instrument has four co-aligned normal incidence off-axis parabolic mirrors. Each mirror has a focal length of 2245 mm and observes energy in the 910- to1180-Å spectrum. To maximize the optical throughput of the instrument, the mirrors cannot accept more than 0.05 mm (0.002 in) of mount distortion resulting from assembly error and from forced induced displacement contributed by both differential actuation and thermal growth. Additionally, the mirror mounting system had to provide adequate strength to support the mass of each mirror for a 15g single-axis launch environment and a 45g random vibration environment. After many iterations of mirror flexure and mount design, a solution was found that satisfied both the launch and on-orbit mirror mount requirements. A two-stage flexure design with a rigid intermediate plate (Figure 1) was found to both minimize mirror distortions and provide a medium to off-load the high lateral launch loads that were unacceptable to the actuator ball screw.

The FUSE instrument structure is a graphite-composite tubular construction which will exhibit dimensional changes in orbit due to both the initial 1g release and moisture desorption. To compensate for these dimensional changes and their effects on the instrument optical prescription, the FUSE primary mirrors will each have a linear actuator assembly to provide sub-micron resolution for z-axis focus and sub-arcsec tip-tilt pointing adjustments. Additionally, the actuator assemblies will provide each mirror with a coarse adjustment mechanism used for integration alignment. This mechanism is also required to be able to maintain alignment during launch.

An actuator proof-of-concept demonstration unit and an Engineering Test Unit have been designed, fabricated, and tested. These designs resulted in many noteworthy

---

* Swales Aerospace Inc., Beltsville, MD

mechanism features and substantial lessons learned, which will be shared in this review.

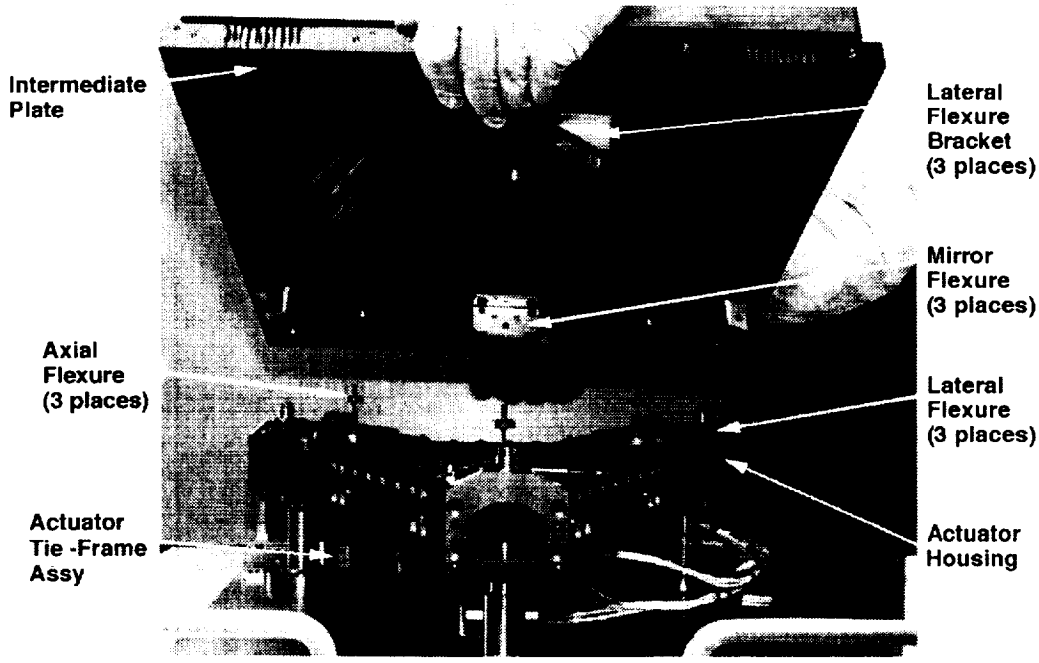

Figure 1 Components of a Mirror Sub-System Assembly

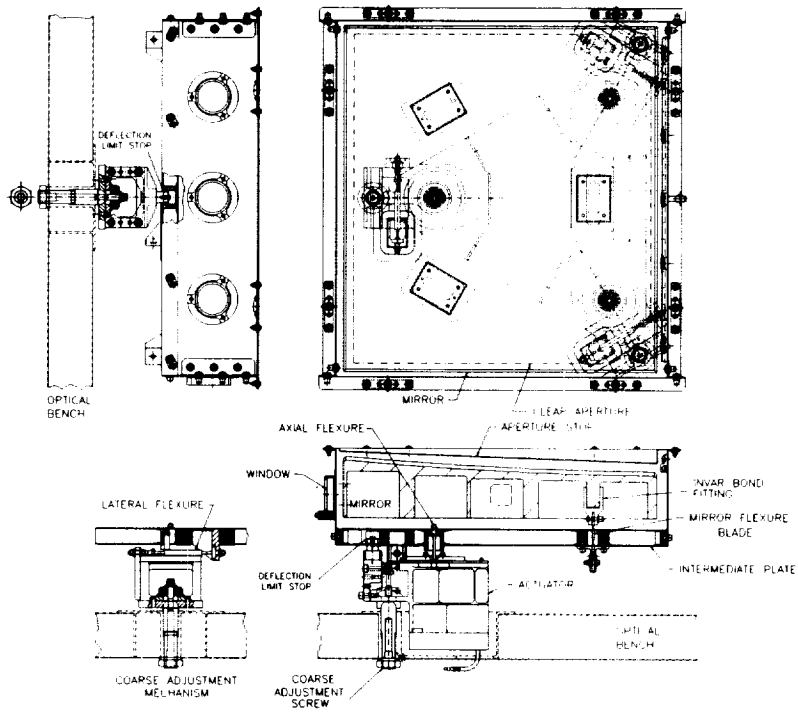

Figure 2 Mirror Sub-System Assembly Detailed Layout

Top-Level Requirements

Design loads for the mirror assembly were derived by evaluating the worst-case environment expected from test and launch. By using Miles' approximation for random vibration response, it was determined that the random vibration test would develop the highest load in the system. With a 75-Hz system, a Q of 25, a PSD of 0.08 G/Hz, and a factor of 3 applied to the Miles' result to account for 3σ events, we arrived at a random-based load of 45g for the mirror and mirror flexures. The predicted dynamic behavior indicated that the first mode had significant participation of the mirror and its flexure system with highest strain energy associated with the intermediate plate bending. The 45g single-axis random vibration acceleration loads were conservatively used as the design load throughout the system, even though attenuation was expected in the lower Mirror Subsystem Assembly (MSA). The MSA design loads and overall requirements are listed in Table 1.

Table 1 Design loads and Overall System Requirements

PARAMETER	REQUIREMENT	QUALIFICATION TESTING	ANALYTICAL PREDICTIONS
Component Acceleration Mirror and mirror flexures	45 g single axis	Comply by Testing	Comply
Random Vibration	10.6 Grms	Comply by Testing	Comply
Sine Vibration	8 g from 18 to 50 Hz	Comply by Testing	Comply
Sine Burst	18.75 g	Comply by Testing	Comply
Stowed Resonant Frequency	> 75 Hz	120 Hz; Q=25	Comply
Factors of Safety	1.25 on Yield / 1.4 on Ult	N/A	N/A
Total Mass per MSA	< 75 Kg	Measured 89.6 kg	83.2 kg
Operational Temperature Ranges	17–27°C	Life Testing in Thermal Vac	Comply
Survival Temperature Range	-10–40°C	Life Testing in Thermal Vac	Comply

The actuators are required to operate for three years and to provide 500 motions on orbit and 500 motions for ground testing. Each actuator is required to have a minimum bi-directional stroke of 1 mm and encounters an electronic soft stop at the end of a maximum travel of ±2 mm. In the event of a soft stop malfunction, a hard stop will provide a force to stall the actuator motor and prevent actuator damage. The actuator kinematic requirements are listed in Table 2.

Table 2 Actuator Kinematics Requirements

MOTION	REQUIRED	PREDICTED	TESTED
Range of Motion (z-axis)	> ±1 mm	> ±2 mm	±2.1 mm
Resolution (z-axis)	< 1 micron	< 0.351 micron	0.350 micron
Tip Range (Rx)	±10 arc-min	±30.8 arc-min	±32.34 arc-min
Tip Resolution (Rx)	< 1 arc-sec	0.165 arc-sec	0.160 arc-sec
Tilt Range (Ry)	±10 arc-min	±30.8 arc-min	±32.34 arc-min
Tilt Resolution (Ry)	< 1 arc-sec	0.165 arc-sec	0.160 arc-sec

Design Description

The FUSE lower instrument section includes four MSA's, with each assembly containing a Zerodur mirror with mounting flexures, Actuator Flexure System (AFS), Actuator Tie-Frame Assembly (ATFA), and a Coarse Adjustment Mechanism (CAM) (Figures 1 and 2). The MSA's are structurally attached in a three-point mount configuration to the instrument graphite-composite honeycomb optical bench. Each mirror is enclosed by an intermediate plate, four composite side walls, and a removable top cover. This containment system provides the mirror with a controlled purge volume before launch and a supporting structure for the mirror aperture stop. A passive launch lock to hold the aligned position of each mirror is provided by the detent torque of each actuator motor.

Mirror Description

The four FUSE mirrors are fabricated from Zerodur, selected for its low expansion property, and are 70% lightweighted with a triangular isogrid rib pattern (Figure 3). For a three-point mirror mount, the triangular isogrid rib structure was found to provide the optimum stiffness-to-weight ratio. The mirror flexure mounts (Figure 4a) are located on the back of each mirror and are positioned radially with an angular spacing of 120° on a common diameter. Three Invar fittings are bonded with Hysol EA 9396 adhesive to three thickened mirror rib sections, which are notched inward to allow the mount bond line to be closer to the mirror neutral axis. Invar was selected as the bond-fitting material because of its low coefficient of thermal expansion (CTE), a critical concern due to its fixed contact area with the Zerodur mirror. The mirror flexure blades, which are fastened to the Invar bond fittings, are constructed of 6AL-4V titanium. The blade geometry was optimized to allow for near kinematic mount behavior and to provide for slight distortion error on the soft axis, lateral movement, when assembled to the AFS.

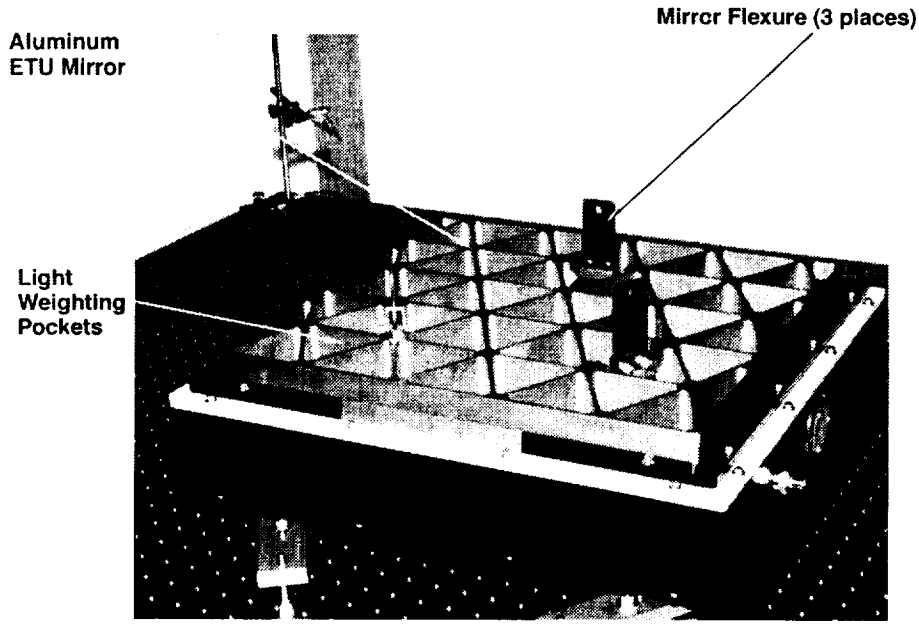

Figure 3 Zerodur Mirror with Flexures

Actuator Flexure System

The mirror and actuators are connected by the actuator flexure system which consists of an intermediate plate, three lateral and three axial post flexures. Each mirror flexure is attached to the intermediate plate by two angle brackets, one on each side of the flexure blade (Figure 4a). The mirror is extremely sensitive to distortion from bending along the strong axis and more compliant along its weak axis. The use of side angle brackets for mounting to the intermediate plate considerably reduced the risk of locking in assembly distortions to the mirror. The ATFA is attached to the intermediate plate by six single-degree-of-freedom posts, three lateral and three axial (Figures 4b and 4c). Each flexure post is fabricated from 6AL-4V titanium alloy and is reduced in diameter at each end to minimize tangential moment stiffness while maximizing buckling stiffness.

The combination of the mirror and the actuator flexures, along with the intermediate plate, has resulted in a multi-functional two-tiered mirror mount design. The two-tiered flexure configuration evolved after many iterations of design and analysis. The design and analysis revealed the complex interdependencies that existed for a mounting system which would satisfy both the mirror and actuator performance requirements. The actuator flexure system had to provide a support system that would isolate the mirror from distortions resulting from forced displacements induced by different positions of the three actuators. Adding a rigid plate between the mirror flexures and the actuator flexures provided a platform that would serve to attenuate these distortions to acceptable levels and react against the lateral launch loads from the actuator ball screws. Providing a lateral load path was accomplished by attaching one

end of each lateral flexure to the actuator housing and the other end to the intermediate plate.

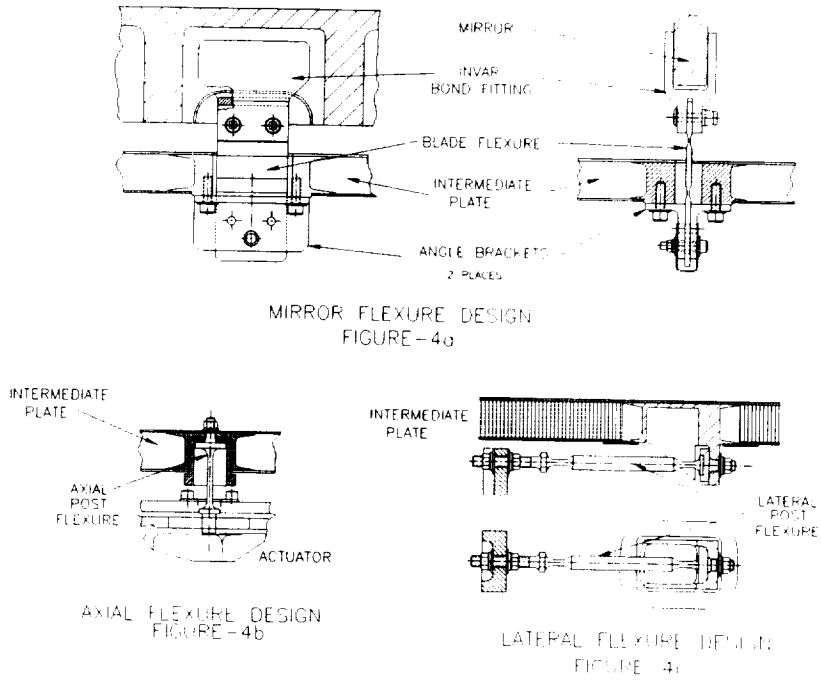

Figure 4 Two-Tiered Flexure Components

Actuator Tie-Frame Assembly

The Actuator Tie Frame Assembly (ATFA) is comprised of three actuators, each radially positioned on a common diameter with an angular spacing of 120° and are joined together by an interconnecting structure (Figure 5). The MSA is required to be co-aligned to the instrument optical axis during integration and then subsequently be structurally attached to the optical bench without losing the aligned position. This requirement dictated that the actuators be structurally connected in a manner that would allow the MSA to be moved as a single system and provide a rigid frame structure to accommodate a three-point attachment to the optical bench. This was accomplished by constructing a rigid actuator frame assembly. A frame structure is produced by locating each actuator housing at the apex of a triangle and joining the housings with three graphite/epoxy composite channels. The triangular section is further stiffened by the use of a composite top closeout plate. The composite components and titanium housings are aligned on a tooling plate and then attached together with high-strength shear fasteners and bonded with Hysol EA 9396 adhesive. This built-up approach was chosen over a one-piece machined titanium frame alternative for its higher stiffness, lower weight, and better CTE match to the optical bench.

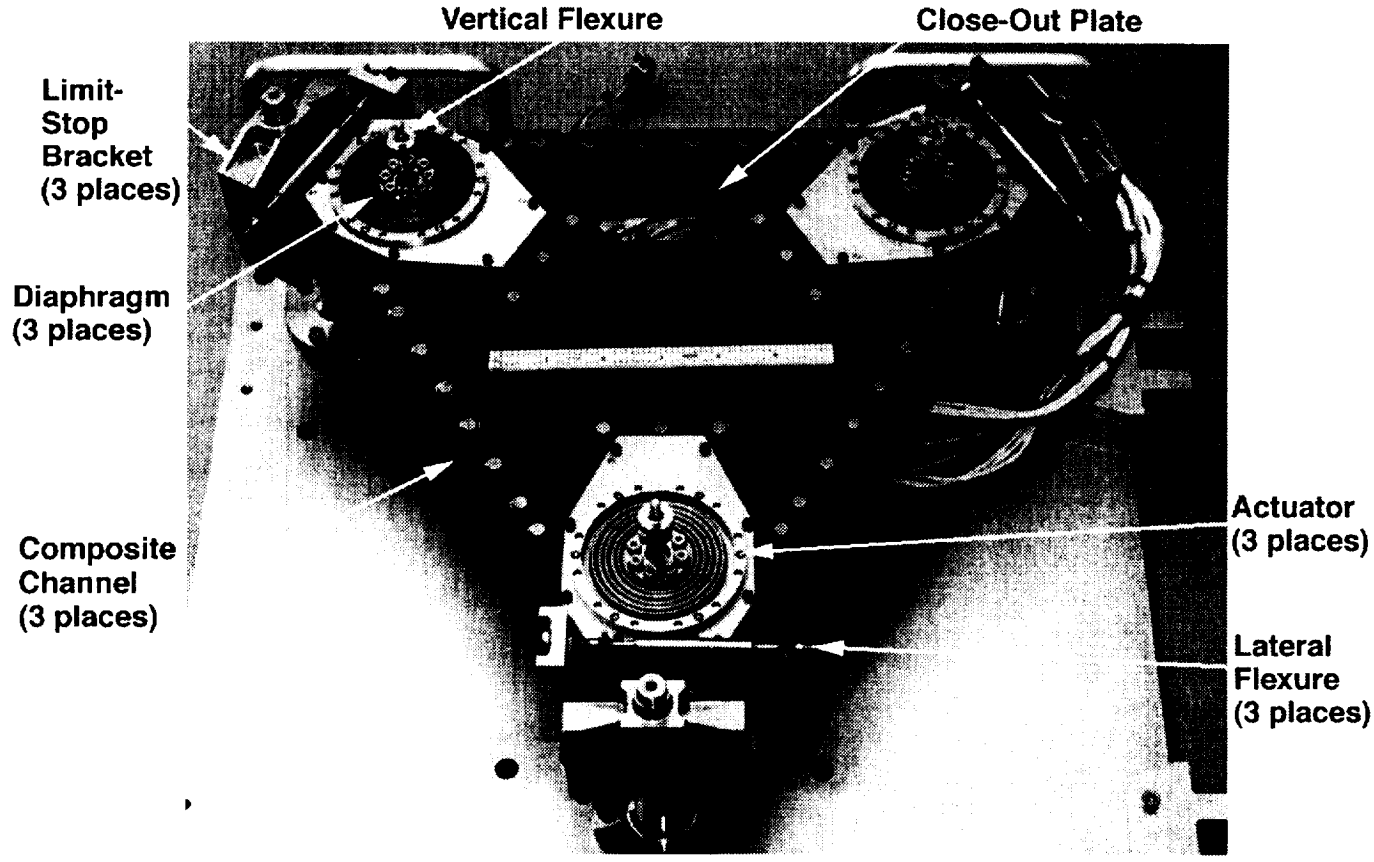

Figure 5 Actuator Tie-Frame Assembly- (ATFA)

Coarse Adjustment Mechanism Design

The MSA Coarse Adjustment Mechanism (Figure 6) is a structural mounting system that provides six independent degrees of movement: three translational and three rotational. The CAM is required to provide a travel of ±200 mm for x-y-z translations with a resolution of 5 microns and ±10 arc-min of rotational motion with a resolution of 1 arc-min. Once the mirror aligned position is found, the CAM must preclude any positional shifts resulting from the severe launch forces.

Three adjustment screws and three slider plates are used to provide a structural mount system and to allow for all six alignment degrees of freedom. Each adjustment screw has a spherical top section which is coupled to the slider plate and is located under each actuator housing. Z-axis focus and tip-tilt rotations are achieved by adjusting the height of the adjustment screws. To allow for lateral X-Y movements and Z-axis rotation, the slider plate is coated with Dicronite, a dry-film lubricant, and is positioned between the top of the adjustment screw and the bottom actuator housing. The slider plate is simultaneously held in place and allowed to pivot by the top spherical section of the adjustment screw. Removable bi-directional micro-adjusters, mounted to the optical bench, are used to impart motion for X-Y movements and Z-axis rotation. To

lock the MSA in the aligned position, each adjustment screw is secured in place by tightening both an upper bolt and a lower locking nut. The upper bolt is used to clamp the actuator to both the top of the adjustment screw and slider plate, and the lower nut clamps the bottom of the screw to the optical bench. To further secure this joint, the actuator housing and slider plate are matched drilled and pinned together.

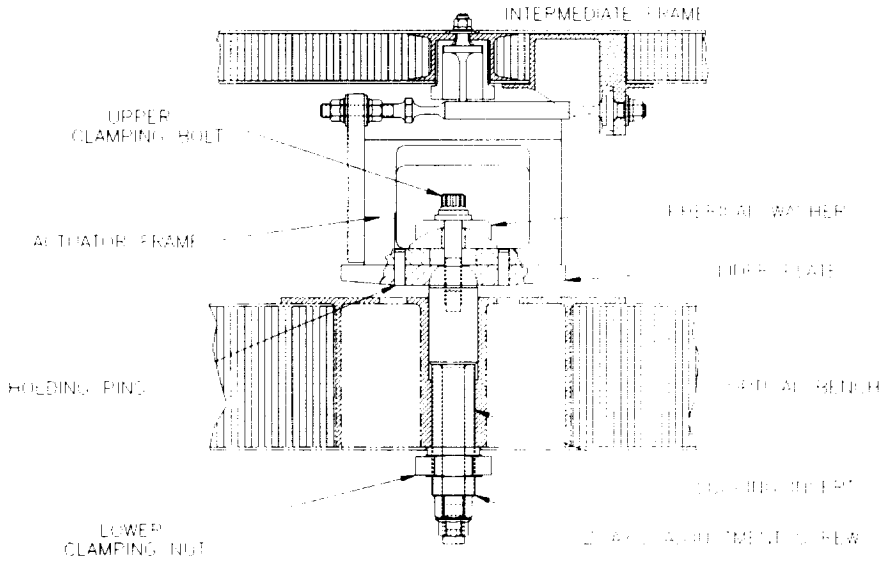

Figure 6 A Single Coarse Adjustment Mechanism

Actuator Design Description

The actuator assembly (Figure 7) consists of a 30° stepper motor with an integral 160:1 two-stage planetary gear reduction system. The motor/gear-head output pinion rotates a large spur gear, providing an additional gear reduction of 4.25:1. The large spur gear has an integral lower housing section which supports a ball screw assembly. The housing section is coupled to a pair of ball screw nuts designed to provide a zero backlash translation of 2.5 mm/rev (0.1 in/rev). The gear housing is supported in the actuator housing by a duplex pair of angular contact bearings, which are in a back-to-back configuration to provide moment stiffness. The ball screw nuts are pinned to the gear housing and rotate together when the motor is stepped. The ball screw shaft is rotationally constrained by a convoluted diaphragm which deflects axially, thus allowing the shaft to exhibit pure translation. The outer diameter of the diaphragm is attached to the actuator housing, and the inner diaphragm is fastened to the top of the ball screw shaft. With a total gear reduction of 681:1 and a ball screw lead of 2.5 mm (0.1 in), an output translation of 0.31 micron per 30° motor step of

rotation is achieved. To signal the positions at the middle and each end of travel, a light emitting diode, in conjunction with an encoder disk coupled to the gear housing, is used. At ±1.2 mm of travel, the operating stroke, the position sensor is enabled and the motor step commands are disabled. In the event the electronic stop malfunctions, a non-jamming hard stop is encountered at ±2.1 mm, which will stall the motor without inducing any damage to the actuator components. To eliminate the cost and complexity of a launch restraint mechanism, the motor was selected such that its detent torque will be used as the braking torque to hold the aligned position of the mirror during launch.

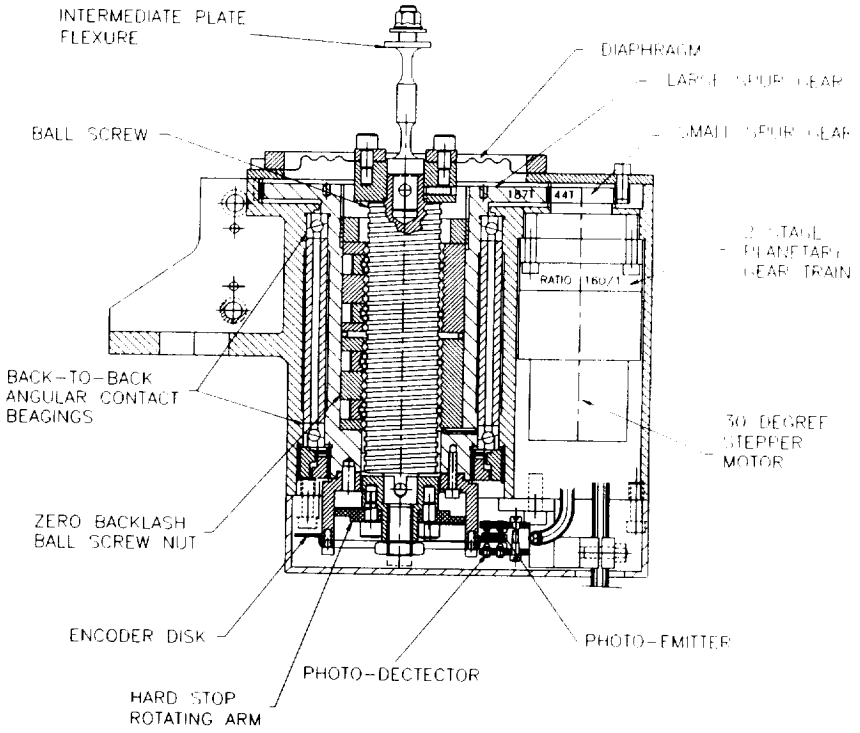

Figure 7 Cross Section of Actuator Assembly

Motor Design

After a mature actuator design had evolved, it become apparent that the selection of the actuator motor was more complex than originally anticipated. Three critical dependent motor design parameters had to be satisfied to meet all actuator performance requirements: (1) provide sufficient detent torque for the actuator launch lock, (2) produce the required pull-out torque at minimum voltage to assure ample torque margin for reliability, and (3) generate a stall torque at maximum voltage less than the torque capacity of the actuator diaphragm. After a lengthy design process in

conjunction with the motor vendor[1], a 30° brushless DC stepper motor with a motor torque constant, Kt, of 0.088 N•m/(watt)1/2 was selected. The motor frame is configured with a 6-pole Samarium Cobalt permanent magnet rotor and a four-phase non-redundant winding stator and has a frame size of 3.2 cm (1.25 in).

A feature unique to the Astro motor is its ability to produce a continuous detent torque of 0.003 N•m (0.40 in•oz), which is independent of the rotor position relative to the armature. This continuous detent torque provides a locking force of 4892.8 N (1,100 lbf) per actuator and will insure that the mirror will not shift from its aligned position during launch vibration.

Rotor pull-in torque at a low voltage condition was a critical motor parameter and required the rotor to produce a 0.016-N•m (2.31-in•oz) pull-in torque. A torque margin of four was added to each resisting torque with all values reflected back to the motor rotor, except for detent torque which has been found not to vary with time. This factor of safety accounts for possible efficiency degradation of the drive train components over the lifetime of the mechanism.

Ball Screw Design

To minimize actuation stiction and to ensure a reliable actuator that will survive the high loads from launch and vibration testing and operate reliably in space vacuum, a ball screw was selected over the traditional lead screw used for sub-micron actuation. A lead screw inherently has high sliding friction due to the large contact area between its moving parts, thus resulting in a low mechanical efficiency of 30% and an unpredictable load reacting behavior. A ball screw (typically 90-95% efficient) produces movements based on rolling contacts and provides a uniform and predictable load reacting behavior. However, the accuracy of a ball screw was in question because no flight or commercial heritage existed for an application that achieved sub-micron resolution. The highest commercially available ball screw lead accuracy is 0.005 mm (0.0002 in) per 4.7 cm (1 ft) and 0.0006 mm (0.000025 in) per 4.7 cm (1 ft) for a lead screw. A ball screw exhibits a linear cumulative pitch error that is characterized per unit length of travel. Within each revolution of the screw, a positional error (pitch oscillation) varies in a sinusoidal manner on top of the cumulative pitch error. This pitch oscillation could affect the overall positional accuracy locally within a single revolution; however, it did not seem to add any gross errors in the actuator resolution performance.

The selected ball screw was a commercial design consisting of a 17-4PH ball screw shaft, a 17-4PH double-nut assembly, and 440C SS balls, manufactured by RBG Beaver (Figures 8 and 9). Launch loads, test vibration, and repeated movement over the same area raised concerns for the potential of galling from the contacting of similar materials. To eliminate this problem, the 440C balls were replaced with silicon nitride balls which have a Rockwell hardness of 90 and dissimilar metallurgical structure, thus ensuring that galling would not occur. The ball screw has a rating of 3558.4 N

[1] Astro Instrument Corp., Deerfield, FL

(800 lbf) axially and 111.2 N (25 lbf) laterally. Applied loads in the 15g load environment were 220 both axially and laterally, though with the addition of the lateral flexures the applied lateral loads on the ball screw shaft were reduced to 44.48 N (10 lb). The precision rating of the ball screw is ISO-class-3, which has an accuracy of 0.167 mm/m (0.0002 in/ft) of travel with a surface finish of 0.81 μm (32 micro-in). All ball screw components are grease-plated in a solution of 5 parts Freon and 1 part Bray-601 EF micronic grease. The void spaces in the ball screw assembly are 30%-filled with Bray-601 EF micronic grease at assembly.

A double nut with an opposing preload was used to eliminate ball screw backlash. Setting and holding the optimum torque for each ball screw is critical to its performance. Ball screw free running torque measurements reflected a preload torque sensitivity range of only ±0.028 N•m (4 in-oz); whereby, any deviation from the optimum setting resulted in excessive torsional friction and grinding of the contacting components. Holding the preload was achieved by staking the preload turret nut and pinning both nuts to the gear housing.

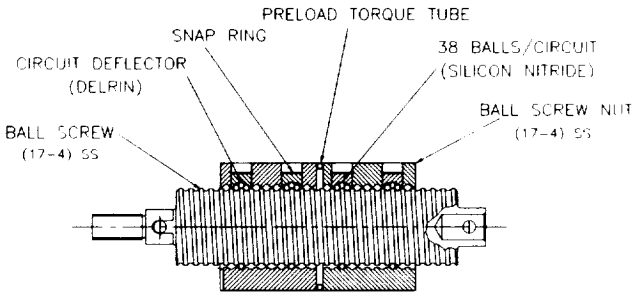

Figure 8 Cross-Section of Ball Screw Assembly

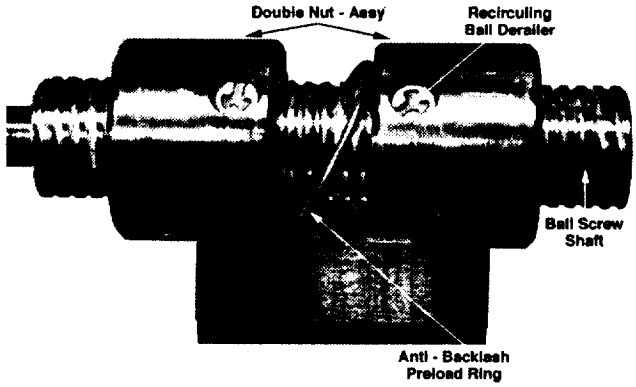

Figure 9 Ball Screw Assembly

Convoluted Diaphragm Design

To achieve pure translation of the ball screw shaft, a device was needed to restrain the shaft from rotating while simultaneously allowing a relatively large bi-directional translation of ±2.1 mm. Additionally, a restraining device had to react elastically to the hard stop 9.6 N•m (85 in-lb) torsional load that is superimposed with a forced displacement induced distortion resulting from the maximum actuator stroke. Initially, a bellows design was investigated as a possible restraining device, but volumetric constraints and low torsional capacity proved the bellows design to be a non-viable candidate. A stainless steel custom-stamped convoluted diaphragm was found to satisfy all actuator requirements. Material selection for the diaphragm turned out to be the most difficult part of the design. The difficulty resulted from the extreme requirements needed to satisfy the multiple loading condition, along with material availability and cost. Material selection was based on optimizing the ratios of material tensile strength, modulus of elasticity, and material thickness. After a lengthy investigation and analysis, the material selected for the diaphragm was 17-7PH stainless steel in the RH-900 condition with a thickness of 0.06 mm (0.0025 in). This proved to be very difficult to obtain without ordering a large quantity required by all mill houses.

Self-Reacting Hard Stop Design

Over-travel of the ball screw in the actuator would be catastrophic to both the actuator and the mission; therefore, a reliable non-jamming hard stop was developed. The hard stop force reacts between the bottom of the ball screw shaft and gear housing and stalls the drive system at the input to the ball screw (as opposed to stalling the high force output end of the screw). As the ball screw shaft reaches its maximum travel, the hard stop arms, which are fastened to the shaft, contact tabs that rotate with the gear housing. Synchronizing the contact of the translating arms on the ball screw shaft with those of the rotating tabs on the bottom of the gear housing set the limits of the actuator stroke. It was found that placing the hard stop components at these locations achieved a self-reacting load path between the ball screw shaft and the gear hub, thereby reducing the probability of damage to the mechanism at the lock-up condition.

Demonstration Unit Testing

Resolution tests were performed using Millitron and Starrett linear position sensors. The Millitron sensor recorded an average uni-directional resolution of 0.28 microns, and the Starrett recorded an average value of 0.33 microns. Backlash tests revealed an average deadband of 0.9 microns, recorded by the Millitron, and an average of 0.45-micron deadband was recorded by the Starrett sensor. Measured values for position accuracy and repeatability were not consistent between instruments and readings. Mechanical means for measuring movements in the sub-micron range were found to be very sensitive to temperature changes, minute vibrations, and unknown causes of position drifts. To further characterize the performance of the actuator in the sub-micron range, additional stability and resolution tests will be performed using a laser interferometer in a thermally stable and vibration isolated room.

To simulate the axial and lateral loading effects on the ball screw, a simulated MMFS with a mock mirror mass was incorporated on the actuator for vibration testing. Actuator resolution and backlash tests were performed after the completion of each axis of vibration and showed no degradation of performance from pre-vibration values.

Post thermal-vacuum life tests for both functional and performance testing showed no degradation of performance. Disassembly of the actuator and ball screw showed that the Braycote grease plate was still uniformly coating both the balls and threads of the nuts and screw.

Convoluted Diaphragm Testing

To simulate both full extension and lock-up loads on the diaphragm, a special test fixture was developed. The diaphragm was extended ±2.0 mm,while simultaneously applying 9.6 N•m (85 in-lb) of torque to simulate actuator lock-up at a full motion stroke. The first diaphragm failed at less than 40 cycles into the test. The cause of the failure was traced to a small radius on the outer diameter of the inner diaphragm clamping ring. The small radius subjected the diaphragm to high bending stresses at a full stroke condition. After doubling the radius, the second diaphragm failed after 200 cycles of testing (50 times the expected life).

Self Reacting Hard Stop Testing

The demonstration unit did not contain a hard stop mechanism; however, the ETU contained three complete flight-like actuators, each having a functional hard stop which was tested once in both directions. The tests showed that, at the full stroke of ±2.1 mm, hard stop contact was made and the motor stalled. After a complete functional test force, each actuator was disassembled, and all components were inspected. No damage was found in any of the relevant drive components.

Actuator System Test

The demo unit contained the lower section of the MMFS, three vertical and horizontal flexures, one live actuator, two dummy actuator mounts, and a mirror mass simulator. The test consisted of a sine survey, sine sweep, sine burst, and random specification. The vertical flexure under the live actuator failed during a lateral axis random vibration test. Examination of the test article revealed slip marks between the actuator and base plate and lateral flexure and support brackets. These parts were fastened together with locking nuts and were not pinned. The actuator flexure was re-made and all mating parts were pinned, resulting in a successful vibration re-test. This failure did expose the sensitivity of the vertical flexures to small lateral deflection; therefore, a limit stop has been added at each actuator to preclude overstress of the flexures from excessive lateral deflection.

An ETU assembly, which contained a complete MSA with an aluminum spherical mirror and a full complement of actuators, was successful in a three-axis sine burst and random vibration test. The first three fundamental natural frequencies were determined to be within 5 Hz of the predicted frequencies.

Launch Lock Testing

Since the launch locking force is provided by the motor detent torque, the load path must travel through the entire drive system. This fact raised concerns of mating gear teeth impacts and positional shifts which might occur as the gear backlash gaps shift. The backlash for all gears was minimized by selecting precision grade AGMA-12 gears. A static load of 889.6 N (200 lbf) was applied to the demonstration unit and 0.018 mm (0.0007 in) of ball screw movement was recorded. After vibration testing of the demonstration unit, 0.025 mm (0.001 in) of z-axis movement was recorded. This displacement was measured between the mirror mass simulator and the actuator fixed platform. Both displacement values are acceptable by the mirror adjustment system. There is adequate margin in the actuator adjustment budget to compensate for these errors.

Conclusions: Design Lessons Learned

- A commercial-grade ball screw can achieve sub-micron resolution.
- Proper mounting of the diaphragm is critical to its fatigue life.
- Proper pinning of flexure supports and actuator components are critical for reacting against vibration loads.
- A reliable self-reacting non-jamming design can be achieved for an actuator hard stop.
- A two-tiered flexure mirror mount can attenuate multiple force displacement-induced distortions to acceptable levels and simultaneously support applied launch loads.

Acknowledgments

I would like to thank Ed Devine of Swales for his invaluable help during the development of the two-tiered mirror mount concept and the ball screw actuator. I would also like to thank Dave Watson and Cengiz Kunts, both from Swales, for their prompt and proficient structural analysis that was crucial to the success of the mirror flexure system and actuator component design. Additionally, I would like to thank Dave Heckle for his innovative concept of the Course Alignment Mechanism and Frank Rowe for his creative design solutions used in the development of the actuator mechanism.

References

Michael J. Kennedy. " Design of the Far Ultraviolet Spectroscopic Explorer Mirror Assemblies", SPIE Volume 2807, pp172-183. Presented at the Space Telescope & Instrument Conference at Denver, CO, on August 6-7, 1996.

Two Unique Methods of Micro-positioning as Implemented in the FUSE Focal Plane Assemblies

Jeffrey Lees*, Gregg Allison*, John Andrews*,
James Green*, and James Westfall**

Abstract

The Focal Plane Assemblies (FPAs) provide a unique opportunity to compare and contrast two quite different design solutions for micro-positioning in a space flight mechanism. The contrast between the designs for the X-axis and Z-axis provides valuable insight for designers of high-force, low-frequency, micro-positioning systems. The FPAs use a High-Output Paraffin Linear Actuator (HOPLA) to actuate the X-axis compound-flexure motion stage. The HOPLA takes an evolutionary step from the usual binary operation of paraffin actuators. The HOP-actuated flexure system can achieve sub-micron positioning accuracy without friction, stiction, mechanical backlash, or hysteresis when driven with a closed-loop control. In contrast, the FPA Z-axis motion stage uses a geared stepper motor/lead screw actuator and parallel-flexure stage with an open-loop control. This paper discusses the mechanism design, selection of actuators, analysis, material selection, and lessons learned during the verification, performance testing, and qualification of the flight FPAs.

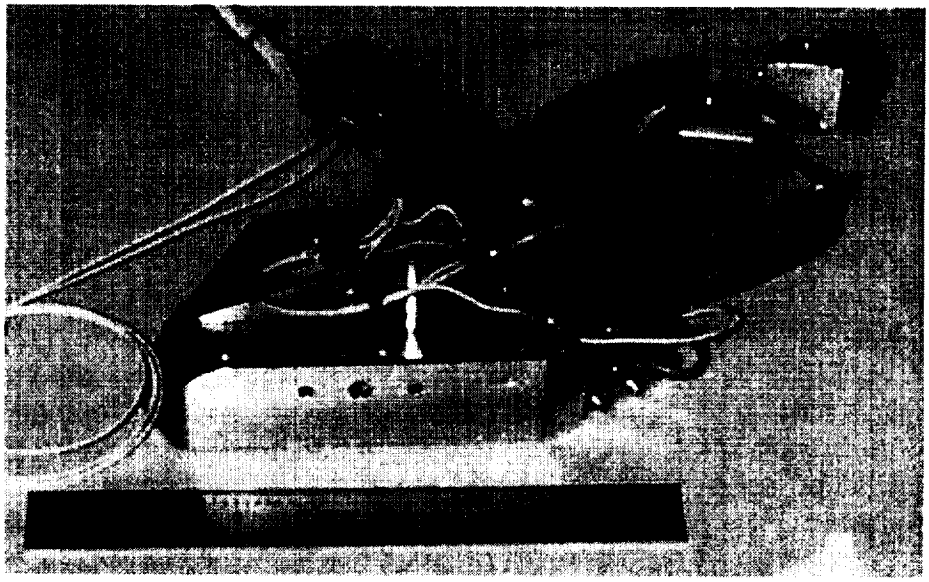

Figure 1 Focal Plane Assembly (LiF-1)

* University of Colorado Center for Astrophysics and Space Astronomy (CASA), Boulder, CO
** University of Colorado Laboratory for Atmospheric and Space Physics (LASP), Boulder, CO

FUSE Mission & Mechanism Requirements

The Far Ultraviolet Spectroscopic Explorer (FUSE) is designed to perform moderate resolution spectroscopy ($\Delta\lambda/\lambda$ = 30,000) from 905–1180 Å. The optical design employs four separate, co-aligned channels to maximize the instrument sensitivity and cover the entire wavelength region simultaneously. Light is collected by four off-axis parabolas and focused onto four FPAs, which act both as movable entrance slits for the spectrometer and also as mirrors for the Fine Error Sensors (FES). The FES acts as a slit jaw camera and provides fine pointing control error signals to the spacecraft. The diverging light passing through the air slit is diffracted and re-imaged by four holographically corrected spherical gratings in Rowland circle mounts. The four spectra are collected on two microchannel plate detectors employing helical time delay anodes.

The primary science goals of FUSE are three-fold. The first is to measure the ratio of deuterium to hydrogen in a variety of galactic and extra-galactic environments. By covering the entire HI Lyman series (other than Lyman α), the instrument allows coincident measurements of the ratio in several Lyman lines and provides a much better accuracy in the determination of the ratio. Second, the instrument will perform a survey of hot gas, particularly in the important 1032- to 1038-Å doublet of OVI in a variety of environments. Finally, a measurement of hot intergalactic gas by observing the red-shifted absorption from HeII will be performed. Of course, numerous other observations can and will be performed, particularly in the study of hot stars, interstellar H_2, and any phenomena which are bright in the FUSE wavelength regime.

The FPA mechanisms are employed in the FUSE instrument to move a small, air-slitted mirror (20 mm by 20 mm) along two axes. In the local X-axis, which is along the spectral dispersion direction, the FPAs move the slit mirror perpendicular to the slits. This X-axis motion is used to accommodate a spectral analysis technique known as the Iterative Restoration Technique (IRT). When using IRT, the spectrograph entrance slits must be moved in small increments, thus causing the position of the spectrum to shift on the detector. The IRT motion requires small step sizes (on the order of 2 μ) and will be used quite frequently over the course of the FUSE satellite three year mission. The local Z-axis motion of the FPAs results in moving the spectrograph entrance slits along the instrument optical path, thus resulting in a focusing capability. It is expected that focusing will be done infrequently and , therefore, the duty cycle on the FPA Z-axis motion is quite low. The general motion requirements for the FPAs is shown in Table 1. In addition to the motion requirements, the FPA mechanism must be designed with the usual space flight considerations of robustness, reliability, cleanliness, low-power, low-mass, etc.

Table 1 On-Orbit Performance Requirements

REQUIREMENT	X-Axis	Z-Axis
Total displacement	+350 μm	±250 μm
Displacement rate	≥50 μm/min	≥50 μm/min
Accuracy	≤±2 μm/orbit	≤±10 μm/orbit
Total # of flight motions	11000	80

Introduction

For micro-positioning to be successful in an ultra-clean, ultraviolet spacecraft environment, friction and stiction must be eliminated to reduce non-linear behavior. For our application, various flexural system configurations for linear motion were evaluated for the FPA X-axis and Z-axis. Some typical flexural system configurations are listed below:

- cantilevers
- parallel flexures
- diaphragms
- flex pivots
- crossed flexures

Through various arrangements of these components, linear motion, approximately linear, rotational, and simulated rotational motion can be achieved.

Z-Axis Flexure System

The flexural system chosen for the Z-axis motion (spectrograph focus) consists of two flat parallel flexures (Figures 2 and 3). The advantages of flat parallel flexures are simple design, fabrication, analysis, and nearly linear motion over the required range of travel (±250 μ). In addition to a friction- and stiction-free design, parallel flexure systems also eliminate wear and lubrication issues and can be designed for near infinite life. The one obvious disadvantage of parallel flexures is the produced motion that is both perpendicular to the translation and parallel to the flexures. This parasitic motion does not adversely affect the optical performance of the FUSE spectrograph (the motion is along the length of the entrance slits). However, it presents several challenges from an actuation standpoint. The non-linearity of the motion prevents the lead screw, nut and actuator from rigidly attaching the motion stage to the FPA base (Figure 2). This does not present a problem for ordinary ground-based systems. However, a space-bound system must be sufficiently robust to survive launch without damaging the mechanism or losing alignment. A frequently employed solution is to employ a launch lock. Envelope and mechanism size constraints preclude the use of a launch lock on the FPAs. Therefore, a system with low mass and a high spring rate was chosen. Achieving the low mass became a significant issue in the design.

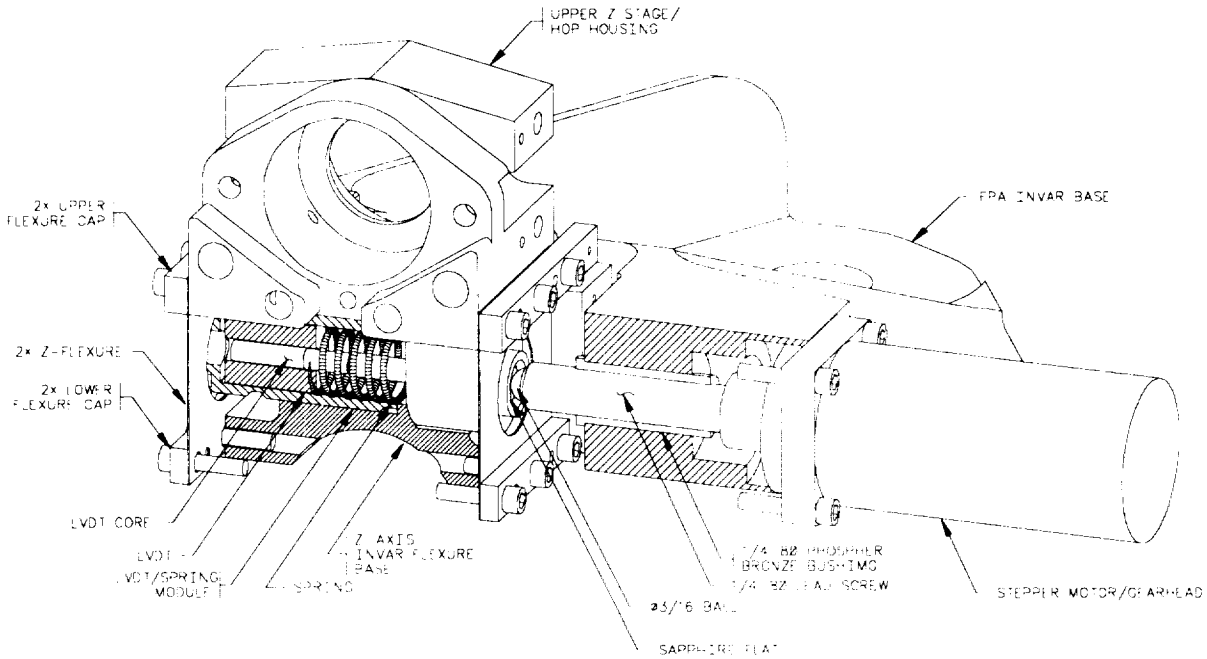

Figure 2 FPA Z-Axis Components Cutaway

For the parallel flexure configuration, the following general equation of motion can be derived [1]:

$$F(\delta) = \frac{12EI\delta}{l^3} \tag{1}$$

For two flexures:

$$F(\delta) = 2 \times I \times \frac{12\delta E}{l^3} = 2 \times \frac{bt^3}{12} \times \frac{12\delta E}{l^3} = \frac{2\delta E b t^3}{l^3} \tag{2}$$

The moment for two flexures can be written as follows [1]:

$$M = \frac{Fl}{4} = \frac{\delta E b t^3}{2l^2} \tag{3}$$

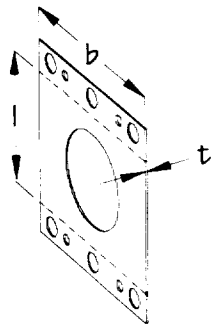

Figure 3 Z-Flexure

Substituting (2) for F for a twin flexure system:

$$\sigma(\delta) = \frac{Mc}{I} = \frac{\delta Ebt^3}{2l^2} \times \frac{t/2}{bt^3/12} = \frac{\delta Ebt^3}{2l^2} \times \frac{12t}{2bt^3} = \frac{3\delta Et}{l^2} \tag{4}$$

The flexures employed on the FPA Z-axis deviate from the ideal theoretical design to accommodate the lead screw and sensor assembly and installation (Figure 4). A finite element model was developed to predict stresses and performance to a higher level of confidence.

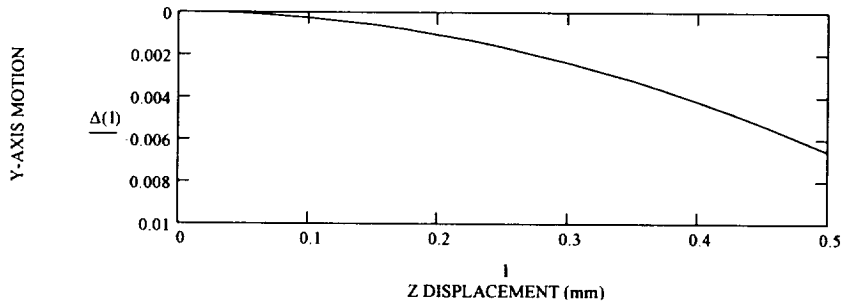

Figure 4 Y-Axis Parasitic Motion

Parallel Flexural Parasitic Motions

The most obvious parasitic motion occurs in the Y-direction (Figure 4) and is approximated by

$$\Delta y(\delta) \cong -\left(l - \sqrt{l^2 - \delta^2}\right) \tag{5}$$

Another error that can be introduced from design constraints is tilt of the stage (α) when the actuation force in not applied to the stage at $\frac{l}{2}$ [3]:

$$\alpha(\delta) \cong \left(\frac{\delta}{l}\right) \times \left[\frac{6(l-2a)t^2}{3b^2 l - at^2 l + 6at^2}\right] \tag{6}$$

Additionally, fabrication errors will also introduce parasitic tilts. Each of the FPA *X*-axis and *Z*-axis flexures were fabricated in a single group to reduce Δl errors of the dowel pin locations and for substitutability. The Δl errors can be approximated by [3]

$$\theta(\delta) \cong \frac{\Delta \ell \delta}{2l^2 b} \tag{7}$$

Another fabrication error, resulting in a parasitic tilt, is unequal spacing of the flexures in the upper and lower stages (i.e., non-parallel flexures) and can be approximated by the following equation [3]:

$$\varphi(\delta) \cong \frac{\delta z}{lb} \tag{8}$$

Flexure Material

The importance of choosing a proper flexure material for the FPAs was perhaps second only to the choice of material for the optic. The following material properties must be carefully considered for space-bound micro-positioning mechanisms:

- Density
- Modulus of elasticity
- Yield strength
- Coefficient of thermal expansion
- Thermal conductivity
- Availability
- Electrical conductivity
- Corrosion resistance
- Operating temp
- Micro yield strength

Several benchmarks of mechanical properties can assist in the decision. One is specific stiffness E/ρ, and another is Y/E, as suggested by Weinstein [4] (Table 2). The latter relationship emphasizes a characteristic of a good spring: low modulus and high strength. The alloy chosen for both the X-axis (0.127 mm) and Z-axis (0.254 mm) was Ti-15V-3Al-3Cr-3Sn, also known as Ti-15-3. The major advantages of Ti-15-3 alloy are [5,6,7]

- Extremely consistent mechanical properties
- Low susceptibility to stress corrosion cracking due to high V and low Al content
- Material is single-phase beta when supplied in solution annealed condition. However, the beta structure is metastable and will precipitate a fine alpha phase upon aging.
- Very low sensitivity to hydrogen embrittlement
- Low notch sensitivity, $K_t = 3.0$, at temperatures above −196°C in annealed or aged conditions
- Consistent yield strengths as high as 1448 MPa in cold rolled aged condition with 2% elongation or as low as 758 MPa in solution annealed condition

Z-Axis Actuator

The Z-axis is actuated by a small stepper motor and lead screw with the nut position fixed with respect to the base and stepper motor (Figure 3). The Astro stepper motor, with 30° steps, is attached to a 100:1 gear head to produce output steps of 0.300°. The output shaft has an internal 22-tooth, 96-pitch gear spline. The LOIC 1/4-80 pitch semi-hardened stainless steel lead screw has an external gear spline hobbed onto the

mating end. On the opposite end, a ball mates to a sapphire disk connected to the upper half of the Z-Axis stage. The phosphor bronze nut and the motor/gear head are both rigidly attached to the FPA base. Hence, the lead screw advances with the Z-axis as it rotates and is not rigidly connected to the stage, thus allowing the stage to move in the Y-direction as the flexures displace from their neutral position. The spring provides a constant preload on the lead screw, with sufficient force to avoid separation of the upper Z-stage to the lead screw during typical launch environments. Through extensive vibration testing, however, it was shown that several separations would not adversely affect performance or alignment.

Lead Screw

Lead screw and nut require careful consideration and several key characteristics were addressed:

- Resolution
- Lubrication
- Torque requirement/margin
- Stresses
- Material combinations
- Stability

The FPA lead screw/actuator resolution was determined as follows:

$$\frac{.0125in}{rev} \times \frac{rev}{360^\circ} \times \frac{300^\circ}{step} \times \frac{25400\mu m}{in} = .265 \, \mu m/step$$

A perfluoropolyether (PFPE) grease was chosen to lubricate the FPA lead screw. The advantages of this class of lubricants are [7,8]

- Low volatility required by UV environment
- Excellent chemical inertness
- Low surface tension/high surface affinity
- Good lubricating properties

The FPAs operate in the spectrograph, and thus, significant attention was given to contamination of FUSE optics operating in the far UV. One significant problem with lubricants in ultra-clean spacecraft environments is lubrication creep. A lubricant will spread or "wet" a surface whose surface energy is higher than the surface tension of the lubricant [9]. A barrier film was employed in several key areas around the bushing and sapphire flat to prevent lubricant migration. The Barrier film consisted of a stable fluorocarbon polymer dissolved in a fluorinated solvent that quickly evaporates after application. This theoretically leaves a monomolecular layer with a surface energy well below the surface tension of the PFPE lubricant as well as silicones [9]. To

ensure that the barrier film would not adversely affect lubricant performance in places it was not supposed to be, it was applied after the lubricant.

Various theoretical torque equations have been proposed in various forms including the following [10]:

$$T_R = \frac{dW}{2}\left[\frac{\pi f_s d_m + l\cos\theta_n}{\pi d_m \cos\theta_n - f_s l}\right] \tag{9}$$

$$T_L = \frac{dW}{2}\left[\frac{\pi f_s d_m - l\cos\theta_n}{\pi d_m \cos\theta_n + f_s l}\right] \tag{10}$$

Extensive torque test were performed on various lead screws and various lubricants. These tests clearly showed that one should not rely solely on theory alone in the prediction of lead screw torque requirements. Quality of thread form and materials play a significant role in performance. Also, note that none of the samples exhibited zero torque with no load applied (Figure 5) due to lubrication viscosity.

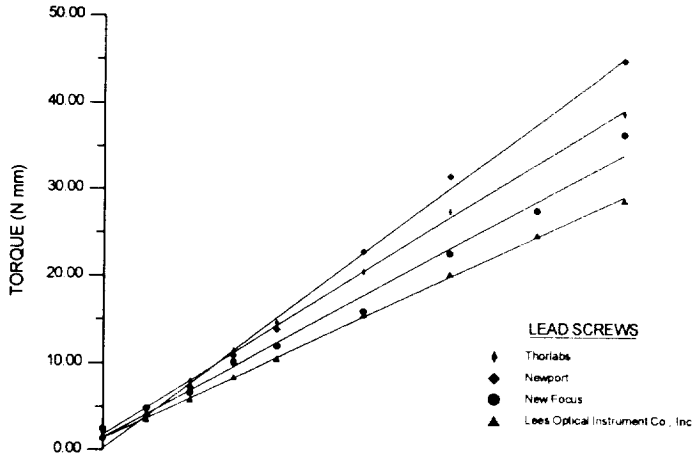

Figure 5 1/4-80 Lead Screw Evaluation

A very detailed discussion of lead screw and nut design can be found in [11]. Additionally, some basic stress equations can also be employed as given by Deutchman *et al.* [10]:

- Bearing pressure $$\sigma_{bearing} = \frac{w}{\pi d_m h n} \tag{11}$$
- Thread bending stress $$\sigma_{bending} = \frac{3wh}{\pi d_m n b^2} \tag{12}$$

$$\tau_{screw} = \frac{3w}{2\pi d_R n b} \tag{13}$$

- Thread shearing stress $$\tau_{nut} = \frac{3w}{2\pi d_o n b} \tag{14}$$

- Tensile/compressive stress $$\sigma_{t\,or\,c} = \frac{4w}{\pi\left(\frac{d_R + d_P}{2}\right)^2} \quad (15)$$

- Buckling $$\sigma_{buckling} = \frac{p}{A}\left[1 + \left(\frac{L}{K}\right)^2 \frac{S_{YP}}{\pi^2 KE} + \frac{ce}{K^2}\right] \quad (16)$$

Finally, the stability of the lead screw design must be considered. Deutchman *et. al.* provide an equation for overhauling, which is the tendency for the lead screw to rotate due to the applied load. This phenomenon is not uncommon in ball screws but occurs rarely in plane screws where the coefficient of friction is higher. To prevent overhauling, the following criterion must be met [10]:

$$f_s \geq \tan\alpha \cos\theta_n \quad (17)$$

The contact stresses of the ball against the sapphire were calculated using the method presented by Boresi and Sidebottom [12].

Z-Axis Control

The Z-axis controller is a simple, open loop, stepper motor driven system. The control logic receives a gated pulse stream and a direction command from the FPA electronics and converts that into the phased, step sequence required to move the motor in the desired direction. The control logic drives the stepper motor through four N-Channel MOSFET switching transistors. Since this is an open loop system, it is possible to step beyond the desired range and damage the drive mechanism. In the event of an extreme excursion, limit switches sense mechanism position and disable the motor drive.

X-Axis Compound Flexure System

The flexural system chosen for the FPA X-axis also consists of two flat parallel flexures. However, to reduce parasitic motion, a compound flexural system, symmetrical about the axial centerline, was developed (Figure 6). The two types of FPA X-axis, *"pushers"* and *"pullers"*, both use HOP linear actuators with an extending push rod and are nearly identical and share all but a few components. The compound nature of the FPA flexural system complicates the equations of motion [11]:

$$\delta(F) = \frac{Fl}{P} \times \left[1 - \frac{\tanh\left(\frac{\psi l}{2}\right)}{\psi l / 2}\right] \quad (18)$$

where $$\frac{\psi \ell}{2} = \sqrt{\frac{3Pl^2}{2Ebt^3}} \quad (19)$$

This is a result of the flexures being in tension from the sides bending in compliance. If the flexures were under a compressive load [11]:

$$\delta(F) = \frac{Fl}{P} \times \frac{\left[\tan\left(\psi l/2\right) - 1\right]}{\psi l/2} \tag{20}$$

The nature of the force required to actuate the X-axis is very linear for the FPA. Several of the implemented design changes included "weakening" the sides, removing a cross member, connecting the free ends of the sides, and moving the LVDT sensor below the axis of motion as originally implemented in the *"puller"* design. Another significant benefit of this change was the reduction of thermal expansion errors and the ability to sense them. Other than the additional element for the *"puller"* HOP to push against, the *"puller"* and "pusher" designs are nearly identical (Figure 6).

Flat parallel flexure strips were also chosen for the same reasons as the Z-axis, as well as Ti-15-3 alloy. The only differences were the thicknesses: 0.127 mm (.005 in) for the X-axis, and 0.254 mm (0.010 in) for the Z-axis. Thinner material was selected due to the increased stiffness of the compound flexure system and to minimize hysteresis.

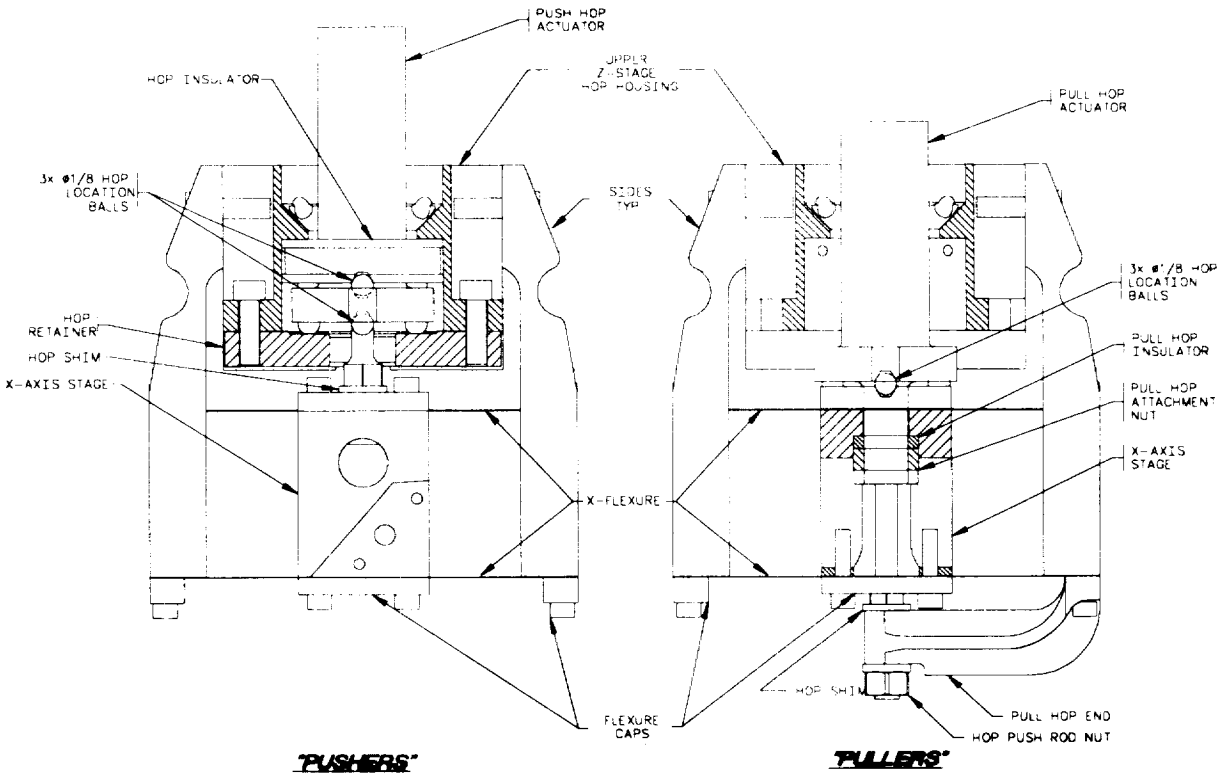

Figure 6 X-Axis "Pusher" and "Puller" Design

HOP Linear Actuator

The Starsys HOPLA is a fairly small, lightweight, and simple device (Figure 7). The HOPLA produces a linear extension due to the volume change of the paraffin as a function of temperature, thus resulting in a high-force, small-displacement actuator. The size, stroke, resolution, mass, and power advantages are comparable with some other solutions shown in Table 2. Internally, the *"pusher" and "puller"* HOPLAs are identical and share the same components. One of the major design challenges for the Starsys team was to develop an actuator with only 500-μm displacement. The paraffin undergoes a 15% expansion when transitioning from a solid to a liquid. In order to limit the stroke to 500 μm, the transition expansion fills a small void to relieve the preload built into the non-powered hard stop (i.e., home position). The HOPLA operates with paraffin entirely in the liquid phase. Therefore, the HOPLA relies solely on the thermal expansion of the paraffin for micro-positioning and does not exhibit hysteresis effects of the phase transition in the controlled region. The minute amount of liquid paraffin and thermofoil heater with an integrally embedded thermistor assembly are contained in a hermetically sealed chamber. Thus, with the heater/thermistor assembly immersed in an extremely small volume and mass of paraffin, thermal lag is reduced and the overall thermal response, control margins and stability are greatly enhanced. Additionally, due to the solid paraffin and stiff bellows, the HOPLA adds a stiff and well-damped connection to the X-Axis stage during the launch environment.

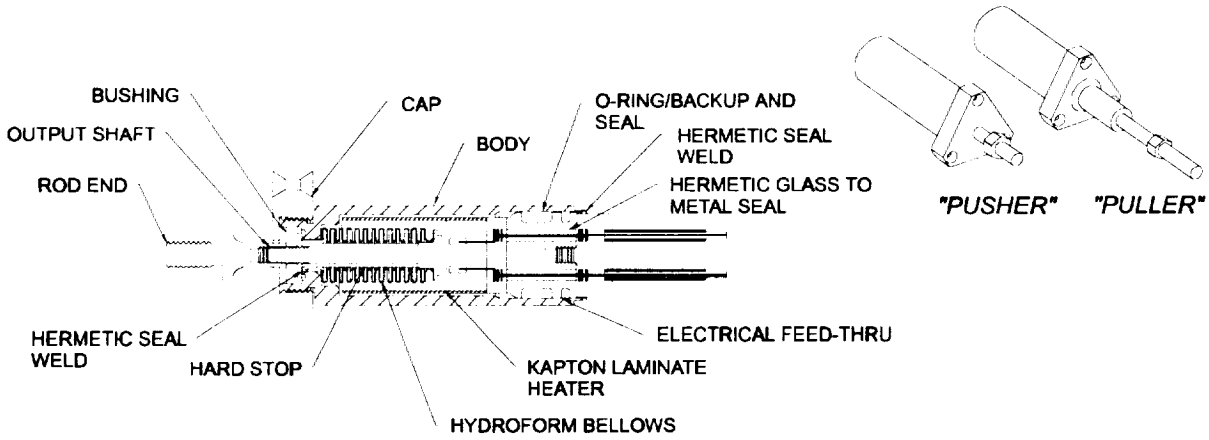

Figure 7 HOP Linear Actuator (HOPLA)

Mounting the HOPLA

A kinematic scheme consisting of cones, vees, and ball bearings was chosen to mount the HOPLAs to the mechanism (Figure 8). The advantages of the mounting concept are

- Kinematic mounting design
- Thermal isolation

- Moderate machining tolerances ±0.025–0.127 mm (±0.001–0.005 in) typ.

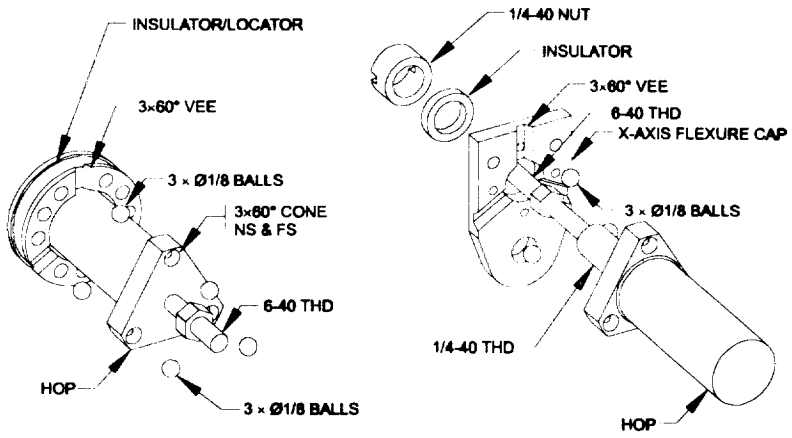

Figure 8 HOPLA Kinematic Mount

The X-axis stage of the *"pusher"* FPA is connected to the HOPLA via a 6-40 screw thread and a shim/washer on the push rod. This thread mounting required that the mount be able to accommodate a random clocking of the HOPLA. Likewise, the *"puller"* design kinematically locates the HOPLA directly to the X-axis stage, and the push rod thread must accommodate a fixed clocking. The primary disadvantages of this design are 1) the difficulty in accurately modeling the thermal losses, even though this system is dominated by thermal contact resistances that make it very efficient; and 2) assembly of the mechanism, which consists of very small components, in a Class 100 clean room.

"Pusher" Mounting

The HOPLA locator/insulator, made from Vespel, contains three radial 60° vee grooves, spaced 120° apart (Figure 8). When three Ø3.175-mm (1/8-in) 440C stainless ball bearings are nested in the HOPLA cones and mate with the insulator, the HOPLA is kinematically located with zero degrees of freedom. The HOPLA, balls, and insulator are fully constrained with three additional balls nested in the three opposite cones with a retainer. A polymeric material was chosen for the insulator because of its low thermal conductivity and its compliance. The system was designed to have about 0.076–0.127 mm (0.003–0.005 in) of axial press to ensure a rigid play-free mount.

"Puller" Mounting

The *"puller"* HOPLA is mounted directly to the X-axis motion stage, and the push rod passes through the stage and connects to the mechanism (Figure 6). Again, three ball bearings nested in three HOPLA 60° cones mate to the three 60° radial vee grooves in the flexure cap of the X-axis stage. The HOPLA is held in place by a Vespel insulator/washer and a silver-plated stainless steel spanner nut with a 1/4-40 thread. The push rod is connected to the mechanism via a shim/washer, a plane bore, and a silver-plated 6-40 stainless steel nut.

X-Axis Controller Design

The X-axis controller is a two-mode, closed-loop system. The first mode, the preheat mode, is a temperature control loop. In this mode, the controller melts the paraffin to raise the temperature nearly to the HOP initial actuation temperature. The controller senses the paraffin temperature using a thermistor embedded in the HOP heating element. There is very little thermal lag between the sensor and melted paraffin. The second mode, the position control mode, uses an LVDT as the feedback element. In this mode, the controller monitors the FPA position using an LVDT with a total linear range of travel of 0.635 mm (0.025 in). FPA displacement occurs as a result of thermal expansion of the paraffin in the HOP. In both modes, the control error is amplified and used to generate a pulse width modulated (PWM) drive signal that applies power, through an N-Channel MOSFET switching transistor, to the HOP heating element.

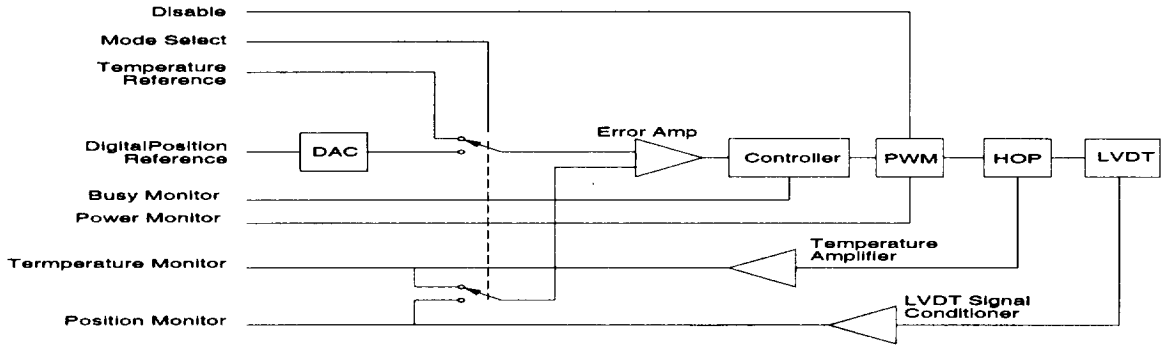

Figure 9 Block diagram of the X-Axis control electronics

Table 2 FPA Materials[1]

	ρ g/cm^3	E×10^3 MPa	Y MPa	η×10^{-6} mm/mm/°C	E/ρ	Y/E
Invar-36	8.055	147.0	440	1.84	18.3	2.99
Magnesium ZK60A-T5	1.828	44.8	248	27.0	24.5	5.54
Neyoro-69	16.0	89.6	124–206	13.5	5.6	1.38-2.31
Sapphire Tensile Compressive	3.97	379.2 431.6	186.4 2060.0	5.0-5.6	95.4	0.492 4.77
Stavex ESR	7.8	215.0	1460	11.0	27.6	6.79
Ti-15V-3Cr-3Al-3Sn	4.77	77.9	773.6 1241.0	9.1	16.3	9.9[2] 16.0[3]
Ti-6Al-4V	4.44	110.3	827.4 999.7	8.8	24.8	7.5[2] 9.0[3]

[1] from [14]
[2] Annealed
[3] Aged

Conclusion

The FPAs have implemented two different methods of micro-positioning. The FPAs also relied on non-conventional materials (Table 2), although most of the metallics are listed in MIL-HDBK-5E, a common material properties reference. In addition, the FPAs also employed an evolution of the HOP actuator by taking advantage of their light weight, long stroke, and high resolution.

Lessons Learned

HOPLAs can achieve micro-positioning in low-frequency systems. Additionally, HOPLAs have a stroke, resolution, and force capability that can be difficult to match by other actuators of equal mass.

High accuracy micro-positioning can be achieved by a plain lead screw and stepper motor actuator in an open loop control system. However, a position sensor should not be eliminated and can serve as a valuable reference.

Properly designed limit switches can aid greatly in the recovery of a system failure.

Non-conventional evolutionary designs should be allowed to continue to advance technology and establish heritage.

Proper material selection (i.e., base material, threaded inserts and fasteners) in an ultra-clean UV environment is essential. A CRES fastener seized in a non-phosphor bronze helicoiled hole in the Invar-36 base used for a ground stud.

References

1. Roark, Raymond J., Youn, Warren C., Formulas for Stress and Strain, McGraw-Hill Book Co., 1982.
2. Jones, R.V. , "Some Parasitic Deflection in Parallel Spring Movements", *Journal of Scientific Instruments*, Vol. 33, Jan 1956
3. R. R. Boyer, H. W. Rosenberg, "Beta Titanium Alloys in the 80's", proceedings of a symposium sponsored by the Titanium Committee of AIME, Atlanta, Georgia, March 8, 1983.
4. Weinstein, Warren D., "Flexure-Pivot Bearings," *Machine Design*, July 8, 1965.
5. W. M. Parris, J. A. Hall, Titanium Metals Corporation of America, Cold Rolled and Aged Ti-15V-3AL-3Sn-3Cr Strip for Springs, Final Technical Report, Contract No. 6603-9169-2290.
6. TIMETAL 15-3 Data Sheet, TIMET, 1999 Broadway, Denver Co, 80202
7. Applications and Benefits of Perfluoropolyether Lubricants, Castrol Specialty Products Division.
8. Nye Lubeletter Digest 1972-1993, Nye Lubricants, Inc.
9. Lubrication in a Clean Room, Castrol Specialty Products Division.
10. Aaron D. Deutchman, Walter J. Michels, Charles E. Wilson, Machine Design, Macmillan Publishing Co., Inc.

11. Handbook H28 (1969), Screw Thread Standards for Federal Services, CODEN:NBSHA, United States Department of Commerce.
12. Boresi, Arthur P., Sidebottom, Omar M., Advanced Mechanics of Materials, 4th ed., John Wiley and Sons, 1985.
13. D. Vukobratovich, R. M. Richard, "Flexure Mounts For High-Resolution Optical Elements".
14. Military Handbook, "Metallic Materials and Elements for Aerospace Vehicle Structures," MIL-HDBK-5E, June 1, 1987.

Symbols

F	force	d_m	mean screw diameter
δ	displacement	f_s	coefficient of friction
E	modulus of elasticity	θ_n	$\approx$ ½ thread angle
I	moment of inertia	w	weight or applied force
l	flexure length	n	number of threads
b	flexure width	z	depth of thread
t	flexure thickness	x	tooth thickness at theroot diameter
M	moment	d_o	major screw diameter
σ	stress	d_r	minor screw diameter
c	$t / 2$	d_P	pitch diameter
α	thread helix angle	P	axial force on flexures/column
a	height of F above fixed flexure base	L	length between column supports
ω	tilt parallel to flexures	K	column support factor
s	distance between flexures	Y	yield strength
θ	flexure stage tilt	e	distance of ecentric load
$\Delta\ell$	variation of l	ρ	density
T	torque	η	coefficient of thermal expansion
τ	shear stress		

A Reactionless, Bearingless Linear Shutter Mechanism for the Multispectral Pushbroom Imaging Radiometer

Les J. Krumel*

Abstract

A shutter mechanism has been developed and flown as part of an airborne imaging radiometer having application to spacecraft or other systems requiring low vibration, high reliability, and long life. The device could be employed in other cases where a reciprocating platform is needed. Typical shutters and choppers utilize a spinning disc, or in very small instruments, a vibrating vane to continually interrupt incident light or radiation that enters the system. A spinning disk requires some sort of bearings that usually have limited life, and at a minimum introduce issues of reliability. Friction, lubrication and contamination always remain critical areas of concern, as well as the need for power to operate. Dual vibrating vanes may be dynamically well balanced as a set and are frictionless. However, these are limited by size in a practical sense. In addition, multiples of these devices are difficult to synchronize.

Introduction

SERDP / ARM - UAV

The Atmospheric Radiation Measurement Program is a multi-laboratory, interagency program as part of DOE's principal entry into the U.S. Global Change Research Program. Two issues addressed are the radiation budget and its spectral dependence, and radiative and other properties of clouds. Measures of 'solar flux divergence' and energy exchanges between clouds, the earth, its oceans, and the atmosphere through various altitudes are sought. Additionally, the program seeks to provide measurements to calibrate satellite radiance products and validate their associated flux retrieval algorithms. Unmanned Aerospace Vehicles fly long, extended missions. MPIR is one of the primary instruments on the ARM-UAV campaigns.

System Description

MPIR is a Multispectral Pushbroom Imaging Radiometer, designed to provide multiple images of a scene as viewed through various wavelengths simultaneously. Each detector array scans in crosstrack to record a line image. Utilizing the forward flight path of the host platform, this line is 'swept' over an area; the pushbroom effect allows for construction of a 2D image. As a multispectral system, information is obtained through multiple, parallel channels. The radiation spectrum is sectioned into various bands of interest, and independent modules can be assembled for specific wavelengths. Each channel therefore, is a dedicated module made up of an optics assembly, a sensor assembly, and associated electronics. The modular concept

* Sandia National Laboratories, Albuquerque, NM

provides for reconfiguration and interchangeability. As a whole, the system includes up to 11 microprocessors, optics, and sensors with cryogenic cooling, and a chopper mechanism used for continuous, on-board calibration. It was intended that the chopper design would be transferable to space based applications, such that it would possess the desirable features of vibration isolation, reliability and long life.

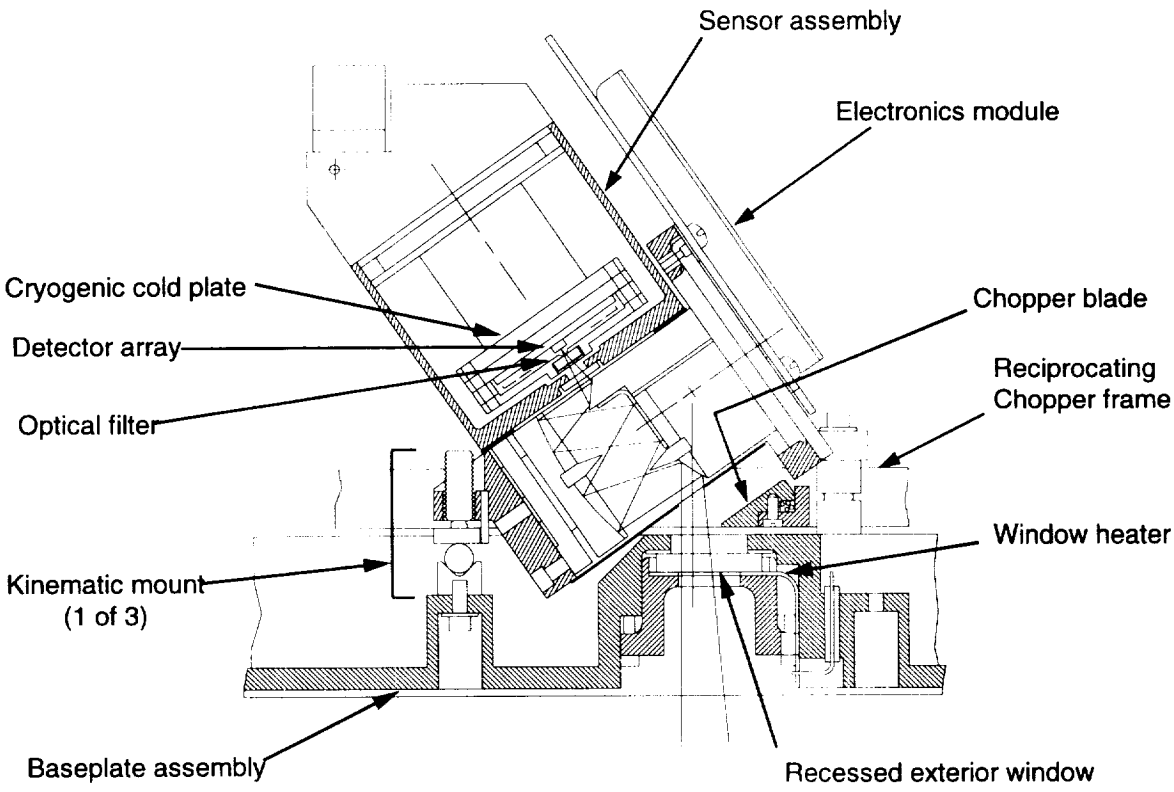

Figure 1: Cross section of a single module, installed

Chopper

The chopper is used for continuous on-board calibration. Incident radiation is scanned by the detector of each module as the chopper blades are retracted (open). At closure, the beam is interrupted, and additional recordings indicate 'dark current' in the visible detectors. To the IR detectors, chopper blades serve as blackbody references. Upon interrogation by the main board processor, each module delivers its data sequentially for formatting with other statistics for transmission via telemetry link.

Typically, a spinning wheel with cutouts is employed as a chopper. For MPIR, each module had to be 'chopped' identically and the size of a sufficiently large wheel was prohibitive. In addition, each module must be oriented in parallel for imaging identical scenes; chopping with radial blades with a fixed center would not create similar effects

on each module. Blades could be articulated for parallel motion only with increased complexity. The only solution would be to use a wheel of large radius and to group all the modules into a small general area, making the blade motion seemingly the same to each module. Actually, only a few blades are necessary, without the need to navigate a full circle. With some logic, this leads to a reciprocating mechanism having only a virtual center that is located at infinity. The concept forms itself into a simple frame that only oscillates back and forth. Nine dedicated chopper blades are attached to a moving grid placed before the 3 x 3 array of modules used on the instrument.

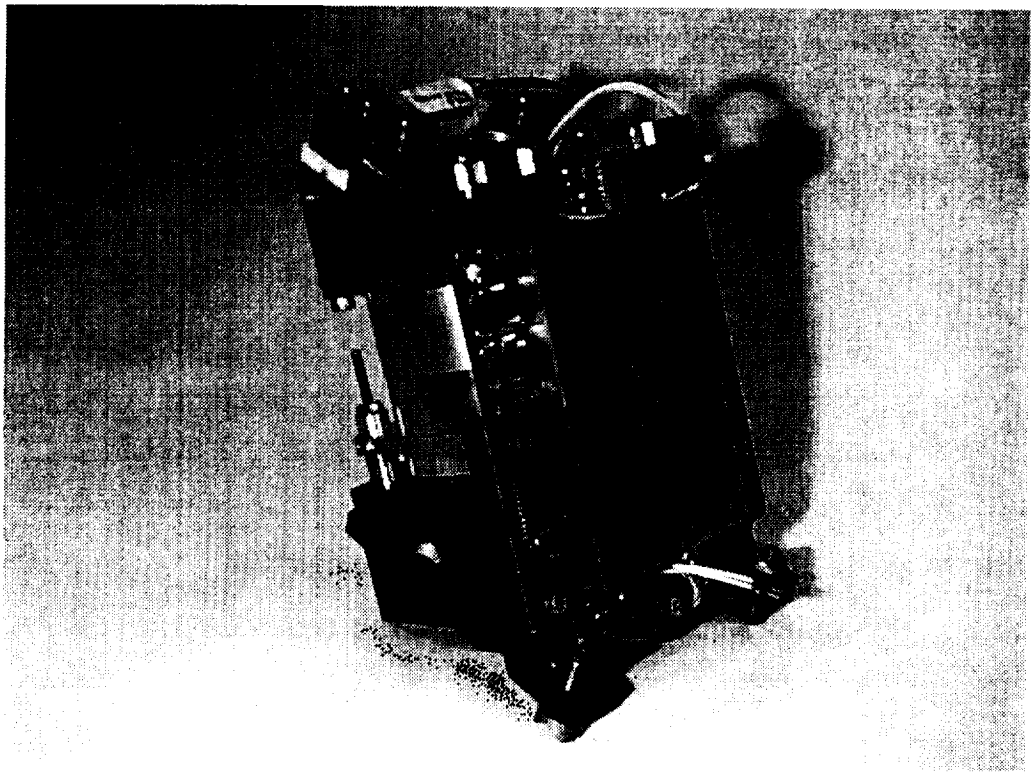

Figure 2: A single, self contained sensor module.

Chopper Mechanism

The mechanism involves an oscillating frame, or grid, to which individual chopper blades are attached, a countermass assembly, and a linear actuator. The uniqueness of the mechanism is the employment of a reactionless, fully flexural, translating shutter without any rubbing or rolling surface contacts. It operates in resonant mode and requires very little power. Being virtually frictionless, it seems to run on its own once set into motion. Dual, reversing countermasses eliminate inertial forces to make MPIR a relatively quiescent payload.

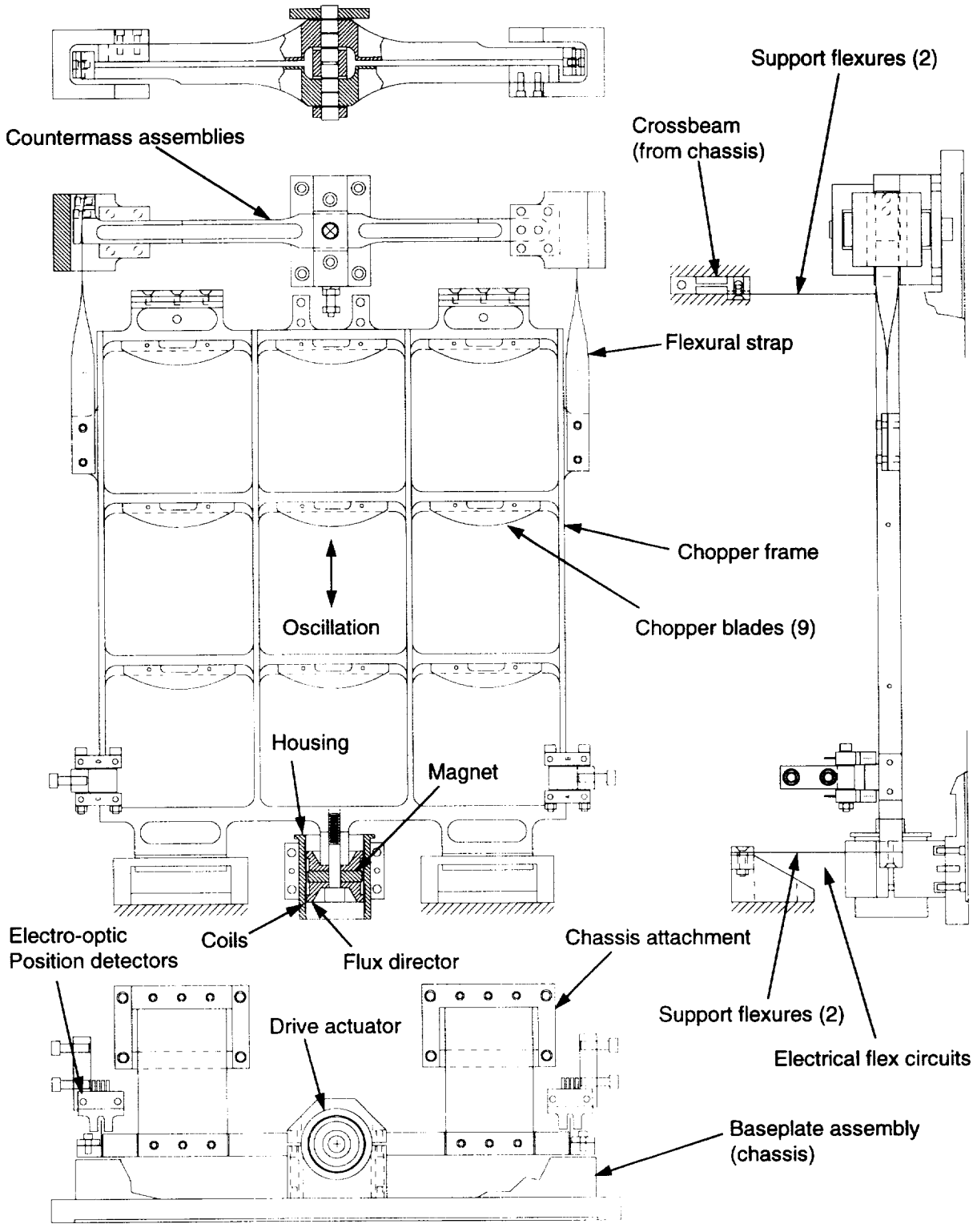

Figure 3: Chopper mechanism

Chopper Frame and Support Flexures

The chopper frame is suspended by four flat flexures, one mounted at each corner. The chopper acts somewhat like the coupler of a four-bar mechanism; flexures are of equal length to maintain parallel motion of the chopper. Deflection of cantilevered springs is almost parabolic, so the dimension between opposite ends of a particular flexure is not constant as it swings. Integrating along the parabolic curves, the height change for the chopper is calculated to be 0.5 mm (0.020 in). Considerable width is required for stiffness against side loads, and inverted flight. One other degree of freedom to be constrained was that of rotation within the plane of the chopper around the yaw axis.

For engineering purposes, these support flexures are viewed as two half-length, flat cantilevered springs *(a-b) & (b-c),* butted together at the center. The inflection point *(b)* is assumed to have zero stress, and no bending moment. Figure 4 shows two parallel flexures *(a-c) & (d-e).* The chopper mechanism actually uses four vertical, parallel elements (one on each corner). The flexures not only support the chopper, but also perform as springs.

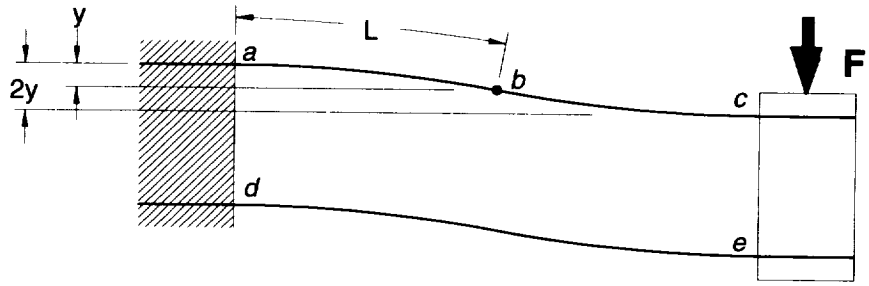

Figure 4: Model for flexural supports

A cantilevered spring (a-b), with force F at point *b* would cause deflection y. On a spring *(b-c),* by itself, the same deflection would be caused by an equivalent force. Consequently, the force F would cause deflection on both parts *(a-c)* an amount 2y. Stiffness is then calculated starting with the well-known equation for deflection of a single cantilevered spring. The 'spring' has rectangular cross-section so that for *a-b:*

$$I = \frac{bt^3}{12} \tag{1}$$

$$y = \frac{FL^3}{3EI} \tag{2}$$

$$= \frac{4F}{Eb}\left(\frac{L}{t}\right)^3 \tag{3}$$

E is the modulus of elasticity, t the thickness of the spring, b the width, and L the length. Substituting deflection y into the formula for stiffness, k = F / y:

$$k_{ab} = \frac{Eb}{4}\left(\frac{t}{L}\right)^3 \qquad k_{ac} = \frac{Eb}{8}\left(\frac{t}{L}\right)^3 \tag{4a,b}$$

Because the flexure *(a-c)* has twice the deflection (forces being equal), stiffness is only half that amount.

Note the division of thickness over length as a sensitive aspect ratio, a cubed entity. Although the length, 2L, remains constant, separation between ends along the x-axis will decrease with more curvature. Each half of the spline is parabolic and separation between ends can be calculated by integration. The difference from that value and one of a flat condition gives height change of the chopper as it swings through the arc.

Failure Analysis of Flexures

To assure long life and reliability, fatigue must be considered. Maximum bending stress at the root of each flexure is simply determined by applying the maximum force of full deflection to the common formula s = M·c/ I. Values used on MPIR show a maximum stress of about 13.8 MPa (2 ksi), which is far below any endurance limit. In any case, edges of the flexures were polished and inspected to eliminate stress risers and cracks before acceptance and installation.

Chopper Actuator and Drive Mechanism

Conventional motors would require some sort of bearings, gears, etc., which involve inherent sources of friction. Designing without vibration specifications, use of mechanisms with direct physical linkages were considered as a contingency plan in the untested state of MPIR. Although not frictionless, they provide direct physical control of position and displacement. Two precursor concepts are described. The integrity of an imaging system is obviously compromised by vibration. Likewise, for any installation to spaceborn platforms, MPIR would be prohibited from inducing vibration to other instruments or systems. The MPIR chopper therefore needed to be designed as a reactionless system. First to be speculated was the obvious slider-crank mechanism. Considering a chopper (slider) of mass m, a crank of length r, angular velocity ω, and connecting rod of length L, inertial forcing imparted to the frame is:

$$F_i = -m\left[r\omega^2 \cos\theta - r\omega^2 \left(\frac{r}{L}\right)\cos 2\theta\right] \qquad (5)$$

Dynamic balance of this mechanism is typically accomplished by using a countermass on the crank. The method is only approximate because of the uncompensated second term (r/L)cos2θ. This can be mitigated by using a long connecting rod, minimizing the factor, r/L. Another would be to include an additional rotating countermass with a gear of half the pitch diameter, running off of the crank at the first harmonic frequency. To offset the lateral force of these rotating masses, the rotating elements (gears) may be installed in complimentary pairs.

A scotch yoke mechanism (Figure 5) has been considered where the second term and harmonic effects of the connecting rod are simply eliminated. In equation (5), length is infinite. Once again, complimentary pairs are employed for lateral balance; two scotch yoke mechanisms with a common yoke are joined together. The pivot at center reciprocates and carries the load. In this way, crank pin forces are equalized on the yoke for load sharing and smoother operation.

However, the double scotch yoke is not without its own drawbacks. Problems involve backlash in the gear mesh and yoke, and the accompanying vibration. Support flexures would need to be very weak springs in order to reduce varying torque feedbacks in the drive train. The solution was to abandon it in view of the linear actuator. Without gears or cranks, etc., these basically consist of a voice coil and a magnet similar to devices found in loudspeakers. Although less efficient than moving coil devices, these actuators use a moving magnet with a fixed coil, which allows the wiring to be rigidized. The magnet, cantilevered on one end of the chopper passes through the coil, where it is acted upon only by magnetic forces. This was the compromise to be made over other mechanisms, in that relatively weak physical restraint exists to control displacements of the moving parts. Various masses are free to move as far as the flexible elements will allow.

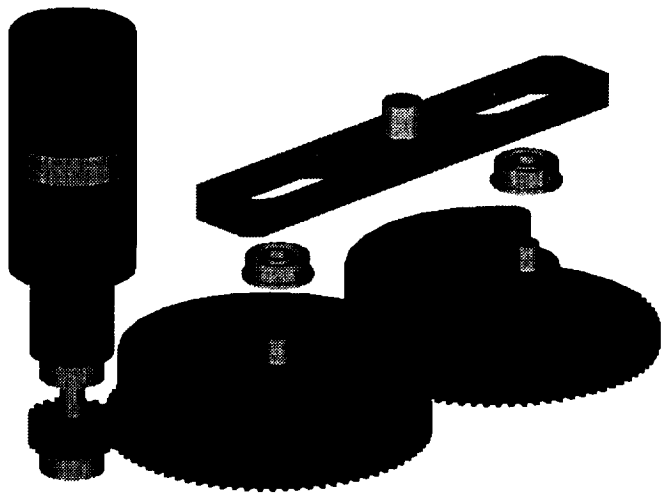

Figure 5: Balanced double scotch yoke

Previously described mechanisms better dictate absolute displacement and amplitude of the chopper. Magnetic coupling is weak in comparison to rigid links, but the linear actuator avails itself to a system without parts in contact. Full PID closed-loop control systems and larger, stronger magnetic circuits are an option to enhance control of this motion. However, the real driver was 'philosophical,' that is, to *choose simplicity.* A design decision was made, recognizing that external disturbances were acceptable on occasion in that the system would tend to restabilize itself without direct connection.

Model No. LA16-19-001A was selected from a line of linear actuators manufactured by BEI Motion Systems Co., having a samarium-cobalt rare earth magnet. The magnetic circuit is comprised of an axial magnet, free to slide within a cylindrical, steel housing (the return path between poles), having sufficient annular gap. The coil is mounted to the inside surface of the housing, situated over the magnet. A cross-section of the device also reveals steel ends integral with the moving magnet acting as flux directors

on the pole faces. Close examination shows that two coils are actually employed in series, each centered over the localized air gap of the flux directors. This configuration provides induced magnetic fields where most influential and flux is more densely located. As the chopper swings in its short arc, allowance for some vertical motion is necessary, the diameter of the ends was reduced to 31 mm (1.219 in) to allow more radial clearance. Increasing the annular air gap was made at the expense of some efficiency, and yet this loss was unnoticeable.

Countermass Assembly

With the linear actuator, a separate means was developed to balance the chopper for lack of an actual drive 'mechanism.' It simply involved adding mass of opposite motion to counteract shaking forces imparted to the instrument. The motion is achieved by a reversing lever, or beam. The 'countermass' is attached to one end; its other end is attached to the chopper by a strap and hidden clamp. A pivot near the beam center acts as a fulcrum. The pivot is a key component, which is also a flexural member, having no rolling or wearing parts or associated friction. Generally, they can be described as criss-crossed flexures packaged as cylindrical components. For the most part, depending on loading and cycling, angles of rotation are limited to less than 10°. For small displacements, the angle of rotation for the beam is small enough (about ±2.7°) that the motion of the countermass can be approximated as being linear.

To provide better centering of the c.g., and to balance any lateral motion, the countermass apparatus is actually divided into two symmetrical devices (Figure 6). They are nested into each other for a compact design, where the pivots share the same axis. Laterally, any errors developed are mirrored and eliminated by cancellation. The key aspect in developing a suitable reactionless system is to cancel out induced vibrations in all degrees of freedom. For the chopper system described, this requires opposing forces to be maintained on the same plane. Hence, the countermasses are nested vertically and lie co-planar with the chopper. Admittedly, the chopper has a small 0.69 mm (0.027 in) vertical displacement as it swings through its arc. Its motion is not purely within the plane, yet this can be ignored for MPIR.

No flexural pivot is without spring rate. The countermass assembly is therefore not purely an inertial device, and will also produce a torque opposing its displacement. The additional spring rate is simply added to that of the others in the system. A stiff, flexural pivot is desirable in at least one respect in that it must support the countermass. Considerable torque is presented to the pivots along a transverse axis. Upright, as installed, the pivots are better suited for shear in the horizontal plane. To counteract the bending moment due to vertical accelerations, two pivots are used in support of each beam. Tension at the top of the beam is reacted by horizontal shear of the upper pivot. Compression at the bottom of the beam is reacted by a similar horizontal shear in the lower pivot.

'Free-Flex' pivots by Lucas Aerospace (Bendix) were selected. With proper orientation, they posses a maximum shear capacity of 51 kg (113 lb) perpendicular to

their axis, and a spring rate of 5.4 mN·m (0.048 in·lb) per degree. Installed at the root of each beam, two of these, with centers essentially separated 15.2 mm (0.600 in) can support a 53.4 N (12 lb) force at the beam's end. This value is then reduced with a safety factor and 3g loadings taken into account. Flexural pivots are rated with respect to number of cycles, loading and deflection.

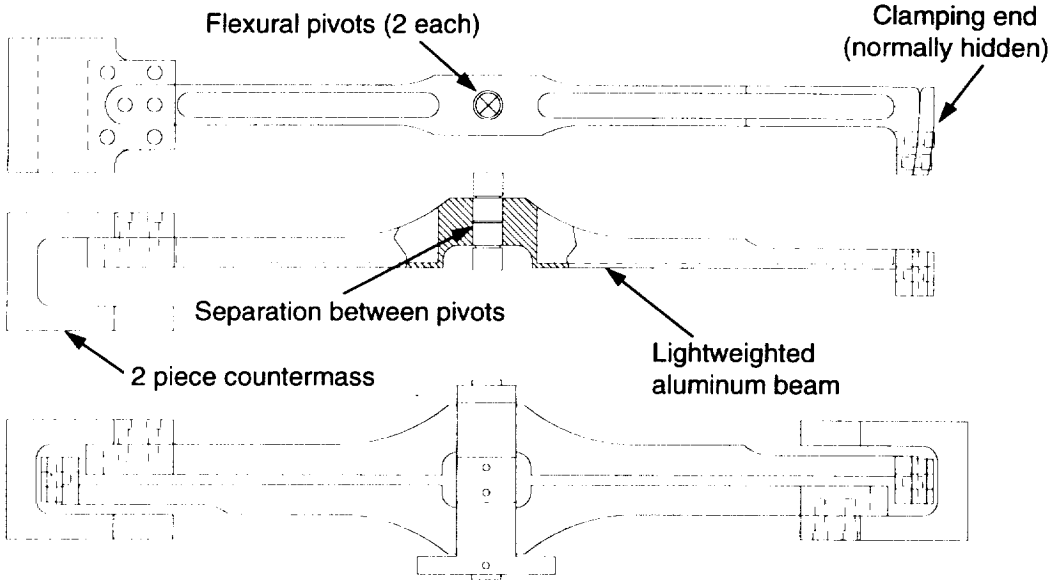

Figure 6: Nested Countermass Assemblies

Deflections are typically less than 10°. In the plane of rotation, the countermass beam for MPIR is required to turn only 2.64° each way. Lifecycle charts indicate that this will bear an infinite lifetime. For the stated springrate and deflection angle, a peak torque of 14.2 mN·m (0.126 in·lb) is calculated for each. Using the approximation of linear motion for these small angles, 1.86 N/mm (10.62 lb/in) is the additional spring rate applied by the countermass assembly. As a protective measure against out of plane bending of the flexural pivots, adjustable nylon-tipped hardstops and 0.5 mm (0.020 in) clearance limit any would-be vertical motion on the countermasses.

Flexural Straps

Connections between the chopper and the countermass assembly are also made with flexural members. Any link between the two assemblies must be compliant in both the vertical and horizontal planes. As described previously, a small vertical displacement occurs with the pendulous motion of the chopper causes a shifting of its plane. Meanwhile, the countermass beams swing a short horizontal arc. While providing congruence between the chopper and countermass motions, the link must allow for conversion between the planar and rotary motions as well. Many ideas were contrived which led to a unique, yet simple, twisted strap. The 'flexural strap' is intended to be compliant, yet also serve as a compression member as the chopper is accelerated in

two instances throughout its cycle. Buckling was not a great concern since the system operates at resonance and parts move in unison. Energy is stored/released by spring elements in both the chopper and countermass assembly. In the plane of motion, hardstops were located in case the device would get over-driven. The chopper frame will stop in one direction while the countermass assemblies are limited in the other so that in either case only tension would occur in the straps and they won't collapse.

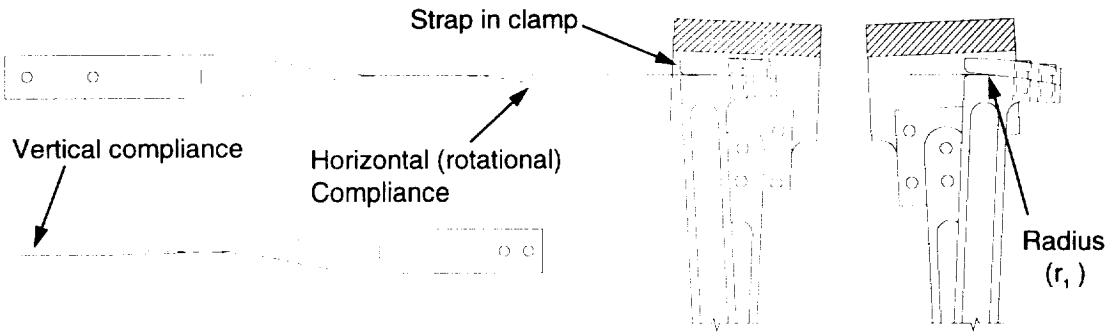

Figure 7: Twisted flexural strap as a connecting link (different positions)

There was no plan to optimize the connecting link. A narrow thickness was sought through several iterations simply to find one of low bending stress where the material would be utilized within its elastic limit. Links were made of 0.25 mm (0.010 in) 304L stainless steel. An assumption was made that any stored energy in the flexural strap would be released back into the system and in this way compliance would be tolerated. The clamping surfaces at the end of each countermass beam were specifically shaped to accommodate the strap. The inner surface is radiused so that action of the strap would be that of a metal band over a pulley. The outer surface is simply a flat relief allowing the strap to remain straight in the 'chopper closed' position. The strap thus rolls over a constant radius with smooth motion.

Dynamic analysis and design

An interesting discovery came about during the analysis, in that the countermass assemblies can be applied in two different ways. Foremost is need to react against generated inertial forces of the chopper. This effectively cancels vibration that otherwise would be induced to the host platform. On space-borne systems this would be of paramount importance. Such jitter could quite effectively impair imagers such as MPIR and other instruments and attitude controls systems. The other application utilizes the inverse philosophy that rather conserves motion of the chopper, as it is susceptible to accelerations and impulses imparted by the host. In other terms, it's possible to optimize the dynamics, with preference given to either the instrument or the host. The difference lies in the residual inertia of the countermass beams. It's very subtle, probably having little consequence; yet the distinction exists.

Figure 8 depicts the free-body diagrams. This shows a springless system with the chopper free to oscillate horizontally in the plane of the page. It is suspended by long, swinging links conceivably mounted above the plane so that for short arcs the motion is practically along a straight line. Countermass assemblies also are free to rotate within the plane as shown.

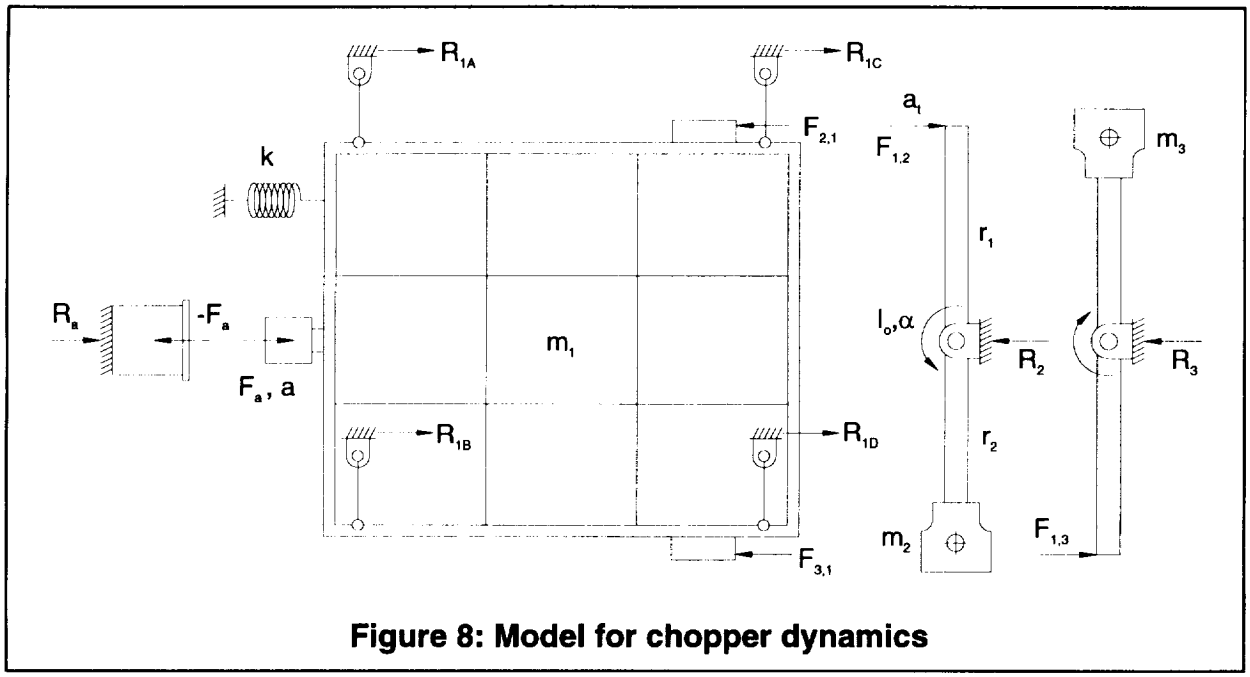

Figure 8: Model for chopper dynamics

Beside the actuator and the frame of the system, three links are indicated, being the chopper, and two countermass assemblies. These carry the subscripts 1, 2, 3, respectively. Reaction forces due to acceleration of the chopper are created in the frame that suspends it. These forces, R_{1A}, R_{1B}, $R_{,1c}$, and R_{1D} may be summed as a whole, designated simply as R_1. Mass m, includes that of the chopper frame, chopper blades, the actuator magnet, etc. Once operational, the forcing function, $F_a = A \sin(\omega t)$ is substantially reduced to provide only a restoring force. Also indicated are the spring forces (F_{flex}) of the support flexures and torques (T_{pivot}) of the flexural pivots. For the current discussion these are not applied.

To size components for the countermass assemblies, an analysis is made from a springless system that employs only the inertial forces. With the assemblies installed, opposing forces F_2, and F_3, are applied to the chopper, with consequent reflections imparting R_2 and R_3 to the frame by purely inertial effects. As with any flight system, its optimization would require the minimization of mass. In this case, m, is controlled as an independent variable. Afterward, with a given set of dimensions the problem becomes one in finding the correct countermasses, m_2 and m_3 for reactionless operation. Finally, by including 'springs' in the model, the frequency is determined with the stiffness parameter, k, of the flexures. Because of the necessary tolerances

allowed for in manufacturing, small correction masses are attached to the chopper during final assembly, testing and alignment. This may require subsequent corrections in the countermass assemblies. The process may be listed as follows:

1. Optimize the chopper to determine minimum mass, m_1 .
2. Determine values for countermasses, m_2 and m_3, and size for manufacture.
3. Calculate necessary overall stiffness, k, and design flexures for proper frequency of operation.
4. Assemble, align, and test, making corrections in mass for chopper and countermasses.

To continue, the intent is to provide an equal but opposite reactionary shaking force (the sum of R_2 and R_3) to cancel the whole of R_1. This application optimizes the dynamics to eliminate shaking forces imparted to the host. As shown in the previous diagram, both countermass assemblies are made symmetrical and dynamically equivalent. Furthermore, with small angles of rotation, it can be assumed that tangential acceleration of the countermass beam is comparable to the acceleration of the chopper imparted by the actuator: $\alpha_t = - a/ r_1$. Any motion of the chopper is mirrored by the countermass assemblies so that the problem is simplified as a quasi-static analysis. The reactionary force R_2 results from the inertial effect of the countermass m_2 being levered on the end of the countermass beam as $F_{1,2}$ is applied. The mass moment of inertia of the beam itself, I_b, is distinguished from that of the countermass, mr^2. Terms r, and r_2 denote radial distances to the point of contact on the beam and the c.g. of the countermass from the pivot point. By design, the countermass assemblies are dynamically equivalent where $m_3 = m_2$ and I_b is the same for each. In selecting a value for the countermasses, inertial effects of the countermass beams always help to counter that of m_1 so that:

$\sum F_{chassis}$: $$R_a + R_1 - R_2 - R_3 = 0 \quad (6)$$

$\sum F_{chopper}$: $$F_a + R_1 + m_1 a - F_{2,1} - F_{3,1} = 0 \quad (7)$$

$\sum F_{C'mass\ Ass'y}$: $$F_{1,2} - \frac{I_o \alpha}{r_1} - R_2 = 0 \quad (8)$$

Use (3) to subst. R_2 in (1):

$$R_a + R_1 - 2\left(F_{1,2} - \frac{I_o \alpha}{r_1}\right) = 0 \quad (9)$$

Use (4) to subst. R_1 in (2):

$$2\left(F_{1,2} - \frac{I_o \alpha}{r_1}\right) + m_1 a - F_{2,1} - F_{3,1} = 0 \quad (10)$$

$$m_1 a = 2\left(I_b + m_2 r_2^2\right)\frac{a}{r_1^2} \quad (11)$$

$$m_2 = \left(\frac{m_1}{2}\right)\left(\frac{r_1}{r_2}\right)^2 - \frac{I_b}{r_2^2} \quad (12)$$

The effect of inertia in the beam I_b helps reduces the requirements for the countermass in a short term dynamics sense. However, in a constant acceleration or gravity field other than normal to the mechanism (this is a 'planar' mechanism), the countermasses alone must balance the chopper in a statics sense. Inertia of the beam ultimately represents a weight penalty so it should be minimized.

As previously stated, this mechanism may be applied to mitigate external disturbance and vibrations. This is accomplished by the static balance just described, where the countermasses alone contradict the mass of the chopper. To use the equation, the difference in application is whether or not to subtract the term with I_b. Now it is evident that with minimized inertia of the beam the system may work in both applications.

In order to utilize a small angle of rotation and maintain the assumption of 'pure' translation for small angles, values for r_1 should be large. Yet to minimize total mass, r_2 should be maximized. The decision was made to make r, and r_2 relatively equivalent. For a compact design, their sum was also limited to being no larger than the width of the chopper, while utilizing a common axis for the flex pivots. In cases where these lengths are equal and the beam has little inertia, the value for m_2 and m_3 becomes half of m_1, as would be expected. For efficiency, the countermass assemblies were optimized for minimum overall weight. The beams themselves are therefore lightweighted and the savings in mass is applied to the countermass on the end.

Tuning

To use minimum power, the spring-mass system is tuned to operate at resonance, the natural frequency being equivalent to the desired operating frequency (4 Hz). A simplified relationship may be utilized where *effective* values for stiffness and mass are employed.

$$f_n = \frac{1}{2\pi}\sqrt{\frac{k_e}{m_e}} \tag{13}$$

Consequently, the model is further simplified to resemble a single spring-mass system consisting of elements m_e and k_e. The two countermasses can be included with the mass of the chopper to describe the *effective* mass of the system:

$$m_e = m_1 + 2\left[m_2\left(\frac{r_2}{r_1}\right)^2 + \frac{I_b}{r_1^2}\right] \tag{14}$$

All flexures working in parallel, the effective combined stiffness is simply a summation of their spring constants. At the end of the beam, rotational stiffness of the flex pivots can be approximated to be linear over small angles. Units of k_{pivot} are N·m / degree. Including the support flexures, the flexural straps, and the flex-pivots in parallel, the overall stiffness is:

$$k_e = 4\left[\frac{Eb}{8}\left(\frac{t}{L}\right)^3\right] + 2k_{strap} + 4\left[\frac{k_{pivot}}{r_1^2}\left(\frac{180}{\pi}\right)\right] \tag{15}$$

Since the operating frequency is usually first to be specified and the various masses are minimized for weight, only the parameters for spring rate remain to tune the system. The pivots were chosen for bearing capacity. The remaining options lie in specifying the support flexures. These are the elastic modulus of the material 'E', and the dimensions for width 'b', half-length 'L', and thickness 't'. Note that the effects of thickness and length are most significant. Substitutions of m_e and k_e into the equation for natural frequency are easily made.

In fabricating the flexural supports, an overall length of 2L is used. By definition, L is the length to midspan. As mentioned previously, long length flexures are desirable to minimize variations in height throughout the arc of motion. A suitable compromise between width and length was found. For thickness, size was selected by commercially available shim stock, available in discrete values.

A particular lesson to learn was finding a reasonable dimension for the width 'b.' Kinematics would disallow the use of four flexures to prevent over-constrained conditions in supporting the shutter. The result would be a 'tin canning,' or buckling effect where a flexure can snap between two possible positions due to misalignment of the installation. The problem is alleviated by loosening the clamps and re-aligning the flexures so all are perfectly flat and straight in their 'at rest' position. If possible, the next increment in thickness and narrower widths would mitigate the difficulty. Later versions of the flexures incorporated extra width and a central cutout to provide relief. The effective number of flexures increases yet the proclivity toward bi-stable condition is reduced. At minimum, an aspect ratio of length to width seems to be roughly 3:1, simply by experience. Designing with good lateral separation between flexures also makes an improvement; and of course, a three part suspension would be even better.

In parallel with the flexural supports are two electrical flex-circuits. They posses practically no stiffness, but could be heard ever slightly on occasion against the air. Better designs would use rolling motion flex leads.

Fine tuning was accomplished with the least sensitive parameter, the width b. 'On the bench' corrections are also possible with modification to masses m_1, m_2, & m_3, so the system was designed for slightly higher frequency that could then be reduced. Corresponding piece-parts were intentionally made with features to accept these corrective masses. The most difficulty lies in minimizing overall mass while using mass for ultimate fine tuning. Seemingly small tolerances on the flexures have pronounced effect. The preventative is good analysis beforehand.

Chopper Motion Control

Except for some amplitude control the drive system is open loop and the chopper mechanism is expected to respond accordingly. As a system of spring-masses, the mechanism is tuned to resonate at the same frequency with sharp cutoffs. Other excitations have little effect, and at resonance very little power is required. Albeit not directly controlled, the mechanism is loosely synchronous. As a tunable system, it has

frequency stability as it attempts to follow the drive excitation. Drive electronics include an 8-bit, 256-level A/D converter operating from the main microprocessor, and a lookup table for the sinusoidal waveshape. This is coupled to filtering and a Class-C push pull amplifier utilizing darlington-pair transistor stages. A control loop in both the A/D converter and the amplifier circuits presents a very stable signal to the actuator.

Amplitude Control

A set of four electro-optical detectors is employed for position/timing information. Two are positioned to detect an upper and lower limit (UL, LL) of the positive half-cycle that give indication to amplitude. The tolerance band is ±18 mm (±0.007 in), centered at the peak displacement of +6.35 mm (0.250 in). Circuitry seeks to maintain a signal above L.L. and below U.L.

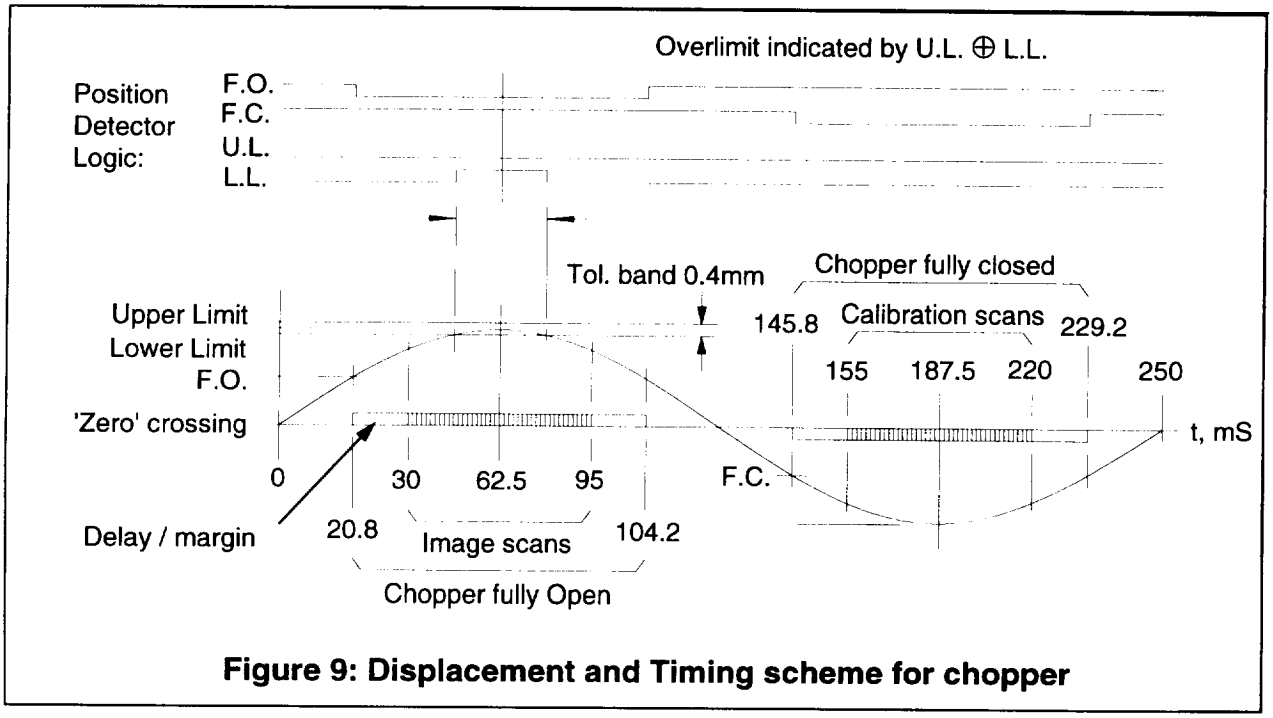

Figure 9: Displacement and Timing scheme for chopper

It is assumed that the frequency is generally well regulated, so the only remaining uncertainty is one of bias. Some difficulty lies in the fact that the spring/mass system has no detent at center. Centering is determined by the force balance of the spring/mass system superimposed by the coil and magnet. This 'zero crossing' can be adjusted by moving any one of the components. Any bias error is seen by unequal duty cycles on waveforms given by the F.O. and F.C. interrupts. These are measured accurately by a digital oscilloscope.

Conclusion

A chopper without gears, bearings, etc. has been designed and is now operational. It is a reactionless system expecting high reliability. Without a countermass assembly, it

would impose a horizontal shaking force upon the chassis an amount $F= -mr\omega^2 \sin(\omega t)$. Accelerations would reach 0.4 g's. Compare this to the reactionless system having peaks of about 0.001 g, as indicated in Figure 10. The difference is a reduction of 400:1, or -26 dB. Additionally, a vertical component of about 0.006 g's exists from the pendulous suspension. Its frequency is double that of the drive signal as a peak occurs at each end of the swing. No compensation was made for this axis; efforts were concentrated upon the horizontal, which was critical to eliminate blur upon imaging. Obviously, long flexures for suspension would reduce the height of swing and vertical accelerations. A set of flexures made as reversed pairs is proposed that could more truly prescribe linear motion for light loads over a small range. To date, the MPIR system has successfully flown on several science campaigns. The chopper continues to operate smoothly without problems. Images are now being reconstructed and geo-rectified from flight data and look very clear.

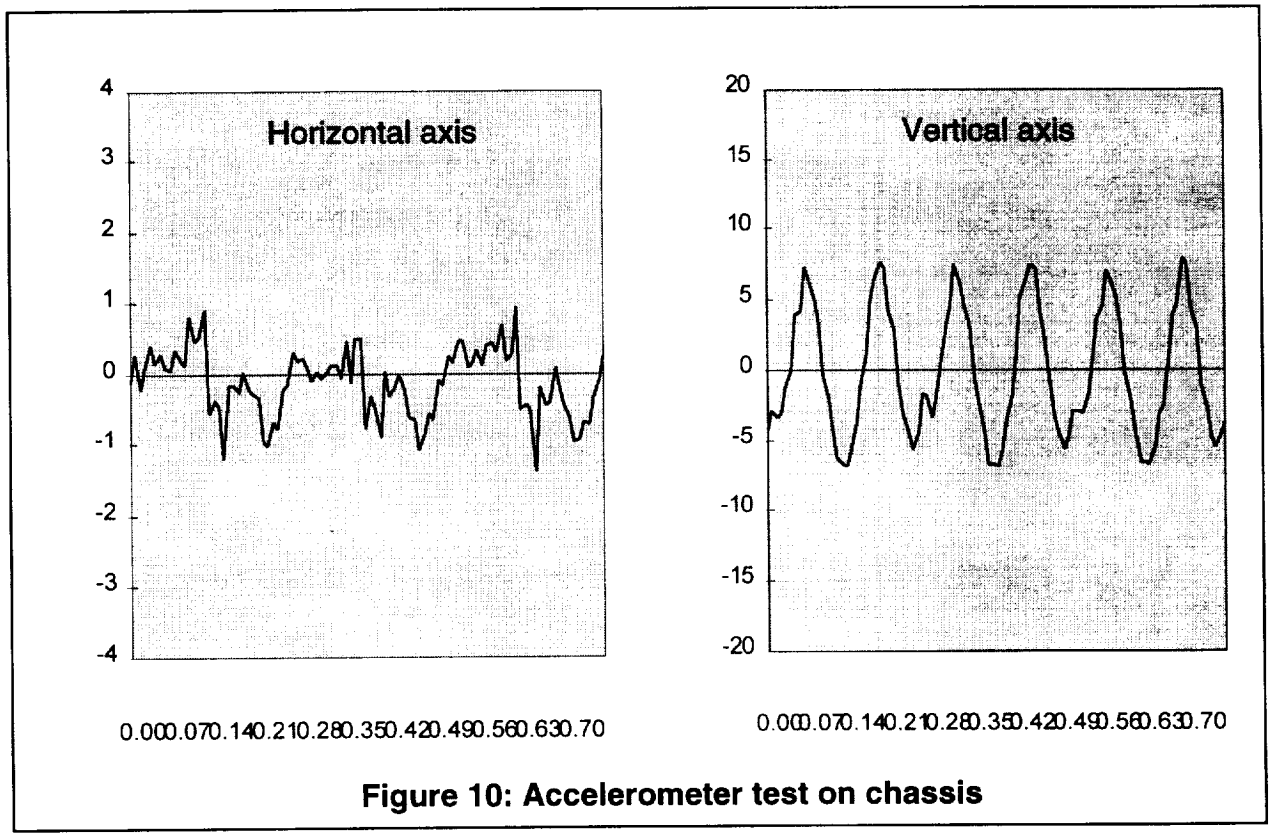

Figure 10: Accelerometer test on chassis

References

1. George H Neugebauer, "Designing Springs for Parallel Motion," *Machine Design*, Aug. 7, 1980, pp. 119-120.
2. Warren D. Weinstein, "Flexure-Pivot Bearings," Selected Papers on Optomechanical Design, SPIE Vol. 770, 1988, pp. 330-347.

Vibration Isolation, Steering, and Suppression Mechanism For Space-Based Sensors

Steve Bennett *, Torey Davis*, Richard Cobb**, Jeanne Sullivan**

Abstract

An experimental Vibration Isolation, Steering and Suppression (VISS) system has been developed and is currently being performance tested as a complete system. Performance testing is scheduled to complete in February of 1997. The VISS will fly on the Ballistic Missile Defense Organization (BMDO) experimental satellite, the Space Technology Research Vehicle 2 (STRV-2). VISS will provide broadband vibration isolation, suppress disturbances created by a payload mounted cryocooler, and steer the payload about multiple axes. The payload for VISS is a Medium Wave Infrared (MWIR) telescope developed by the United Kingdom Ministry of Defence, also experimental hardware on STRV-2. STRV-2 is part of an ongoing collaborative effort between BMDO and the United Kingdom Ministry of Defence to provide key space data to enhance design and risk reduction efforts for space-based, advanced, new technologies. STRV-2 is scheduled to fly in 1998.

Introduction

The need for vibration isolation and damping system resonances is not new, nor uncommon in today's world of engineering high performance, lightweight, stiff (undamped), aerospace structures. As spacecraft components evolve and performance demands on them become more stringent, so goes the demands placed on their interface mounts. Sensitive pointing devices, such as optical payloads, are now limited in performance by the quiescence of their mounts. Advanced optical payloads serve as prime examples of hardware in need of advanced vibration isolation technology. By limiting disturbances transmitted to these devices, their performance can be dramatically improved.

There are several ways to limit vibration disturbances to sensitive payloads. Passive or active vibration isolation mounting configurations abound. The method of attacking vibration problems discussed in this paper is a unique blend of passive and active vibration isolation using the Hybrid D-strut™ (or actuator).

The Hybrid D-strut combines damping strut (D-strut) technology with linear magnetic actuator technology to produce hardware that can be used for broadband vibration isolation as well as steering, or any other active control schemes desired. Another benefit of hybrid isolation that deserves mention is "graceful performance degradation". By this we mean that if anything should fail on the active portion of the isolation system, the passive portion of the isolation system would still allow degraded (passive only) performance without catastrophic failure. Other all-active systems cannot boast this feature. A cross section of the hybrid actuator used on the STRV-2 VISS program is

* Honeywell Satellite Systems Operation, Structural Control Group, Glendale AZ.
** United States Air Force, Phillips Laboratory, Kirtland AFB, NM.

presented in Figure 1. For VISS, six hybrid actuators are mounted in a "hexapod" or Stewart Platform[1] configuration, as shown in Figure 2. Mounting in this manner allows six Degree Of Freedom (DOF) isolation, steering, and suppression. Similar mounting schemes have been successfully used for both passive and active vibration isolation of spacecraft components[2,3].

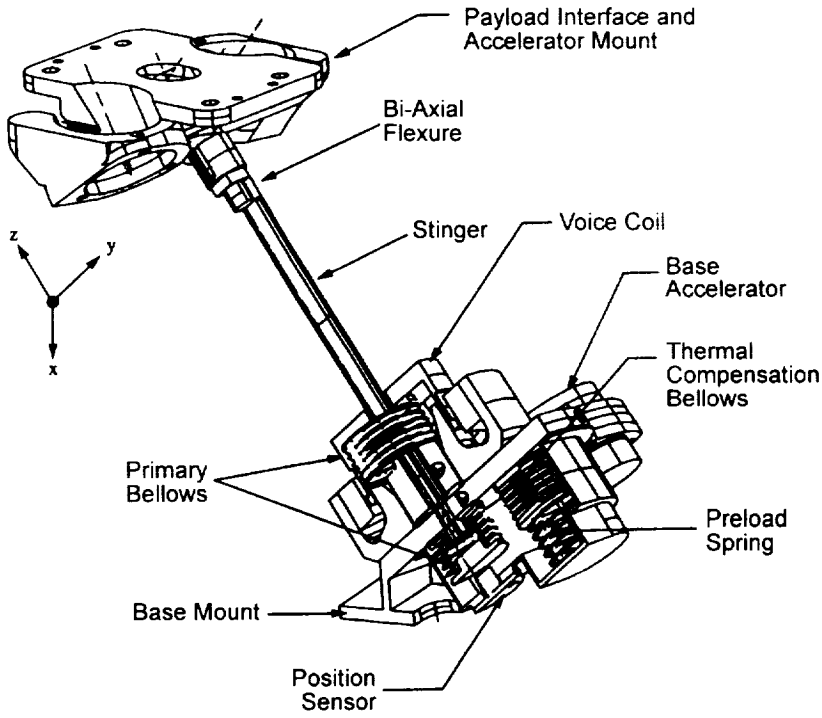

Figure 1. Hybrid Actuator.
The hybrid actuator combines "tuned" passive damping with a linear magnetic actuator to provide vibration isolation, steering, and suppression of on-board disturbances for an optical payload.

The hexapod, along with payload motion-sensing accelerometers, control electronics, and interconnecting cables make up the complete VISS system. VISS will isolate broadband base disturbances to an optical payload at least 20 dB (a factor of 10) between 5 and 200 Hz. VISS will also actively steer the payload ± .3 deg. Finally, VISS will actively suppress on-board cryocooler first harmonic disturbances 20 dB. STRV-2 is part of an ongoing collaborative effort between the BMDO and the United Kingdom Ministry of Defense to provide flight heritage for new, and potentially beneficial space technologies. The VISS flight experiment is sponsored in part by the United States Air Force's, Phillips Laboratory. The focus of this paper will be the mechanical hardware used in the STRV-2 VISS program, and more specifically, the lessons learned during build and test of the mechanical hardware.

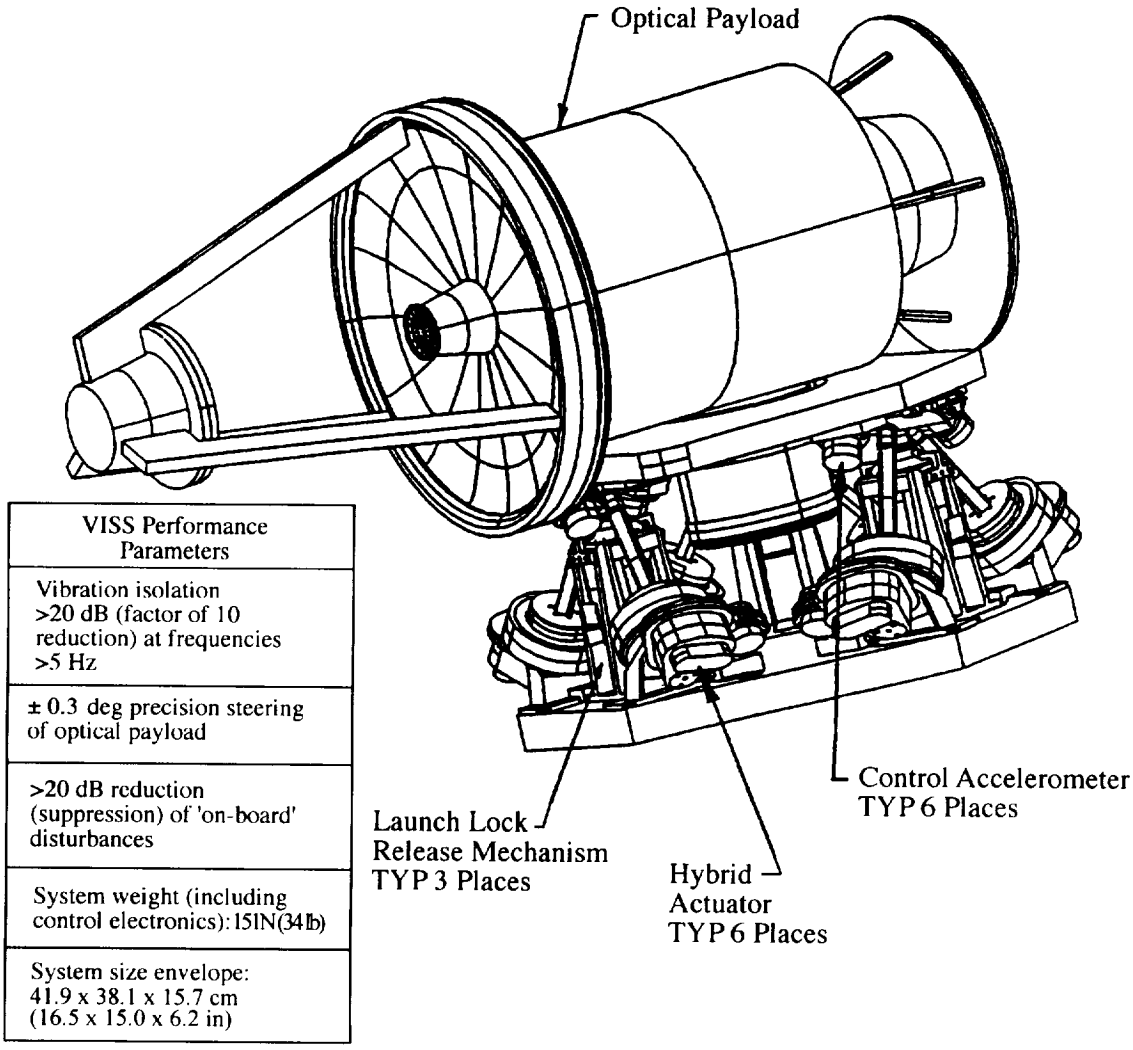

VISS Performance Parameters
Vibration isolation >20 dB (factor of 10 reduction) at frequencies >5 Hz
± 0.3 deg precision steering of optical payload
>20 dB reduction (suppression) of 'on-board' disturbances
System weight (including control electronics): 151N(34lb)
System size envelope: 41.9 x 38.1 x 15.7 cm (16.5 x 15.0 x 6.2 in)

Figure 2. STRV-2 VISS Hexapod.
The VISS Hexapod will provide 6-DOF vibration isolation for an optical payload, as part of the STRV-2 experimental satellite scheduled to fly in 1998.

VISS Hybrid Actuator

Again, the hybrid actuator is a combination of active (voice coil) and passive (D-strut) components. These components must be designed to complement each other to provide optimum actuator performance.

The passive D-strut hardware consists of primary bellows, secondary bellows, preload springs, damping fluid, end caps, stinger, pivot flexure, and through rod (refer to Figure 1). The primary bellows provide the static stiffness (K). The primary bellows, in conjunction with the endcaps, also serve as the hermetically sealed fluid chambers of the damping element. Damping (C) is provided by viscous fluid flow through the damping annulus from one primary bellows chamber to the other as the actuator strokes. The secondary bellows, along with the preload springs, provide fluid thermal

expansion and contraction compensation for the D-strut, since the primary bellows are tied together "rigidly" by the through rod. The preload springs also provide preload pressure to the damping fluid. This preload pressure prevents fluid cavitation when the D-strut strokes. This simple device can be designed to provide almost any combination of stiffness and damping (K, C), thereby tuning the passive D-strut to provide desired system performance.

General passive system constraints include the primary bellows allowable operating pressure and stroke capability. If the isolation system is ground-based, 1-g sag and structural integrity are always concerns. Because the STRV-2 VISS system hybrid actuator was designed for weightless space, actuator structural and stroke requirements were reduced from those normally imposed on ground-based systems. Thus, lower isolator resonant frequencies could be achieved. For VISS, passive isolator resonant frequencies ranged from just below 1 to almost 3 Hz for all six DOF. Passive performance requirement specification is < 5 Hz. The optical payload mass supported by VISS is 15 kg, (33 lb).

VISS also includes an integrated launch lock and release system that will serve as the primary load path for reacting launch loads experienced while delivering the payload into orbit. Once in orbit, the launch locks will be released, and the payload will be supported by the six soft hybrid actuators. The soft hybrid actuators need only be structurally sound enough to survive the launch environment, supporting their own mass.

To achieve the low isolator resonant frequencies (1 to 3 Hz), the actuator primary bellows wall thickness was a minute 3.3×10^{-5} m, (.0013 in). This fly-weight bellows met all the launch and thermal requirements, while still leaving some margin on system passive isolator resonant frequencies. Some of the lessons learned, to be discussed later in this paper, focus on utilizing and proofing these fly-weight bellows.

The active portion of the hybrid actuator is a voice coil linear force motor. A cross-sectional representation of the voice coil is shown in Figure 3. The voice coil operates on the Lorentz force principle, and can be designed to operate with a linear force vs. input current relationship over a large range of actuator stroke. This linear relationship can greatly simplify active control routines.

The VISS voice coil was specially designed for low power consumption and good heat dissipation properties. This was done mainly to safeguard the device if accidental overload commands were issued, either during test or flight. Current limits were set in the control electronics motor drivers based on the voice coils' energy absorbing and dissipating capabilities. These current limits could not be set so low as to prevent the voice coil from generating the necessary forces needed to meet performance goals. Thus, the need for good heat conduction paths away from the voice coil windings. Heat conduction was enhanced by special bobbin construction. The voice coil bobbin for VISS is made from a graphite epoxy composite material with graphite strands oriented in such a way as to conduct heat away from the copper windings while avoiding Eddy current effects.

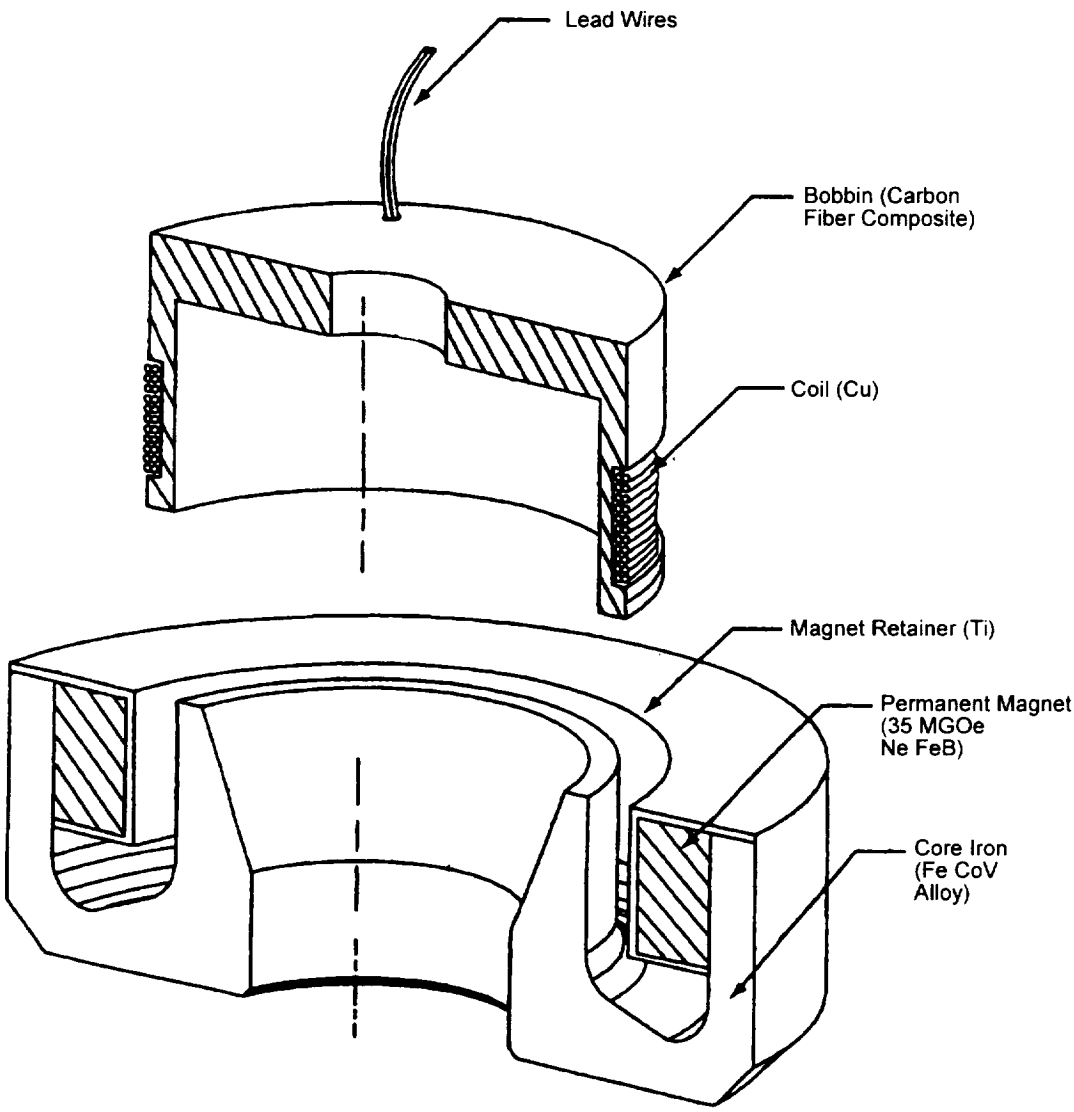

Figure 3. Voice Coil X-Section
The voice coil has been designed as an integral part of the Hybrid D-strut for the VISS application

The voice coil magnets are made from rare earth Neodidium Iron Boron material, selected for maximum flux density. The fragile magnets are protected by a titanium cover that has no effect on the electromagnetic field. The outer housing is made from iron cobalt material and its cross section has been designed to afford optimal voice coil performance.

The voice coil assembly has been designed as an integral part of the Hybrid D-strut where the bobbin is supported by the primary bellows, and the magnet/housing attaches to the base actuator bracket.

A summary of performance parameters for the VISS Hybrid Actuator is presented in Figure 4.

Parameter	Value
Rated force	8.9 N, (2 lb)
Stroke	± 0.001 m, (± 0.04 in.)
Power at rated force	3.5 W
K	525.4 N/m, (3 lb/in)
C	105 N•s/m, (0.6 lb•s/in)
Weight	11.12 N, (2.5 lb)
Size envelope	0.102m x 0.127m x 0.203m, (4in x 5in. X 8in.)

Figure 4. Summary of VISS Hybrid D-strut Performance Parameters

VISS Launch Lock

As briefly discussed earlier, the soft VISS actuators cannot adequately support the optical payload during the rigors of launch. For this purpose a launch lock system was devised, comprised of a launch lock tower, a Frangibolt® release actuator[4], and an interface bracket. A single assembly of the launch lock system is presented in Figure 5. Three of these launch lock assemblies support the payload. The upper interface bracket also serves as the payload attach point for the hybrid actuators.

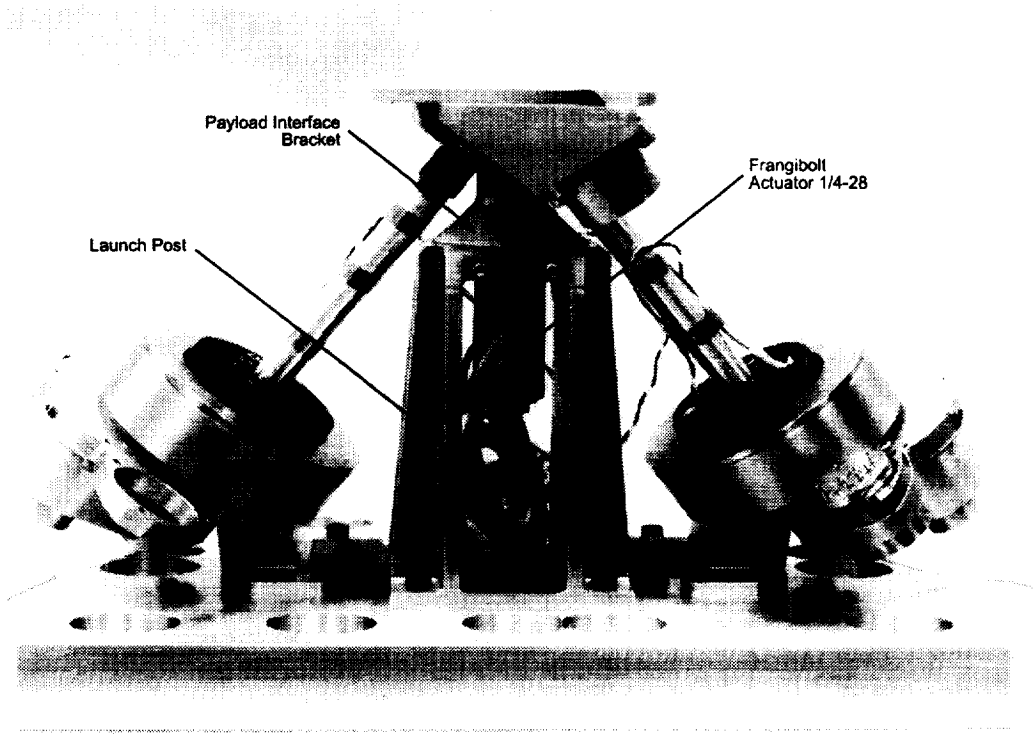

Figure 5. Launch Lock X-Section
The launch lock system provides structural support to the payload and safeties the Hybrid Actuators during launch.

The Frangibolt, manufactured by Ti Ni Alloy Company, is a flight-proven release mechanism which employs a titanium fastener (0.25 - 28UNF hex bolt) and a nitinol (also known as a shape memory alloy or smart material) spacer specifically designed to stretch and fracture the bolt when heated past its phase change temperature (80 °C). A silicone rubber heater provides the energy necessary to realize this phase change. This 90 Watt heater runs off the standard 28 V bus and takes just under 25 sec to fracture the bolt once powered up, (under ambient conditions). The titanium bolt is notched in an area where fracture is desired to occur. This notch has been designed by Ti Ni Alloy company to minimize stress risers and has surprisingly good fatigue characteristics.

Benefits from using the Frangibolt are its simplicity, reliability, cost, and the device imparts an order of magnitude less shock to the sensitive payload than a comparable pyrotechnic device. A fraction of the strain energy of the stretched bolt is all that is released into the payload when fracture occurs. Evaluation tests of the launch lock system show this energy to be on average 0.52 N-m (4.6 in.-lb) for the 0.0064 m (0.25 in.), separation bolt. For VISS, the majority of this release energy is absorbed by the Hybrid Actuators and not the payload. This gives the payload an extra margin of safety from shock loading during launch lock release.

For launch, the Frangibolt clamps the launch post to the interface bracket in much the same fashion as a normal bolted joint. The interface bracket and launch post have been fabricated with a matched cone and cup interface that reacts shear loads during launch, and also affords the necessary lateral clearance for VISS isolation performance once released. The launch lock structure has been designed to provide a stiff load path from which payload acceleration loads can be transferred to the spacecraft without excessive deflections that could be detrimental to the payload and/or the soft actuators.

Fabrication and Test

Challenging applications for isolation systems, i.e., VISS, often require low break frequencies to ensure the isolation system break frequency is well below any resonant frequencies of the equipment being isolated. As the required break frequency of an isolator continues to drop, the axial stiffness, K, required to allow this lower break frequency also lessens. With this lower axial stiffness comes design, fabrication, and testing challenges. The VISS isolator has two bellows in series with the stinger. These two bellows determine the axial stiffness of the isolator. The bellows are utilized to form a hermetic seal between the actuator stinger and the mounting bracket assembly. Taking into consideration the available bellows material, diameter, stroke and working pressure, a thickness of 3.3×10^{-5} m, (0.0013 in.), was chosen to optimize the design. The process of actually manufacturing the "flyweight" bellows is not new or difficult for the skilled craftsman involved in this technology. The difficulties arose after manufacture, during installation and proof testing these delicate components at the VISS actuator assembly level.

The thin bellows for VISS were manufactured using the nickel deposition method by MS Bellows located in Huntington Beach, CA. This process includes manufacturing an aluminum mandrel with the shape of the desired bellows on the outside surface of the

mandrel. This mandrel is then nickel-plated to the desired thickness, typically using proprietary methods. The nickel-plated mandrel is then dipped in an acid bath that dissolves the aluminum mandrel leaving only the nickel bellows. Normally, bellows are inspected for surface defects or anomalies and then leak checked; a popular leak check method includes submersing the bellows in an alcohol bath. The bellows is first fitted with end caps, then, while in the alcohol, pressurized with helium to a safe level pressure for the bellows under test. While in the alcohol bath, the bellows is inspected using a borescope to search for bubbles indicating a bellows leak. Alcohol is used for its low surface tension and clarity. Helium is used because it is such an incredibly small molecule. To detect smaller leaks, the assembly is evacuated utilizing a mass spectrometer and associated vacuum pump. A controlled source of helium is then sprayed on the outer surfaces to detect any passage through the bellows into the mass spectrometer.

The bellows for VISS could not be economically leak checked as piece parts by the bellows vendor because they were too delicate. Attaching inspection end caps and fittings for a leak check would put the bellows at too great a risk as well as significantly adding to the price. Additionally, the VISS actuator design did not lend itself to leak inspections or proofing until the actuator was completely assembled. To get some confidence as to the lot metallurgy and quality, a sample from each lot was fitted with end caps and leak checked in an alcohol bath, as described above. The testing was destructive for the bellows tested.

The risk of costly reworks, if leaks were found late in the actuator assembly, were thought to be minimal. Actuator assembly rework, if leaks were encountered, was the option taken in lieu of redesigning the mechanism to allow end caps to be assembled to the bellows as a subassembly. By having caps for leak checking integral to the design, leak checking the bellows could have been performed before many hours were invested, completing the actuator assembly to a stage at which it could be leak checked as a completed assembly. The end caps for the VISS actuator were epoxied to the bellows as part of the actuator assembly. This made removal of a suspect bellows without damaging it, or a companion bellows in the assembly next to impossible.

Again, when the entire actuator is completed it is leak checked using helium and a mass spectrometer. This leak check is typically very thorough. After the leak check the actuator is evacuated and filled with silicone fluid. One of the VISS actuators passed all of the above testing only to leak fluid after a few hundred cycles during post-assembly proofing. The leak was not severe, but any defect allowing fluid to pass was much too large for the VISS application. Given 24 hours under preload pressure, a single droplet of silicone was forming between the convolutes of the bellows.

With the leaking actuator still assembled the bellows were put under pressure and checked for leakage using an alcohol bath. With a residue of silicone fluid in the actuator, finding the leak proved difficult. The reason being, the viscous silicone fluid actually helped seal the small defect, considered unacceptable.

The bellows was removed from the actuator assembly and returned to the manufacturer for further analysis. Removing the bellows did destroy the ends, also called cuffs, of

the bellows. This wasn't a big concern as the droplet was forming on an intermediate convolute. The microscope typically used for examination revealed no obvious anomalies. The bellows was thoroughly cleaned with alcohol and soldered to inspection end caps; then it was leak checked with pressure in an alcohol bath. The leak was apparent with the bellows in this condition; the alcohol removed the silicone residue allowing the helium to pass though the pinhole freely. The pinhole was marked and the bellows taken to an analysis house for further inspection. The pinhole was very interesting under the electron scanning microscope. (refer to Figures 6 and 7) The pinhole appeared to be at the location of a "nodule". A "nodule" is a minute area on the bellows where a small bump forms in the bellows during the plating process. The exact cause of a nodule is typically not known. Some of the causes are believed to be a microscopic contaminant on the bellows mandrel, or a minute contaminant in the plating material, or other irregularity in the plating bath metallurgy. Close inspection of the nodule in question revealed the appearance of filing at the location. Often during inspection the nodule is dressed with a file to improve appearance. Typically the nodule area is plated more heavily, such that filing does not create any problems. It is important to note that even under the strictest quality assurance guidelines, as was the case here, nodules will occur, making it most important to thoroughly proof these fragile devices.

Figure 6. External View
An electron scanning microscope image of the external surface of the leaking area. Close examination reveals what might be file marks from the attempted "repair" of a nodule.

Figure 7. Internal View
An electron scanning microscope image of the internal surface of the leaking area. The texture reveals the acid etching performed on the aluminum mandrel surface before the nickel plating.

Oddly, when first assembled into the actuator, the bellows in question did not leak when checked with a mass spectrometer. On previous programs this inspection has always successfully found defective hardware. It wasn't until pressure was applied to the bellows internally, that the problem area was found. Although the reason for this occurrence hasn't been fully explained, it has been surmised that foreign material could have been dislodged from the nodule during cycling, or when positive pressure was applied inside the bellows during actuation, or even a combination of the two. In any case the experience did provide lessons to be learned. Bellows that appear leak-free when checked with positive pressure external to the bellows may not be leak-free when tested with positive pressure inside the bellows. Therefore, positive and negative pressure cycling is crucial for proofing these lightweight devices. Also, when a bellows cannot be easily leak checked by the manufacturer, and the assembly in which they are integrated is complex, consider a design that allows bellows leak checking before the assembly is complete.

Once rework of the defective actuator was complete, it was positive and negative pressure cycled, and no other leakage problems have been encountered.

The VISS actuator is assembled using a space-qualified epoxy. The cure time on this epoxy is eight hours at room temperature, reaching full strength after 24 hours. The cure time is shorter if the temperature is elevated. An obvious key to a quality glued assembly is having the glue only on the joints intended per the design. For the VISS

actuator this proved to be less straightforward than was originally believed. The problem of epoxy migrating to areas not intended for epoxy began to become apparent when assembly procedures began taking advantage of shorter cure times by elevating the cure temperature. Extraneous epoxy was discovered when interference was noticed in the stinger travel on a few of the flight actuators.

Upon tear down extraneous epoxy was observed on the through rod of the stinger. Closer observation revealed epoxy had run from the glue joint between the bellows end cap and the through rod, (refer to Figure 1 for joint detail). Review of the assembly procedure revealed two epoxy steps joining components with areas that could be adversely affected by epoxy overrun caused by gravity. Careful re-engineering of the assembly procedure produced an assembly methodology that worked in conjunction with gravity. No further problems caused by epoxy migration have been encountered.

After VISS actuator assemblies were complete, they were then incorporated into the VISS hexapod assembly. As part of this assembly a shim was installed between the end of each stinger and the titanium flexure. The reason for the shims is to allow the actuators to center the payload at a neutral position in a zero gravity field. The bellows, in series with each actuator stinger, have a natural neutral position. The neutral position of each actuator was found by resting the stinger horizontally on a low friction rest. This unloads the bellows from the gravity force vector. With the stinger in this neutral position the gap reading from a gap sensor built into each actuator was recorded. The actuators were then assembled in their respective flight configurations. This entails pairing the actuators as they will be mounted in flight, as well as pairing the actuators with their respective launch post and payload bracket. With the actuators mounted in their flight configuration each actuator gap sensor was reread. Using the calibration sheet for each gap sensor, a shim was manufactured to bring the stinger back to the neutral position recorded when the actuator was horizontal. Each shim was installed and fine-tuned to repeat the neutral gap sensor reading while the actuators were in their flight configuration. With the shims installed, the actuators will passively maintain the MWIR telescope level at the design elevation.

Preliminary Performance Testing

The VISS system is currently undergoing performance testing at the USAF Phillips Laboratory. Modifications to the system software are still being made, therefore only preliminary results are currently available. The two fundamental performance issues for VISS are passive and active vibration isolation. The passive isolation was first demonstrated in a modal test which included the VISS system. The goal of the modal test was to identify flexible base (plate/ring/breadboard) modes which could adversely affect the passive and active isolation. The setup for this test is shown in Figure 8.

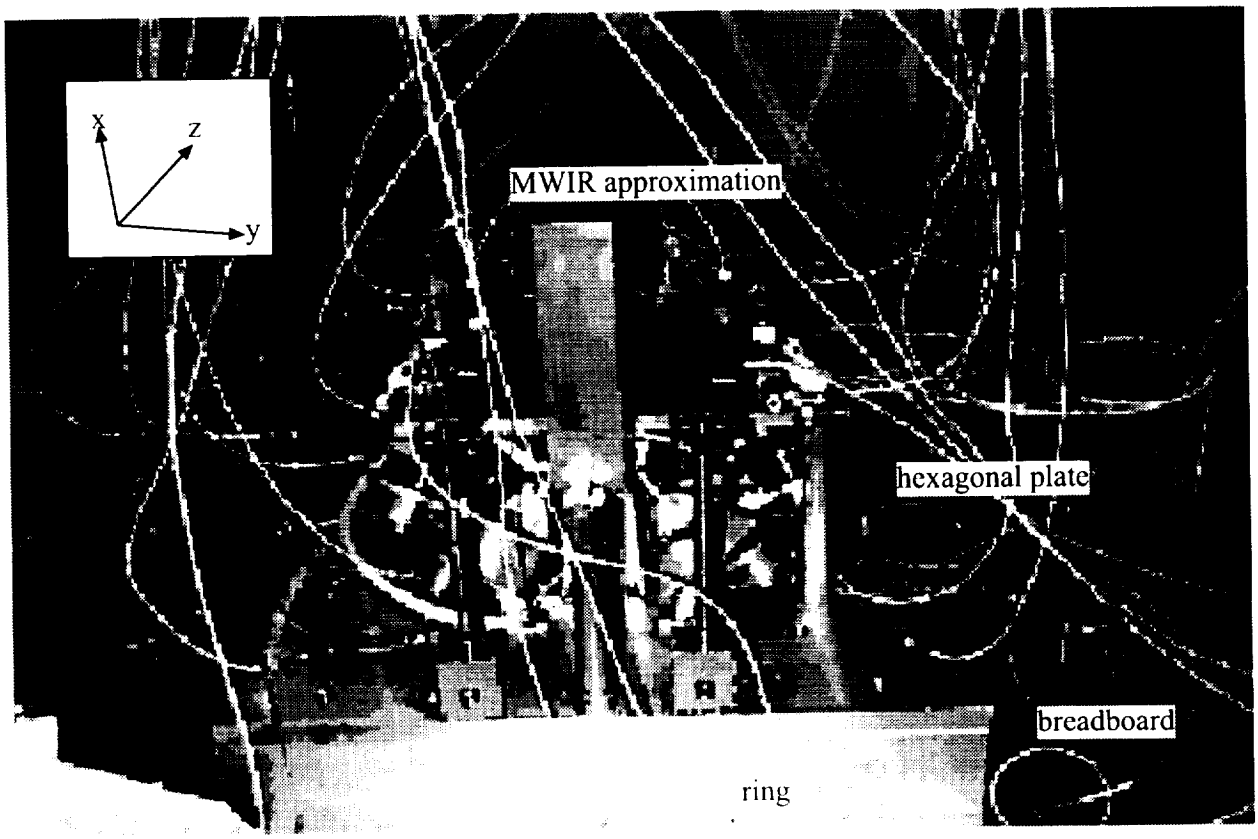

Figure 8. Modal test setup for VISS with MWIR approximation.

VISS is shown attached to a hexagonal plate and ring fixture which were designed to approximate the flexible dynamics of the flight bus structure. The plate and ring fixture were connected to a small optical bench, or breadboard. The mass and inertia values of the hexagonal plate, ring fixture, and breadboard are greater than the mass and inertia values of the MWIR by a factor of ten, but were chosen to be smaller than the mass and inertia values of the satellite. The payload attached to VISS in this experiment was a rigid-body approximation of the MWIR telescope. The MWIR approximation was gravity off-loaded with two CSA Engineering, Inc. active/passive gravity off-load devices. The passive component of the device is pneumatic while the active component includes a voice coil with displacement sensor and accelerometer feedback.

Instrumentation consisted of twelve triaxial accelerometers placed around the perimeter of the breadboard (on the underside) and four triaxial accelerometers placed on the corners of the MWIR approximation. In addition, thirteen single-axis accelerometers were placed on the hexagonal plate.

A 100-pound electrodynamic shaker, was used to provide disturbance input. The shaker force was applied at one corner of the breadboard with the line of action oblique

to all three coordinate directions. A load cell was used to measure the shaker input force, and was also placed at the point of shaker input

The Phillips Laboratory VTVD modal system was used to acquire the data and estimate the modal parameters in the tests. Modal parameters were estimated from the measured Frequency Response Functions (FRF).

Figure 9 shows the magnitude and phase of three FRFs obtained during the modal testing. A continuous random input to the VTS100 shaker was used and a zoom analysis was made between 150 and 278 Hz. The driving point FRF of the breadboard is shown as compared to the FRFs measured between the shaker load cell and accelerometer measurements in the x-direction on the plate and the MWIR. The motion in the x-direction on the MWIR is at least a factor of 10 (20dB) less than that of the plate so passive isolation has been obtained in this frequency range. Figures 10 and 11 show two of the mode shapes of the system as obtained by the modal test. The mode shown in Figure 10 shows torsion of the breadboard, some motion in the plate, and no motion of the MWIR - the rectangle at the top of the picture. The mode shown in Figure 11 shows bending of the breadboard, some motion in the plate, and again, no motion of the MWIR.

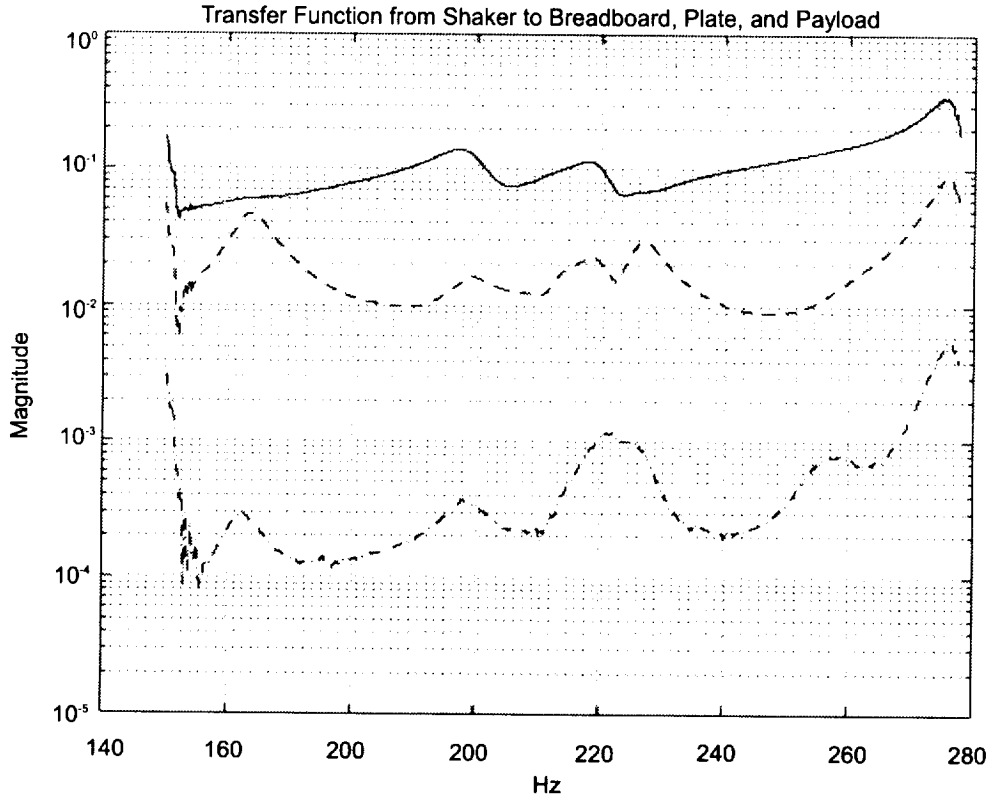

Figure 9. Magnitude and phase of frequency response functions obtained during VISS modal testing for the breadboard

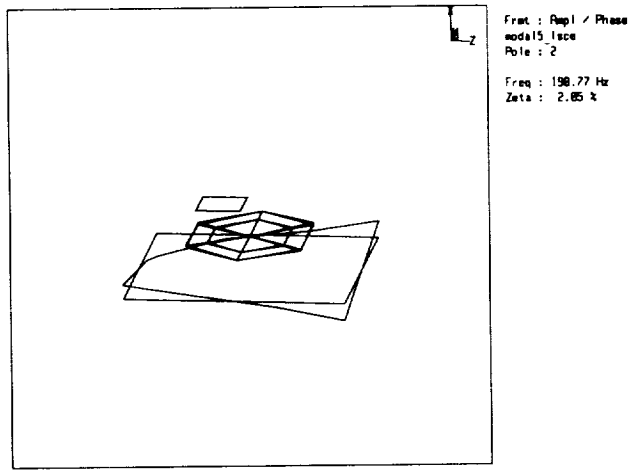

Figure 10. Mode 2 of the base structure: 198 Hz, 2.05% damping.

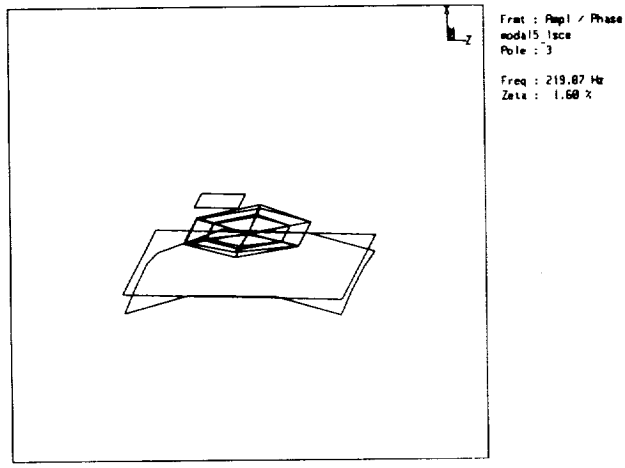

Figure 11. Mode 3 of the base structure: 220 Hz, 1.60% damping.

A preliminary closed-loop isolation test was conducted by closing a Single Input/Single output control loop around the payload accelerometer and voice coil of one VISS strut. The setup for this test is shown in Figure 12 with an engineering model of the MWIR being utilized as the payload for VISS for the test. The resulting active transmissibility is shown in Figure 13 and is compared to the passive transmissibility. These measurements were made by measuring the FRF from the shaker load cell to the strut base accelerometer and from the shaker load cell to the strut payload accelerometer. As can be seen from the plot, the active transmissibility shows isolation over a wider frequency range than the passive transmissibility, but the active input to the voice coil was rolled off at higher frequencies so that the active/passive transmissibility merges with the passive transmissibility. Peaks in the transmissibility were caused by test fixture dynamics. The peak at 40 Hz is due to the dynamics of the gravity off-load system. The higher frequency peaks are due to flexible modes of the base fixture which includes the plate, ring, and breadboard.

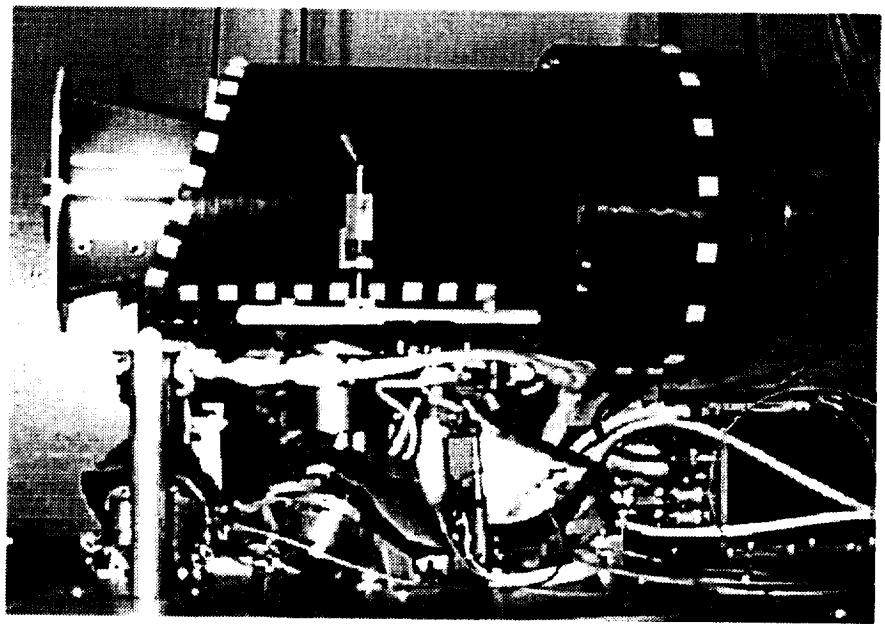

Figure 12. Performance test setup for VISS with MWIR approximation

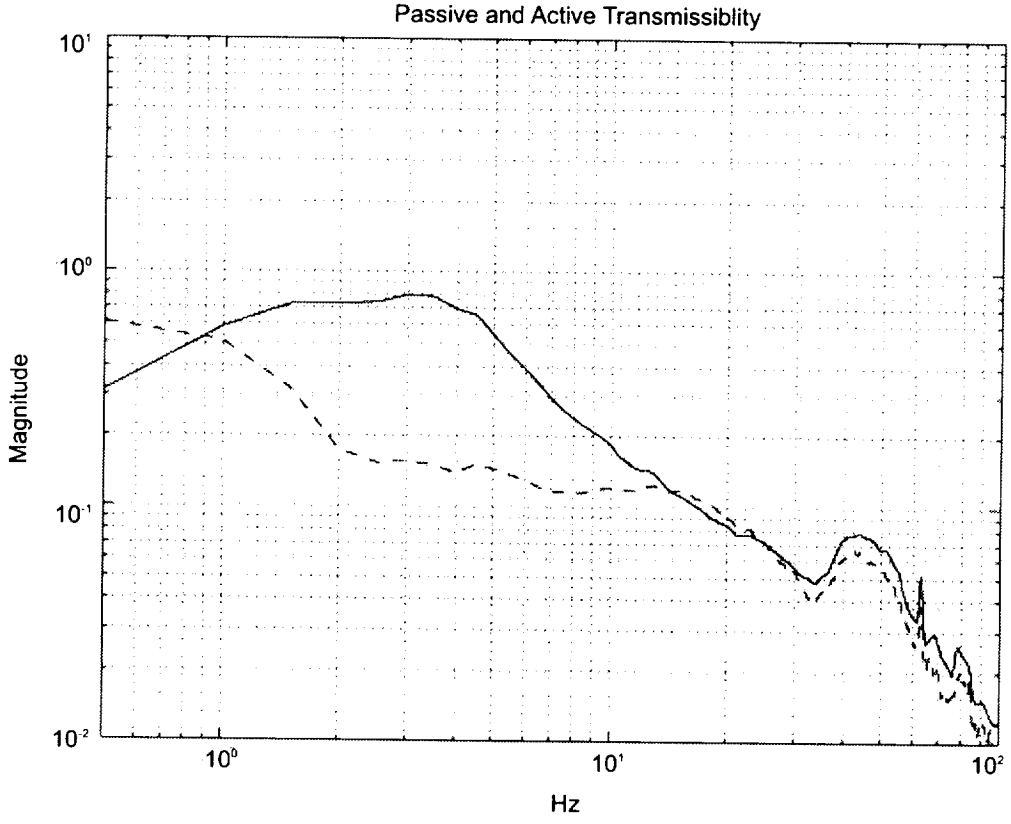

Figure 13. Initial closed-loop (active) transmissibility compared to passive transmissibility measured across one VISS strut.

Conclusion

In conclusion, though system testing is in progress and control software for the active performance of the VISS isolators is still under construction, results to date indicate the actuators will perform per design. The VISS isolators have exhibited the vibration isolation set forth in the design using simple control law regimes. As the control laws become more refined, the active performance of the isolators will only improve. The VISS isolation system has proven to be a flight qualifiable, high performance, relatively low cost solution to vibration isolation for sensitive spacecraft payloads. Very soon the design will also have flight heritage.

Acknowledgments

This work has been partially funded by the Ballistic Missile Defense Organization (BMDO). We would like to thank Dr. John Stubstad, Maj. Gary Hay, and Lt. Col. Michael Obal for their support and contributions.

References

1. Stewart, D. A Platform with six Degree of Freedom, Institution of Mechanical Engineers, (1965).

2. J. Spanos, Z. Rahman, G. Blackwood. "A 6-axis Active Vibration Isolator, American Control Conference, Seattle, (June 1995).

3. D. Cunningham, P. Davis. A Multiaxis Passive Isolation System For a Magnetic Bearing Reaction Wheel. Damping' 93, (Feb 1993), Hotel Nikko, San Francisco, CA.

4. J. Busch, W. Purdy, A. Johnson. Development Of A Non-explosive Release Device For Aerospace Applications. 26th Aerospace Mechanisms Symposium.

Selection, Preparation and Lubrication of Middle-Size Ball Bearings for Infrared Instruments

Jean Louis Lizon*

Abstract

Infrared astronomical instrumentation normally requires cooling to cryogenic temperatures in order to minimize thermal radiation inside the instrument. These infrared instruments are equipped with various optical components which, in order to be remotely selectable, are mounted on wheels or turntables. Both the recent developments in infrared detector technology and the construction of the new generation of large telescopes lead to a growing demand for large size infrared instruments. The past generation of instruments was generally working with an optical beam diameter of 20 to 30 mm. In order to fully exploit the performances of the detector and the modern telescopes one needs instruments which can accommodate an optical beam diameter of up to 150 mm. This very large increase in the size of the optical components led us to start experiments with larger size bearings with a bore diameter of up to 200 mm.

Introduction

The European Southern Observatory is currently building one of the largest telescopes in the world: the Very Large Telescope (VLT). One of the first instruments to be installed on this telescope is an infrared imager spectrometer working in the wavelength range 1 to 5 mm. This instrument includes 13 movable functions amongst which the grating unit is the most demanding one. This unit on which 2 gratings are mounted back to back carries a total rotating mass of about 8000 g. The following table summarizes the most important parameters of the technical specification of this grating unit:

Table 1 Technical requirements

1. Angular stability (while the instrument is rotating)	< 2 arc sec
2. Angular positioning accuracy	< 3 arc sec
3. Angular run out (wobbling movement of the axis)	< 3 arc sec
4. Operating temperature	< 70 K
5. Operating pressure	< 1E-6 mbar
6. Cooling time (from room temperature to 80K)	< 24 hours

As the VLT is being installed on a remote site in the Atacama desert in Chile, these performances have to be guaranteed over a period of 10 years with minimum human intervention.

* European Southern Observatory, Munich, Germany

Choice and Adaptation of the Ball Bearing

As the requirements clearly show, the unit needs to position and support the optical elements rather accurately. During observations of astronomical objects the telescope follows the movement of the stars. The instrument is attached to the telescope and therefore all instrument components are subject to a permanent rotation of the gravity vector.

A first assumption would lead to consider a very rigid bearing as the only solution possible of meeting the angular positioning accuracy requirement. The rigidity of a bearing depends directly on its internal preload (preloading of the balls onto the races). The experience gained with optical instruments operating at room temperature has shown that it is not advisable to increase the internal preload until the bearing can meet this specification. An excessive preload will directly lead to an increase of the running torque and eventually to a premature damage of the races. A better approach is to balance the rotating mass on both sides of the bearing plane. If this operation is done very carefully by the addition and the fine tuning of a counter-weight, an angular stability of a fraction of an arc second can be reached even with a very low internal preload.

The second main driving parameter in the choice of the bearing is its thermal conductivity. Ideally we would like to cool the rotating mass through the bearing itself in order to avoid either a slipping cooling finger which would lead to a higher drag or a flexible thermal connection which would not allow a continuous rotation of the unit. The thermal conductivity of a bearing depends mainly on the following parameters:

- number, diameter and material of the balls
- nature of the ball/race contact
- contact pressure of the balls on the races

Three different types of preloaded bearings have been tested: i) a single four-point bearing, ii) a preloaded pair of thin ring bearings and iii) a pair of angular contact ball bearings. Further tests have been carried out on this last bearing type in order to improve the thermal conductance by using ruby (Rb) and tungsten carbide (WC) balls. A last attempt to improve the thermal behavior was done by using a gold coating on the races.

The poor thermal performance of the four-point bearing (Figure 1, curve 1) can easily be explained by the low number of balls it includes. The thin ring bearing (curve 2) which uses some 200 balls showed a disappointingly low conductivity. This is mainly due to the fact that only a restricted number of the balls is in contact at any one moment, and this is even the case when the bearing is mounted on a seat with high geometric quality. Using a material for the balls with high thermal conductivity has a direct impact on the conductance of the bearing (curves 3, 4 and 5). The use of balls from material which is different from the races has the additional advantage of preventing any cold welding which could possibly take place in the high vacuum

environment. The lack of experience and the high fragility of ruby lead us to abandon this material even if the results were very promising. As can be seen from curve 6, the material and the coating of the races are very important factors. The mounting of the bearing also plays an important role in the thermal behavior as can be seen from curve 7.

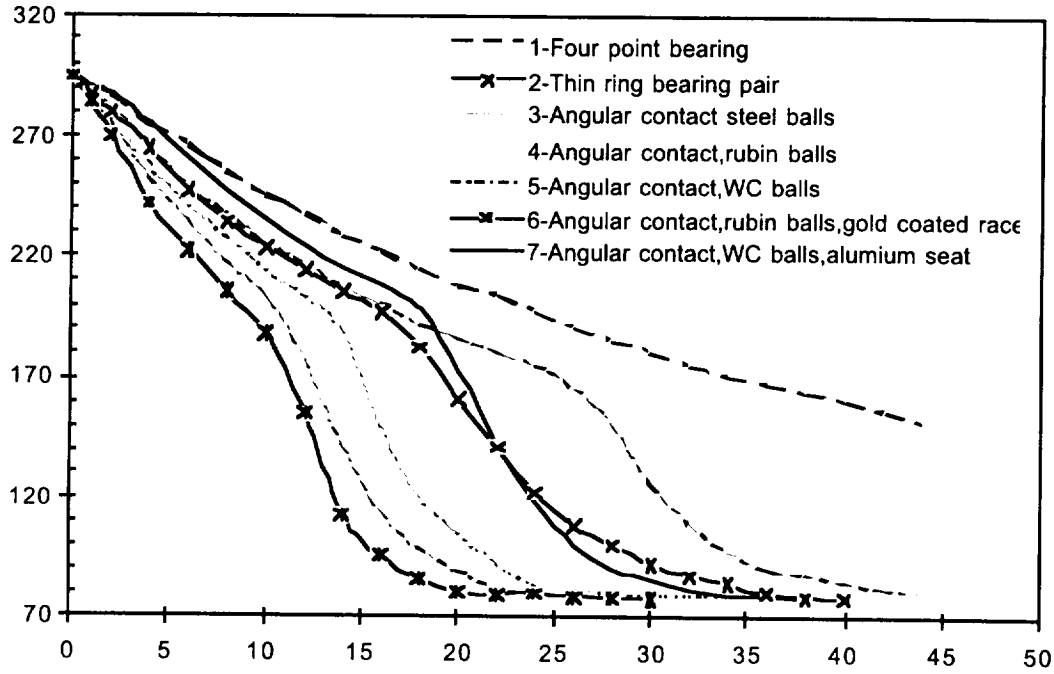

Figure 1. Cooling of a 8000 g aluminium mass through various ball bearings

In order to ensure the mechanical performance, the inner ring of the bearing is to be mounted with a press fit on a seat machined in a geometrical quality 5. The best thermal performance is obtained when a similar fitting is also used for the outer ring. The use of an aluminium seat for the outer ring can only be realized with a clearance allowing for the differential thermal shrinkage. This gap also causes some delay in the cooling time (curve 7).

Finally, the following angular contact bearing has been chosen:
71920 E TPA PA7 UL from IBC in "O" arrangement, with a 250 N preload and fitted with tungsten carbide balls. Both the inner and the outer races are mounted with press fit in seats machined from martinsitic stainless steel. The thermal conductance of this bearing was measured to be 0.7 W/K at 300K and 0.3 W/K at 80K.

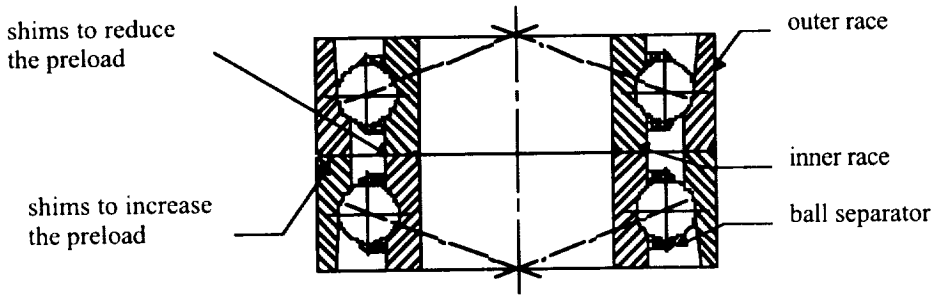

Figure 2. Preloaded pair of dis-mountable oblique contact ball bearings
Choice and application of the lubricant

Pure molybdenum disulphide (MoS_2) is well known to be one of the most efficient lubricants in vacuum for cryogenic applications. This coating is generally applied by sputtering and suffers the disadvantages of being expensive and of having a rather long delivery time. Moreover MoS_2 is a very good lubricant under vacuum only when it is very pure and when it has its lamelar structure. In order to simplify the test procedures for the movable functions of the instrument, it was very important to have a solution for the lubrication that can be used both at ambient temperature in air and in vacuum at cryogenic temperature without significant differences. A series of tests allowed us to qualify a commercial dry lubricant for this application.

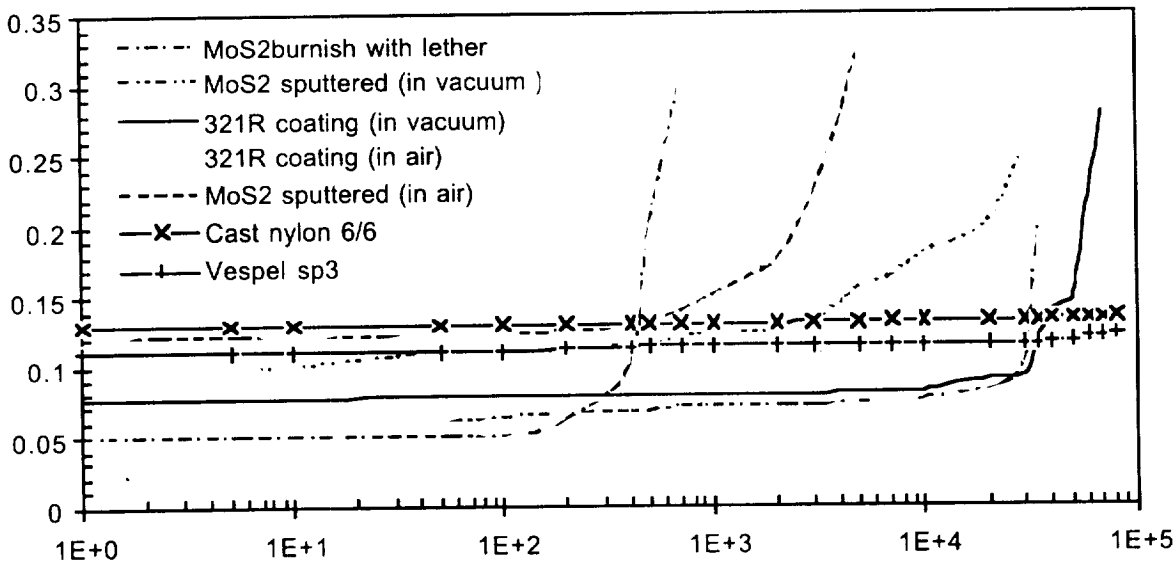

Figure 3. Coefficient of friction and life time comparison of various lubricants

When looking at the dynamic behavior of a bearing, one can see that the ball separator is the only part which is subject to sliding, whilst the balls are rolling on the races. Therefore, special attention needs to be taken when selecting the material for the manufacturing of this cage; a non-metallic self-lubricating material needs to be employed. One of the best candidates for this application would be Vespel SP3 from

Dupont, which is a polyamide filled with MoS_2. As this material is rather expensive and very difficult to obtain in large quantities, we started an investigation to find an alternative material. A good replacement material has been found with the Cast nylon 6/6 (*Nylacast Oilon Ltd., Leicester, LE5 OHD, U.K.).*

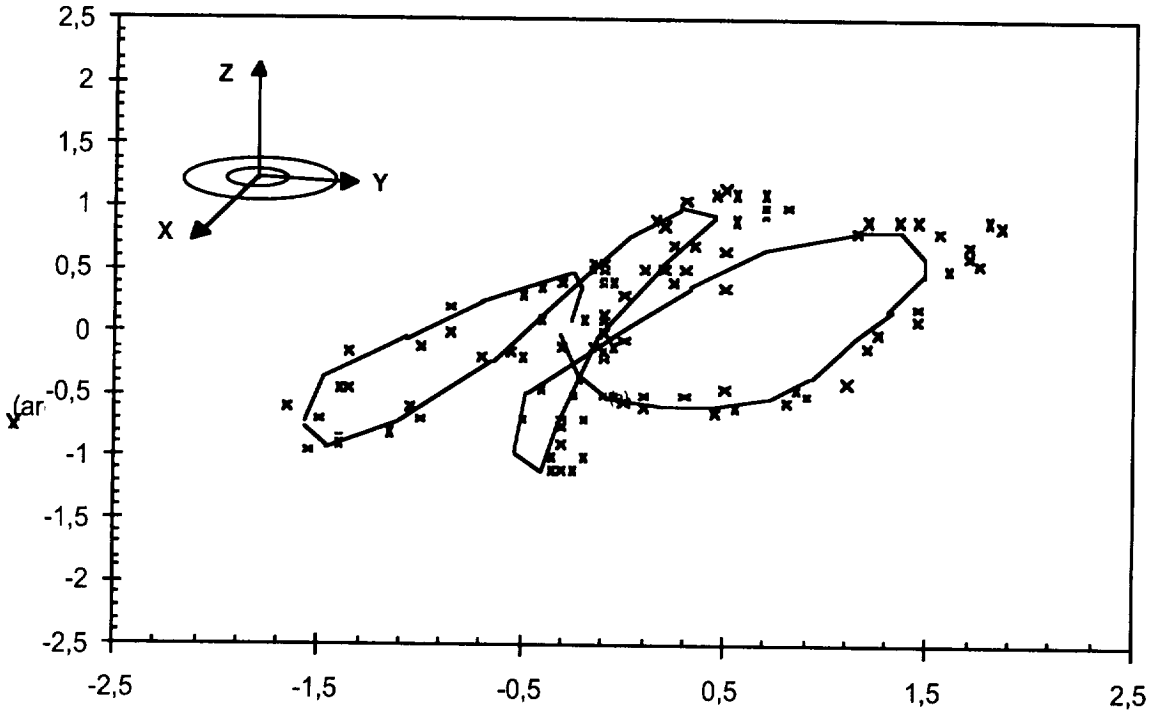

Figure 4. Run out error of the bearing after coating

The choice of a lubricant which is commercially available as a spray (*321R from Dow Corning*) was only the first step. This needed to be completed by the development of a method of application that could guarantee the proper mechanical quality and the accuracy of the races. A variation of one micron in the thickness of the lubricant film is enough to cause a run out error of 2 arcseconds. During many months of experimentation and various unsuccessful trials, an application procedure was developed that allowed to fully keep the mechanical quality of the bearing and that ensured a smooth and reliable operation at cryogenic temperatures. The bearing is disassembled and carefully cleaned in an ultrasonic bath filled with acetone. The bearing is then reassembled with a ball separator that has been generously coated. The pair is assembled with only 50% of the original preload for a first run-in operation (≈5000 rev). The run-in continues with 3 more periods using respectively 75, 100 and 110% of the preload. During this process the lubricant is transported from the ball separator onto the races. Using different preloads ensures that a somewhat larger area of the races is coated.

The bearing is then disassembled and the races are wiped with cleaning paper. The final ball separator is coated with a very thin film of lubricant. Great care is taken to brush it strongly with a nylon brush in order to remove all the excess coating that could otherwise later become a source of pollution. The bearing can be finally assembled with the final tungsten carbide balls.

Results, Status

In the pre-design phase, two prototypes of the grating unit have been built in order to fully qualify both the bearing technology and the drive principle. The design of the drive is based on a worm wheel mechanism powered with a 5-phase stepper motor. As the positioning accuracy relies only on the motor steps, it is extremely important to keep friction and torque along the complete kinematic chain as low as possible. The running torque at 80K has been measured on ten sets of the selected bearings after complete adaptation. The dynamic torque is in all cases lower than 0.55 Nm while the static torque was never measured to be above 0.6 Nm.

The various measurements that have been carried out clearly demonstrated that these two prototype units met the technical specifications in all points. At the end of the test cycle, the prototypes have been used for a lifetime test. In order to simulate utilization over a period of 10 years, the unit has been rotated over 1 million revolutions. During this lifetime test, the positioning accuracy has been regularly measured. Figure 5 shows measurements recorded at two different stages of the test.

The two units survived without any failure the 10 years lifetime simulation. When analyzing the results of the positioning accuracy measurements, we have to distinguish between the following two cases. In the plane of the bearing (r.X) the accuracy improved. This parameter, which directly depends of the bearing, seems to indicate that a longer run-in would be beneficial. The degradation of the angular positioning around the rotation axis (r.Z) is caused by two sources: the torque noise of the bearing, which increased significantly during the test, and the degradation of the drive mechanism, which performed a total of 400 million revolutions. At this time, the final grating unit, as well as all other units of the instrument, have been built and tested. The complete instrument is now entering into the system test phase.

Conclusion

The lubricant and its application procedure have proven to be extremely reliable. The same coating has also been successfully applied to the roller screw which provides the translation of the instrument collimator. The technology we have applied has proven to be a very simple and cheap alternative for many mechanisms operating in a cryogenic environment.

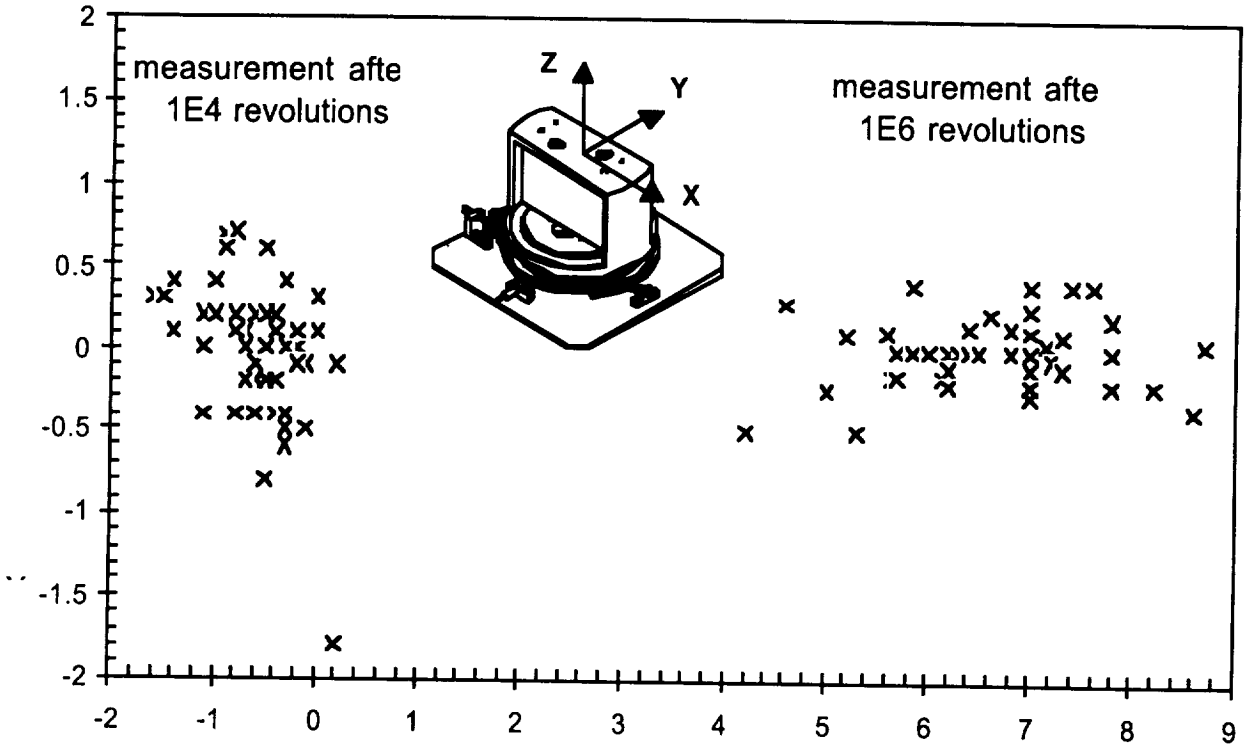

Figure 5. Angular positioning accuracy

References

1. Testard, O.A. "Thermal contact through mechanical moving parts in low thermal budget optical cryogenic assemblies." Cryogenics, (1987), 27-87.
2. Van Seiver, S. "Thermal and electrical contact conductance between metals at low temperature." Proceedings of the Space Cryogenic Workshop, Berlin.
3. Claus, F.J. "Solid lubricant and self lubricant solid." New York: Academic press, 1972.

The Advanced Microwave Sounding Unit-A, Antenna #2 Bearing Assembly Life Test

Charles E. Powers*

Abstract

Four bearing assemblies, lubricated with Apiezon C oil with 5% lead naphthenate (PbNp), were life tested in support of the Advanced Microwave Sounding Unit-A (AMSU-A). These assemblies were tested continuously for five to six years using the scanning pattern of the flight instrument. A post-life-test analysis was performed on two of the assemblies to evaluate the lubricant behavior and wear in the bearings.

Introduction

The AMSU-A will be flown on five National Oceanic and Atmospheric Administration (NOAA) meteorological satellites and the Earth Observing System (EOS) PM. The AMSU-A instrument is built by Aerojet ElectroSystems Company (Azusa, CA) and consists of two scanning dish antennas (AMSU-A1 and AMSU-A2) that measure temperature and humidity at altitudes up to 40 km above the Earth using microwave radiometry.

In January 1991, the Materials Engineering Branch (MEB) at the Goddard Space Flight Center (GSFC) began life testing the first of four bearing assemblies used to support the AMSU-A2. This testing was done to meet GSFC assurance requirements [1], prompted by failures and problems with past scanning instruments and by conclusions in a report published in April 1987 [2]. This report concluded that the antenna position accuracy could degrade due to a decrease in the bearing preload and the depletion of the bearing lubricant. The bearing assembly for the AMSU-A2 was selected for the life test because it will be supporting more weight and will be rotating at a slower speed, thus giving it the more severe operational mode.

The life test was originally scheduled to last four years, which is the mission requirement for the NOAA satellites. In 1995, the life test was extended to meet the six-year mission requirement of the EOS-PM satellite. To achieve the mission equivalent for these satellites in less time, two bearing assemblies were tested using an "accelerated" stepping pattern. The accelerated stepping pattern was similar to the flight pattern, but with reduced dwell times. This allowed these bearing assemblies to complete a four-year mission equivalent in three years of ground testing.

Objectives

The objective of the life test program was to demonstrate that the bearing assembly for the AMSU-A2 will operate within the design specifications for the NOAA and EOS-PM satellites. With this in mind, the MEB pursued the following specific objectives:

- Developed a motion control system to simulate the AMSU-A2 stepping pattern,
- Developed a monitoring system to evaluate bearing performance,

* NASA Goddard Space Flight Center, Greenbelt, Maryland

- Developed a test facility to simulate the space environment,
- Performed a six-year mission equivalent life test on several bearing assemblies,
- Performed a post-life-test analysis to determine bearing/lubricant wear mechanisms.

Experiment

Description of Test Equipment

The equipment used to perform the life test can be described as several systems. These systems include the test fixtures used to house the bearing assemblies, the vacuum system in which the test was performed, the motion control electronics and hardware, and the monitoring system.

Test Fixtures

The fixtures being used for these tests were designed by Swales Associates, Inc. (Beltsville, MD). As shown in Figure 1, a fixture is composed of two sections. One section is used to house and preload the bearing assembly, and the other to house an optical shaft encoder and DC brushless motor. The outer casing and the shaft are electrically isolated so that capacitance measurements can be made across the bearings to monitor lubricant behavior. Isolation is achieved by constructing one end of the outer casing from Delrin and by using a bearingless optical encoder. Electrical contact to the shaft (the inner race of the bearings) is made by pressing a nickel pin against one end of the shaft. Electrical contact to the outer race is made through the outer casing.

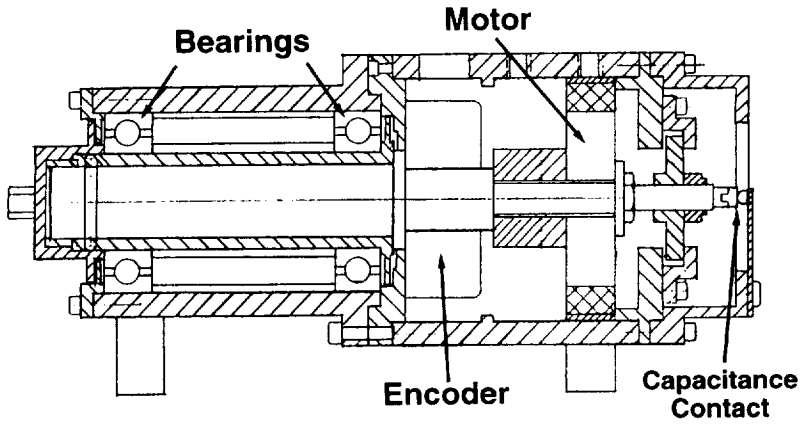

Figure 1. Bearing Assembly Test Fixture (1/2 scale)

Vacuum System

The vacuum system used for the life test is a diffusion pump system. Each fixture (station) is housed in its own chamber that can be isolated from the rest of the vacuum system. Each test chamber also has a viewing port, a port for a pressure gauge, and an electrical feed-through.

Position Control System

The position control system consists of an IBM PC-compatible computer, a control module, a DC brushless amplifier, a DC brushless motor, and an optical encoder for each test station. The computer continuously sends position commands via an RS-232-C communication line to the control module. The control module uses these commands to generate an output voltage that is converted into a motor current by the brushless amplifier. The control module uses the output from the encoder for position feedback. The encoder is a bearingless quadrature incremental encoder with 1200 lines per revolution. By tracking the individual transitions from the encoder (4 per line), the angular position of the shaft can be measured to 0.075°.

Monitoring System

The monitoring system is built around a Macintosh computer with an analog-to-digital interface card. The computer uses a LabVIEW® program to monitor the life test. A high-speed capacitance meter is also a part of the monitoring system. During the life test, the motor current, the bearing electrical capacitance, and encoder outputs from each station were monitored using this system. Each of these quantities was simultaneously sampled at 10 kHz over several cycles of the stepping pattern, three times a week. The room temperature, vacuum pressure, and number of AMSU-A2 cycles were also recorded.

After the data is recorded, the motor current is used with angular position information derived from the encoder outputs to calculate bearing torque. The bearing torque and angular position data are used to determine if the bearings meet the failure criteria for the life test. The bearing capacitance data is used to study the dynamics of the lubricant in the bearings.

Test Conditions

The bearings were tested at room temperature (+22.5 ± 1.5°C) in a vacuum which was typically about 5×10^{-4} Pa (4×10^{-6} torr). The temperature of two test fixtures was measured to be between +36 to +39 °C near the location of the bearing assembly, which is probably close to the actual temperature of the bearing assemblies during the life test. The temperature of the fixture and bearing assembly was above room temperature because of both the heat generated by the motor and thermal isolation of the fixture and vacuum system. The operating range for the flight bearings is expected to be between −10 and +36 °C.

Several differences between the operating conditions of the flight bearing assemblies and the life test units should be noted. The flight assemblies will have a Fluorad barrier film applied to the outside of the bearings. This film will help prevent the lubricant in the bearings from migrating out of the bearings. No barrier film was used with the life test units. The flight bearing assemblies will be supporting a 13.6-kg antenna dish, while the life test assemblies only supported a shaft, motor, and encoder weighing 0.5 kg. The life test assemblies were subjected to gravity, which may have caused an asymmetric loading in the bearings, since they were tested in a horizontal configuration. This orientation may also cause the lubricant to settle at the bottom of the bearings, thus aiding in the lubrication of the bearings. A horizontal configuration was selected to prevent migration of the oil from the bearings and for ease of constructing the test setup.

Description of Bearing Assembly

The bearing assemblies used for this life test have angular-contact duplex bearings made of 440C stainless steel with a nominal preload of 13.6 kg (30 lb). This preload produces a peak hertzian stress of about 900 MPa (125 ksi). The bearing retainers are made of Meldin 9000 polyimide. All four bearing assemblies were manufactured, cleaned, and lubricated by Barden Precision Bearings (Danbury, CT) and came from the flight lot for the NOAA KLM AMSU-A2. Two assemblies received further processing at Ball Aerospace Systems (Boulder, CO), as did the actual flight assemblies. The processing done at Ball included additional cleaning, inspection, and lubrication.

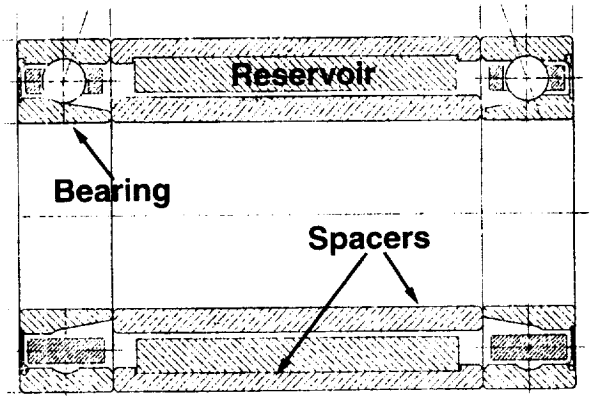

Figure 2. AMSU-A2 Bearing Assembly (actual size)

As shown in Figure 2, the bearing assembly consists of two ball bearings, two spacers and a lubricant reservoir. The reservoir is a porous nitrile-acrylic elastomer ring that is attached to the outer spacer. All bearings, retainers, and reservoirs are impregnated or lubricated with Apiezon C oil with 5% PbNp. The total lubricant weight must be at least 10.2 g.

Table 1. Life Test Matrix

Station #	Full Flight Processing	Accelerated
1		
2		x
3	x	
4	x	x

Description of Test

Table 1 shows the heritage of the four bearing assemblies and how they were tested. The bearing assembly tested in station 1 did not receive the additional processing done on the flight assemblies and was operated using the actual AMSU-A2 stepping pattern (Figure 3). This assembly completed 19.0 million cycles (608 million stop-starts) of the stepping pattern before it was stopped for post-life-test examination. The bearing assembly in station 2 also did not receive the additional processing done on the flight assemblies and was tested using an "accelerated" stepping pattern. Acceleration was achieved by reducing the dwell times in the stepping pattern so that

the shaft takes about 5.5 sec, instead of 8, to complete a revolution. To date, this assembly has completed 25.4 million cycles (813 million stop-starts) of the accelerated AMSU-A2 stepping pattern. The bearing assembly in station 3 received full flight processing and was tested using the actual AMSU-A2 stepping pattern. To date, this assembly has completed 16.8 million cycles (538 million stop-starts). The assembly in station 4 also received full flight processing and was tested using the accelerated AMSU-A2 stepping pattern. This bearing assembly completed 23.9 million cycles (765 million stop-starts) before it was stopped for post-life-test examination. Note that a one-year mission equivalent is about 4 million cycles of the stepping pattern.

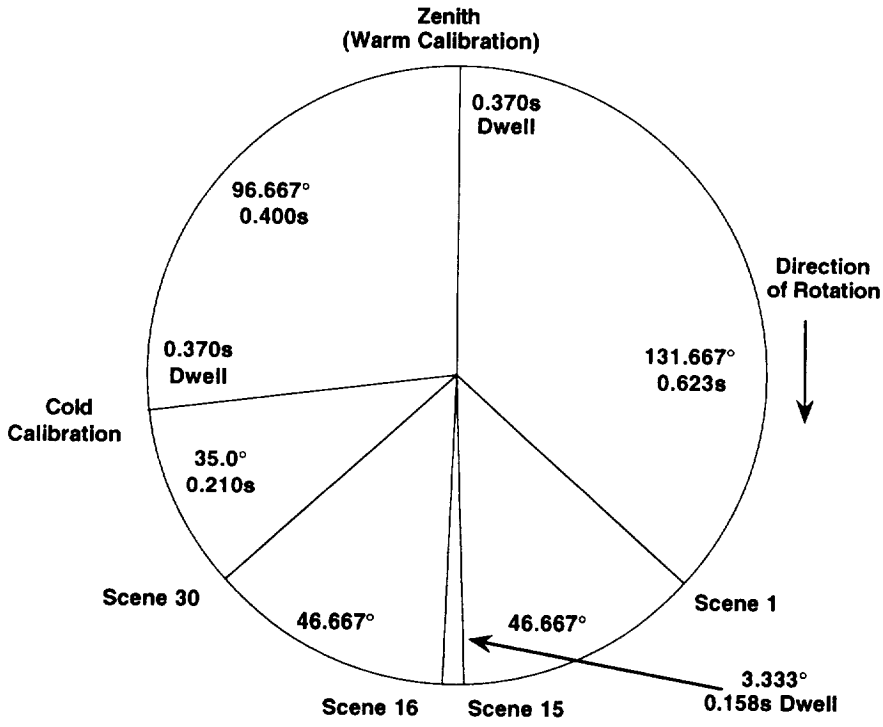

Figure 3. AMSU-A2 Scan Pattern

Failure Criteria

Prior to the start of the life test, two failure criteria were determined for the termination of any particular test station. These criteria are based on the AMSU-A2 positioning accuracy and friction torque specifications [3]. If the bearing assembly causes a deviation from the AMSU-A2 stepping pattern of more than 0.13° during the dwells or if the bearing torque increases three times its initial value, the test will be stopped.

Results and Analysis

Bearing Torque

The torque being supplied by the DC brushless motor is calculated by multiplying the measured motor current and the torque constant for the motor. If the shaft is rotating at a constant angular velocity, the motor torque will equal the bearing torque. The torque

constant for the motors used in these tests is 34 mN•m/amperes ±10%. The instrumentation used to measure the torque (motor current) has a resolution of 0.2 mN•m (5 mA). Since the bearing torque is typically between 1 and 2 mN•m, the signal-to-noise ratio for these measurements is between 5 and 10.

During the AMSU-A2 stepping pattern, there are several times that the shaft is rotating at constant velocity: the 35° slew to the cold calibration position, the 97° slew to the warm calibration position, and the 132° slew to scene 1. The latter of these steps was used to calculate the bearing torque.

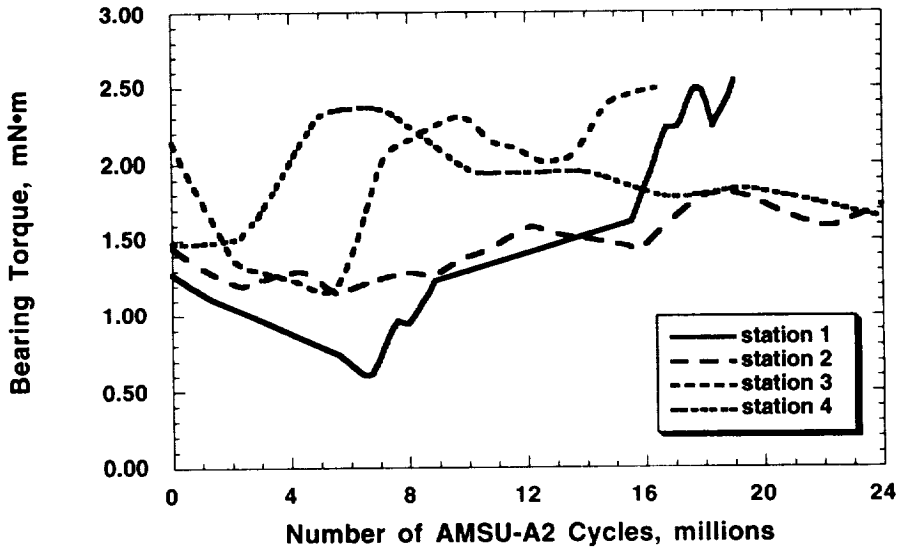

Figure 4. Bearing Torque vs. Number of AMSU-A2 Cycles

The data shown in Figure 4 is a plot of the average bearing torque (calculated during the step to scene 1) versus the number of AMSU-A2 cycles completed for the four bearing assemblies tested. The data was fit to the shown curves using a weighted least-squared error routine with a smoothing factor of 22% to show long-term trending. Smoothing was required because of the low signal-to-noise ratio for these measurements.

Three of the four bearing assemblies had an initial decrease in torque during the first 2 to 6 million cycles, followed by a steady increase for the remainder of the test. The assembly in station 4 was an exception to this behavior. The torque for these bearings was unchanged for the first 2.5 million cycles, followed by an increase to a value 60% above its initial value at 5 million cycles. From 7 to 24 million cycles, the torque slowly decreased to a value 10% above its initial value. None of the bearings exceeded the torque limit set for the life test of three times its initial value.

In all four bearing assemblies, there appears to be periodic increases in torque followed by a decrease, with a typical period of about 6 to 8 million cycles. This behavior is indicative of a deposit or build-up of material until it reaches an unstable amount, which then breaks away [4]. This appears to have occurred several times in each of the assemblies.

Angular Position

Figure 5 shows the angular position data from the optical encoder versus time. This plot shows a couple of the 3.3° steps (scenes) from the AMSU-A2 stepping pattern. The angular position data was graphed and examined visually during the life test to determine if the bearing assemblies were maintaining the required positioning accuracy. All four bearing assemblies operated within the position requirements set prior to the start of the life test.

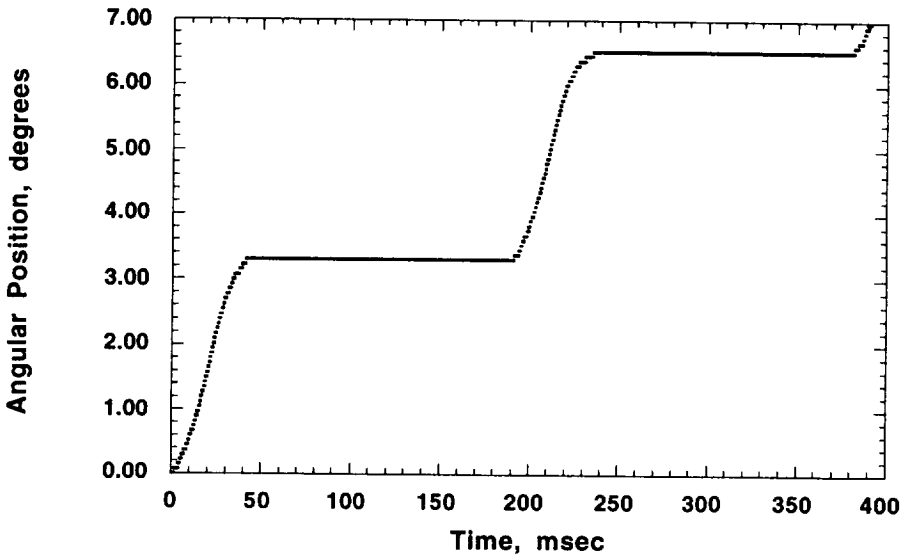

Figure 5. Shaft Angular Position vs. Time

Bearing Capacitance

The capacitance meter has an analog voltage output which is proportional to capacitance. When the meter is shorted across its inputs (infinite capacitance) or the measured capacitance is above the range set on the meter, the analog output will normally go "off-scale" to a value of +3.6 V. When measuring the capacitance of the bearings, the meter puts out a value of –3.6 V (-3600 pF) when shorted by the bearings. This effect is caused by the resistance of the leads (about 1 ohm) between the bearings and the meter. This makes interpretation of the capacitance measurements difficult, since a thinner lubricating film should cause an increase in the capacitance, but, because of the resistive component of the leads, the measured capacitance eventually becomes more negative as the "real" capacitance increases. As a result, these measurements can only be used to determine if metal-to-metal contact (–3600 pF) is occurring, or if there is an elastohydrodynamic lubricating film between the balls and races. These measurements presently cannot be used to determine the thickness of the lubricating film.

The capacitance being measured is that of two bearings with thirteen balls each. Since there are two capacitors per ball (one between the inner race and the ball, and one between the outer race and the ball), the measured capacitance involves 52 separate "capacitors". This makes a bearing in boundary lubrication a very dynamic

system, since some of these "capacitors" can be shorted, while others will have a lubricating film separating the ball from either race.

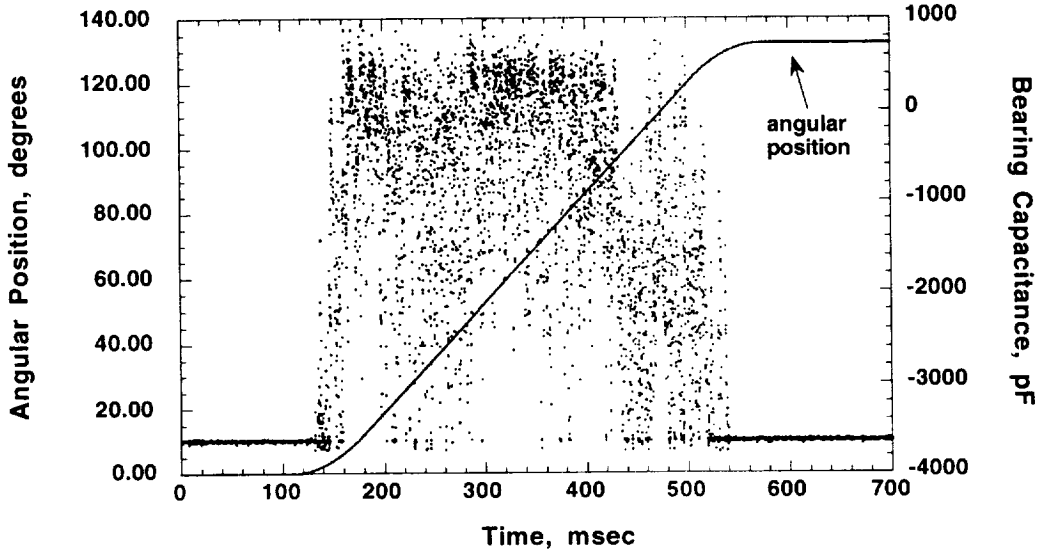

Figure 6. Angular Position and Bearing Capacitance vs. Time

The capacitance measurements shown in Figure 6 indicate that metal-to-metal contact occurs while the bearings are not rotating and becomes partially lubricated when performing a step or slew. This was typical behavior during the early part of the life test for all four bearing assemblies. Later in the life test, the capacitance measurements indicated that metal-to-metal contact was occurring almost continuously. Note that the negative capacitance values are not a true capacitance, but occur from the conversion of negative analog output values into capacitance.

Figure 7 shows the behavior of the measured bearing capacitance versus the number of AMSU-A2 cycles for the bearings tested in station 4. The capacitance values represent the average bearing capacitance during the step to scene 1. The bearing torque is also shown for comparison. This graph shows that the bearing capacitance was about 500 pF for the first 1 million cycles. Thereafter, the capacitance meter was indicating it was mostly shorted (–3600 pF). There were occasional periods during the life test when the capacitance meter indicated some lubrication of the bearings was occurring while they were rotating. These periods seem to correspond with events occurring in the bearing torque. The capacitance measurements from station 4 were typical of all four sets of bearings.

Post-Life-Test Analysis

Upon removal from the test fixture, the bearing assemblies and fixtures from stations 1 and 4 were examined visually. This examination found that all the bearings surfaces were still covered with oil. As shown in Figure 8, about 70–80 mg of oil migrated to fixture surfaces near the bearings.

All bearing components from stations 1 and 4 were weighed before and after the life test. The oil on the test fixture and in the storage bags of the bearing assemblies was

also weighed. These measurements found that the bearing components in station 1 lost about 1.5 of 10.8 g of oil, and the components from station 4 lost 1.3 of 10.7 g. Most of this weight loss was from the reservoir. The bearings themselves actually had an increase in weight. This oil loss was most likely due to evaporation of the lubricant. A small amount of lubricant was probably lost during the handling of the bearings, and a small amount of lubricant was probably lost as a result of some deposition on the bearing surfaces. Thermogravimetric Analysis (TGA) of some oil from one of the reservoirs predicted about a 10% weight loss at 39°C for these two assemblies. This is consistent with the 12 to 14% oil loss that occurred during the life test, since the TGA uses a "softer" vacuum that the life test vacuum system.

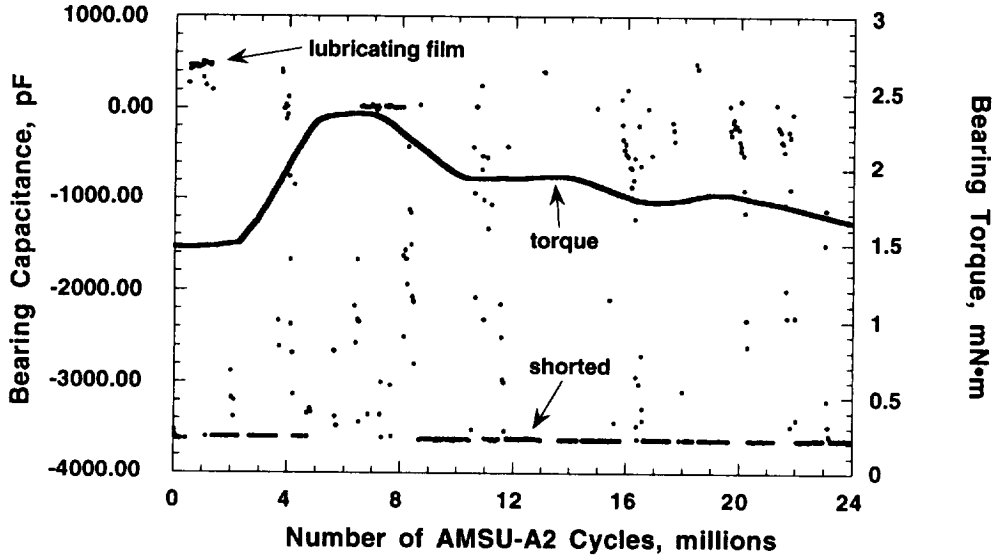

Figure 7. Bearing Capacitance vs. Number of AMSU-A2 Cycles

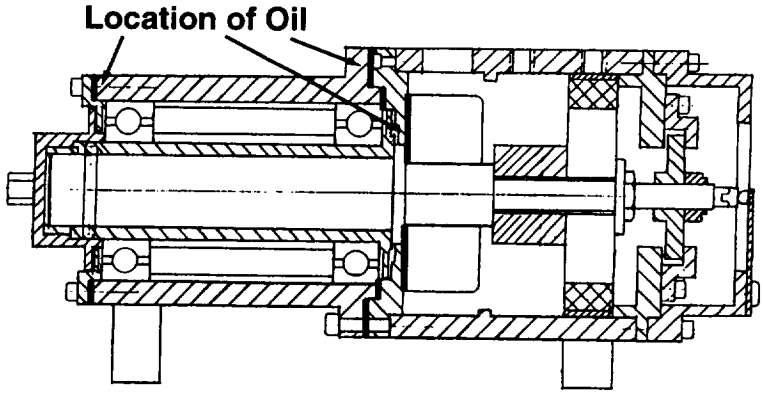

Figure 8. Bearing Assembly Test Fixture (1/2 scale)

Fourier Transform Infrared Spectroscopy (FTIR) of the Apiezon C oil removed from the bearings found a decrease in the PbNp percentage as compared to oil samples from the storage bags of the bearing assemblies. FTIR also found a small amount of a

carbonyl compound in the oil from the bearings. This compound is mostly a breakdown compound from the PbNp or sebacate ester additive in the oil.

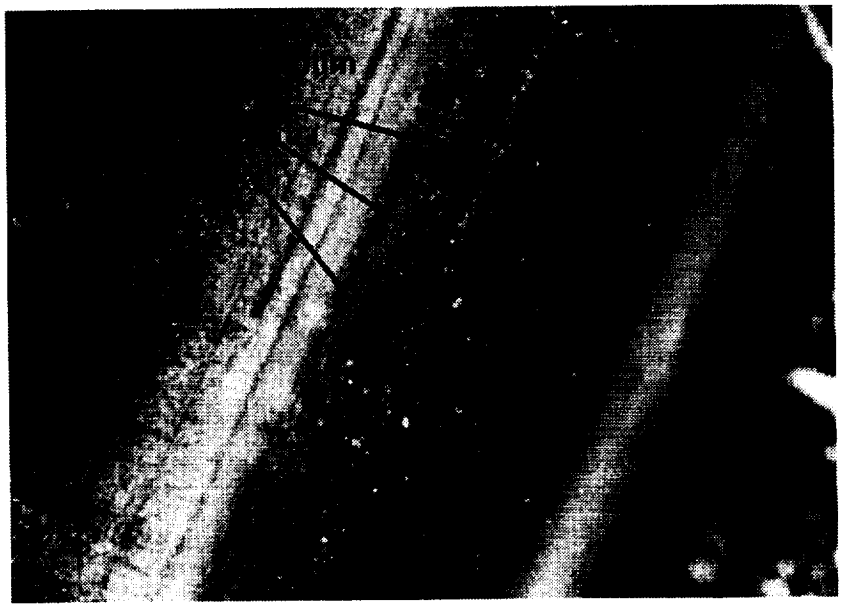

Figure 9. Ball Wear Track on Outer Race (27.5x)

Examination of the bearing balls using Scanning Electron Microscopy found no evidence of wear. X-ray Photoelectron Spectroscopy (XPS) of the balls detected a small amount of partially reacted PbNp on the surface. Visual examination of the inner and outer races also found no wear, but did find black- and brown-colored deposits in the ball wear track. As shown in Figure 9, a black colored deposit formed in the ball wear tracks with brown deposits to either side. The width of the black deposit on the outer race varied between 0.52 and 0.58 mm, which is close to the calculated width of the hertzian contact area of 0.61 mm. The width of the black deposit on the inner race was between 0.58 and 0.69 mm, which is also close to the calculated width of the hertzian contact area of 0.76 mm. Inspection of the ball wear track using a Confocal Scanning Laser Microscope found the deposit to be thinner than the resolution of the instrument (< 1 μm). The microscope also found the surface of the deposit areas to be smoother than adjacent areas of the race, as if the deposit had filled in the tool marks in the ball wear track. There was no evidence of material loss due to wear in either the balls or races.

XPS of the surface of the black and brown deposits found them to be partially reacted PbNp and iron oxide. These findings are similar to those from a previous study of PbNp adsorption on 440C stainless steel [5]. Sputtering into the black deposit found partially reacted PbNp, iron oxide, chromium, and sulfur. Typical 440C stainless steel has an iron oxide and chromium oxide layer on the outer most surface, followed by the bulk material. The sputtering results suggest that the PbNp deposit has reacted with the iron oxide and chromium oxide layer during the life test, since both were found in the deposit. Optical Emission Spectroscopy of some of the Apiezon C oil confirmed that it was the source of the sulfur.

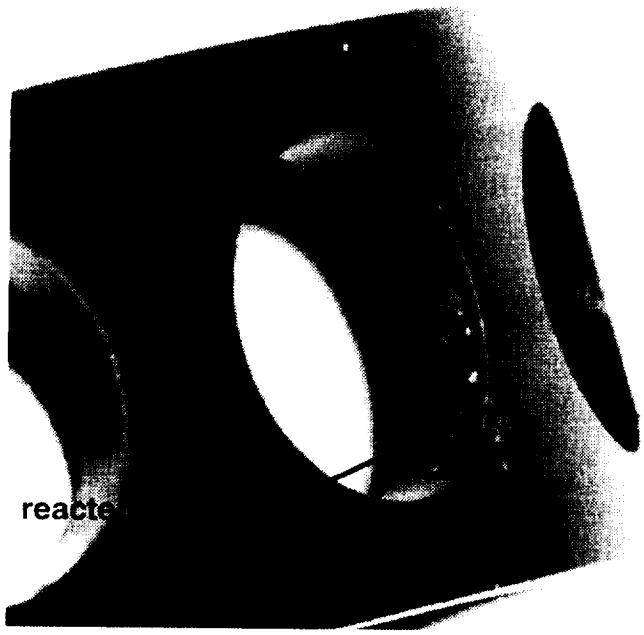

Figure 10. Particles found on Retainer (7.5x)

Visual examination of the bearing retainers found worn areas in the ball pockets that also appear to have the same black deposit that was found on the races (Figure 10). Foil-like particles were also found on the retainers. XPS found these particles to be partially reacted PbNp and sulfur. The composition of these particles is similar to the deposits in the ball wear tracks, except for the lack of iron oxide and chromium. These findings, as well as those in the bearing torque data, suggest that a build-up of partially reacted PbNp is occurring in the ball wear tracks and/or the retainer ball sockets with some of it eventually breaking free.

Conclusions

All four bearing assemblies operated within the AMSU-A2 flight specifications (positioning accuracy and friction torque limits) for the duration of the life test (4.2 to 6.4 years mission equivalent). The largest torque increase occurred in the station 1 bearings, which doubled after operating for 4.8 years mission equivalent. This change is below the 3x increase allowed for the AMSU-A2. The largest torque increase observed in the flight processed bearings was 60% and occurred in the station 4 bearings after 5 million cycles, followed by a steady decrease to the end of the life test. Based on these results, the bearing assemblies for the AMSU-A1 and AMSU-A2 should meet the mission requirements for both the NOAA and EOS-PM satellites.

The use of an accelerated stepping pattern has shown no observable effect on the performance or wear of the bearings. The post-life-test analysis found identical wear characteristics in both the nominal and accelerated bearings. Therefore, acceleration of the life test by reducing the dwell times did not affect the lubricant behavior and is a valid means of testing these bearing assemblies.

As mentioned previously, there was concern that the loss of lubricant would affect the performance of the bearings [2]. Even though there was a decrease in the total amount of oil on the bearing components, there was an increase in the amount of lubricant on the bearings. This demonstrates that the lubricant reservoir performed as designed, maintaining an oil supply to the bearings for the duration of a mission. The post-life-test analysis also found little (if any) degradation of the lubricating oil.

The preload in the bearings was not measured during or after the life test. Also previously mentioned, there was some concern about the loss of preload due to wear [2]. The analysis found no wear in the balls or ball wear track but did find a partially reacted PbNp film in the ball wear track. These results suggest that the preload did not change during the life test.

Little wear of the bearing metal surfaces was observed in either bearing assembly examined. A partially reacted PbNp film was observed in the ball wear tracks on both inner and outer races, and most likely in the ball pockets of the retainers. Flakes of partially reacted PbNp were also found in the ball sockets of the retainer. These findings are consistent with the periodic increases and decreases observed in the bearing torque data. These results together suggest that a deposit is forming on the races and/or in the ball pockets of the retainer until it reaches a critical thickness, when some of it then breaks away. This build-up of a partially reacted PbNp film may also explain the capacitance measurements which mostly indicated metal-to-metal contact only a few million cycles into the life test. With a layer of material in the ball wear track, there will be less clearance between the balls and races for lubricant to flow. The presence of flakes in the bearings may also be causing shorting of the capacitance meter to occur as well.

Acknowledgments

The author would like to recognize the many contributors to this bearing study over the past seven years. I would like to recognize Carl Taylor, who has faithfully gathered and stored the data from this test for the last five years. I would also like to thank Bruno Munoz for his support in maintaining the life test equipment. I would like to recognize Alex Montoya, Gloria Park, and Joanne Uber for all their excellent work on the post-life-test analysis. Other members of the Materials Engineering Branch who have also supported this study include Mary Ayres-Truesdell, Mike Barthelmy, Betsy Forsbacka, Patricia Friedberg, Peggy Isaac, Diane Kolos, Mark McClendon, Joe Petitto, Roamer Predmore, Jackie Townsend, Tim Van Sant, Mike Viens, Carl Walch, and Len Wang. I would like to thank Ed Devine of Swales for designing the test fixtures and for his many consultations before and during the life test. I would like to thank Al Conti of Barden for supplying all the pre-life-test data on the bearings. This study was also supported by Claef Hakun, Sid Johnson, and Claudia Woods of the Electromechanical Systems Branch at GSFC. Financial support from the NOAA Project Office is also greatly appreciated.

References

1. Goddard Space Flight Center publication entitled "Guidelines for Standard Payload Assurance Requirements (SPAR) for GSFC Orbital Projects", pp. 7-S, 5-I, 7-5, March 1990.
2. Aerojet ElectroSystems Company report #8187-1 entitled: "Limited-Life List for the Advanced Microwave Sounding Unit-A (AMSU-A)", pp. 2-3, April 1987.
3. Aerojet ElectroSystems Company report #8172A entitled: "Preliminary Design Review for the Advanced Microwave Sounding Unit -A (AMSU-A)", pp. 2-68 - 2-69, June 1987.
4. Blau, P.J., Friction and Wear Transitions of Materials, pp. 385-396, Noyes Publications, Park Ridge, NJ, 1989.
5. Didziulis, S.V. and Fleischauer, P.D., "Chemistry of the Extreme-Pressure Lubricant Additive Lead Naphthenate on Steel Surfaces," LANGMUIR, 1991, 7, pp. 2981-2990.

02712-7

The GSFC Combined Approach of ODC Stockpiling and Tribological Testing to Mitigate the Risks of ODC Elimination

278 756

p. 14

Roamer Predmore* Claudia LeBoeuf* and Andrew Hovanec**

Abstract

In response to the elimination of production of several Ozone Depleting Chemicals (ODCs) which have been widely used in successful space flight mechanism cleaning and lubricating procedures, GSFC developed and implemented an overall philosophy of mitigating the risks to flight hardware during the transition phase to ODC-free cleaning procedures.

The short term leg of the philosophy was the stockpiling of an appropriate amount of ODC solvents such that all short term GSFC missions will be able to stay with or revert to heritage cleaning and lubricating procedures in the face of life issues. The long-term leg of that philosophy was the initiation of a several tier testing program that will deliver increasing amounts of information over the next few years, starting with accelerated lubricant life tests that compare lubricant life on surfaces cleaned with ODC solvents with lubricant life on surfaces cleaned with ODC-free solvents.

While tribological testing, mechanism life testing and space-flight experience will ultimately bring us into the 21st century with environmentally friendly means of cleaning long-life precision mechanism components, many satellites will be launched over the next few years before a number of important tribological questions can be answered. In order to prepare for this challenge, the Materials Engineering Branch in cooperation with the Electromechanical Branch launched an intensive review of all ongoing missions. The failure risk was determined for each long-life lubricated mechanism based on a number of parameters, including a comparison of flight solvents used to clean the heritage/life test hardware. Also studied was the ability of the mechanism manufacturers to stockpile ODCs based on state laws and company policies. A stockpiling strategy was constructed based on this information and subsequently implemented.

This paper provides an overview of the GSFC ODC elimination risk mitigation philosophy as well as a detailed examination of the development of the ODC stockpiling plan.

Introduction

For many years, the successful heritage of most long life lubricated mechanisms for satellites has been based on cleaning procedures which utilize the chlorofluorocarbon solvent CFC-113 and 1,1,1,-trichloroethane (1,1,1-TCA). Most satellites require long life lubricated mechanisms for successful orbital operation

* Goddard Space Flight Center, Greenbelt, MD
** Unisys, Goddard Space Flight Center, Greenbelt, MD

up to 10 years. Spacecraft use reaction wheels, momentum wheels, antenna gimbals, solar array drives, gyros and despin mechanisms for control and power acquisition. Satellite instruments require spatial scan mechanisms, spectral scan mechanisms and focus mechanisms for scientific and earth observations. In order to qualify a lubricated mechanism, a successful mechanism life test for up to 5 years or an orbital heritage for 10 or more years has to be successfully accomplished.

Elimination of Ozone Depleting Solvents

In 1993, GSFC discovered that the Montreal Protocol had mandated the termination of CFC-113 and 1,1,1-TCA solvent production at the end of 1995. In September 1994, lubrication engineers and members of the Montreal Protocol Solvents Committee held a workshop in Denver to assess the state-of-the-art of new ODC-free cleaning process development, requirements imposed by the Montreal Protocol and the requalification status of heritage lubricated mechanisms [1]. The workshop entitled "Non-Ozone Depleting Chemical Cleaning and Lubrication of Space System Mechanical Components for Multi-Year Operations," was sponsored by Aerospace Industries Association, The Aerospace Corporation, Air Force Space and Missile Systems Center, International Cooperative For Ozone Layer Protection, Instrument and Bearing Working Group, Draper Laboratory, NASA, Honeywell, Inc. and EPA.

The workshop discovered that most bearing manufacturers, spacecraft mechanism suppliers and satellite instrument fabricators had or were about to remove ODC solvents from their cleaning processes which had been qualified for long life space mechanisms. To resolve the requalification problem of heritage mechanisms, the workshop recommended stockpiling CFC-113 and 1,1,1-TCA to extend the use of heritage mechanisms, repeat life testing to requalify mechanisms cleaned with ODC-free solvents and conduct generic lubricant life studies with ODC and ODC-free solvents in an attempt to show that ODC-free cleaning processes did not degrade lubricant life and therefore eliminate the necessity for requalification. Short life satellite and rocket lubricated mechanisms were not included because they could be requalified quickly with a short duration life test. Aircraft mechanisms were not included because they are redundant and receive periodic maintenance.

Inadequate Time for Mechanism Requalification

After the Denver Workshop in September 1994, GSFC tribologists had to define stockpile needs for all the long life mechanisms on GSFC satellites and persuade the project managers to purchase a stockpile of CFC-113 and 1,1,1-TCA solvents. In early 1995, GSFC discovered that manufacturing of CFC-113 and 1,1,1-TCA was scheduled to be terminated by the suppliers in April 1995 instead of December 1995.

The Materials Engineering and Electromechanical Branches proposed a stockpiling plan to the Engineering Directorate, Flight Projects Directorate and the Office of Flight Assurance in March 1995. With the support of project management, resource management, procurement, safety logistics and all GSFC flight hardware contractors, the survey team reviewed CFC-113 and 1,1,1-TCA usage in manufacturing all long life lubricated mechanisms.

ODC/ODC-Free Solvent Usage Survey Questions

In order to provide a reasonable estimate of GSFC stockpiling needs, it was necessary to develop a database of cleaning procedure information from all current GSFC projects. One of the main objectives was to ascertain which mechanism suppliers were either still using ODC cleaning procedures or were in the process of switching from ODC to ODC-free processes but had not completed the mechanism requalification after cleaning with their new procedures.

Long life lubricated mechanism suppliers were asked the following survey questions:

1. Which company supplied the bearings?
2. Which ODC and ODC-free cleaning solvents were used for each mechanism?
3. What is the distribution of your ODC and ODC-free cleaned bearings in flight, life test, and heritage mechanisms?
4. Which solvents were used to clean the long life mechanisms that were originally qualified by life tests or successful flight heritage?
5. What requalification is being planned after you switch to ODC-free cleaning solvents?
6. Are you stockpiling ODC solvents in order to continue ODC solvent cleaning until ODC-free cleaned mechanisms are requalified?
7. Who is your company executive responsible for environmental policy decisions?

Criteria for Stockpiling ODC Solvents

If the mechanism and bearings had been cleaned with ODC-free solvents and had successful space flight heritage or had completed a life test, the mechanism was qualified and ODC solvent stockpiling was unnecessary. If companies had stockpiled ODC solvents to continue building heritage mechanisms, there was no need for GSFC to stockpile solvents to support fabrication of the heritage mechanism.

Most companies are under extreme public pressure to comply with the Montreal Protocol and therefore they will not stockpile ODC solvents. Many companies were reluctant to use ODC solvents even though ODC solvent usage is acceptable under the Montreal Protocol. Therefore, GSFC had to stockpile the ODC solvents

and provide the solvents to the mechanism suppliers until the mechanisms could be fabricated with ODC-free solvents and requalified.

All precision bearing manufacturers have implemented ODC-free cleaning methods in the past few years for all of their bearings. Therefore, even if the mechanism manufacturer was using the heritage cleaning procedure for the current flight unit, the overall cleaning history of the mechanism bearings was quite likely different due to the changes in the bearing manufacturers cleaning methods. Unless life testing had been repeated with ODC-free cleaned bearings, solvent stockpiling and requalification were planned.

Space mechanisms that operate at slow speed or possess a stop/start motion operate in the boundary lubrication regime. Moving metal parts are in constant contact during boundary lubrication and therefore sensitive to surface chemistry changes. Stockpiling ODC solvents was accomplished for mechanisms that operate in the boundary lubrication regime and used to fabricate the mechanisms until requalification is completed for the ODC-free solvent cleaned versions of the mechanisms.

The newly developed low outgassing synthetic hydrocarbon (Pennzane) will accept boundary lubrication additives and has great potential for use in all lubricated space mechanisms. Several GSFC mechanisms have been lubricated with Pennzane and are being life tested but only one mechanism has flown. Stockpiling was accomplished for these mechanisms so that the low outgassing Braycote 815Z or Krytox could be used as a replacement if the Pennzane lubricated mechanisms fail life testing.

The perfluoropolyalkylethers (PFPE) like Braycote 815Z or Krytox oils will not dissolve boundary additives and have been found to autocatalytically break down to form solid polymers in the presence of bare iron surfaces [2, 3]. CFC-113 is the solvent used for PFPE cleaning. Preliminary data has shown that ODC-free cleaning methods have accelerated the PFPE breakdown process. All long life mechanisms which had or were continuing to use a PFPE lubricant were candidates for ODC stockpiling. Stockpiled CFC-113 solvent will be used until ODC-free solvent cleaned mechanisms can be requalified by life testing.

CFC-113 and 1,1,1-TCA Solvent Stockpile

The list of long life lubricated satellite mechanisms and the satellite instruments with their associated solvent stockpile quantities are shown in Table 1, ODC/ODC-Free Cleaning Survey.

The first column lists the GSFC project and satellite. The second column identifies the spacecraft long life lubricated mechanisms. The third column lists the instruments on the satellite. The fourth column identifies the qualification status, potential failure status, heritage status, stockpiling status and other information

used to identify stockpiling needs. The fifth column shows examples of solvent stockpile quantity computations. The sixth column lists the CFC-113 solvent quantity selected for each mechanism. Column seven lists the quantity of 1,1,1-TCA selected for each mechanism. The lubricant, cleaning processes, qualification status and project schedule were compared with the criteria for stockpiling in order to select the quantity of solvent to stockpile. With only a few months to stockpile, GSFC stockpiled 1055 gallons of CFC-113 and 122 gallons of 1,1,1-TCA.

Since the stockpile was purchased in May 1995, CFC-113 has been used by Miniature Precision Bearing, Aerospace Corp., Lockheed Martin Missiles & Space, Wedeven and Assoc., and Marshall Space Flight Center for the generic study of ODC-free cleaning effects on lubricant life. The Bearing Consultants used CFC-113 for bearing failure analysis. Barden used CFC-113 to process flight bearings like the bearings that are flying. Hubble Space Telescope (HST) needed 250 gallons of CFC-113 to fabricate additional gyros in December 1995 but was able to purchase the solvent from warehouse stocks. If Goddard has need for four more future applications like HST, the GSFC stockpile will be gone.

Accelerated Lubricant Life Testing

The NASA Chief Engineer's Office is sponsoring a generic study of ODC-free cleaning processes on lubricant life. Marshall Space Flight Center is leading the NASA study. Three existing accelerated lubricant life testing techniques were selected because there was very little time to identify ODC-free cleaning effects on lubricant life if any. None of the accelerated lubricant life test methods had demonstrated the capability of measuring the effect of cleaning on lubricant life when the testing started.

The transient elastohydrodynamic apparatus at Lewis Research Center consists of inner and outer race drive motors (the latter containing a torque sensor) and a loading mechanism [4]. The upper bearing is an AISI 52100 steel test bearing. The outer race of this bearing is driven by a synchronous hysteresis motor through a toothed belt drive. A keyed bushing is press-fit into the inner race. The load ring is keyed into the bushing and a spindle, which is driven by a second synchronous motor through another toothed belt drive. This allows the bearing to be run in a counter-rotating mode, where the races spin in opposite directions such that the ball complement is stationary. The bearing is loaded axially through the load ring and the central load shaft that extends down through the spindle. A lever arm system and a scissors jack are used to load the shaft. The four lower bearings provide support and alignment.

The bearings were cleaned with UV-ozone, super critical carbon dioxide, and Freon 113 [5]. Only the balls in the retainerless test bearings were lubricated with 3 to 6 milligrams of perfluoropolyether oil based on hexafluoropropene oxide (Krytox 143 AC) and rotated at a 4600 rpm effective speed in dry air. When the preset values of bearing temperature, lubricating film capacitance or resistance warned of

imminent test bearing failure, the test apparatus would automatically shut off. The variation in residual surface chemistry from the cleaning processes produced a 50% reduction in life for the UV-Ozone cleaning and a 70% reduction in life for super critical carbon dioxide cleaning when compared to Freon 113 cleaning (Figure 1) [5].

The second accelerated lubricant life test apparatus that is being utilized is the Lewis Research vacuum rolling element tribometer [6]. The vacuum tribometer is a retainerless steel thrust bearing with three balls placed symmetrically on flat plates. The top plate rotates at 4 rpm and drives the 12.7-mm-diameter balls to roll in an near circular 21-mm orbit on a stationary bottom plate. The orbit is a spiral with the balls moving out 0.5 mm per revolution. A guide plate pushes the balls back to the 21 mm diameter location and measures the return force. The 445 N (100 lbf) load produces approximately a 1.39 GPa (200 ksi) hertzian stress. The balls are dip coated with approximately 100 micrograms of oil that results in an approximate film thickness of 100 nm (4 microinches). Gaseous tribological reaction products will be continuously monitored with an in situ residual gas analyzer.

Krytox, Brayco 815Z and Pennzane oils will be tested with plates cleaned in ODC Freon 113 and ODC-Free aqueous Brulin, UV-ozone and supercritical carbon dioxide. The accelerated lubricant life will be determined by an increase in the guide plate force or friction force and oil degradation as shown by x-ray photoelectron spectroscopy and Raman microspectroscopy.

The third accelerated lubricant life test apparatus utilized was The Aerospace Corporation's bearing test fixture operated as a lubricant screening test in an eccentric motion mode [7]. A modified GT-1 thrust bearing is used in the test, with a grooved upper race of AISI 52100 steel, twelve 440C balls (a stamped steel ball retainer separates the balls) and a flat 440C disk counterface. The rotation axis of the flat disk is intentionally misaligned with the axis of the thrust race, creating an eccentric motion that forces the system into a mixed/boundary lubrication regime at the ball/flat interface at high speeds (1800 rpm for these tests). A fixed amount of lubricant is applied to the bearing at the start of a test. The test load is applied by a spring loaded plate mounted on the upper thrust race housing. This upper race housing is mounted to the test fixture via aluminum flexures, and the bearing reaction torque is monitored by a proximity gauge attached to the housing. The fixture is contained with a turbomolecular-pumped ultrahigh vacuum chamber, which has a base pressure of $1 \cdot 10^{-9}$ torr and a typical operating pressure of $1 \cdot 10^{-7}$ torr. Tests have been conducted on bearings cleaned with various processes. Preliminary results have suggested that the ODC-free Brulin aqueous detergent reduces the life of bearings lubricated with Bray 815Z relative to bearings cleaned with Freon 113. Tests are continuing with alternative fluorinated solvents.

Life Testing of Long Life Lubricated Space Mechanisms

Preliminary data from accelerated lubricant life testing has shown that ODC-Free aqueous Brulin, UV-ozone and supercritical carbon dioxide cleaning methods reduce the lubricant life substantially. In order to access impact on actual lubricated space mechanisms, actual flight bearings have to be tested to evaluate the effect of ODC-Free cleaning. Mr. S. Loewenthal of Lockheed Martin Missiles & Space has developed a bearing life test capability to measure the life of space flight bearings, lubricants and cleaning methods [8, 9].

Computer-controlled bearing test rigs are used for the life tests. Bearing torque and torque ripple are continuously monitored. Eight pairs of hard-preloaded (rigidly clamped), precision angular contact ball bearings are circumferentially spaced inside each vacuum bell jar tester. Turbo-molecular pumps provide clean vacuum levels of $1 \cdot 10^{-6}$ Torr. The bearings are fitted into individual bearing cartridges. Each cartridge is grounded to the base plate through a strain gage flexure system which measures the reaction torque acting on the bearing pair. A central drive motor system drives a large collector gear through a rotary, ferrofluidic vacuum feedthrough. The collector gear meshes with gear pinions fixed to the bearing cartridge spindle and thus provides inner race rotation. A computer was used to drive the test stand motors over a scan cycle of ± 12.5 degrees of revolution or less than one ball spacing as well as record the torque signature data on disk for later analysis.

Duplex pairs of ABEC 7 Miniature Precision Bearing 2532 angular contact bearings containing 34 grade 10 balls were utilized. The balls and races were made from AISI 440C stainless steel. The balls were separated with Teflon toroids. Preload was set to provide a peak mean hertzian stress of 0.75 GPa (110 ksi), which is much higher than flight instrument bearings. Bearing pairs were cleaned with ODC Freon 113, ODC-Free Brulin aqueous, ODC-free Dupont Vertrel XF and ODC-free 3M PF-5052 cleaners. They were lubricated with Brayco 815Z or Pennzane 2001 oil. When the bearings built up torque bumps at the ends of the cycle and the lubricant was visually degraded, the test was stopped, disassembled and analyzed. Although most bearings are running over 50 million cycles, some bearings started to fail life testing after 35 million cycles which demonstrated that none of the cleaning methods caused catastrophic short term failure. The details of the testing and early results can be found in Ref. 10.

New Long Life Lubricated Mechanism Designs

New lubricated mechanism designs should be qualified with a life test of actual flight hardware. If the bearings and new mechanisms are cleaned with ODC-Free cleaning processes, the cleaning processes will be qualified by the life test along with all features of the new design.

Heritage Long Life Lubricated Mechanisms

Heritage mechanisms lose their qualification when the original ODC cleaning processes are replaced with new ODC-Free cleaning processes. Requalification requires repeating the life test with the new ODC-Free cleaning processes. If the schedule will not allow a life test to be repeated before the satellite launch date, mechanism fabrication can be continued with stockpiled ODC solvents while the repeat life test is completed with the ODC-Free cleaned hardware. For Goddard Space Flight Center satellites, ODC solvents are available to temporarily continue fabrication until life tests are completed and the mechanisms requalified. For NASA satellites, stockpiled Freon 113 or 1,1,1-TCA may be available through Goddard Projects.

Acknowledgments

The authors thank the GSFC project managers, Mr. W. Denoon of the Office of Flight Assurance, Mr. B. Keegan, Mr. E. Powers and Mr. K. Hinkle of Engineering Directorate, Ms. D. Williams, Mr. T. White and Mr. L. Ramsey, Management Operations Directorate, Mr. G. Warner and E. Stuckrath, Cortez, the Electromechanical Branch members and the Materials Engineering Branch members for their assistance. Without the Goddard team effort, the stockpiling task would not have been accomplished.

References

1. Non-Ozone Depleting Chemical Cleaning and Lubrication of Space System Mechanical Components for Multi-Year Operations--Workshop, Sponsored by Aerospace Industries Association, The Aerospace Corporation, Air Force Space and Missile Systems Center, International Cooperation for Ozone Layer Protection, Instrument and Bearing Working Group, Draper Laboratory, NASA, Honeywell, Inc, EPA, Denver, Colorado, September 26/27, 1994

2. W.R. Jones, Lewis Research Center; O.O. Ajayi, A.J. Goodell, L.D. Wedeven, Wedeven Associates; E. Devine, Swales and R.E. Predmore, Goddard Space Flight Center; Enhancement of Perfluoropolyether Boundary Lubrication Performance. I. Preliminary Results, NASA TM-10937, June 1995

3. P. Herrera-Fierro, W.R. Jones and S.V. Pepper, Interfacial Chemistry of a Perfluoropolyether Lubricant Studied by XPS and TDS, J. Vac Sci. Tech. A., 11(2), P 354, (1993)

4. Schritz, B., Jones, W.R., Jr., Prahl, J., and Jansen, R., "Parched Elastohydrodynamic Lubrication: Instrumentation and Procedure," Trib. Trans., 37, 1, (1994)

5. W.R. Jones and T.T. Toddy, Lewis Research Center; R.E. Predmore, Goddard Space Flight Center; B. Shogrin, Case-Western Reserve University and P. Herrera-Fierro, Ohio Aerospace Institute, The Effect of ODC-Free Cleaning Techniques on Bearing Lifetimes in the Parched Elastohydrodynamic Regime, Aerospace Environmental Technical Conference, Huntsville, Alabama, August 6-8, 1996

6. Pepper, S. V., E. Kingsbury and B. T. Ebihara, "A Rolling Element Tribometer for the Study of Liquid Lubricants in Vacuum," NASA Technical Paper 3629, October 1996

7. Kalogeras, C., M. Hilton, D. Carre, S. Didziulis and P. Fleischauer, "The Use of Screening Tests in Spacecraft Lubricant Evaluation," TR-93(3935)-6, The Aerospace Technology Operations, El Segundo, CA, Oct. 1993

8. Loewenthal, S. H., and G. Hopple, "Life of Liquid and Solid Film Lubricated Gimbal Bearing", International Rolling Element Bearing Symposium 1994, San Diego, CA, April 11-14, 1994.

9. Loewenthal, S. H., R. G. Chou, G. B. Hopple and W. L. Wenger, "Evaluation of Ion-Sputtered Molybdenum Disulfide Bearings for Spacecraft Gimbals," Tribology Transactions, V. 37(1994), 3, p. 505

10. Loewenthal, S. H., W. Jones, J. Grout, R. Predmore and R. Thom, "Instrument Bearing Life with Non-CFC Cleaners," Fourth International Rolling Element Bearing Symposium, Orlando, Fl, April 1997

TABLE 1
ODC/ODC-Free Cleaning Survey

PROJECT	Spacecraft Mechanism	Satellite Instrument	CFC - 113 Stockpiling Rationale	CFC - 113 Stockpile Computation Gal.	CFC - 113 Stockpile 4/26/95 Gal.	1,1,1 TCA Stockpile Gal.
LANDSAT 7	X- Band Antenna Gimbals		1 of 2 Life Tests	0.5 x 50 = 25	25	6
	Solar Array Drive		Failures - New	0.5 x 50 = 25	25	6
	Reaction Wheels Assy.		Heritage			
				LANDSAT 7 Total	**50**	**12**
HST	Fine Guidance System		Fabrication of Bearings & Mechanism		40	
	Reaction / Momentum Wheels				0	
	Solar Array Drive				0	
	Gyros				0	
	CATS				5	
	FSS / BAPS Ring Gear / CDU / 10 Latches				0	
	SI Latches		Retain Flight Heritage		5	
	SAC		Short Life / Seldom Lubed		5	
	ORUC LIS/FSIPE		Short Life		5	
		NICMOS			55	14
		STIS			55	14
		ACE			110	28
				HST Total	**280**	**56**
EOS - AM	Solar Array Drive		In Life Test	0.5 x 80 = 40	40	10
	High Gain Antenna Gimbal		In Life Test (No Heritage)	0.5 x 80 = 40	0	10
	Reaction Wheel Assy.		No Life Test or Heritage		50	
	Earth Sensor Assy.				20	
	Inertial Reference Unit		NAVY Stockpiling at Kearfott		20	
		CERES	In Life Test		0	20
		MISR	JPL Stockpiling		0	
		MOPITT			0	
		MODIS	8152 Heritage		20	
				EOS - AM Total	**150**	**40**

TABLE 1
ODC/ODC-Free Cleaning Survey

PROJECT	Spacecraft Mechanism	Satellite Instrument	CFC - 113 Stockpiling Rationale	CFC - 113 Stockpile Computation Gal.	CFC - 113 Stockpile 4/26/95 Gal.	1,1,1 TCA Stockpile Gal.
EOS - PM	Reaction / Momentum Wheels				40	
	Solar Array Drive				0	
	Gyros				0	
	High Gain Antenna Gimbal				0	
		AIRS	JPL Stockpiling		0	
				EOS - PM Total	**40**	**0**
ACE	N/A	N/A			0	
				ACE Total	**0**	**0**
METSAT	Solar Array Drive				10	
	Reaction Wheels Assy.				400	
	Gyros				?	
		AVHRR	ITT Stockpile		0	0
		HIRS	ITT Stockpile		0	0
		SBUV	Ball Stockpile		0	
		AMSU			0	
				METSAT Total	**410**	**0**
XTE	Solar Array Drive		Passed Life Test		0	
	Antenna Gimbal		Passed Life Test		0	
	Momentum Wheels		In Life Test		0	
		ASM			15	
		HEXTE			15	
				XTE Total	**30**	**0**
TRMM	Solar Array Drive		In Life Test		0	
	Antenna Gimbal		In Life Test		0	
	Momentum Wheels		In Life Test		0	
		VIRS	In Life Test & Bearing Stockpile		0	
				TRMM Total	**0**	**0**
SMEX	Momentum Wheels				0	
	Gyros				0	
				SMEX Total	**0**	**0**
TOMS	Momentum Wheels		In Life Test		0	

TABLE 1
ODC/ODC-Free Cleaning Survey

PROJECT	Spacecraft Mechanism	Satellite Instrument	CFC - 113 Stockpiling Rationale	CFC - 113 Stockpile Computation Gal.	CFC - 113 Stockpile 4/26/95 Gal.	1,1,1 TCA Stockpile Gal.
	Gyro				0	
		TOMS	1 of 3 Instrument Failure		55	9
				TOMS Total	**55**	**9**
SSBUV		SSBUV	Instrument Failure		0	5
				SSBUV Total	**0**	**5**
AXAF		XRS			0	
				AXAF - XRS Total	**0**	**0**
GGS	Despin Platform		Passed Life Test		0	
				GGS Total	**0**	**0**
GOES	Solar Array Drive				0	0
	Momentum Wheel Assy.		Heritage		0	0
	Gyro (DIRA)		Northrop		40	
		IMAGER	ITT Stockpile & Life Test		0	0
		SOUNAR	ITT Stockpile & Life Test		0	0
				GOES Total	**40**	**0**
				Lubricated Mechanisms Total	**1055**	**122**
BLDG. 29	Quadex Cleaner				275	0
				BLDG. 29 Total	**275**	**0**
					[illegible]	[illegible]
				Total Volume Gal.	**1385**	**122**
					[illegible]	[illegible]
				Total Cost ‡	**$ 208,013**	**$ 1,245**

† CFC-113 = 13.06 lbs/Gal. ; 1,1,1-TCA = 10.97 lbs/Gal.

‡ CFC-113 = $11.50/lb. ; 1,1,1-TCA = $0.93/lb.

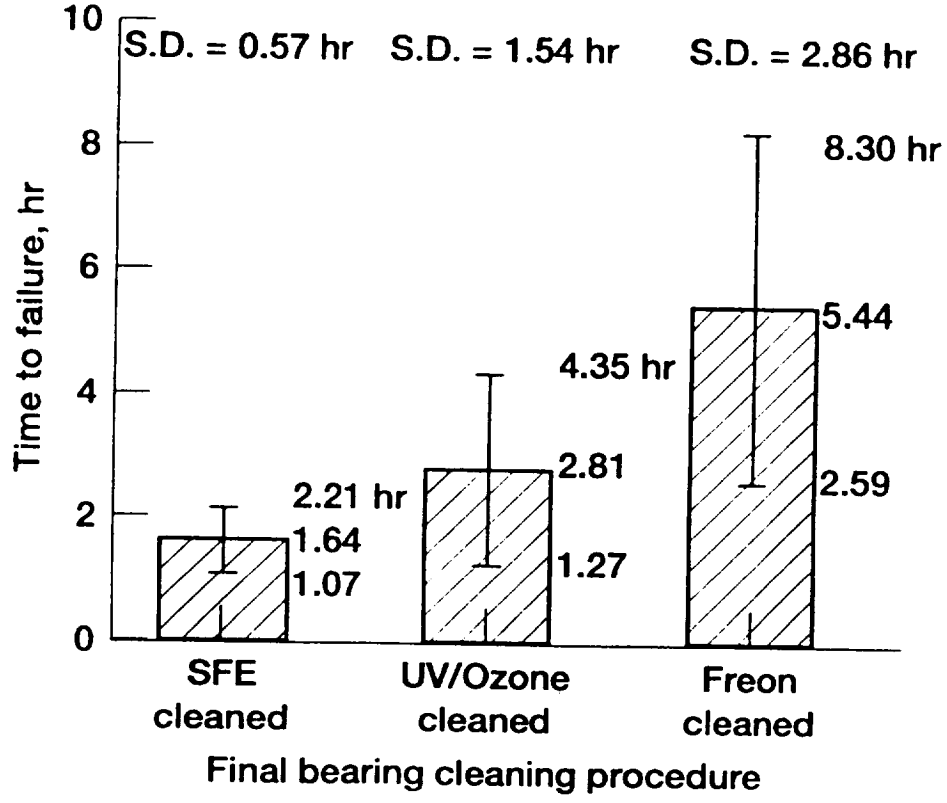

Figure 1. Effect of ODC-free cleaners on bearing lifetimes (Parched EHL apparatus, air, 4500 rpm, room temperature, Krytox 143 AC)(From reference 5)

Bearing Assembly, Thermal Radiator Rotary Joint

Ed Kibel*

278757
p.16

Abstract

The Bearing Assembly, Thermal Radiator Rotary Joint (TRRJ) is a rotating mechanism for the International Space Station (ISS). The TRRJ was designed, built, and qualified by Honeywell Inc., under a contract to Lockheed Martin Missiles and Space Corporation to deliver two flight units and one spare unit. The TRRJ protoflight unit 1 is complete and is undergoing structural testing. Units 1 and 2 are scheduled for customer delivery in December, 1996, and August, 1997, respectively.

The TRRJ mechanism design, as well as the major manufacturing problems, will be explained, and some lessons learned and problems encountered during the testing will be discussed.

Introduction

The TRRJ is a rotating mechanism that provides the structural support to the ISS thermal control system radiator assembly. The uniqueness of the TRRJ mechanism is due to the size, bearing type and suspension of the design, the very low rotational speed, and the complexity of the structural load testing. An Engineering Development Unit (EDU) was built and partially tested (some operational and non-operational load tests were conducted, but no random vibration tests) about four years ago. A qualification TRRJ unit was planned but was never built due to financial constraints. The level of the program was then reduced to proposal support and some trade studies for about a year. When the program was restarted to full level in the first quarter of 1994, significant changes to the loads and testing requirements resulted in a redesign of the TRRJ unit. The revised TRRJ specification and statement of work omitted the fabrication and testing of a qualification unit and called instead for the design, fabrication and test of protoflight units. Since the TRRJ protoflight units are the actual flight units, test levels were lower than the established norms for a qualification unit (i.e., a random vibration test composite 8.8 grms level versus 11.9 grms level specified for design and qualification testing). The present ISS design includes two TRRJ units, each mounted to the pre-integrated truss structure (P1 and S1), which is the backbone of the ISS.

TRRJ Layout

The TRRJ consists of a rotor and stator, separated by a set of thin cross-section angular contact bearings, in a DB type arrangement, with a diaphragm suspension system, preloaded to 7562 N (1700 lb). The front of the rotor contains a large bull gear with two sets of teeth spaced 1.16 mm (0.050 in) apart for redundancy (Figure 1). The TRRJ contains provisions for mounting two Drive/Locking Motor Assemblies (DLA).

---

* Honeywell Inc., Satellite Systems Operation, Glendale, AZ, USA, Mechanisms Structures and Control Department

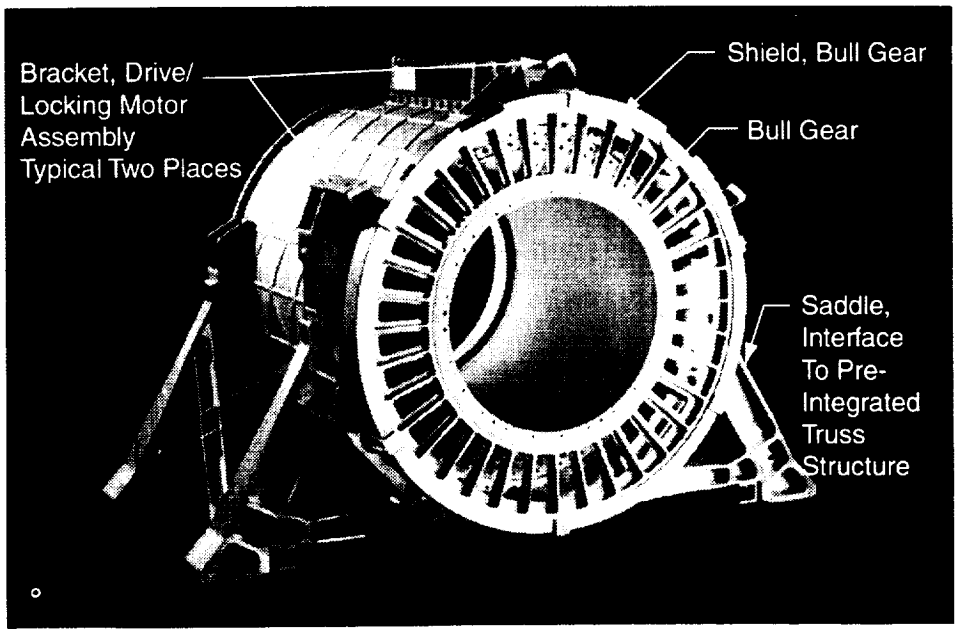

Figure 1. Bearing Assembly, Thermal Radiator Rotary Joint (TRRJ)

The DLA pinion engages the bull gear to drive the unit. During shuttle docking with the space station or during routine maintenance Extra Vehicular Activities (EVA), the pinion is disengaged from the bull gear, and a lock rack is engaged with the teeth to prevent TRRJ rotation. For redundancy, the TRRJ may be driven in both directions by either DLA. An EVA handhold for the astronaut is provided at the top of the unit (Figure 2).

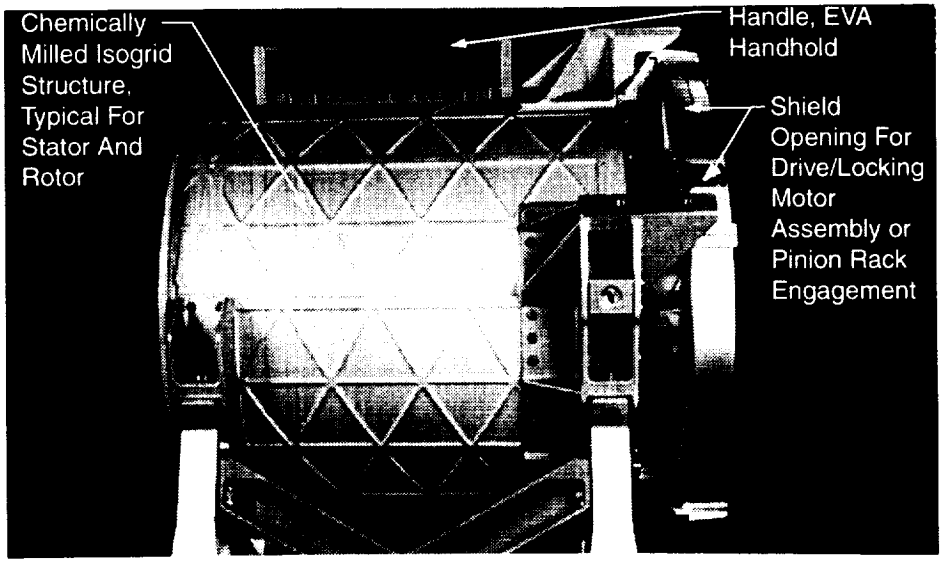

Figure 2. Side View, Bearing Assembly, TRRJ

The center of the rotor is open (Figures 3 and 4) to allow the radiator working fluid hoses to pass through the TRRJ and plumb into the radiator assembly. At the back of the unit, there is an interface to the Flexible Hose Rotary Coupler (FHRC) unit.

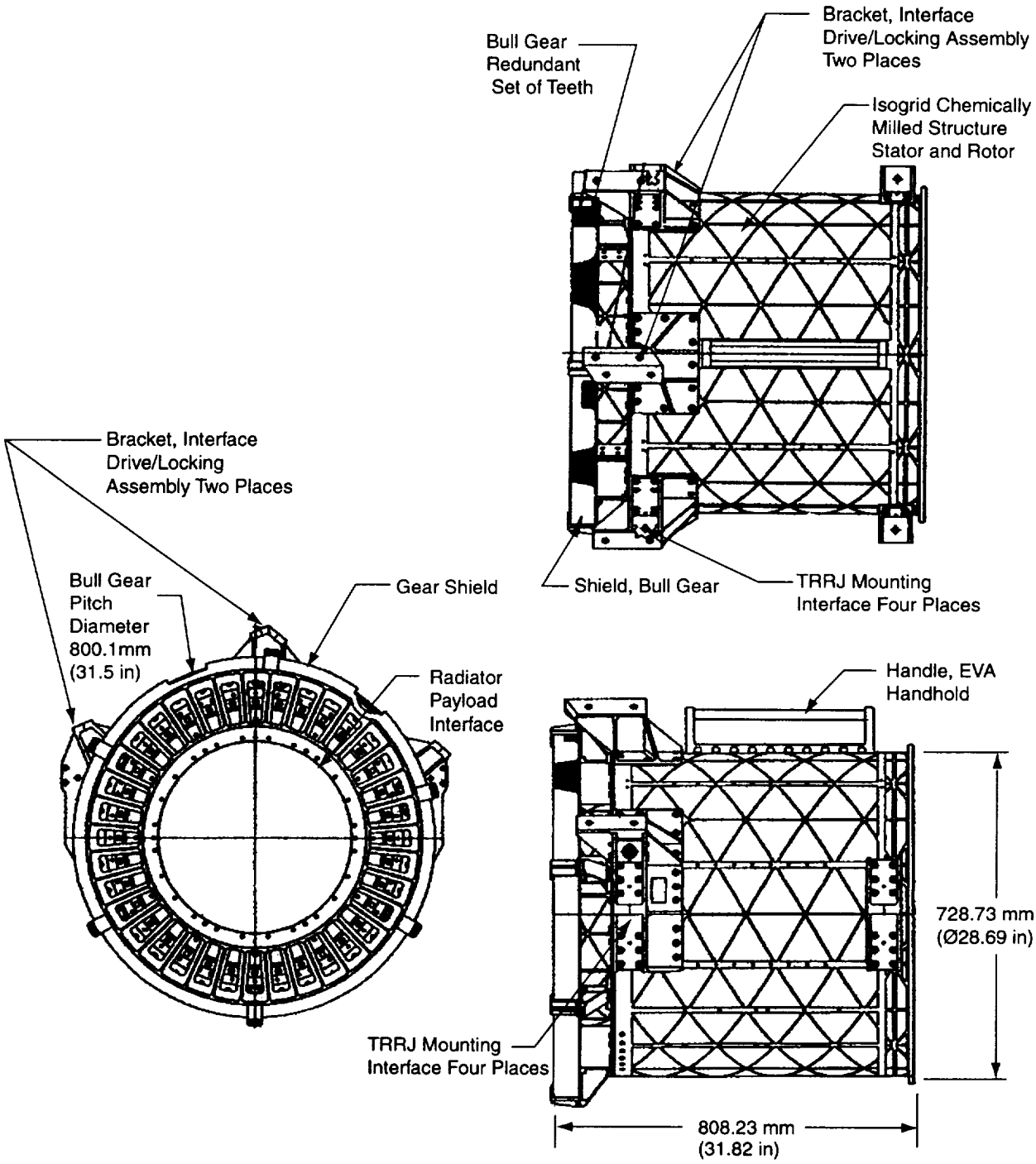

Figure 3. Layout, Bearing Assembly, TRRJ

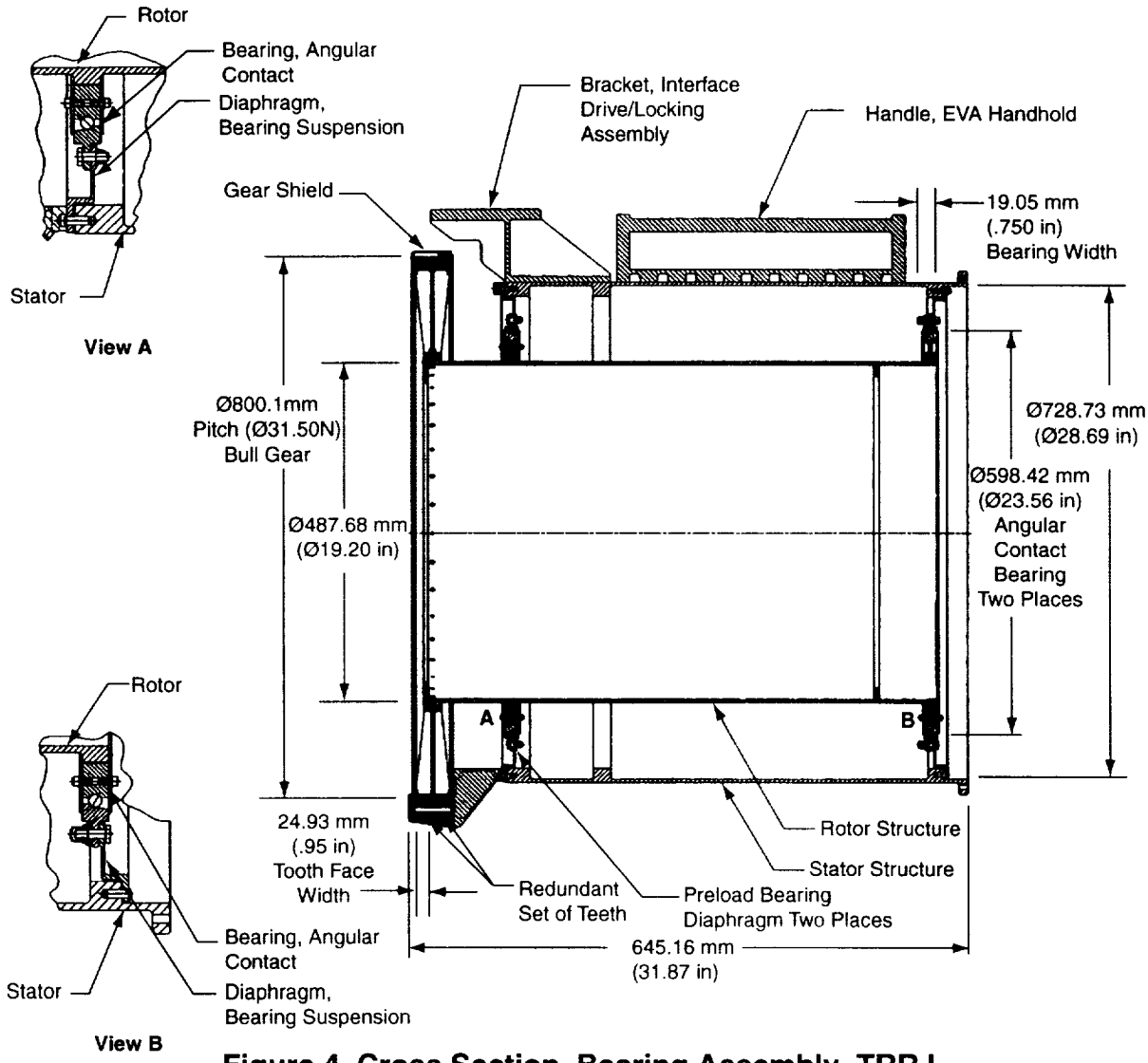

Figure 4. Cross Section, Bearing Assembly, TRRJ

TRRJ Features

Bull Gear

The bull gear pitch diameter is 800.1 mm (31.50 in).

- Materials
  - 2219-T851 machined aluminum hub with 4340 steel rings heat treated to Rc42-45, thermally-fitted to the hub
  - 378 redundant set of teeth, AGMA quality 10, machined into the steel rings (Figure 4)
- Weight: 15.9 kg (35 lb)
- Coating
  - Ion gold deposition 2000-7000 Å thickness on teeth for corrosion protection and enhanced lubrication

Rotor and Stator

- Materials
  - 2219 aluminum forgings; machined bearing surfaces; isogrid structure, chemically milled skins for high strength and stiffness-to-weight ratio. The chemical milling resulted in weight savings of 35% for the rotor and 20% for the stator.
  - Clear, anodized finish
- Weight
  - Rotor, 12.5 kg (27.5 lb)
  - Stator, 22.7 kg (50 lb)

Bearings/Diaphragms

Angular contact, thin cross-section 19.05 mm wide x 563.63 mm inner race Ø (0.75 in wide x 22.19 in).

- Materials
  - 52100 steel races
  - 440C balls, AFBMA grade 5 (quality 144, size Ø 9.53 mm (Ø 0.375 in)
  - Ball retainers, segmented phenolic cages
- Weight 9.2 kg (20.3 lb)
  - Bearing diaphragm, A286 corrosion-resistant steel
- Weight
  - Front - 4.8 kg (10.6 lb)
  - Rear - 4.4 kg (9.8 lb)
- Lubrication
  - Braycote 601™ (as specified by customer)

Table 1: TRRJ Performance Requirements

Bearing Drag Torque	≤8.1 N•m (6 ft•lbf) unloaded at steady state rotation of 45 deg/min. ≤176.28 N•m (130 ft•lbf) while subjected to operational loads applied and rotating at 45 deg/min.
Rotational Speed	≤45 deg/min.
Stiffness	Bending 3.96 x 10^4 N•m/deg (2.0 x 10^7 in•lbf/rad) Axial 1.75 x 105 N/cm (1.0 x 10^5 lbf/in)
Operational Loads (unit rotates)	Combined bending moments about two orthogonal axes 2825 N•m (25,000 in•lbf), torsional load 113 N•m (1000 in•lbf), shear load 3145 N (707 lbf), axial load 2224 N (500 lbf)
Non Operational Loads	Combined bending moment about two orthogonal axes, 1130 N•m (10,000 in•lbf) about one axis, 10,170 N•m (90,000 in•lbf) about the other axis (the bull gear is locked from rotating using a lock rack while loads are applied), torsional load 5085 N (45,000 in•lbf), shear load 3145 N (707 lbf), axial load 2224 N (500 lbf)
Vibration	Random vibration, composite G level 8.8 grms
Temperature	Operating Temperature -40 to +60 °C (-40 to +140 °F)
Weight	107 kg (235 lb)
Life	Storage ≥10 years, operating ≥10 years

Manufacturing Lessons

Bull Gear

Weight savings of over 7.0 kg (15 lb) were realized by combining the aluminum hub with the steel rings in the bull gear design. The two-gear steel blanks, spaced 1.16 mm (0.050 in) apart, were thermally fitted to the hub with an interference of 0.7 mm (0.030 in), and will react 217 N•m (160 ft•lbf) at –65°C.

Initial difficulties with the bull gear cutting resulted in failure to achieve either the profile tolerance of 0.016 mm (0.00063 in) or the lead tolerance of 0.0076 mm (0.0003 in) for a face width of 24.13 mm (0.950 in). These difficulties were caused by gear deflection, thus resulting in excessive runout of the cutting head. The final fix for the manufacturing problem was to sandwich the gear between two precision plates which stiffened the cutting setup, thereby producing acceptable gear tolerances.

Bull Gear Gold Sputtering Process

To the best of our knowledge, the TRRJ bull gear is the largest mechanism ever qualified for space flight using the gold sputtering coating process. The bull gear teeth were gold-coated using the process of triode sputtering. The purpose of the coating is corrosion protection and enhanced lubrication properties.

An extensive process development on small gear segments, and on scraped but otherwise finished bull gears, was conducted prior to processing the flight gears. To remove all machining and storage oil, the bull gear teeth were first thoroughly cleaned under a controlled process, which included immersion in heated clean trichlor (43 to 49°C) ultrasonic cleaner for 3 to 4 minutes, then air-blowing the teeth and groove. The cleaning process was repeated once.

The greatest difficulty during the development process was the cleanliness of the bull gear teeth. During machining operations, minute amounts of oil became trapped at the interface of the steel rings and the aluminum hub and seeped out during the vacuum process, thereby contaminating the gear surface and resulting in poor gold adhesion to the gear surface. The process development concentrated on the cleaning issue; for example, it was found that placing the cleaned bull gear in the vacuum chamber and pumping down to 10^{-4} torr (total time of 1 to 1.5 hr) pulled the remaining small amounts of trapped oil to the surface, where it could easily be wiped off with alcohol. This process was repeated once or twice, thus resulting in a very clean gear surface.

The triode sputtering process involved placing the bull gear horizontally on a rotating table inside a vacuum chamber with the aluminum hub covered top and bottom (to prevent it from being coated). Thin silicon wafer coupons, for verifying the coating thickness, were placed in four places close to the gear teeth. Pure gold (better than 99.50% purity) targets were placed on each side of the bull gear. The vacuum chamber was evacuated to pressure on the order of 10^{-5} torr and back-filled with argon gas. Negative voltage was applied to the gold targets to turn them into cold cathode electron emitters, thus resulting in ionization of the gas in the chamber. The positive gas ions were accelerated to the negatively charged targets with enough energy to dislodge gold atoms from the target surface. The dislodged atomic particles moved through the

plasma in all directions, some striking the substrate (bull gear teeth) with sufficient energy to create an atomic bond with the substrate material. The triode auxiliary electron- emitting source ionized the gas in the chamber at lower pressure than would otherwise be possible, thus providing better control over the coating physical properties. The thickness, which was cited in the Honeywell specification base on a previous heritage gear design, and much smaller than the TRRJ bull gear, was 1500 to 2000 Å on the teeth profile. This thickness turned out to be very difficult to control on such a large gear. Once all the process parameters, such as cleaning, proper applied voltages, pressure, process time, and others had been characterized, excellent process control and adhesion were obtained. In all cases, the thickness was greater than 2000 Å, and the drawing was changed to increase the coating thickness tolerance to 2000 – 7000 Å. This increased coating thickness provides better corrosion protection and enhances lubrication, yet is thin enough to assure that no flaking will occur.

Testing Lessons

Bearing Drag Torque

The TRRJ unit utilizes large Ø563.63-mm inner race (22.19 in) by 19.05 mm wide (0.75 in) angular contact bearings, which are highly loaded. The bearing lubrication, selected because of space flight heritage, was Braycote 601™, a product of the Castrol® corporation. Braycote 601 is a grease system with Brayco 815Z™ perfluorinated polyether as the base oil. The drag torque requirement, from the specification for the unloaded TRRJ under steady-state rotation of 45 deg/min, was ≤40.68 N•m (30 ft•lbf). Under operational loads, the drag torque specified was ≤176 N•m (130 ft•lbf), under steady-state rotation of 45 deg/min. The design rotational speed was 45 deg/min.

For engineering information, the customer had requested drag torque data at low speeds of 1.35 deg/min and 4.0 deg/min, which resulted in an increase of the drag torque (Table 2, Figure 5). The increase of the drag torque at low rotational speeds correlates well with data from other sources. In particular, a study of the drag torque characteristics of a much smaller angular contact bearing set of 83.82 mm (3.30 in) by 139.7 mm (5.5 in) showed an increase of the drag torque in the order of 300-400 % when measured at speeds ≤4.2 deg/min, as compared with speeds of ≥60 deg/min. Using the 45 deg/min as a baseline, the average running drag torque of the TRRJ increased by 224% for the 4 deg/min run and by 676% for the 1.35-deg/min run.

Despite the differences in the bearing type, size and suspension systems between the study and the TRRJ, similar drag torque characteristics were demonstrated. It appears that the drag torque increase phenomenon at low speeds is a function of the surface velocities of the balls. The lowest drag torques occur at surface velocities in the order of 3.81 cm/min to 25.4 cm/min, (1.5 to 10.0 in/min).

Table 2: Drag Torque at Various Speeds

Rotational Speed (deg/min)	Initial Break Away Drag Torque N• m (ft•lbf)	Average Running Drag Torque N• m (ft•lbf)	Final Break Away Drag Torque N• m (ft•lbf)
45	2.3 (1.7)	5.1 (3.7)	9.8 (7.2)
4	22.6 (16.7)	11.3 (8.3)	2.8 (2.1)
1.35	20.3 (15.0)	33.9 (25.0)	20.3 (15.0)

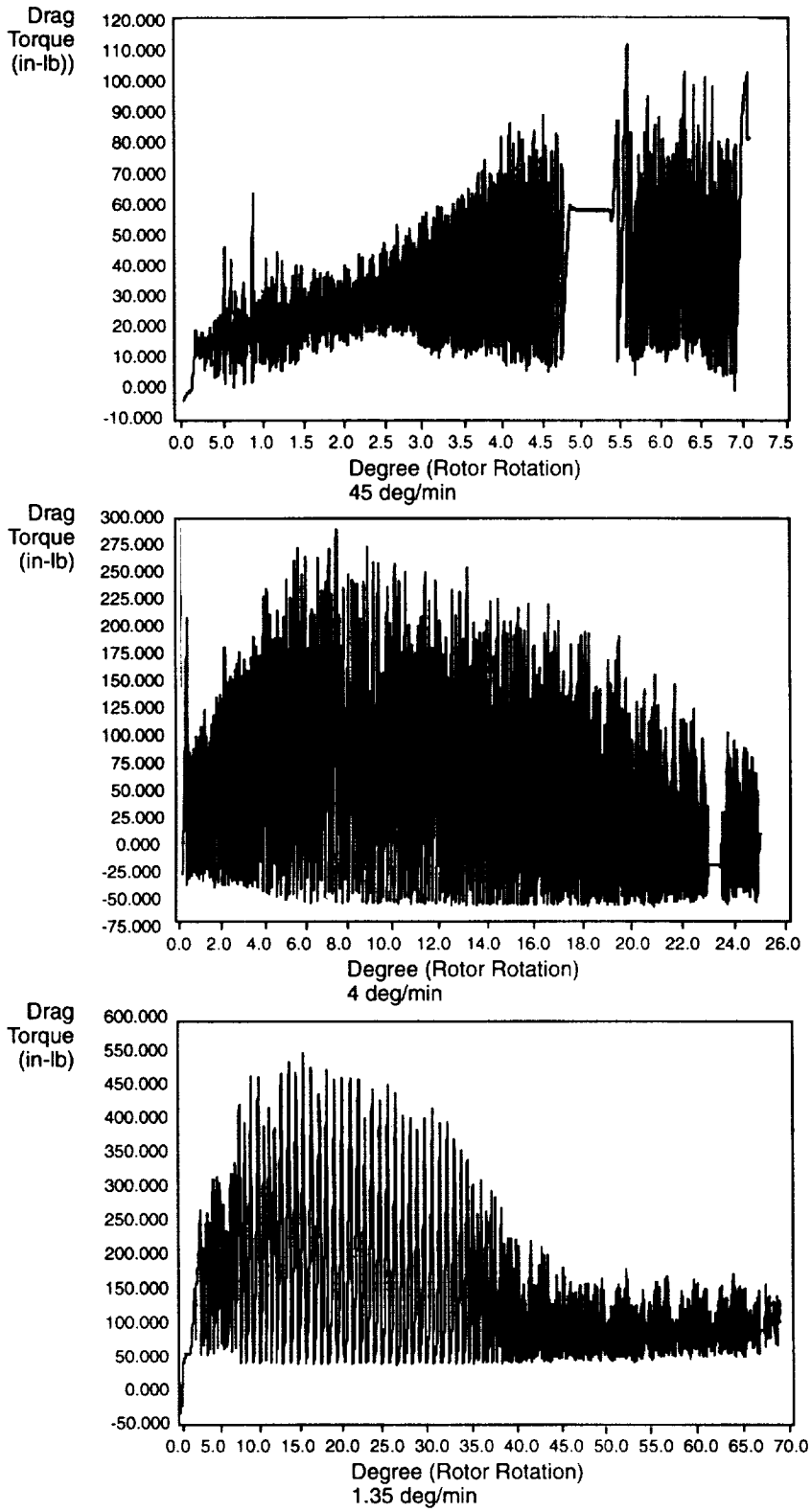

Figure 5. Bearing Assembly Drag Torque as a Function of Rotational Speed

Structural Tests

A considerable portion of the TRRJ program is devoted to testing. All the testing is mechanical in nature, as shown in Figures 6, 7, and 8. The Lab-View™ software package was used for all the data collection, analysis, and documentation.

The TRRJ unit required complex loading combinations of up to 8 loads, applied simultaneously, and individual loads as high as 31,137 N (7000 lb) and as low as 89 N (20 lb), thus resulting in bending moments about two axes, torsional, axial, and shear loads. The TRRJ unit was instrumented with strain gages at various critical locations, determined by analysis, in order to measure the stresses resulting from the structural loads (Figure 6).

A hydraulic control console, with manual reducing valves and manual bi-directional valves to control up to eight independent hydraulic cylinders, was designed and procured early on in the program (approximately five years ago). The console was originally intended to control applied static loads only.

During the testing of the TRRJ EDU, it was important to apply the loads in a particular sequence to minimize interaction between the loads as they were being applied (Figure 7). Constant adjustment of the controls was necessary to maintain the loads: as one load was applied, it affected the next one and so on, until some equilibrium could be sustained long enough to record strain gage data.

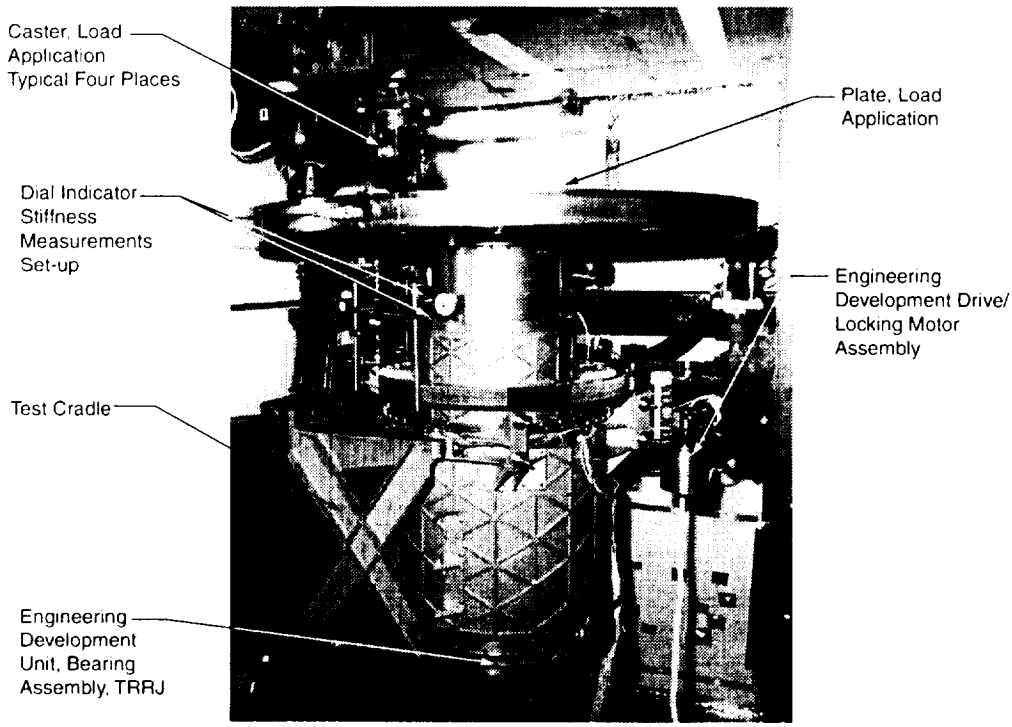

Figure 6. Typical Test Setup with the Bearing Assembly, TRRJ Engineering Development Unit (EDU) in the Test Cell.

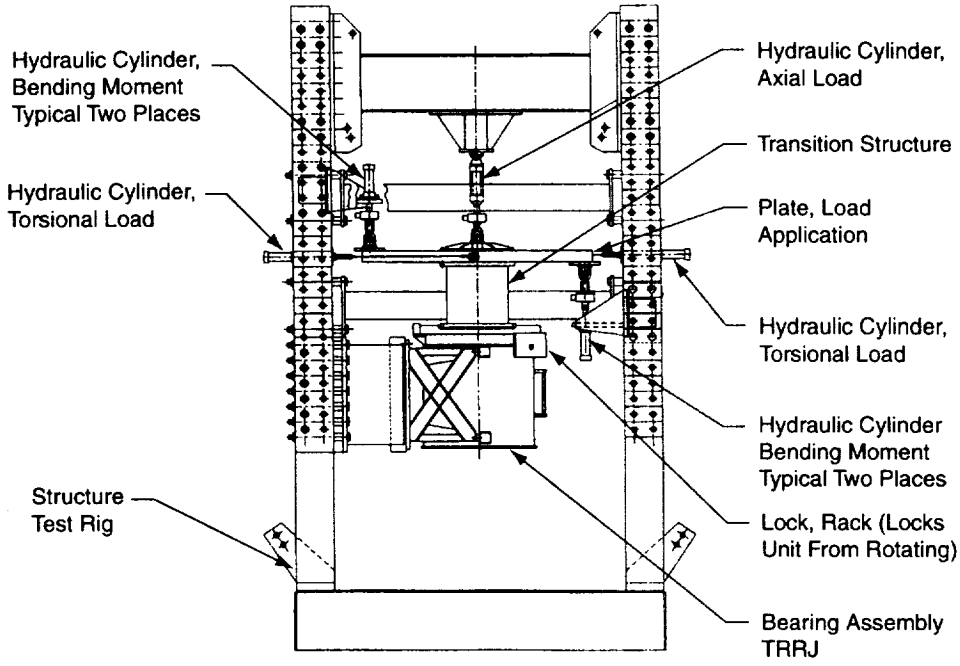

Figure 7. TRRJ Non-operational Loads Test Set Up

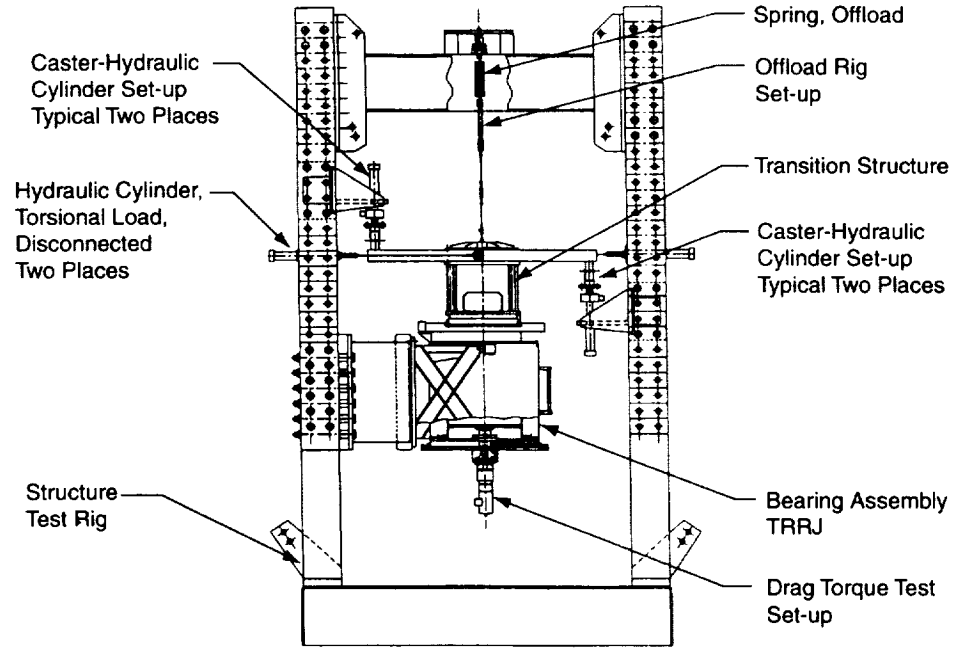

Figure 8. TRRJ Operational Loads Test Setup

As the program grew and evolved over the years, the test requirements became substantially more complex, without a corresponding increase in the test equipment budget. With the existing control console, a difficult requirement to implement was

maintaining the level of the applied loads while the unit was rotated; five loads were applied, with each required to be held to ±5%. This requirement was needed in order to record the drag torque of the TRRJ while subjected to operational loads. The loads were applied to a 1526-mm (60.0-in) diameter plate, attached to a transition structure mounted to the rotor interface. Casters, attached to the hydraulic cylinders, were used to apply the loads (Figure 8).

Due to test equipment limitations resulting from mechanical tolerances, such as caster roundness, load plate flatness, hydraulic control console limitations, the operational loads drift could only be maintained to ±25%. However, it was observed that the drag torque was fairly stable and was not affected much by the drift of the applied loads during the operational loads test.

A request to deviate from the required ±5% tolerance for the applied operational loads was submitted to the customer and approved. There was no concern over the applied loads damaging the unit, even if the combined applied operational loads were 25% higher, which was not the case. Some loads were increased, while others were decreased. The non-operational loads test applied much higher loads than the operational loads test, and the unit passed the non-operational test with no problems.

It was possible to modify the control console to automate the operational loads and achieve much better stability. This improvement would have required a closed-loop system utilizing electrically actuated proportional hydraulic valves available off-the-shelf. The signal of the load cell, amplified, would have been used to drive the electrically actuated proportional valves to modulate the pressure required for each cylinder in order to maintain the required load. However, since the drag torque variation is minimal due to the loads drift of the loads and the cost of modifying the existing system was high, the decision was made by Honeywell, in consultation with the customer, to stay with the existing system.

Vibration Test

The bearing assembly and TRRJ were random vibration tested to the Power Spectral Density (PSD) shown in Figure 9. The unit was tested in the X, Y, Z axes (Figure 12).

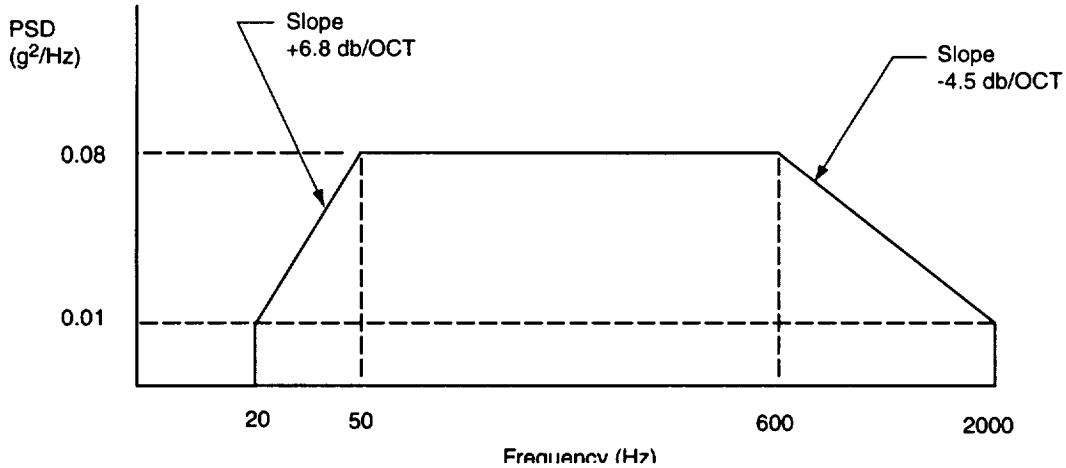

Figure 9. Bearing Assembly, TRRJ Random Vibration PSD Spectrum

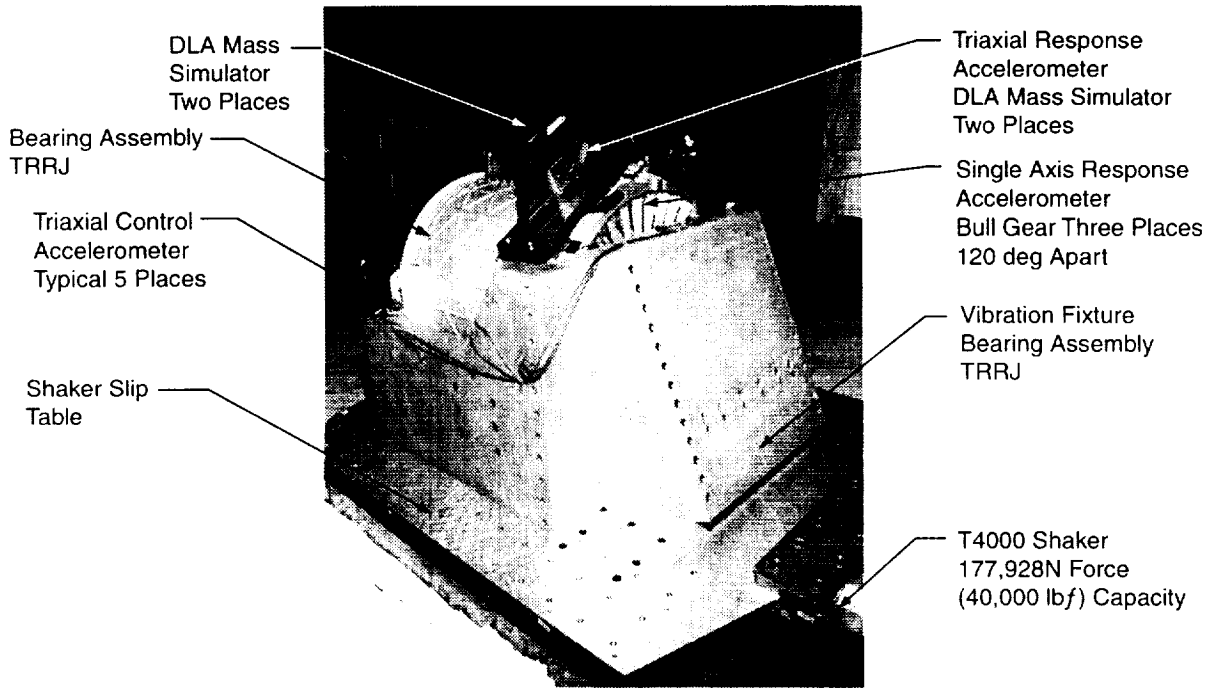

Figure 10. Random Vibration X-Axis Test Setup

For each axis, low-level characterization runs were conducted, starting with –12 db and proceeding through –6 db and –3 db, to full level. The lower-level tests were run for 30 seconds — only long enough to obtain sufficient data for review and analysis. The full-level tests were run for 120 seconds, per the customer requirements. Two (DLA) mass simulators, each weighing 45.5 kg (100 lb), were mounted to the bearing assembly. The weight of the combined bearing assembly unit with the DLA mass simulators is 198 kg (435 lb). The weight of the vibration fixture is approximately 545 kg (1200 lb).

The customer has established a criterion for notching of the PSD input levels to ensure that the unit was not subjected to loads higher than the design loads [2]. The specified random vibration test level was a workmanship level; therefore, notching was allowed. Notching was required because of the size, weight, and complexity of the mass under test [the weight of the combined TRRJ and vibration fixture was 743 kg (1635 lb)].

Finite element analysis of the random loads acting on the bearing assembly predicted high stress levels on the bull gear and DLA brackets. The bull gear shield was analyzed for EVA- and astronaut-induced static loads, but not for random vibration loads.

During the random vibration testing, it was found that notching of the PSD input levels was required in each of the shake axes due to high accelerations of the bull gear and the DLAs. It was also observed that portions of the bull gear shield were resonating, thus resulting in large deflections. Large deflections were observed around the cutouts of the shield, which provide access to the bull gear for the DLA pinion and lock rack engagements. The shield had contacted the flat side of the bull gear in one area, thus resulting in a 12.7-mm (0.5-in) diameter spot where the gold coating was worn off. There was no damage to the gear, since the worn-off gold spot is in a non-functional

location, and Braycote 601 grease was used to coat the exposed spots on the gear. Single-axis response accelerometers were mounted on the shield in the front of one cutout and in the back of the other cutout, and the –12-db runs were repeated (Figures 11 and 12). Because of the very high acceleration levels on the shield cutout due to the resonances, it was found that notching, using the criteria established by the customer, was not possible.

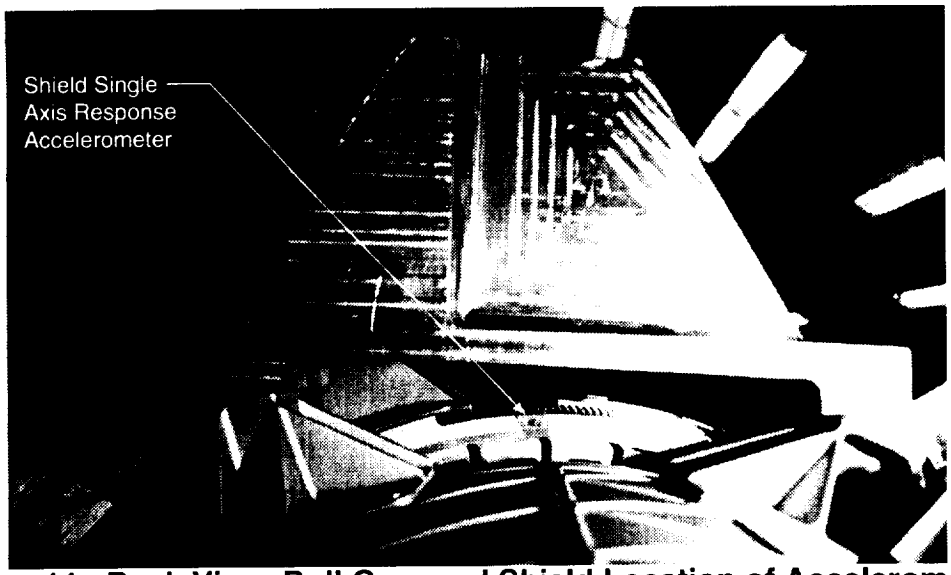

Figure 11. Back View, Bull Gear and Shield Location of Accelerometers

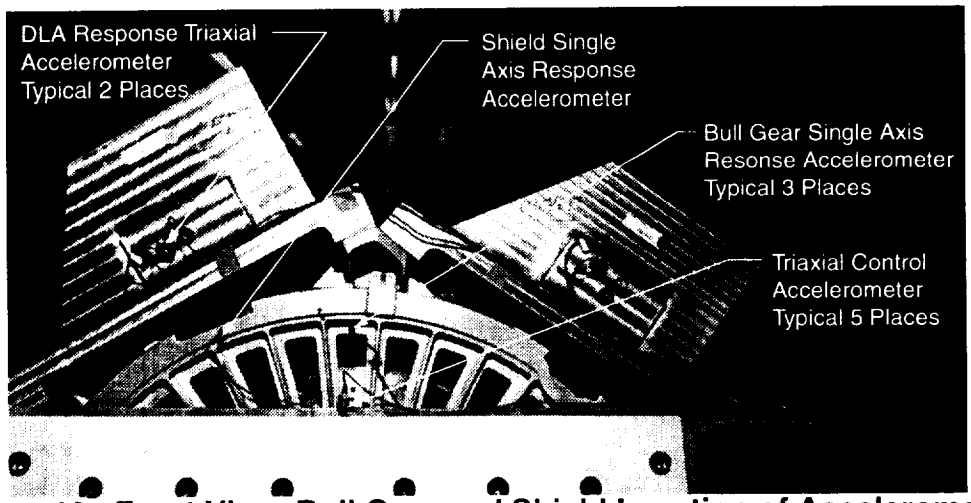

Figure 12. Front View, Bull Gear and Shield Location of Accelerometers

Typical Notch Calculation for the X-Axis

The gear shield was re-designed to reduce its deflection under random vibration loads. Random vibration analysis, resulting in positive margins, was performed for the new shield using a higher grms level than the test grms. The protoflight unit 1 will be retrofitted with the new gear shield, and all subsequent TRRJ units will incorporate the new shield design.

Review of the data obtained at the –12-db run in the X-axis indicated that the single-axis accelerometer identified as M1 (Figure 13), mounted on the bull gear, was subjected to high acceleration levels of 4.75 g^2/Hz at a frequency of 228 Hz.

The following is a typical calculation conducted to establish the notch levels required for the bull gear:

$$Q = \text{Structural Damping} = \sqrt{\frac{\text{Output PSD}}{\text{Input PSD}}}$$

$$Q = \sqrt{\frac{4.75 g^2/\text{Hz}}{0.05 g^2/\text{Hz}}} = 31$$

$$\frac{1}{2}\text{Power Bandwith} = \frac{fr}{Q} \quad (fr = \text{resonate frequency of mode of interest})$$

$$\frac{1}{2}\text{Power Bandwith} = \frac{228\ \text{Hz}}{31} = 7.3\ \text{Hz}$$

Per the customer, notching procedure:

$$\text{Notching bandwith} = 4 \bullet \frac{1}{2}\text{Power Bandwith}$$

$$\text{Notching bandwith} = 4 \bullet 7.3 = 29\ \text{Hz}$$

$$\text{Projected full level PSD (from -12db)} = 16 \bullet 4.75 = 76 g^2/\text{Hz}$$

$$\text{The predicted finite element analysis PSD Level} = 23.8\ g^2/\text{Hz}$$

$$\text{Reduction ratio} = \frac{76}{23.8} = 3.2$$

$$\text{PSD Level at -12 db} = \frac{0.08}{16} = 0.005\ g^2/\text{Hz}$$

$$\text{The revised PSD input level} = \frac{0.005}{3.2} = 0.0016\ g^2/\text{Hz}$$

$$\text{The revised full input level} = 0.0016 \times 16 = 0.0256\ g^2/\text{Hz}$$

$$\text{The notched frequency bandwidth} = \frac{29}{2}\ \text{Hz} = \pm 14.5\ \text{Hz} \qquad (1)$$

Minimum notch frequency: $228 - 14.5 = 214$ Hz

Maximum notch frequency: $228 + 14.5 = 243$ Hz

A similar type of calculation was made to establish the required notching for the DLAs (Figures 13 and 14).

Figure 15 shows the notched X-axis Random Vibration PSD spectrum.

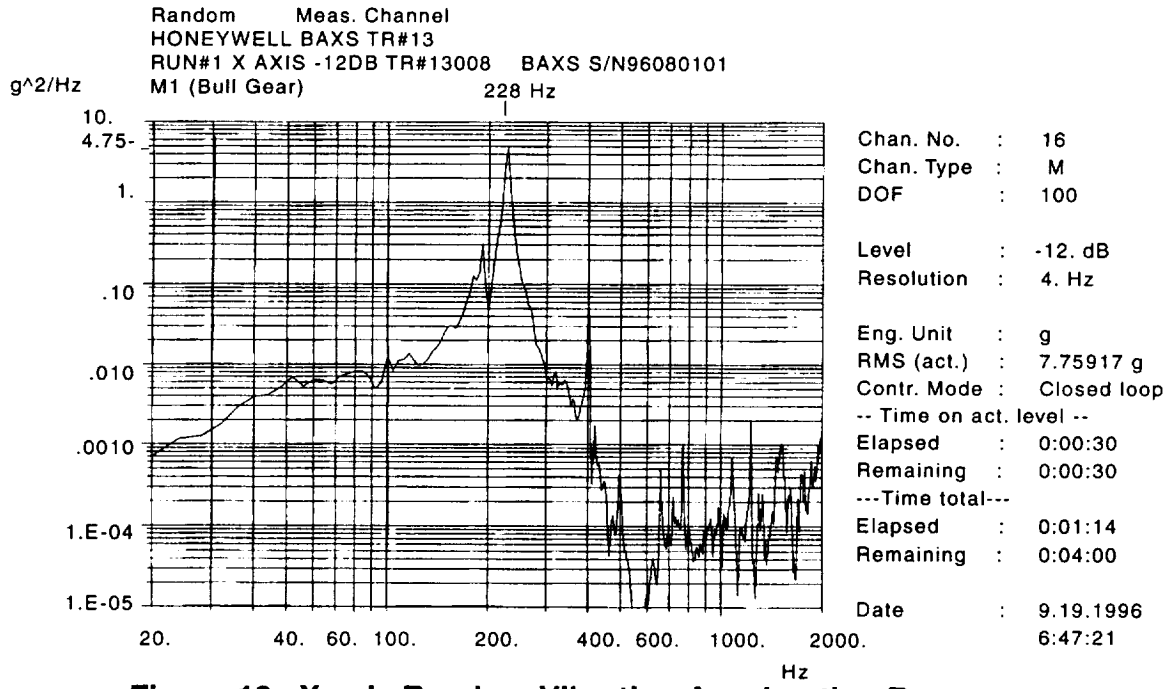

Figure 13. X-axis Random Vibration Acceleration Response of Bull Gear at -12 db-Prior to Notching

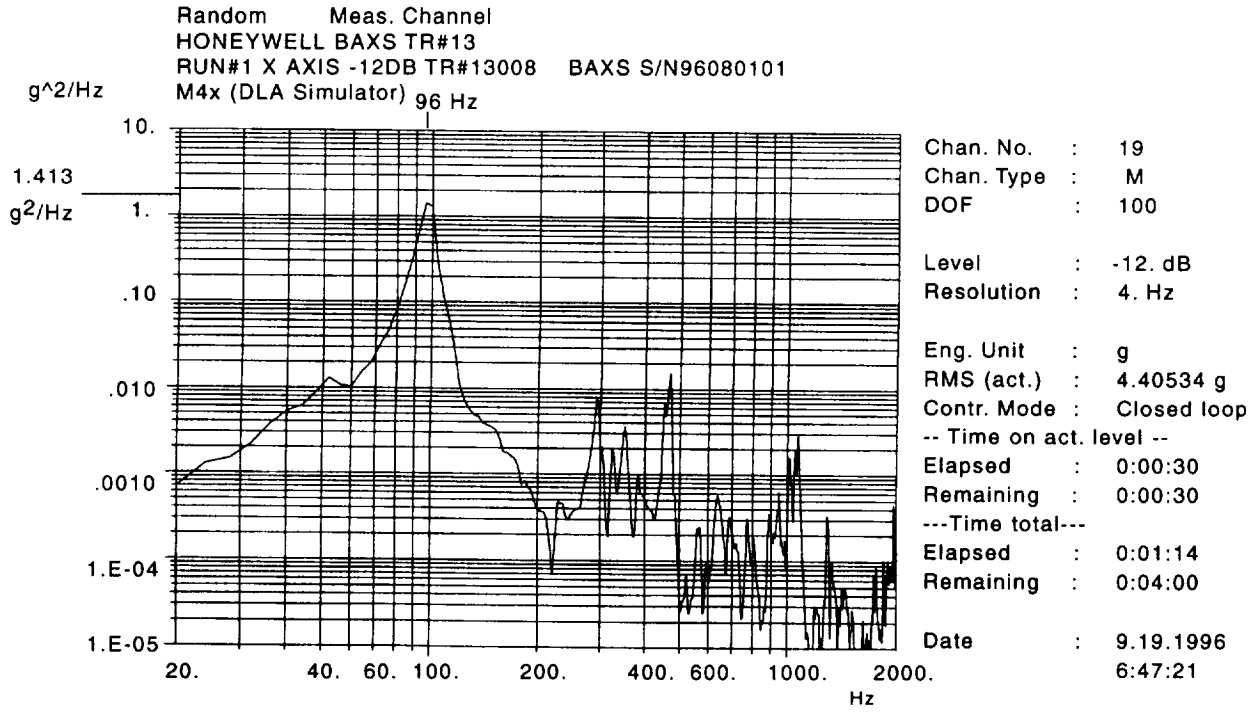

Figure 14. X-axis Random Vibration Acceleration Response of DLA at -12 db - Prior to Notching

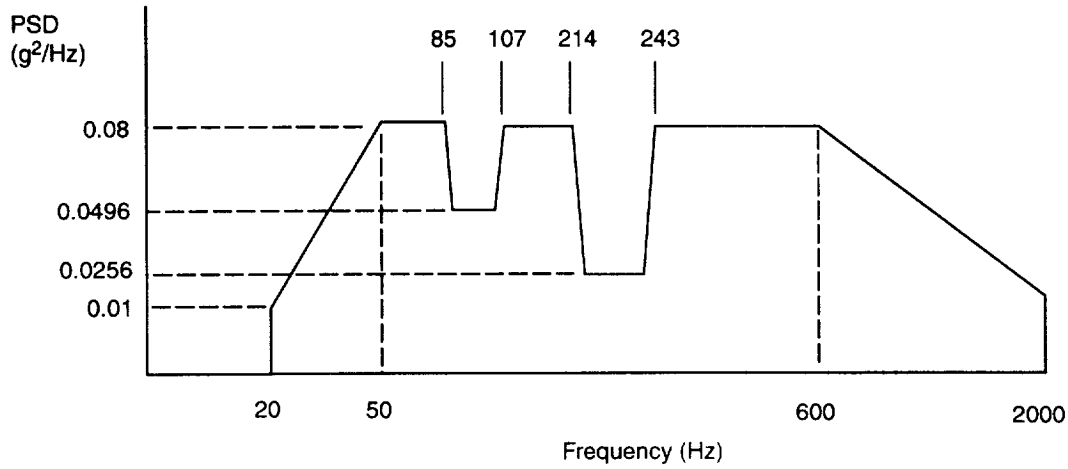

Figure 15. X-axis Random Vibration PSD Spectrum after Notching

Conclusions

A successful gold sputtering process that met all requirements was developed. A more comprehensive up-front planning prior to the fabrication of the bull gears could have avoided some of the problems encountered. Random vibration analysis of the gear shield and random vibration testing of a qualification unit, had one been available, would have revealed the issue with the gear shield design. Some problems with test equipment are inevitable in a dynamically changing program. However, built-in flexibility in the test equipment and test setups for future growth and changing requirements are crucial.

References

1. Encoder Bearing Torque Investigation, Lockheed Martin Missiles and Space Corporation, EM SL-054, dated 20 October 1992.

2. New Notching Procedure Memorandum, Lockheed Martin Missiles and Space Corporation, A95-J012-LGS-M-9502411, dated 13 December 1995.

Acknowledgments

John Leonard, Bearing Assembly Technical Director, for his review and technical input.
Roger Nagel, Structural Analysis Group, for his review and technical input.

The Chemical and Physical Properties of Aerospace Grade Lubricants

Paul A. Bessette*

Abstract

Lubricants serve a vital role in reducing the destruction of contacting solids when in motion. This presentation provides a brief synopsis of the chemical and physical properties of polyalphaolefins and multiply alkylated cyclopentane. Two important lubricants that have been used for aerospace applications. Lubricating oils and grease are discussed.

Introduction

Selecting a lubricant for aerospace applications must be based on specific design requirements. Criteria differ for rolling element bearings, gearboxes, or LOX valve stems. However, the process of lubricant selection should be based on factors that will increase the likelihood of mission success. As a general guideline, lubricants should be chosen based on their vapor pressure, operating temperature range, and tribological effectiveness. In this presentation, lubricants prepared from polyalphaolefins, PAO's, and multiply alkylated cyclopentane, MCP are discussed in terms of their chemical and physical attributes.

Lubricant Classification

Lubricants may be classified into three distinct types:

1. Lubricating Oils
2. Lubricating Greases
3. Solid Films

Only oils and greases will be discussed here. Lubricating oils are fluids that are effective under EHD conditions due to their viscosity which is directly related to the fluid's molecular weight and to a lesser extent on intermolecular affinity. Under boundary conditions, the chemical properties of the lubricant are responsible for minimizing asperity contact while viscosity becomes less important. Polar fluids like esters are intrinsically better lubricants under boundary conditions than non-polar PAO's; however, polar fluids respond less favorably to additive fortification than do non-polar oils. The explanation for this behavior is apparently due to the competition for active sites on metallic surfaces.

A lubricating grease is simply lubricating oil compounded with a thickening agent which serves to immobilize the fluid. The primary advantages of grease over oil are its

* Nye Lubricants, Inc., New Bedford, MA

ability to remain where applied, the ability to function as a reservoir liberating oil during thermal excursions, it serves to seal out moisture and airborne contaminates, and greases may be fortified with special additives that would otherwise be insoluble in the corresponding base fluid. Greases are less effective than oils at reducing noise, produce higher torque levels, are poorer heat conductors, and are more likely to starve the inlet zone in a concentrated contact although filtered greases are less likely to do so. Grease properties that are often used to specify physical characteristics include unworked and worked penetration, oil separation, evaporation, temperature limits and dropping point. For rolling element bearings, an NLGI Grade 2 Grease , P_{60} = 265 to 295, is usually the consistency of first choice. However, slightly softer and firmer greases have also been used successfully. The dropping point of a grease which is defined as the lowest temperature at which a drop of oil separates from the grease under the conditions of the test should never be used to assess its high temperature capability. The ability of organic lubricant to remain serviceable at high temperatures is a function of the stability of the base oil and not dropping point of the thickener and oil combination.

For aerospace applications, lubricant evaporation should always be minimized. However, this rather straightforward requirement is difficult to achieve in practice since most lubricating fluids, including synthetics, are composed of molecules with a range of molecular weights. Distillation can narrow the distribution, but will not eliminate it.

Oil separation from a grease is a more difficult parameter to quantify. Although excessive oil separation would be undesirable, some oil bleed is essential for many applications where the bulk grease is unable to reach the mated surfaces. For example, between a shaft and gear hub. For many lubricating greases, oil separation tends to be self-limiting. As oil is lost from the grease matrix, the ratio of thickener to oil increases making it more difficult for further fluid loss. But as oil is lost from the grease structure, it becomes firmer and will eventually be transformed from a pliable substance into an intractable mass. When approximately 50% of the original oil quantity is lost, failure is imminent.

The incorporation of a solid thickening agent into a lubricating fluid usually raises the low temperature usefulness of the base fluid. Polytetrafluoroethylene, PTFE, telomers appear to have the least impact on low temperature fluid properties due to the intermolecular inertness of the fluoropolymer. Low temperature usefulness is primarily a function of the base fluid, but the influence of the thickener can not be ignored.

Channeling is a grease property that many believe to be a desirable attribute for producing low torque in rolling element bearings. This grease behavior has nearly universal appeal, but very little exits in the technical literature to substantiate the broad based belief regarding the channeling phenomenon. From a theoretical standpoint, two distinct types of channeling can be described:

1. Channeling due to consistency. A firm grease, such as an NLGI Grade 3 or firmer, will have a tendency to be displaced from the ball path after initial rotation and will tend to remain where displaced. Since the consistency of a grease can be altered by changing the ratio of thickener to oil, it should be possible to make any grease channeling by simply making it firmer.

2. Rheological channeling occurs when certain grease structures rapidly breakdown under the mechanical energy imparted by ball rotation. Torque is reduced due to the semi-fluid nature of the grease in the ball path. Sodium based and polyurea thickened grease are thought to function in this manner.

Place a drop of oil on a clean metal surface and a tug-of-war results. Molecules of oil are attracted to each other with an affinity dependent on the type of lubricant. But lubricant molecules at the metallic interface are usually more strongly attracted to the metal than to their own kind and the resulting pull causes the drop to enlarge. The process continues until some equilibrium point is reached where the film thickness of the original oil drop approximates monomolecular dimensions. The tendency of a lubricant to migrate is determined by its surface tension and viscosity. Although most lubricating oils intended for space applications will spread spontaneously under a thermal gradient, low surface tension fluids exhibit the greatest tendency to spread. The surface tension of four commonly used aerospace base oils is reported in Table 1.

Table 1. Surface Tension

Type	Chemical Description	Surface Tension, dynes/cm
PAO-6	Polyalphaolefin	28
PFPE-K	Branched Perfluoropolyether	16 to 18
PFPE-Z	Linear Perfluoropolyether	21
MCP	Multiply Alkylated Cyclopentane	31.4 at 100C

Lubrication migration and subsequent lubricant depletion is perhaps the most overlooked cause of component failure in aerospace mechanisms and deserves more attention in the aerospace community. A few milligrams of oil placed in a rolling element bearing can be reduced to micrograms prior to mission completion. When appropriate, grease can replace oils since, as mentioned earlier, they remain where applied. But another alternative includes the application of an oleophobic fluoropolymer barrier coating which is highly effective in preventing oil loss if the only driving force for oil depletion is surface wetting. The application of a thin, invisible film of pentadecafluorooctylmethacrylate with a surface energy of only 11 dynes/cm will

effectively retard surface wetting. Ultraviolet dyes added to the barrier coating solution serve to identify the application of the material.

A second lubricant attribute that is frequently overlooked is cleanliness. Grease manufacturing processes on a microscopic scale are inherently dirty as are finishing operations such as filling and packaging. To reduce noise levels, improve micro-flowability of grease into a concentrated contact and greatly reduce or eliminate particulate contamination that may jeopardize fatigue life, lubricants intended for any precision devices should be ultrafiltered. Ultrafiltration is the process by which microscopic debris is removed from specialty lubricants. Table 2 summarizes typical specification requirements for ultraclean oil and grease.

Table 2. Cleanliness Requirements

Lubricating Oil:

Particle Size range	Maximum Number of Particles/100 ml
0 to 14 microns	75
15 to 24	3
25 or larger	None

Lubricating Grease:

Particle Size Range	Maximum Number of Particles /cc
10 to 34 microns	500
35 microns and larger	None

Polyalphaolefins, PAO's, Synthetic Hydrocarbons

Polyalphaolefins have been commercially available for approximately twenty years. They are synthetic fluids prepared by oligomerizing decene-1 monomer. As a family of fluids, they are available in seven standard viscosity grades ranging from a 2 mm^2/s PAO-2 to a 100 mm^2/s fluid, PAO-100. The specific grade is determined by the kinematic viscosity measured at 100° Centigrade. Intermediate grades are available by blending the two neighboring standard grades to the desired target viscosity. A useful expression used to approximate the required percentages of the two components to prepare a blended fluid is:

$$\log KV\ 100°C = X_1 \log n_1 + (1-X_1)\log n_2$$

Where KV 100°C is the viscosity of the desired fluid at 100°C, X_1 is the % of Component 1, $1-X_1$ is the % of Component 2, n_1 is the viscosity of Component 1 at 100°C, and n_2 is the viscosity of Component 2 at 100°C.

PAO's have been successfully used for aerospace bearing applications for many years and are the successors to the highly refined KG-80 type mineral oils. Moreover, PAO's can serve as a viable lubricant type to better understand the structure and activity relationship relevant to all lubricants intended for the environmental demands of hard vacuum, extremes of temperature, and mission-limiting tribological constraints. Whether lubricating oil or grease, the demands of aerospace require lubricants with low vapor pressure and low temperature fluidity. Table 3 lists the molecular weight, approximate low temperature limit, and vapor pressure of five PAO base lubricating oils qualified to MIL-L-53131.

Table 3. PAO Base Oils

Grade	Molecular Weight	Low Temp. Limit °C	Vapor Pressure at 25°C
4	437 g/mole	-62 °C	N/A
6	529 g/mole	-57°C	8.8×10^{-6} Pa
9	823 g/mole	-57°C	6.8×10^{-6} Pa
14	971 g/mole	-48°C	6.8×10^{-6} Pa
40	1400 g/mole	-27°C	2.1×10^{-6} Pa

From the table, it is evident that as molecular weight increases, a fluid's vapor pressure decreases, but the low temperature performance suffers. This is a good example of two desirable physical attributes that from a molecular standpoint are structurally antagonistic. Others abound. Since most lubricants are composed of various molecular weight fractions, narrow molecular-weight distributions are desirable to achieve low vapor pressure and reduce volatility. Precision distillation and vacuum hardening are two techniques when used in conjunction can greatly reduce the vapor pressure of a lubricant. In terms of additives, very little has been done to determine their suitability for vacuum environments. In the author's laboratory, the amount of tricresylphosphate in a PAO was reduced by fifty percent after 24 hours at 100°C and 10^{-4} Torr.

With improved system reliability, mission longevity or even success is now dependent on the lubricant. When considering the hard vacuum of space, approximately 10^{-13} torr, we seldom consider the thermooxidative stability of the lubricant; however, in the author's judgment we perhaps do so at some risk. The thermooxidative stability of a lubricant refers to the simultaneous affect of temperature and oxygen on the chemical stability of the lubricant. Oxygen may be viewed as a pair of molecular scissors that literally cut lubricant molecules into shorter pieces. Severed fragments can subsequently recombine to form non-lubricating films or volatilize to contaminate sensitive optical systems. Without antioxidant fortification, hydrocarbon-based lubricants, whether synthetic or petroleum, can be degraded as temperatures rise. Antioxidants do not prevent oxidation, but they are effective at appreciably extending the induction time for degradation. Oxidation is not expected to be a factor at 10^{-13};

however, proper lubricant fortification can give us some assurance that the lubricant will remain intact during prolonged terrestrial storage.

PAO's are synthetic hydrocarbons and can be compounded with additives to improve performance related characteristics. For applications where EHD conditions prevail, the most important lubricant property is viscosity. However, under boundary conditions, the chemical properties of the lubricant determine tribological effectiveness. PAO's are inherently less responsive than other lubricants under incipient metal to metal contact, but are greatly enhanced by the addition of small amounts of phosphate ester. Phosphate esters do jeopardize the vapor pressure of PAO lubricants formulated for space applications; however, the contribution to vapor pressure of chemisorbed boundary lubricant remains unknown. Work continues in the author's laboratory to identify boundary additives with better volatility characteristics than tricresylphosphate, TCP or the various synthetic analogs.

The typical properties of a PAO Grade 6 lubricating oil used for rolling element bearings are listed in Table 4.

Table 4. PAO Properties

Property	Typical Value
Color	Clear to Light Yellow
Appearance	No visible suspended matter
Viscosity at 100C	5.5 mm^2/s
Viscosity at 40C	28.5 mm^2/s
Viscosity at -40C	7720 mm^2/s
Pour Point	<-57°C
Flash Point	245°C
Acid Number	0.04 mg KOH/g
Evaporation, 24h at 149C	1.4%
Lubricity, 400N, 75C, 1h	0.45 mm wear scar

Although few have been prepared to date, greases thickened with organic soaps, lithium 12-hydroxystearate, organo-modified clay, amorphous fumed silica, and PTFE could be prepared from all of the MIL-L-53131 PAO's.

Multiply Alkylated Cyclopentane

One of the more recent additions to the world of synthetic lubricants is Tris(2-octyldodecyl) cyclopentane commonly referred to as a multiply alkylated cyclopentane, (MAC) or Pennzane SHF X-2000. The most unique feature of this fluid, with a molecular weight of only 910 g/mole, is its vapor pressure. The vapor pressure of two different lots of the uninhibited oil is summarized in Table 5.

Table 5. Pennzane Vapor Pressure

Lot Number	Vapor Pressure, Pa
PCC-1	1.2 x10^{-9} Pa
PCC-2	2.5 x10^{-9} Pa

Other typical physical properties of the fluid are reported in Table 6

Table 6. Pennzane Properties

Property	Typical Result
Viscosity at 100°C	14.3 mm^2/s
Viscosity at 40°C	107 mm^2/s
Viscosity at -40°C	80,500 mm^2/s
Viscosity Index	137
Flash Point	300°C
Pour Point	-55°C
Density at 25°C	0.84 g/ml
Coefficient of Thermal Expansion, 25 to 100°C	8 x 10^{-4} cc/cc/°C
Lubricity, 400N, 75°C,1h, 1200 RPM	0.34 mm wear scar

MAC has a vapor pressure similar to that of linear perfluorpolyether and superior lubricating properties under boundary lubricating conditions. Moreover, it can be fortified with antioxidants and special additives to improve lubricity or load carrying capacity.

Phenolic antioxidants such as Thiodiethylene bis-(di-tert-butyl-4-hydroxy) hydrocinnamate do not contribute to the vapor pressure of the base oil at temperatures below 75°C and lead naphthanate, if molecularly distilled to remove the solvent vehicle, also has negligible impact on the vapor pressure of the formulated lubricant. However, phosphate ester boundary lubricants do jeopardize vapor pressure at the 1% loading level.

Some of the recognized deficiencies of the MAC fluid are its low temperature limitations, the kinematic viscosity at -40°C is about 80,000 mm^2/s, a susceptibility to oxidation at elevated temperatures if not stabilized with antioxidant, and the fact that only one viscosity grade is available.

Grease Based on MAC

Only one lubricating grease is currently available prepared from Pennzane SHF X-2000 and its vapor pressure is much less than that of the corresponding MAC base oil. The reason for the increase in volatility results from chemical contaminates being incorporated into the grease during the formation of the thickener. However, vacuum hardening of the finished lubricant appreciably reduces volatility. The grease

thickener is Sodium octadecylterephthalamate and represents approximately 20% of the formulation. This particular thickener behaves as a complex soap in that the dropping point of the grease is approximately 260°C and being sodium based it is expected to have good rheological characteristics for high speed rolling element bearing applications. Some of the typical properties of Rheolube 2000 are reported in Table 7.

Table 7. Rheolube 2000 Properties

Property	Typical Result
Color	Light Brown
Odor	Slight Amine
Unworked Penetration	265
Worked Penetration, 60X	276
NLGI Grade	2
Oil Separation, 24h at 100°C	3.3%
Ultrafiltered	Yes
Density, 25°C	0.89 g/cc
Lubricity, 400N, 75°C, 1h, 1200 RPM	0.38 mm wear scar
Oxidation Stability, 168h at 100°C	10 kPa pressure drop
Vapor Pressure at 25°C	1.3×10^{-5} Pa

It should be noted that the vapor pressure of the grease is determined at 150°C, 100°C and at 75°C. At these elevated temperatures there is also contribution from the various additives that are compounded into the grease. The reported vapor pressure at 25°C is extrapolated using the Classius -Clapeyron equation.

Other approaches to manufacture a low vapor pressure grease from the Pennzane base oil include using hydrophobic fumed silica, and high efficiency polytetrafluorethylene. A grease has been prepared in the author's laboratory using PTFE and initial results look promising.

Conclusions

A discussion of some of the relevant properties of two important lubricant classes has been presented. It is hoped that this synopsis has provided some insight into the factors that must be considered when selecting lubricants for aerospace mechanisms.

References

1. Buckley, D.H. and Johnson, R.L., "Evaporation Rates for Various Organic Liquid and Solid Lubricants to 10-8 Millimeters of Mercury at 55 to 1100F," NASA Technical Note NASA TN D-2081, Washington, DC (1963).

2. Didziulis, S.V. and Bauer, R., "Volatility and Performance Studies of Phosphate Ester Boundary Additives With Synthetic Hydrocarbon Lubricant," Aerospace Report Number TR-95(5935)-6., The Aerospace Corporation, El Segundo, CA.
3. Betrand, P.A. and Carre, D. J., "The Vapor Pressure of Lead Naphthanate," Aerospace Report Number TOR-93(3478)-3, The Aerospace Corporation, El Segundo, CA.
4. Bessette, P. A., "The Vapor Pressure of Oils and Greases," NLGI Annual Meeting, Orlando, FLA., 1993.

Development of a New, No-Shock Separation Mechanism for Spacecraft Release Applications

Shawn H. Smith[*] , Bill Purdy[**] , Bill Nygren[***]

Abstract

A new release mechanism has recently completed development which solves the pyro-shock and strain-energy shock problems inherent in existing pyrotechnic and non-pyrotechnic release alternatives. The Fast-Acting, Shockless Separation Nut (FASSN) uses no pyrotechnics and converts strain energy built up in the release shaft into harmless rotational energy during release. The FASSN releases loads greater than 44.48 kN (10,000 lbf) in less than 30 milliseconds and meets all the other basic requirements of competitive separation alternatives.

Introduction

As spacecraft get smaller and lighter, the need for fast, low-shock separation between the spacecraft and launch booster becomes more important. Current methods of releasing payloads from spacecraft boosters typically employ pyrotechnic separation devices which offer the advantage of fast, simultaneous release, but deliver extremely high shock loads to surrounding structure and create a stressing environment for spacecraft components.

Traditional non-pyrotechnic release devices which maintain the fast-release time characteristics of pyro-devices do not address the shock generated by the release of strain energy stored in the release bolt. Slower-acting, non-pyrotechnic release alternatives which may be motor or thermally driven, solve this strain-release shock problem, but at the cost of substantially slower release times and decreased simultaneity between units.

An innovative new mechanism that eliminates both the pyro-shock and the shock induced by strain-energy stored in the release shaft while still maintaining the fast, simultaneous release times has recently completed development. The FASSN uses no pyrotechnics and converts strain energy built up in the release shaft into harmless rotational energy during release. The FASSN also releases loads in excess of 44.48 kN (10,000 lbf) in less than 30 milliseconds at ambient conditions. Figure 1 shows a photograph of one of the prototype mechanisms, while Figure 2 shows comparative shock data of the FASSN versus an equivalent pyrotechnic separation nut.

[*] Starsys Research Corporation, Boulder, CO
[**] Naval Research Laboratory, Washington, D.C.
[***] Lockheed Martin Astronautic, Denver, CO

The FASSN is designed to be a "drop-in" replacement for existing pyrotechnic separation devices and uses a firing pulse identical to that used to fire pyrotechnic separation devices. The FASSN is fully resetable without removal, retrofit or refurbishment of any hardware. The FASSN also meets all the other basic requirements of competitive separation nuts with respect to fast function times, load carrying capacity, environments, electrical requirements, simultaneity, and misalignment.

The FASSN was developed jointly by Starsys Research and Lockheed Martin Astronautics, with assistance from Swales and Associates, and Naval Research Laboratory. Additional assistance was provided by TiNi Aerospace. The FASSN recently completed development testing in August 1996 and enters qualification testing in February of 1997. The development testing program consisted of over 300 tests which encompassed all of the tests to be performed in the qualification program including baseline functional testing (8.90 kN (2000 lbf) to 62.27 kN (14000 lbf)), random vibration (24 Grms), shock (8000 G's), thermal vacuum (-25C to +60C), performance, misalignment (1 degree and 0.762 mm (0.030") offset), maximum load (62.27 kN (14000 lbf)), life (50+ load and release cycles), and others. The first flight of the FASSN is on a classified satellite for Lockheed Martin Special Programs scheduled for sometime in 1997.

This paper will discuss the following topics:

1. The FASSN design.
2. Testing and performance of the mechanism.
3. The development history of the FASSN.
4. Design evolution and problems encountered.
5. Conclusions and lessons learned.

The FASSN was invented by Bill Nygren of Lockheed Martin, Denver, Colorado. The technology has been patented by Lockheed Martin and is licensed exclusively by Starsys Research.

Design, Testing, and Performance

Design

The FASSN is designed to release a satellite from its launch booster in the same manner as a typical pyrotechnic separation nut except that negligible shock is imparted to the surrounding structure and instrumentation. The way this is achieved is described in the following paragraphs.

Illustrated in Figure 3, the FASSN consists of 5 main components: a Housing, a long-lead threaded Bolt/Flywheel Nut assembly, an internal Latching Mechanism, a Nitinol

Actuator[1], and a Bolt Catcher. Under tension, the long-lead thread of the Bolt/Flywheel Nut assembly creates a backdrive torque which is reacted internally in the FASSN by the Latching Mechanism. Similar to a standard gear reduction, the Latching Mechanism reduces the backdrive torque by a factor of over 1000:1. This reduced torque is reacted on a face cam attached to the shaft of the Nitinol Actuator.

When energized, the Nitinol Actuator rotates the face cam and releases the internal Latching Mechanism, which retracts from all latching points and locks in place. This allows the Flywheel Nut, which is mounted on a stack of thrust-needle bearings, to rotate freely under the backdrive torque. This action releases the load and ejects the bolt into the Bolt Catcher. The Bolt Retractor captures the bolt and retains it past the separation plane. During release, strain-energy in the Bolt is converted to harmless rotational energy in the spinning Flywheel Nut, thus achieving a shockless release.

The FASSN is reset when the long-lead Bolt is manually pushed back through the separation interface and inserted back into the Flywheel-Nut. Upon full thread engagement in the Flywheel Nut, the Bolt activates a plunger which allows the Latching Mechanism to re-engage the latching points. In a separate step, the Nitinol Actuator is reset and the FASSN is ready for reloading and another release.

Axial load on the FASSN is applied using a SuperNut ® which allows loads in excess of 44.48 kN (10000 lbf) tension to be applied with maximum torques of only 5.09-5.65 N•m (45-50 in•lbf) on each jackbolt.

The Nitinol Actuator makes the FASSN electrically transparent with pyrotechnic separation nuts. The Actuator is energized using a standard 3.5 amperes minimum current. The more current applied to the Actuator, the faster the release occurs. The Actuator has two completely redundant firing circuits either or both of which will actuate the device when current is applied. In order to allow repeated ground test firings without the risk of overheating the Nitinol wire, cut-off switches have been incorporated on each circuit which shut off the current to the Actuator after functioning.

Testing and Performance

Several hundred tests were performed on the FASSN during development. Table I illustrates the testing conditions and environments. Table II illustrates the FASSN performance specifications determined during the test program. All testing was designed to envelop anticipated Special Program design requirements.

Development History of the FASSN

The FASSN was developed under an aggressive schedule. The initial idea and proof-of-concept unit evolved over a period of approximately 5 years before a patent was awarded. The development thrust, however, was given just 12 months from initial

[1] Manufactured by TiNi Aerospace Corporation, San Leandro, CA

creation of pre-production drawings through completion of all development testing. The devices for each iteration were tested intensively with the intention of aggressively exposing design weaknesses so that design improvements could be made in the next iteration. This method was painfully successful in exposing potential failure modes within the mechanism.

The development relied heavily on "back of the envelope" calculations and test results and was done in parallel with stress and dynamics analysis and modeling. The eventual correlation of test results with analytical efforts was crucial to the decision to use the FASSN for a flight critical application.

The development team included the manufacturers of the FASSN and the Nitinol Actuator, the FASSN inventor, a government laboratory, and their subcontractor. This was necessary for a variety of reasons. Assembly of such a diverse team brings an array of talents, resources, and viewpoints to the development and engineering process. Also, the teamwork between larger and smaller organizations on the team proved especially advantageous. For the FASSN team, technical expertise between the organizations was shared, however, analysis capabilities and test facilities were generally provided by the larger organizations while significant time and cost savings were achieved by procuring materials, machining parts, and building hardware through the smaller organizations.

The one main challenge for the FASSN team was communication between group members located across the country. This was resolved by performing critical testing and design reviews with all members present. This provided an invaluable advantage on numerous occasions when problems or failures occurred and quick resolution was required. It also provided for a general unity of effort towards a common cause which resulted in time and cost efficiency.

The success of this build and test-based development process using a diverse team consisting of both large and small organizations is one of the key lessons learned during this project.

Design Evolution and Problems Encountered

The current design evolved through essentially 4 major design iterations:

1. Initial concept unit, EDU 1.0.
2. A modified version of EDU 1.0, referred to as EDU 1.5.
3. Completely rebuilt, working development units, EDU 2.0A and 2.0B.
4. Final design used for qualification and flight.

EDU 1.0

From the start, the primary goal of the FASSN program was to produce a device which would release large tension loads very quickly with essentially no shock. We were also looking to provide an alternative release device which would provide the benefits of low-shock while eliminating the use of explosives. Towards this end, all the FASSN's from initial concept to the flight design have maintained essentially the same design concept required to produce a shockless release; that is, a long-lead threaded bolt is engaged with a mating Flywheel Nut that is mounted on a stack of thrust needle bearings. Under tension, the long-lead thread creates a backdrive torque which is reacted and reduced by an internal latching mechanism. When this latching mechanism is released by a rotary actuator, all strain energy in the bolt is transferred to the Flywheel Nut in the form of harmless rotational energy and the bolt is ejected and retained by a Bolt Retractor. Another important, but secondary goal was to make the FASSN easily resetable and reusable.

The key to the design, however, and the main source of its evolution was initially in the answers to the following questions:

1. How can enough torque be generated to reliably release internal Latching Mechanism, given the current , function time, and simultaneity constraints established by other release alternatives?
2. Since the design concept inherently requires sliding between mating and latching parts, how can the effects of sliding friction be minimized so that the design is repeatable and reliable?
3. What are the optimum materials for high stress parts?
4. How will the axial load be applied?
5. How can the device be reliably reset and reloaded without affecting its primary function which is to unload and release?

EDU 1.0 was the first attempt to address these questions. For this unit an electric rotary solenoid was selected as the means to provide the torque required to release the internal latching mechanism. As the solenoid rotates in this design, the lockarm slides away from the single point of engagement with the internal Latching Mechanism. The effects of sliding friction in other parts of the mechanism were minimized by designing the parts such that the friction vectors at sliding surfaces were directed through the axis of rotation of each part. Thus, the friction vectors created at sliding points of contact effectively generated no moment. Friction between the long-lead threaded Bolt and Flywheel Nut was minimized by application of solid-bonded lubricant along with generous amounts of Braycote 602 grease. These two methods of handling friction proved extremely successful are were maintained as part of the baseline design all the way through flight.

The highest stressed components of the Latching Mechanism were fabricated from 440C stainless steel which was hardened to RC 56-60. The bolt was fabricated from Aermet 100 alloy. The Housing, which contained latching points to engage with the

internal Latching Mechanism, was of single piece construction fabricated from PH13-8 stainless steel, heat treated to condition H1000. Axial load was applied by means of a torque nut on the end of the bolt opposite the long-lead thread.

On EDU 1.0, a one-step reset was achieved when the Bolt was re-inserted into the Flywheel Nut. Upon full engagement with the Flywheel Nut, the Bolt would activate a plunger which would not only allow the internal Latching Mechanism to reset (by spring action), but also allow the Solenoid to return to its reset position under the power of its own return spring.

Although successful in demonstrating the shockless release concept, EDU 1.0 failed by almost every other design standard. The problems can be summarized as follows:

1. The Solenoid failed to respond quickly enough to the quick actuation pulse. Typically, the solenoid could not reach full torque at ambient temperature for at least 30 ms. This was much too slow to achieve the goals of the FASSN program. Even at full torque, the functional margins were insufficient.
2. There were no provisions to visually verify proper reset. Since the reset didn't always work inadvertent load paths and structural failures of internal parts occurred.
3. The torque output of the solenoid was highly variable with temperature.
4. The solenoid was heavy.
5. The single point of engagement of the lockarm with the internal Latching Mechanism was pure sliding friction. This created very unpredictable results and made prediction of the torque required to release the internal Latching Mechanism almost impossible. This design also had the embarrassing tendency to release uncommanded during vibration or shock.
6. 440C stainless steel was extremely brittle and fractured under high loads and under creep conditions.
7. The torque nut as a means to apply axial load proved extremely cumbersome. Torques as high as 203 N•m (150 ft•lbf) were required to apply 44.48 kN (10000 lbf) to the Bolt and difficulties were experienced in maintaining the load over time.

EDU 1.5

EDU 1.0 obviously needed some improvement. At that point, however, there was neither time nor money to redesign and manufacture new parts. Fortunately, TiNi Aerospace had joined the FASSN team and had offered the use of a Nitinol Rotary Actuator to replace the rotary solenoid. EDU 1.5 took the EDU 1.0 mechanism and replaced the electric rotary solenoid with the Nitinol Rotary Actuator. The Nitinol Rotary Actuator offered the following advantages:

1. It generated over 4 times more torque.
2. The torque output was created by an internal, redundant, mechanical torque springs. Thus, the torque was not affected by temperature.

3. The design of the actuator was such that no uncommanded releases could occur.
4. The actuator weighed 1/4th as much as the solenoid.

The tradeoff was that the Nitinol Actuator did not lend itself to a 1-step reset of the FASSN. The Actuator instead had to be reset in a separate operation. This was considered an acceptable tradeoff since the time to reset the device was still minimal. The other shortcomings identified under EDU 1.0 testing were not addressed. This was particularly true with respect to ports in the FASSN which would allow visual confirmation of proper reset.

EDU 2.0

Naval Research Laboratory along with Swales and Associates entered into the FASSN team at that point with funding from the ARTS II program for continued FASSN development. Under the ARTS II program, EDU's 2.0A and 2.0B were created to address these and the remaining problems with the initial designs. The two units had packaging differences and were tested in parallel so that we could settle on a flight configuration with confidence in a minimum amount of time.

EDU's 2.0A and 2.0B represented significant improvements to EDU's 1.0 and 1.5 in the following ways:

1. The single point release of the internal Latching Mechanism was changed to a two-point, symmetrical face cam design which rolled away from the latching points. This design significantly reduced the effects of frictional forces by changing from sliding friction to rolling friction. This design also changed the load path so that zero net force is acting on the center shaft of the rotary actuator. This decoupled the torque to release from the applied axial load to the bolt.
2. The material of the highly stressed components of the internal Latching Mechanism was changed to Custom 455 Stainless Steel, condition H1000.
3. A SuperNut® was used to apply the axial load to the bolt. This reduced the torque required to generate 44.48 kN (10,000 lbf) from 203 N•m (150 ft•lbf) to 5.1 N•m (45 in•lbf).
4. Viewports were added at critical latch engagement points to provide visual verification of proper latching and proper latching sequence.

EDU's 2.0A and 2.0B were identical internally. EDU 2.0B was even a little bit more evolved from early designs in that it used a 3-piece, aluminum and steel housing instead of a 1-piece steel housing. This reduced weight, saved machining time, and improved assembly. After significant testing to both of these units, it was felt that the original design questions had been answered. However, other questions surfaced which were more pertinent to flight applications and general reusability concerns. Among these are the following:

1. The Nitinol wire in the Actuator cannot be reused if too much current is applied for too long a time. While not a flight concern, this presented serious testing constraints and raised the question of: How can the Actuator be made insensitive to higher currents applied for a longer duration of time?
2. In preparation for flight, how can it be determined if the FASSN is properly loaded and those loads are properly shared in the internal Latching Mechanism?

The final flight/Qualification design addressed these problems in the following manner:

1. Cut-off switches were incorporated into each redundant circuit of the Nitinol Actuator which would cut-off current to the nitinol wire after functioning. This prevented the nitinol wire from overheating and allowed for complete electrical transparency. In order to avoid questions about switch reliability, bypass circuits were added which would allow firing current to bypass the cut-off switches in the event of switch failure.
2. Strain gages were added to the Housing of the FASSN near the engagement point with the latches of the internal Latching Mechanism. This allows direct verification of backdriving torque and load sharing of the latches.

The issue of electrical transparency is worth some discussion. A typical pyrotechnic separation nut has a 1.0Ω bridgewire. In order to provide a typical 5A current pulse from a 30 VDC bus voltage, an in-line resistor is required. After functioning, the circuit opens when the bridgewire burns out. The same scenario exists for the FASSN except that the resistance of the in-line resistor is different, since the FASSN circuit resistance is approximately 4Ω. Also in the same manner as bridgewire burnout for a pyro-device, the cut-off switches on the FASSN open the circuit after functioning.

One other change worth noting was that the long lead threaded Bolt material was changed from Aermet 100 Steel to MP35N Steel. This change was made because the stress corrosion properties of MP35N are superior to those of Aermet 100, although no problems were experienced with Aermet 100.

Reliability of the Mechanism

One of the most significant problems that must be overcome for a new mechanism is how to demonstrate reliability. This is especially true when the mechanism is designed to replace pyro-devices which show many 9's reliability based on a large data base of demonstrated firings. To illustrate the scope of the problem, consider the following:

The formula for demonstrated reliability, R, given n successful releases is:

$$R = (1 - \text{confidence level})^{(1/n)}$$

For a 95% confidence level it would take 3000 successful releases to demonstrate a 0.999 reliability. Since 4 FASSN's must operate for mission success, the reliability under these conditions is as follows:

$R_{system} = R^4 = (0.999)^4 = 0.996$

In order to get the system reliability up to 0.999, it would take 12,000 successful FASSN releases.

Therefore, the only practical way to prove reliability is through structural and functional margins. With the FASSN, this is achieved in the following ways:

1. During in-process testing, measurements or the torque required to release the device manually are made on each FASSN and compared with measurements of the output torque of the Nitinol Actuator.
2. The force to manually actuate every Nitinol Actuator is measured as part of its acceptance testing. This is compared with the measured force output of the lot of nitinol wire when energized.
3. On every FASSN, axial load is monitored in the Bolt and direct strain measurements are taken from the notched section on the Housing where the latches engage. This data can be used to verify backdrive torque and compare component allowables with applied stresses.

With the above data, the following coupling equation for the interference of two normal distributions can be used to calculate reliability:

$Z = (\text{mean available} - \text{mean required})/(\text{std\_dev\_available}^2 + \text{std\_dev\_reqd}^2)^{(1/2)}$

Z is used to obtain a value from reliability tables and then the reliability can be determined from:

R = 1 - table value

Conclusions and Keys to Our Success

Development of the FASSN was highly successful. The end result was a robust, well-tested mechanism that evolved from napkin sketch to achieving flight heritage in one year and 8 months. Numerous lessons were learned or confirmed during development of the FASSN which can be described in both engineering as well as philosophical terms. From an overall perspective, the following can be stated:

1. Test with an eye for establishing failure modes and functional margins. Nobody likes to have failures, particularly when time and money are critical, but the limits and capabilities of a new mechanism must be known.

2. Build and test, build and test. The FASSN computer model resembles a mixture of many types of pasta all mixed together and makes even the most powerful Pentium chip beg for mercy. There simply is no substitute for human hands touching hardware and evaluating fits and function.
3. Build a team. The assembly of a design/development team consisting of user, vendor, subcontractor, and test support proved extremely valuable and effective. This requires extra efforts in communication, but it is well worth it since it allows considerable parallel efforts and pooling of expertise.
4. Two minds are better than one. No design solutions on the FASSN were done alone. The best designs were team efforts, the key is knowing at what point the design is complete.
5. If it ain't broke, don't fix it. The fundamental concept of the FASSN did not change from EDU 1.0 to flight. This was because it was determined early on that the basic concept worked. There was, however, considerable temptation to improve it, even though we all knew it worked. This is hard to resist sometimes, but one has to continually evaluate the benefits of improving an already good design against the risks of introducing a new failure mode.
6. Avoid sliding friction. Minimization of the effects of sliding friction by clever design makes the mechanism more predictable, consistent, and reliable.
7. Don't use materials susceptible to stress corrosion cracking whenever possible. Just say no to materials susceptible to stress corrosion cracking.
8. Determine reliability by measuring functional margins. This is achieved by thorough in-process and lot acceptance testing. Its hard to argue about reliability when functional margins on the flight units can be tested and measured on the ground.
9. Use a SuperNut® to apply large tensile loads. They are an extremely efficient means of applying axial load.
10. Avoid blind assemblies. Visual verification of critical mechanism conditions provides an extremely easy verification of mechanism setup.
11. Fly what you test, test what you fly. Also see lesson #8. With a new mechanism in particular, considerable confidence is gained if this simple rule is followed.

References

1. Shigley, J.E. and Mischke, C.R., "Mechanical Engineering and Design.", 5th edition, McGraw-Hill, Inc., 1989.
2. Dovich, R.A., Reliability Statistics, ASQC Quality Press, 1990.

Table I: Development Test Matrix

Test	Description
Break-in Tests	8.90 kN (2000 lbf) 22.29kN (5000 lbf)
Baseline Functional	31.34 kN (7000 lbf)
Random Vibration	24 G_{rms}, 3 minutes/axis, 31.34 kN (7000 lbf)
Shock	8000 G's, 1 shock/axis, 31.34 kN (7000 lbf)
Thermal (non-Vacuum) -40°C -25°C -10°C +50°C +70°C	31.34 kN (7000 lbf) all tests
Thermal Vacuum -25°C +60°C +70°C	31.34 kN (7000 lbf) all tests
Angular Misalignment	½ °, 1°, 31.34 kN (7000 lbf)
Creep	31.34 kN (7000 lbf), 30 days 31.34 kN (7000 lbf), 60 days
Life	31.35 kN (7000 lbf), 50+ cycles
Maximum Load Test	44.48 kN (10000 lbf) to 62.27 kN (14000 lbf)

Table II: FASSN Specifications

Description	Specification	Comments
Thread Size	12 mm(½ in)	
Nominal Load Range	22.24 kN to 44.48 kN (5000 lbf to 10000 lbf)	
Ultimate Load Capacity	62.27 kN (14000 lbf)	
Function Time	< 50 msec	First application of current to 10% load on bolt
Temperature Range	-25°C to +60°C	
Misalignment/offset	1° max angular/ .030" offset	
Simultaneity	± 7.5 msec	units at same temperature
Random Vibration	24 Grms, 3 min/axis	
Shock	8000 G's	
Vacuum	1 x 10^{-4} torr	Higher vacuum acceptable
Firing Current	3.5 A, min 70 msec min pulse	Higher currents result in faster acuation times. Cut off switches in Actuator allow for ground testing at higher currents.
All-Fire	2.4 A with 70 msec firing pulse	
No-Fire	.6 W	
Circuit Resistance	3.7 Ω ± .20 Ω	
EMI/RFI	20 dB	

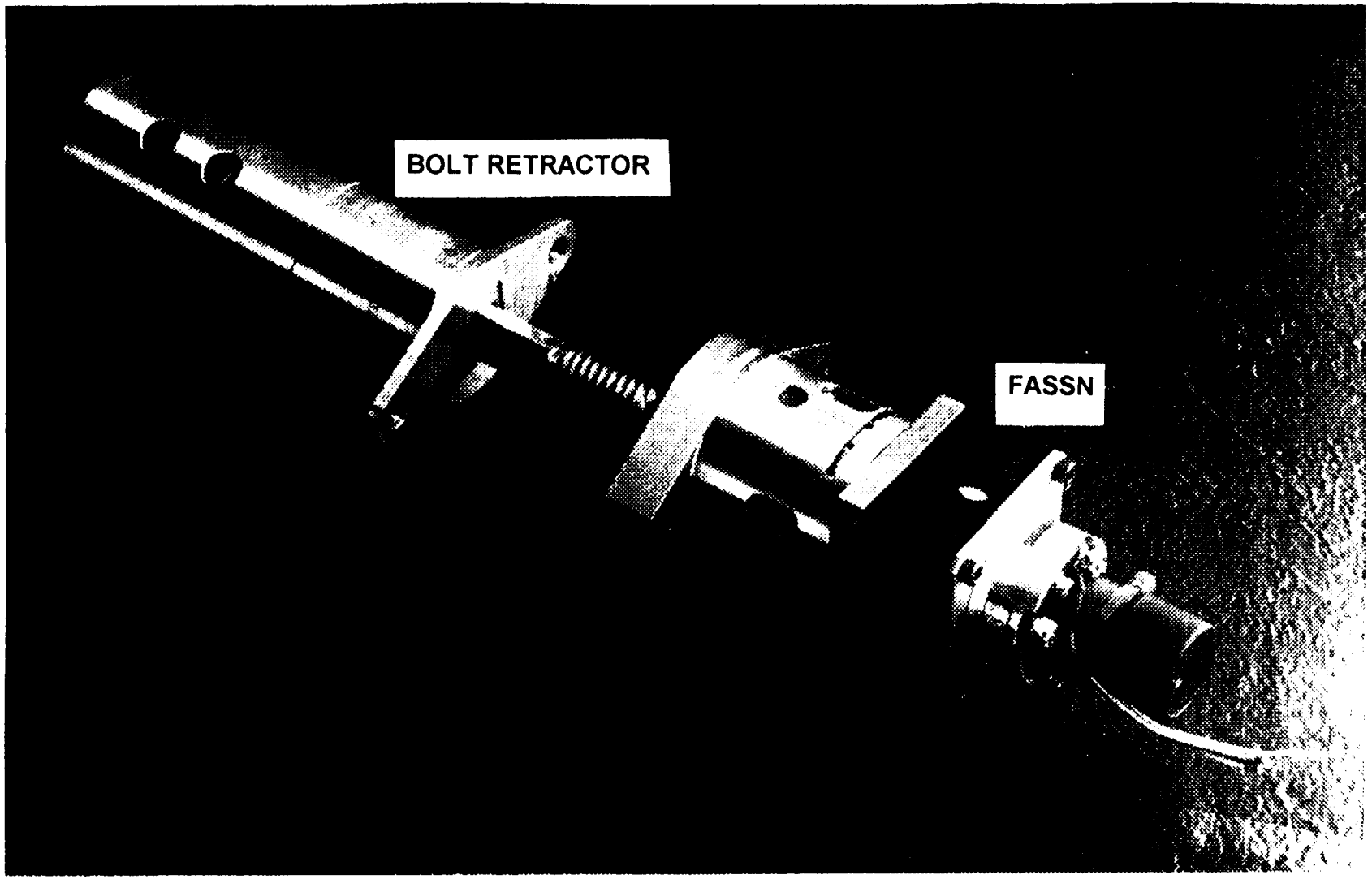

FIGURE 1: FASSN ASSEMBLY

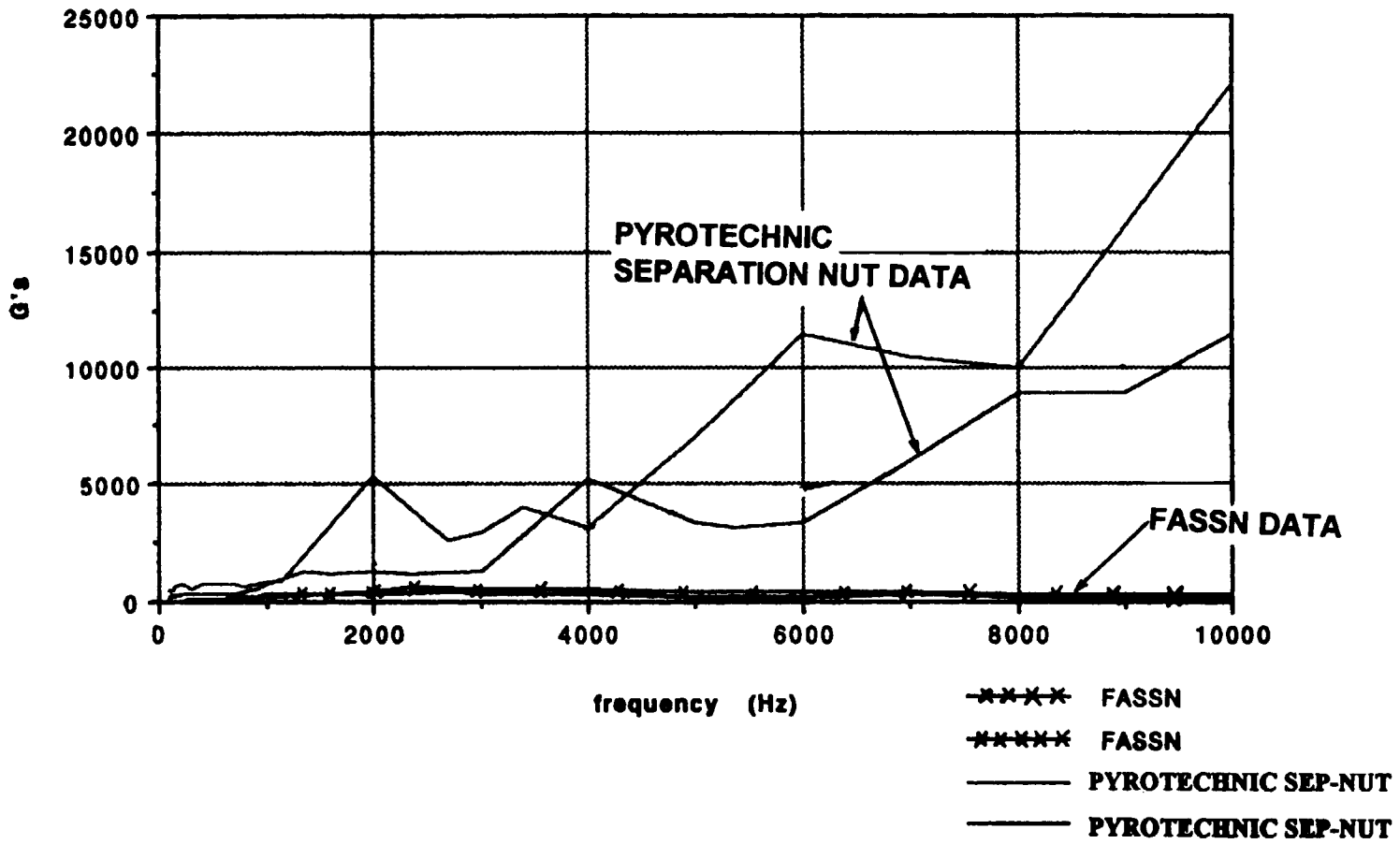

FIGURE 2: COMPARATIVE SOURCE SHOCK DATA

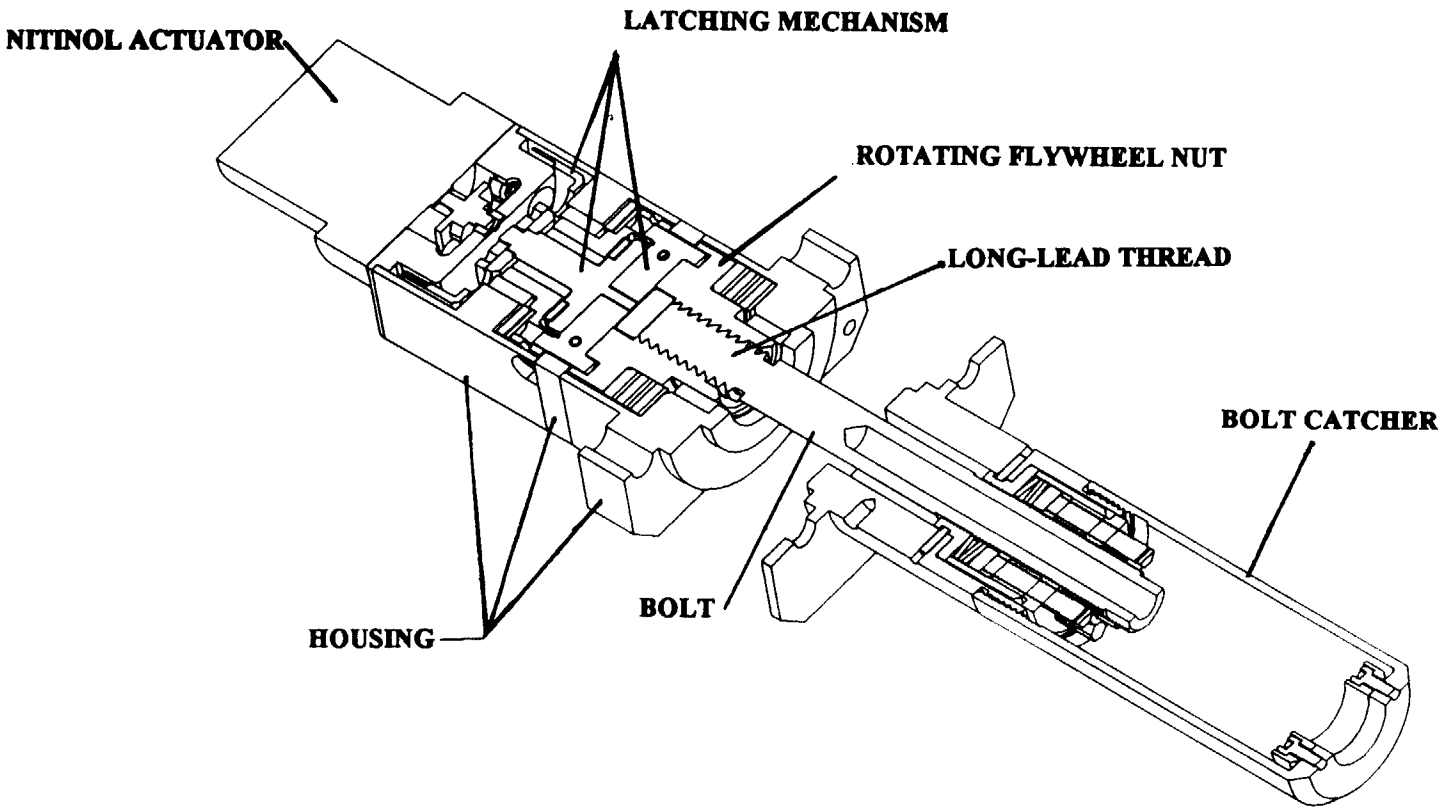

FIGURE 3: FASSN ASSEMBLY CROSS-SECTION

Environmental Sensor Boom Experiment Using Shape Memory Alloys for Release, Deployment, and Final Lockup

Steven P. Robinson*, Robert T. Gammon*, John E. Koch*, Jerry D. Stephenson*

Abstract

An experiment was recently flown in space which demonstrated the capability of the Shape Memory Alloy(SMA), NiTiNOL, to perform a variety of deployment functions normally accomplished by more conventional technologies. The deployable element was a 127 cm(50 in) experiment boom mounted to the host spacecraft via a rigid strongback. This paper will describe the overall design of the experiment, including detailed descriptions of the various SMA-actuated mechanisms. In addition to the aforementioned devices, a novel "bearingless" joint design, developed at Boeing, was successfully demonstrated.

The design of this experiment, from initial concept generation through subsequent fabrication, test, and on-orbit operation yielded valuable information about the potential usefulness and practical limitations of SMA materials in this application area. The paper will also describe lessons learned from environmental and qualification testing in addition to actual on-orbit operation.

Introduction

Since the late 1980s, the Boeing Defense & Space Group has been investigating the viability of SMAs, particularly NiTiNOL, as an alternative approach to conventional devices used for deployment and operation of appendages on spacecraft. NiTiNOL, a Nickel-Titanium alloy originally developed by the Naval Ordnance Laboratory in the early 1960's, was the alloy of interest due to its combination of unique mechanical properties. The most unusual was its ability to "remember" a given shape when heated to an intermediate temperature(~100°C). Though NiTiNOL can be plastically deformed by as much as 8%, heating to its shape recovery temperature returns the material to its predeformed shape while accomplishing useful work. Several proof-of-concept devices were developed under Independent Research & Development (IR&D) demonstrating NiTiNOL's ability to perform mechanical functions such as structural release, controlled precision movement, active vibration suppression, as well as shape control, without the need for explosive nuts, electrical motor/gear sets, springs, or other conventional technologies. This preliminary work showed the material has the potential capability of revolutionizing mechanism development for aerospace applications. Improvements in packaging flexibility, size, force/weight ratio, shock mitigation, and cost are possible using these materials.

* All of Boeing Defense & Space Group - Kent, Washington

System Requirements

The initial system requirements were straightforward and are listed below in Table 1. However, concept application and requirement evolution imposed additional constraints on the design. Because of the evolving nature of the system requirements definition, complete identification was not accomplished until late in the experiment design development phase. This disrupted fabrication and testing because of design iterations required to satisfy the evolving system requirements. The biggest impacts were the requirements to restow the boom in the event of deploy or lock failure and provide information on experiment performance without discrete telemetry channels. Table 1 also shows the final approved system requirements list.

Environmental Sensor Experiment Description

The experiment is a 2-piece system consisting of a strongback and the environmental sensor boom. The strongback, which is the main structural attachment between the host vehicle and the deployable boom, housed the electrical cabling and hardware, release device, locks, rotation joint, and deployment actuators. The boom housed two(2) environmental sensors in addition to the preload pin assembly, deployment actuator attachments, and the studs used for locking the boom in its deployed state.

The boom was a 7.62 cm(3.0") diameter aluminum tube 127 cm(50 in) long on which two(2) experimental sensors were mounted. The boom is released and rotated by NiTiNOL actuators through a 180 degree arc locking the boom mounted sensors to the outboard side of the rigid strongback. The experiment configurations, both stowed and deployed, are shown in Figure 1.

The release device, deploy actuators, and ring locks were operated in autonomous sequence once power was applied to the experiment. High reliability was achieved by having two(2) independent electrical circuits - one for the primary and the other for the redundant string of actuators. Using NiTiNOL, provided the ability to add redundancy very easily by simply including another actuator element with minimal scar weight.

Boom release and deployment used NiTiNOL wire to provide the torque required for both of these operations. At the end of the deployment operation, locks used NiTiNOL rings that clamped onto boom mounted studs inserted into the lock openings. NiTiNOL lock mechanisms used externally mounted strip heaters to provide the thermal energy for shape recovery because the rings were too bulky to be electrically heated with the power available for the experiment.

The electrical circuit was designed to accomplish two(2) functions. The prime function was application and autonomous transfer of electrical power to each device as the sequence of deployment operations occurred. The other was providing telemetry to monitor the experiment's performance to indicate success or failure. The circuit was essentially a resistor network where strip heaters were used as ballast resistors to dissipate power and produce the desired voltage drop across each device to indicate

Table 1 - Experiment System Requirements

Initial Requirements List	Final Requirements List
1) Autonomous operation	1) Autonomous operation
2) Redundant capability	2) Redundant capability
3) Single fault tolerant	3) Dual fault tolerant
4) Power: 2-28V/5A circuits	4) Fail-safe operation
5) Stowed frequency >14 Hz	5) No self-actuation below 74 C(165 F)
6) Deployed frequency >7 Hz	6) No discrete telemetry channels
7) Max. shock:240 Gs @1KHz	7) Restow capability
8) Discrete telemetry channel(s)	8) Min. operational temp. -25 C*(-13 F)
	9) Max. operational temp. +50 C*(122 F)
* These apply to release and deploy operations only. Lock rings have the following temperature limits:	10) Stowed frequency >14 Hz
	11) Deployed frequency >7 Hz
	12) Max. shock:240 Gs @ 1KHz
Min.: -70 C(-94 F)	13) Power: 2-28V/5A circuits
Max.: +35 C(95 F)	14) Total weight: < 14 Kg(31 lbs)

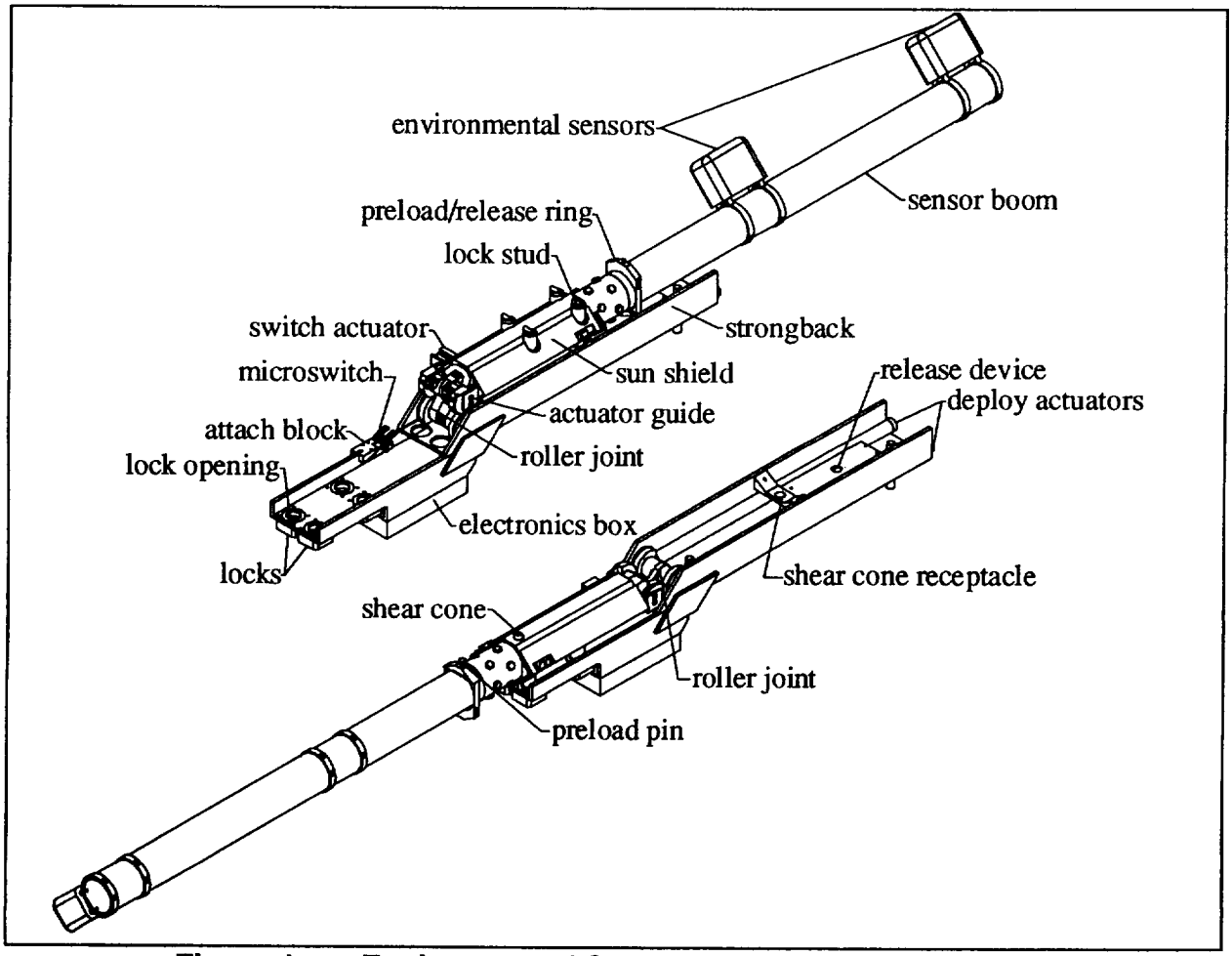

Figure 1: Environmental Sensor Experiment Description

the experiment's operational state. Microswitches were used to change circuit voltage providing unique voltage drop values which corresponded to specific deployment operations. Total circuit voltage drop was the only experiment telemetry monitored during the boom's deployment. As each function occurred, total circuit resistance was controlled by microswitch operation. The sequential change in circuit resistance was the core of our simple telemetry scheme. The voltage monitoring telemetry showed boom release, deployment angle of 180°, and sensor boom latching by increases in the circuit voltage drop. Both A and B circuits incorporated this feature which provided redundant telemetry channels. Predicted voltage drop telemetry steps are shown in Figure 2. Boom latchup was not verified as part of the initial deployment. After power was turned off, the actuators were cooled down for a period of up to 2 hours. Power would be reapplied to measure circuit voltage. If the voltage drop indicated a 180° position, a positive lock would be declared.

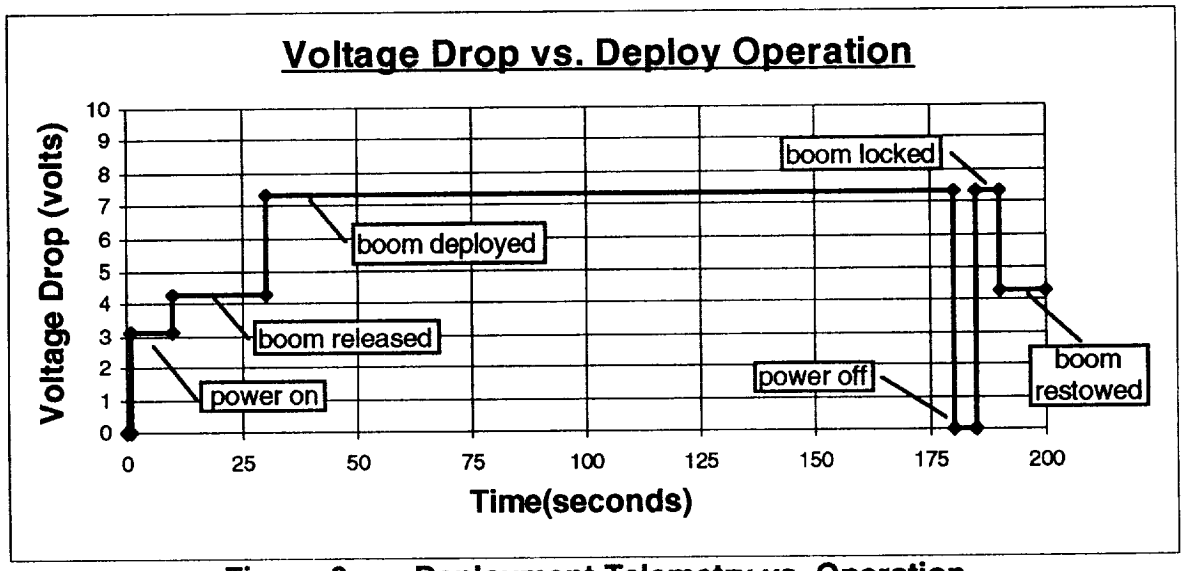

Figure 2: Deployment Telemetry vs. Operation

Experimental Mechanism Description

Boeing Developed "Roller" Joint Design

At the interface of the strongback and the boom was a unique rotation joint. The design was a Boeing developed "bearingless" joint, demonstrated under IR&D, with several potential advantages over conventional joints. These are listed below in Table 2:

Table 2 - Boeing Developed "Roller" Joint Features

1) Little or no lubrication required	6) Angular mechanical advantage = 2
2) No sliding surface contact	7) Non-concentric rotation
3) Larger contact area	8) Variable or constant moment arm capability
4) Very low rotational friction	9) Built-in "zero" position
5) Precise positioning capability	10) Built-in retarding torque from flexures

The roller joint design consists of two(2) equal diameter cylinders bound together by three(3) parallel flexures. The two(2) outboard flexures are wound around the cylinders in one direction and the center flexure is wound in the opposite direction. They are mounted to the stationary roller and attached to blocks, each with two(2) alignment pins, which are inserted into the movable roller. The alignment pins in each block are used as guide elements to maintain alignment of the flexures with respect to the two rollers. The pins also allow the blocks to be displaced outward by the action of a preload screw which was used to induce flexure preloading. This was required to maintain intimate contact between the two rollers and provide positional repeatability during joint rotation. Cams were mounted on the ends of the rollers for routing of the deploy actuators. The cams were positioned to produce an increasing moment arm with respect to boom angle. Figure 3 shows both stowed and deployed configurations of this unique joint design.

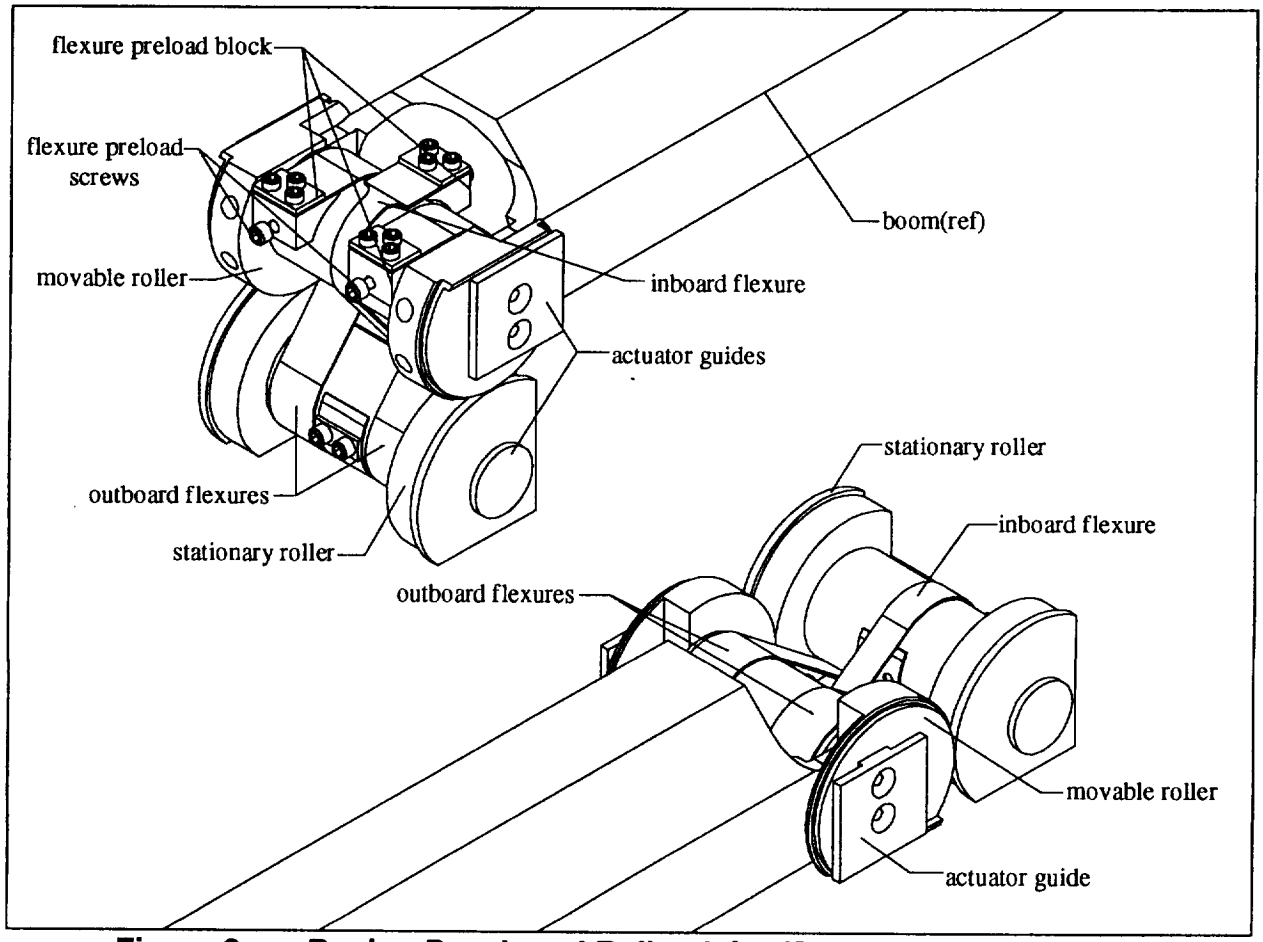

Figure 3: Boeing Developed Roller Joint (Stowed And Deployed)

Since joint rotation relied on surface rolling instead of surface sliding, rotational friction was reduced significantly thereby minimizing the need for lubrication. Vacuum testing revealed no significant increase in friction between lubricated and non-lubricated joints. Testing also demonstrated cold welding was not a concern. However, rolling surfaces produced non-concentric rotation which provided unique benefits such as a built-in

restow feature and variable deploy torque profile offering potential rotation damping to control rotation speed. It also produced a side effect not seen in conventional joint designs. The boom loading line of action across the joint changes with respect to rotation angle. This allowed the line of action to be optimum in the deployed state, but it minimized the joint stiffness in the stowed position. This would not be a problem since the boom was held by a shear cone positioned 33 cm (13") away from the joint which adequately reacted any lateral loads during launch. The joint design was rigid enough to withstand predicted operational accelerations.

NiTiNOL Actuated Preload/Release Device

The preload/release design incorporated two(2) functions. The main function was the release of the preload and physical separation of the sensor boom from the strongback. The secondary function was mechanical preloading of the boom against the strongback to react launch loads. The design incorporated two(2) independent NiTiNOL actuators each controlled by independent circuits. The preload pin is mounted to the boom by a two-piece ring assembly and held by two jaws. The preload is applied by torquing a screw, located in the ring assembly, against the boom forcing the shear cone into its receptacle and engaging the tapered pin in the jaws. When release occurs, the jaws are spring loaded to move apart eliminating any pin hang-up. Once the pin is released, a small spring, located within the preload ring assembly, pushes away from the release jaws eliminating interference between the sensor boom and release device if restowing was necessary.

The jaws were mounted on studs which not only provide free rotation, but up and down motion as well. This forced the jaws to bear against the underside of the housing creating a direct load path between boom, housing, and strongback when the pin was engaged and preloaded. The pivot end of each jaw interfaced with a set of two(2) microswitches. These configured the circuit resistance to perform the release function first, then transfer power to the deploy actuators to begin boom rotation when the switch state changed.

The jaws were held together by a center lock mechanism on a spring flexure mounted to the bottom plate of the release device. NiTiNOL actuators were attached to the lock and anchored at the other end of the release housing with phenolic blocks isolating the actuators from surrounding metallic parts. Electrical isolation was required because electrical current was used for heating the NiTiNOL to its recovery temperature. The release actuators were manually prestretched after each operation to provide full recovery stroke prior to re-installation and locking of the preload pin. The actuators had to disengage the lock under a 1.2 kN (275 lbf) preload. Each actuator, by itself, was sized to overcome the preload and pull the lock mechanism away from the jaws. Molybdenum disulfide was used at this interface to reduce the friction created by the mechanical preloading of the pin. Due to limited electrical power, sizing of the actuator element was a difficult compromise between release force, recovery stroke, available power, and minimum operational temperature. The NiTiNOL actuators were 0.50 mm(0.018") diameter wire. This provided 81 N(18 lbf) of retraction force on the lock flexure from each actuator. The shape recovery temperature of the NiTiNOL actuators was ~

100 C (212 F). This satisfied the "no self-actuation" condition imposed when using NiTiNOL. Figure 4 shows the mechanism design of the preload/release device.

NiTiNOL Actuated Deployment Actuator Design

The deployment actuator design encompassed the experiment boom, "roller" joint, and the strongback as part of its overall design. The deployment actuators were mounted on either side of the experiment boom, routed around the "roller" joint and terminated in the tube at the end of the strongback. Figure 5 shows the general arrangement of the actuator deployment design in the stowed and deployed orientations. The length of the

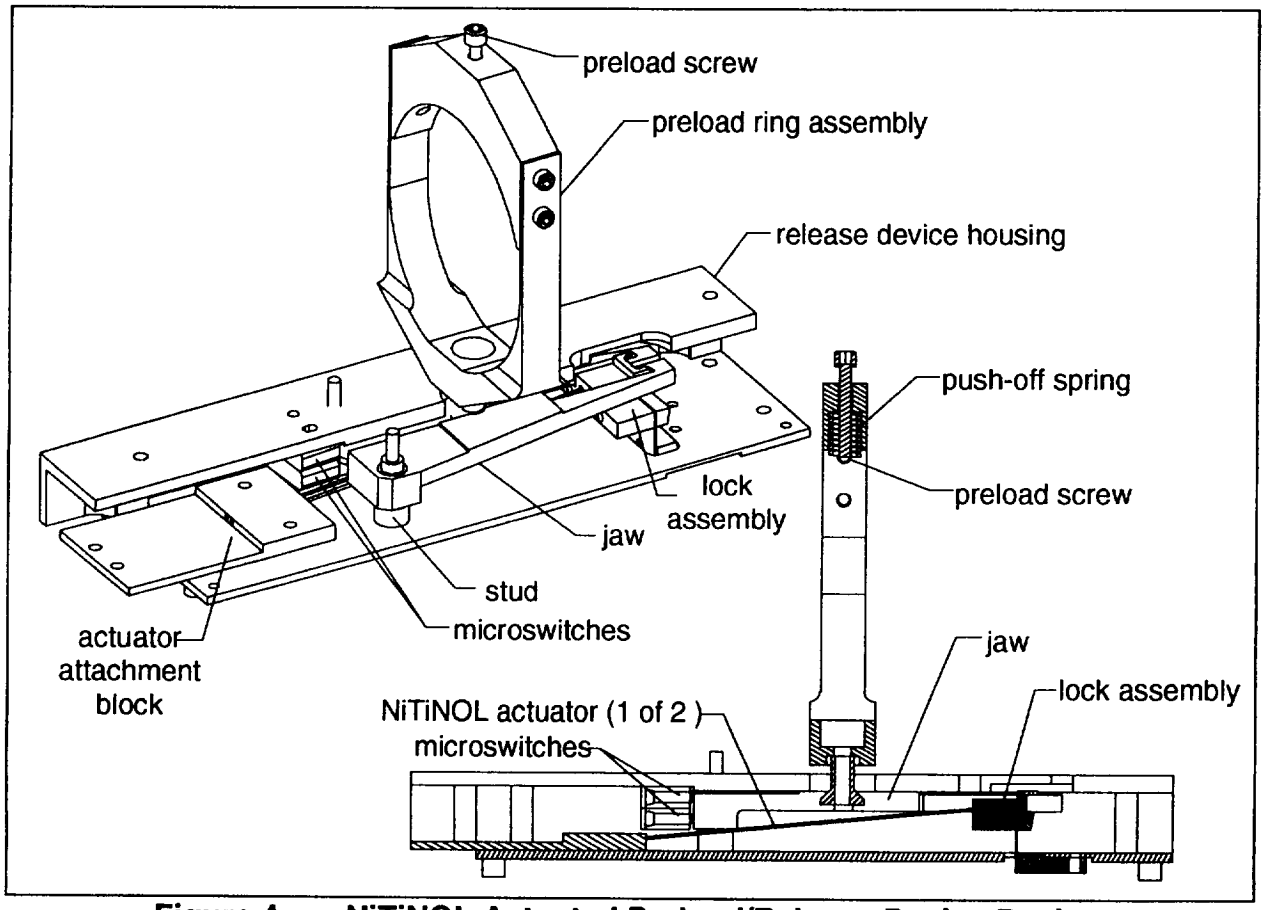

Figure 4: NiTiNOL Actuated Preload/Release Device Design

actuator element was 102 cm(~40"). This resulted in a shape recovery stroke of 2.5 cm (1.00") at approximately 2.5% recovery strain. NiTiNOL is capable of 8% max. recovery strain but using more than 3% strain required an external force to reset the NiTiNOL actuator for the next cycle. The internal restow torque of the roller joint was too low to accomplish this task. Since multiple operations would be required for ground testing and may be required for operational deployment, it was decided to utilize another of NiTiNOL's unique attributes: **two-way memory**.

Two-way memory is a byproduct of the primary shape memory effect. NiTiNOL has the ability to be "trained" to remember not only a "warm" shape but a "cold" shape as well.

The "cold" shape occurs as a result of multiple actuation cycles under a specific loading regimen. This "training" generates an internal stress field favorably oriented in the direction of the initial deformation. The maximum recovery strain associated with this "cold" memory is about 3%. Therefore, the length of the NiTiNOL actuator was based on this limited recovery strain capability. This provided the recovery stroke without the need for the restow springs to reset the actuators. In fact, the actual stroke necessary for deployment was only 70% of the total capability. The residual recovery stroke was needed for two reasons. First, NiTiNOL deployment actuators were required to hold the boom in the deployed state for a period of 15 minutes to engage the locks and latch the boom in place. Actuators must also have a maximum operational life of 10 cycles before replacement due to ground testing requirements. Each cycle induces creep which decreases the effective recovery stroke. Therefore, residual recovery strain was

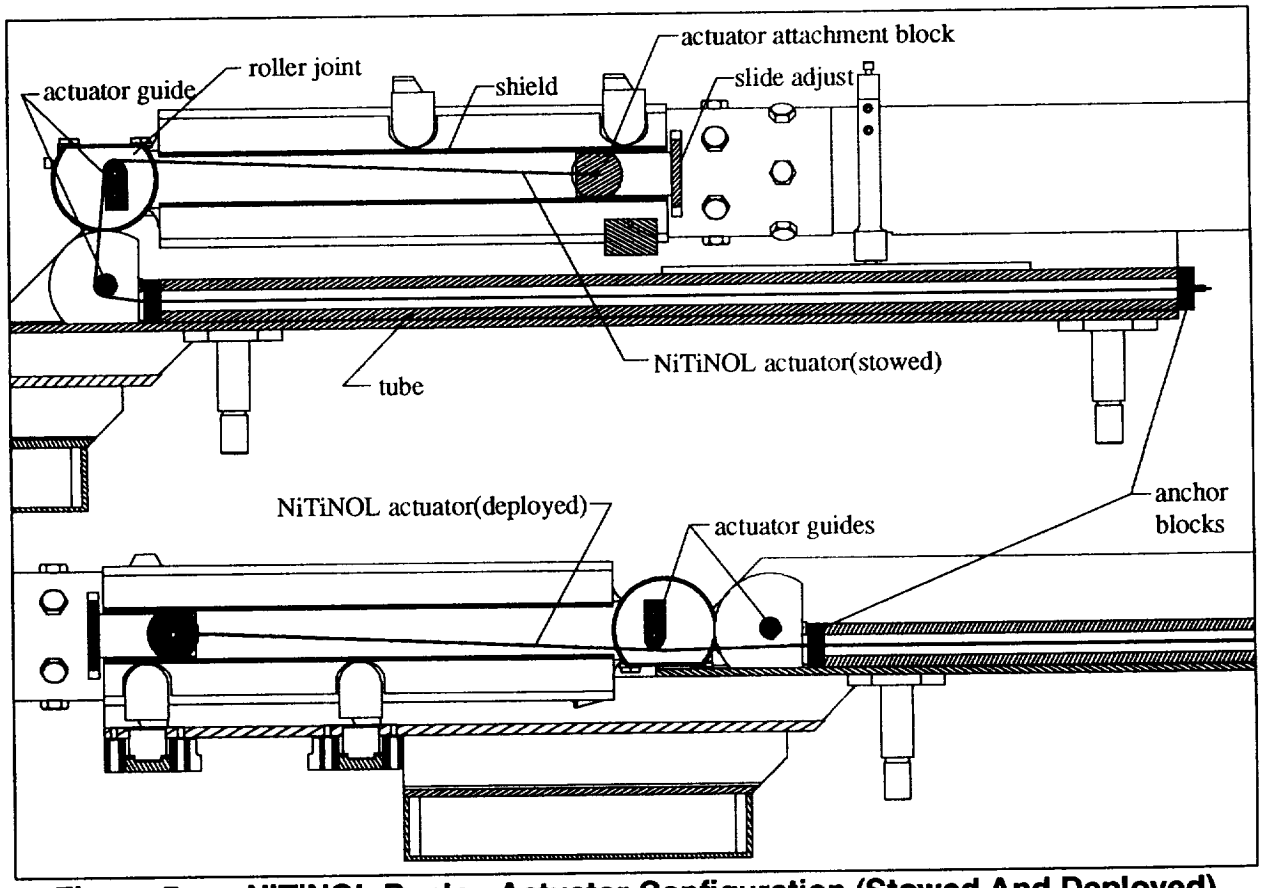

Figure 5: NiTiNOL Deploy Actuator Configuration (Stowed And Deployed)

used to provide additional operational cycle life margin.

The moment arm associated with these deployment actuators was designed to increase with rotation angle. Figure 6 shows the moment arm variation with respect to boom deployment angle. The change in the moment arm is approximately linear except for the jump near the end of deployment. This is due to the actuator(s) coming off the cam and providing an increased torque output to offset the operation of four microswitches used to transfer power to the NiTiNOL lock rings. Each microswitch

required a force of approximately 1.5 N (0.33 lbf) to change state. Unfortunately, this was multiplied by a factor of 4 due to parallel mounting. This generated a substantial torque increase the actuators had to overcome to accomplish full deployment. The design of the deployment actuators also required shielding from solar illumination to prevent self-actuation. An aluminum tube and angle were used to enclose and shade the NiTiNOL from the sun. This required the wires to be enclosed in Teflon sleeving. The tube had phenolic caps at each end to ensure the actuator would be positioned in the center and isolated from metallic parts. Adjustment of the NiTiNOL was provided by a movable bracket at the end of the aluminum shield. A screw was torqued to bear against the end of the aluminum shield forcing the bracket away from the shield thereby removing any slack in the NiTiNOL actuator.

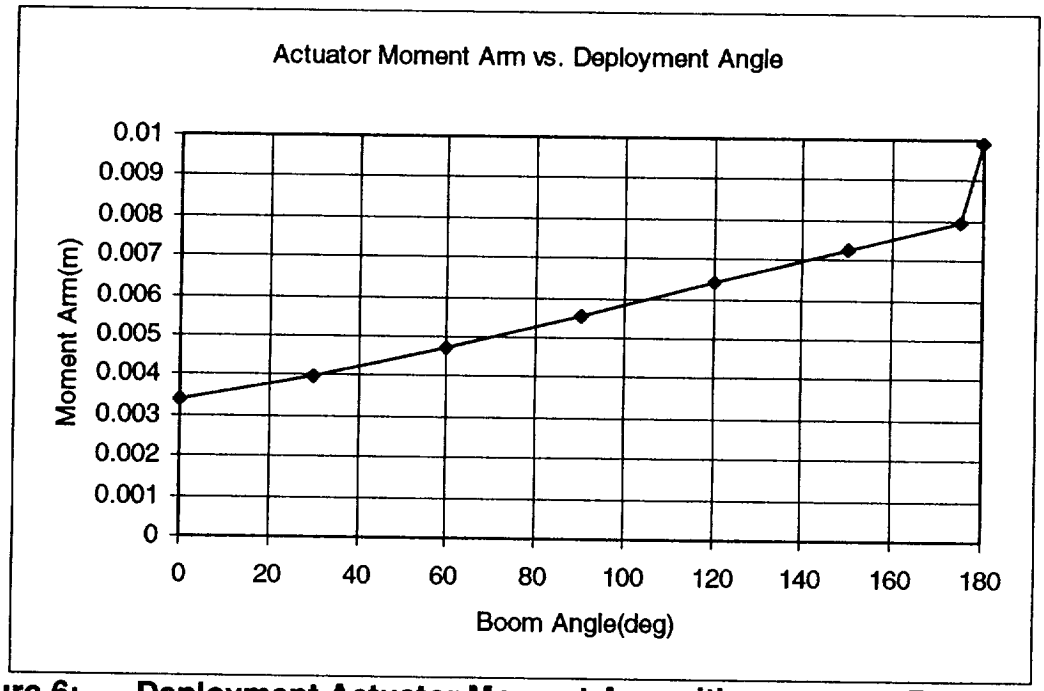

Figure 6: Deployment Actuator Moment Arm with respect to Boom Angle

NiTiNOL-Actuated Ring Lock Design

Four(4) lock assemblies comprised the boom locking system. They were arranged in a rectangular pattern with each diagonal pair operated by independent circuits. The lock design was the simplest and least complicated of all the mechanisms. The design, shown in Figure 7, consists of a two-piece housing, thick-walled NiTiNOL ring, phenolic spacers, and a flexible strip heater. The ring lock was sandwiched between phenolic spacers providing thermal isolation from the surrounding aluminum structure. Since the lock mechanisms were exposed to deep space, the lowest temperature predicted was different than the specified minimum temperature listed in the system requirements. Because of the predicted minimum temperature of -70 C, a 55 Watt strip heater was used to provide adequate heating. The strip heater was bonded to the ring and double wrapped around the periphery because of its extra length. The mating piece of the lock design was a boom mounted stud inserted into the lock mechanism prior to application of thermal energy from the strip heater. The stud OD was 24.2 mm(.954") with a 0.15

mm(.006") lip around the edge of the stud to provide positive interference ensuring permanent boom latchup. Since deployment torque margin was low, the lock design incorporated a zero insertion force feature to eliminate stud/ring interference. Nominal clearance between the stud and ring was 0.71 mm (0.028"). Each ring lock was held in place by four(4) fasteners on the backside of the strongback. These forced the rings to bear against the strongback. Even though held against the strongback, the NiTiNOL rings easily overcome frictional effects allowing them to clamp the studs.

The ring was a Niobium doped NiTiNOL exhibiting a unique wide thermal hysteresis feature associated with some SMAs. This was required to maintain maximum strength at low temperatures The ring had an initial ID of 25.7 mm(1.010"). Upon heating the ring above 45°C with the bonded strip heater, the ID shrank to 24.2 mm(.954") with a compressive stress on the stud of approx. 250 MPa(36 KSI) providing a substantial clamping force with the stud creating a permanent joint.

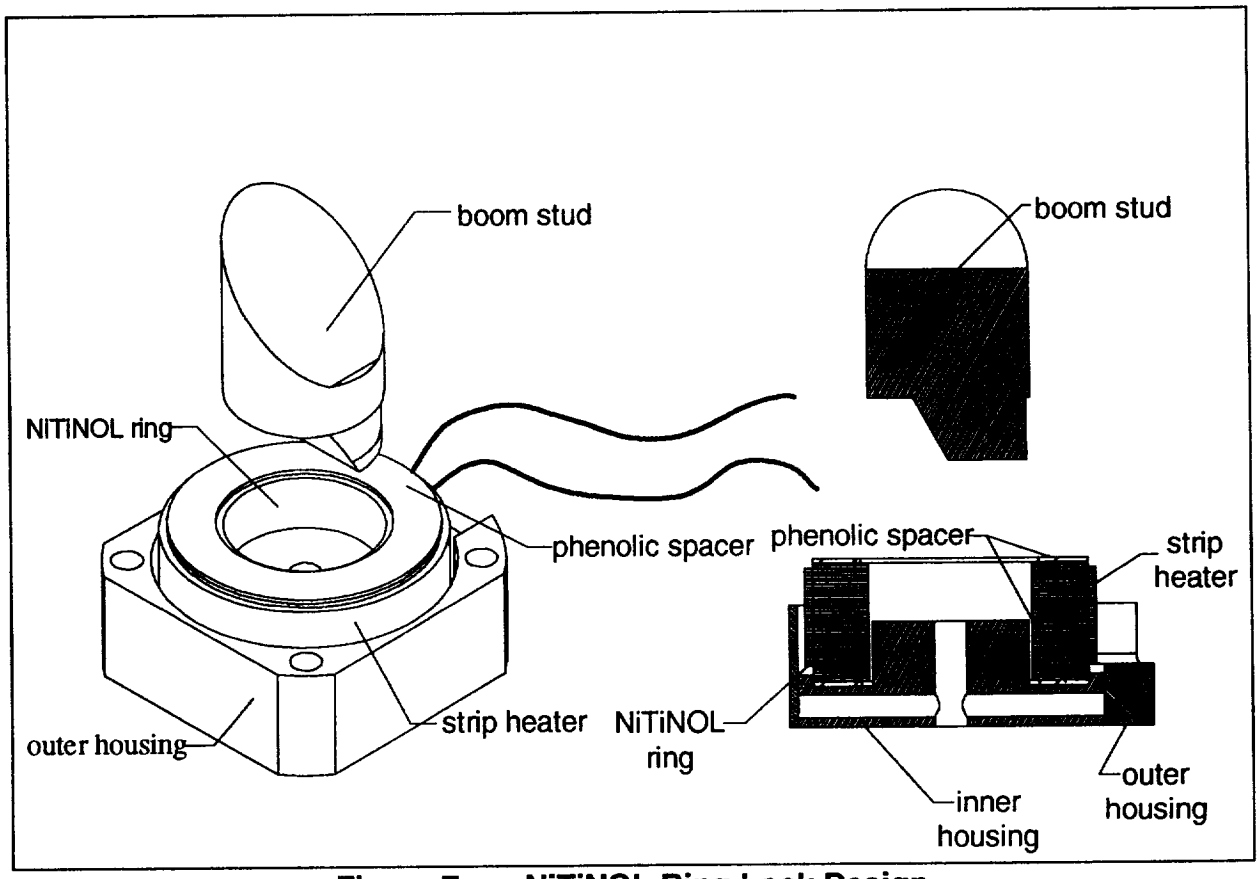

Figure 7: NiTiNOL Ring Lock Design

Mechanism Testing

Boeing Developed Roller Joint

Flight joint thermal testing showed rotation friction was very low and independent of min. and max. temperature extremes. Vacuum testing used an engineering model joint with a dumbbell weight assembly to simulate the sensor boom inertia. The test joint

performed as expected. Vacuum testing was only performed with the engineering joint because the flight joint had been assembled on the experiment to support integration schedules and was not available for testing. The engineering joint was identical to the flight joint in order to qualify by similarity. The test setup did not include the eccentric loading condition caused by the boom because this was a condition peculiar to a 1-G environment and not required for roller joint qualification.

The change in the line of action of the cantilevered boom across the joint was not viewed to be a problem. The joint, with preloaded flexures, could react any eccentric loading generated by the experiment boom due to predicted operational accelerations. However, the joint stiffness was not sufficient to overcome the twisting moment generated, in a 1-G environment, by the cantilevered boom. This required offloading the boom to perform functional testing and minimize any potential damage to the joint and actuator elements. This also prevented full-scale functional testing of the boom experiment in an available vacuum chamber because of the size required to allow full rotation and any offloading fixtures. One engineering test was performed to determine if the joint could overcome the 1-G twisting moment and deploy the boom without offloading. Not only did it deploy the boom but precisely located the studs in the four(4) lock mechanisms without interference. However, it was decided that offloading would be used for functional testing to preclude potential damage.

In order to characterize joint performance, the design was tested to identify the desired flexure preloading for satisfactory rotational performance and restow torque profile required to bring the boom back to its stowed position while allowing a single actuator to accomplish the deployment function. The addition of the boom restow feature late in the design development phase required several iterations of the flexure designs. These iterations investigated cross-section, material, and forming of the flexure shape to provide the best combination of restow capability, 'zero' position, and bending stress, without overwhelming the deploy actuator torque availability. Fortunately, the natural tendency of the joint to return to a nominal "zero" position allowed the boom restow feature to be incorporated easily once the flexures were developed. The preferred flexure material was a corrosion resistant steel called Elgiloy due to its exceptional high yield and ultimate strength values.

NiTiNOL-Actuated Preload/Release Design

Testing was performed using a Thermal/Vacuum chamber simulating the predicted operational temperature extremes. Conventional thermal testing prevented operation of the release device at the cold temperature limit due to limited power. Switching to the vacuum chamber eliminated the excessive convective heat loss which prevented the NiTiNOL from recovering its memory shape. Functional release operations were performed to validate the design and its ability to overcome the mechanical preloading at specified temperatures. All testing was accomplished using one actuator to demonstrate the robustness of the design. In addition to functional testing, the release device demonstrated no self-actuation at a maximum non-operational temperature of 74 C (165 F). Over 50 releases were successfully accomplished. This however, led to concerns regarding the operational life of the NiTiNOL actuators. This concern was

reinforced by subsequent release function failures indicating limited actuator life. Once failure occurred, the recovery stress level in a single actuator was determined by precision load cell. This was compared to the maximum recovery stress level derived from IR&D testing. The stress was 310-331 MPa(45-48 KSI). The actuator was sized for a maximum recovery stress of 276 MPa(40 KSI), based on IR&D testing. This was a not-to-exceed value which maximized the predicted cycle life by reducing creep in the NiTiNOL actuator. Another concern was the heating rate and maximum temperature of the actuator element. If the temperature rose too high, this would increase the amount of creep from each operation reducing the number of useful cycles. The solution to both of these problems was reducing current through release circuit redesign and increasing the mechanical advantage of the actuator acting on the lock reducing the apparent stress level. Because of the number of functional test operations, releases, with preload, were limited to no more than 15 before replacement of the NiTiNOL actuators was required. Fortunately, by this time, the basic design had been thoroughly tested with little additional testing required other than to verify design modifications.

The only other unusual "failure" occurred during final functional release and deployment checkout. The release device jaws were locked in place without pin preload to reduce wear and tear on the NiTiNOL release actuators. When release operation was initiated, the lock mechanism pulled back normally. Instead of the jaws being held tight against the underside of the release housing by the preload pin, the jaws dropped following lock mechanism motion. When recovery stroke was complete, the jaws were engaged in the lock conceivably preventing boom release. As it turned out, gravity was the culprit. The test was rerun with the release device mounted upside down to simulate a preloaded pin holding the jaw in place. The lock mechanism released the jaws and functional checkout was completed successfully.

NiTiNOL-Actuated Deployment Actuator Design

Since two-way memory was to be used in this application, insufficient data relating to heat treatment and training of NiTiNOL to optimize this effect was readily available. Characterization testing was performed to identify the heat treatment and training processes required to achieve acceptable two-way memory in NiTiNOL. The other test goal was to determine the deployment time, required current, deploy and restow characteristics of the boom in a vacuum.

The heat treatment process that produced an acceptable shape memory effect was an inert atmosphere(Argon) at 550 C for approx. 1 hour. Water quenching was used to cool the material. NiTiNOL can be annealed anywhere from 450 C to 850 C, but the lower annealing temperature maximized the two-way memory effect.

Several test cycles were performed to reach an acceptable training process producing the proper amount of two-way memory with repeatable results. A two-step procedure produced the greatest two-way memory results. The first step was large loading cycles(3-5) which severely strained the material. This removed almost all the permanent deformation induced in NiTiNOL that normally occurs in the first 100-200 loading cycles. The stress level was over 415 MPa(60 KSI). The second phase was

performed with a stress level 60% of the first. After 40 cycles, creep was lower but not eliminated at the lower stress level. The max. two-way memory approached 3.0%. A minimum cycle life of 10 operations was also demonstrated to verify the process would produce actuators with the required operational performance.

Boom rotation speed, in a vacuum, created the most surprising results. The test joint, with the dumbbell shaped inertia fixture, was used to accomplish qualification testing of the deploy actuators. Even though the fixture weight was not offloaded, the rotation speed was impressive. However, flight restow springs were not included in the testing and the impact at the 180° stop caused concern about shock to the sensors. Flexure redesign, limiting the current to the NiTiNOL actuators and additional joint testing with modified restow flexures and electrical circuit showed the impact velocity was reduced sufficiently to eliminate shock damage to the sensors. Functional testing with restow flexures was accomplished to compare deploy torque against restow torque. This is shown in Figure 8 based on a single actuator. Two actuator performance is shown in Figure 9. Torque margin is also shown for both.

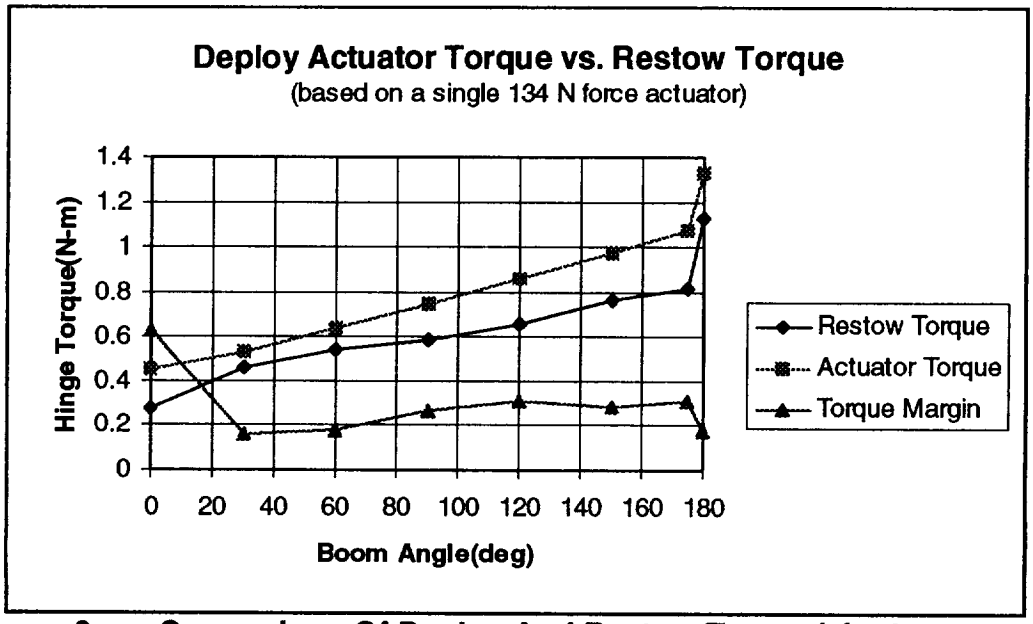

Figure 8: Comparison Of Deploy And Restow Torque(single actuator)

However, the stop/start deployment motion appeared because the stiffer flexures and the slower heating of the single NiTiNOL actuator would generate a large torque pulse allowing the boom to swing freely. This, in turn, caused the NiTiNOL to go slack until the boom slowed down and started restowing. The NiTiNOL would catch up and jerk the boom again. This was repeated until the boom was at the 180° position.

NiTiNOL-Actuated Lock Design

Testing of the lock design was straightforward. The only two areas of concern were the time required for the ring to shrink for proper engagement and the ability of the lock to withstand a maximum heating time of 15 minutes. The other uncertainty was whether it would operate at the minimum predicted operational temperature of -70 C.

The design worked as expected with time for initial lock engagement of 5-6 minutes. Endurance testing was also performed to demonstrate the design's robustness to meet the 15 minute heating time required to provide margin for successful boom latchup. Maximum ring temperature leveled off at approx. 200 C (400 F) without failure. Post inspection showed significant outgassing and scorch marks which created concerns regarding shorting of the strip heater. Since the strip heater was long enough to be wrapped around the periphery of the ring by approximately 2.5 times, this was a possibility. Subsequent resistance checks showed strip heater resistance to be

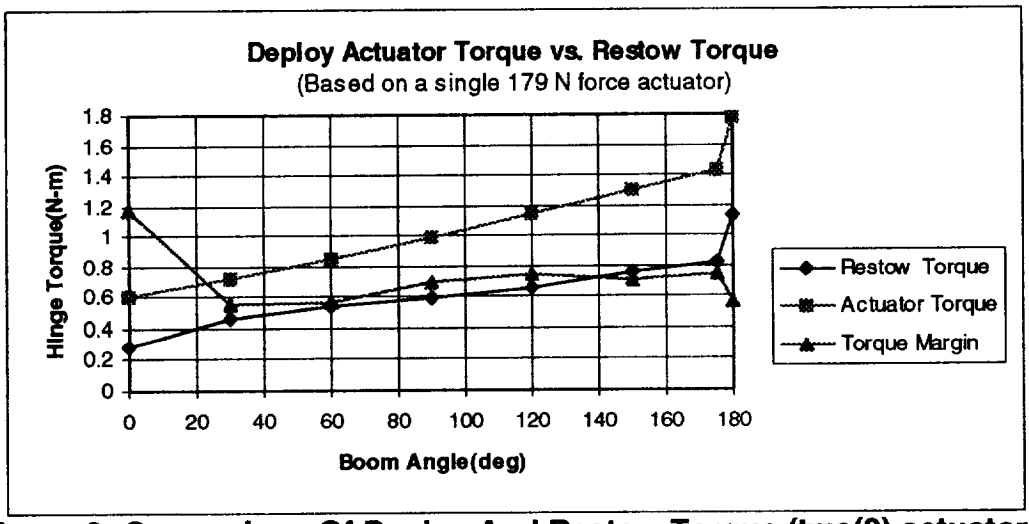

Figure 9: Comparison Of Deploy And Restow Torque (two(2) actuators)

unchanged. This showed that shorting had not occurred during this test. Since there were four rings used for latchup, losing one ring lock to an electrical short would not prevent the experiment from successfully deploying and locking in place

Other testing was performed to verify the deployed resonant frequency requirement would be met. One of the locks was activated to rigidly latch the boom in its deployed configuration. A "tap" test was done to determine the first mode frequency. The deployed frequency was 31 Hz as compared to 42 Hz when the boom is stowed.

Experiment Deployment and Operation

As in any good experiment, the "acid" test was the actual operation. The deployment of the Environmental Sensor Experiment proceeded smoothly with power to both A and B circuits simultaneously. This resulted from tests showing minimum margin with a single actuator. Dual actuator operation was determined to be lower risk.
Release occurred within 6-8 seconds of power on. This was faster than tested because dual actuator release was not part of ground test and checkout. Typical release times for a single actuator were 12-25 seconds. After release, power was transferred to the dual deploy actuators. Rotation proceeded rapidly with no bouncing due to two(2) NiTiNOL actuators being used simultaneously. When the 180° position was reached, microswitches transferred power to heat the lock rings. At this time power was to be

maintained for a period of 15 minutes after which it would be turned off. However, at the 5 minute mark, the voltage drop reading became erratic. At 6 minutes, telemetry indicated an open on both A and B circuits. Analysis showed an electrical short circuit blew both 5A fuses on the experiment's power bus. The short circuit was in one of the strip heaters used to heat the NiTiNOL lock rings. This was apparently a consequence of overwrapping the strip heater onto itself around the NiTiNOL lock rings because of its length. Since the 15 min. heating period was not reached there was concern that the boom had not successfully latched. The other problem was there was no independent means of showing the locks worked since power could not be restored. Fortunately, independent host vehicle telemetry provided indirect proof the experiment was fully deployed, locked and functioning. The actual telemetry trace is shown in Figure 10.

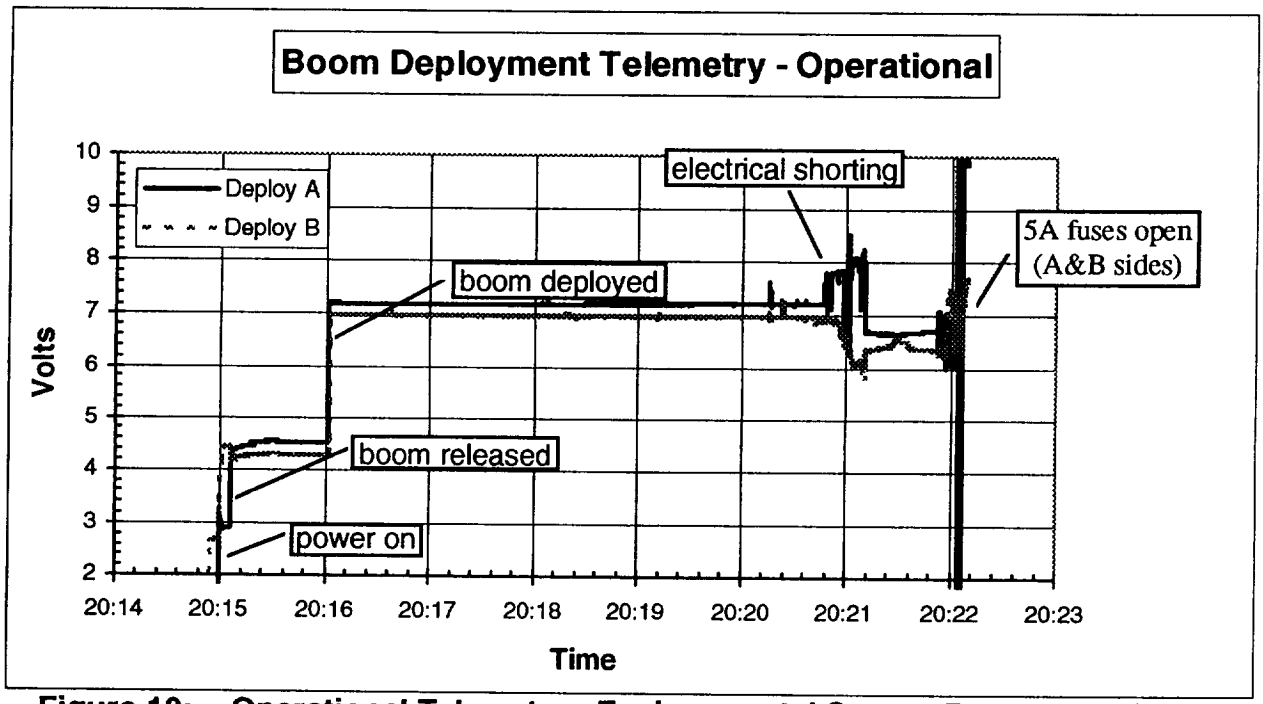

Figure 10: Operational Telemetry - Environmental Sensor Boom Experiment

Lessons Learned

The experiment's successful deployment in a space environment provided valuable insight into the practical implementation of Shape Memory Alloys, such as NiTiNOL, into aerospace systems. It also identified limitations and design unknowns which could seriously affect any NiTiNOL development effort. These "lessons learned" are listed below:

1) NiTiNOL has limitations which **must** be identified and addressed early on to minimize situations requiring substantial redesign and retest.
2) Thermal environments must include NiTiNOL self-actuation phenomenon.
3) Bulk NiTiNOL elements heating schemes must be thoroughly investigated to eliminate unusual failure modes.

4) Size force output of NiTiNOL actuators to be 3 times larger than predicted reaction forces to maintain acceptable margins at end of life.
5) Do not base predicted vacuum performance of NiTiNOL on ambient testing.
6) Lower recovery stress maximizes NiTiNOL's cycling capability and useful life.
7) Two-way memory eliminates the need for external resetting mechanisms.
8) To maintain linear performance, stay above minimum residual recovery strain.

Conclusion

The experiment's successful use of NiTiNOL to release, deploy and rigidly lock the sensor boom in place as part of an on-orbit demonstration proves this class of material has a place in the design of aerospace mechanisms. The design of these devices must take into account the virtues and vices of Shape Memory Alloys. The main problem is due to the lack of standardized and acceptable engineering data. Adequate material performance data must be acquired and disseminated into the engineering community in order to take full advantage of this technology. This is especially true when using the lesser known capabilities such as NiTiNOL's two-way memory in mechanism design.

The positive influence on shock mitigation, elimination of explosives and their safety hazards, adaptability to changing requirements, and improvements in basic deployment functions showed promise that this technology will be useful in the faster, better, cheaper development environment of future aerospace systems.

Acknowledgment

The authors wish to thank F.C. Reddaway(Systems Engineering), John Anderson (Electrical Circuit Design), Ronald Bondy(Manufacturing), Romald Sikora(Mechanical Design), and Phil Robertson(Consulting) for their invaluable experience and perseverance in this effort. Without their inputs and expertise, this experiment would not have been successful in demonstrating the unique benefits and possibilities Shape Memory Alloy Technology can bring to future aerospace mechanism developments.

Shape Memory Activated Adaptive Antenna

Dr. Bernie F. Carpenter and Duane Grosskrueger*

Abstract

Creation of an antenna system that could autonomously adapt contours of reflecting surfaces to compensate for structural loads induced by a variable environment would maximize performance of space-based communication systems. Design of such a system requires the comprehensive development and integration of advanced actuator, sensor and control technologies. As an initial step in this process, a test has been performed to assess the use of shape memory alloy as a potential actuation technique. For this test, an existing, offset, cassegrain antenna system was retrofit with a subreflector equipped with shape memory alloy actuators for surface contour control. The impacts that the actuators had on both the subreflector contour and the antenna system patterns were measured; the measured data is presented herein. The results of this study indicate the potential for using shape memory alloy actuation techniques to adaptively control antenna performance; both variations in gain and beam steering capabilities were demonstrated. Future development effort is required to evolve this potential into a useful technology for satellite applications.

Introduction

The performance of large space antenna systems can be enhanced through the addition of adaptive components. These adaptive structures have the ability to sense their own response to environmental and operational stimuli, and adapt that response in such a way as to maintain or optimize structural performance. Accurate control of the reflector surface offers a means of steering and distributing gain across the beam footprint, providing substantial advantages over existing systems. Combined with adaptive feedback control, reflector operating parameters (i.e., gain and focal point) can be optimized for variable environmental conditions.

Shape Memory Alloys (SMAs) utilize a thermally activated reversible phase transformation to recover their original heat-treated shape (up to 8% strain) or to generate high recovery stresses (>7 MPa) when heated above a critical transition temperature. Metallurgical conditioning processes have been developed to improve cyclic stability and obtain reproducible mechanical response. NiTi SMA actuators have been integrated into a composite antenna structure based on a communication antenna system to demonstrate shape control phenomena.

---

* Lockheed Martin Astronautics, Denver, CO

Technical Approach

The cassegrain antenna, developed by TRW for the NASA Advanced Communications Technology Satellite program, was selected as the baseline system for this study. This antenna consists of a 106.8 inch diameter primary reflector that is offset fed by a pair of subreflectors and a cluster of feed horns. For this study, the baseline design was modified to use a single subreflector and a single feed horn. The test subreflector was designed to be dimensionally equivalent to one of the baseline subreflectors.

Figure 1 shows the general construction of the adaptive subreflector. In general, it consists of an aluminum honeycomb panel with Lexan facesheets. The 12-mil RMS reflective surface face sheet was made conductive by plasma deposition of aluminum. SMA tendons were arranged in an isogrid pattern to attain overall deflections of 1 inch with minimal curvature inflection. This is in excess of the deflection associated with the operational wavelength of 19.5 GHz (0.6 inch).

Smooth curvatures were obtained by varying the level of SMA contraction to impose face sheet strains. As can be seen from the Finite Element Model (FEM) in Figure 2, face sheet strain is responsible for producing linear deflection of the reflector surface. Modeling of the reflector surface demonstrated that the ratio of bonding stiffness to membrane stiffness (D/A) is critical to avoid anticlastic and "pillowing" behavior of the reflector surface. A large D/A ratio is preferred.

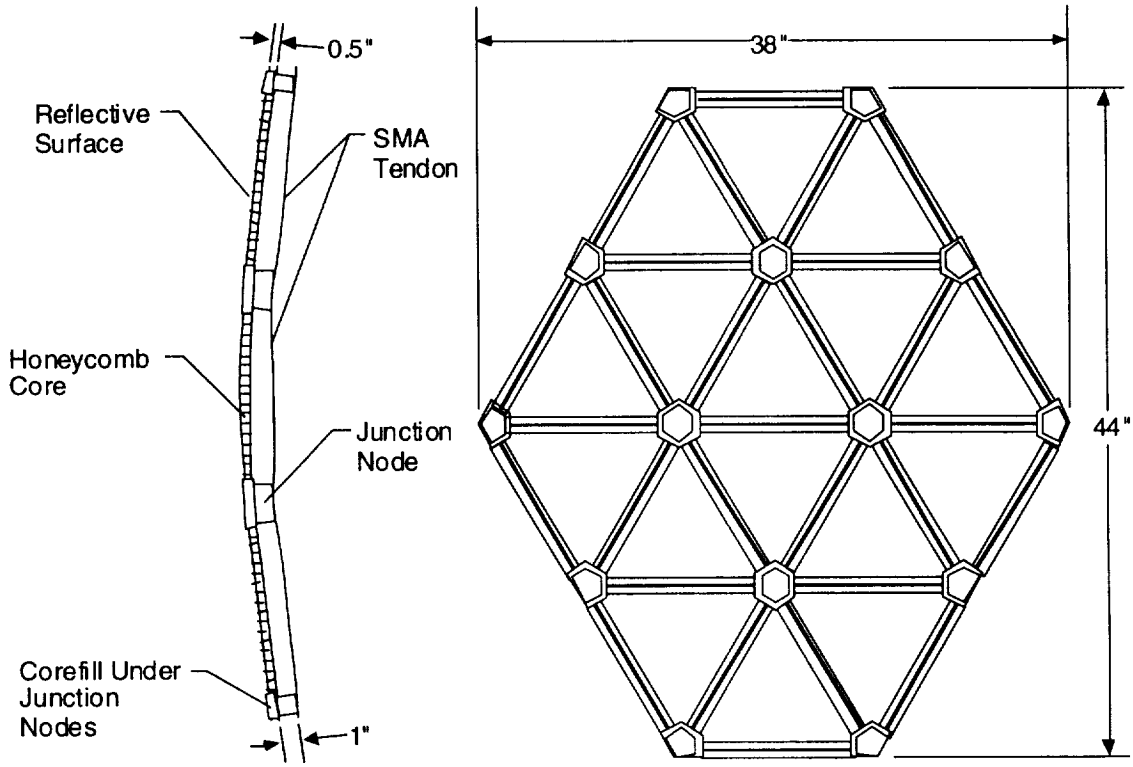

Figure 1. Shape Memory Actuated Subreflector.

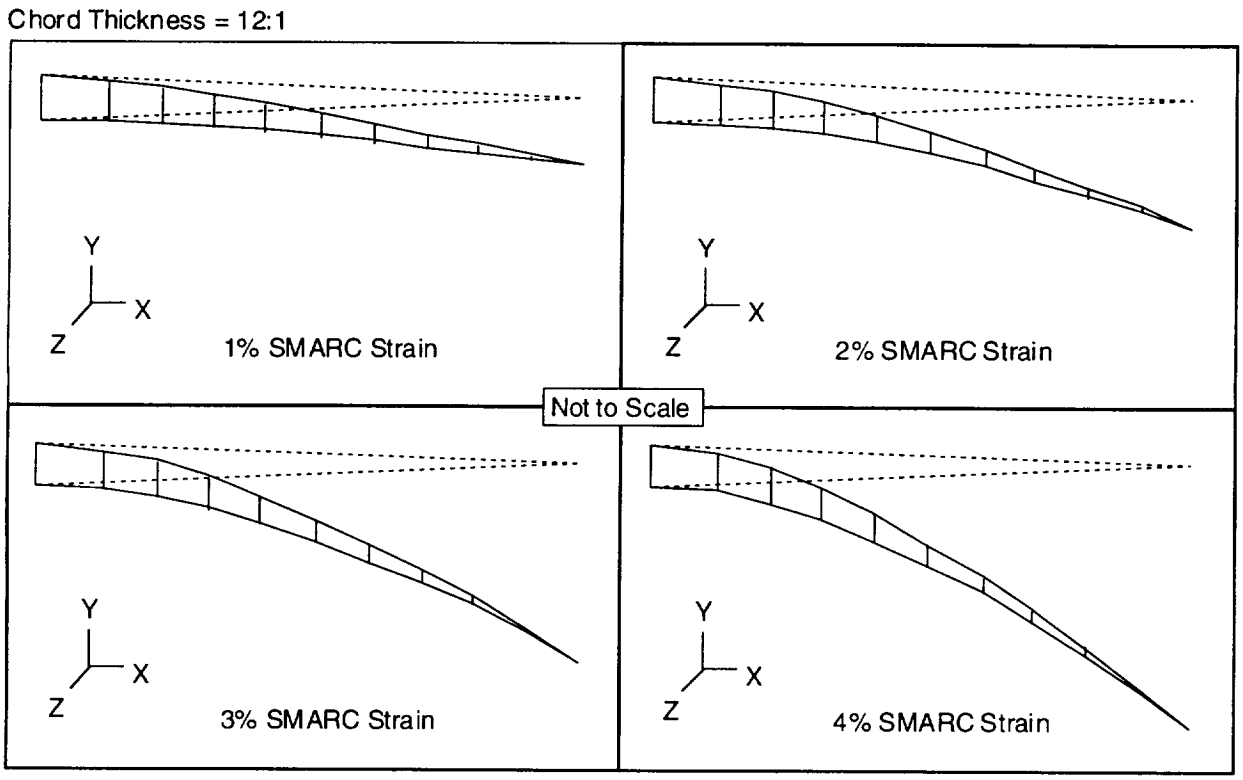

Figure 2. Adaptive Reflector Section with Varying Isogrid Rib Strain.

Adaptive Antenna Fabrication

Fabrication of the reflector is facilitated by the incorporation of prepackaged shape memory actuators. Packaged actuators such as these consist of conditioned shape memory material attached to substrates that are compatible with traditional composite fabrication approaches. The package maintains the properties of the actuator such as prestrain, electrical connection and isolation, and mechanical restraint throughout the fabrication process. As such, actuator reproducibility and reliability can be maintained while providing an actuator package that can be easily installed and aligned into a subassembly.

A typical embodiment of a shape memory actuator packaging approach is in the form of a shape memory alloy (SMA) tow. SMA tows may incorporate thermoset or thermoplastic face sheets bonded directly to SMA wires (Figure 3). After collimation of SMA wires in a lay-up fixture, they are prestrained to 4% and then bonded to the face sheets. By fabricating SMA tows in this manner, the SMA wires remain collimated, prestrained and electrically isolated after being embedded into a reflector subassembly.

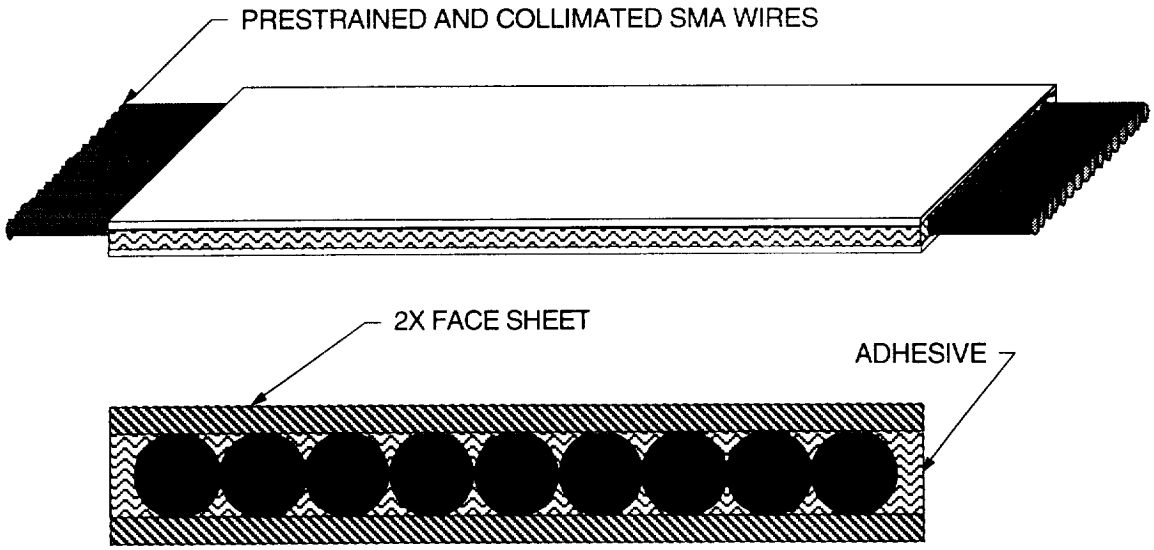

Figure 3. Shape Memory Wire Tow Actuator Detail.

SMA foil, rather than wire, may also be incorporated into an SMA tow actuator package. Foil tows are fabricated in a very similar manner to wire tows, except that SMA foil is substituted in place of wires (Figure 4). SMA foils are placed into a tow lay-up fixture and prestrained just as wires are, but there is no need to provide collimation since the foils have a contiguous solid cross section. The key advantage of using SMA foils, rather than wires, is that foils greatly reduce tow fabrication time and effort, and provide a much more dimensionally uniform and robust SMA tow actuator when finished.

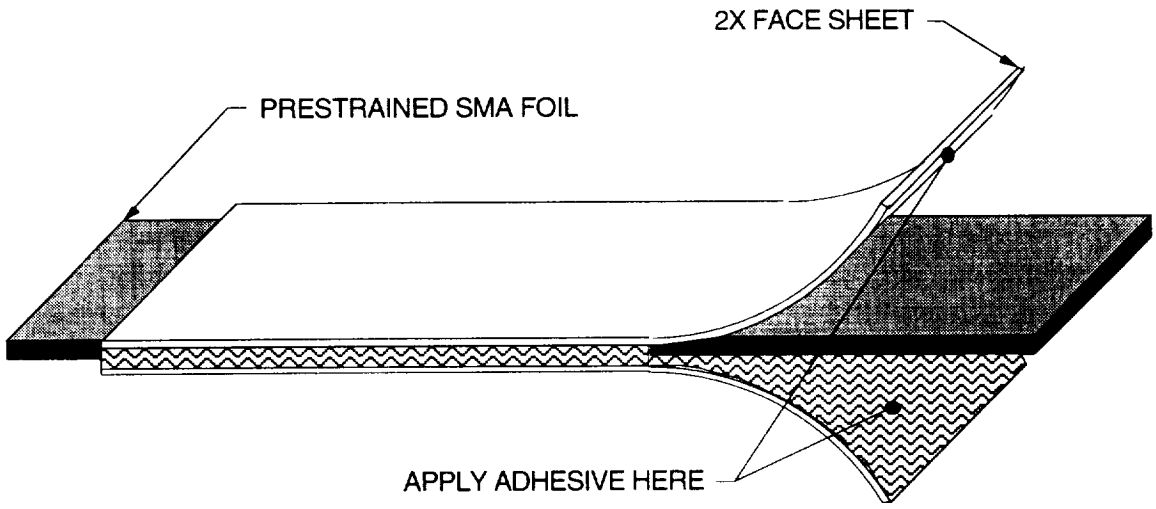

Figure 4. Shape Memory Foil Tow Actuator Detail.

Adaptive Antenna Testing

The adaptive reflector has been tested using the multibeam antenna system shown in Figure 5. This Cassegrain system has been fully characterized using a conventional subreflector. This subreflector was then replaced with the adaptive reflector. Activation of the 24-element isogrid arrangement of SMA actuators was accomplished using a closed-loop control system. The controller is based on a strain gage (displacement) measurement along the axis of each SMA actuator. This value is compared to a user-defined displacement. The difference between these two values results in an error signal that controls the current flow for an individual actuator. Current flow is reduced as the reflector approaches the desired displacement.

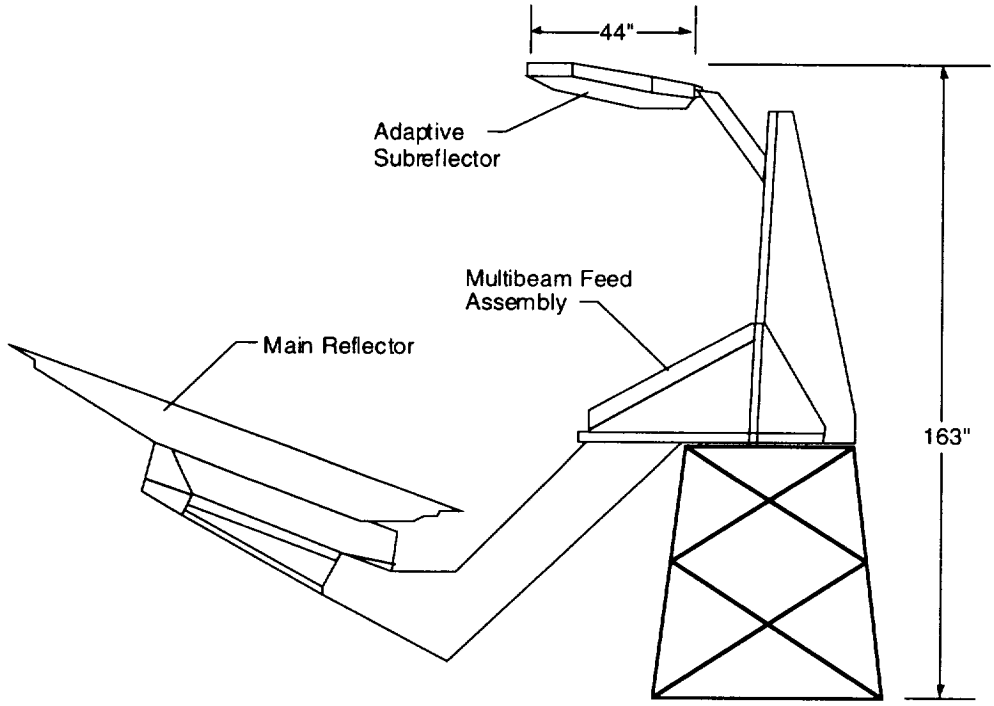

Figure 5. Cassegrain Antenna Test Configuration.

The overall control scheme is presented in Figure 6 for a single actuator. A proportional control law is used to generate a current based on the difference between a position command and a truth sensor measurement. This current is converted to a temperature and read into a thermo-mechanical model that describes shape memory behavior in terms of actuator force, displacement and temperature. The closed loop response is shown in Figure 7. In general, the predicted response agrees with the test data. Control current and deflection are within ten percent of the predicted values.

A series of tests was performed at Lockheed Martin Astronautic's Near-Field Measurement Laboratory on the adaptive antenna system to determine the impact of

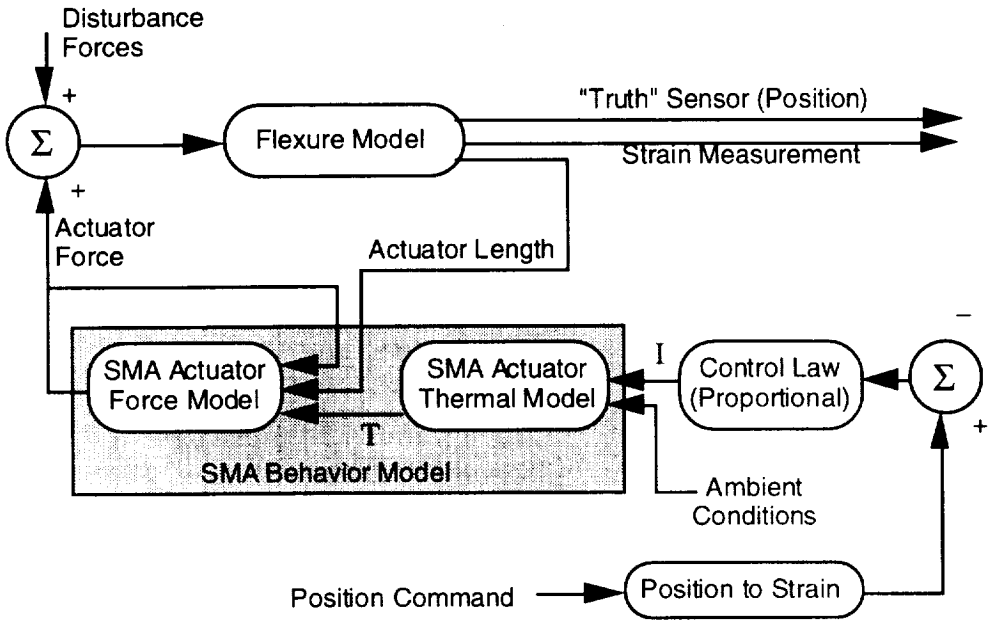

Figure 6. SMA Response Simulation and Control Implementation.

the shape-actuated subreflector on system performance. These tests were conducted following an initial boresighting operation during which the subreflector was aligned within the antenna system and baseline performance was measured with no subreflector actuation. The subreflector actuation schemes considered in this test series include symmetric actuation of all strings, asymmetric actuation across subreflector axes and selective actuation of strings to attain desired deformations. The results obtained from these tests reveal the relative efficacy of using shape memory actuation technology to attain adaptive antenna control.

Figure 8 shows the nominal (non-actuated) phase pattern measurement. The uniformity in color represents the imperfections in surface contour. The relatively little change in color (circle consists of yellow and green colors out of eight available colors) indicates less than 45° (1/8 wavelength) variation through the entire system demonstrating correct subreflector design fabrication and setup. Figure 9 is the near-field pattern with all shape memory actuators actuated to 50% of their design capability. The pattern shows smooth contours and the color is observed to change from green through the eight available colors to green. This shows that the shape memory actuators have the capability to distort the subreflector enough to obtain at least one cycle of phase shift (about 0.5-in. deflection). This implies that the shape memory actuators have the capability to remove externally induced distortions that cause phase shifts of roughly one cycle.

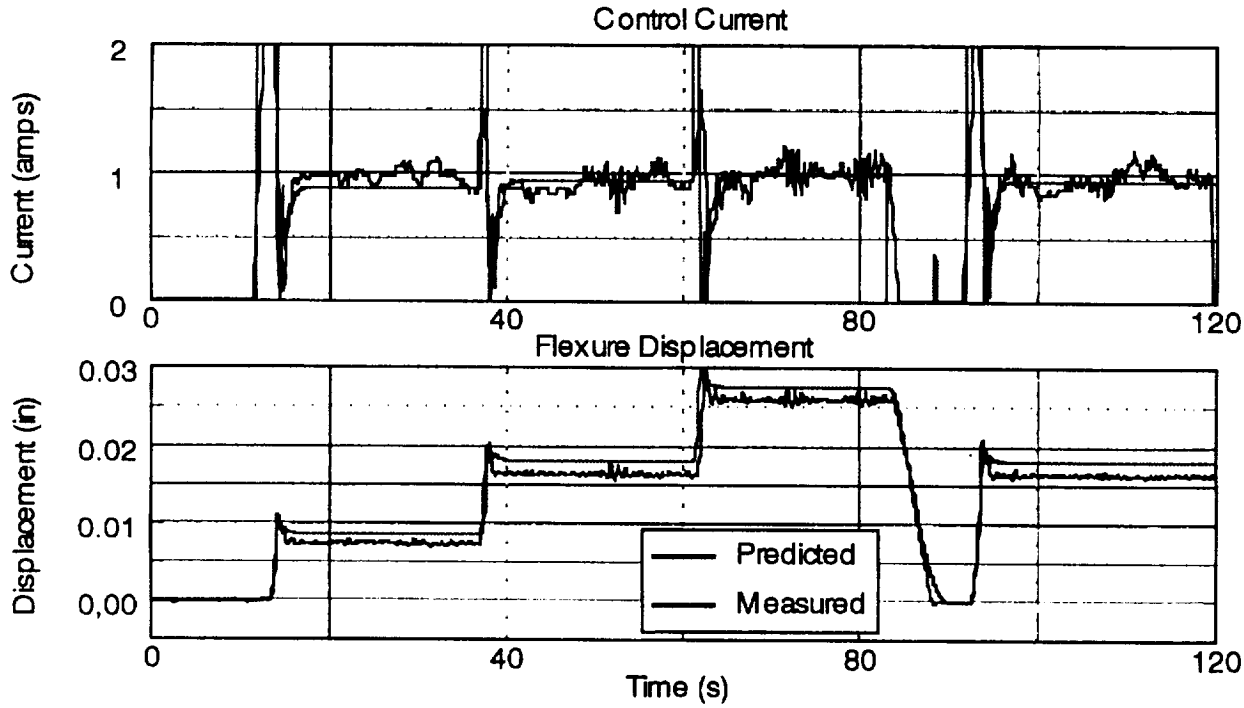

Figure 7. Closed Loop Flexure Response.

Performance spectra have been acquired for a number of actuation cases to demonstrate phase correction ability, beam steering feasibility, and the effectiveness of SMA tendon actuation. An example of beam steering is provided in Figure 10 in which alternate halves of the reflector have been actuated to demonstrate 0.15 degree beam steering. Similar patterns have been acquired to show that local or global reflector deformation may be achieved by proper selection of actuator elements.

Proposed Applications and Recommendations

The subreflector surface control system used for these tests obviously has several iterations to go through before it can be considered a viable technology for satellite use. This method of surface control could be used on microwave antennas is the same way corrective optics are used on telescopes to compensate for thermal or gravitational loading that introduce a systematic distortion of the main reflector. Also, as the method becomes more refined with more nodes of control on the active surface, the surface could compensate for surface errors in the main reflector and atmospheric distortion. Compensation for the large cubic phase errors seen in beam steering could also be implemented to allow steering with only minor loss for smaller f/d antennas. Currently, the most convenient way to minimize steering losses is with the large f/d antennas which can be extremely awkward to deploy. The important feature in whether the shape memory wire actuator technology has an application in the antenna field is whether the technology is cheaper, simpler, and more reliable as a mature

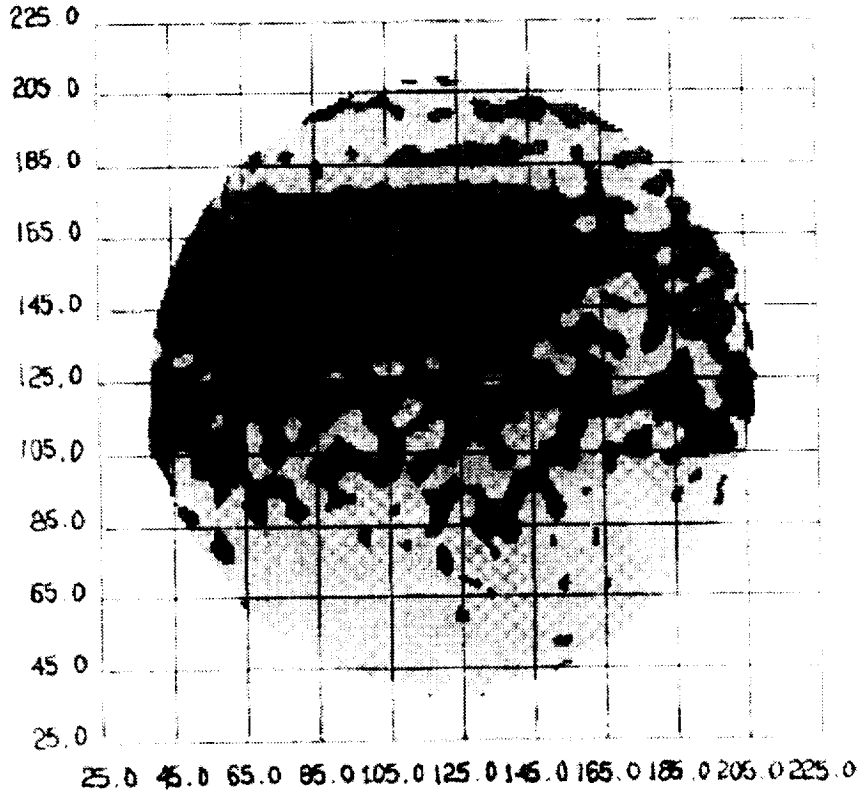

Figure 8. Nominal (Non-Actuated) Phase Pattern)

technology than the other methods currently in use, such as beamformers and mechanical actuator/gimbal systems.

Conclusions

The adaptive antenna test program demonstrated that noticeable changes to antenna patterns could be caused with minimal actuation of the subreflector, 20% actuation of an actuator string could easily be detected in the near-field measurement. Because the subreflector was shaped for near optimal performance with all actuators turned off, the only variance in gain attained during actuation was negative. Gain loss was accomplished by beam broadening, a similar implementation using a beamforming network would be much more lossy. Beam steering was less than a beamwidth, but this is reasonable for a system designed to produce small deflections. Much larger steering angles could have been achieved using a long shape memory wire actuator pulling perpendicular to the surface like a mechanical actuator. The overall test program described herein is considered to be a success in that the use of shape

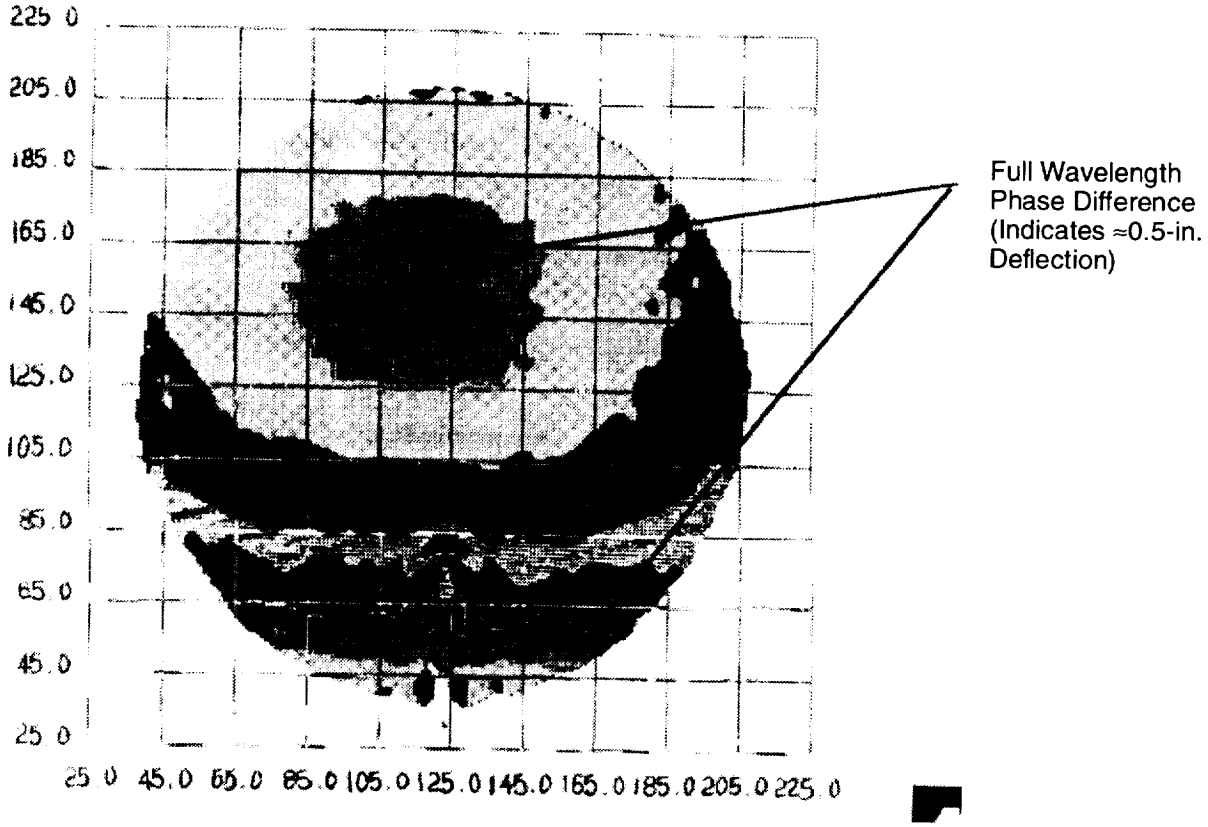

Figure 9. Phase Pattern With All Shape Memory Actuators Actuated to 50% of Design Capability.

memory wire actuation to perform adaptive antenna control was proven feasible; however, the technology demonstrated obviously needs to go though several more development iterations to become a useful technology for satellite applications.

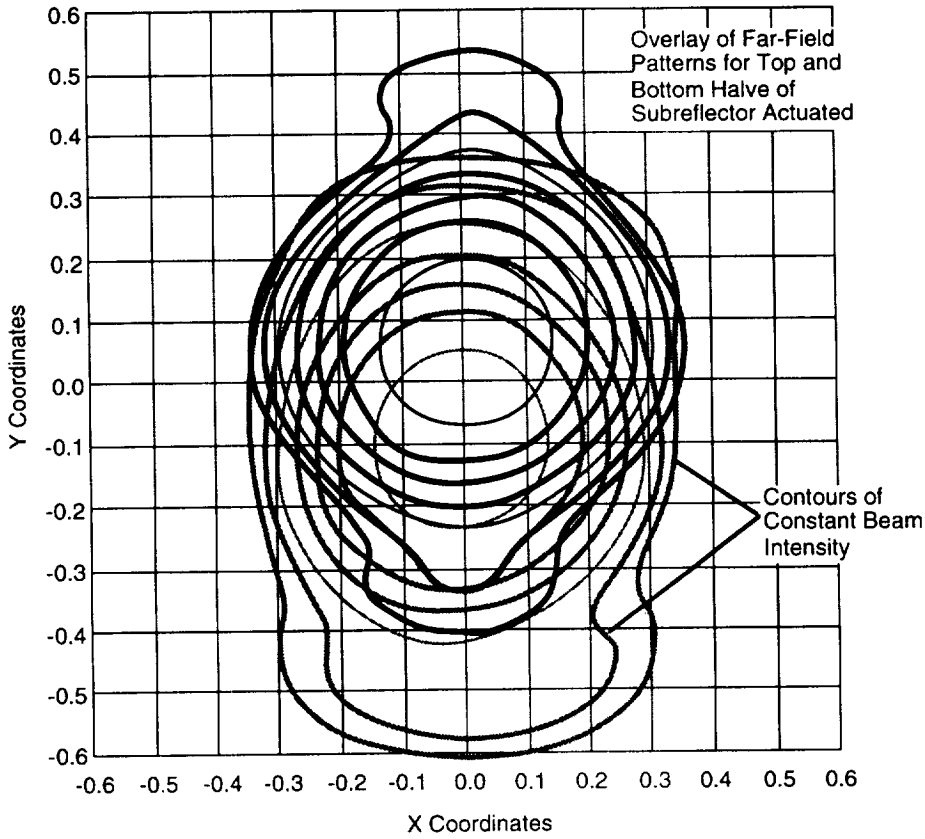

Figure 10. Beam Steering Using Adaptive Subreflector.

The Cassini Magnetospheric Imaging Instrument Ion and Neutral Camera Shutter Door Mechanism Design

Douglas Mehoke and Steven Vernon*

Abstract

This paper describes the design of the Cassini Magnetospheric Imaging Instrument (MIMI) Ion and Neutral Camera (INCA) shutter door actuator mechanism. The actuator uses a standard bimetallic spring element to open and close a shutter door that covers the instrument aperture. However, its design differs from the typical approach to this type of mechanism by having the heater element mounted directly to the spring. The design of the mechanism, the engineering and life tests necessary to qualify the design, and the results obtained during instrument-level thermal vacuum testing on the flight sensor are discussed.

Introduction

Using a bimetallic spring as the actuator in a door mechanism is a standard design that has been used on many flight programs. In an active configuration, a heating element is used to change the temperature of the structure surrounding the spring. Eventually, enough heat is transferred through the structure to the spring, and the actuator moves. This method can also be used in a passive application, such as a louver, where the spring reacts to changes in the local environment. In either case, the spring element relies on changes in the surrounding structure to trigger its movement. This type of design is effective because it is simple, has few moving parts, and is lightweight. Its major drawbacks are its limited operational temperature range, its slow reaction time, and its high power requirement.

The design for the INCA sensor called for a new approach. The sensor required fast operation, at low power, over an extended temperature range. To satisfy all three requirements, the heater element was moved onto the spring itself. This location increased the efficiency of the mechanism operation, but increased the complexity of the design. The two major design considerations were controlling the heater maximum temperature and eliminating abrasion of the heater due to spring movement. A series of tests were performed to demonstrate the concept feasibility, to optimize the specific performance, and to verify the proper operation.

INCA Aperture Door Mechanism

The Cassini MIMI INCA sensor consists of a collimator assembly on top of a sensor electronics housing. The aperture and door mechanism is located inside a trough in the upper electronics housing. The complete unit is shown in Figure 1. Figure 2 shows the sensor with the collimator removed. The details of the door-actuating mechanism are listed on the figure. The INCA door design consists of two doors. The first is an acoustic door with two functions: (1) to seal and protect the extremely fragile

* Both authors are from The Johns Hopkins University Applied Physics Laboratory, Laurel, MD.

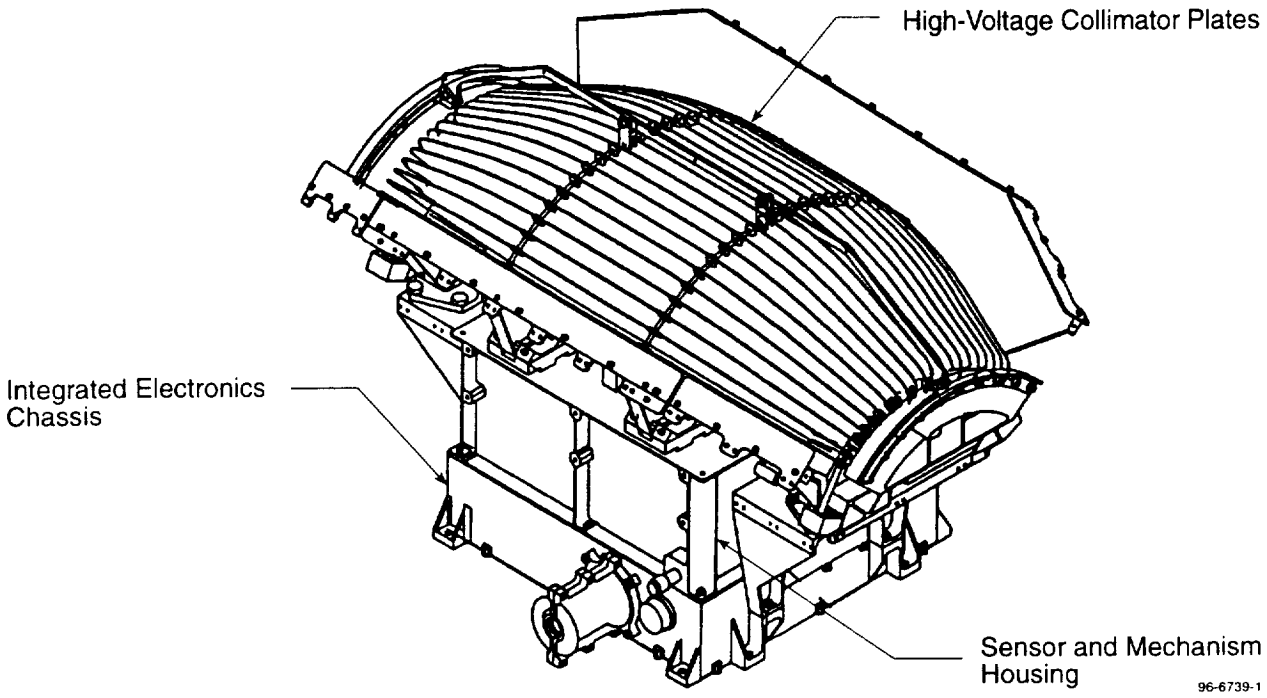

Figure 1. Cassini MIMI INCA Sensor

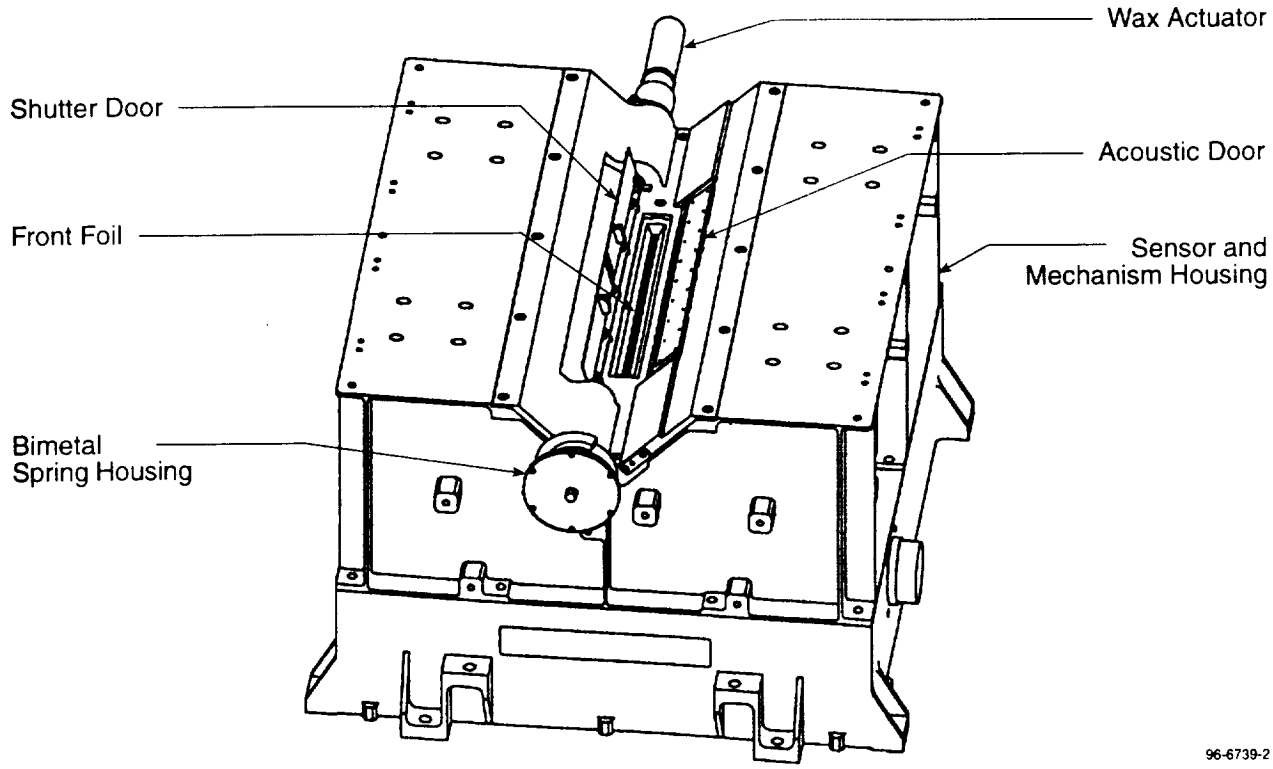

Figure 2. INCA Sensor with Collimator Removed to Show Door Assembly

front foil from acoustic energy during launch, and (2) to cage the shutter door for launch. After launch, the spring-loaded acoustic door is deployed via a wax actuator and latching mechanism. This door must be resettable for ground testing and sensor qualification. After launch, the acoustic door is deployed, and it releases the shutter door from the stowed state. After releasing the shutter door (the second door), its role is complete. This second door, the subject of this paper, has two functions. One is to scale the geometry factor down when high saturation of the microchannel plates occurs during different observing modes. This scaling is accomplished via a small opening in the door. It functions when the door is rotated from the stowed position to the closed position. The second purpose is to provide an in-orbit calibration function (when closed) through the use of two radioactive sources mounted on the door.

Spring Design

Bimetallic springs have been successfully used in space flight mechanism actuation for years. Typically, these uses were not sensitive to the time needed for the mechanisms to perform quickly. The INCA required relatively quick operation, compared to our previous experience. Torque requirements were nominally (without friction and applicable safety margins) small and on the order of 3.04×10^{-4} N•m. There are approximately 70 different bimetallic materials (sometimes referred to as thermoset metals) available with many associated properties. It quickly became apparent that the design of the spring was going to be an iterative process that combined material properties, shape, and available suppliers. Unfortunately, our needs (5–10 springs) were small and quite unprofitable for most manufacturers to make custom springs. We realized that, as a first-order approximation, we needed to choose a highly reactive material. The material chosen was the Truflex P675R, which has the following characteristics:

Number of coils	9 (≈48.3 cm long)	Modulus of elasticity (E)	1.3×10^{11} N/m^2
Width (w)	0.635 cm	Thickness (t)	0.0254 cm
Radius ®	1.75 cm	Rotation angle (A)	135°
Force (P)	0.33 N	Maximum temp.	427°C
Usable temp range	–75 to 260° C	ASTM flexivity (F)	2 3 10^{-7} 1/°C

Figure 3 depicts the various parameters used to calculate mechanical force and thermal deflection. The calculations for mechanical force yielded 0.33 N at 1.74 cm, or 5.74 3 10^{-3} N•m, which provided a nominal margin of 19 times the required torque. The calculations for thermoset metals and Figure 3 are quoted from [1].

Standard Bimetallic Spring Design

As mentioned above, the use of bimetallic springs as actuators is a common approach. The early INCA mechanism assumed this type of design, based on a mechanism used in the Ulysses LAN instrument. The need to achieve better operational performance drove the INCA mechanism to a new design. However, it is important to look at the details of the standard bimetallic spring design to understand how this type of design inherently limits performance. Figure 4 shows a standard conceptual bimetallic spring design for louver and actuator applications.

Thermal Deflection

$$A = \frac{67F(T_2 - T_1)L}{t}$$

Mechnical Force

$$P = \frac{0.0232EAwt^3}{Lr}$$

Thermal Force

$$P = \frac{1.55EF(T_2 - T_1)wt^2}{t}$$

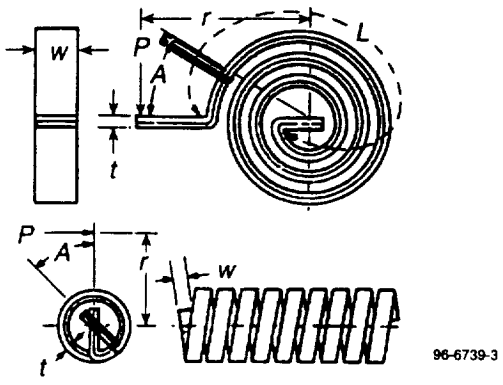

Figure 3. Bimetallic Spring Force Calculations

In mechanism door applications, the spring housing is thermally isolated from the mounting structure. The mechanism is required to open or close without relying on a specific temperature condition. A heater is used to heat the housing to a temperature that will cause the spring to move through its entire range of movement. Removing the power allows the spring to return to its original shape. Clearly, the normal operating temperatures of the unit must be below those necessary to cause some rotation in the spring. In this design, the heater may be mounted to an internal "hot plate" rather than the spring housing. This feature adds some complexity, but allows a wider range in temperatures and decreases the operating time.

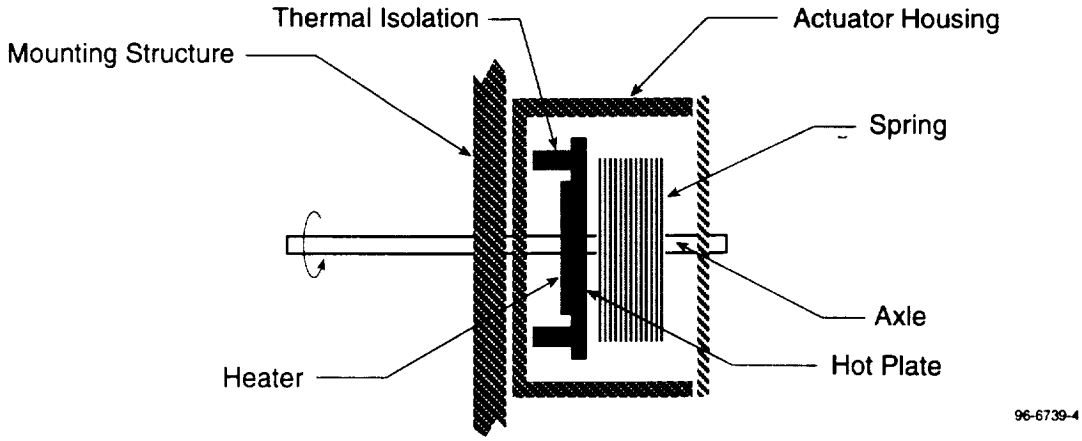

Figure 4. Bimetallic Actuator Block Diagram

The common problem in all these designs is the separation between the temperature source and the actuating element. In each case, it is the spring housing that induces a temperature change in the spring, which in turn causes the movement. The housing is typically more massive than the spring body, so the spring response is slowed. Also, it is difficult to have a good thermal coupling between the spring and housing. This poor coupling creates an additional time lag. These factors combine to produce a mechanism that operates very slowly.

Figure 5 shows the operational performance of the bimetallic spring used in the Ulysses LAN cover door actuator. Door opening and closing times were measured at the two operating temperature extremes. Heater power for each actuator was about 0.75 W. The figure shows the typical trade-off between operating temperature and open/close time. At warmer temperatures, the door opens faster than it closes.

Initial Design

The initial INCA shutter door actuator design assumed a standard bimetallic spring mechanism. The spring temperature was controlled by a heater mounted to the external structure. The spring twisted as its temperature increased, and this twist was transferred by an axle to the shutter door. Motion from fully open to fully closed required a rotation of 135°.

The goal of these initial tests was to determine whether this design was practical. Operational tests were run for a variety of powers at ambient temperature in vacuum conditions. The results, given in Figure 6, show that the heater power must be increased to more than 10 W to get the closing time near the desired goal of 5 minutes. Furthermore, the opening time was about 30 minutes for all cases. Due to the weak conductive coupling between the spring and housing, there was a significant lag in the response time of the spring. The sensitivity of the spring to temperature changes was about 3°/°C. Both the power and operating times were well outside our requirements.

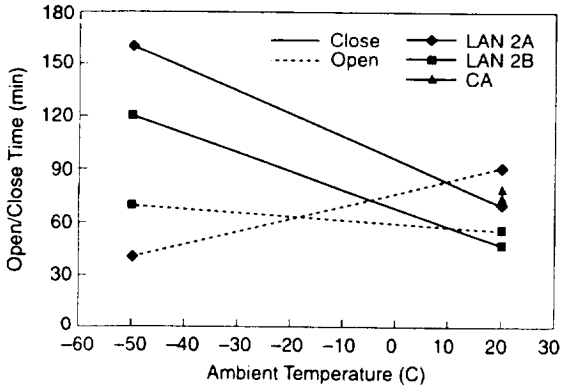

Figure 5. Ulysses LAN Actuator Performance

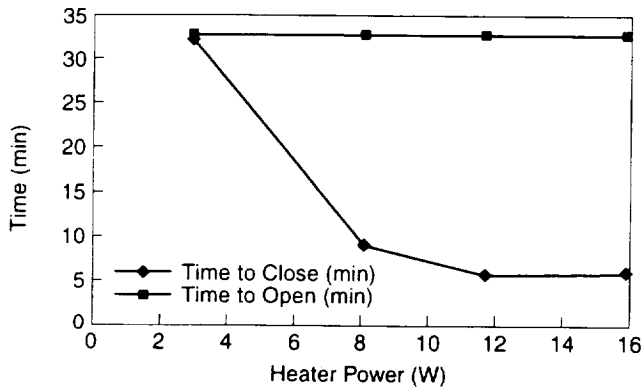

Figure 6. Initial Design Performance Sensitivity to Applied Power

New Approach

The INCA mechanism needed a new approach. Eliminating the housing as the thermal driver was the only way to speed up the mechanism. The actuator would be more responsive if the heater was moved from the housing to the spring itself. Whereas this approach had the potential of producing better performance, it also presented a series of design challenges. The most serious of these challenges were the inclusion of a potential entanglement hazard into a moving mechanism, the need to maintain the spring below the adhesive bond-limiting temperature, and the need to protect the heater from damage.

The development of the new spring mechanism proceeded in three series of tests. The first tests were designed to see if the basic approach was feasible. These tests addressed the following topics: (1) whether a material could be found that would operate over the required temperature range, (2) how the heater installation would affect spring performance, and (3) whether the spring would stay bonded. After the design was shown to be feasible, a set of engineering tests tuned the specific parameters necessary to optimize spring operation in the flight housing. Lastly, flight unit testing provided a comparison against the engineering tests and demonstrated the final end-to-end performance.

Feasibility Testing

The first set of tests were run to quantify the effects of the heater on spring performance. Testing was done on a spring with and without the heater. These tests calibrated the spring performance in an unconstrained condition. They were used to verify the spring material choice and to make initial estimates of heater sizing and the spring "clocking" angle. The test results were also used to predict the final system performance and to demonstrate the feasibility of the design concept.

The first step was to calibrate the performance of the unconstrained spring over a range of temperatures. For this test, the spring was placed in a Thermatron oven, and the temperature was varied between –25°C and 95°C. The results are shown in Figure 7. The slope of the performance curve is also shown in the figure. The spring sensitivity to temperature varies between 2.8°/°C and 3.2°/°C.

Proper actuation was required over the entire protoflight test range of –35°C to 50°C. To keep the door from closing prematurely at hot operating conditions, it was necessary to preload the spring to keep it in its stowed position up to 50°C. The spring required a temperature change of about 50°C to completely close the door. Therefore, the maximum required spring temperature was about 100°C. To allow for the design margin on the spring operation and for the adhesive limit, an upper temperature limit of 130°C was imposed on the spring. Based on a practical temperature limit, it was decided that the spring material was acceptable.

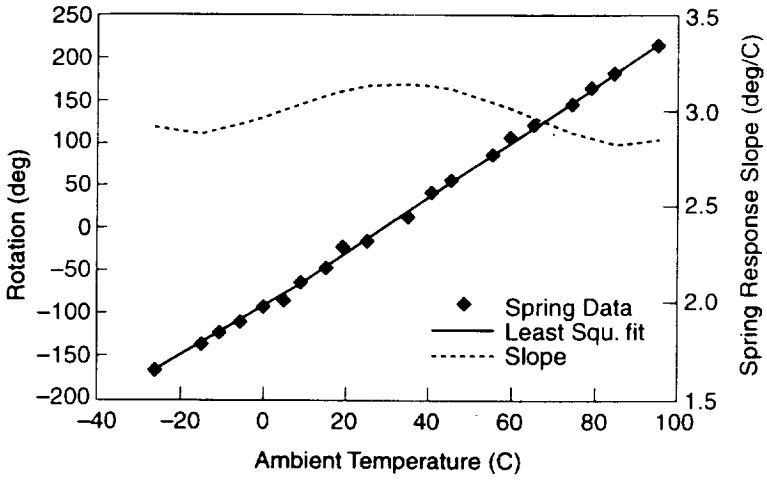

Figure 7. Bare Spring Rotation/Temperature Characteristics

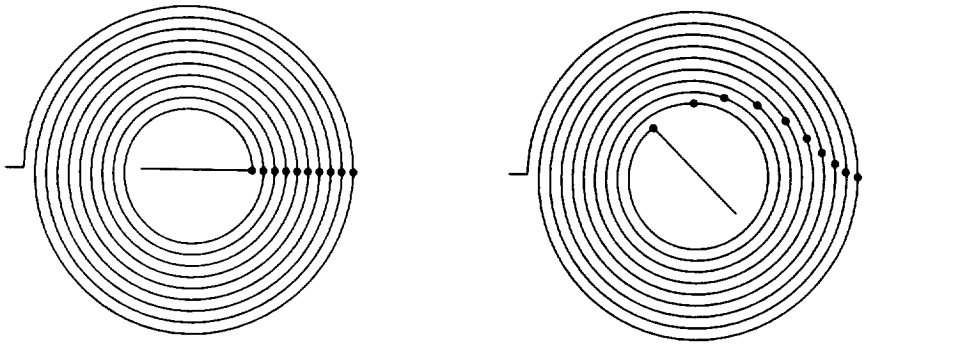

Figure 8. Spring Rotated Position of Different Coils

How much of the spring should be covered with heater was decided based on a trade-off between temperature control and potential delamination. To minimize the effect on the spring, a thin-film Kapton foil heater was used. Provided that both ends of the spring are reasonably isolated, there would not be a large temperature gradient between the heated and unheated sections. It is desirable to keep the heater on those parts of the spring that experience minimal movement. As can be seen in Figure 8, as the central axis rotates through its entire range of 135°, the spring at the end of the heater only rotates about 8°. Restricting the heater to areas of little movement minimizes the potential for abrasion of the heater and the possibility of entanglement.

The second step in the test process was to quantify the impacts of the spring/heater assembly. As shown in Figure 9, a thin heater was wrapped around the outside three coils of the spring. A layer of aluminum tape was added on top of the heater. The tape

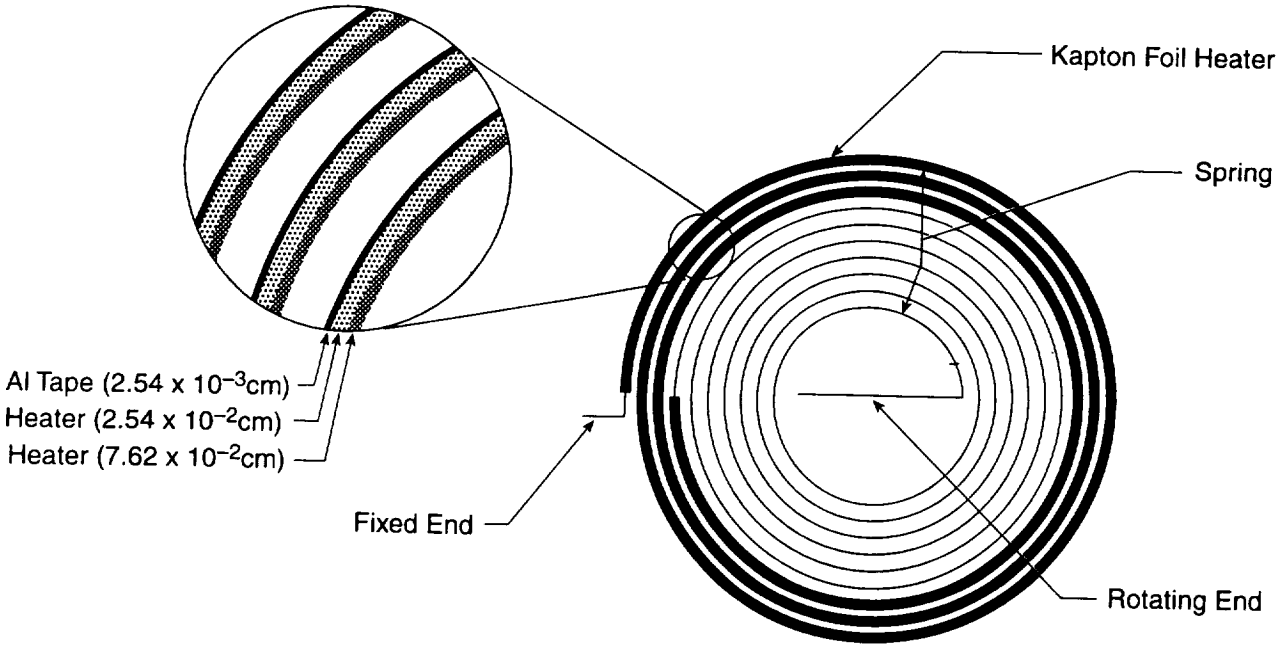

Figure 9. Heater Installation on Spring Details

provided both mechanical protection and thermal insulation for the spring. The bare spring calibration tests were duplicated for the spring/heater assembly. Again, the unit was placed in the oven and cycled between –25°C and 95°C. The results, shown in Figure 10, are not significantly different from the curve in Figure 7. The slope of the curve shows that there is a definite retarding of the performance at low temperatures, whereas the performance at high temperatures remains relatively unaffected. Because reduced performance at cold temperatures was not a concern, adding the heater to the spring did not affect its performance.

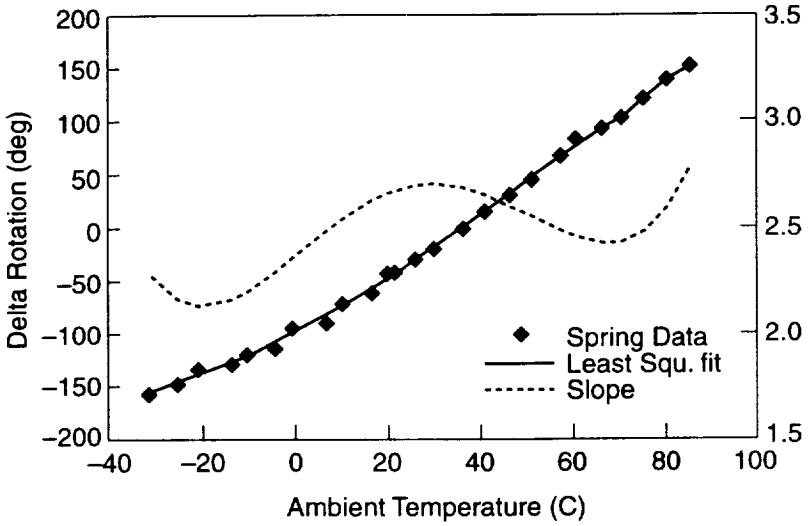

Figure 10. Spring/Heater Assembly Rotation/ Temperature Operating Characteristics

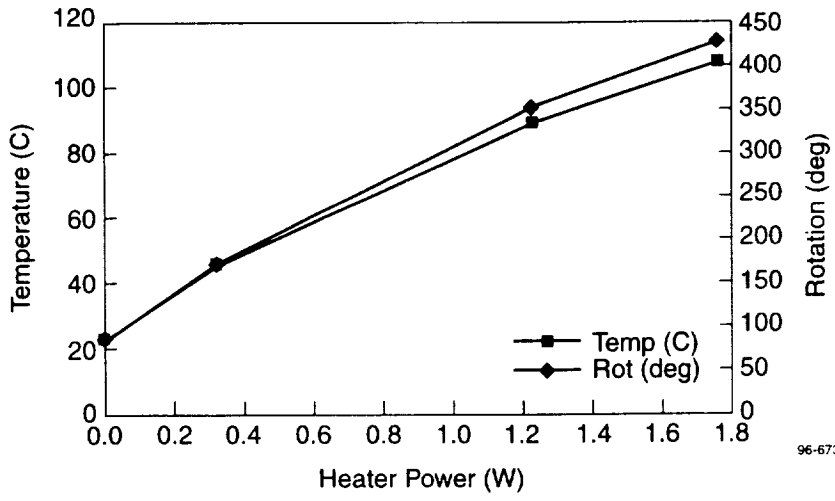

Figure 11. Spring Performance in Vacuum Using Heater

The next step in the test program was to estimate the heater size and to verify spring operation in vacuum conditions. The oven produced a nearly uniform spring temperature. In flight operation, the spring would operate in vacuum and be heated over only a portion of its length. To test this condition, it was placed in a vacuum chamber, and the heater was used to change its temperature. The heater must be sized large enough to produce a quick response, but not too large to overheat when powered. To find the right power level, heater voltage was incrementally increased, and the steady state temperature and rotation were noted. A desired maximum temperature of 110°C was set to provide the maximum activity while protecting the adhesive. The results of that test are shown in Figure 11. Transient results indicate that the system was close to equilibrium after 20 minutes (Figure 12).

The temperature/rotation profiles from the cases shown in Figures 7 and 10 were checked against the best-fit curve generated in the oven tests (Figures 13 and 14).

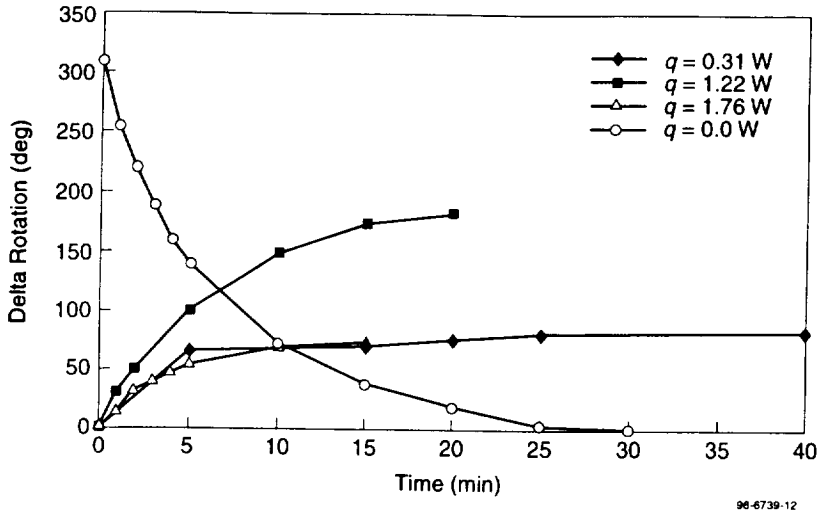

Figure 12. Spring Transient Response in Vacuum

The figures show that the best-fit curve follows the data well. In the hot case, the spring cooling down shows the greatest offset. This effect may be due to the outside cooling faster than the inside of the spring. Most of the data lie above the best-fit curve, thus indicating a more active spring. The actual temperature response of the spring is important in setting the opening and closing points and defining the associated times.

The clocking angle is the amount that the spring is preloaded to move the null point higher on the temperature scale. The null point is the point at which the spring generates no torque. It was a design requirement that if there is some failure in the door, it should fail in the open condition. The INCA temperature limits and effective spring rotation are shown in Figure 15. The spring null point needs to be chosen high enough to ensure that the door does not close due to the normal temperature change of the sensor. The fully closed position is 135° above the null point.

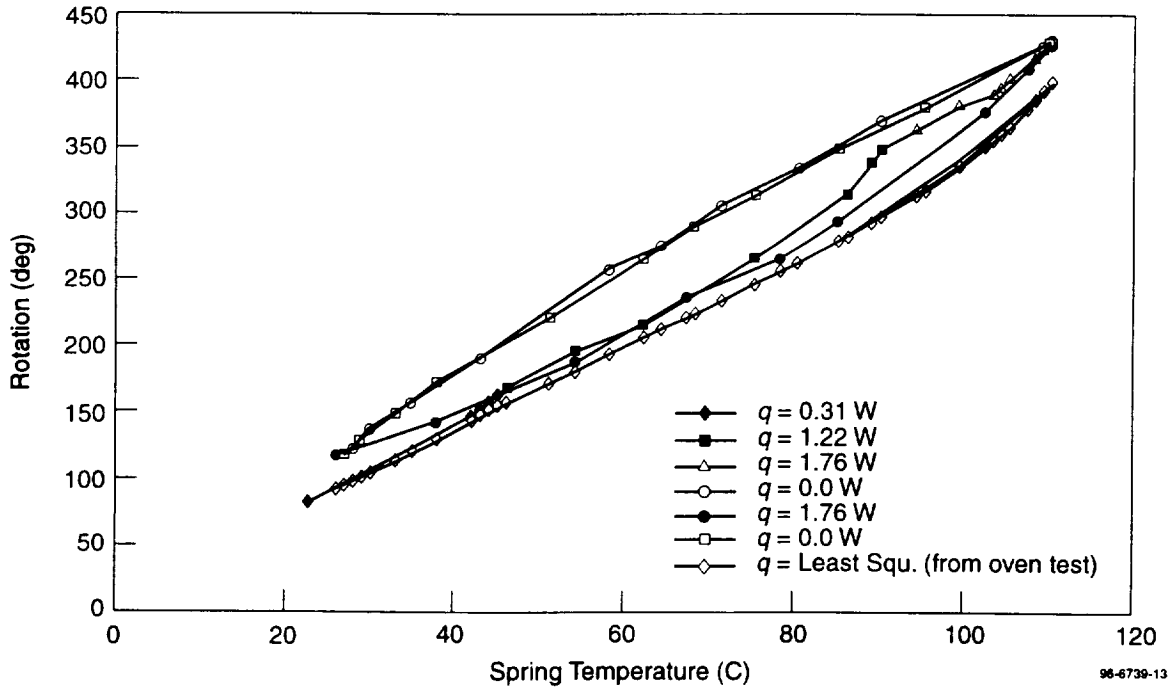

Figure 13. Oven/Vacuum Performance Comparison at 23°C

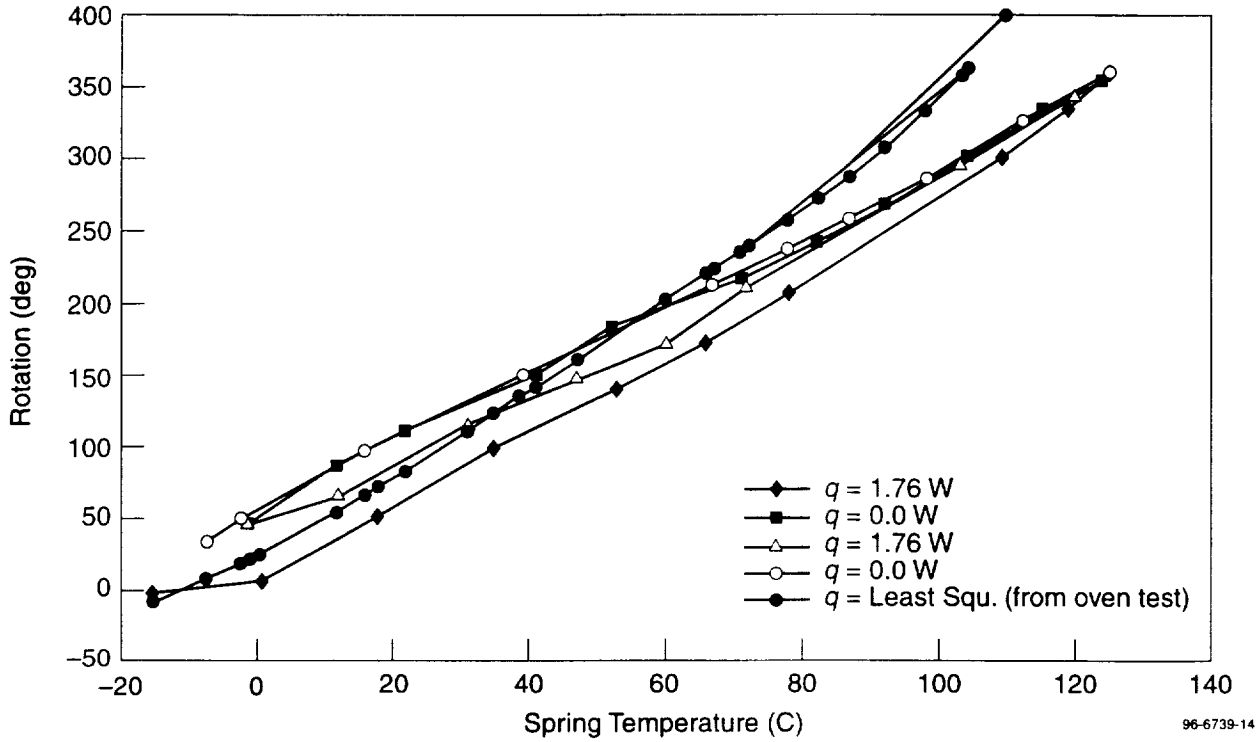

Figure 14. Oven/Vacuum Performance Comparison at –25°C

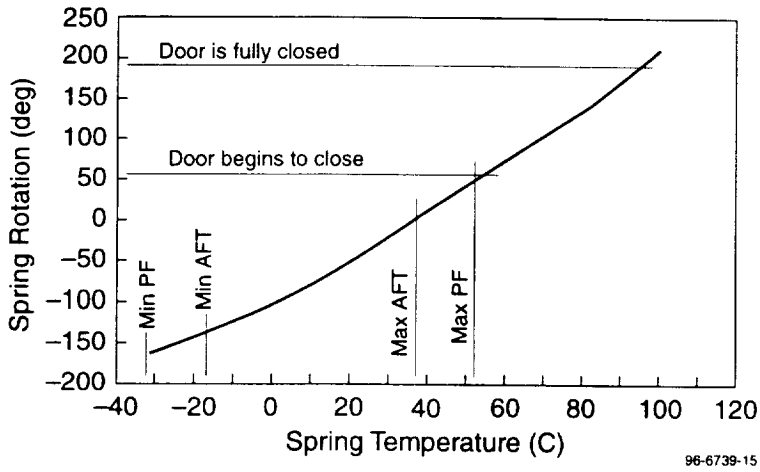

Figure 15. Predicted Spring Response to Temperature Showing INCA Operating Limits (AFT = allowable flight temperature; PF = protoflight)

Door actuation times were predicted for the proposed spring design. Spring rotation values of 100° and 235° were determined as the spring open and closed points, respectively. Spring temperature/rotation profiles were taken from the cases shown in Figures 7 and 10. The resultant spring response for the door closing is shown in Figure 16. The heater is turned on at time zero. It takes between 2 and 5 minutes for the door to reach the null point, depending on the case. It takes between 4 and 10 minutes for the door to actually close. The latter time is longer than desired. There is a valley in the warm-up curve that may account for this effect, or the null point may have to be set lower. Again, the time starts when the power to the heater is switched off. The door begins to move in 1 to 3 minutes. It takes between 7 and 8 minutes for the door to open (Figure 17). These operating times show a great improvement over the initial design, but do not include the effects of the housing.

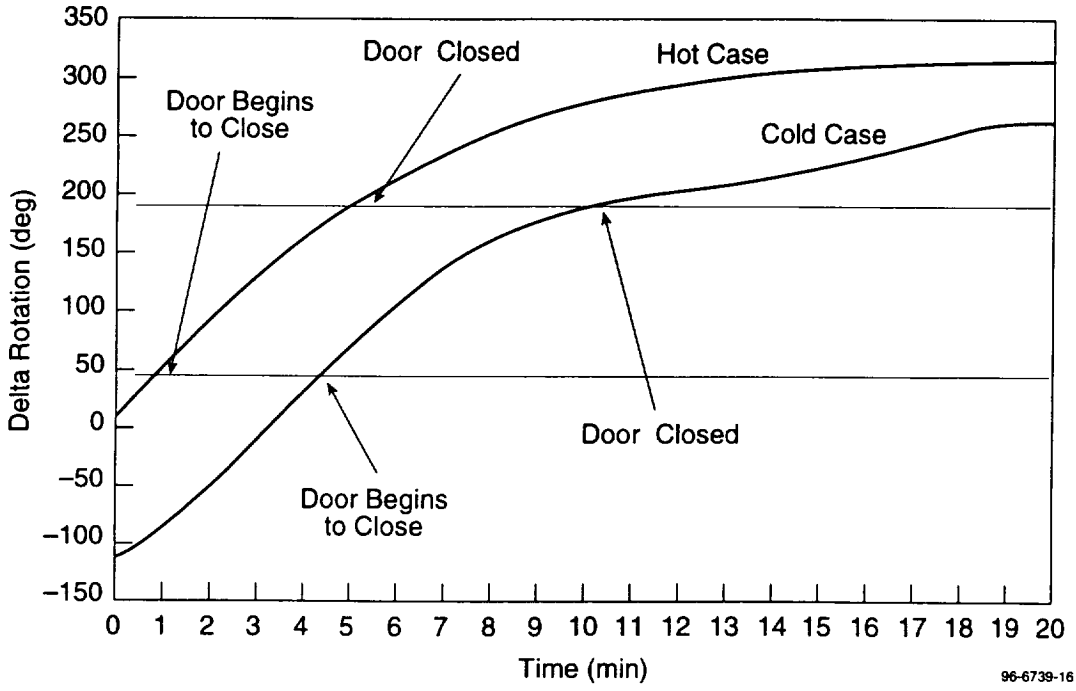

Figure 16. Predicted Spring Response During Door Closing

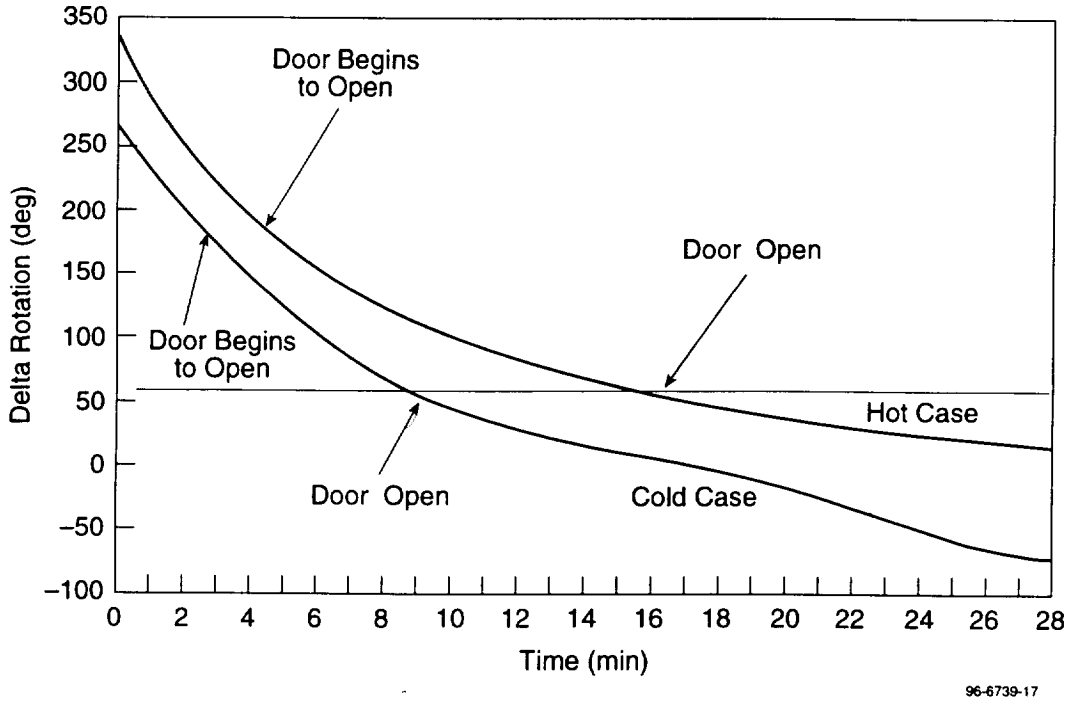

Figure 17. Predicted Spring Response During Door Opening

Engineering Testing

Based on results of the feasibility testing, the proposed spring design concept was shown to be feasible. The temperature range, heater power, and operating times were all reasonable. The last question to be answered was how to ensure that the heater would stay bonded. Answering this question required defining the final heater sizing and clocking angle, including the effects of the specific housing. Tuning the design would be critically important.

The effect of the clocking angle on spring performance was tested. The oven temperature was changed from 20°C to 120°C for two different clock angles. The spring position and temperature were recorded to determine the temperature at which the spring would begin to respond. The results of those tests are shown in Figure 18. With a clock angle of 15°, the spring began to move around 30°C and was fully closed at 85°C. The same test was run with the spring preloaded another 30°. The movement began around 55°C and was fully closed around 105°C.

The next step was to size the heater. Based on the spring/heater vacuum tests, the maximum power used should be about 1.75 W. Design bus voltage limits were 28.36 V to 30.25 V. The spring was tested over a range of heater powers and over the range of potential housing temperatures to optimize the design for the specific application. Due to the need to simulate accurately the heat leakage paths, these tests were run in vacuum. The installation of the spring into the housing would have an unknown effect on the spring temperature. The conduction losses from the spring should increase, but the radiation losses might decrease. Setting the heater power required the delicate balance of not overheating the spring in the hot case, but heating it enough to close in the cold case.

The plan for this balancing effort was to determine how much power would get the spring assembly to 120°C in the hot case, and then see how hot that same amount of

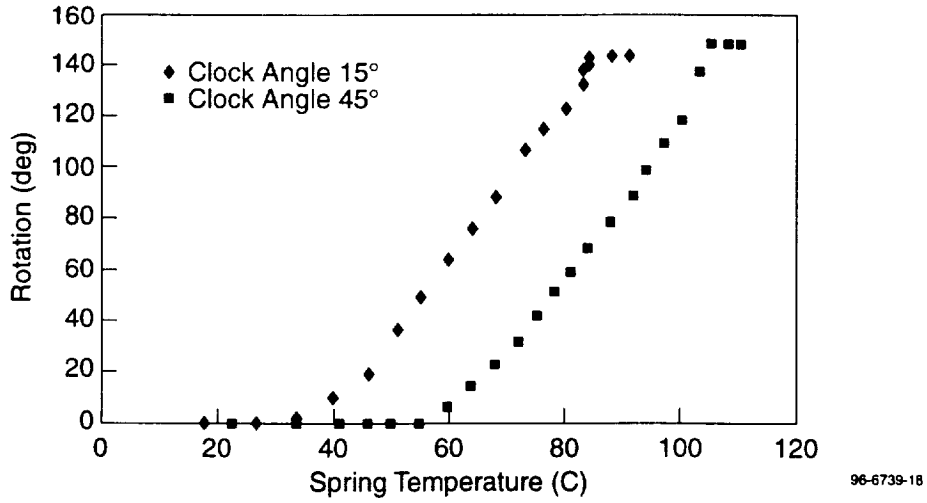

Figure 18. Spring Movement at Two Different Clocking Angles

power would get the spring in the cold case. Thermocouples were placed near the center of the heater and near the fixed end of the spring. Power was supplied to the heater from an external power supply. Initially, the chamber was set to 35°C. With 1.2 W applied to the heater, the spring temperature nearly reached 120°C. There was an 8°C difference between the center and edge thermocouples, thus indicating that the conductive heat loss was minimal. When the chamber temperature was increased to 55°C, 0.98 W brought the spring temperature to 111°C. About 1 W seemed to be the maximum that the spring could receive without overheating. It was now necessary to ensure that 1 W could get the spring hot enough to close in the cold case.

At first, cold testing indicated that the design would not work, but later demonstrated that the design was more robust than initially thought. It is this unforeseen robustness that makes this type of design truly practical. When the thermal vacuum chamber was lowered to –35°C, and 1 W of power was applied to the heater, the spring only rotated through 90°. It was still 45° away from being fully closed. Dropping the housing temperature from 55°C to –35°C resulted in a reduction in the spring steady-state temperature of 30°C. More power was needed, but then the spring would be too hot in the hot case. To test the spring sensitivity to temperature, the heater voltage was increased in steps until the spring was fully closed. Spring temperatures for these power increases are shown in Figure 19. It was necessary to increase the power to 1.2 W before the spring temperature reached above 110°C. However, this result was interesting because that point was the same power level needed to get the spring above 110°C from a +35°C ambient.

It appeared that the maximum spring temperature was not too dependent on heater power. Some heat leak was changing as the temperature increased. To investigate this variable heat leak, spring temperature sensitivity to power was tested over several hot temperatures.

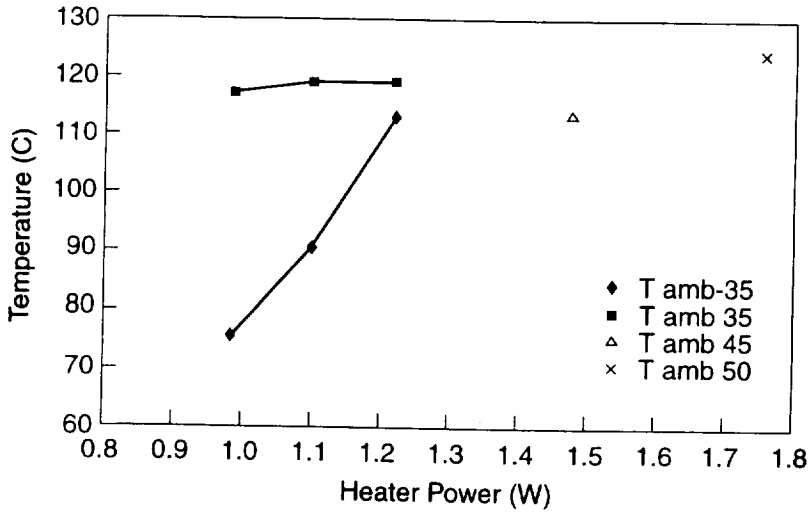

Figure 19. Maximum Spring Temperature for Different Ambient Conditions and Power Levels

In investigating this behavior, it was discovered that there was a heat leak in place that self-regulates the temperature of the spring. In normal operation, the spring makes contact with the housing only at the two ends. These contacts are intentionally poor so that the heat loss is minimized. However, as the spring expands, a large section of the outer coil is pushed up against the inside wall of the housing. While in contact, the heat from the spring is transferred directly to the housing wall. In

effect, this contact acts like a thermal shunt for the system. The maximum spring temperature can be regulated, over a small range of powers, by controlling the size of the housing. This discovery makes the design much more flexible, as it increases the range of usable heater powers. Finally, as the heat is directed specifically to the spring, the power required by the system is relatively small. In this case, 1.5 W was chosen as the design value. There is a tuning process involved, but the process is based on the spring and housing dimensions and therefore not difficult.

Once the clocking angle and heater size were chosen, it was necessary to demonstrate that the spring/heater assembly would stay intact over extended operations. The spring/heater assembly was installed in the engineering unit housing and subjected to an operational life test between January 25–31, 1996. Mission planning predicted that the door would be closed about 150 times. Using a 150% margin of safety, a life test was scheduled for 225 close/open cycles. Based on the engineering test results, a 40-minute on/off cycle was chosen to ensure that the heater would reach a stable temperature in the powered state. The test was run in the 3D3 thermal vacuum chamber. The cold wall chamber liner was set at the following steps: 55°C, 35°C, 20°C, 0°C, –20°C, and –35°C. The mechanism was operated six times at each temperature plateau until 225 heater cycles were completed. After testing, the mechanism was inspected and no degradation was found.

Flight Testing

After the system was shown to be feasible and was tuned to the specific housing, the flight unit could be built. Flight testing had two goals: to provide traceability to the earlier engineering tests and to demonstrate end-to-end performance in the required flight environment. The tuning parameters had been chosen but would have to be verified in the final design.

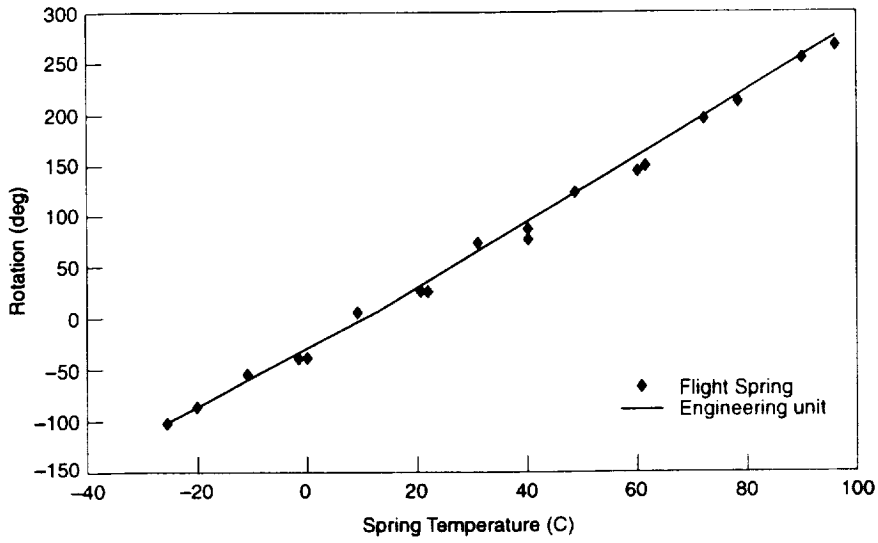

Figure 20. Comparison of Flight and EU Bare Spring Performance Data

The flight tests followed the same pattern as the engineering tests. The spring performance was calibrated with and without the heater. The bare spring calibration test data are shown in Figure 20. The data compare very well with the engineering test data, thus indicating good repeatability between springs. A four-cycle fast warm-up/cool-

down series was performed to test heater adhesion. The results show the performance was repeatable, thus indicating good adhesion. Maximum spring temperatures were just over 110°C, again comparing well with the engineering unit data (Figure 21). The final assembly of the unit was completed quickly. The clocking angle was set so that the spring null point was just above 50°C. A flight temperature sensor was attached near the fixed end of the spring.

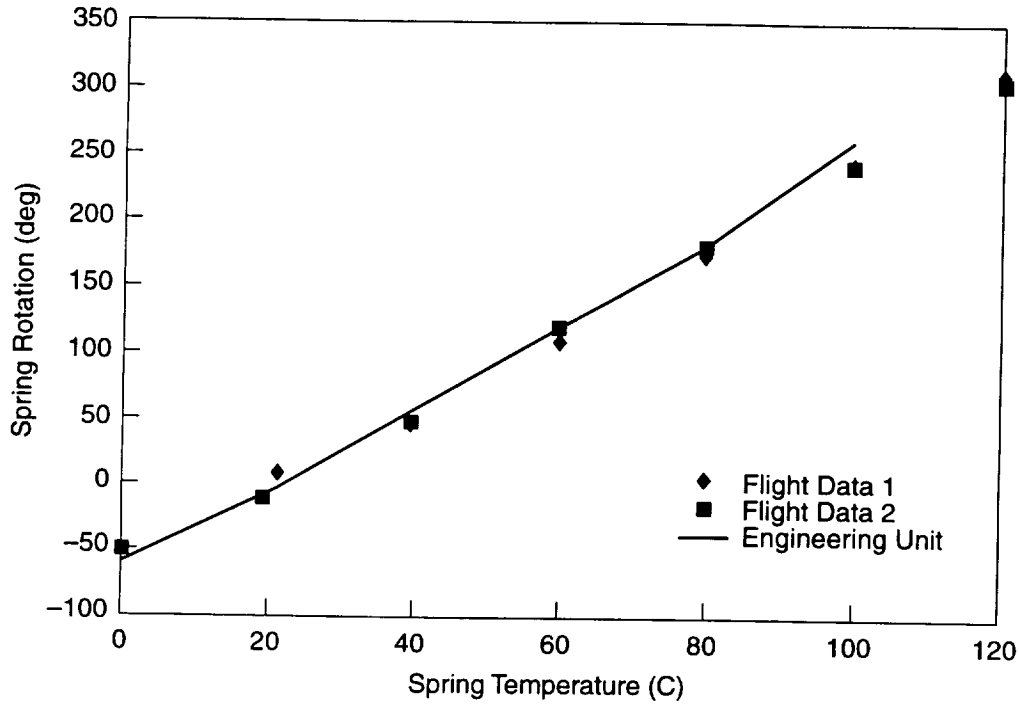

Figure 21. Comparison of Flight and EU Spring/Heater Performance Data

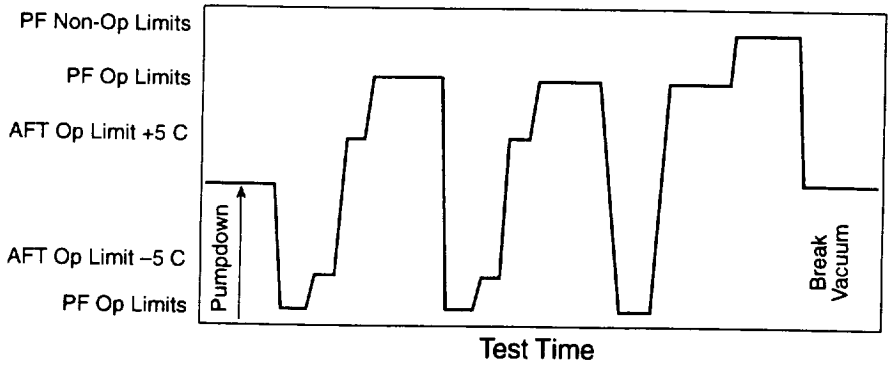

Figure 22. INCA Thermal Vacuum Test Profile (AFT=allowable flight temperature; PF=protoflight)

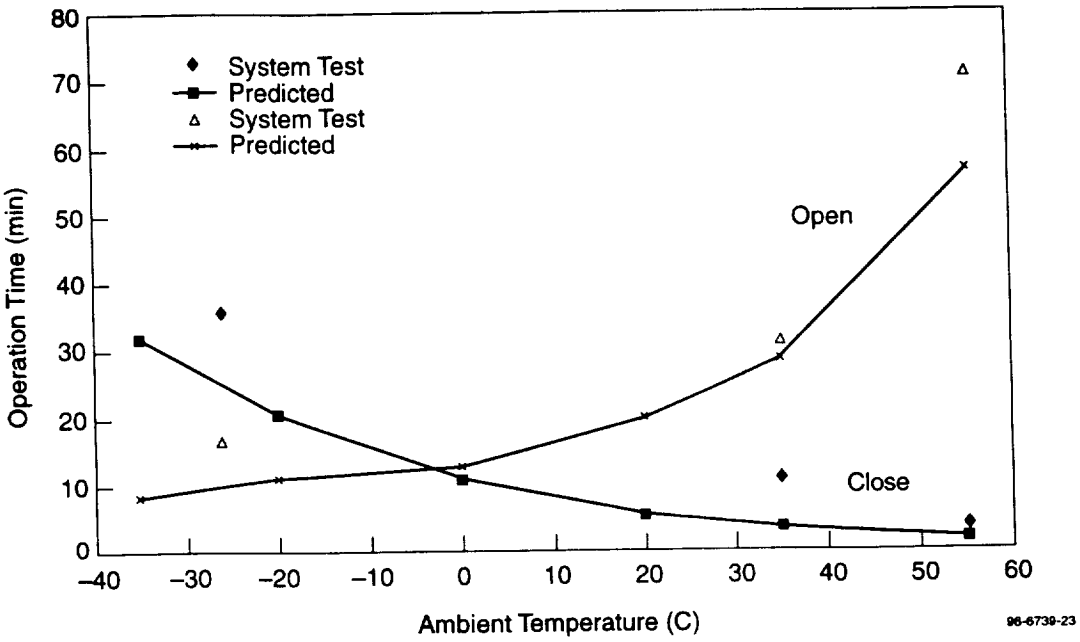

Figure 23. INCA Shutter Door Assembly Flight Performance Data

The final flight testing on the unit was performed in instrument-level thermal vacuum testing [2]. The thermal vacuum test profile is shown in Figure 22. Because there is no flight telemetry indicating the cover location, a television camera was included in the test setup. By watching the movement of the central axle in the actuator mechanism, the operation of the door could be monitored. During each plateau, the actuator was operated, and the closing and opening times were recorded. Figure 23 gives the end-to-end flight performance results compared against the earlier test predictions. The results show that the flight unit is slower than predicted. However, some of this performance degradation may be attributed to the difficulty in taking the readings.

Conclusion

The performance of the INCA actuator door mechanism proved that a bimetallic spring mechanism could have quick response, over an extended temperature range, with little power. The successful performance of the mechanism also demonstrated that a heater can be integrated onto a bimetallic spring in the tight schedule constraints of a flight program. Some tuning of the system is required, but this can be done easily.

The mechanism performance could be improved by a factor of three by changing the spring material. The INCA mechanism material was chosen for performance, schedule, and cost constraints. Bimetallic materials are available with performance characteristics that are three times better than the materials used, but they would not meet our schedule and cost constraints.

Acknowledgments

The authors would like to thank Bill Hamilton, Dennis Miller, and Tony Scarpati, who were responsible for all testing of the INCA sensor mechanism. Their dedication and efficiency are much appreciated, and they were important in allowing the mechanism testing to meet the tight schedule demanded.

References

1. *Texas Instruments Thermostat Metals Designers Guide*, (January, 1992).
2. Test Specification for the Cassini MIMI Thermal Vacuum Test (7348-9201).

SEPTRA 14 Gear Development

Luc Chatenet* and Frederic Canedi*

Abstract

SEPTRA® 14 (Solar Electric Power Transfer Assembly) is the trade name given by Société Européenne de Propulsion (SEP) to the Solar Array Drive Mechanism (SADM) developed for the Polar Platform, Envisat. Since many of the requirements for this mechanism were similar to those of the SPOT ERS and HELIOS SADMs, most of the selected technologies were well proven except the gear device. In fact, a new gear device was developed specifically for the SEPTRA 14. This paper is focused on the design and lubrication problems met during the device development. Due to the high level of torque applied on it, as well as to the speed stability requirements, this device has from the beginning been identified as a critical element. The critical path method led to the realization of an Engineering model and to the decision to perform a complete qualification testing on it comprising of vibration testing, high torque testing, and life testing under vacuum. The initial choice for lubrication was a SEP well-proven technology of a dry lubrication process by Nuflon deposition (Teflon deposition at hot temperature). Back-up solution studies were delayed to the end of the Engineering Model tests. After test completion, the gear had an unacceptable amount of particles and gear tooth degradation. Consequently, a modification trade off was made. It considered different lubricants and materials and was based on test results made on samples. A new solution was then selected, and led to an important number of modifications and then to a successful qualification.

Introduction

Since 1970, SEP has been developing and producing a range of Solar Array Drive Mechanisms for various types of satellites. The product line consists of seven different mechanisms composed of a mechanical subassembly and the associated electronics.

- The SEPTRA 11 and SEPTRA 12 are direct-drive mechanisms developed for Earth observation satellites (SPOT, ERS, HELIOS).
- The SEPTRA 14, which was developed for the Polar Platform, has the same basic characteristics, and will be described in this paper.
- The SEPTRA 21, 22 or 23 are dedicated to geostationary satellites. They have a gear with dry lubrication of Nuflon type that was used on the first version of SEPTRA 14.
- The SEPTRA 31 is a mechanism for small satellites.

The SEPTRA1X line has the motor characteristic that its current compensation is able to rotate very large solar arrays with minimimal micro gravity perturbation induced to

* Société Européene de Propulsion, France

the platform. This performance is considered an improvement for Earth observation and ensures a better reliability of pictures taken by the satellite.

The SEPTRA 14 gear has to be compatible with speed stability (or micro-g induced to the platform), high torque, and anti-backlash. These requirements led to a critical development including:

- Initial choice
- Engineering test
- Modification trade off and validation tests
- Final design
- Qualification tests

SEPTRA 14 Description

The SEPTRA 14 is composed of an electronic box and a mechanism. The electronics are dedicated to the motor current powerization by micro-stepping adapted to the dedicated mechanism. They also interface with the position sensor. The mechanism main functions are to:

- Rotate the solar array (SA) continuously clockwise or counter-clockwise
- Transfer the power and the signals coming from the solar array to the platform as well as deployment motor powerization from the platform to the solar array
- Sustain very high load during launch and solar array deployment
- Present a stiffness well adapted to SA characteristics in order to avoid any overstress of the deployment system
- Provide the rotor angular position.

The design of the mechanism is based on qualified technologies (through SPOT and ERS program) and comprises:

- A locking system able to sustain very high loads during launch and deployment: the locked configuration is obtained by blocking the rotor between two cones using a preloading system that is unlocked by a pyrotechnic cutter
- A set of lead lubricated bearings, softly preloaded by membranes
- A slip ring with silver races and silver MoS_2 brushes preloaded on the races by means of flexible blades
- Two motors (primary and redundant) of 57PPP Sagem type that are 1200 step motors specifically controlled for torque and speed stability
- A one-stage gear device with an anti backlash system with two pinions preloaded by a torsion shaft (this device was not from SPOT and ERS development).
- Two magnetic position sensors
- A stiffness adapter

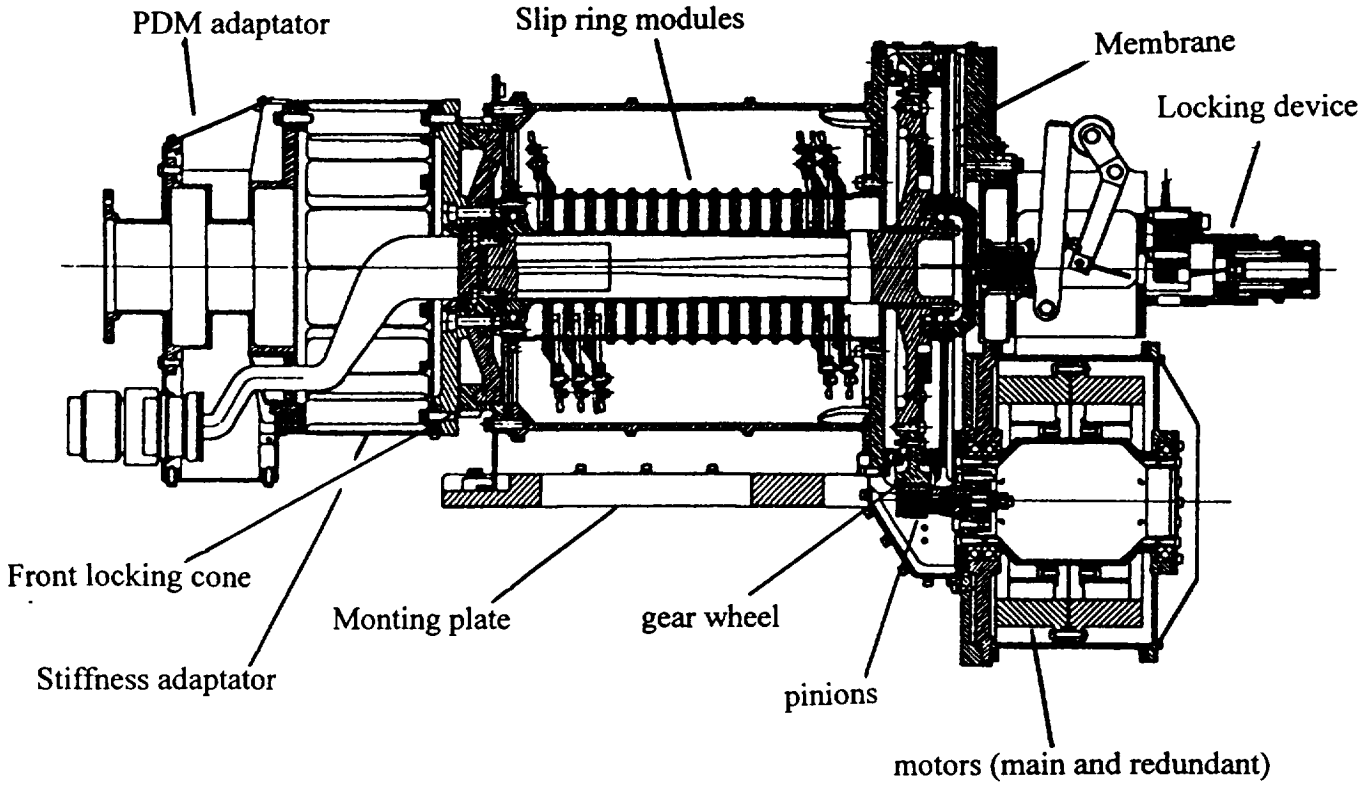

Figure 1 SEPTA 14 Cross-section

SEPTRA 14 requirements are as follows:

- Power transfer: 48 tracks rated at 14 ampere
- Signal transfer: 72 tracks rated at 2 ampere
- Rotation speed:
  nominal: 1 rev/100 minute
  maximal: 8 rev/100 minute
- Position sensor accuracy: ± 1°
- Torsional stiffness: 2660 N•m/rad
- External load in locked configuration:
  Bending moment: 275 N•m
  Torque (around rotation axis): 115 N•m
  Radial or axial load: 1875 N
- Available motor torque in unlocked configuration: >50 N•m

Life requirements are defined in Table 1, and have to be demonstrated by test for two lifetimes.

Table 1

	CYCLE	Environment	Revolution	Loads
	* Running in and speed compensation	Vacuum	810	0
	* Acceptance tests			
	- tests before vibrations	Ambiant		0
G	- vibrations	Ambiant		1500 N simulated
R	- tests after vibrations	Vacuum		0
O	* Transport/storage	N2		0
U	* Platform tests (3 years max)			
N	- tests before vibrations	Ambiant	1160 rev (nom, speed,	0
D	- vibrations	Vacuum	ambiant)	1500 N simulated
	- tests after vibrations	Ambiant	300rev (nom, speed, vacuum	0
	* Transport/Storage (11 years max)	N2/ambiant	650 rev (acceler.	0
	* Launch preparation	Ambiant	speed ambiant)	0
	* Launch (vibrations)	Ambiant		2000 N specified
	* SA deployment	Vacuum		chock
	* Unlocking	Vacuum		
	* Life orbit (5 years)	Vacuum		
	- nominal mode		27500 rev (2 Nm)	
	- survival mode		10 rev (18 Nm)	
	- altitude corrections		550 rev (10 Nm)	

Speed stability harmonics amplitude (at nominal speed) due to the gear are:

0.5% at 0.045 Hz; 0.3% at 0.09 Hz
0.7% at 0.135 Hz; 0.2% at 0.18 Hz

and due to the motor are:

3% at 0.8 Hz; 1.5% at 1.6 Hz
1.5% at 2.4 Hz; 6% at 3.2 Hz

Initial Gear Design

Due to the speed stability requirements which are to be correlated to the torque stability by calculations at the platform level, the choice of a single-stage gear was made in order to minimize the number of critical harmonics in the low frequency range (from 0 to 1 Hz). The speed reduction ratio has to be equal to 16 in order to keep acceptable margin in front of the torque requirements as well as to comply with the electronics frequency range. Thus the gear was designed with a modulus at 1 and a pressure angle (inclination of the drive line) at 15°. The three parts of the gear system are:

- the wheel: 272 teeth; width 21 mm
- the pinion: 17 teeth; width 15 mm
- the counter pinion: 17 teeth; width 2.5 mm

The preload at the counter pinion is applied by means of a torsional shaft. The torque between pinion and counter pinion is applied after assembly. A bearing placed between the pinion and counter pinion controls the alignment between the two parts. Nuflon deposition is made on the wheel, but the pinion and counter pinion are not treated.

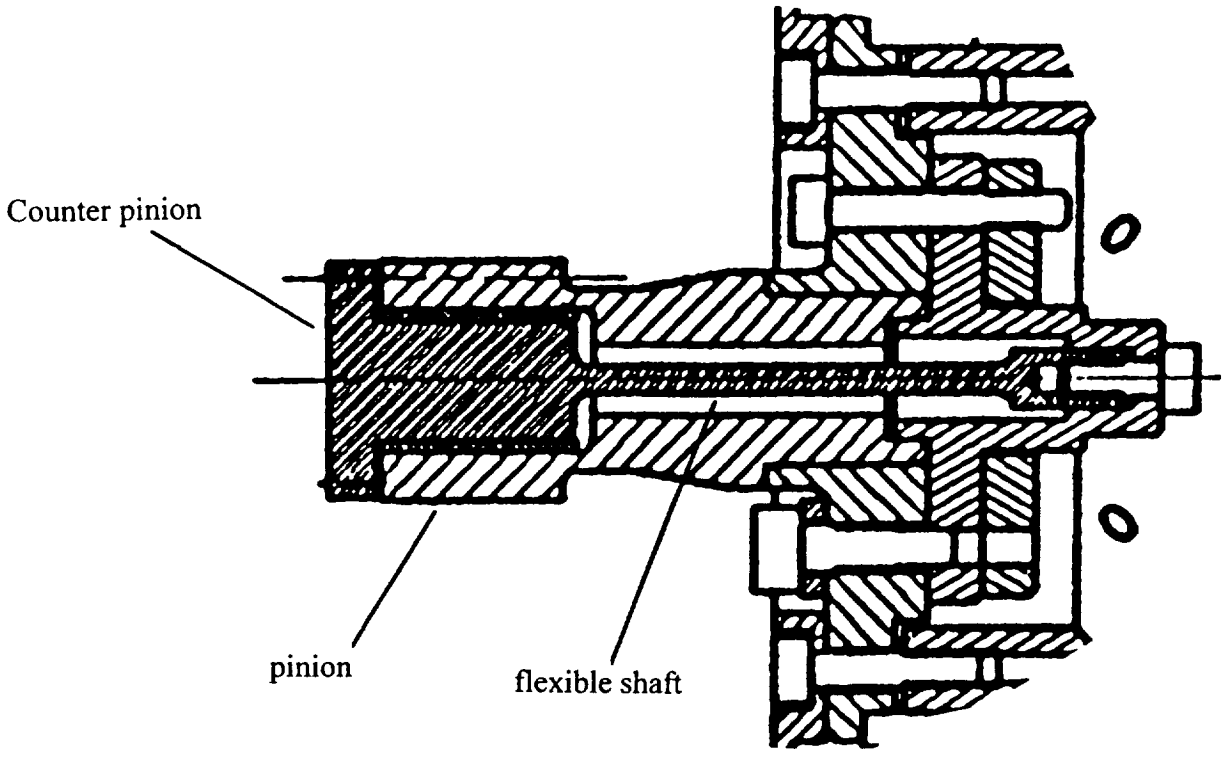

Figure 2 Pinion Details

According to the requirement (anti-back/slash functioning range), the torque applied between the pinion and counter pinion after assembly is between 0.14 and 0.16 N•m. Thus the Hertzian pressures calculated after application of the safety factors (ESA requirements) were:

- nominal external torque: $410 \cdot 10^6$ Pa
- survival mode torque: $600 \cdot 10^6$ Pa
- attitude correction torque: $550 \cdot 10^6$ Pa

Tests Performed on the Engineering Model

The main purpose of the Engineering Model was to test the gear device resistance and to check the speed stability before and after the life tests. Thus this model had a gear device in the flight configuration and a motor with a speed stability compensation in order to minimize the noise level of the speed measurement. A brake was added in order to simulate the torque that is applied during the flight by the Solar Array. The speed stability was checked by a gyrometer using a transfer slip ring. This campaign aimed also to take brushed preload and friction measurement throughout the life span. The Engineering Model design is given in Figure 3.

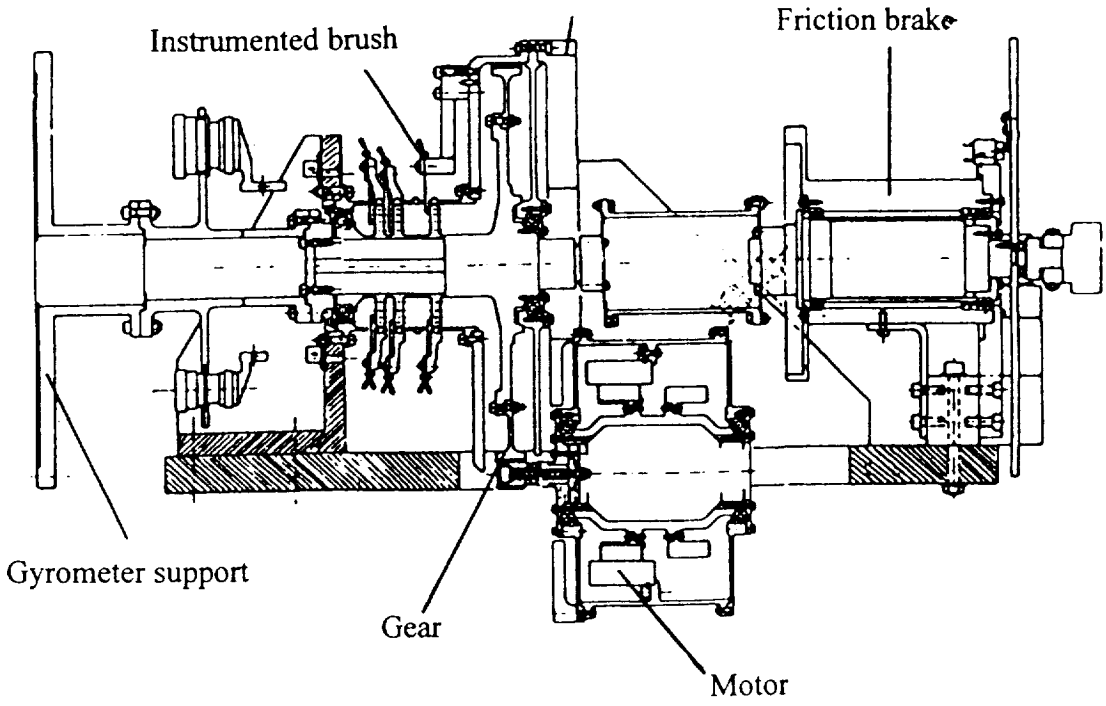

Figure 3 Engineering Model

The tests applied on this model were at the same level as a qualification test, including:

- vibration test (three axis at qualification level)
- running in under vacuum
- running in under atmospheric pressure
- life span under vacuum
  - 10 revolutions with a survival mode torque
  - 550 revolutions with an attitude correction torque
  - 27500 revolutions with a nominal torque

All the torques applied on the mechanism were increased by a qualification factor and then by another factor due to the friction uncertainty. The results of this test campaign are illustrated by the three following major items:

- After vibration, the Nuflon deposed on the wheel was damaged at the spot in contact with the counter pinion. The depth measurement of this area was not accurate since it could only be done by comparison of the two tooth profiles. This depth measured did not seem to exceed the 8 microns Nuflon thicknesses. Thus the damage was not considered as a critical one and it was decided to continue the tests.
- After the life tests, the torque margin was the same as at the beginning of life and the speed stability still met the requirements even though the amplitude of the harmonics increased by a ratio of 1.5.
- The examination made after the life tests revealed that the tooth erosion as well as the amount of particles were unacceptable.

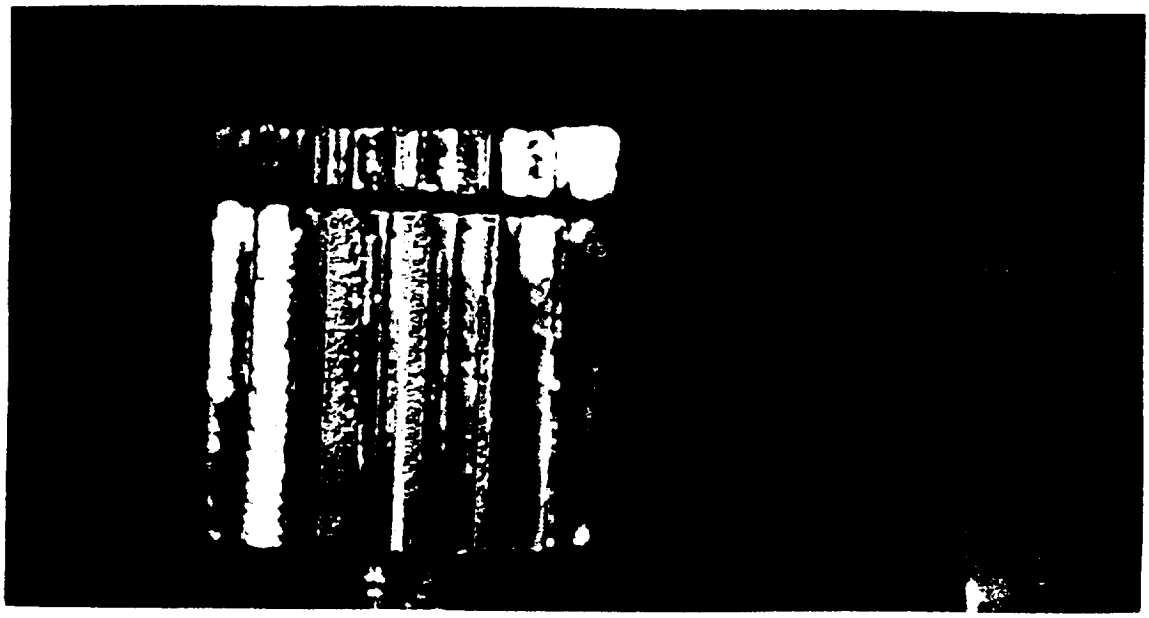

Figure 4 Gear Teeth

Results Interpretation and Complementary Tests

The Nuflon coating was qualified for a number of cycles far greater than have be applied during the life span. The Hertzian pressure applied during qualification was equivalent to the attitude correction torque ($550 \cdot 10^6$ Pa), but under survival mode torque ($600 \cdot 10^6$ Pa) the degradation of Nuflon coating was could be initiated during 10 revolutions with the high torque level. Thus tests with different levels of torque have been applied on a new gear. Each torque level was applied on a few teeth. Figure 5 shows that for torques of 30 N•m and 40 N•m, small degradations can be observed.

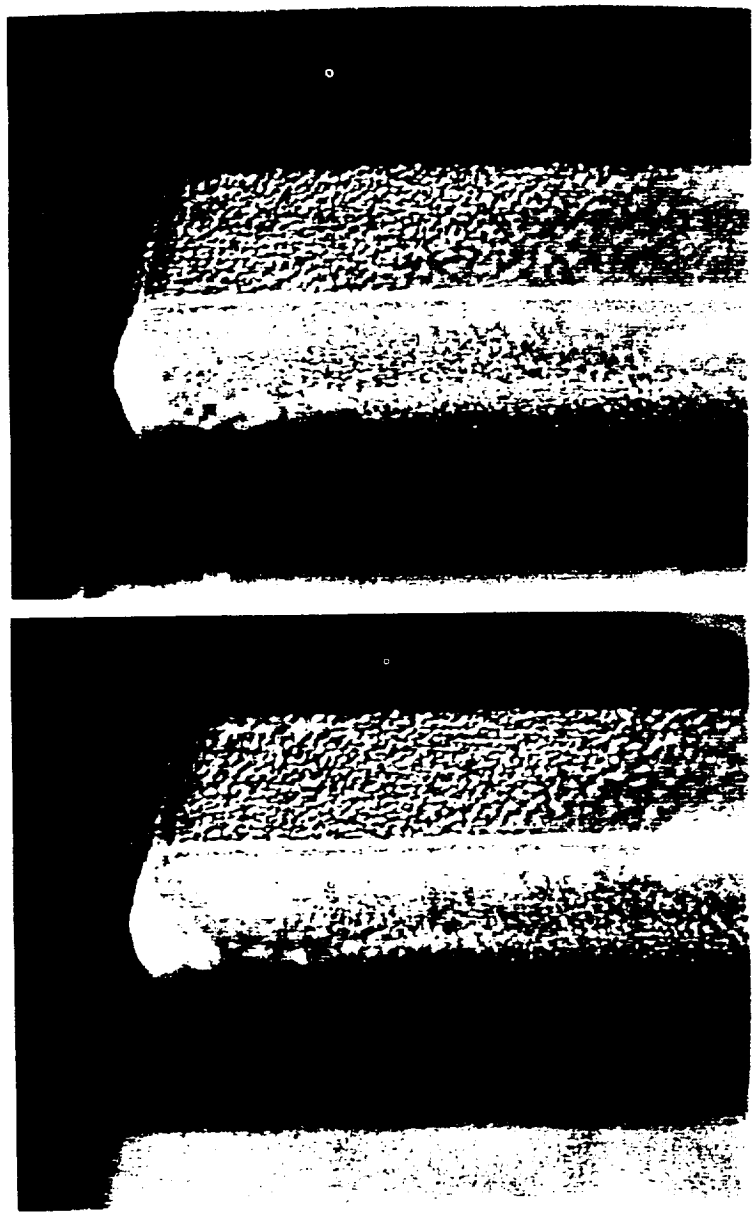

Figure 5 Degradation after 30 Nm solicitations (20 cycles)

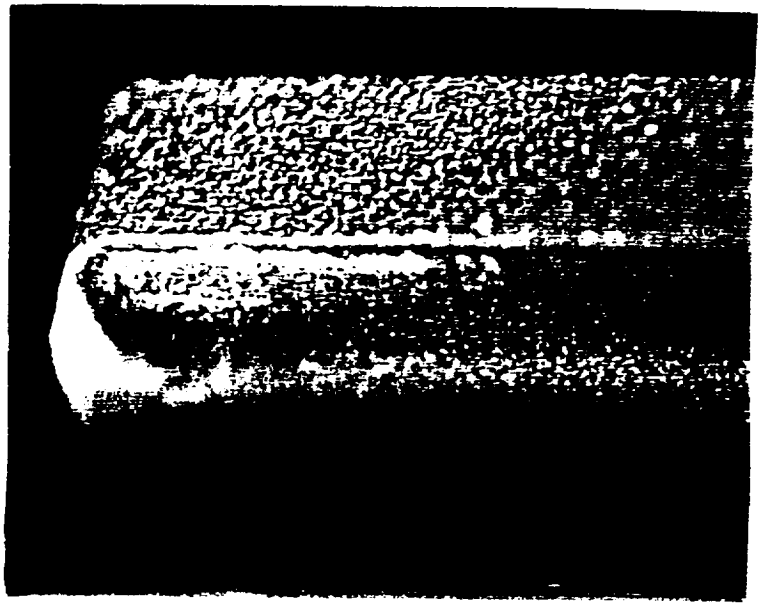

Figure 6 Degradation observed after 20 cycles under 40 Nm

Another vibration test was performed on a new gear and the degradation was analyzed just after this test. Figure 7 shows the degradation of the Nuflon coating and Figure 8 shows measurements indicating that the coating is completely removed in front of the counter pinion.

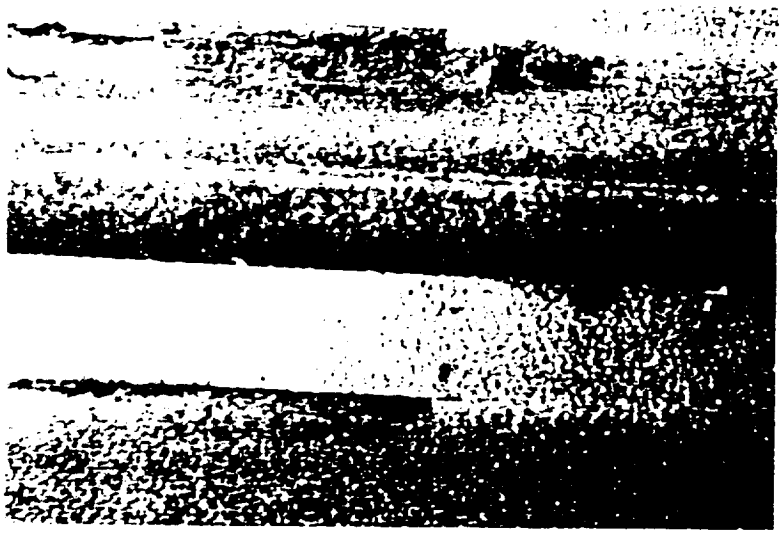

Figure 7 Degradation of the Nuflon coating due to solicitations

One side of the wheel tooth (in contact with the pinion).

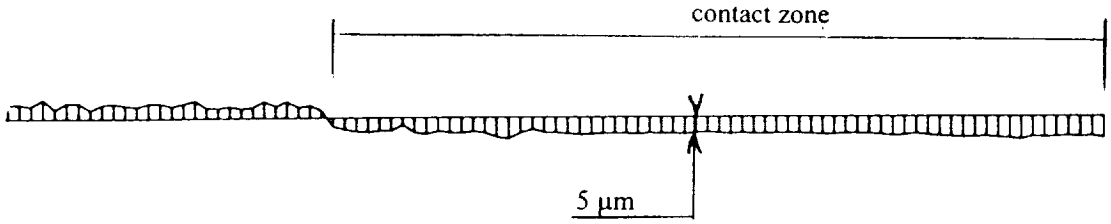

Other side of the wheel toot (in contact will b counter-pinion)

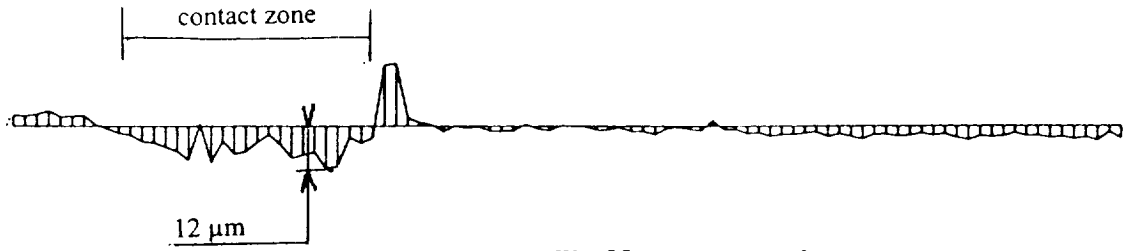

Figure 8 Tooth Profile Measurements

After thorough test analysis, it was concluded that:

- The hertzian pressure on the tooth was higher than the one expected. This was due to the deflection of both pinion and counter pinion shafts. This generated degradation that appears already at 30 N•m when expected at 45 N•m
- Nuflon damaging during vibrations was important. The degradation could be amplified by the interference that could be locally generated in the configuration by the counter pinion as shown in Figure 9.

Modifications Implemented on the SEPTRA 14

To decrease the displacement amplitude during vibrations and also the bending deflection of the pinion, four modifications were decided. An additional one was delayed until completion of a new test campaign to be performed very quickly on samples.

- The first modification was made in order to increase simultaneously the bending and the axial stiffness of the bearing assembly (shaft linked to the pinion). The comparison of the two configurations is given in Figure 10.
- The width of the counter pinion was increased from 2.5 mm to 4 mm. At the same time, the tooth profile was changed from a flat tooth to a rounded one. This modification was made in order to avoid any edge contact.

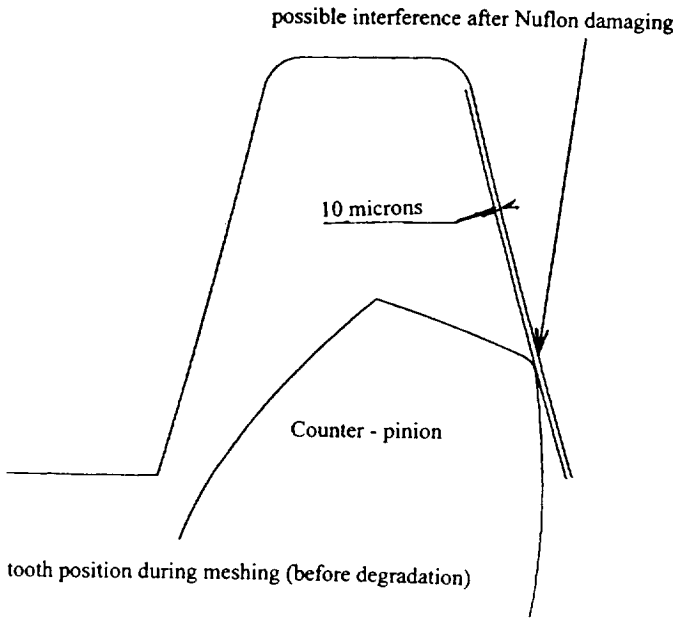

Figure 9 Counter Pinion Interference

- Modification of the Vespel bearing between pinion and counter pinion. This modification was made to increase the bearing stiffness:
  - the bearing length was increased
  - the gap was reduced from 32 microns to 8 microns
  - the thickness was deceased
- The surface treatment of the gear was changed in order to increase the hardness. The new process selected was nitriding.

The change of the lubricant was decided after a comparative fretting test performed on samples. The comparison was made with nitrided samples and the five following configurations:

- Nuflon coating
- MoS_2 deposition
- without lubricant
- Pennzane oil
- Braycote 601

The test plan was determined in relation to the expected PV factor, with P corresponding to the hertz pressure and V to the speed of the displacement. The comparison of all the frequency ranges led to an equivalent test in three phases:

Phase 1: 75000 cycles at 22 Hz with a displacement of ±0.027 mm
Phase 2: 30000 cycles at 150 Hz with a displacement of ±0.041 mm
Phase 3: 50000 cycles at 70 Hz with a maximum displacement of ±0.25 mm

All of the tests were performed with a hertzian pressure of $290 \cdot 10^6$ Pa.

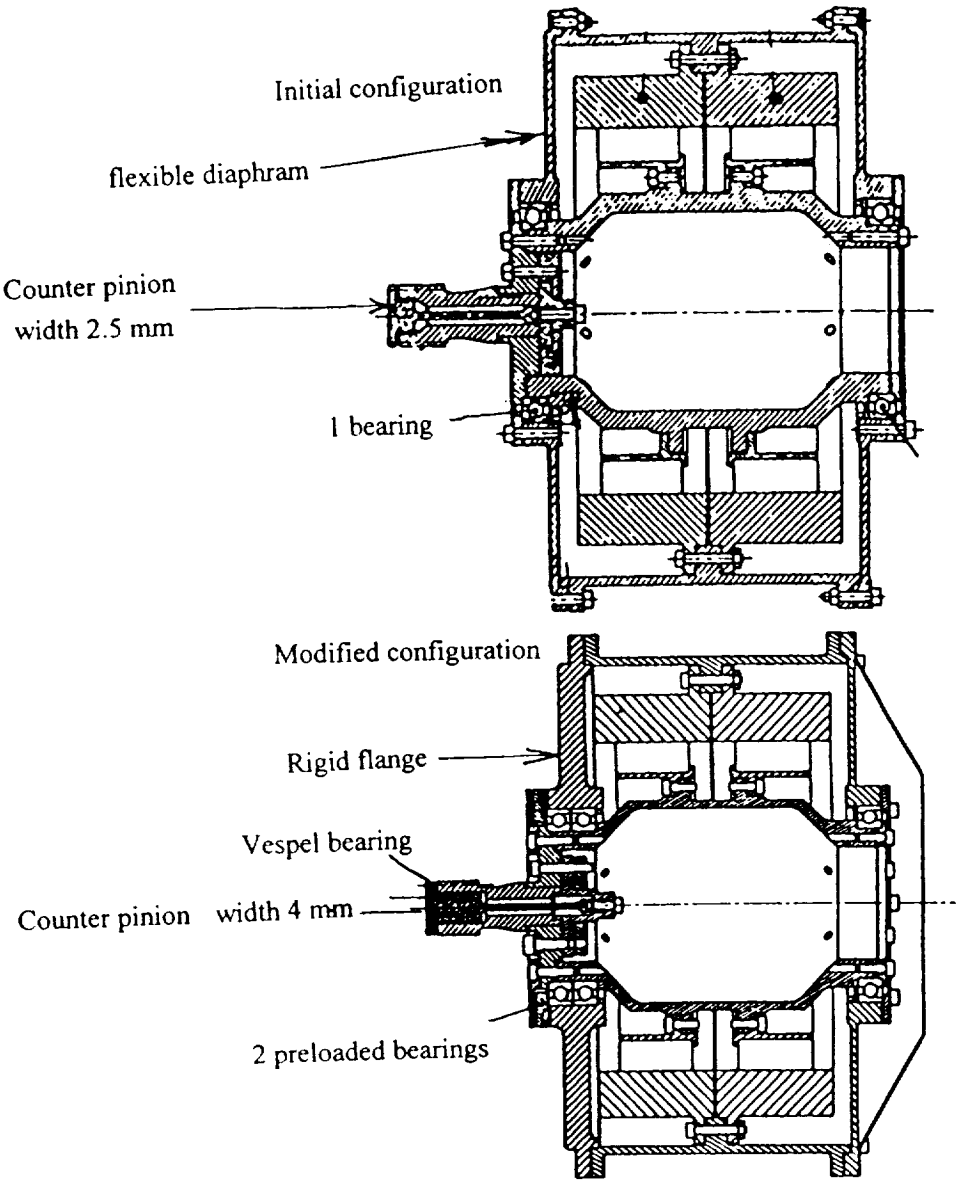

Figure 10 Bearing configurations

The comparison concluded that:

- Tests with dry lubrication presented unacceptable wear (6 to 8 microns)
- Tests without dry lubrication presented nearly the same metallic wear as those with dry lubricant (2 microns)
- Samples with lubricant of Pennzane or Braycote type presented a wear corresponding to the top of machining score (0.5 micron)

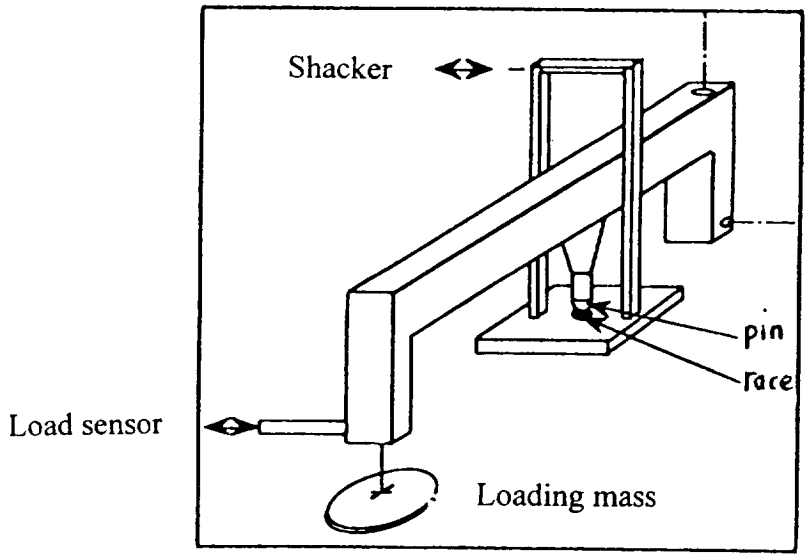

Figure 11 Fretting test set up

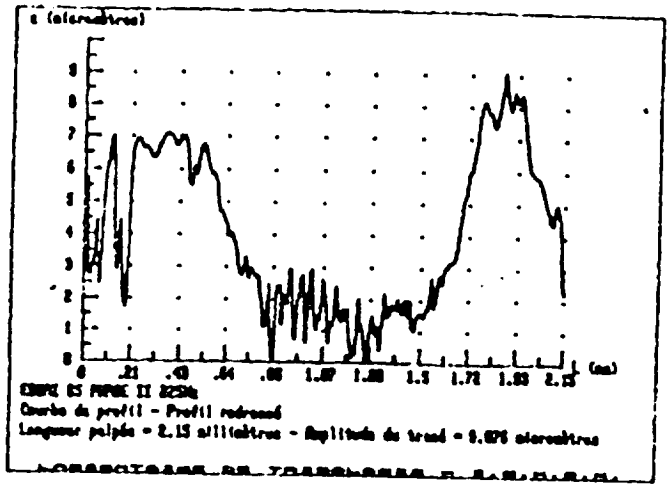

Figure 12

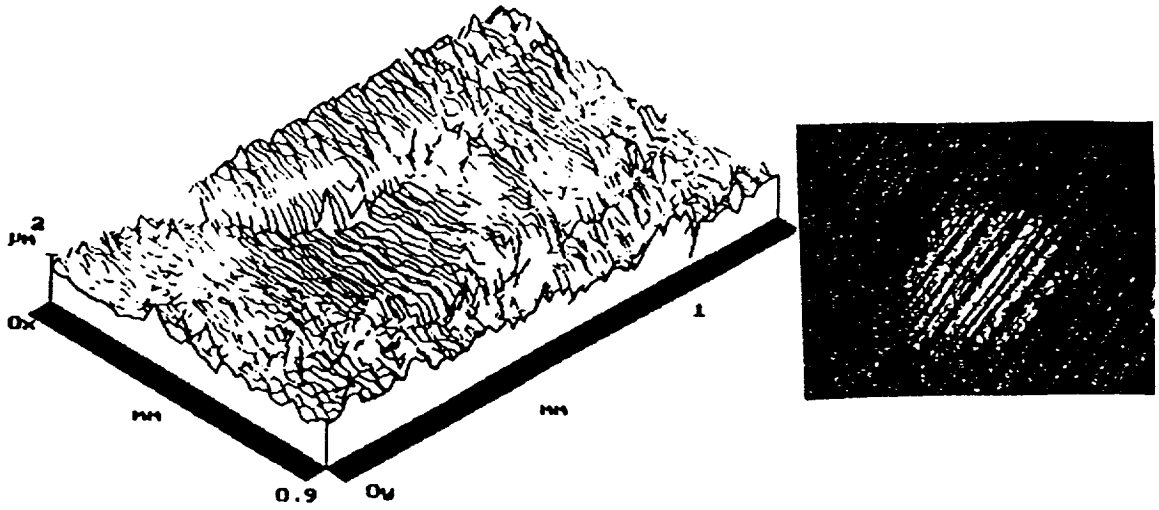

Figure 13 Wear measurement on race lubricated with Braycote oil

Conclusion

After implementation of all modifications on the Engineering Model, a new qualification campaign with vibrations, constant acceleration test, and ife cycling was successfully performed.

The experience realized on the Engineering Model provided the design of a gear that had excellent behavior after two lifetimes.

This program taught us the following lessons:

- Fretting effect during vibrations shall not be neglected
- Deflection and the stress concentration factors behavior shall be taken into account (for the evaluation of the coating)
- The choice of a lubricant can be done through very simple tests that have to be performed at the beginning of the development. It is worth taking this precaution to save a lot of time and effort.

The Cassini Main Engine Assembly Cover Mechanism

Donald R. Sevilla*

Abstract

This paper describes a micrometeroid protection system for the main engines of the Cassini spacecraft. The engine Cover Assembly is a deployable/restowable half sphere of multilayer insulation mounted to an articulatable frame over 2 meters (7 feet) in diameter. The Cover folds into a compact wedge only 25 cm (10 inches) at its maximum thickness. The micrometeroid environment and typical protection methods are described as well as the design details and development problems of the Cover Mechanism Assembly.

Introduction

Cassini is thought by many to be one of the last immense interplanetary spacecraft the United States will produce. Standing over 6.7 meters tall and weighing over 5,600 kilograms, Cassini will orbit Saturn for a four year tour of the rings and moons (Figure 1). Cassini is an international collaboration between the National Aeronautics and Space Administration (NASA, supplying the Orbiter), Agenzia Spaziale Italiana (ASI, supplying the High Gain Antenna) and the European Space Agency (ESA, supplying the Huygens Titan Probe). In all, the scientists and engineers on the Cassini team come from 16 European countries and 33 states of the U.S. Using its main engines and numerous gravity assists, each orbit around the planet will be unique to allow Cassini to perform close-up observations of many of Saturn's satellites. Due to the criticality of the main engines for this mission, the Main Engine Assembly (MEA) is block redundant, consisting of dual engines, gimbals and linear actuators (Figure 2). Late in the development of the spacecraft, it was determined that these high performance engines were particularly sensitive to damage from the micrometeroid environment of interplanetary space. Thus, a protection scheme had to be implemented for the MEA after the entire Cassini spacecraft had been designed and built. This paper presents the design of the MEA Cover Mechanism Assembly and some of the more interesting problems encountered during its development.

The Micrometeroid Environment

Interplanetary spacecraft have been designed with micrometeroid protection features since the early 1970s. When Galileo was built in the early 1980s, protection was incorporated according to a micrometeroid fluence model based on data collected by Pioneer 10 and 11, Helios 1 and flux measurements near Earth (spacecraft and lunar craters). For Cassini, the model had been updated with data from the Galileo and Ulysses spacecraft. The interplanetary environment is considered to have a nearly omnidirectional flux of micrometeroids ranging in mass from 10^{-13} grams up to 10^{-4} grams, with an average impact velocity of 20 kilometers per second (44,700 mph).

* California Institute of Technology, Jet Propulsion Laboratory, Pasadena, CA

The concentration of these high speed particles is highest at low heliocentric distances and falls off rapidly outside of 2 astronomical units (AU). Essentially, protection from micrometeroids is required between the Sun and the asteroid belt, and becomes less important as you approach the outer planets [1].

The protection methods are usually quite simple and fall into two classes. Provisions must be made either for a single, thick *first surface protection* or for a thinner *second surface protection* which in itself is shielded at a distance by a first surface. This latter method is the preferred design because it is a lower mass solution. The key is providing the spacing between the first and second surfaces. A typical example is a mission critical electronics bay, exposed to space. The electronics box enclosure must have a wall thickness of 5.8 mm (0.23 inch) of aluminum if it is a single first surface protection for micrometeroids. However, the aluminum enclosure can be a more reasonable 1.6 mm (0.06 inch) thick second surface if it is shielded by multilayer insulation (MLI) spaced off at least 6.1 cm (2.4 inch) from the first surface. The idea here is to break up these small high velocity particles with the first surface into even smaller particles that are stopped by the second surface. A volume of the first surface and the micrometeroids are partially vaporized, and the "shotgun blast" is sprayed against the second protecting surface. The density of the shielding materials, the field of view to space and the sensitivity of an item to damage are the primary parameters that determine the required thicknesses. MLI thermal blankets, usually already required for temperature control, are spaced off with thin wall Mylar or fiberglass spacers and fastened by Kapton tape. Most of the spacecraft is provided adequate micrometeroid protection by the thermal blanketing alone.

The sensitivity of Cassini's main engines was uncovered late in the program. The engine combustion chamber is thick walled and is protected by its limited exposure to space and the density of its construction. However, the engine nozzles are thin walled columbium with a crucial 0.08 mm (0.003 inch) thick disilicide coating. This coating protects the base columbium material from oxidation. It is this coating that is sensitive to micrometeroid damage, since a single small damaged area in a strategic location along the nozzle can result in a "burn through" when the engine is fired. The micrometeroid protection of these nozzles was complicated by the fact that cooling is provided by the field of view to space Simply covering the nozzle exterior with a thermal blanket wouldn't be acceptable. A deployable shield was required that could protect the entire nozzle yet provide a full view of space for cooling and plume exhaust.

Primary Design Requirements

One of the most fundamental design requirements of the micrometeroid protection mechanism for Cassini's main engines was that the retrofit could not adversely impact the integration of the Radioisotope Thermoelectric Generators (RTGs) and the Linear Separation Assembly's electric Detonators. These items are the last components to be integrated to the spacecraft, and they are installed on the otherwise completely assembled stack on the launch pad. Furthermore, integration of the three RTGs is an extremely sensitive activity that must operate like clockwork, since each technician performing the installation can only be exposed for a few minutes to close proximity of

these radioactive components. No holdups, interferences, or delays could be tolerated.

The Cover Assembly must be deployable (Cover closed to protect the MEA) after separation from the launch vehicle, with a life requirement of 25 cycles to restow (Cover open) for engine firings during the cruise to Saturn. Just prior to Saturn orbit insertion, the MEA Cover will be re-stowed (opened) permanently. Due to the mission criticality of this device blocking the main engines, it was deemed that the Cover Mechanism should be fail-safed to an open position. This was implemented by designing the Cover to be ejectable in the event of a failure of the motor drive, bearings or gears.

The Cover had to provide 100% area protection of the Main Engine Assembly with multiple layer insulation (MLI) spaced a minimum of 20 cm (8 inch) away from the engine nozzles. The Cover must also restow (open) sufficiently to provide an adequate field of view of the engine nozzles to space for thermal cooling. In addition, it was highly desirable to be able to verify the Cover Mechanism Assembly at the spacecraft system level solar thermal vacuum test. Thus, a design goal was to provide an operational capability under Earth gravity without external assistance.

Design Implementation

The overall design concept was to provide a collapsible half sphere that pivots at the equator to accomplish the deployable protection. For simplicity, the Cover Assembly would be driven from one end pivot only, with an idler pivot on the other end that would be driven by the Cover structure. Therefore, the Cover Assembly would consist of two half circle *Bows* pivoting at one end on a *Drive Mechanism* and at the other end on an *Idler Mechanism,* with a MLI envelope that folds between the Bows. By configuring the Cover to mount outside of the Launch Vehicle Adapter (LVA), only JPL designed hardware would have to be modified, no volume restrictions existed except for the RTG and Detonator integration issues, and the resulting deployment would then consist of a simple rotation about a single pivot axis. After separation of the spacecraft from the launch vehicle, the Cover would then be deployed over the MEA. The size of the Cover was determined by the volume needed for the Drive Mechanism to clear the LVA. Selection of JPL's largest predesigned redundant actuator for the Drive Mechanism resulted in a Cover that was over 2.1 meters (7 feet) in diameter.

The addition of the Cover changed the spacecraft thermal design, which must now meet the allowable flight temperature ranges *with or without* the Cover deployed. Deploying (closing) the Cover over the bottom of the spacecraft, in addition to enclosing the main engines, also blocks the Propulsion Module's view to space. Therefore, a Thermal Skirt was required to provide a space-facing radiator for the Propulsion Module as well as to close out the open annulus of the Cover for micrometeroid protection. The Cover Assembly must also be supported through the launch dynamics environment. This was accomplished by the addition of two Launch Restraint Assemblies (LRAs) to support the Cover Bows and protect the Cover MLI envelope from damage. The LRA spring capsules each provide a 935 Newton (210 lb) preload through the Cover from the LVA, through each Bow, across the separation

plane to the spacecraft structure. The required stroke of 0.5 cm (0.2 inch) is to compensate for the potential deflection of the spacecraft during launch vibration and keeps the LRA ball-and-socket interfaces together. When spacecraft/launch vehicle separation occurs, the LRA interfaces are self-releasing as the two bodies part. Small kickoff springs within each joint insure proper release (Figure 5). Each LRA is spring loaded to rotate away from the Cover Bows, enabling an unencumbered deployment.

Cover Design

The Cover structure consists of a leading *Drive Bow* made from 3.2 cm (1.25 inch) aluminum tubing and a *Fixed Bow* made from 2.5 cm (1.00 inch) tubing of the same material, each formed into a half circle. These Bows pivot at their ends at a *Hub*. The two Cover Bows together result in the full equator of a sphere. Intermediate *Full Stays*, sliding within a groove in each hollow Hub, then assemble to make up the Cover frame. The Hub design consists of the intermediate Cover stiffeners (the Stays) sliding in a slot of the hollow Hub, being retained by the "lollipop" head of the end fitting. The Stay fittings allow efficient compaction because they can translate axially (due to the flexibility of the Cover envelope) within the Hub interior volume to stack flatly when stowed (Figure 6). Each Stay is made from 3.2 mm (0.13 inch) thick graphite-epoxy sheet cut into the shape of an arc. The "lollipop" shaped end fittings, machined out of 15-5 stainless steel, are bonded on the ends of the Stays. Graphite-epoxy was used for the Stays rather than a metallic rod to insure that if hit by a micrometeroid, metal particles could not spray out like shrapnel. The flat shape of the Full Stay end fittings allow the Cover frame to collapse to a relatively compact stowed position. The MLI deployable half sphere micrometeroid shield is attached to the Bows, and eight Full Stays slide into pockets sewn within the envelope. Seven *Partial Stays* (that do not extend all the way to the Hubs) are sewn into pockets within the envelope between each set of Full Stays to further support the shape of the half sphere.

The Cover envelope is fabricated from two layers of 0.20 mm (0.008 inch) thick Beta cloth (Teflon-impregnated glass cloth) sandwiched between two layers of 0.03 mm (0.001 inch) carbon-filled Kapton. The spherical shape is a result of cutting the envelope pattern out of gore-shaped pieces and sewing them together. (Imagine peeling a globe). In this way, the Cover becomes a half sphere accordion, collapsing into a relatively flat package. Applying torque to the Drive Bow allows it to pull the Cover envelope to the spherical shape, or push it back to the stowed position. Because Cassini must have an isopotential exterior surface to meet its science requirements, the Cover must be grounded to the spacecraft structure. The carbon-filled Kapton outer surface is sufficiently conductive, but it must be provided a electrically conductive path to the spacecraft to bleed off any potential that develops. This is accomplished through the Bows and the Full Stays, and the materials and finishes within the Hubs were selected to meet this requirement. The Stay fittings were left as bare polished stainless steel sliding within titanium Hubs coated with Nedox SF-2 (product of General Magnaplate, Ventura CA). This Nedox is a hard nickel coating filled with Teflon, and was selected because it is one of the few dry lube coatings that is electrically conductive.

Cover Development

Although JPL has developed a number of deployable sunshades and similar structures, consisting mainly of stiffened multilayer insulation blankets, this was the first time that a complete half sphere had to be deployed. It was felt that key to the success of the development was insuring proper articulation of the frame, particularly in the area of the Hub. Design of the Cover envelope was originally assumed to be the major challenge, but the person responsible for design and fabrication of Cassini's thermal blankets was unperturbed. Essentially "eyeballing" the shape of the individual gore segments, he fabricated a half scale mockup within days of receiving an articulatable frame to build upon. This half scale mockup was built as a proof-of-concept for the Hub design and the Cover envelope fabrication techniques. The compacting material between the Stays is prevented from interfering with the stowage by removing a 20 cm (8 inch) radius of Cover envelope about each pivot point. Small semicircular fixed shields close out these openings in the Cover.

After the original half scale mockup proved the task attainable, a full size prototype was fabricated with the expectation that new surprises would reveal themselves. Eventually, two engineering model units had to be made in addition to the prototype. The progression from using the MLI materials available from stock to current flight-approved materials caused a number of problems. The first and primary problem became evident with the initial engineering model. The flight materials were significantly stiffer than the materials used for the full size prototype. The inner and outer layer of Kapton was stiff and brittle, buckling into large lumpy wrinkles when stowing. As the Cover folds (like an accordion) while stowing, the radius of the inner edge of each fold gets smaller, but the material is cut to the larger radius of the deployed sphere. Therefore, the material must buckle along the direction of the folded edge. The material of the earlier prototype was more forgiving, resulting in distributed small wrinkles and a maximum stowed height of about 15 cm (6 inch). The new Beta cloth was similarly much stiffer, such that the stowed height due to the buckling increased to between 28 to 38 cm (11 to 15 inches). It was attempted to produce shaped cuts in the internal Beta cloth, and different methods of suspending the Stays to the envelope were tried. One of the causes of the problem was that the original Kapton materials were manufactured with a rip-stop scrim that didn't stiffen the material excessively, whereas the new materials were manufactured with a different scrim. While old material stocks were pursued for the task, eventually all new materials were used. The completed flight unit substituted carbon-filled Kapton for the original aluminized Kapton. Although the carbon-filled Kapton was twice the thickness of the aluminized material, it was more flexible due to the use of different scrim and didn't exhibit some cracking seen in test. While the final design never did perform as well as the prototype, its stowage improved to a maximum height of about 25 cm (10 inches). The Launch Restraint Assemblies (LRAs) had to be re-manufactured to accommodate the larger stow envelope.

Drive Mechanism Design

Ejection of the Cover was made possible by coupling the drive elements to the Hub with a single spur gear set, configured in such a way that the Cover could "drop away" from the mesh (Figures 3 & 7). The drive gear is simply supported between the bearings internal to the motor actuator and a needle bearing in the Drive Mechanism

housing. The driven gear is cantilevered from the Hub to complete the gear mesh. To minimize the size of the assembly, the gears are designed with high strength (and high toughness) Maraging steel C300. The gear blanks were machined, heat treated to 200 MPa (290 KSI) and then fabricated to final form by wire electrostatic discharge machining [2]. The drive actuator used is a size 20 JPL Dual Drive Actuator (DDA). This is a fully block redundant actuator, combining two paths of 20:1 dual stage spur gears into coaxially mounted 605:1 pancake Harmonic output gears with a common drive output (Figure 9). Two independent, electronically commutated DC brushless motors provide the drive torque [3]. This Dual Drive Actuator is the one of the same units that were built for the Shuttle Imaging Radar foldable antenna. The SIR-C antenna design was changed mid-project and these actuators were not needed. Ten years later, the existence of fully machined and kitted components for Cassini's usage really helped in getting the MEA Cover development performed in time. The bearings and gears are lubricated with Bray 600 or 601, appropriate to the corrosion resistance of the materials. JPL has always used the "off-the-shelf" nodular cast iron Harmonic gears with 52100 bearings for its DDAs rather than the custom stainless steel units used elsewhere in the industry. No ill effects have resulted in this practice, and delivery schedule problems are alleviated. The drive/driven gears were only grease-plated with Bray 600.

The rotation of the Cover is limited by adjustable stops within the Drive Mechanism. To reduce the loads on the actuator bearings, a balanced stop design is used. A lever is allowed to pivot about the actuator bearing centerline and contacts equidistant stops for the stow and deploy positions. This lever also contacts the microswitch actuating levers to provide stow and deploy telemetry indications (Figure 10). One subtle detail that was required to be incorporated in the design was to accommodate the deflection of the Drive Bow during the launch dynamics. The actuator is non-backdrivable, so to prevent the output gears from being overtorqued due to the applied loads from the Drive Bow, sufficient backlash had to be incorporated in the load path from the Bow to the actuator. The drive/driven gear mesh provided approximately half of the total required 3.3 degrees of backlash, while the spline connection from the driven gear to the Hub was fabricated to provide the other half. Only a small amount of backlash was available within the Harmonic gear mesh. The required amount of backlash was maintained at the lowest practical level by the use of a larger diameter tubing for the Drive Bow. For launch, the Cover's position must be rotated to the center of the backlash region, 1.7 degrees towards the deploy direction from the stow hardstop.

Idler Mechanism Design

The Idler Mechanism consists of a simple pivot using the same high load bearing configuration of the Drive Mechanism primarily to simplify the design and procurement needs (Figure 4). Similarly, the same mounting interface as the Drive Mechanism was used. Lightweight Delrin gears transfer the rotary motion of the Cover Bow to a potentiometer. The pot was a flight spare 5000 ohm Cermet unit (manufactured by Beckman Industrial) left over from the Mars Pathfinder project. To replicate the resistance range of a temperature transducer circuit, a series/parallel set of resistors was packaged in a box next to the pot.

Ejection Mechanism Design

Each Cover Hub is fastened to the mechanism's structure with a 6.3 mm (0.25 inch) bolt passing through the throat of a Bolt Cutter (manufactured by Special Devices, Incorporated, Newhall Ca). The Hub interface retains the shear loads by the use of 30 degree male/female wedges, and is hardcoated with Nedox dry lubrication to insure release while maintaining electrical conductivity for Cover grounding purposes. A pair of linear spring capsules in both the Drive and Idler Mechanism provide kickoff energy to the Hubs (Figures 7 & 8). An "ejected state" microswitch is also installed at both Mechanisms to provide telemetry. Extensive modeling using ADAMS kinematics analysis was performed to insure that the ejected Cover could not recontact the spacecraft. The Cover was modeled as 9 rigid bodies connected by revolute joints with stiffness and friction forces incorporated. The initial center of gravity of the deployed Cover resides directly in line with the Hubs, while a large offset exists in the stowed condition. While there would be no reason to eject a Cover failed in the stowed position, the partially stowed position equivalent to a 30° wedge was determined to be the maximum limit of a "safely stowed" position. Any further deployment (closing) of the Cover would adversely affect the thermal environment of the engines when ignited. By analysis it was determined that additional linear spring capsules located at the Launch Restraint Assemblies, each providing 40 Newtons (9 lb) of force, could push off the Fixed Bow and solve the problem. The ADAMS analyses confirmed that the Cover would tumble off the spacecraft as before, but the additional LRA pushoff springs decreased the tumble rate while increasing the translation rate, thereby allowing the Cover to clear the main engine nozzles with adequate safe clearance.

Testing And Integration

The verification of the design for acceptable flight performance began with the prototype Cover Assembly, in which flex cycle testing was performed in the ambient environment to see if any unexpected wear occurred in the envelope materials and the Stays sliding within the Hubs (Figure 12). The engineering model (EM) Cover and Mechanisms were then fabricated, and a test fixture was produced that allowed the Assembly to be tested with the pivot axis horizontal or vertical. In this way the operating performance could be characterized for both the spacecraft system test orientation as well as in a partial gravity-compensated configuration. The integrated Assembly was placed with the pivot axis in a vertical orientation in JPL's 10 Foot Space Simulator (over 3 meter diameter test chamber) for thermal vacuum qualification. The Mechanisms were controlled with separate heat exchangers to maintain their test temperatures between -50°C to +65°C, while the chamber shroud controlled the temperature of the Cover to -115°C. The Assembly was calibrated for torque versus deployment angle, and a 100 cycle life test was performed (4 times the life requirement). Full stowage to the launch position was not achievable although the Cover was positioned within the "safely stowed" angle. At this juncture it was decided that the drive actuator should be redesigned to provide more output torque.

The EM actuator for the MEA Cover Mechanism was originally assembled with a 363:1 Harmonic gear ratio, which was predicted to provide an output torque of 76 N•m (670 in•lb). The actuator was fully temperature/atmosphere dyno tested, which

consists of generating clockwise and counterclockwise speed/torque/current plots for each motor and both motors operating conditions. The EM unit's output torque was not only lower than the prediction, but the performance was severely degraded under cold operating conditions. While predicting the performance of Harmonic gear systems can be an inexact science, this shortfall in output torque was unprecedented at JPL (See "Problems and Lessons Learned" below). A flight unit with 605:1 Harmonic gears was assembled, flight acceptance temperature/atmosphere dyno tested and retrofitted to the Drive Mechanism. The flight Mechanisms and EM Cover were integrated on the lower portion of the spacecraft structure with all the new modifications and was subjected to flight acceptance dynamics testing (Figure 11). Afterward, the hardware was delivered to Assembly, Test and Launch Operations (ATLO) for flight spacecraft integration in preparation for the system testing. New materials for the flight Cover had still not been delivered.

The flight Cover was eventually completed The final mass of the deployable Cover as delivered was 18.3 kg, which included the LRA spring capsules. Assembly level thermal vacuum characterization testing was performed in the 10 Foot Space Simulator, including a 25 cycle life test. The test actuator, retrofitted with the 605:1 ratio, was used to operate the flight Cover and for the torque versus angle characterization (Figure 16). The flight Cover was inspected, and delivered to ATLO in time for system dynamics and solar thermal vacuum testing. In all, the mass increase to Cassini for the retrofit of the MEA Cover Mechanism Assembly, support structure and associated thermal structure totaled over 41 kg.

Problems And Lesson Learned

Two significant problems occurred during the development of the Cover Mechanisms, both involving the Dual Drive Actuators. The first episode appeared when the DDA's Harmonic gears were received and the actuator was dyno tested. The output torque was far below predictions. Although the torque requirement was expected to be less than 12 N•m (100 in•lb), the "desirement" for the capability to operate in the system level testing drove the design for the production of the most torque possible. The 363:1 output ratio was predicted to produce approximately 76 N•m (670 in•lb) at room temperature. Its actual output peaked at 65 N•m (575 in•lb) but dropped off substantially at cold temperatures. The unit would stall as low as 28 N•m (250 in•lb) at -50°C. These torques were insufficient to fully stow the engineering model Cover during the thermal vacuum qualification tests. At cold temperatures the torque requirement to stow the Cover, made from the stiffer flight materials, to an acceptable position turned out to be almost 34 N•m (300 in•lb) (Figure 15). While grasping for an explanation it was concluded that the higher ratio 605:1 gears from the SIR-C program must be installed to obtain more torque.

A torque limiting clutch was originally mounted to the actuator in the SIR-C program to insure that the output torque would not exceed the maximum torque rating of the gears, and to protect the actuator during ground testing of that very large deployable. The original qualification unit from SIR-C was tested to motor stall with the torque limiting clutch removed to ascertain whether the Harmonic gears would ratchet. The maximum torque developed was 79 N•m (700 in•lb), safely below the ratchet limit of 96

N•m (850 in•lb). Another actuator was assembled for Cassini using the 605:1 gears, and flight acceptance dyno testing commenced. Again, the output torque was lower than expected! Something unexplained was occurring.

While not ever fully explained, one primary cause of the anomaly was attributed to the Bray grease. The formulation of Bray grease was changed since the SIR-C actuators were originally tested in 1987. Although it is still identical chemically to the original, the grease is now formulated without the use of ozone depleting chemicals. In the past the base oil and Teflon particles were mixed in Freon, and the volatiles were evaporated off, until the usual buttery consistency resulted. Now the base oil and Teflon are mixed without any liquifier or solvent. A number of times in the last couple of years assembly technicians have noticed that some tubes of the Bray grease have exhibited lumps. The original SIR-C qualification unit was then fully dyno tested, cleaned and relubricated with the new grease, and re-dyno tested. Figure 13 shows a significant degradation of performance of the size 20 DDA with 605:1 Harmonic gears at -50°C, apparently due only to the new grease formulation. Finally, with side-by-side testing of an actuator showing differences in performance, the grease came under more focused scrutiny.

Samples of the old Bray 601 EP were compared to the new Bray 601 EF under a scanning electron microscope. While the old grease displayed consistent-sized spherical particles ranging from 3 to 5 microns, the new grease showed inconsistent, jagged edged particles ranging as large as 30 microns diameter. Although testing at other NASA facilities have indicated no performance differences between the old and newly formulated Bray grease, including cold temperature operation, JPL's experience with this one A-to-B comparison showed otherwise. However, while no other explanation was found, testing was limited and schedule restrictions dictated that the investigation be halted. The manufacturer of Bray grease (Castrol of North America) was contacted and the problem explained. It is believed that Castrol has initiated better mixing procedures for a more consistent product. Interestingly, the biggest mystery involved the cold temperature performance of the first actuator built for Cassini, using the 363:1 Harmonic gears. While the actuator with the 605:1 gears demonstrated a speed reduction from room temperature to -50°C ranging from 19% (old grease) to 30% (new grease), the 363:1 gears exhibited a whopping 71% reduction in no-load speed. Figure 14 shows how this speed difference at cold temperatures was remarkably high compared to the 605:1 unit. Also compared are the speed differences due only to the change to the new grease formulation. No further explanations were pursued due to the workload in completing the MEA Cover Mechanism.

A second problem that emerged after delivery of the MEA Cover Mechanism to Cassini involved the electronic packaging of the DC brushless motors. A motor in another assembly failed to operate properly after dynamics testing. Disassembly revealed that one of the drive transistors had broken free from the circuit board and the lead wires disconnected. Further inspection revealed that 4 of the 6 transistors were debonded. The vibration levels were very nearly the same as the levels these flight spare motors were originally qualified to in 1982. The conclusion of the investigation was that the conformal encapsulant used to bond the TO5 cans to the circuit board had aged, and

did not have adequate bonding strength. After closely scrutinizing the electronics packaging, it was observed that workmanship standards have improved vastly in the last 14 years. It was decided to remanufacture the entire electronics packaging for all of Cassini's DDA motors. The MEA Cover DDA was removed from the spacecraft after system test and the motors replaced. Each motor had been reworked and re-dyno tested over its qualification temperature range. After retrofit to the DDA, actuator dyno and vibration testing was repeated prior to reassembly into the Drive Mechanism and redelivery to Cassini.

Another late change related to the Cover ejection occurred. The original ejection kinematics analysis did not provide any energy to the separation from the Bolt Cutters. During the lot acceptance testing of the Bolt Cutter, fixturing was included that allowed a 7 kg mass to be swung as a pendulum and the velocity was recorded. Upon cutting of the bolt, this mass was propelled over 5 cm (2 inch) in 110 milliseconds! Incorporation of this imparted energy in the ADAMS analysis determined that the Cover would contact the engine nozzles under some ejection conditions. Fortunately, merely deleting the four Hub kickoff spring capsules accomplished safe ejection under all conditions.

In terms of the design and development of collapsible MLI envelopes, it appears that there is no magic involved. However, one should plan on the fabrication of a number of prototypes because so many parameters are derived empirically. Compensation for seam thickness in the blanket pattern varies not only with the thickness of the material but also in the stiffness of the material, which affects the way it is sewed. One can also vary the number of rigid supports to find the optimum number and spacing. One feature that was incorporated between the fabrication of the last engineering model and the flight unit was that the radius of the Stays were made 13 mm (.5 inch) or so smaller than the radius dictated by the Bows. The Cover folded more effectively because the Stays would stack within the radius of the Bows, resulting in a smaller overall stow thickness.

References

1) Divine, N., E. Grun, and P. Staubach; "Modeling the Meteoroid Distributions in Interplanetary Space and Near Earth"; *Proceedings, First European Conference on Space Debris*; Darmstadt, Germany; April 1993.
2) Gillis-Smith, Greg: "Mars Pathfinder Lander Deployment Mechanisms"; *Proceedings, 30th Aerospace Mechanisms Symposium*; May 15 -17, 1996; NASA CP-3328
3) Packard, Douglas T.; "Dual Drive Actuators"; *Proceedings, 16th Aerospace Mechanisms Symposium*; May 13-14, 1982; NASA CP-2221.

Acknowledgments *

This work was performed at the California Institute of Technology's Jet Propulsion Laboratory, under contract with the National Aeronautics and Space Administration. Reference herein to any specific commercial product, process or service by trade name, trademark, manufacturer, or otherwise does not constitute or imply its endorsement by the United States Government or the Jet Propulsion Laboratory.

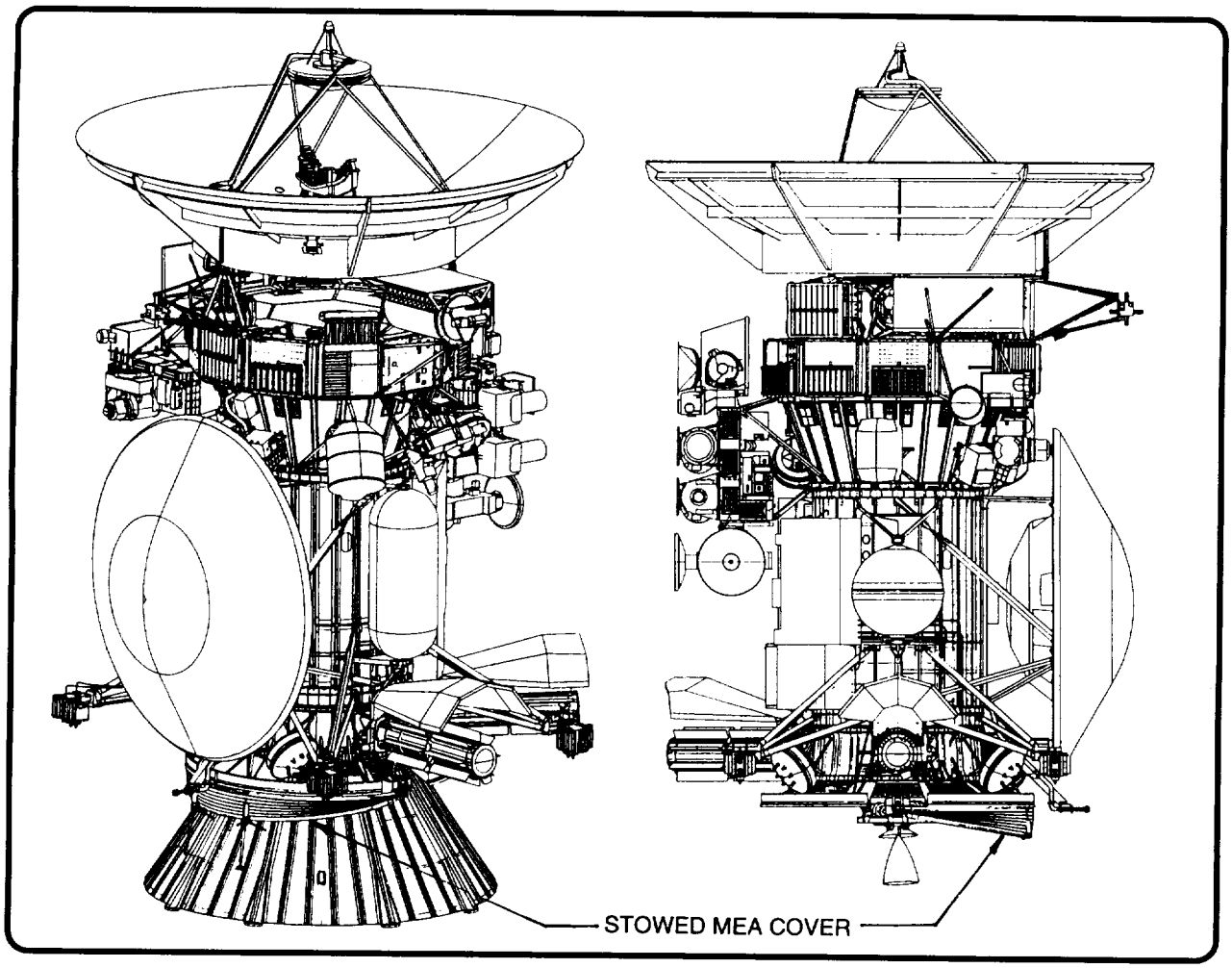

FIGURE 1 - CASSINI, BEFORE AND AFTER SEPARATION FROM LAUNCH VEHICLE ADAPTER

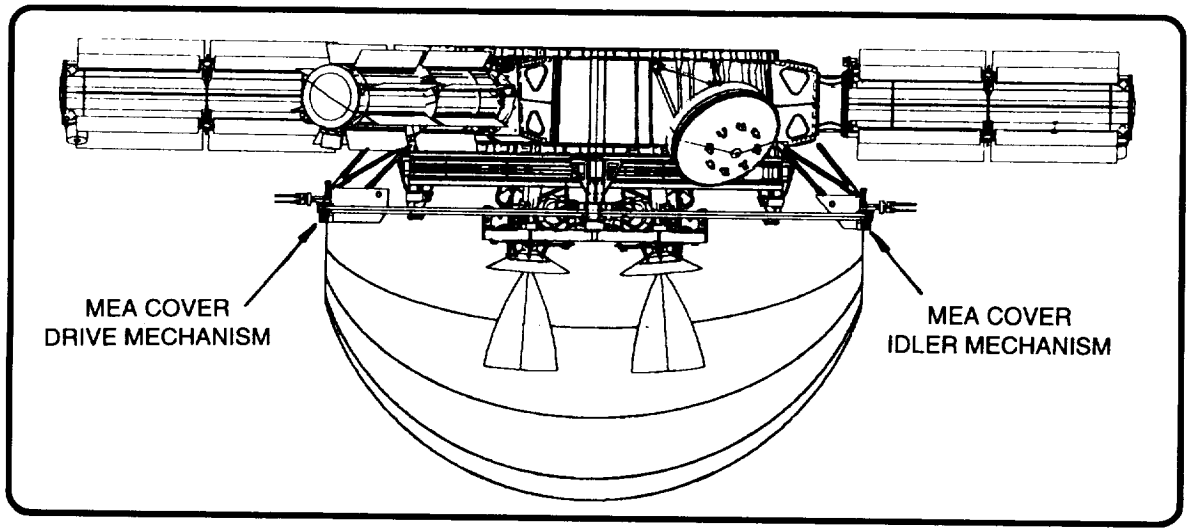

FIGURE 2 - VIEW OF CASSINI'S REDUNDANT MAIN ENGINES

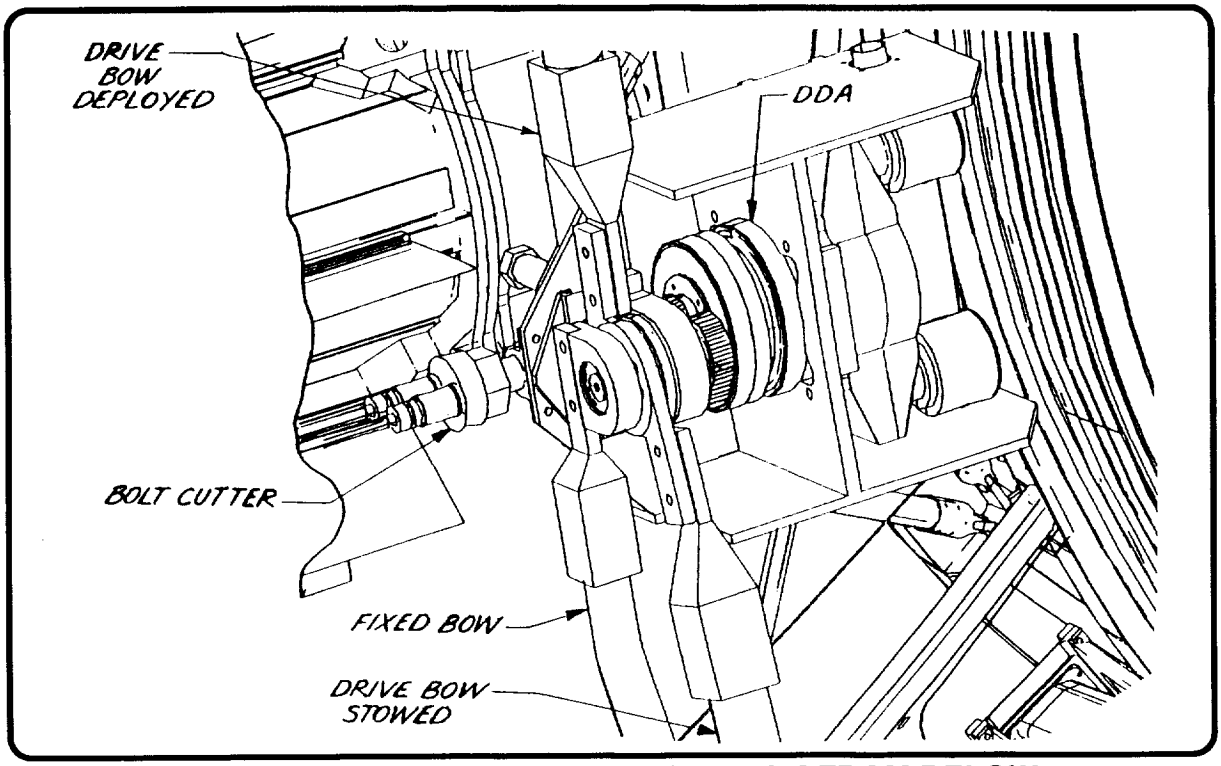

FIGURE 3 - VIEW OF DRIVE MECHANISM FROM BELOW
(SOME COVERS REMOVED)

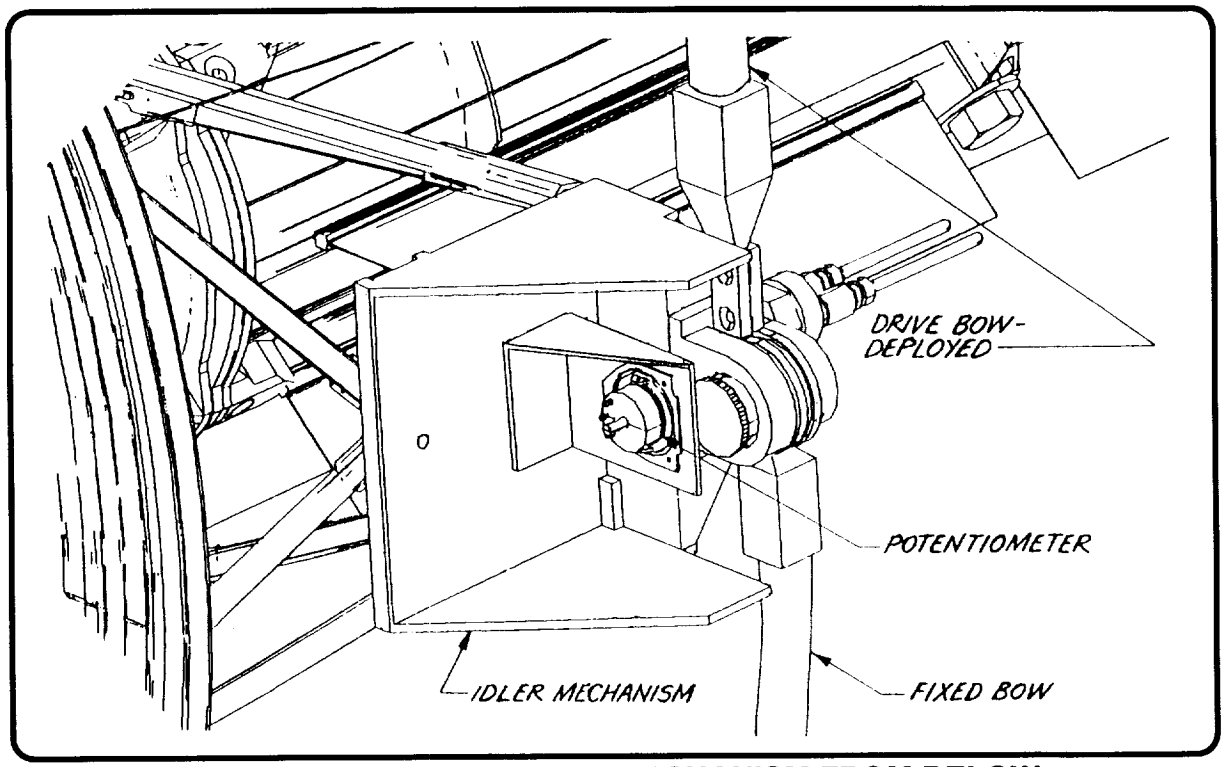

FIGURE 4 - VIEW OF IDLER MECHANISM FROM BELOW
(SOME COVERS REMOVED)

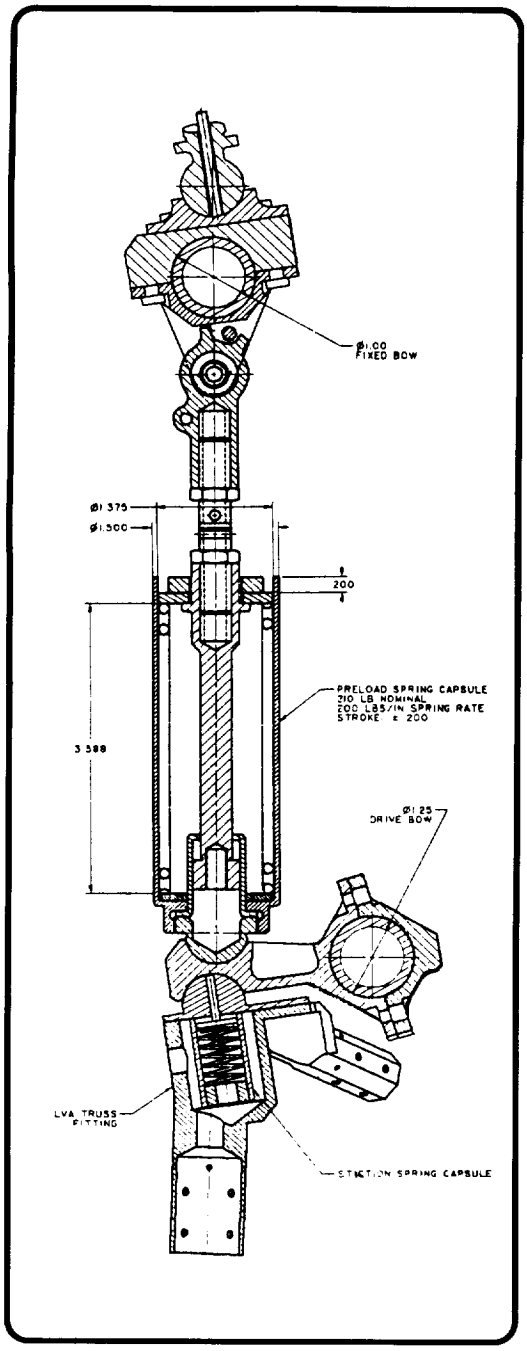

FIGURE 5 - DETAIL OF LAUNCH RESTRAINT ASSY

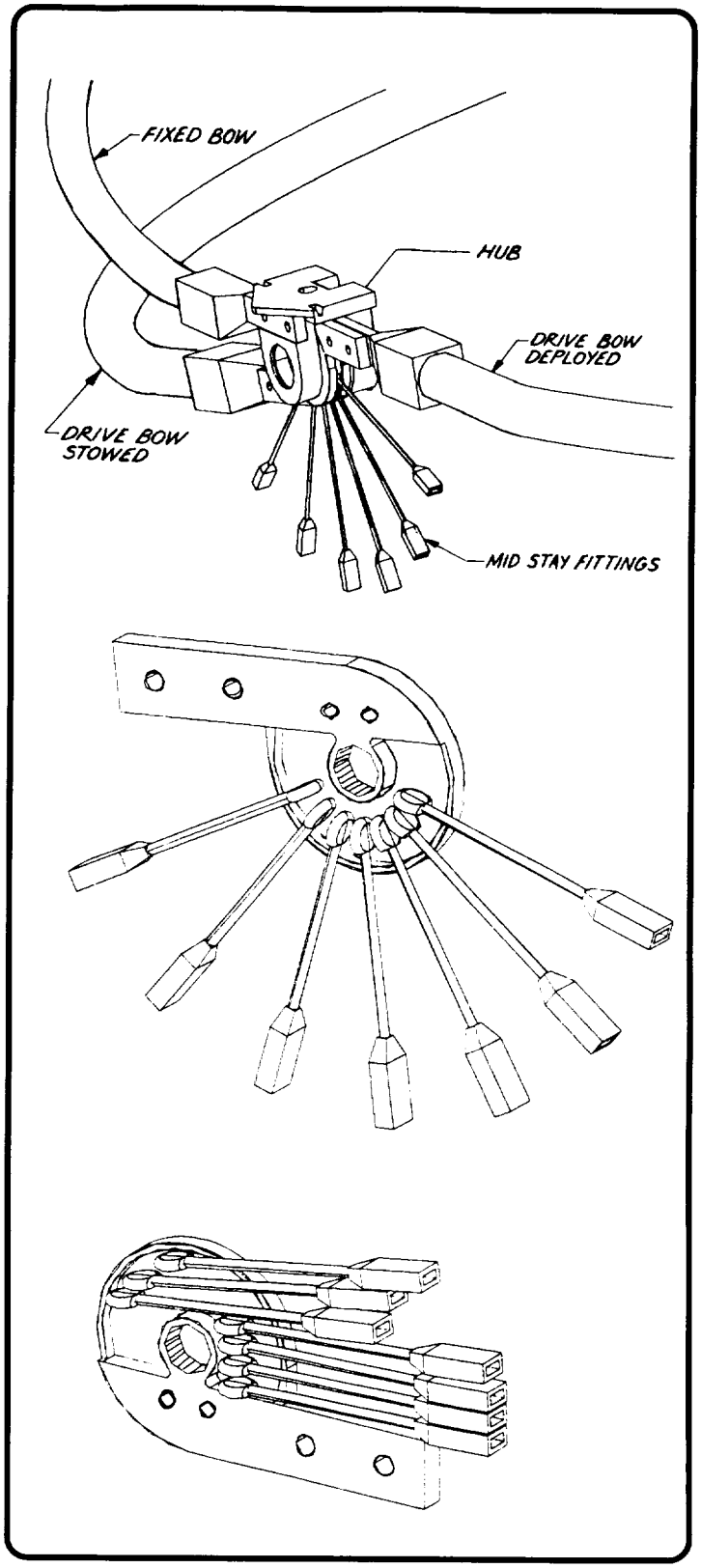

FIGURE 6 - DETAILS OF COVER HUB

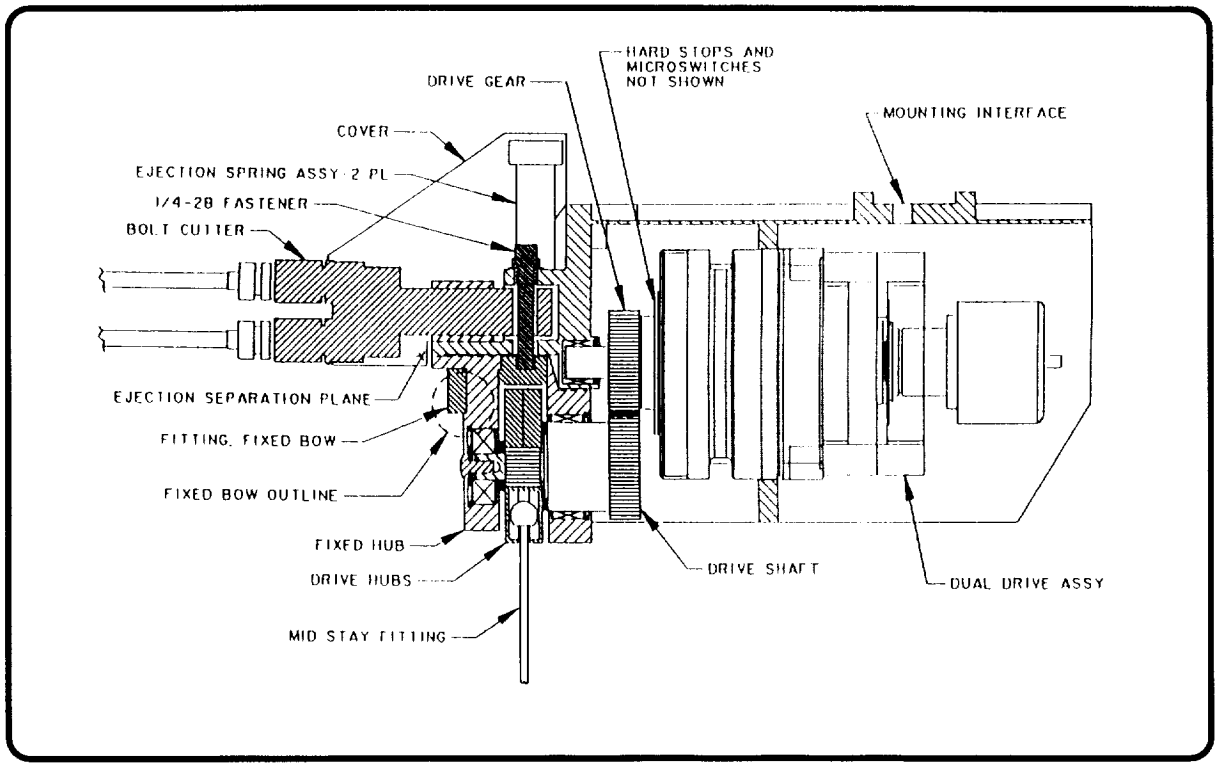

FIGURE 7 - CROSSECTION VIEW OF DRIVE MECHANISM

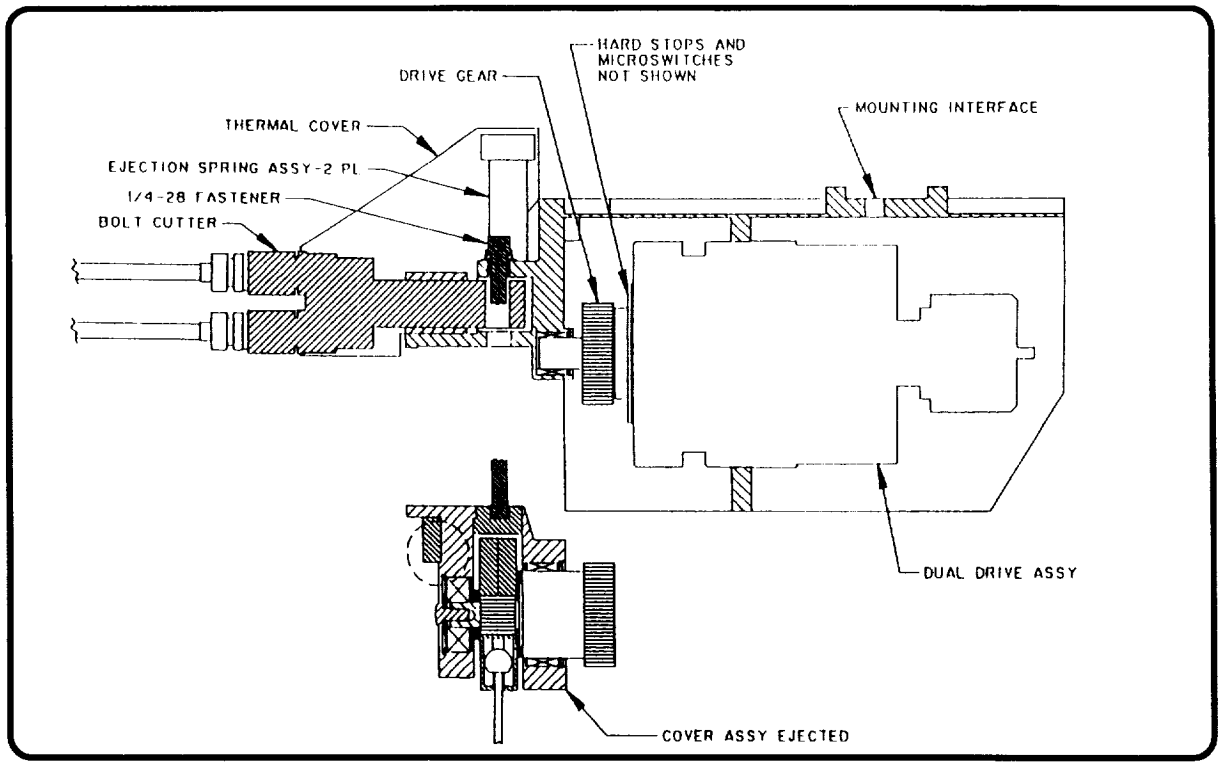

FIGURE 8 - CROSSECTION VIEW SHOWING COVER EJECTION

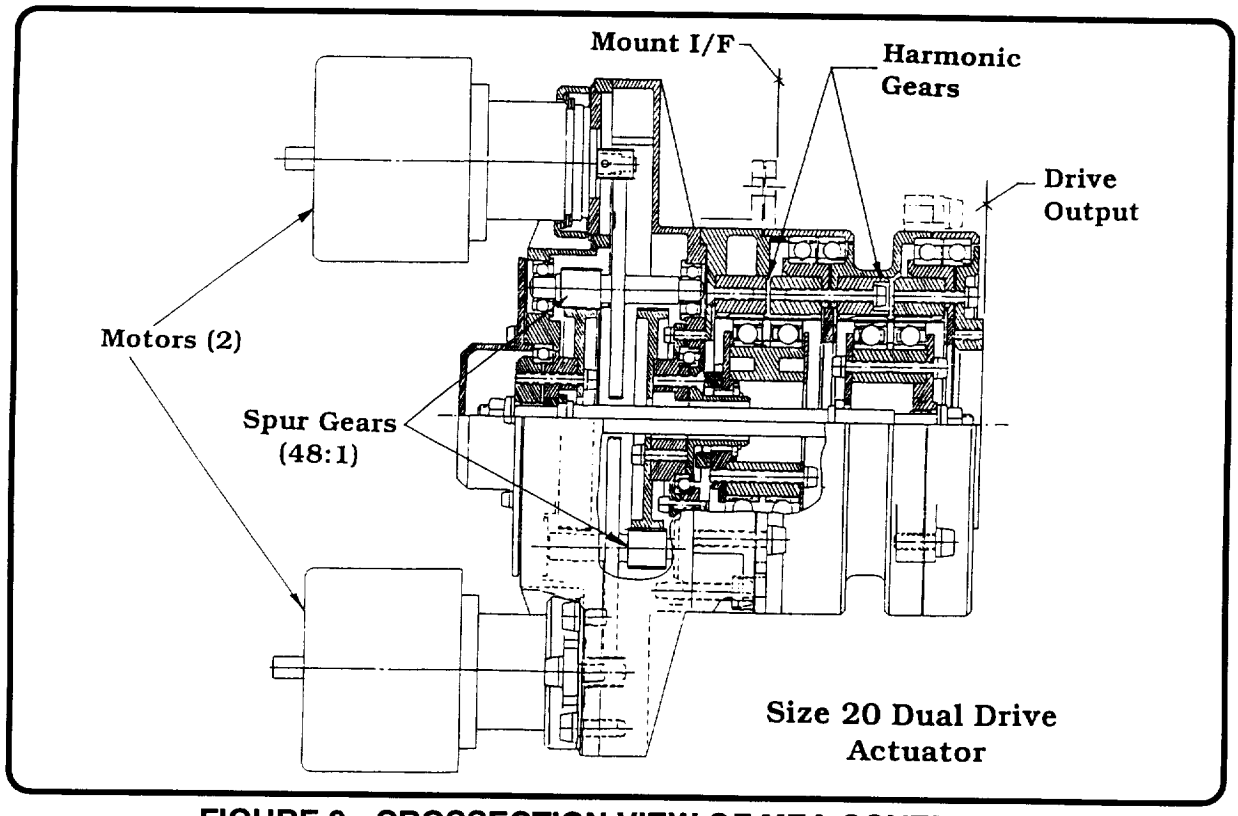

FIGURE 9 - CROSSECTION VIEW OF MEA COVER DDA

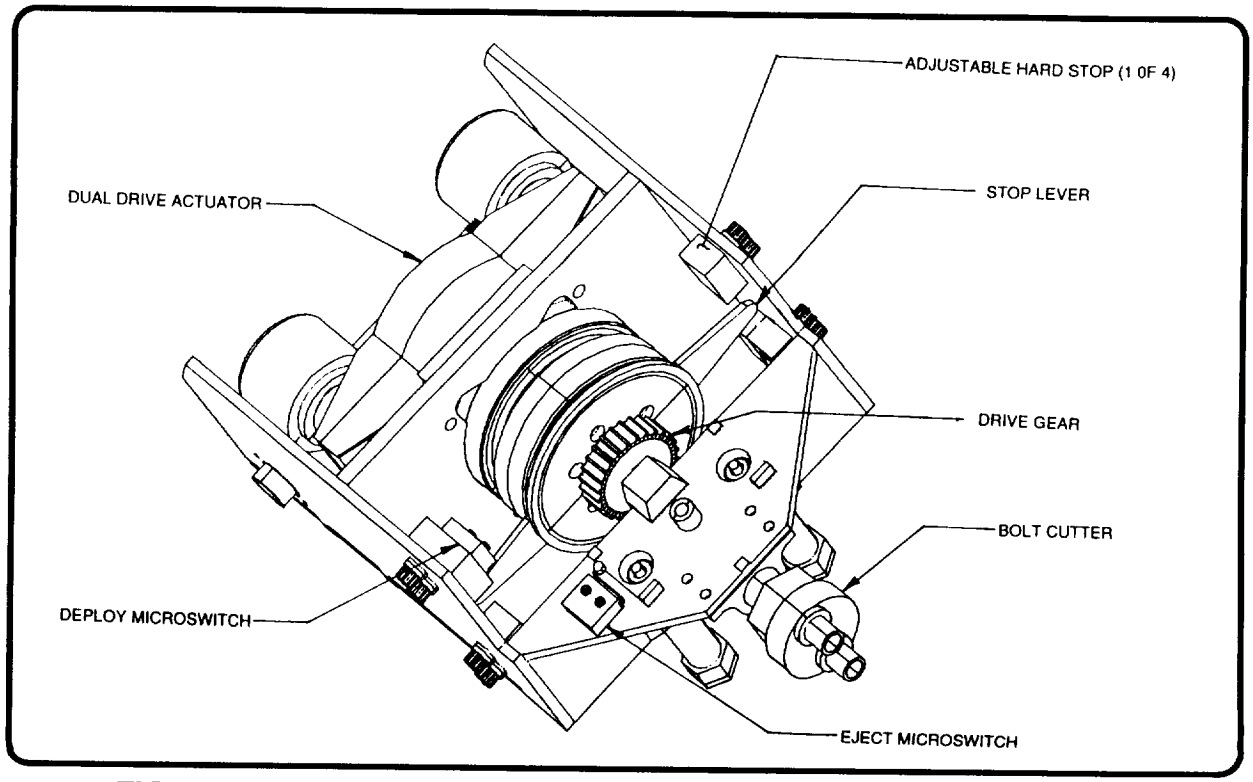

FIGURE 10 - VIEW OF DRIVE MECHANISM SHOWING STOP LEVER

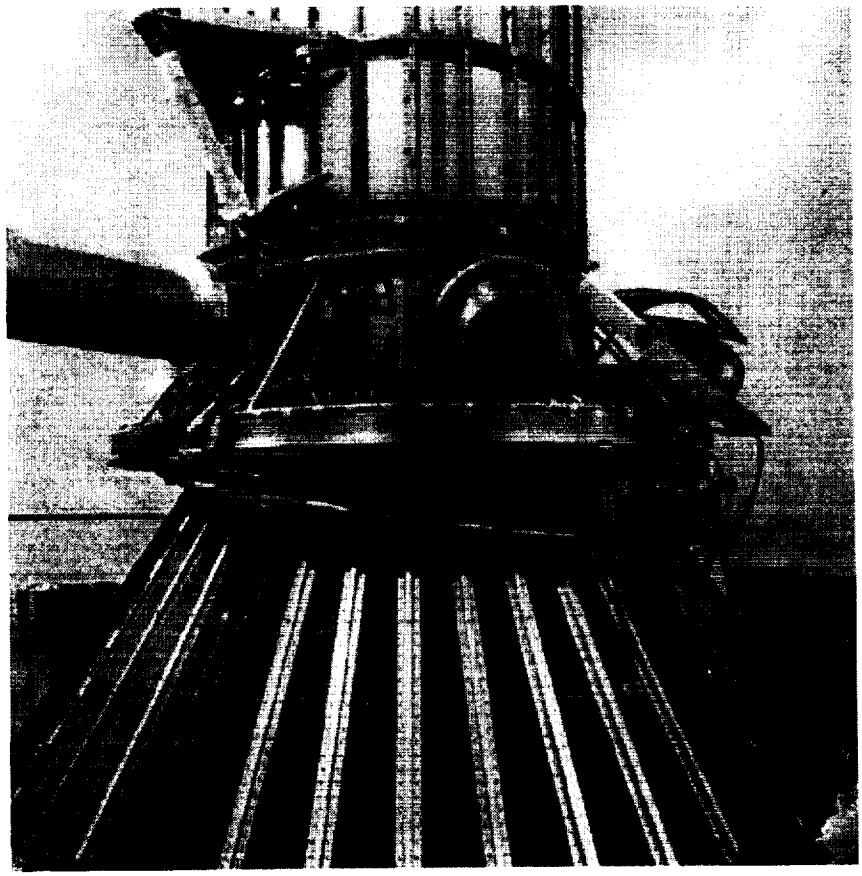

FIGURE 11 - EM COVER ASSEMBLY, DYNAMICS TEST CONFIGURATION

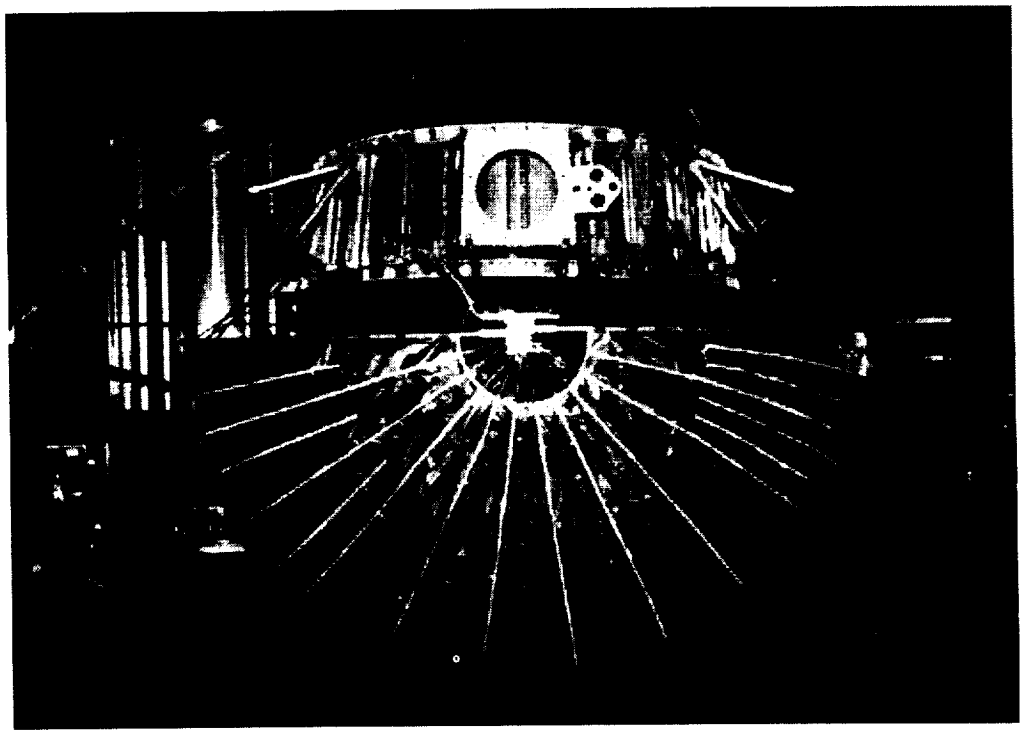

FIGURE 12 - PROTOTYPE COVER ASSEMBLY TESTING

FIGURE 13 - BRAY GREASE COMPARISON TEST
(605:1, 23° C to -50° C)

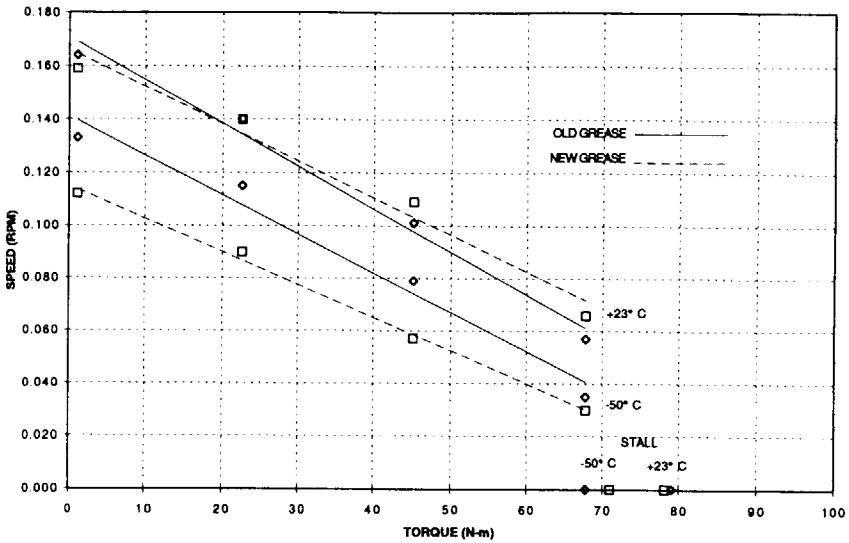

FIGURE 14 - SPEED REDUCTION DUE TO TEMPERATURE DROP
(23° C to -50° C)

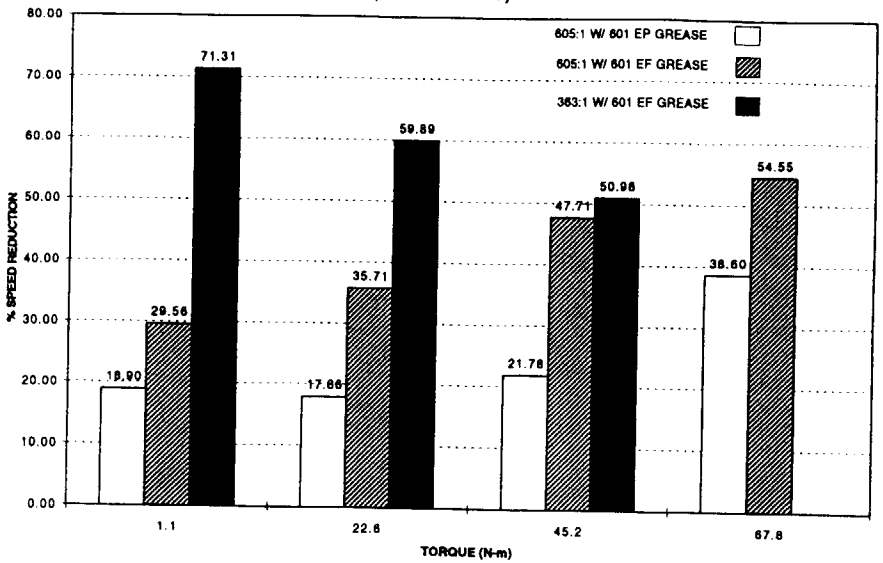

FIGURE 15 - ENGINEERING MODEL MEA COVER
TORQUE TO STOW VS. ANGLE

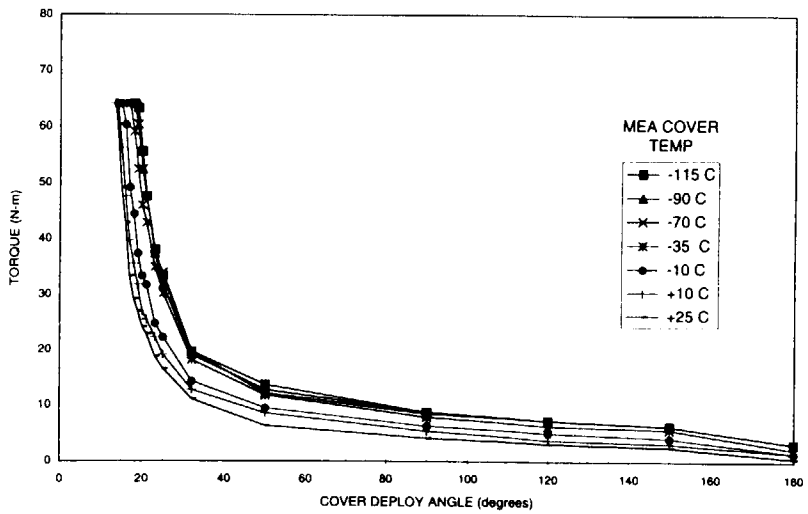

FIGURE 16 - FLIGHT MODEL MEA COVER
TORQUE TO STOW VS. ANGLE

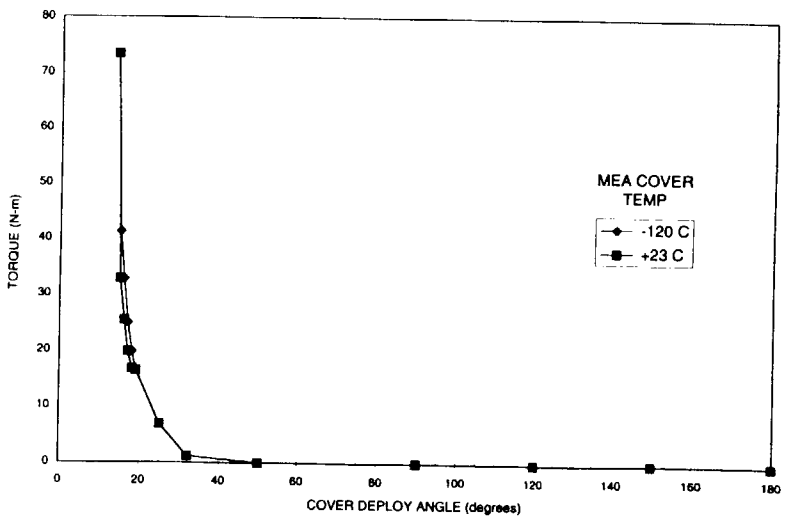

Hexapod Pointing System for Space Applications

Luis Genovese*, Walter Gallieni*, Piero Galeone** and José Gavira**

Abstract

This paper presents the mechanical design of the Hexapod Pointing System (HPS) designed to support the NASA Stratospheric Aerosol and Gas Experiment (SAGE) III mission on the International Space Station (ISS) truss. The HPS is designed to compensate ISS attitude deviations in order to provide Nadir pointing to SAGE III. The key item of the mechanical assembly is represented by the electromechanical high accuracy linear actuator (LA). The development and testing of the LA's from the ground application upgrading activities up to the HPS Development Model (DM) are described hereafter, along with the most important design features of the flight version of the system.

Introduction

Hexapod systems are composed of six LA's disposed as legs of three trapezia and connected by means of twelve joints to two mounting platforms (lower and upper ones). The overall assembly is statically determined (isostatic), so that the length of each LA can be changed independently from the length of the others, if needed, without jamming the mechanism. The coordinated motion of the six LA's, controlled by computer, allows the determination of the relative displacement and orientation of one platform with respect to the other. The location of the axis of instantaneous rotation of the upper platform is selectable by software. Normally, the lower platform remains fixed while the upper one accommodates the payload instrument, whose position and attitude — six degrees of freedom (DOF) — are determined by the lengths of the six LA's. The achievable positioning and pointing ranges depend on the overall geometrical and mechanical characteristics and may be differently optimized, depending on the specific payload requirements.

Background

Conceptual studies performed in ESA identified the need to control five DOF for the accurate positioning/alignment of the secondary mirror assembly of large space antennas [1]. A suitable solution for this requirement could be the use of hexapod systems. Feasibility studies performed in 1993/94 by the ESA Directorate of Manned Spaceflight and Microgravity identified the possibility of using hexapods as multi-purpose positioning/pointing systems in space applications, and also proved the possibility to upgrade the existing ground applications hexapod technology for use in space [2,4,5,6]. In spite of the high number of DOF that they can control, hexapods

* ADS Italia S.r.l., Lecco, Italy

** European Space Agency (ESA), ESTEC, Noordwijk, The Netherlands

were identified as relatively simple devices. Their electromechanical assembly is essentially based on the design of just one LA, to be built in six identical units and assembled in a suitable geometry; in principle, the same LA control electronics could be used in different applications with different electromechanical assemblies. Aspects of design modularity and the potential capability of the six legs to withstand all or part of the launch/re-entry loads were also identified as potential advantages for space applications.

In the frame of the ESA/NASA negotiation on the Early Utilization of the ISS, ESA included a Hexapod-based pointing device in the list of enhancement items that ESA offered to develop and provide to NASA in exchange for early flight opportunities for European payloads. NASA identified the proposed Hexapod as a suitable pointing mechanism for their SAGE III instrument, since its version to be flown on ISS requires a pointing platform to compensate the ISS attitude deviations from its nominal Local Vertical Local Horizontal (LVLH) attitude. Following the notification of the NASA interest in the Hexapod, a 1994 feasibility study identified the possibility of accommodating SAGE III on a Hexapod [3]. The ESA Member States participating in the Space Station program approved the HPS for SAGE III, to be developed by Italian Industry. The Hexapod for SAGE III is going to be the first European mechanism based on the Hexapod principle to be flown in a space application. Its complete development is funded, and the delivery to NASA of the HPS Flight Unit is planned for first quarter solar year 2000, one year before launch (flight UF-4 in first quarter 2001).

A pre-development oriented Pre-Phase B, aiming at developing and testing a few design options of LA prototypes, has already been completed (Dec. 1994 – Oct. 1995, contractor ADS Italia). Phase B is now in progress (Alenia Spazio is prime contractor; ADS Italia and Carlo Gavazzi Space are sub-contractors), and the activities are planned to be completed in January 1997. Phase B includes the development and testing of an HPS Development Model (DM).

Hexapod for SAGE III Mechanical Assembly

The SAGE III instrument is the fifth in a series of space-borne remote-sensing instruments developed by NASA Langley Research Center for monitoring the global distribution of aerosols and gaseous constituents in the Earth atmosphere by using the solar occultation approach. In addition, SAGE III is also able to operate with the lunar occultation and detects the distribution of some typical night constituents of the atmosphere. The SAGE III payload is composed of the Sensor Assembly (mounted on the Hexapod Upper Platform) and by the electronic boxes.

During each orbit, SAGE III will perform up to four observations: sunrise, sunset, moonrise, and moonset. The Hexapod task is to compensate ISS attitude deviations from its nominal LVLH attitude in order to provide Nadir pointing to SAGE III before each observation event starts, but remaining fixed during the event itself. The upper part of the SAGE III Sensor Assembly (scanning unit, telescope, and spectrometer) is driven in azimuth around its vertical axis by the onboard sun/moon sensors, while the

elevation mirror performs the scanning. The selected Hexapod/SAGE III Sensor Assembly mechanical configuration is extremely compact, with the Hexapod Upper Platform shaped as a ring flange, thus allowing the SAGE III Sensor Assembly to be accommodated by partly protruding inside the volume among the six legs (Figure 1) in order to optimize volume allocation and minimize moment of inertia of movable parts. The Upper Platform provides the mechanical interface to the Sensor Assembly and to the launch Off-Loading Device (OLD). The HPS Lower Platform is mounted on an Express Pallet Adapter (EPA) of an Express Pallet which is accommodated on the ISS truss looking towards the Earth.

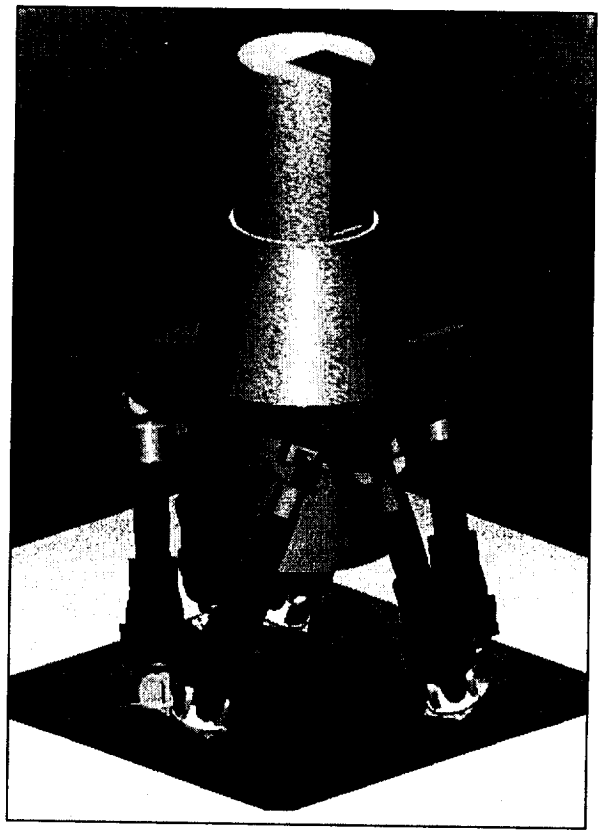

Figure 1. Hexapod/SAGE III Sensor Assembly Mechanical Configuration (Launch Off-Loading Device not shown)

Although SAGE III operation needs only two DOF (rotation around two perpendicular axes, i.e., pitch and roll), the hexapod offered capability to control more degrees of freedom and allows partial recovery from electromechanical failures of the LA's (via software reconfiguration). Moreover, the six-DOF control capability, together with the structural characteristics of the six legs, are also used to simplify drastically the design of the launch OLD: a vertical translation of the Hexapod Upper Platform allows both positioning for latching to the OLD for launch, as well as positioning for on-orbit operation without mechanical interference of movable parts.

Hexapod and Linear Actuator Requirements

The following two tables summarize the HPS requirements and the corresponding LA requirements:

Table 1. Hexapod Requirements

REQUIREMENT	VALUE	REMARKS
Pointing Range	± 8°	with respect to the Hexapod vertical axis
Pointing Accuracy	± 0.0083° (± 30 arcsec)	Measured between the Hexapod Upper and Lower Platforms
Pointing Rate	1.2 °/s	tilting rate of the Hexapod Upper Platform
Pointing Stability	0.0035 °/s	applicable only during the SAGE III observation time with Hexapod in a fixed position
Payload Accommodation	SAGE III	Hexapod is the pointing platform of SAGE III Sensor Assembly
Maximum Height	≤ 1.0 m (target)	height of the composite Hexapod/SAGE III mechanical assembly in launch configuration
Mass	≤ 70 kg	Hexapod plus SAGE III
On-orbit Lifetime	5 years	mounted to the EPA on ISS Truss Express Pallet
Launch Vehicle	NSTS	

Table 2. Linear Actuator Requirements

REQUIREMENT	VALUE	REMARKS
Linear Stroke	95 mm	70 mm are used to achieve ± 8° range, another 20 mm are necessary to avoid contact with OLD during on-orbit operation; and 5 mm is an extra-stroke required at launch to allow actuator backdriving
Positioning Accuracy	± 25 micron	applicable to the 70-mm nominal stroke
Positioning Repeatability	± 5 micron	3σ value
Positioning Resolution	(10 ± 1) micron	maximum allowed error for 10-micron positioning step is 1 micron
Maximum Linear Speed	5 mm/s	required to achieve 1.2 °/s pointing rate

Hexapod Linear Actuator Development and Testing

Pre-development Activities: Upgrade of Ground-based Hexapods

The main study objective of Pre-Phase B was the technological development (design and testing) of Hexapod LA prototypes. In addition to the feasibility studies performed for ESA on Hexapod space applications, Pre-Phase B was initiated by considering the

required space qualification during the program and taking as a starting point the ADS Italia available experience of ground-based HPS in the astronomy field.

The LA movement is driven by an electrical motor through a preloaded spindle-nut mechanism which transforms the shaft rotation into a linear displacement of the nut housed in the movable part. The spindle is mounted in the fixed part of the actuator. An optical incremental rotative encoder is coupled to the spindle free end and is used for positioning control feedback as an angular sensor. Although an encoder of the absolute type would be easier for the application, an incremental one was preferred because of the availability of an existing space-qualified version of a similar encoder. Two cardan joints are mounted at the end of the actuator movable and fixed parts housing, thus allowing the relative tilting of the Hexapod platforms once assembled. Limit switches, placed at the beginning and at the end of the nominal actuator stroke, allow for protection during testing and for coarse calibration. Fine calibration is achieved by the accurate reference mark of the encoder.

As part of the Pre-Phase B initial trade-off activities for the actuator design, two main options were identified :

- Option "A" prototypes use a roller screw as the driving unit and ball bearings for spindle support and for the cardan joints.
- Option "B" prototypes use a standard spindle-nut device with the nut made of plastic material which can be designed to be intrinsically irreversible, plastic bushings for spindle support and for the cardan joints, and plastic wheels for the reduction gears (if present). Among the most common plastic materials already used in space applications, DELRIN and VESPEL were considered. The advantage of this option is self-lubrication.

In addition, direct drive, spur gear reduction, and worm gear reduction configurations were also considered (called configurations 1, 2, and 3, respectively).

Because of the simplification of the overall Hexapod design, a special effort was made to investigate the reversibility/irreversibility of the driving mechanism and to determine if a solution could be found, such that all the launch/re-entry loads could be withstood through the LA's. Reversibility means that an axial load applied to the actuator movable part produces a displacement, and therefore a motion of the actuator occurs. The minimum axial load capable of producing the actuator motion (backdriving limit) depends on the preload of the spindle-nut assembly for a reversible device like the roller screw. This reversibility can be avoided with an intrinsically irreversible spindle-nut assembly or with a component able to resist the torque on the spindle —a brake or an irreversible reduction, for example.

An extensive testing campaign in ambient conditions was performed for each of the LA prototypes:

- Positioning Accuracy, Repeatability, Resolution, Hysteresis tests
- Axial Stiffness test
- Motor current absorption at constant speed and applied load

Loads ranging from 10 N (on-orbit loads) up to 100 N (Hexapod assembly ground testing), and different loading conditions (tension and compression) were considered during testing. Table 3 contains the most important results of the LA accuracy testing campaign in ambient conditions.

During testing, option "B" was modified as part of the development process:

- The plastic bushings used to support the spindle were substituted by bearings, since the too high thermal expansion coefficient of DELRIN material produces a thermal deformation of the bushings and blocks the spindle rotation.
- DELRIN components were substituted by VESPEL ones because of the better thermal properties and wear resistance of the latter.
- Two plastic bushings were added to the nut ends in order to support directly the action of the actuator weight and provide a guiding capability of the nut along the spindle (Figure 2).

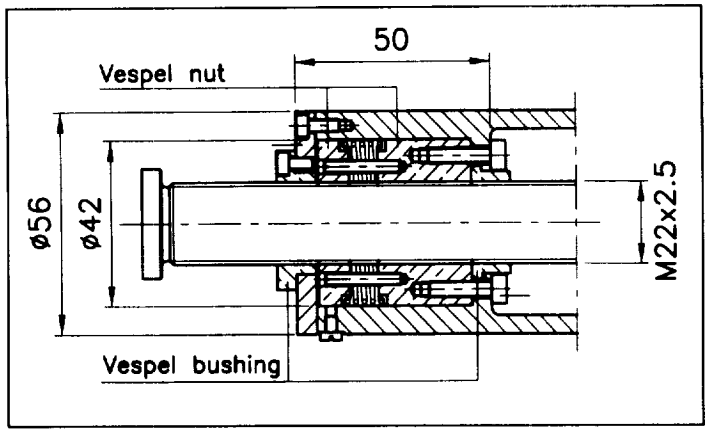

Figure 2. VESPEL nut assembly

- The test setup was improved by adding weights on both the fixed and movable parts of the actuator to counterbalance the effect of the actuator weight.
- Finally, the spindle-nut assembly was re-designed by increasing the screw diameter and changing to a trapezoidal thread shape with 2.5-mm pitch instead of 1 mm (to improve the guiding capability by maintaining the same specific pressure on the thread).

The actuator with the VESPEL nut was also subjected to lifetime testing, performing 74,000 stroke cycles of ±3.75-mm amplitude (equivalent to ±1° Hexapod pointing compensation) in ambient conditions at 5 mm/s with 10 N applied tension load to simulate about 5 years on-orbit Hexapod operation. Before and after lifetime cycling, accuracy tests were performed for comparison reasons and also at 20,000-cycle

Table 3. Hexapod Linear Actuator Prototypes Test Results Summary

LA Prototype configuration :	**1 "A"**	**2 "A"**	**3 "A"**	**1 "B"**	**1 "B" modified**	
Main Features :	• direct drive • roller screw • 2-mm pitch	• parallel drive • roller screw • 2-mm pitch	• worm gear drive • roller screw • 2-mm pitch	• direct drive • DELRIN nut • 1-mm pitch	• direct drive • VESPEL nut • 2.5-mm pitch	
Test Parameter :						**Requirement**
Positioning Accuracy [micron]	± 14	N/A	± 14	± 16	± 26	± 25
Positioning Repeatability (3σ) [micron]	± 1.7	± 2.4	± 2.4	± 3.0	± 9.2	± 5
Positioning Resolution [micron]	7 ± 1.4	6 ± 1.2	6 ± 1.2	2 ± 0.4	4 ± 0.8	10 ± 1
Positioning Hysteresis [micron]	5	5	5	4	7	N/A
Axial Stiffness [N/micron]	5.0	6.0	6.6	2.5	4.9	N/A
Motor Current Absorption (*) [A]	1.56	1.22	0.97	2.33	N/A	N/A

(*) : measured during 100-N load lifting at 5-mm/s nominal pointing speed.

intervals. At the conclusion of the life cycle test, the VESPEL nut was disassembled, and visual inspection showed that few plastic particles inside the nut were abraded during the first cycles. The accuracy tests performed at the end of life cycling demonstrated the absence of degradation of the overall performances; only a shift of about 30 microns between the reached positions during the tests can be considered an index of some wear of the nut.

The last test performed on one LA prototype was the evaluation of the accuracy performances due to the effect of cardan joints placed at the actuator ends. An actuator was mounted using a test setup representing the real actuator inclination when assembled into the Hexapod. The cardan joints were therefore subjected to angular displacements equivalent to the ±8° Hexapod Upper Platform tilting. The cardan joints have a cross mounted on preloaded ball bearings, so this test gives an evaluation of the bearing behavior when subjected to small oscillations (stick-slip effect). The test results show that the accuracy performances are not degraded when the cardan joints effect is considered.

The results of the testing campaign demonstrated that the LA performances are able to fulfill SAGE III requirements for Hexapod use. Different design solutions were proposed for selection during the design of the complete mechanical assembly.

Linear Actuator Prototypes Thermal-Vacuum Testing

The following two LA prototypes were considered the most significant design solutions and selected for thermal-vacuum testing (TVT) at the beginning of Phase B: worm gear drive actuator with roller screw (config. #3 "A") and direct drive actuator with VESPEL nut (config. # 1 "B" modified).

Thermal Vacuum Test on LA Prototype Config. 3 "A":
Before the start of TVT, some changes were introduced:

- As proposed by the manufacturer for space applications, the roller screw lubrication was changed from standard commercial grease to a dry lubrication treatment called Microseal 200-1 (MoS_2 based).
- Fomblin vacuum-compatible grease for bearings lubrication (spindle support, worm screw support, and cardan joints) was used instead of standard commercial grease.

The following results were obtained:

- Accuracy performances were not degraded by the execution of the TVT.
- The LA was still capable of performing the functional test at maximum (70°C) and minimum (–20°C) operative temperatures after exposure to maximum (80°C) and minimum (–35°C) non-operative temperatures.
- Increase of current absorbed by the motor at high temperatures (70°C) was interpreted to be the effect of the high thermal expansion coefficient of DELRIN material of the worm wheel inside the worm gear reducer.

- Problems due to the applied lubricants were not found.

Thermal Vacuum Test on LA Prototype Config. 1 "B" modified :
Also in this case Fomblin grease was used for bearings lubrication.

The following results were obtained:

- Accuracy performances were not degraded by the execution of the TVT.
- The actuator was still capable of performing the functional test at maximum (70°C) and minimum (–14°C) operative temperatures after exposure to maximum (80°C) non-operative temperature.
- During the first cold passage, one of the two VESPEL bushings guiding the actuator movable part slipped off the nut support because of insufficient fixation capability of the screws. The VESPEL bushing was thermally contracted on the stainless steel spindle and remained jammed when the actuation was commanded.
- The VESPEL nuts worked well at all tested temperatures.

The TVT campaign helped to identify the best LA prototype configuration to be used for Phase B development:

- The satellite roller screw solution was preferred to the VESPEL nut one because
  - ⇒ the design maturity of the latter was not considered sufficient to guarantee good mechanical behavior at low temperatures, and
  - ⇒ the accuracy performances of the first one were better.
- The Microseal dry lubricant treatment did not evidence tribology problems during the test, but it is not a must for the roller screw. Other treatments and lubricants selection (Braycote, Fomblin, etc.) could also be used, particularly if they are supported by more space application experience in Europe.
- If irreversibility is no longer needed in case the Hexapod configuration presents an off-loading device, then the preferred actuator configuration is the direct drive one (instead of the worm gear one).

Linear Actuator Design for HPS Development Model

The selected configuration of LA for development during Phase B was the direct drive one with a DC brushless motor and an encoder mounted on the same shaft of the motor rotor (Figure 3). For backlash elimination, a preloaded nut is mounted to the nut housing on the driving unit, a roller screw, and represents the actuator movable part (translation).

The electrical motor is a DC brushless unit in a frameless configuration: the motor stator housing is part of the actuator housing, and the motor rotor is mounted directly on the roller screw spindle. Phase commutation is achieved using an embedded Hall sensor. The available room foreseen for the motor takes into account that the flight version of the actuator will mount a redundant (windings and Hall sensor) motor. The

selection of a frameless motor is advantageous from the structural point of view, since it provides a load carrying path through its housing and has no support bearings on the motor shaft.

The encoder is an optical incremental rotative type in frameless configuration: the disk hub is directly mounted on the shaft (spindle), and the scanning unit plus electronics is placed on a fork-shaped disk connected to the actuator housing. Also in this case, there are the advantages of no support bearings in the encoder and direct connection of the disk hub to the shaft through grub screws, thus producing a high torsional stiffness to reduce the angular error with respect to the torsional spring coupling solution normally used to mount housed encoders to a shaft. This type of encoder is the commercial version of an existing space-qualified one with redundant reading stations. It was selected because of its simple mechanical interface and the few electronic components present in it. In fact, this encoder provides two analog incremental signals (sine and minus cosine) and one reference signal per revolution (analog). The disk hub has 3600 line counts; therefore, the output consists of 3600 incremental signals per revolution. For actuator positioning control purposes and due to the required accuracy performances, the encoder incremental signals need to be interpolated/digitized to increase the number of impulses per turn. The signal interpolation/digitizing electronics are not embedded in the encoder.

The planetary roller screw is a very high accuracy device that is normally used for precise micropositioning in instruments. The nut is a cylindrical split type with an interposed calibrated spacer for preload application (stiff type) and is mounted in its housing through the nut flange. Preload dimensioning is very important because it produces a constant torque without load due to friction and defines the maximum axial load on the actuator under which backlash and backdriving take place. The nut contains non-recirculating rollers (planetary type).

A mechanical end-stop, consisting of two spacers with Belleville washers in between, is placed at the free spindle end to provide a shock absorber capability during re-entry and landing (without latching capability to the launch off-loading device). It is also a helpful feature to recover an eventual motion that is out of nominal stroke range during ground testing at actuator level when adjusting control loop parameters.

The roller screw is supported by ball bearings. A pair of preloaded angular contact ball bearings in back-to-back configuration is used to provide central spindle support, while a deep groove ball bearing was placed at the spindle end to help withstand overturning moments due to lateral loads. The bearings pair is configured, such that the correct preload is obtained during mounting operation by eliminating the determined free space of contact faces created by the manufacturing process. In this way, the tightening torque applied to the threaded locking ring that is used to lock the central bearings does not influence the preload level. The deep groove bearing is mounted on a diaphragm (low axial stiffness and high radial stiffness) to allow for shaft

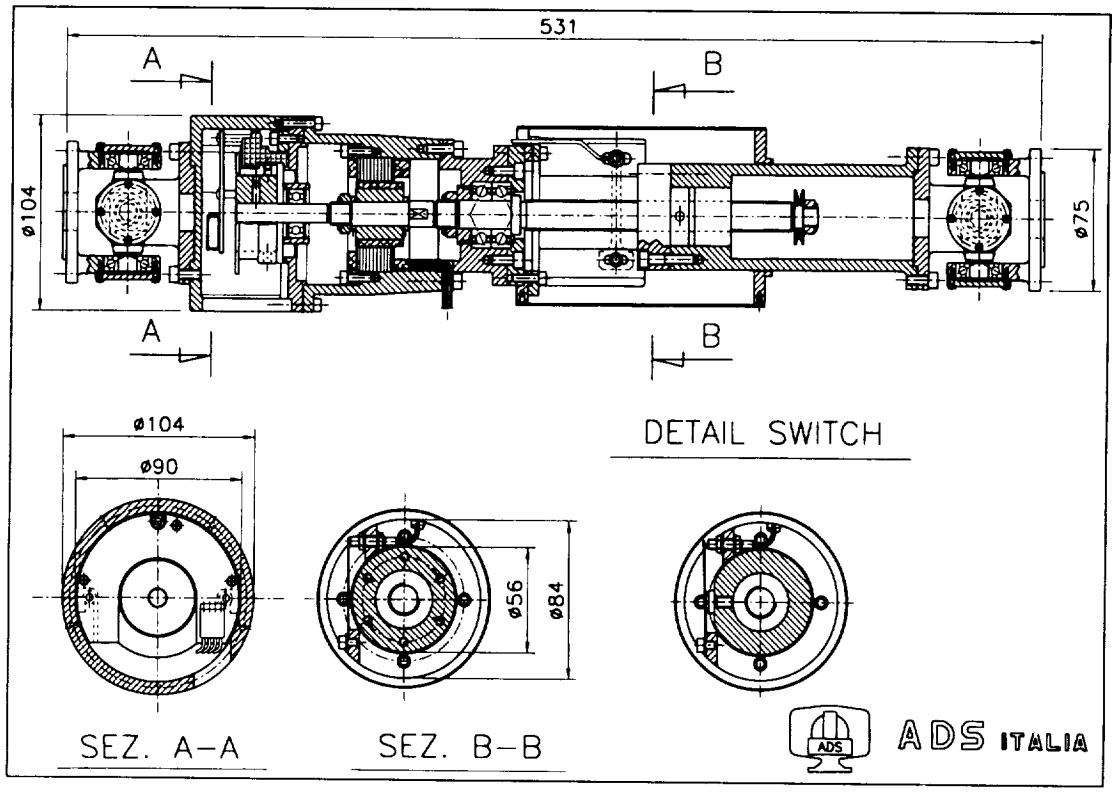

Figure 3. HPS DM Linear Actuator Assembly Drawing

axial displacements (thermal effects) without causing blocking or friction increases in the bearing.

At the end of the actuator movable and fixed parts, there are two cardan joints to allow rotation around two perpendicular axes. The cardan joint is composed of two flanged perpendicular forks connected through a cross that is mounted on four low preloaded ball bearings. The forks and bearings covers are made of aluminum alloy, while the cross is made of stainless steel.

The actuator housing is made of aluminum alloy, and the connection screws are stainless steel. The threaded locking rings are self-locking and are also made of stainless steel.

A hollow cylinder, covering the exposed part of the screw, is used for both contamination and thermal control purposes. The gap between the cylinder and the nut housing needs to be optimized.

A proximity switch of the inductive type is placed in correspondence to the minimum nominal stroke of the actuator and is used only for calibration purposes (to conduct accuracy testing and actuator length calibration before Hexapod assembling).

HPS DM Linear Actuators Accuracy Testing Campaign

Prior to assembly in the Hexapod, each of the six LA's of the HPS Development Model were subjected to an extensive accuracy testing campaign in ambient conditions for both acceptance procedure and mechanical characterization. In addition, the DC brushless motors and the roller screws were also tested at the manufacturer.

Since the roller screw is the key mechanical element that defines the whole actuator accuracy, the following parameters were measured before actuator assembly:

- Spindle accuracy (to verify spindle lead error within specified value, as defined by the tolerance class: in our case, DIN G1 class with 6-micron maximum error over 300-mm stroke)
- Displacement error of the complete spindle-nut assembly along the stroke, using a high-precision laser interferometer system
- Torque without load (the friction torque due to nut preload)
- Nut axial stiffness
- Backdriving limit

The following tests were performed on the LA's:

- Full-stroke positioning accuracy
- Positioning repeatability, resolution, and hysteresis
- Measurement of motor torque at constant speed and applied load
- Actuator axial stiffness
- Recovery after jamming at nominal speed (only for two actuators)

Tests were conducted at nominal speed (5 mm/s) and 10-N tension load. Full nominal stroke is 70 mm. Test results are shown in Table 4, and the test setup is shown in Figure 4.

All the measured accuracy performances parameters meet the corresponding DM specification requirements for all six actuators. Moreover, the whole group of six actuators shows very similar accuracy performances, which demonstrates a benefit for the complete Hexapod DM performance characterization.

Recovery from jamming of the actuator movable part hitting the spindle mechanical end-stop at 5 mm/s was successfully achieved on repeated tests without the necessity of increasing the motor torque limit (set at nominal value for normal operation).

Hexapod Development Model Mechanical Assembly Design and Testing

The complete Hexapod DM mechanical assembly design was completed, including the Upper and Lower Platforms, a SAGE III Sensor Assembly dummy mass, and the interface blocks to the LA cardan joints that are needed to obtain the correct inclinations of the actuators after assembling the Hexapod (system geometry). Extensive dimensional control of parts at each assembly stage was performed to

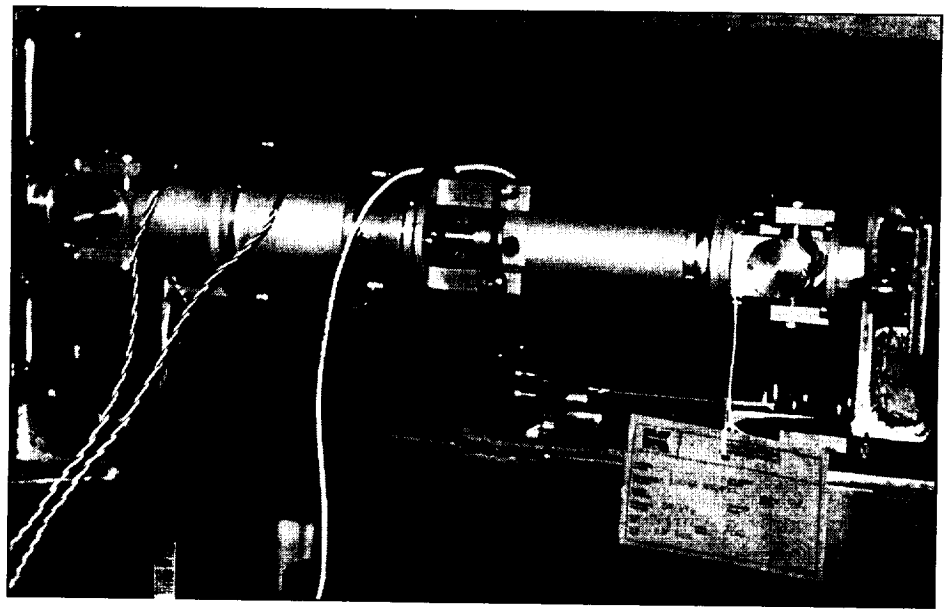

F gure 4. DM Linear Actuator under Testing

guarantee low mechanical alignment errors and to establish preliminary procedures for Flight Unit integration. The HPS DM mechanical assembly is shown in Figure 5.

Testing in ambient conditions of the HPS DM is being performed during preparation of this paper and includes the following:

- Pointing range, accuracy, and rate measurements
- Thermal gradient and thermal stability tests (to characterize the system thermal behavior in terms of pointing error induced by the thermo-elastic deformation of the LA's)

The following table reports the preliminary results:

Table 4. Hexapod DM Test Results

Test Parameter :	Test Value :	Requirement :
Pointing Range	± 8 deg (around two perpendicular axes)	± 8 deg
Pointing Accuracy	± 13 arcsec	± 30 arcsec
Pointing Repeatability	± 5 arcsec	± 10 arcsec

Hexapod Flight Unit Key Design Solutions

Most of the linear actuator design activities related to the flight version were concentrated on the mechanical components. Since the utilization of roller screws in space applications is relatively new and very little test data are available, testing of this component is foreseen as part of the Hexapod program. The two types of roller screws

Table 5. HPS Development Model Linear Actuators Test Results in Ambient Conditions

Test Parameter	Actuator S/N 01	Actuator S/N 02	Actuator S/N 03	Actuator S/N 04	Actuator S/N 05	Actuator S/N 06	Requirement
Global Positioning Accuracy [micron]	± 15	± 15	± 16	± 19	± 16	± 19	± 25
Positioning Repeatability (3σ) [micron]	± 2.5	± 2.3	± 2.0	± 2.0	± 3.1	± 2.9	± 5
Positioning Resolution [micron]	1 ± 0.3 10 ± 0.8	1 ± 0.1 10 ± 0.8	1 ± 0.2 10 ± 1.0	1 ± 0.5 10 ± 1.0	1 ± 0.1 10 ± 1.0	1 ± 0.3 10 ± 0.8	N/A 10 ± 1.0
Positioning Hysteresis [micron]	-10	-12	-10	-11	-10	-9	N/A
Axial Stiffness [N/micron]	4.9	5.4	5.6	4.9	9.2	5.1	≥ 5.0
							Prediction
Motor Torque [Nm]	0.082	0.114	0.151	0.131	0.102	0.076	0.120

Note : 1 micron linear actuator displacement is equivalent to approximately 1 arcsec Hexapod Upper Platform tilting angle.

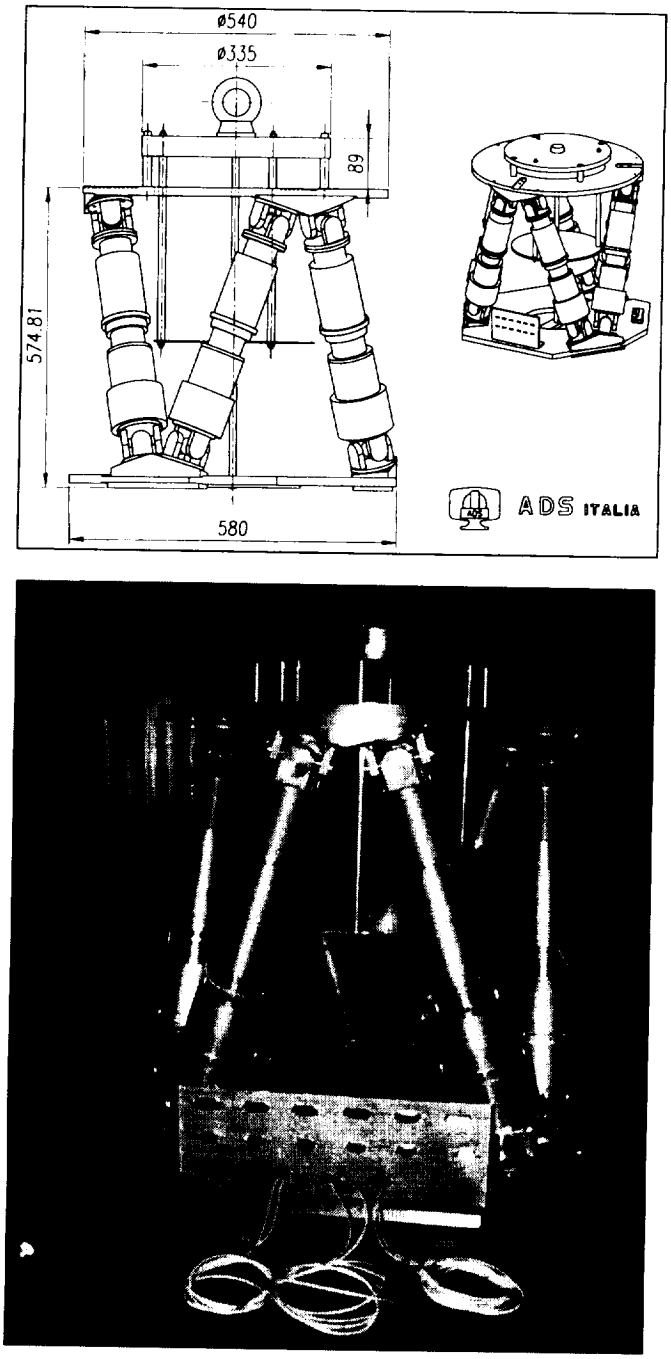

Figure 5. HPS Development Model Mechanical Assembly

(planetary and re-circulating) will be subjected to a random vibration test to simulate Hexapod launch. This test will be followed by a lubrication lifetime test in vacuum conditions with thermal cycling to simulate five years of on-orbit operation. The roller screws used for testing will be at flight-quality level, and lubrication baseline consists of an ion-plating lead treatment on the stainless steel spindle and nut, followed by fluid lubrication using Braycote 601 grease. Of particular interest is the random vibration

testing on the re-circulating roller screw because the disengaged roller, excited by the vibrations, hits the spindle and nut to produce micro-shocks that could degrade the accuracy performances. A key aspect of lifetime testing is the nut preload loss due to wear, an effect which must be controlled and maintained above the minimum required value needed to counteract on-orbit backdriving and eliminate backlash. These test results will be inputs for the selection of the roller screw type for the flight actuators.

Conclusions

This paper presented the mechanical design of the first European pointing system based on the Hexapod principle to support the NASA-provided SAGE III instrument mission on the International Space Station truss. Early breadboarding activities on the required high accuracy linear actuators during a pre-development phase allowed the selection of the design baseline. A complete Development Model, manufactured and tested during Phase B, confirmed that the system pointing performances measured in ambient conditions are well within imposed requirements. Main design aspects that were needed to complete the mechanical design of the system flight unit were identified, and a testing campaign on the still not well-characterized roller screw space component is foreseen as an anticipation to program Phase C/D.

Acknowledgment

The authors would like to thank Media Lario S.r.l. for the support given during manufacturing and integration of the Hexapod Development Model mechanical assembly. An acknowledgment is also dedicated to the SAGE III team (NASA LaRC and Ball Aerospace) for the tight cooperation they are having with the Hexapod Team in the frame of the ESA/NASA Agreements for the ISS Early Utilization Opportunities.

References

1. "Study for the IVS antenna", Future Science Projects, Scientific Projects Department, ESA/ESTEC, 1991.
2. "Hexapod Pointing Mechanism for Space Applications - Feasibility Study", ESA Contract N° 132302, ADS Italia S.r.l., June 1993.
3. "Accommodation Assessment of SAGE III on Hexapod" and "Accommodation Assessment of UTEF on Hexapod", ESA Contract N° 141103, ADS Italia S.r.l., March 1994.
4. "Preliminary Analysis of an Hexapod Pointing System for Space Applications", ESA STM-253, G. Isella, ESTEC, May 1994.
5. "A Proposal for In-orbit Demonstration of a Pointing System Based on the Hexapod Principle", F. Ongaro, G. Isella, ESA/ESTEC, 1994.
6. "Pointing System Feasibility Study", ESA Contract N° 11202/94/NL/AE, Prime Contractor Sener, 1994.

The Galileo Tape Recorder Rewind Operation Anomaly

Michael R. Johnson* and Greg C. Levanas*

Abstract

On October 11, 1995, the Galileo spacecraft executed a sequence to record three approach images of Jupiter on the spacecraft's tape recorder, rewind the tape, and play back the images at the appropriate data rate consistent with the downlink performance. The recording of the images was performed and the spacecraft computer commanded the tape recorder to rewind the tape to the beginning of the first image. The rewind command was started at the proper time but the tape never got to the beginning of the image data. The analyses and tests that followed allowed a conclusive determination of the failure mechanism and indicated a strategy that could be used to prevent the untimely demise of the mission.

Introduction

The Galileo spacecraft's mission is to drop a probe into the atmosphere of Jupiter and then tour the Jovian system for two years with an encounter of a moon every one to two months. The data will provide information on the system and the individual moons' structure, composition, and environments. The spacecraft was launched from Kennedy Space Center aboard the Space Shuttle on October 18, 1989. Galileo's trajectory involved a gravity assist from Venus and two gravity assists from Earth. Galileo released its Jupiter atmospheric probe on July 13, 1995, for a ballistic trajectory to the giant planet. The spacecraft reached its destination at Jupiter on December 7, 1995, and the atmospheric probe entered Jupiter's atmosphere exactly as planned. The data from the probe was recorded on the spacecraft's digital data tape recorder and has all been returned to Earth for study. The spacecraft is currently approaching another moon for its next encounter and significant data return.

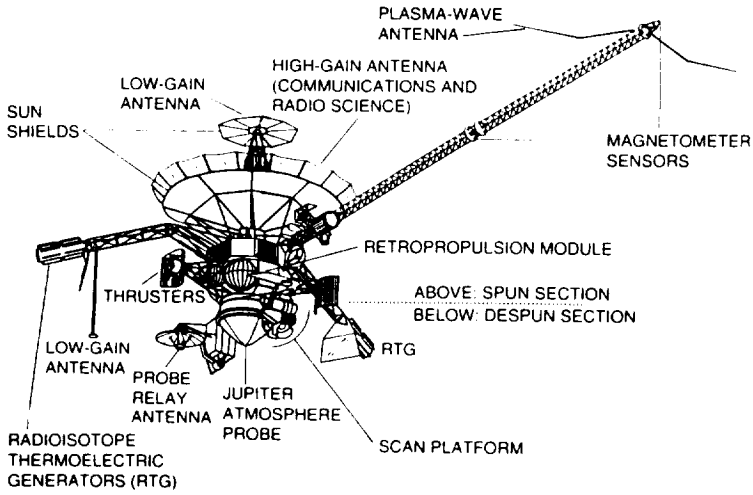

Figure 1.
Galileo Spacecraft Configuration

The Galileo spacecraft (Figure 1) is a spin stabilized spacecraft with seven fields and particles instruments and four imaging instruments. There are two antennas in the

* California Institute of Technology, Jet Propulsion Laboratory, Pasadena, CA

high gain antenna assembly, the high gain dish and a low gain wide beam antenna. The second low gain antenna seen in the figure was only deployed for use during the first five years of the mission and is no longer usable for communications. The primary transmission source for returning the science data to Earth was designed to be the High Gain Antenna (HGA) which was capable of transmission rates up to 134 kilobits-per-second (kbps). In the event the real-time downlink could not be maintained during the probe descent into the atmosphere of Jupiter, a tape recorder capable of record rates up to 806.4 kbps was incorporated into the spacecraft design. There are several operating modes for the tape recorder at different data rates from 7.68 kbps to 806.4 kbps. The different data rate modes include different combinations of the various science instruments. The lowest data rate for recording and playback on the tape recorder is 7.68 kbps, and this mode does not include any imaging science. To obtain imaging science data, the recorder must be operated at a higher data rate than 7.68 kbps.

On April 11, 1991, the Galileo spacecraft's High Gain Antenna failed to deploy properly which had serious mission implications [1]. The only remaining data downlink was the Low Gain Antenna (LGA). This antenna's downlink data rate performance was only 10 bps at Jupiter. With the slowest data rate from the instruments (no images) of 7.68 kbps, the data could not be sent over the LGA. The solution to this problem seemed to be the tape recorder. The data from a single encounter could be recorded onto the recorder and played back at a rate that the LGA link could be used to return the data. The quantity of science data from a single encounter is enough to fill up all of the space on the tape. This approach had the limitation that a complete return of the data from a full tape recorder would take over three years. This time frame was inconsistent with the need to dump the entire recorder between each encounter: one to two months.

From October 1991 through February 1992, a JPL team worked on developing options to solve the data return problem with the HGA unusable. The total strategy developed by this team consisted of adding compression, editing, and encoding software to the spacecraft and arraying the ground based Deep Space Network antennas to obtain a higher signal to noise ratio. The software added to the spacecraft was installed in the main computer as well as some of the instruments' computers. Science data during an encounter will be recorded onto the tape recorder, played back from the recorder, modified, and sent through the LGA to Earth. This total strategy reduced the downlink time for a full tape from over three years to just around two months. The mission was possible again with the caveat that the tape recorder went from being a backup piece of hardware to a mission critical item.

The Rewind Anomaly and Telemetry Description

On October 11, 1995, the spacecraft recorded three approach images of Jupiter on the beginning of the tape and then attempted to rewind the tape for playback of the images. The telemetry from the spacecraft indicated that the tape never reached the beginning while the motor was running at the proper speed for several hours. The

rewind operation should only have taken 26 seconds to complete. If the motor was running the wrong direction, the end of tape should have been reached within five minutes. At this time, Galileo was only two months from Jupiter arrival and the return of the atmospheric probe data. Since the atmospheric probe data was of the highest priority and the tape recorder was required for complete data return, the rewind anomaly had to be understood and a solution determined in time for the December 7 arrival at the giant planet.

There are four types of telemetry provided from the tape recorder. These four are:

1. Motor current
2. Tape position
3. Presence of servo lock
4. Beginning of tape or End of tape (BOT/EOT)

The motor current telemetry provides a Data Number (DN) that is proportional to the current drawn by the tape drive motor. Since the motor is a brushless dc type, the current is proportional to the torque load on the motor.

The tape recorder provides pulses, or tics, while its motor is running that are proportional to the length of tape passed through the drive mechanism (no slippage). These are incremental tics from the tape recorder itself. The incremental tics are summed up in the spacecraft computer and a "tic count" number is generated for tape position telemetry. This telemetry should always be between 200 and 7183 representing the beginning and end of the tape, respectively.

When the tape drive mechanism is operating, it is very important that the speed of the tape be maintained accurately. The drive motor has a rotor encoder that provides speed data for the tape drive mechanism's servo control loop. When the recorder is operating in the slew or record modes, the encoder is used as the speed sensor and the control loop is closed around it. When the recorder is in the playback mode, the actual recorded data is used by the servo control loop to determine the tape speed. When the control loop has obtained a speed error signal within certain limits, a servo lock indicator in the recorder's telemetry changes state to indicate servo "lock-up".

The ends of the tape in the recorder have clear sections that are sensed by a photoelectric device. This device outputs a bi-level signal indicating that the tape has reached the end of travel. The tape recorder has internal circuitry that detects the presence of an end of tape indicator. If an indicator is detected, the circuitry stops the tape drive immediately and reverses the tape direction if appropriate. The machine's internal circuitry will only accept commands that move the tape away from the end of travel. The presence of an end of tape indicator is provided through the recorder's telemetry outputs.

Figure 2 shows the motor current telemetry received during the rewind anomaly. The expected nominal motor current for the tape position and speed at the time was 160 DN which was right in the center of the data. This telemetry did not indicate that a

problem had occurred. A stalled motor would saturate the current telemetry signal since its dynamic range is 255 DN (the equivalent stall value would be 738 DN). Figure 3 shows the tape position telemetry decrementing and then rolling over to the maximum value to continue decrementing. The large gaps correspond to missing groups of telemetry data. The rolling over of the count indicates that the data is going beyond the allowable limits for this telemetry. Using the tape position telemetry to determine the motor speed yields the result that the motor was running at exactly the commanded speed of 806.4 kbps. Since the rewind command uses a slew mode for the recorder, the servo lock telemetry as well as the tape speed are both determined from the motor rotor encoder. The servo lock telemetry indicated that the motor was in lock to the commanded speed. The fourth telemetry, BOT/EOT, never indicated that either end of the tape had been reached.

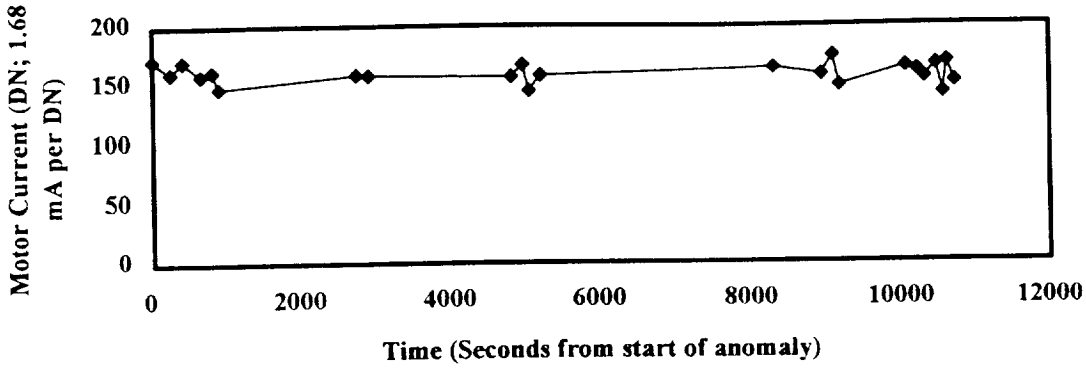

Figure 2.
Motor Current Telemetry vs. Time

Tape Recorder Mechanical Design

The tape recorder used on the Galileo spacecraft is an Odetics, Incorporated, Model 3100. This type of recorder uses AMPEX type 799 one-quarter inch wide tape. The tape is constructed of a polyethylene terephthalate base film (Mylar), gamma ferric oxide in a polyester urethane binder, and a backcoat of carbon black in a polyester urethane binder. The backcoat materials were selected to provide a good friction surface for driving the tape as well as a conductive surface to minimize the generation of static charge from the motion of the tape. The polyester urethane binder is produced from the combination of carboxylic acid and an alcohol. This process produces esters and water, and the reaction is reversible. Since the reaction is reversible, there are always some unreacted components present in any sample of tape, corresponding to the equilibrium quantities for the temperature and humidity level within the tape. The generation of the alcohol and carboxylic acid from environmental humidity is known as hydrolysis and the hydrolysis products are sticky (this is the technology behind the licking of a postage stamp to "activate" the adhesive) [2]. In the late 1960's it was learned that all tape recorders had to be run in an atmosphere with a certain humidity level to prevent the generation of huge static discharges in the machine. The ideal humidity level was determined to be between

30% and 50% for the temperatures that tape recorders were operated [3]. This humidity level has a corresponding concentration of hydrolysis products within the tape. These products remain suspended in the tape and do not present a threat to proper operation of the recorder. Because of the requirement to maintain a certain level of humidity around the tape in a recorder, all Odetics recorders are sealed with a 30% to 40% relative humidity atmosphere of nitrogen and helium [4].

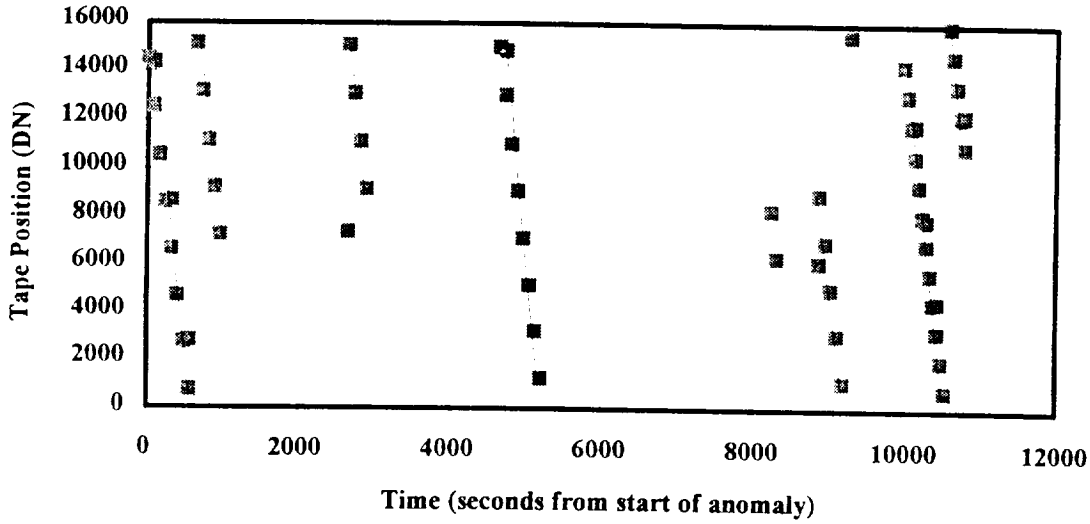

Figure 3.
Tape Position vs. Time

The tape is wound onto two reels that are stacked on top of each other and counter-rotate to minimize the uncompensated momentum that is injected into the spacecraft. Figure 4 is an outline drawing of the tape path in the recorder. The circles with numbers in them represent rollers or capstans that control the tape. Starting on the upper reel, the tape exits and wraps around roller #1. The path then takes the tape through the "BOT Block" which houses the photoelectric sensors for detecting the beginning of the tape. Roller #2 is tilted relative to the axes of the reels and lowers the tape half of the distance to the lower reel. Rollers 3 and 5 guide the tape to the first capstan, #4. The tape then passes over a playback head, roller #6, and another playback head. The second capstan in the drive system is the apex capstan at location #7. The next two heads in the path are the record heads with roller #8 in between. The third and final capstan in the drive system is #10. Roller #9 performs the same function as roller #4 and maintains the large wrap angle around capstan #10. Roller #11 positions the tape so it can be lowered the remaining distance to enter the lower reel by tilt roller #12. The tape then passes through the EOT block (same as the BOT block but detects the end of the tape), over the "dummy" erase head, around roller #13, and onto the lower reel. From the tape entrance and exit angles on the reels, the counter rotation of the reels is evident. The tape is driven through the group of rollers and onto the reels by the three capstans 4, 7, and 10. The drive force to

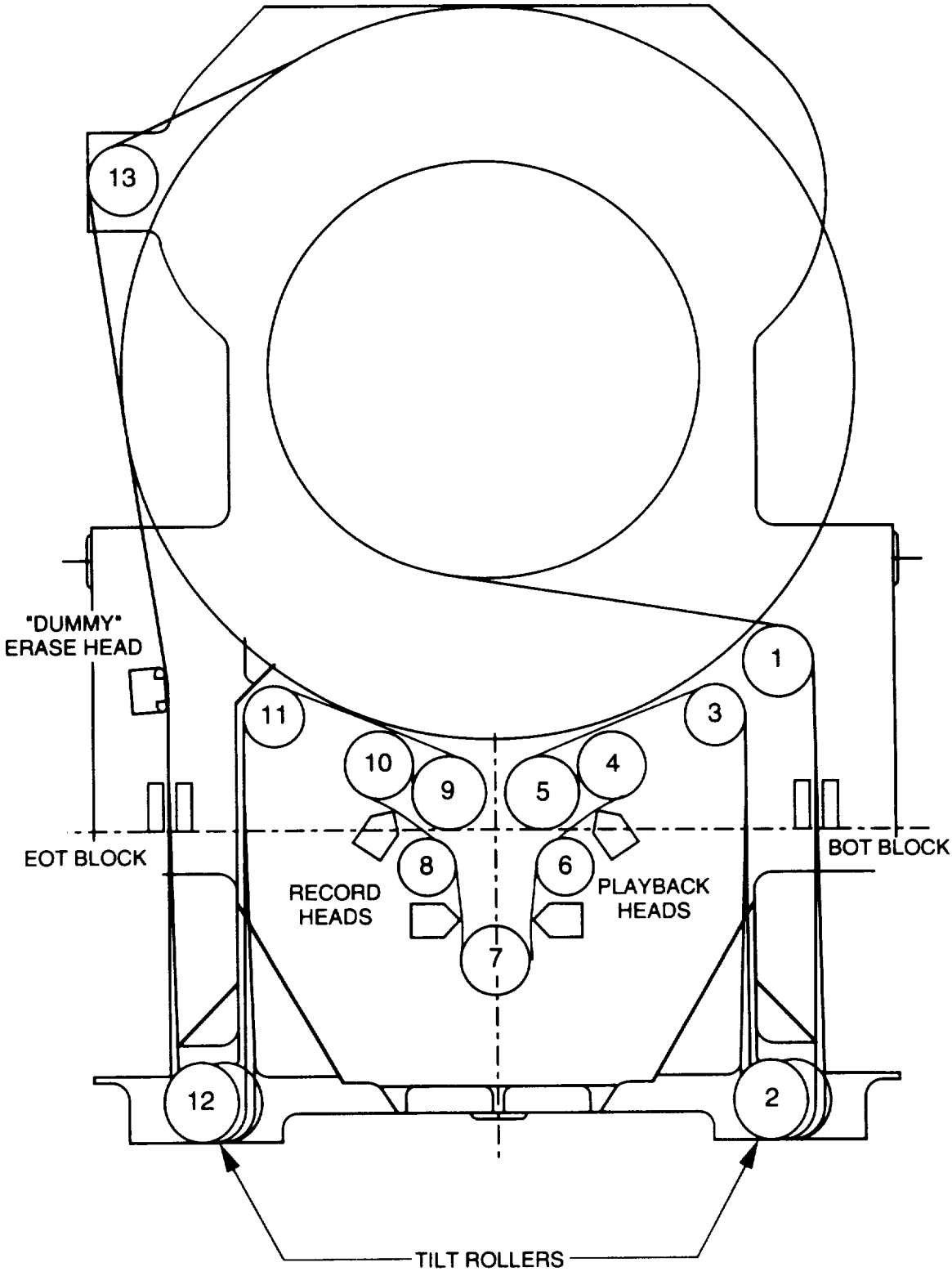

Figure 4.
Tape Path Outline
Drawing courtesy of Odetics, Inc., Anaheim, CA

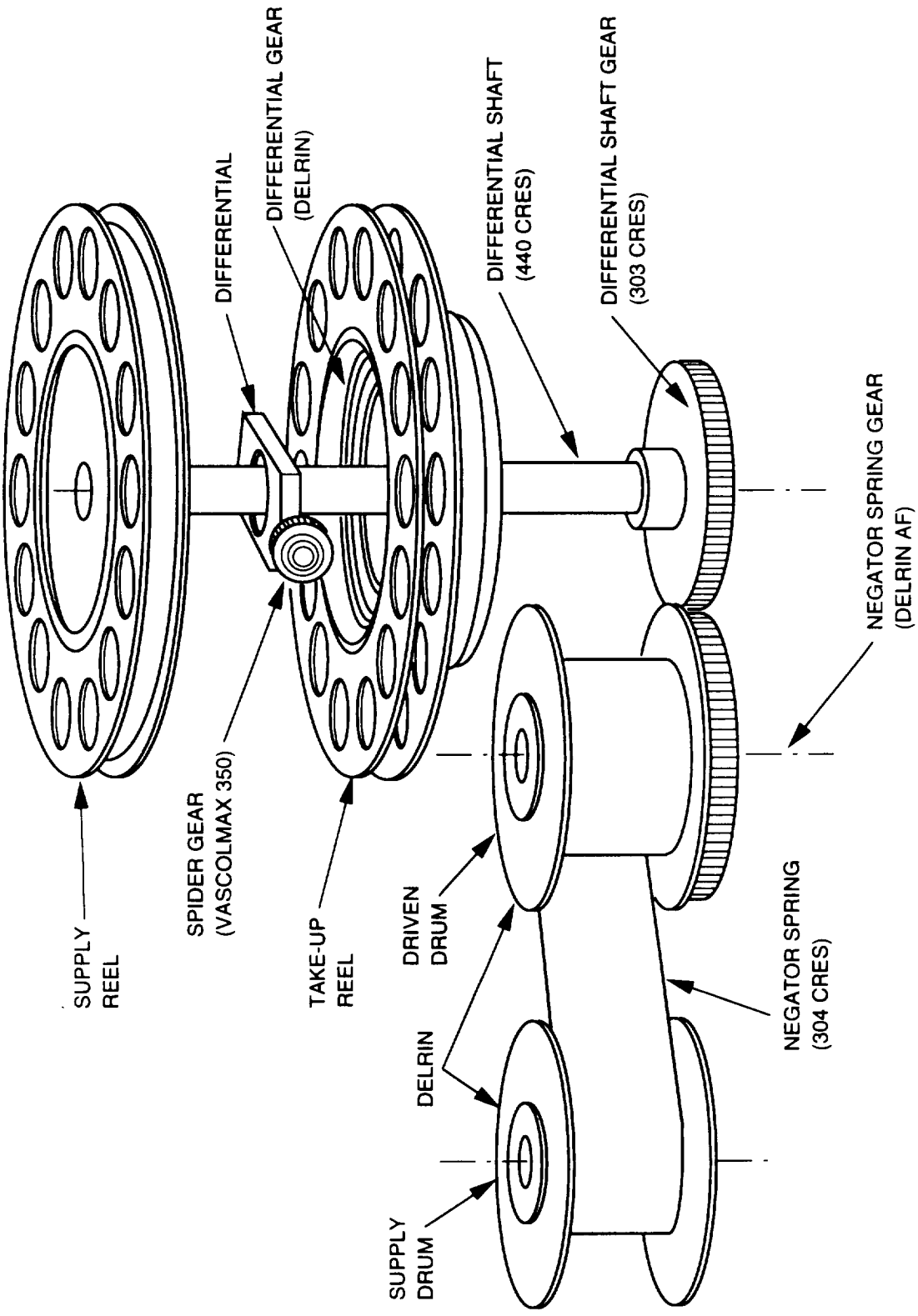

Figure 5.
Spring and Reel System
Drawing courtesy of Odetics, Inc., Anaheim, CA

move the tape comes from friction between the backside of the tape and the capstans. For this drive technique to work properly there must be continuous tension on the tape.

The required tape tension is provided by a single negator spring operating on the two reels through a differential mechanism as shown in Figure 5. The reels are independently supported on the differential shaft by a preloaded pair of bearings for each reel. This allows the reels to move freely relative to the differential shaft and each other. The negator spring applies torque to the differential shaft. This torque is reacted through the spider gear to the reels and provides the tape tension needed for the friction drive system to work. Refer to Figure 4 to see how both ends of the tape are tensioned by a single applied torque. The spring is always trying to pull the tape onto both reels. The capstan drive system pulls the tape off one reel and the spring winds the tape up onto the other reel.

During any move of the tape, the reel speeds will not be the same; the reel that has more tape on it will rotate slower. The differential mechanism shaft rotation rate will be proportional to the difference of the two reel speeds. At the exact center of the tape where there is the same amount of tape on each reel, the reel speeds will be the same and the differential shaft will stop rotating. As the tape passes the exact center, the difference in rotation rates of the two reels will change sign since the reel with the most tape will have changed position (that is from the upper to the lower reel). The result of this motion is the negator spring is unwound, stops, and then rewound as the tape goes from one end to the other. If the tape is released at any position, the spring system will drive the tape to the center of tape where the negator is fully unwound. The nominal motor current to move the tape from one end to the other is shown in Figure 6 and is independent of the direction of tape motion. The monotonic nature of

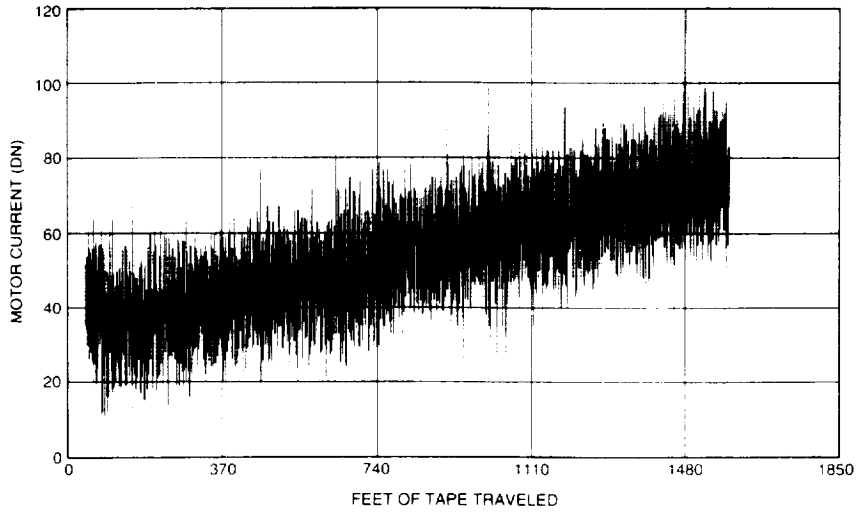

Figure 6.
Nominal Motor Current Trace at 7.68 kbps
1400 Feet of Tape, Reverse or Forward

the current is due to the motor holding back the negator (acting as a brake) as the center of tape is approached, and then rewinding the negator after passing the center

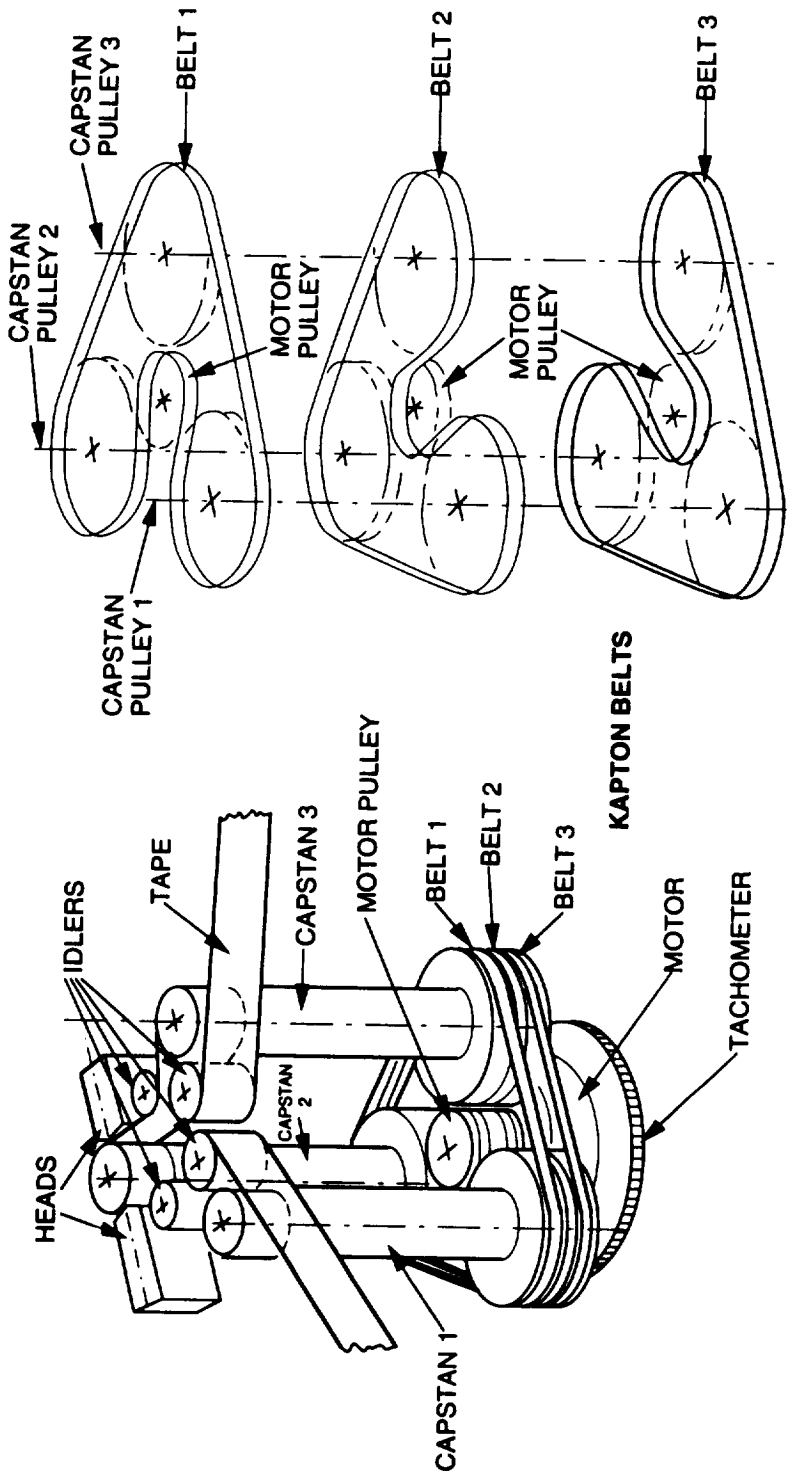

Figure 7.
Three Capstan Drive System
Drawing courtesy of Odetics, Inc., Anaheim, CA

of the tape. This current profile requires the knowledge of tape position to determine what the nominal motor current should be for a given operation.

The drive system for the three capstans is shown in Figure 7. The motor drives a central pulley that has three Kapton belts wrapped around in the configuration shown. This approach guarantees that all three capstans run at the same speed and do not introduce any drivetrain noise in the tape motion. The wrapping technique of the belts minimizes the radial load on the motor bearings providing for a longer life. The tachometer (encoder) wheel is connected directly to the motor rotor to maintain the highest speed accuracy during slew and record modes.

The tape recorder contains a total of 21 preloaded pairs of radial contact ball bearings. All of the bearings are mounted in housings and on shafts of the same material as the bearings (440C) to minimize changes in the drag torque due to thermal expansion. When the recorder was assembled, the drag torque of the bearing pairs was measured and screened for applicability. Only assemblies with acceptable drag torque and ripple are used in the final mechanisms. All bearings are lubricated with EXXON ANDOK C. This grease is filtered to 10 microns absolute and applied to the bearings through a syringe. This technique is used to maintain a very accurate volume of grease and even distribution within the bearings.

The tape recorder contains a total of five heads. Two of the heads are for playback, two of the heads are for recording, and the fifth head is a dummy head. Many of the recorders that had a lot of flight heritage prior to the Galileo build used a dc erase head in the fifth head location. Since the surface of the head is also a tape guide, the dummy head was installed for the purpose of maintaining the tape path heritage. Figure 8 shows the construction of the dummy erase head. The interface to the tape, the two sapphire rods, is the same as the previous machines from which the heritage was obtained. The four active heads are constructed of AlFeSil which is a standard recorder head material.

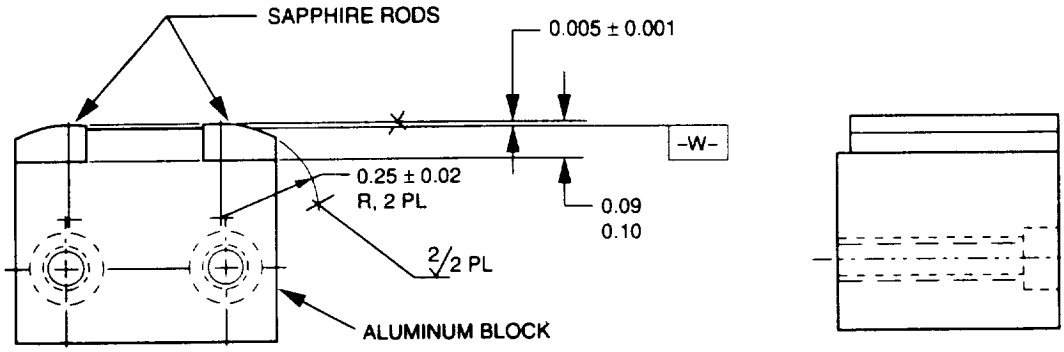

Figure 8.
Dummy Erase Head Construction

Failure Analysis

A complete study of the recorder mechanisms was performed following the anomaly on October 11, 1995. This effort produced a fault matrix that pointed to the following failure possibilities:

1. Tape slippage at the capstans
2. Tape sticking to the dummy erase head
3. Tape sticking to a roller on the BOT side of the drive

With this knowledge, the recorder could be operated in the forward direction and the data from this operation would provide more information on the possible failure. On October 20, 1995, a test was performed that moved the tape forward in playback mode for ten seconds. The motor current from this test is shown in Figure 9 and showed a high startup current with all recorder status and operations nominal afterward. The

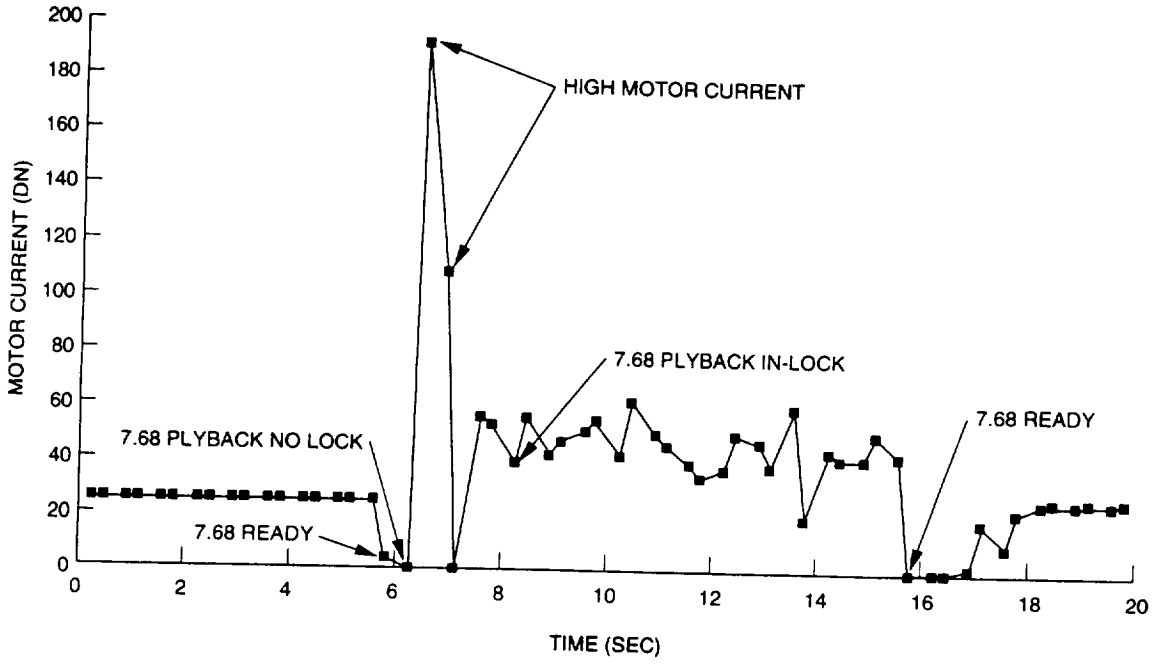

Figure 9.
Motor Current Telemetry
10/20/95 Spacecraft Recorder Test

tape position is recorded with the data on the tape and the playback information showed the tape never moved during the rewind anomaly. This indicated that the tape recorder was still usable and the capstans must have slipped on the backside of the tape. Since there was concern that the tape was structurally compromised where the capstans spun against it, the next motion of the tape recorder was to wrap the compromised section onto the reel. During this motion there was a drop in the servo lock signal indicating an out of lock condition. Since the move was done in the playback mode, this indicated that the data on the tape was damaged at the drop out point (since the servo lock signal is derived from the tape data in this mode). Previous

motions of the tape recorder were researched and two other cases of unexplained tape position error were found. The characteristics of each of the three failure situations are listed below (the preceding numbers are the year - day of year):

1. 95-284: 806.4 kbps rewind failure.
    - No leader indication after 15 hours at 806.4 kbps reverse slew.
    - Motor current not erratic.
    - No loss of servo lock.
    - Incremental tape position pulse rate consistent with commanded speed.
    - No motion of tape as determined by subsequent recorder operation.
    - Initial high motor current at startup of subsequent tape move.
    - Servo lock drop out after moving tape 20 inches forward from the anomaly position.
2. 95-186: 806.4 reverse rewind failure for 4.4 seconds near center of tape.
    - Tape position telemetry count after completed rewind was 83 while the expected count was 191.
    - Only slip in reverse could account for this discrepancy since forward slip would produce an ending count higher than the expected value.
3. 95-258: 7.68 kbps reverse record failure near center of tape.
    - Motor current 70 DN higher than expected for the first eleven minutes of a 22 minute move.
    - After an 806.4 kbps slew to the end of the tape, the end was reached 155 tape position pulses earlier than expected.
    - 155 pulses early is consistent with eleven minutes of tape slippage in reverse at 7.68 kbps.

Note that all of the failures occurred while the tape recorder was operating in the reverse direction. In January 1996, a tape conditioning operation (consisting of winding the entire tape from one reel to the other) was performed that produced another (fourth) sticking failure with the following signature:

4. 96-019: 100.8 kbps forward playback to 7.68 kbps reverse playback.
    - Motor current 80 DN higher than expected with servo in-lock at 100.8 kbps forward playback.
    - 7.68 kbps reverse playback showed servo out of lock.
    - 7.68 kbps forward playback was then executed and showed an initial high motor current.
    - 7.68 kbps reverse playback was executed again and showed nominal tape recorder operation.

The fault matrix was updated with the four failure signatures listed above incorporated. This led to a single conclusion for the failure that could produce all of the failure signatures. This matrix is shown in Figure 10. The failure signatures are listed above

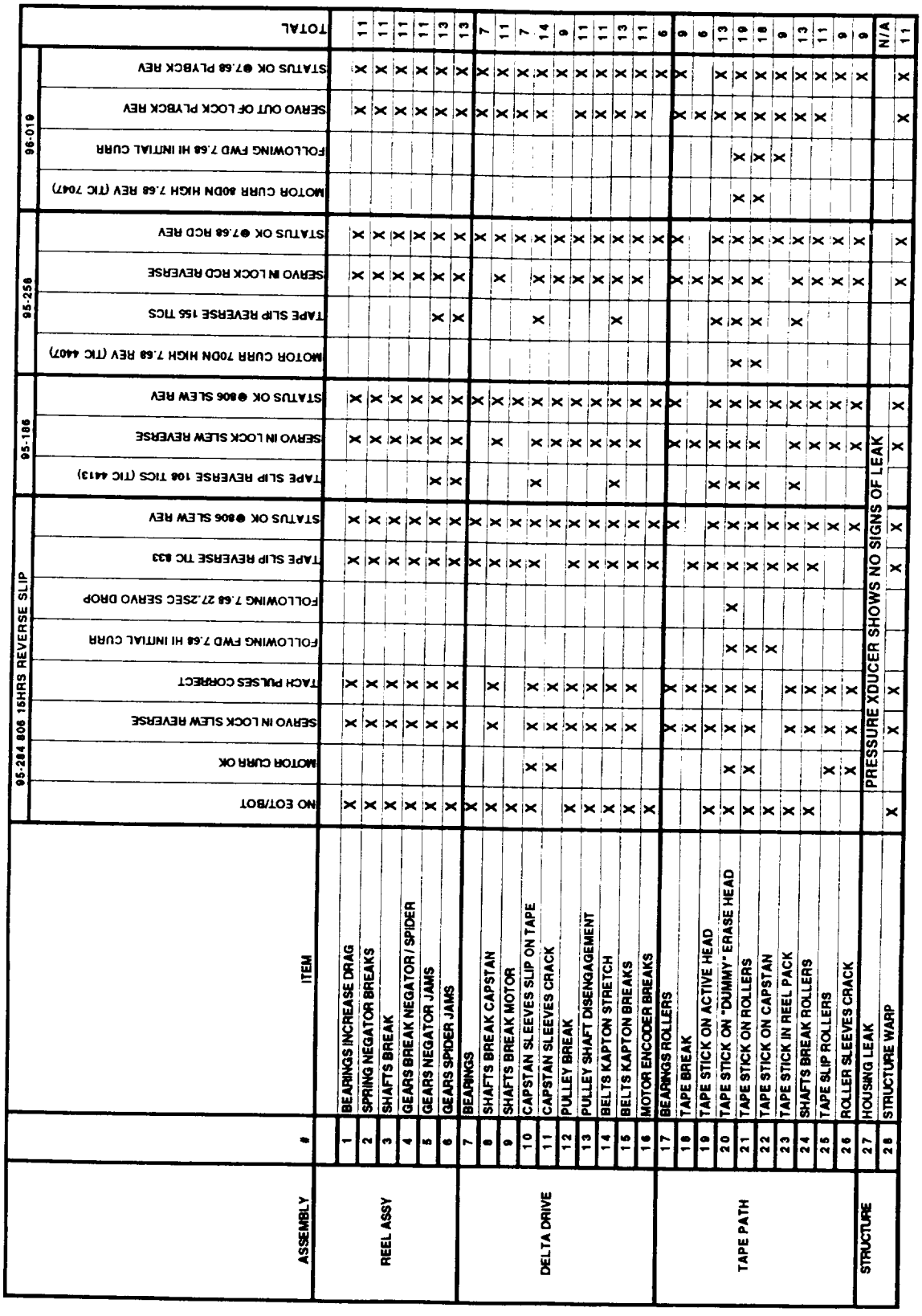

Figure 10.
Tape Recorder Mechanical Fault Matrix

each column and the failure scenarios are listed to the left of each row. The presence of an X indicates that the failure scenario could account for that particular signature. The total number of X's for each scenario are listed in the far right column. Only the failure scenarios that have an X in all of the columns are candidates. The tape sticking to the dummy erase head is the only scenario that fits all of the signatures.

Failure Mechanism

Once the failure scenario had been identified, the next questions were how does the tape stick to the erase head and why don't all of the recorders built by Odetics have the same problem. A significant amount of testing was performed to answer these questions. Several sticking mechanisms were investigated while a search for spare recorders of the same vintage took place. The result of the search yielded a Magellan spacecraft spare recorder that was built at the same time as the Galileo recorder and used the same lot of magnetic tape. This spare recorder was obtained and operated to see if it exhibited any of the sticking characteristics that the Galileo flight recorder had. After the first move to the end of the tape, the Magellan recorder stuck with the same signature as the Galileo flight recorder.

After the Magellan recorder became stuck, it was carefully opened and inspected. The tape had stuck at the erase head (the Magellan units used the dc erase head function and had an active head at this position with the same sapphire rod interface) and there was a visible film of brown residue on the head. The head was then removed for inspection of the debris. The debris was chemically analyzed for composition and found to be composed solely of magnetic tape constituents. A diagram of the debris distribution on the head is shown in Figure 11. Note that the debris is located on both sapphire rods yet appears to be interleaved (as if the debris from one rod broke off and was transferred to the other rod). This investigation found that the sticky stuff is in fact the normal tape debris generated by the passing of tape over the erase head.

The best model identified to date for depositing tape constituents on the erase head maintains that the generation of debris from running tape over the erase head is a natural process that occurs with new tape. New tape is naturally abrasive and "wears in" during the first operation of the machine. The sapphire rods on the erase head promote a high tape wear rate (compared to the AlFeSil active heads) as observed in laboratory tests. This wear-in process creates the tape debris as well as wears flat spots on the sapphire rods. A large portion of the tape debris is swept up by the tape into its surface. After a sufficient amount of tape is passed over the head, the wear rate drops to essentially zero. This was verified by taking a worn-in tape and running it through a machine with a new sapphire head for two million feet. The result was that no discernible tape debris was generated. However, when a new tape is installed with a new head, the tape produces visible amounts of debris in less than two thousand feet of travel.

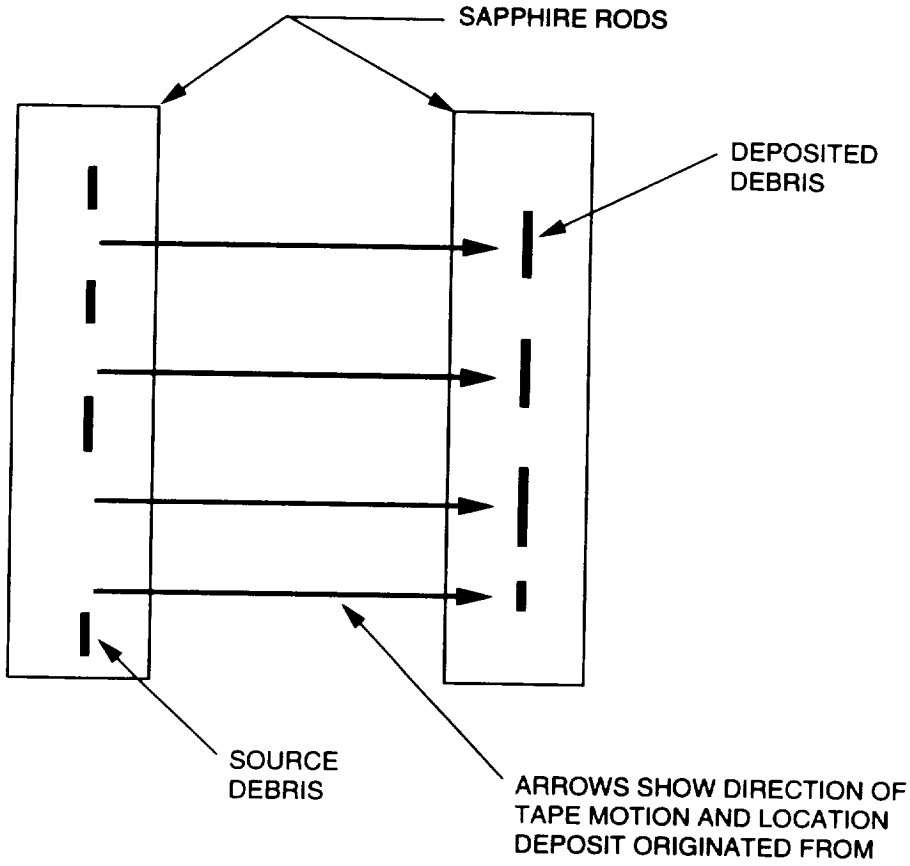

Figure 11.
Magellan Recorder Erase Head Debris Distribution

This information led to the development of a debris model, consistent with all data uncovered to date. The required order of events that leads to a sticking recorder are

1. New tape is installed and operated in the machine. This process wears the tape and erase head sapphire rods, producing debris.
2. Once the tape recorder meets its performance requirements (but prior to completion of the debris generation phase), the machine is thoroughly cleaned by Odetics and then sealed for flight.
3. The tape machine is sealed with the appropriate atmosphere inside.
4. The tape continues to generate significant amounts of debris until its high wear cycle is complete.
5. This generated debris is collected outside of the tape-to-head contact area, presenting no threat to recorder operation.
6. At some point in flight and for unknown reasons, a portion of the debris beaks off the collection area and is swept by the tape into the tape-to-head contact area on the opposite rod.

7. The debris caught in the contact area is worn by the moving tape causing an intimate contact area with a resultant stick.
8. The tape is broken free from the head by operating the recorder. This severs the debris leaving some debris stuck to the tape and some debris left behind in the contact area.
9. The debris left in the contact area acts as a gathering agent and collects more debris from the tape.
10. Steps 7 through 9 repeat.

The tape debris collected at the head is currently believed to contain a high concentration of hydrolysis products. This would explain the sticky behavior of the material. Two tests have been performed to verify this hypothesis. The first consisted of applying a solution of hydrolysis products to the erase head and operating the tape recorder to see if the sticking performance matched the observed behavior on the flight unit. The second test involved putting a reel of unused tape from the same lot as the Galileo flight tape onto the recorder. This tape has hydrolysis products on the entire oxide surface as determined by chemical analysis. The recorder was then operated to produce the sticking condition. The results from both of these tests showed that the sticking behavior of the tape matched the flight unit for a time. Eventually, the sticking phenomenon disappeared because all of the debris deposited on the erase head was removed. This result is consistent with what was seen on the Magellan flight spare unit. When the tape was pulled off the head, the debris was sheared, removing some of the debris from the head. If this process continues every time the tape is torn from the head, the quantity of debris available to cause the tape to stick will continue to reduce to the point where the tape no longer sticks.

To answer the second question of why don't all of the Odetics tape recorders stick, the entire operational history of three units was investigated. The three units were:

1. The Galileo flight unit on the spacecraft
2. The spare Galileo flight unit located on the ground
3. The spare Magellan flight unit located on the ground

The spare Galileo unit was built at the same time as the unit on the spacecraft and has never shown any evidence of the tape sticking. The assembly and testing history suggest that the difference between the units that stick and others that don't is the amount of tape passes put on the machine prior to the final cleaning and closing of the unit. This is consistent with the stick model because the units that stick had not completed their high wear cycle and so continued to produce debris in significant quantities after the units were sealed. On other units, the debris generation had dropped to the nearly imperceptible level prior to final cleaning at Odetics and no longer produced enough debris to cause the sticking phenomenon throughout their entire life.

Galileo Tape Recorder Operation Strategy

All of the testing that has been performed with several sticking tape recorders has shown that the magnitude of the stick does not exceed the ability of the motor to break the tape free by operating the recorder in the forward direction. The limiting factor in the ability to release the tape from the erase head is the drive motor stall torque. The stall torque can produce about 32 ounces of tension in the tape at the erase head. This tension is not enough to break the tape but is about 30% greater than the strongest stick measured during all of the ground testing.

The stick model (item 7 above) requires the debris on the head to be worn in order to obtain an intimate contact area with the tape. This implies the need to run a minimum distance of tape over the head before a stick condition exists. The data from the flight recorder indicates that this is the case. If the recorder is only moved a short distance, the tape will not stick to the erase head and there is no danger in moving the tape in the reverse direction. The current Galileo strategy is to always move the tape recorder in the forward direction for a short distance prior to any motion in the reverse direction. To date this strategy has proved acceptable since the spacecraft has had five encounters consisting of over twenty reverse operations of the tape recorder per encounter with no detectable slipping of the drive. Any slipping events would be detected by the tape position telemetry not being consistent with the expected position.

Conclusions

The Galileo flight tape recorder is critical to the completion of the spacecraft's mission to study the Jovian system of moons and the giant planet. The rewind anomaly that occurred on October 11, 1995, seriously threatened the mission's data return. After exhaustive review of the tape recorder design it was determined that the recorder could be operated and the tape was sticking to the erase head in the machine. The cause of the tape sticking to the head was traced back to the tape itself and the natural generation of debris. The current model indicates that the bulk of the tape debris is generated during the early operation and testing of the recorder. This high debris generation at the start of the recorder's life coincides with the maximum tape and head wear period. The major factor that determines the potential for tape sticking in a particular recorder is where in the tape/head wear cycle the erase head was last cleaned prior to sealing the unit for flight. Testing also indicates that the wear rate of the sapphire rods used as "rubbing surfaces" on the erase head is significantly greater than the AlFeSil material used in the other four heads. This characteristic results in the tape debris deposition occurring mostly at the erase head. The continued production of debris inside a closed and sealed recorder could then lead to a sticking condition at the erase head. Once a machine has set up a sticking condition the recorder must be operated in a certain way to prevent tape slippage. All tests indicate that several sticking events can remove the debris from the erase head until the tape no longer sticks to the head. This means that the possibility of the Galileo flight recorder problem healing itself exists, leading to a recorder that operates normally in the future.

References

1. Johnson, M. R. "The Galileo High Gain Antenna Deployment Anomaly," Proceedings of the 28th Aerospace Mechanisms Symposium, p. 359, May 1994.
2. Cuddihy, E. F. " Aging of Magnetic Recording Tape," IEEE Transactions on Magnetics, Volume MAG-16, NO. 4, July 1980.
3. Cuddihy, E. F. "Kinetics of Humid Aging of Magnetic Recording Tape," IEEE Transactions on Magnetics, Volume MAG-18, NO. 5, September 1982.
4. Cuddihy, E. F. "Hygroscopic Properties of Magnetic Recording Tape," IEEE Transactions on Magnetics, Volume MAG-12, NO. 2, March 1976.

Acknowledgments

The work presented in this paper was made possible by the excellent technical support from the tape recorder manufacturer, Odetics, Inc. of Anaheim, CA.

This work was performed at the Jet Propulsion Laboratory, California Institute of Technology, under a contract with the National Aeronautics and Space Administration. Reference herein to any specific commercial product, process, or service by trade name, trademark, manufacturer, or otherwise, does not constitute or imply its endorsement by the United States Government or the Jet Propulsion Laboratory, Pasadena, California.

Design Improvements for a Second Generation Mirror Gimbal

Scott P. Stanley*
Ruben Nalbandian*
Jeffery T. Williams*

Abstract

Space-borne instruments directed towards the study of the Earth are assuming greater importance as global resources are depleted and man's effect on the environment is becoming more pronounced. In support of one of these scientific inquiries, Schaeffer Magnetics developed a Scan Mirror System (SMS) for an Earth-study instrument which was recently placed into service. After this initial delivery a second generation system was developed, improving the performance of the original unit and adding additional functionality. This paper describes the Scan Mirror System with particular emphasis on the Mirror Gimbal and discusses the performance enhancements and lessons learned during the development and manufacturing phases.

Introduction

Mission

Man's intervention has accelerated changes in the Earth's environment to a rapid pace. Understanding the processes of the environment and monitoring changes are key to evaluating man's influence and possible future results. To gather the data required by the scientific community to evaluate these phenomena, scientific satellites whose primary mission is Earth observation are being developed by the international community. Sophisticated optical devices are crucial to these data-gathering missions, and Schaeffer Magentics has supported and continues to support these instruments through the development of advanced scan mirror systems.

Scan Mirror System Description

The principal function of both Scan Mirror Systems is to provide fine pointing and tracking of a mirror used to illuminate a sensor array within the instrument. The systems presented in this paper include a cantilevered two axis mirror gimbal and a microprocessor based servo-controller closing the loop around a sun-position error signal sent from the spacecraft. Figure 1 is a view of the system.

* Schaeffer Magnetics, Inc., Chatsworth, California

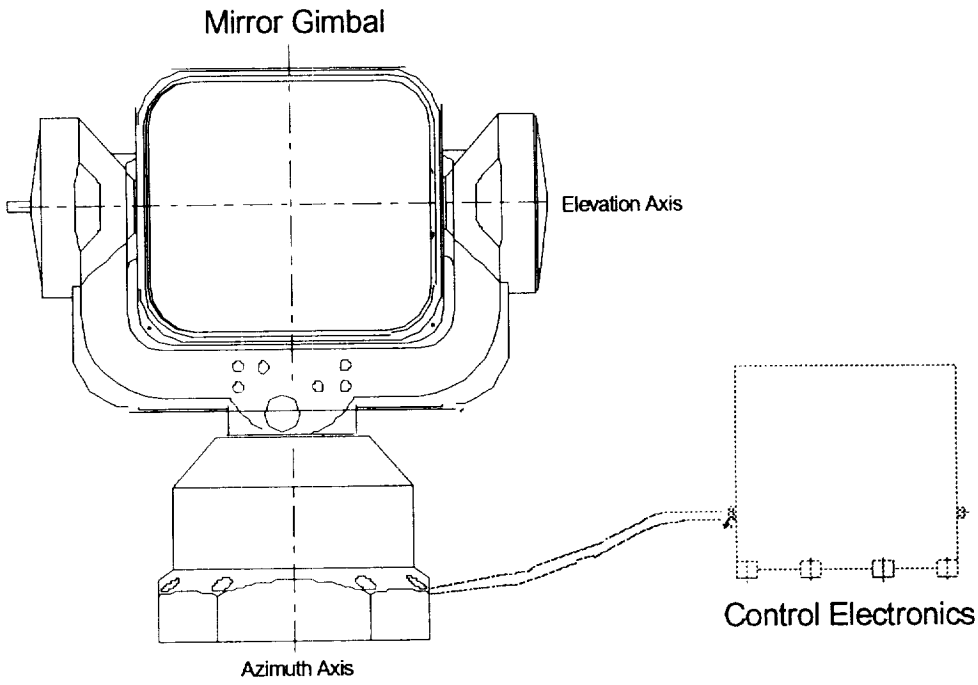

Figure 1. Scan Mirror System

The following are system requirements with key design implications:

- Support required mirror motions
- Accommodate specific interface requirements
- Provide constant velocity scanning
- Provide precise mirror positioning
- Maintain pointing accuracy and optical performance during and after exposure to environments
- Provide telemetry feedback to sun tracker and control assembly
- Minimize weight

The system is designed to meet the following specific functional characteristics:

Position Control

- Settling time less than 1 second at 1 degree command
- Steady state accuracy and repeatability less than 6.81 arc seconds
- Resolution of 0.681 arc seconds
- Rate limiting to 2 deg/s
- Acceleration limit of 20 deg/s^2

Rate Control

- Resolution of 0.00039 deg/s
- Settling time of 0.15 s after command scan mode
- Steady state accuracy of ± 2% minimum

Tracking Control

- Track acquisition less than 4 seconds with tracking accuracy of less than 8 arc seconds

Control Architecture

Each SMS is a computer-controlled two channel servo system. Three performance modes are required: position control, tracking, and scan. The positioning and scan modes are common to both systems, while the scan mode is an added feature to the second generation SMS. The scan mode requirement calls for constant velocity at 0.02 deg/s ±10%. Since this is a direct drive system using DC motors, driving at this very slow rate presents problems of fine motor control, feedback signal generation, motor characteristics, and control system architecture.

The performance requirements for the three modes are:

1. Position Mode: 21 bit resolution, 6 counts steady state error
2. Track Mode: Error signal tracking, 0 to 0.06 deg/s rate
3. Scan Mode: Constant velocity regulation, 0.02 deg/s ±10%

Schaeffer employed a systems engineering approach that functionally allocated performance characteristics that were necessary to ensure the performance of the specification requirements to each subsystem. As design and prototype testing progressed actual values and characteristics, such as scale factors, filter characteristics, bearing friction levels and cable windup characteristics were in turn incorporated into the computer simulation. Subsystem performance was predicted and tracked and thereby overall system performance managed during development by constant iteration and control. Figure 2 is the overall simulation block diagram of the system.

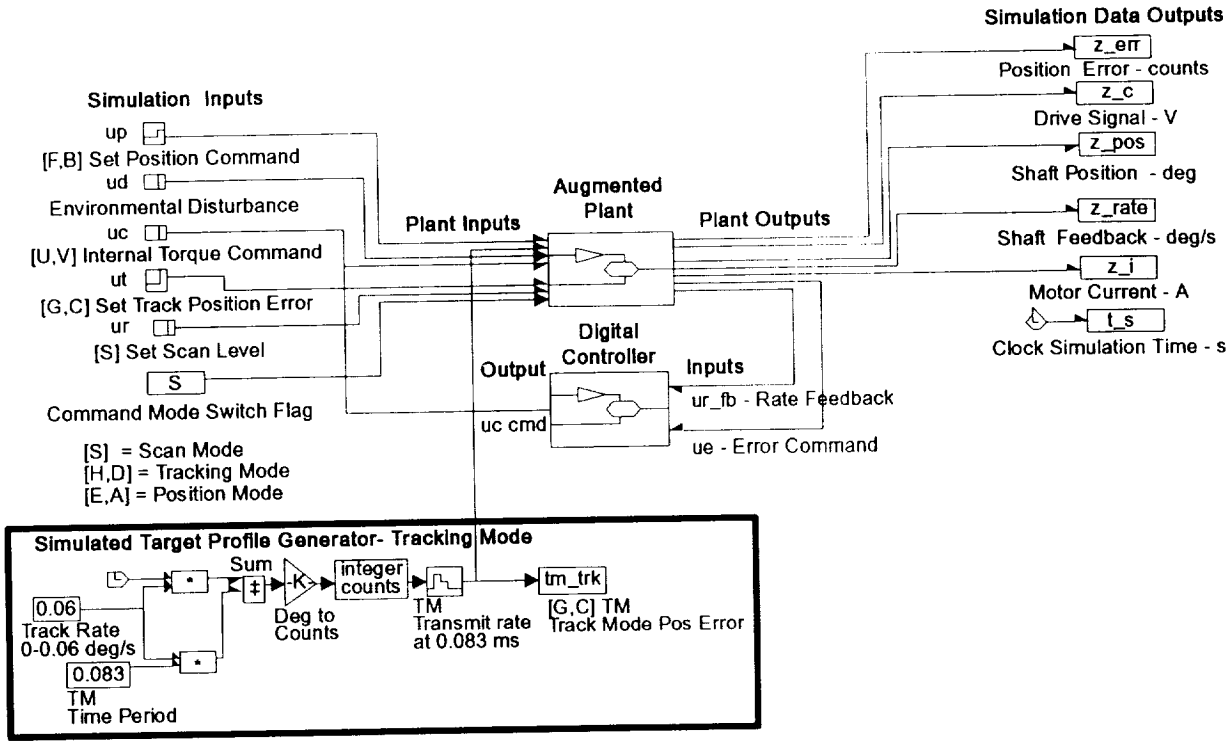

Figure 2. Control System and Augmented Plant Simulation

Electronics

The electronic design solution employed by Schaeffer based around the high speed Analog Devices AD2100 digital signal processor, replacing the 8088 processor used on the first generation system. The solution was found to be primarily centered around the resolution of the feedback signal with sufficient dynamic range to provide control authority over the target speed, with very high bandwidth servo control. This provides the tracking and disturbance rejection necessary to overcome the non-linear effects of stiction, cogging, detents, cable wrap and temperature.

The system feedback is provided by a two-speed 32X resolver. The resolver outputs were processed in the first generation SMS by a Natel 1625 resolver to digital converter (RDC) operated at 100 Hz. While this performance was adequate for the initial requirement, the analog velocity output was not sufficiently accurate for the range of rate control required by the second generation system. Continued support of the Natel component was also in question.

As a result the RDC was replaced in the second generation SMS by Analog Devices AD2S80s to provide 2000 Hz bandwidth for rate control. The RDC is configured from

two S-level monolithic RDCs. These are used in a coarse/fine arrangement with additional combining logic for a 21-bit resolution position output and 7.5 arc seconds of accuracy. The 21-bit position resolution is accomplished by allocating to each resolver output a separate AD2S80 to the fine and coarse channels and combining the digital output to form a 21-bit word. Additionally the fine AD2S80 is used to generate an analog signal proportional to velocity. This velocity signal is then sampled with 12-bit analog to digital converter (ADC). Because the velocity range spans three orders of magnitude (0.02 - 2.0 deg/s), the ADC has a software selectable gain to match the input to the velocity range depending upon the operational mode.

The motor driver is a two-phase sine drive that is controlled by two 14-bit digital to analog converters (DAC), one for each servo channel.

The system servo software is written entirely in AD2100 assembly level code. The controller code operates the two servo channels simultaneously, and regularly updates the telemetry even at 12 hertz. A background loop processes spacecraft controller telemetry requests or any commands which may require a mode change. The servo loop operates at 600 hertz with a 10 to 20 hertz small signal bandwidth depending upon the mode - position or velocity control. The loop is fundamentally a constant rate velocity regulator that can switched in and out of position control. The control architecture requires both the 21-bit position and the selectable range 14-bit velocity feedback for control. Because of the very small speeds detents at very small angles appear as localized compliances, in effect giving the otherwise rigid body system a flexible body mode within the control loop. In order to mitigate this effect, an inverse non-linear lookup table inversely proportional to the detent characteristics is applied to the DAC drive signal, linearizing the motor for control purposes[1]. There are also two single stage pole/zero compensators to further overcome the compliance effect.

An RS 422 serial interface is employed with control and telemetry events occurring at 12 Hz or every 0.083 seconds. These events are governed by an extensive command and telemetry protocol.

Main Discussion

Mirror Gimbal Description

The mirror is supported by a two-axis gimbal, the inner gimbal providing elevation motion and the outer gimbal rotating about the azimuth axis. The mirror is 170 mm (6.7 in) by 200 mm (7.9 in), and the mirror gimbal assembly stands 400 mm (15.75 in) tall maximum. The inner gimbal is supported on a one-piece machined yoke structure which is optimized for minimum weight and maximum stiffness. The azimuth and elevation axes intersect. A detail of the mirror gimbal is shown in Figure 3.

---

[1]See Franklin, Powell, Workman, Digital Control of Dynamic Systems, Second Edition, 1990. P 561, Nonlinear Control Structures for a discussion concerning inverse non-linear control (INL).

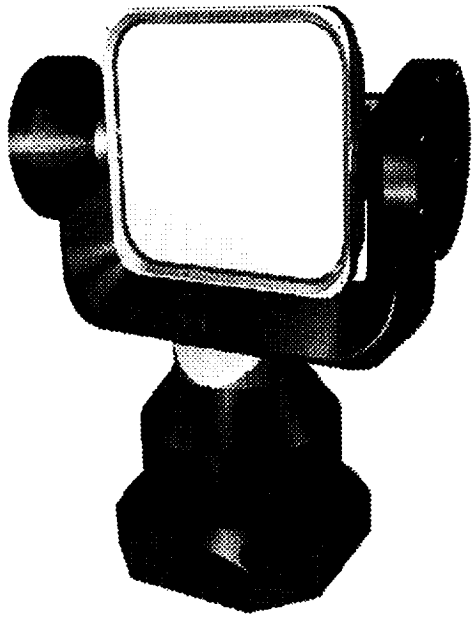

Figure 3. Two Axis Mirror Gimbal

Rotating components required for operation of the gimbal include dc motors, resolvers, and the electromechanical brakes. For both axes, motors and resolvers are mounted on one end of the shaft, while the brake is mounted on the other end of the shaft. Motor and resolver stators are mounted directly in the motor housings, providing short and efficient thermal conductive paths for dissipated heat.

Electrical service to the gimbal is provided through a molded cable-wrap module housed in the pedestal that carry conductors across the rotating interface. Additionally, leads to the motor, resolver and the brake on the inner gimbal axis are passed through the cable wrap on the outer axis.

Mirror

The original mirror was a machined aluminum construction supported on a magnesium mount. The mirror is designed to provide a clear aperture of 200 mm by 170 mm, with a maximum offset of 10 mm from the rotation axis. The mirror was designed for stiffness and detailed finite element analysis was performed to evaluate deformations during not only dynamic loading but also through temperature variations and during 1 g testing. Optically the design is suitable for visible spectral and far infrared regions, from a wavelength of 700 nm to 13 μm. The mirror surface is gold plated and polished. The mirror is mounted on three-point kinematic mount to maintain optimum surface figure.

Motors

The inner and outer gimbals are driven by conventional direct drive, two-phase brushless dc motors with resolver feedback. The motor design employs a permanent magnet rotor and a wound stator. Sine/cosine commutation of each motor is accomplished using the outputs of respective 32X resolvers on each axis. This requires that the motors have 64 poles (32 electrical cycles per mechanical revolution), and that they be two-phase. By using sine/cosine commutation, the torque ripple that would be associated with the sinusoidal torque characteristic of each winding is eliminated. This constant torque response to current input independent of shaft angle allows the servo loop gain to be constant but more importantly allows the drivers to operate more efficiently. Proprietary design software and fabrication processes were used to produce exceptionally smooth low ripple motors.

Resolvers

Position feedback and motor drive commutation is achieved by use of dual speed resolvers on both elevation and azimuth axes. The resolver, a 32-cycle design, provides sine/cosine commutation signals, and when used with a resolver-to-digital converter, provides velocity feedback to the internal servo controller and position data for transmission by the serial interface. The use of sine/cosine commutation to the motor drive windings produces a flat torque characteristic with respect to angular position, and permits drive amplifiers to operate with higher power efficiency than would be attainable if switched commutation were used.

Bearings

Rigidity and stability of the structure were the primary design drivers, with structural strength a concern in the launch phase. Ball bearings were selected to support the output shafts for their ability to withstand launch loads while minimizing operating drag. The elevation axis is supported on both ends with DF duplex pair bearings, while the azimuth axis is supported in cantilever fashion by two pairs of duplex pair bearings. The tail end bearings of the azimuth axis are floating to accommodate thermal changes.

Structure

The structure is a conventional two-axis inner and outer gimbal arrangement with intersecting axes of rotation. The basic cantilever construction is mandatory because of the required mounting arrangement and field of view, and this is implemented with machined aluminum and magnesium alloy. The cantilevered gimbal construction provides for ± 45 degree movement in azimuth axis and ± 15 degree in elevation axis. Important design elements in this area are the previously discussed support bearings on both axes. Bearings are important structural elements, especially at launch, but their drag torques must be controlled to avoid impacting the performance of the servo.

Brakes

Use of brushless DC motors requires an external means of holding position for launch and power-off holding of position. A spring-applied brake (power to release) is part of the gimbal design, this basic design having been used on other programs at Schaeffer. Brake release is accomplished with application of power to a brake coil.

Power-off holding or braking of position is provided on both axes by friction discs, with pressure applied by springs so that the braking force is passive - no action or application of electrical power is required. An electromagnetic coil is mounted in the housing next to the friction discs, and the friction discs are mounted on the ferromagnetic armatures, which complete the magnetic circuits. Application of voltage to the coil produces a magnetic attractive force that draws the armature away from the brake discs, thereby disengaging the brakes.

Required brake maintaining torque is approximately 0.34 N•m (48 in•oz) on both axes. The available operating radius is sufficient to readily produce this torque.

Profiled application of current to the brake coil was used with a short duration (100 ms) relatively high current to initiate pull-in of the armature, tapering to a low maintaining current during normal gimbal operation in which the brake is released. The brake coil is relatively low impedance with a resistance of approximately 45 ohms at room temperature. Steady state power dissipation during servo operation is less than 0.5 watts.

Friction materials were chosen for friction coefficient and cleanliness of operation (no particulate generation). Energy absorption and dynamic effects are not considerations, since the brake is applied only to members that have ceased rotation. The rotating disc has been designed for torsional rigidity but with axial compliance so that excessive net axial forces are not exerted on the bearings when the brakes are applied.

Cable Wrap

An important element of the design is the power-transfer device which carries electrical service to the inner and outer gimbal components, and is a potential source of disturbance torques.

Transfer of electrical power across a rotating interface is always a requirement for a two-axis gimbal - at a minimum, the inner gimbal must be serviced.

For small travel angles, simple flex cables can be used. For larger angles, however, unsupported cable lengths become too long and cable position too indeterminate. This is the case with the SMS. A managed, contained cable wrap was necessary. These have been built in two forms at Schaeffer, namely the spiral or clock spring cable wrap and the rolling cable wrap.

The first generation SMS used the clock spring cable management system. To reduce the torque variations on the cable management device, the wires were separated into individual loops supported between flat separator rotating shelves. The clock spring loop directions were reversed in sequence, thereby reducing the torque variations on the system. However these were still of sufficient magnitude to cause the reevaluation of the cable management scheme during the second generation gimbal development.

Second Generation Gimbal Requirements

After the first SMS was delivered and placed into service, changes in requirements for a follow-on system were established based both on evolved customer requirements and also Schaeffer-driven enhancements for margin and producibility improvements.

Several of these improvements centered on the controller. Customer requested changes included the addition of the scan mode and increased component compliance to S-level requirements. Schaeffer modifications included upgrade of the microprocessor and replacement of the RDC components.

Changes to the gimbal requested by the customer centered on structural and mirror issues. The fundamental frequency of the original mirror gimbal dropped below 100 Hz after integration into the satellite, raising concerns regarding coupling into other modes within the instrument. In response the second generation gimbal was required to have an increased first modal frequency of 115 Hz minimum. Mirror performance parameters were modified to match the new mission requirements. These changes included an increase in mirror area, a small reduction in the gimbal height, and a very difficult improvement in mirror surface figure.

Schaeffer wished to incorporate several improvements into the gimbal for the second generation system as well. The original cable management system had proven difficult to assemble and still introduced significant drag into the system. Additionally the brake proved temperamental at low temperatures, requiring a pulse train to disengage after initial stiction. Though this disengagement sequence of initial sticking then release after a series of pulses was very repeatable both during test and subsequently on orbit during initial deployment, it was not a comforting feature and a redesign was deemed desirable. Several other more minor enhancements were also incorporated.

Development Strategy

In order to minimize risk early in the program and garner as much actual data for the simulation as possible, Schaeffer embarked on an extensive prototyping effort. Full prototypes of the revised brake and cable wrap assemblies were fabricated and tested over temperature to verify performance and characterize behavior. Simpler models were built of other areas of concern such as the cable loop for the elevation resolver.

Solid models for all gimbal components were constructed using advanced CAD software, and detailed finite element models were developed to evaluate both structural

and optical performance over the specified environments.

Finally a very detailed structural model was fabricated and tested using many components fully reflective of the final unit. All structural components including bearings were included, as were the cable details which contributed to losses in the system which would have to be overcome by the servo. Model testing was aided by the design and construction of a highly sensitive and accurate loss measurement fixture.

Second Generation Gimbal Development

Mirror

To achieve the very tight surface figure requirements and to aid in meeting the increased natural frequency requirement, a mirror material change from aluminum to beryllium was necessary. The resulting mirror is of machined beryllium construction supported on a kinematic mount, also of beryllium for stiffness and thermal expansion match. Designed for stiffness, the first fundamental frequency is 2606 Hz, outside of the random and sinusoidal dynamic environmental spectrum.

The mirror surface is gold plated and polished and provides the following optical performance:

Reflectivity	>95% λ for 0.75 - 0.785 μM >97% λ for 3.0 - 13.0 μM at angle of 30 - 55 degrees
Optical Figure (irregularity and deformation)	0.8 λ
Surface Roughness (maximum)	80 A

Motors

While no motor design changes were introduced for the second generation gimbal, increases in performance were realized. Insight gained into which fabrication variables contribute to motor performance led to improvements in assembly methods, decreasing torque ripple 75% from the original unit to 9.9 mN•m (1.4 in•oz).

Structure

The goal of the structural design modifications was to raise the natural frequency of the gimbal above 115 Hz. Several factors affected this goal. First the mirror surface area requirement was increased, and adding mass to the end of the gimbal cantilever is detrimental. However the mirror height requirement was slightly decreased, shortening the cantilever, and the customer was able to increase the number of gimbal mounting bolts.

To ultimately achieve the increase in natural frequency it was deemed necessary to design and build the yoke, mirror support and mirror from beryllium. Though costly, the high strength to density ratio was required and as an added benefit using beryllium as the mirror material increased the likelihood of achieving the surface figure requirement.

Additionally Schaeffer utilizes beryllium on a routine basis so the design and processing expertise was already in place.

After initial finite element analysis predicted that the frequency requirement would be met, the structural model was subjected to shock and vibration testing. All components demonstrated structural adequacy, and the first structural mode was measured at 118 Hz.

Brakes

The original brake design showed stiction at cold temperature during qualification and acceptance testing. After application of a few release commands the brake released and performed satisfactorily. This anomaly repeated itself during satellite integration testing and on-orbit deployment.

The design was modified in areas were it seemed the assembly may be flexing, causing binding and the resulting stiction phenomenon. However actual testing over temperature on the enhanced development brake assembly presented similar stiction. Detailed inspection revealed that the sticking was between the brake pad and its mating surface. Since this appeared to be a surface to surface effect, the mating area was slightly abraded by grit blasting and the stiction was completely eliminated. The enhanced brake assembly design with sand-blasted disks was incorporated into the second generation gimbal.

Cable Wrap

Control difficulties had resulted in the original design from non-linearities and higher than expected drag in the azimuth axis cable management scheme. The assembly was also quite labor intensive.

In an effort to reduce torque and facilitate assembly, a premolded rolling cable loop was incorporated. The rolling wrap requires a molded flat cable - its circular curvature is molded into the cable itself rather than being formed by bending a flat cable, and the cable lays in the wrap in planes normal to the axis of rotation. Attachment of the cable to the structural parts of the wrap is on radial lines, the attachment consisting of connectors that terminate the molded cable to a standard wiring harness. Rotation of the joint is accommodated by a rolling transfer of the cable from one plane to the other. The rolling wrap offers low drag torque, short cable lengths, tight cable bend radius, lower weight, but it needs adequate axial dimension. Application of this concept to space-based rotary interconnections is a patented Schaeffer innovation.

Testing over temperature showed an 80% decrease in cable torque to 17.7 mN•m (2.5 in•oz) or less. The tests also revealed that the magnitude and direction of the cable torque changed with direction and position. This was not anticipated but because of the early characterization could be accommodated in the control simulations.

For the elevation axis a simple loop of ultra-flexible cabling was used for resolver connection. Though the cable itself was the same as that used the first unit, the clamping and service loop arrangement were revisited and optimized using a torque measurement fixture. This not only minimized cable drag but also provided accurate data for the control simulation.

Structural Model Testing

The structural model was fabricated not only to verify structural adequacy of the gimbal components but also to measure bearing loss torque both before and after environmental exposure. An additional benefit was the system level torque data available because of the inclusion of relevant segments of the cable management system. A sophisticated fixture was designed and fabricated for these sensitive measurements at Schaeffer and also for subsequent measurements made by the customer.

Special features were incorporated into the structural model for interface with the torque measurement fixture. After attachment, each axis was driven by a smooth running electric motor via a belt drive and large inertia pulley to reduce induced ripple. Torque measurements were made via a highly accurate torque transducer mounted to the fixture drive shaft via a flexible coupling. The torque measurement fixture is shown below in Figure 4.

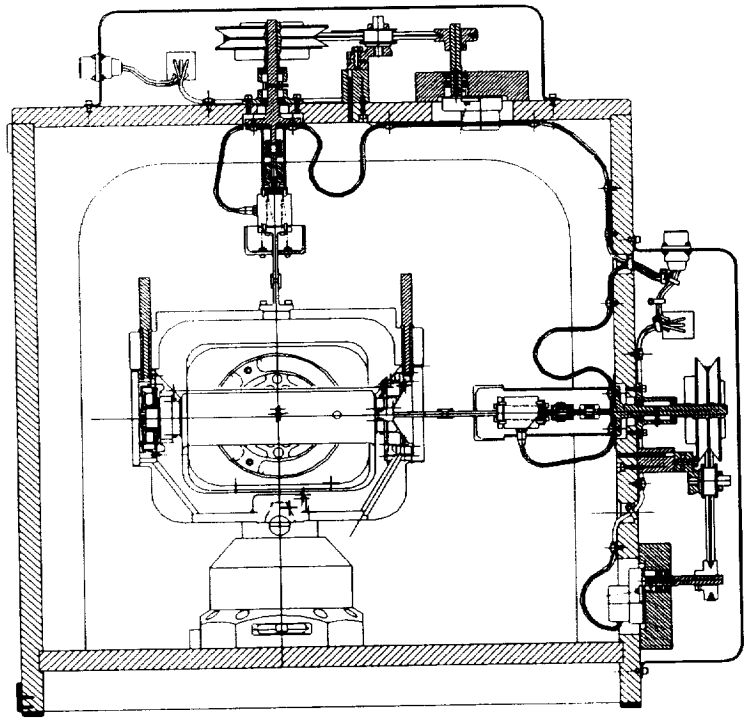

Figure 4. Torque Measurement Fixture

As discussed in the preceding paragraphs, significant improvements in the plant performance were achieved between the first and second generation mirror gimbals. Figure 5 below shows the actual plant performance.

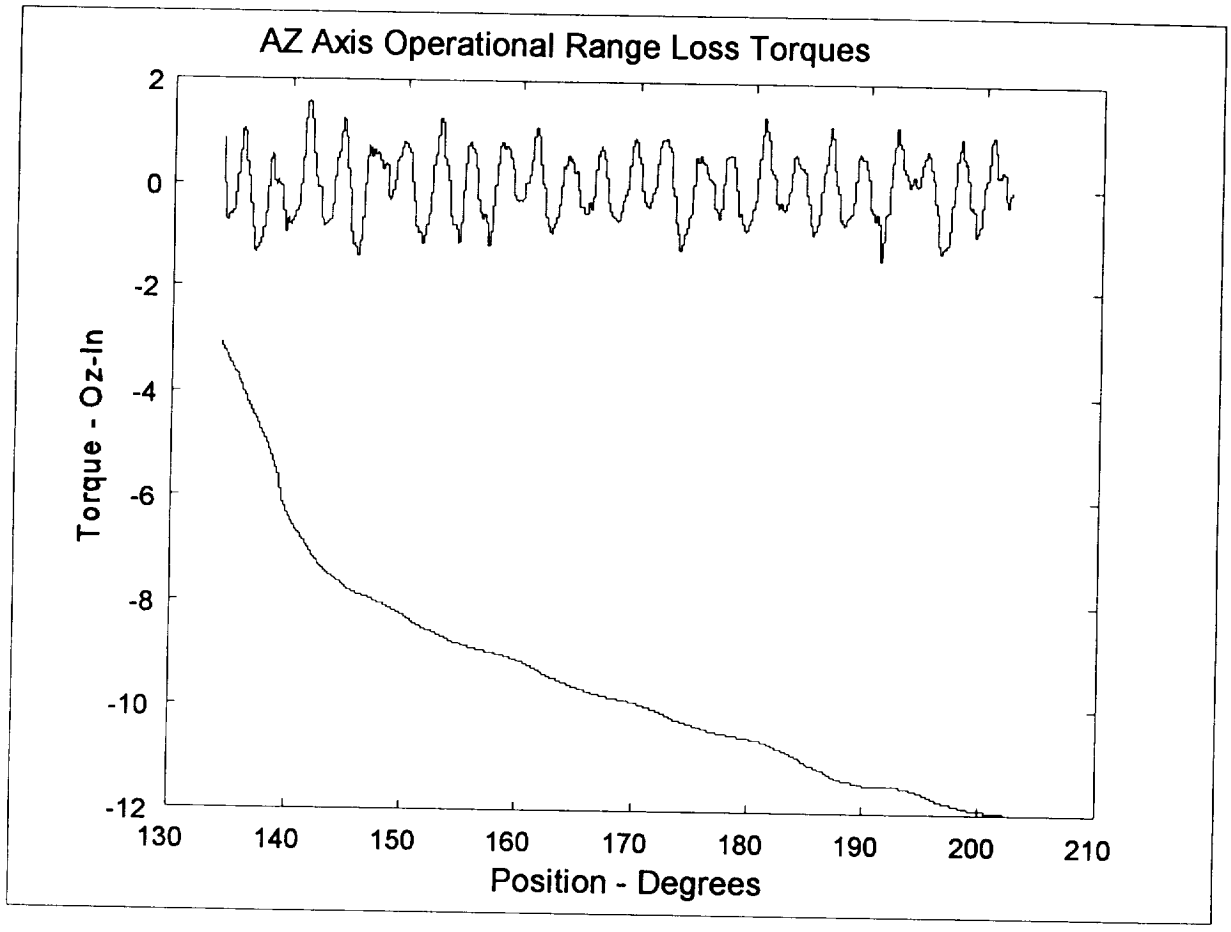

Figure 5. Actual Plant Results

Engineering and Flight Model Testing

The Engineering Model is currently undergoing final integration and entering qualification testing with the assurances provided by the early development and structural model tests. One feature of these flight level tests is devoted Ground Test Support Equipment (GTSE) which allows rapid automated functional testing of the Scan Mirror System. Completely self-contained in a wheeled enclosure, the GTSE allows full functional tests to be performed at any assembly workstation or test site. The GTSE has proved to be an invaluable diagnostic tool during the integration phase, and an added feature is a modem interface which will allow Schaeffer to perform diagnostics even after delivery in support of customer integration.

Lessons Learned

Prototyping

As previously discussed, the root of the brake stiction phenomenon proved to be interaction between the brake mating surfaces rather than a binding problem. The solution of slightly abrading one surface was very simple but the cause was not readily obvious since the phenomena in no way exhibited itself at other temperatures. Subsystem prototyping was not performed as extensively on the first generation unit.

- Prototyping is extremely beneficial, identifying problems early enough for careful investigation and relatively painless resolution.

Plant Characterization

Several loss parameters during the initial development program caused control difficulties for the servo. Loss contributors during the second generation development, particularly the cable management system and slow running motor, showed unexpected behavior.

- Actual measurement cannot be replaced to characterize the behavior of system elements. A simulation is only as good as the input parameters.

Dedicated Test Equipment

Diagnostic tools are crucial during the late assembly and integration periods of system development. Tests must often be run at multiple locations both within a manufacturing facility and also off site.

- A dedicated GTSE rack not only keeps the required test equipment in one place and available, it permits rapid testing and evaluation and provides a readily available diagnostic tool.

Conclusions

Scan Mirror Systems are a key element of Earth study instruments which are becoming increasingly critical to the scientific community. A rigorous, conservative development strategy for these systems reaps benefits even on second generation designs based on already successful systems. Thorough characterization using development hardware is crucial to successful simulations.

Updating Gimbal Actuators for the Long Journey to Saturn

Theodore Iskenderian, Benjamin Joffe and Edward Litty*

Abstract

The Cassini mission requires extraordinary life and reliability from the linear servo-actuators which position the spacecraft's redundant rocket engines. Both commercial actuators and existing in-house actuator designs were studied for this application. Ultimately a device inherited from JPL's Mariner and Viking missions to Mars was selected because of its close match to functional requirements and its flight pedigree. However, several design improvements were necessary to meet life and reliability goals. Special attention was focused on reliability testing of the motor and mechanism at all stages of procurement and assembly because a brush type of DC motor was retained from the old design. These improvements and, in particular, efforts to develop new component sources are discussed in this paper.

Background

The Cassini-Huygens mission to Saturn is a joint effort between NASA and the European Space Agency. Cassini uses a redundant pair of 445-N rocket engine thrusters mounted in a Modular Engine Assembly (MEA) to provide thrust for the following maneuvers:

- In-course trajectory adjustments
- Saturn orbit insertion
- Trajectory control while in orbit around Saturn

The MEA comprises redundant two-axis gimbal subsystems. Each gimbal subsystem includes fuel lines, filters, bearings, structure, and two Engine Gimbal Actuators (EGAs). The EGAs are furnished by JPL to Lockheed Martin in Denver, CO who designed and built both the MEA (Figure 1) and the larger Propulsion Module Subsystem into which the MEA fits [1].

JPL had to choose between either procuring a complete EGA or building the assembly with purchased components. Two considerations drove our decision process: a short schedule and uncertain requirements. Our schedule was critical because we had to deliver tested and proven actuators to JPL's subcontractor in time for it to perform the necessary subsystem tests. Faced with similar concerns, the engine gimbal electronics were designed and fabricated at JPL. In addition to the tight schedule, complex interactions among the various systems involved in the control of spacecraft attitude and many unique spacecraft system constraints made that an easier choice.

---

* Jet Propulsion Laboratory, California Institute of Technology, Pasadena, CA

We had to prepare a Request for Proposal while requirements were still fluid. This process took much longer than anticipated because, at the time, fundamental issues such as launch vibration forces, mass, and power were irreconcilable.

As we pushed hard to define a workable set of requirements, it became apparent that our application fell into a design space that did not include any commercial designs. Instead, some modifications to an existing JPL design, the Mariner/Viking gimbal actuator, which successfully flew on three spacecraft destined for Mars, promised to satisfy all the design constraints. The following narrative is interspersed with lessons we learned as we proceeded with our design process.

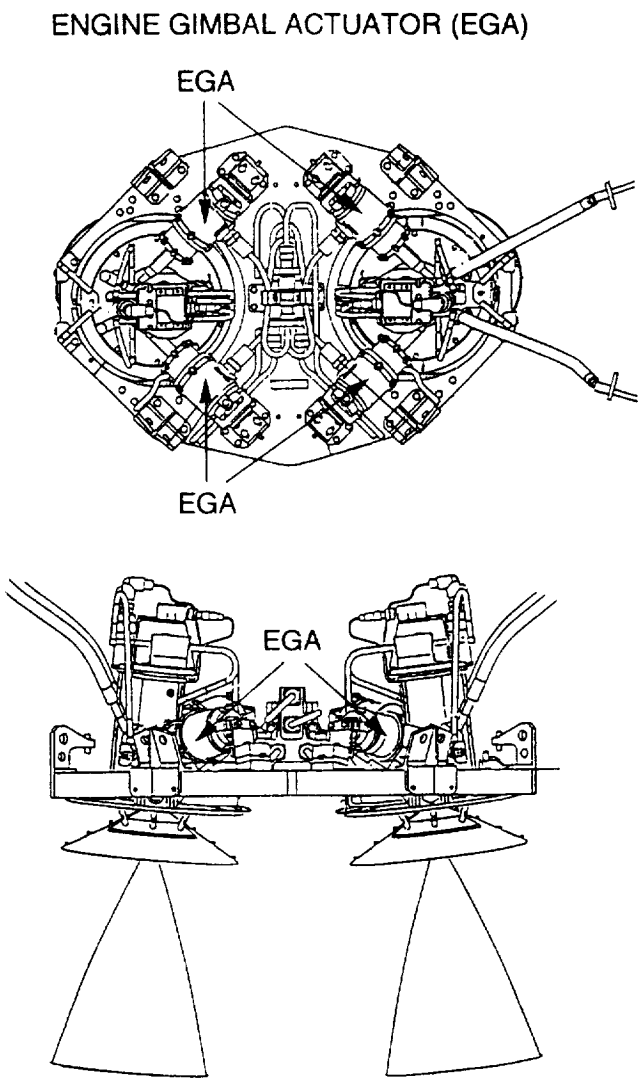

Figure 1

The Cassini Main Engine Assembly as Designed by Lockheed Martin

Choice of Approach

Mariner/Viking Actuator and US Patent

When first published in 1971, the Mariner/Viking linear actuator design was novel enough to earn United States Patent [2] No. 3,660,704 on the basis of improved reliability, responsiveness, and lower weight compared to existing technology (Figure 2). These characteristics were partly achieved by using a DC brush motor whose rotor was mounted directly on the nut of a ballscrew, instead of driving through a conventional geartrain. This design's direct drive approach required only one duplex pair bearing, enhancing reliability. A dust seal separated the

mechanism from debris created by the motor brushes, and the device's output position was accurately sensed by a coaxial LVDT embedded within the ballscrew. The brush motor was particularly attractive because it relied on very simple electronics compared to what is required to drive a brushless motor.

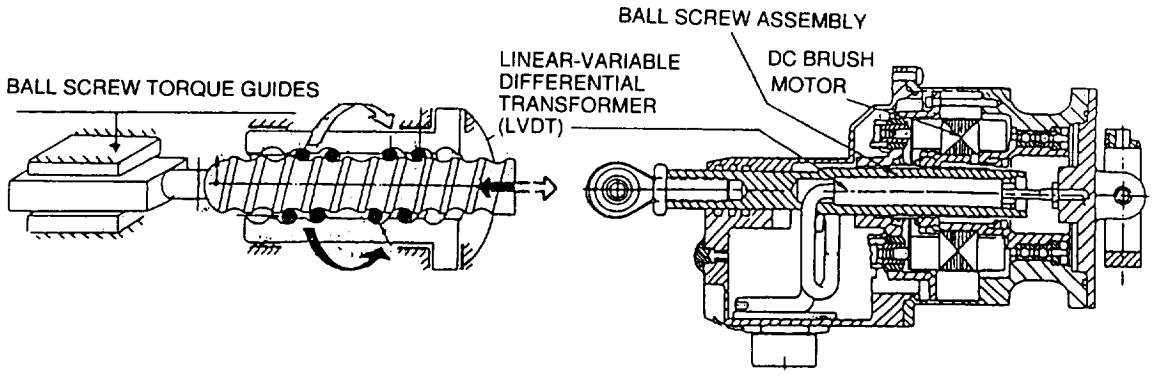

Figure 2

The Mariner/Viking Engine Gimbal Actuator

Requirements Comparison

The relatively short mission durations for Mariner/Viking were the most challenging to reconcile with the new Cassini mission. However, the actual life test results from the Mariner/Viking actuator development were very encouraging. Also, there were no failures or anomalies reported in the earlier missions.

As our investigation of the Mariner/Viking actuator progressed, other problems began to surface. Some of these problems came to light when we disassembled and inspected a Mariner/Viking actuator after more than 17 years in storage. For example, we found:

- The Kynar® shrink sleeve, which wraps the four wire leads of the service loop to the Linear Variable Differential Transformer (LVDT) coil assembly, had become almost glass-hard
- There was a significant amount of brush wear debris present (we could not find a record of how much the actuator had been used)
- The LVDT ferrite probe displayed an alarming degree of wear
- High resistance and high starting voltage on three of the stored units
- The motor rotor had been epoxied to the ballscrew's nut because the small pin used for transmitting torque proved to loosen in operation.

Lesson 1: If you plan to use leftover hardware, test it, open it up and inspect its components as soon as possible.

Solutions to these problems are discussed below in the section on design upgrades. To satisfy ourselves that this basic layout would work, a modified interim design was produced. Figure 3a shows what the Mariner/Viking actuator would look like if it met the functional requirements of Cassini. Figure 3b compares the final design after all modifications to optimize it for the Cassini mission.

Because the requirements were still volatile and there was significant risk of design changes, JPL committed to making the actuator assembly in-house.

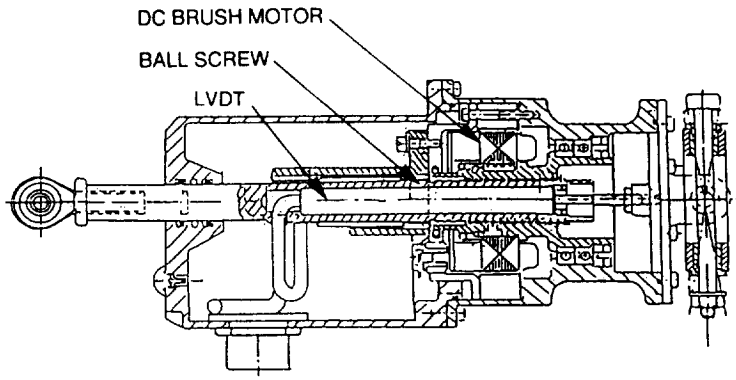

a. Viking Design, But Modified for Cassini Length and Stroke

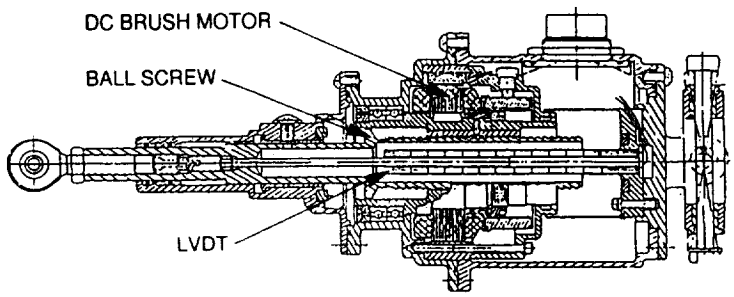

b. Final Design Optimized for Cassini Mission

Figure 3

Interim and Final EGA designs

Lesson 2: Decide on make-or-buy commitments as early as possible.

We established that the basic EGA design was acceptable; parameters such as stroke length, lubricant type, load rating of mechanical components, etc. could all be worked through "business as usual." Enough time remained to do the inevitable redesign work that Cassini's extended duty and reliability requirements demanded. Table 1 summarizes the scope of design upgrades that would be required [3].

Table 1

Design Requirements for Actuator Development

Requirement	Mariner Mars/Viking Orbiter EGA	Cassini EGA	Design Change Code*
Mission Duration	2.8 years	12 years	A, B, C
Longest Engine Burn	45 minutes	3.3 hours	F, K
Total Operating Time	2 hours	142 hours	A, C
Range of Motion	19.9 mm	28.4 mm	C, D, E, H, L
Number of Full Stroke Actuations	100	1,300	C, D, E, H, L
Number of Small Actuations (up to 1/20 of total stroke)	3,000	80,000	A, C, D, E, H, L
External Magnetic Fields: • Static • Dynamic	N/A 5 nT @ 1 meter	2.5 nT @ 1 meter 5.0 nT @ 1 meter	F
End of Travel Stop Integrity	N/A	No damage at full rate impact with 105 kg inertial load	D, G, L
Launch Loads	?	Thrust = 827 N (188 lbf) Lateral =71 G on 2 axes	C, G, I, J, L

* A= Lubricant upgrade; B= Upgrade brush/commutator materials; C= Demonstrate reliability early in program; D= Eliminate flexing LVDT service loop; E= Add flexure rod to reduce wear; F= Change motor magnet material and orientation; G= Added soft stops to end of travel; H= Torque guide upgrade; I= Housing partitioned into modules for easier assembly & test; J= U-joint bushings and spider structure strengthened; K= Motor stator temperature sensor added; L= Ballscrew design improved. [4].

What Spare Parts?

The first difficulty to slow progress was the availability of components for the inherited design. Although some spares had been stocked for the earlier missions, these either turned out to be substandard components or were undersized for the higher projected loads. Other parts simply had to be procured again. This was true for all major components including motors, LVDTs, bearings, and ballscrews.

Design Upgrade Process

Pressurized Design

Our actuators group had experience using pressurized inert gas in spaceflight actuators to help ensure a favorable operating environment . In these earlier applications, nitrogen gas at 136 kPa and a trace amount of Helium for leak measurement were used. These gases were contained with static and dynamic O-ring seals, effectively excluding particulate contamination and loss of lubricant. The use of Nitrogen gas also promised to minimize motor brush wear for the life of the mission.

We debated a long time about the need for internal pressure. On the one hand, our research indicated that even slight pressure (more than ~1 Pa) of inert gas was adequate to improve brush life, no matter what material combinations were selected. On the other hand, the 12-year mission presented us with the reality that internal pressure would certainly leak down to very low levels. This raised a concern that arcing due to the phenomenon of corona discharge could occur at an intermediate point in the mission's cruise phase. Further research indicated that, in a mix of gases much like our actuator's, this phenomenon was most likely to occur at a pressure of about 120 Pa. To estimate end-of-life pressure conditions, we performed an analysis with three different assumptions: Worst-case leak, nominal leak rate as measured from the Mariner/Viking actuators, and an ideal leak rate. Ordinary O-rings were assumed in the analysis; other, more positive seals would have required too much mass or volume.

The result of our analysis indicated that there was no realistic hope of maintaining pressures above the corona discharge level. This presented us with a choice: should we abandon the pressurized mechanism and invest all our hopes in achieving a full 12- year mission life with purely vacuum operation, or should we attempt a mixed approach of both pressurized and vacuum operation? Persuasive arguments on both sides of the issue did not lead to a clear choice. In the end, the flight heritage of the Mariner/Viking actuators gave us the justification to embrace the mixed approach. If it failed, we could fall back on purely vacuum operation. Figure 4 offers a cutaway view of the final EGA configuration.

Performance Over Temperature

As we progressed in modeling the new design, it became apparent that the Mariner/Viking actuators were not required to meet their performance specifications at temperature extremes. Cassini did specify performance over a temperature range, however, so this drove the following design considerations:

- Lubricant viscosity (use a lubricant with a high viscosity index, or a dry film)
- Bearing friction (minimize preload and preload change with temperature)
- Motor parameters such as resistance and torque constant [5]

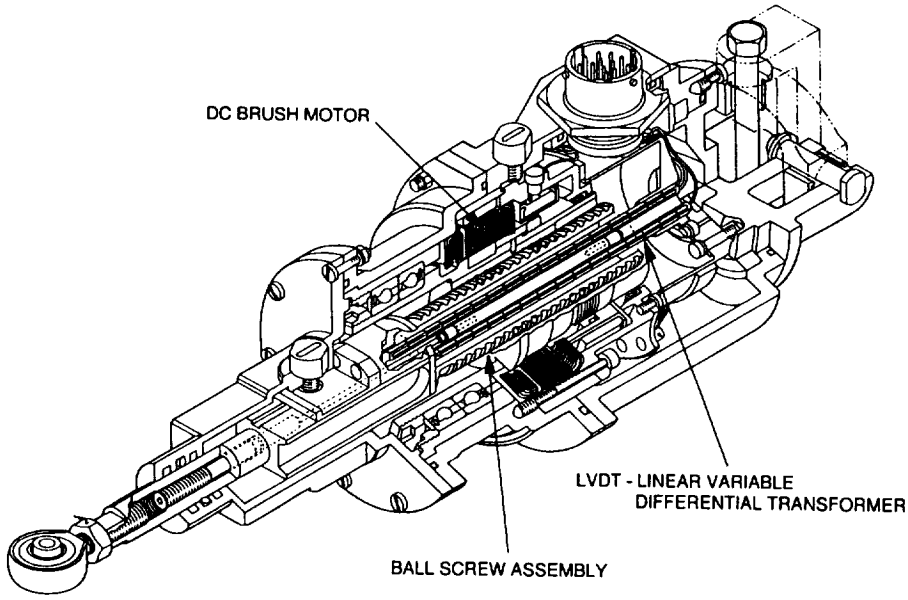

Figure 4 Detailed View of Final Cassini Actuator Design

Search for a Motor

The original motors were designed and produced at a local contractor. The original design was thought to be adequate, but there were two reasons why identical motors could not be manufactured: first, there were no extant prints in sufficient detail. (Perhaps there never were any!). Second, the contractor was not interested in performing the follow-on work.

Even if the original contractor agreed to produce more motors, we could not duplicate the materials and manufacturing processes of the original. Because any claim of heritage relies heavily on the ability to duplicate these factors, it would have been risky to proceed with the original vendor for heritage reasons alone. Moreover, the requirement for minimum stray magnetic field was considered to be very firm, and the contractor had no experience in designing for extremely low emitted fields. It was necessary to seek a new motor vendor and motor design.

Again, the simplicity of the Mariner/Viking EGA brush motor compared to a brushless design made it very attractive and, because of the high radiation environment, commutation electronics for a brushless motor would present a significant reliability problem. The Engine Gimbal Electronics design was also fairly mature at this point, so changes to it were not welcome. Designing for adequate reliability in commutation electronics would have required allocations of power, volume, and workforce that were in short supply.

We decided to proceed with a brush motor, and take every opportunity to establish procedures which would either eliminate problems or reveal them as quickly as

possible. A Request for Information yielded several interested vendors. We specified that the vendors should present their experience in brush motor technology with special attention to vacuum applications.

At the same time, we began preparing a controlling specification for the procurement. Our search for literature to guide us in the specifics of brush motor design for vacuum led to a document by the Fairchild Space Company [6]. This guide gave us valuable insight into design features that need special attention. The following list summarizes most of the significant design features that we controlled in our specification:

- Brush design parameters [7].
- Features to accommodate brush debris and prevent short circuiting.
- Welded terminations of the winding to commutator bars.
- Two close-fitting keys locked the rotor to the shaft with so that it remained snug after many torque reversals.

Brush Basics

With the help of the reference from Fairchild, further literature search, discussions with brush vendors, peer reviews at JPL, and materials specialists, we elaborated on the above requirements in the motor specification. We anticipated the most likely failure modes and designed processes, tests, and backup measures to minimize any delays if these occurred. We learned that there was indeed a large content of "art" in designing and executing a brush DC motor for vacuum applications, most of which centered on brush-related design nuances. Our vendor, American Electronics Incorporated (AEI), cooperated with us in working out all of the design details.

Several details were specified to enhance the reliability of the motor. For example, cartridge-type brush holders with coil springs were chosen over the cantilever type. The corners of each brush holder were relieved to preclude binding in the presence of debris, and they were machined out of Vespel ® to ensure stability over temperature. Average brush contact pressure was specified as 22.5 to 40.2 kPa. We chose to use conventional, undercut commutator segments, although some evidence suggested that no undercut was necessary. To survive the high temperature resulting from the long thruster burn for Saturn Orbit Insertion, or for unexpectedly high duty cycle, we designed for much higher local temperatures at the rotor by welding the winding terminations to the commutator bars.

The most important provision in our contract with AEI was that an engineering unit had to be built and tested as soon as possible. Our specification test plan schedule anticipated up to two failures in selecting an acceptable brush material; we required AEI to identify at least two substitute brush materials and to present these at Critical Design Review for JPL's approval. Furthermore, these substitutes had to be

immediately available in the event that the previous attempt failed under any circumstances. These lessons learned from experience in potentiometer testing for the Topex/Poseidon Solar Array Drive [8] bear restatement:

> Lesson 3: When developing flight hardware, reduce risk for flight hardware by building and testing engineering hardware of sufficient fidelity as early as possible.

> Lesson 4: To protect your schedule, minimize cost, and get maximum benefit, development plans must include:
> - Rationale for what you are doing (purpose)
> - What you intend to accomplish (objectives)
> - Contingency measures to take in case of failure (anticipated outcomes)

Table 2 is extracted from the motor specification test section. It delineates all of the environments and operating conditions required for the engineering motor life testing. The life test was performed in thermal/vacuum conditions, with a constant torque load of 50% of stall, 28 Vdc excitation, and an inertial load of 144×10^{-5} kg•m^2.

Two other concerns drove motor design: Performance and stray magnetic fields. These considerations are coupled to some extent. The required torque-speed curve of the original motor was adequate, but the motor exceeded the static magnetic field requirement of the Cassini mission by a large margin. When we measured the unpowered, stray field of the overall Mariner/Viking EGA, we found it to exceed 26 nT at 1 meter.

Table 2 Motor Life Test Conditions

Sequence	Temp, °C ± 5 °C	Ambient Pressure, Pascals	Oscillating Motion, radians ± 1 radian	Continuous Rotation (50% CW, 50% CCW) radians
1	+ 20	1 atmosphere Nitrogen	942,500	392,070
2	+ 115	120 ± 20%	141,375	
3	+ 115	120 ± 20%		43,375
4	+ 115	< 1.3 E-3	141,375	
5	+ 115	< 1.3 E-3		43,375
6	- 25	120 ± 20%	141,375	
7	- 25	120 ± 20%		43,375
8	- 25	< 1.3 E-3	141,375	
9	- 25	< 1.3 E-3		43,375

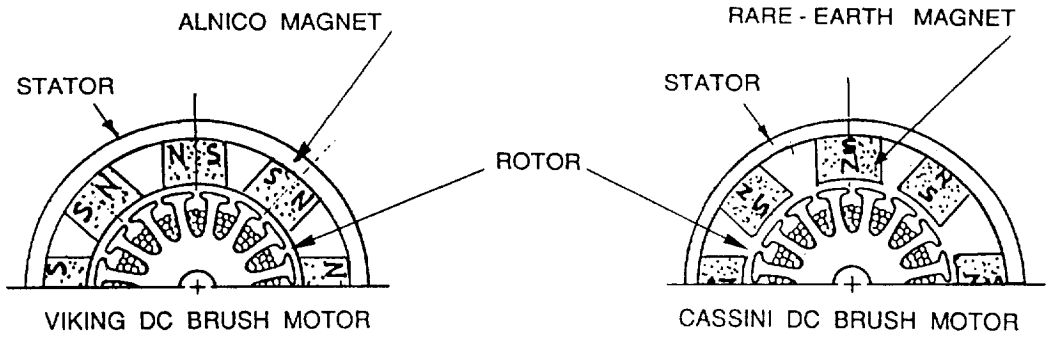

Figure 5 Re-orientation of Motor Magnets

The Mariner/Viking motor employs Alnico magnets to generate its stator field. We chose to use Samarium-Cobalt magnets for their higher energy product which, in turn, requires less volume to achieve the necessary flux density within the motor. We found that the Mariner/Viking motors were designed with the magnets in an orientation that exacerbated the offensive stray flux. The new motors used a different orientation whose magnetic circuit traps more of the flux within the steel stator ring (Figure 5). Some of the flight actuators did not achieve the goal of 5 nT at 1 meter, but all reached very low levels from 11 to 25% of the Mariner/Viking values. This accomplishment is highlighted because it conflicts with a difficult mass constraint. More steel in the magnet ring would have improved our results even further.

Reconfigure for Easier Assembly and Testing

The new EGA configuration is designed for ease of assembly and testing. It is built up from three modules, each with special tooling intended to shorten the calendar time required for many serial procedures in the single elaborate assembly of the Mariner/Viking actuator. The larger ballscrew permitted the LVDT's orientation to be reversed, thus opening up several opportunities for reliability-enhancing improvements. The tooling dedicated to each subassembly made it easy to catch assembly and fit-up errors early, instead of puzzling over what part of a fully assembled actuator is responsible for unexpected problems.

Lesson 5: Invest early in planning the assembly and test sequence. Attempt to isolate mechanism subassemblies at a reasonably simple level, where their fits and performance can be checked against expectations. This approach is often perceived as an unnecessary extravagance and omitted from small lot production runs. Not only will problems be identified at an early stage, but the delay and embarrassment of not meeting a published specification may be avoided.

Bearings and Ballscrew

The original ball bearings were no longer available from the manufacturer, so we elected to buy a commercial "extremely light" standard section made out of 440C stainless steel from the New Hampshire Ball Bearing company. This resulted in a healthy margin of load capacity as the bearing thrust rating was more than twice that of Mariner/Viking's original bearings. Dual, contacting lip seals were deemed necessary to seal out motor brush debris, and seal in lubricant.

Next, we substituted a larger ballscrew of 20 mm outside diameter. Although not necessarily required for load capacity, the extra mass paid important dividends: First, it enabled the new actuator configuration because we also specified a larger ID which accommodates the LVDT coil assembly. The original, hollow 16-mm-diameter component was difficult to manufacture with the necessary precision (our older ballscrews displayed a large variation in friction and backlash), and this choice promised the shortest possible lead times and least likelihood of errors in manufacturing. Ballscrew vendors would more readily quote to industry-standard sizes, and our vendor, Schrillo Corporation, agreed that these decisions would enhance reliability and minimize schedule risk.

Lesson 6: Use of limited resources (e.g. mass) can simplify procurements and enhance a product's robustness.

Use a Real Lubricant

One important lesson that JPL has learned from its experience with the Voyager Spacecraft is that the lubricating fluid used in some of its mechanisms was not a real lubricant at all. (Versilube G-300 silicone grease and f-50 fluid were employed back then.) When they first became commercially available, silicone fluids held tremendous attraction because of their low vapor pressure and high viscosity index, i.e., their stable viscosity with temperature variation. Problems with the scan platform mechanisms led to research that showed silicone fluids are non-Newtonian. Worse yet, the hygroscopic fluid turned into a gritty paste of microscopic crystals under high shear conditions in the presence of water.

In keeping with the conservative project guidelines, we selected Bray 600 grease/815Z oil to replace silicone fluid. With about 15 years of spaceflight mechanism history, this material has been well characterized. Design parameters such as bearing preload were carefully adjusted to avoid the oil's tendency to polymerize. Special provisions were designed-in to ensure a lubricant reservoir for the ballscrew slider and ballnut. To minimize friction, the ball bearings were loaded with relatively little grease, but the lubricant is captured by the lip seals on the bearings.

Use a Flexure, Reverse the LVDT

One of the most disturbing findings when we disassembled the Mariner/Viking actuators was the degree to which the LVDT probe had worn. It turned out that this had been noticed before, but not documented. The reason was that each end of the LVDT was held in a separate subassembly of the actuator, and there was a substantial tolerance build-up between the two parts. We remedied this by mounting the LVDT ferrite probe on a flexure rod of 1.52 mm (0.06 inch) diameter (Figure 6). This forced us to use careful handling methods while assembling the actuator to avoid bending the flexure, but the approach allowed us to analytically bound the forces acting on the probe.

Also, we moved the transformer coil attachment so that, unlike the old design, a flexing service loop would not be required. As noted above, the shrink sleeve on the service loop of the old actuators had hardened and become brittle. The new wiring was analyzed and approved to survive longer than the 12 year mission and the higher radiation dose of the mission.

Lesson 7: Risk is mitigated whenever an analytically determinate design is employed.

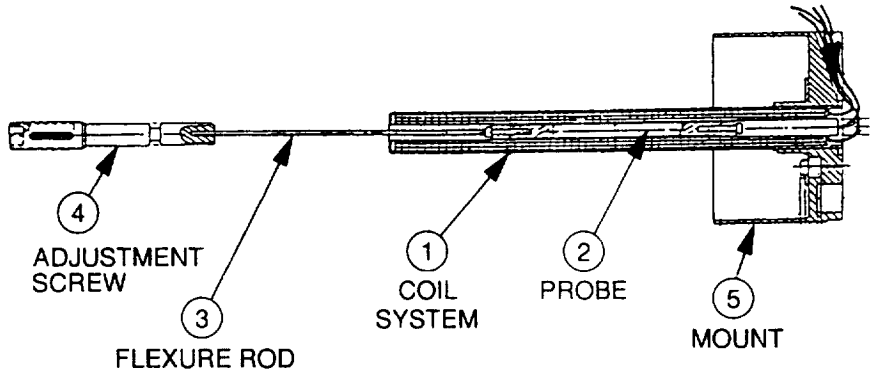

Figure 6 Linear Variable Differential Transformer design concept.

Mount (5) and coil assembly (1) are clamped to the EGA housing . This figure also shows how the adjustment screw (4), flexible rod (3), and probe (2) are screwed into the EGA ball screw. As a result the probe moves with the ball-screw relative to the stationary coil to indicate actuator position. (Figure 4 shows the relationship of LVDT parts to the top assembly)

Soft Stops

In the course of an early peer review, we found that the Mariner/Viking actuator did not have a design feature specifically for absorbing the mechanism's energy at its end of travel. With the help of our materials engineers, we designed custom-molded urethane stops to cushion the ballscrew at each end of travel. The wide temperature range made this a particularly challenging materials problem.

Slippery Restraint

Mariner/Viking actuators employed a simple, square spline as a torque guide to resist the ballscrew's tendency to rotate. We considered improving the design with a sophisticated involute spline, but eventually settled on a flat, broad rectangular section with brass slipper plates as diagrammed in Figure 2. The final design results in less backlash while permitting the same reasonable tolerances.

Magic Vespel

The Mariner/Viking actuators' U-joints employ bushings made of Dupont Vespel®. While redesigning these for the higher anticipated loads, we investigated alternatives for the material. In a Space Mechanisms Videoconference [9] we learned that Vespel has the valuable property of reducing its coefficient of friction in a vacuum, unlike most other materials. We retained Vespel not only because it offered less friction in a vacuum, but also because it simplified our life test configuration. We obtained conservative test conditions (higher friction) during mechanism life testing by leaving the external U-joint in 1 atmosphere of air. At the same time, for the vacuum portions of the test a neat and compact turbopump system evacuated the interior of the EGA through its gas ports!

New Rod End

The challenging radiation environment of Saturn forced us to investigate alternative liner materials for the Teflon® used in the original spherical rod end bearing. Not only was the lining exposed to more radiation than the interior components of the EGA, but because it attaches to a bracket on the rocket engine, it needed to retain lubricity at temperatures even higher than the bulk average value predicted for the mechanism. We agreed with our vendor, Aurora Bearing Co., to use Microseal 200-1 MoS_2 dry film lubrication.

Maintenance Actuations

Because of the short duration of the Viking mission, no procedure had been established to regularly "exercise" the Mariner/Viking actuators. After investigating brush motors, however, we determined to proceed with caution. "Cold welding" or vacuum welding of asperities between the brushes and commutator posed a significant risk in a very long, 12-year mission. Even though the brush/commutator material combination was selected for maximum reliability, we still feared that a nonconductive film may build up under the brush. This phenomenon is illustrated by our measurements of Mariner/Viking actuator characteristics. When we first pulled the machines out of mothball, our first impulse was to "fire them up" and see how they would run. Restraining ourselves, we instrumented the power supply first, and then measured the resistance at the motor terminals. We found resistance as high as 10 KΩ and starting voltage as high as 32 V. After a few strokes, the starting voltage settled down to 16 V. Later on, we subjected the parts to analysis and found commutator corrosion products and silicone F-50 fluid on the commutator surface. The supply voltage was nominally 28 V.

The importance of lesson No. 4 was again demonstrated in the benefits of patience in planning what parameters we wanted to measure and how to measure them.

To avoid any recurrence of this conductivity problem, we initiated a flight rule requirement that the flight actuators would be operated every 3 months, whether in ground storage or in space.

Test Results and Summary

We built a PreProduction Model (PPM) EGA for the purpose of early design validation and life testing. Another application of lessons 3 and 4, the PPM employed flight-specification components and housings as they were made available, which enabled the development team to work out any surprises in manufacturing methods, component fits, or performance. We saved cost on this model by eliminating Quality Assurance oversight of its construction.

Four life test series were performed with the PPM EGA, each patterned on the series in Table 3. Each series approximates the duty of a full life cycle. The first life test was run at specification gas pressure, and the second in a partial vacuum. The last two were performed in a hard vacuum environment to emulate the effects of a failed seal or unexpectedly high leak rate. Only the internal components (Figure 4) were subjected to partial and hard vacuum via the two vent ports in the actuator housing.

After these life tests, the actuator was disassembled and inspected. We found no visible signs of wear, except for the motor brushes, which showed between 9 and 13 percent wear.

Finally, two Protoflight actuators, built specifically for qualification life testing in the fully assembled MEA, were sent to Lockheed Martin. The actuators were commanded to gimbal the MEA for most of the 3 hours and 20 minutes duration of the test in a vacuum environment. This test emulated not only the temperatures and forces of MEA operation, but also the corrosive effects of the combustion environment. No adverse effects on performance or material condition were observed.

Table 3 Life Test Series

Sequence No.	Operating Mode	Temp. ±5°C	Commands and Stroke Lengths	Test Duration	Load N (lbf)
1	Static Launch Simulation.	+20 °C	Powered and commanded to null position.	63 hours	155 (35)
2	Early cruise activity. Internal pressure 136 kPa N_2	+40 °C	200 full strokes. Then 3,000 short strokes ranging from 0.25 to 1.00 mm at a frequency of 1 second per stroke.	Execute motion cycle 11 times.	155 (35) both directions
3	Cruise activity at mid-life pressure of 120 Pa	+20 °C	200 full strokes. Then 3,000 short strokes ranging from 0.25 to 1.00 mm at a frequency of 1 second per stroke.	Execute motion cycle 11 times.	155 (35) both directions
4	End of life pressure < 1.3 E-3 Pa	+20°C	200 full strokes. Then 3,000 short strokes ranging from 0.25 to 1.00 mm at a frequency of 1 second per stroke.	Execute motion cycle 11 times.	155 (35) both directions
5	Evaluate wear and refurbish	Ambient	Measure wear of critical components. Refurbish as required.	N/A	N/A

Future Improvements

We have studied ways of modifying the EGA to make it suitable for continuous duty requirements [10]. The most promising areas were determined to be lubrication and the motor. Specifically, we identified geometry changes that would increase the volume of oil and grease reservoirs. Also, a brushless motor would be superior to achieve a higher duty cycle and longer life.

Conclusion

At least seven tenets for successful hardware development were applied to the Cassini EGA task. A detailed analysis of the actuator design we inherited from the Mariner Mars and Viking spacecraft was a necessary first step in this task. We then validated the overall benefit of some risk-reduction methods that would minimize schedule surprises and overall cost. Although these methods have a substantial up-front cost, and were therefore unpopular at first, they were adopted because of the importance of meeting commitments on time. These methods, as well as the upgraded LVDT, ballscrew and motor, may prove useful in other applications where reliability is critical, and servicing is either difficult or impossible.

References

[1] Rudolph, D,. Design and Development of the Cassini Main Engine Assembly Gimbal Mechanism, 30th Aerospace Mechanisms Symposium, May 1996, Denver Flight Systems, Lockheed Martin, Denver, CO

[2] Paine, T. O., and G.S. Perkins, U.S. Patent No. 3,660,704, May 2, 1972

[3] Joffe, B., T. Iskenderian, and R. Shrake, *Cassini AACS Engine Gimbal Actuator Critical Design Review,* JPL Publication D-14186, Jet Propulsion Laboratory, September 1993.

[4] National Aeronautics and Space Administration, Improvements in Ball-Screw Linear Actuators, NASA Technical Brief , Vol. 20, No. 1, Item 39, January 1996.

[5] Joffe, B., T. Iskenderian, and R. Shrake, JPL Memo 343-94-016, Cassini Thrust Load and Rate Versus Load Estimate, January 1994.

[6] Morin, J. P., General Guidelines for Brush Motor Spaceflight Applications, April 24, 1992, Fairchild Space Co., Germantown, MD

[7] Joffe, B., T. Iskenderian, and R. Shrake, Cassini Engine Gimbal Actuator DC Motor Design Trade Study, JPL Memo 343-93-267, Jet Propulsion Laboratory, Pasadena, CA, July 1993.

[8] Iskenderian, T, Lessons Learned From Selecting and Testing Spaceflight Potentiometers, 28th Aerospace Mechanisms Symposium, May 1994, California Institute of Technology, Jet Propulsion Laboratory, Pasadena, CA

[9] Siebert, M., Report on polyimide roller friction in vacuum vs. air, Space Mechanisms Videoconference, hosted by R. Fusaro at NASA Langley Research Center, December 13, 1993

[10] Bejczy, A., *MLS Antenna Scan Actuator System Study, Final Report,* JPL Memo 3450-95-128, Jet Propulsion Laboratory, Pasadena, CA, July 31, 1995.

Acknowledgments

The authors wish to thank Russ Allen, Randy Braun, John Knox, Ted Kopf, Robert Kovac, Gary Parker, Howard Primus, Walter Proniewicz, Ray Schliesmann, Richard Silva, Robert Summers and Paul Willis for their contributions to this development program.

Design and Flight Qualification of the CRSS Antenna Gimbal

G. Cameron Dales * & Mark C. Calassa *

Abstract

This paper describes the design and qualification testing of an Antenna Gimbal Assembly for use on a commercial spacecraft. The application requires an agile design that minimized jitter of the spacecraft. Discussion will include challenging problems encountered, as well as lessons learned.

Introduction

The Commercial Remote Sensing System (CRSS) satellites are intended for operation in a sun-synchronous, low earth orbit from which the satellites will collect one-meter resolution panchromatic and four-meter resolution multispectral imagery and, in near-real time, transmit this data to worldwide ground stations. Critical to the CRSS mission is the satellite's Wideband Antenna Gimbal Assembly (AGA), shown in Figure 1, which provides the mechanisms required for a 56 cm (22") downlink antenna to track a ground station and hold a communication link while the spacecraft is performing imaging maneuvers. The need to slew the AGA during imagery collection while minimizing jitter of the spacecraft telescope bore sight has led to challenging requirements for the gimbal mechanism and its components.

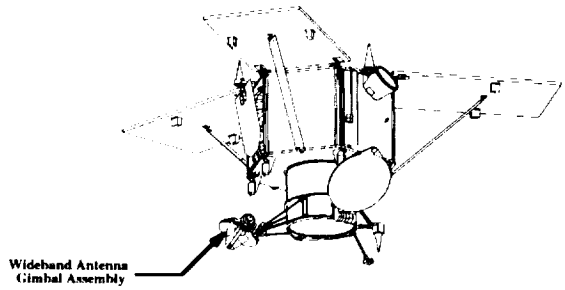

Figure 1: CRSS Spacecraft Configuration.

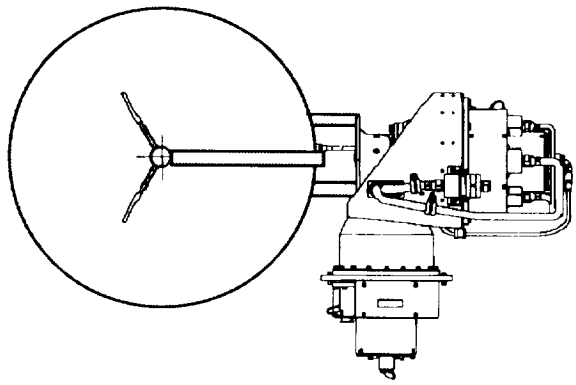

Figure 2: Wideband Antenna Gimbal Assembly.

The AGA consists of two identical drive modules mounted by a yoke in an orthogonal "T" configuration, as shown in Figure 2. The azimuth drive module mates to the spacecraft support structure, while the elevation axis provides a mounting interface for the wideband antenna. Electrical power and signals must be continuously transmitted through two rotating joints with a rotational range of ±135°. To accomplish this, each gimbal drive module incorporates a wire twist capsule consisting of flat conductors imbedded in Kapton tapes mounted in a clock spring configuration. Nested within each twist capsule is a choke-coupled, rotary RF coupler for transmission of the

* Lockheed Martin Missiles and Space, Sunnyvale, CA

wideband RF signal across the rotary interface. Other significant drive module components include redundant, inverted, brushless DC motors, redundant single speed resolvers, and a matched pair of angular contact ball bearings. Figure 3 shows a cross section of the drive module in which the resolvers are located inboard of the motor stators and act as bearing spacers for the bearing pair. Bearing inner and outer races are clamped and preloaded with threaded clamp rings using a clamping procedure which minimizes the parasitic drag torque resulting from minute differences in length between the precision ground resolver housings. The two permanent magnet, brushless DC motor rotors are supported within a thin wall aluminum housing. Drive module materials were chosen for thermal compatibility and consist primarily of aluminum and titanium. During spacecraft launch the gimbal axes are not caged but rather are restrained from rotating using two fully resetable and electrically redundant High Output Paraffin (HOP) actuators.

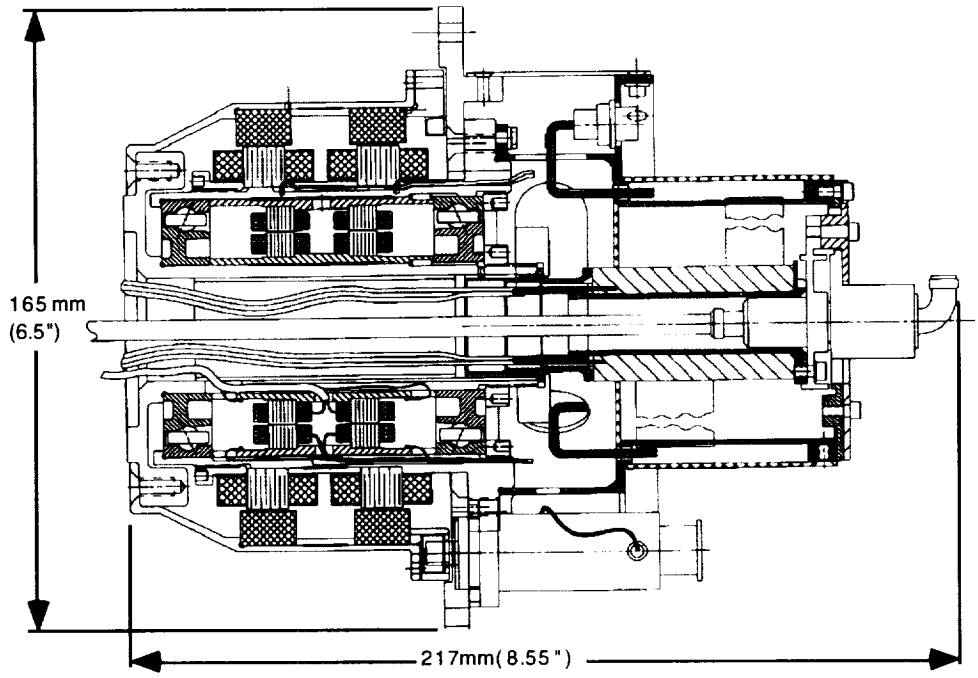

Figure 3: Gimbal Drive Module Cross Section.

The assembly and test of the Antenna Gimbal Assembly occurs on a laminar flow bench in a Class 10,000 clean room within the Lockheed Martin Mechanisms Product Center in Sunnyvale, CA. Special tooling and procedures were developed to install and preload the bearings and to prevent damage to the internal components and wiring during assembly. Potential spacecraft disturbances due to the drive module bearings, motor cogging torque and twist capsule windup were characterized in both the time and frequency domains on a precision rate table with a computerized data acquisition system. Data from these tests is used to show conformance to the CRSS satellite's image quality requirements. Disturbance torque data was also used to trouble shoot unexpected misalignments within the non-contacting RF coupler. Additionally, the bearings, twist capsule and RF coupler were life tested to more than

twice the antenna gimbal's expected operating profile, which was derived from the CRSS image targeting algorithm.

For the CRSS program, three Antenna Gimbal Assemblies were built and tested, one development / qualification unit, and two flight units. This paper describes the design and test philosophies that were implemented for the AGA flight qualification program, as well as lessons learned through the solution of various development problems.

Critical Process Risk Mitigation

During the design phase, critical drive module manufacturing and assembly processes were identified. In order to minimize the risk associated with the assembly of the AGA drive modules, as well as maximize the probability of meeting performance requirements, three critical processes were identified: the bearing installation, the rotor shaft and motor rotor housing installation, and the RF coupler choke installation and alignment. Special tooling was developed to ensure process success, and specific tests were designed with clear pass/fail criteria in order to verify the successful completion of each critical process. These tests were performed immediately after the completion of each critical process so that any problems would be detected before moving on to the next assembly step. In the event that a performance discrepancy was found, this incremental build/test approach minimized the amount of rework and disassembly required to solve a problem. A simplified flow diagram of the drive module assembly and test process is shown in Figure 4.

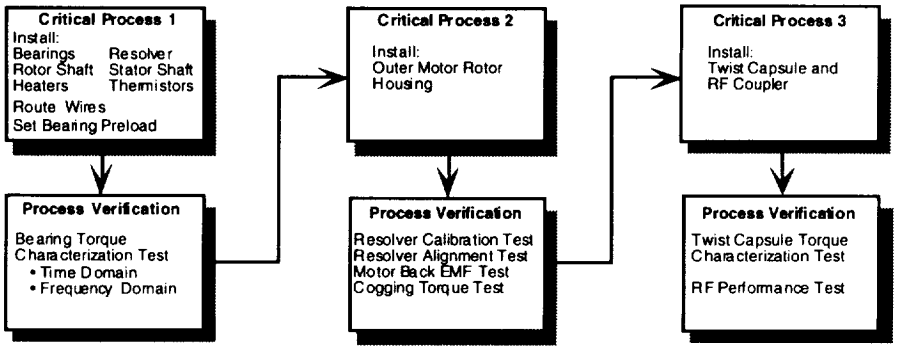

Figure 4: Drive Module Critical Process Flow

Critical Process 1: Bearing Installation

The rotor of each AGA drive module rotates on a pair of custom designed angular contact ball bearings, separated by precision ground, titanium spacers, which also serve as resolver housings. In the bearing installation procedure, the drive module rotor shaft and a resolver alignment pin must be inserted through the bearing inner races. This is considered to be a critical process due to the difficulty of inserting the shaft through the tight fitting bearing races while preventing damage to delicate resolver and thermistor wires which must be lined up and threaded through slots in the shaft. Special tooling was developed which automatically routed wires and aligned the pin while the rotor shaft was pressed through both bearings and the resolver

housing. Additionally, if any contamination or debris generated during the bearing installation were introduced into the bearing race, it could cause reduced bearing life and unacceptably high disturbances to the vehicle line of sight stability, degraded gimbal control system performance, and decreased motor torque margin. Finally, the proper bearing preload must be set in order to maintain the optimum bearing parasitic drag and stiffness over the required thermal environment.

The preload characteristics of each bearing pair was measured after installation using a test fixture and a series of weights which were hung from the partially assembled rotor shaft in order to simulate different preloads. For each different weight, the parasitic drag torque of the bearing was measured with a torque watch and plotted as shown in Figure 5. From this curve, the parasitic drag torque was determined for the desired preload. This axial preload was then applied to the bearings incrementally, using the actual threaded clamp ring, until the measured parasitic torque matched the proper preload.

Consistent with the build-test philosophy described above, after the critical bearing installation process, a series of bearing characterization tests were run in order to prove the success of the process. The partially assembled drive module was mounted to a precision rotary rate table, and a computerized data acquisition system and load cell were used to measure the bearing disturbance torques that were reacted out of the system as the rate table was rotated at various speeds.

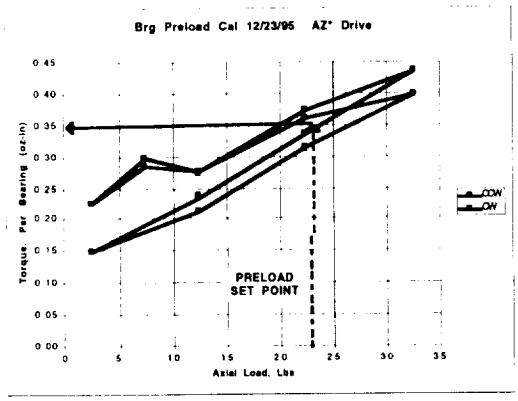

Figure 5: Azimuth Drive Module Preload Calibration Curve

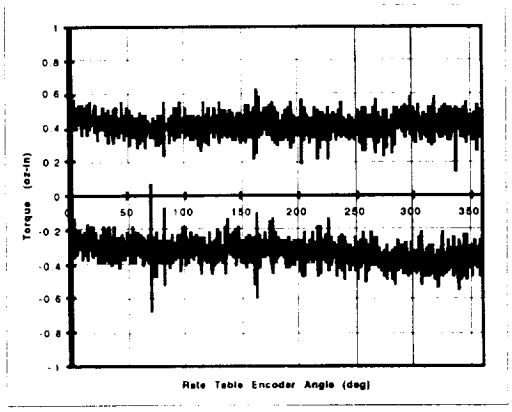

Figure 6: Azimuth Drive Module Bearing Bearing Signature @ 1°/sec

The bearing torque traces were analyzed in both the time and frequency domains in order to show compliance with the disturbance requirements. Figure 6 shows a representative plot of the qualification unit azimuth axis bearing signature in which the rate table was rotated at 1°/sec through an angle of 0° to 360° and back to 0°. Although these bearing torques are within specified limits, note the 5.7E-03 N-m (0.8 oz-in) torque transient found at approximately 65°, as well as those found at 160°. As will be shown, the spacing of the disturbances at 40° intervals is indicative of specific bearing defects or of a contamination particle between the balls and races.

As was mentioned in the discussion above, clues to the nature of the disturbances in any given bearing signature can be gleaned from looking at the frequencies of the disturbances. The frequency of the disturbances is also important in assessing the disturbance torque impact on the satellite's line of sight pointing performance. By knowing the geometry of the bearing and the speed at which it is rotating, we can analytically predict the frequencies at which torque disturbances might occur. Predicted disturbance frequencies (or angular spacings) for various defects for the CRSS AGA bearings running at 10°/sec are shown below for the first three harmonics:

Defect	1x Freq., Hz	2x Freq., Hz	3x Freq., Hz
Unbalance	0.028	0.058	0.086
Cage Defect	0.012	0.025	0.037
Ball Defect / Cage	0.124	0.248	0.372
Ball Defect / Race	0.247	0.495	0.742
O. Race Defect/Ball	0.250	0.500	0.749
I. Race Defect/Ball	0.306	0.612	0.917

Using the rate table and load cell described above, a Digital Signal Analyzer (DSA) was used to produce Power Spectral Density (PSD) plots, such as the one shown in Figure 7 for the qualification azimuth axis drive module rotating at 10°/sec.

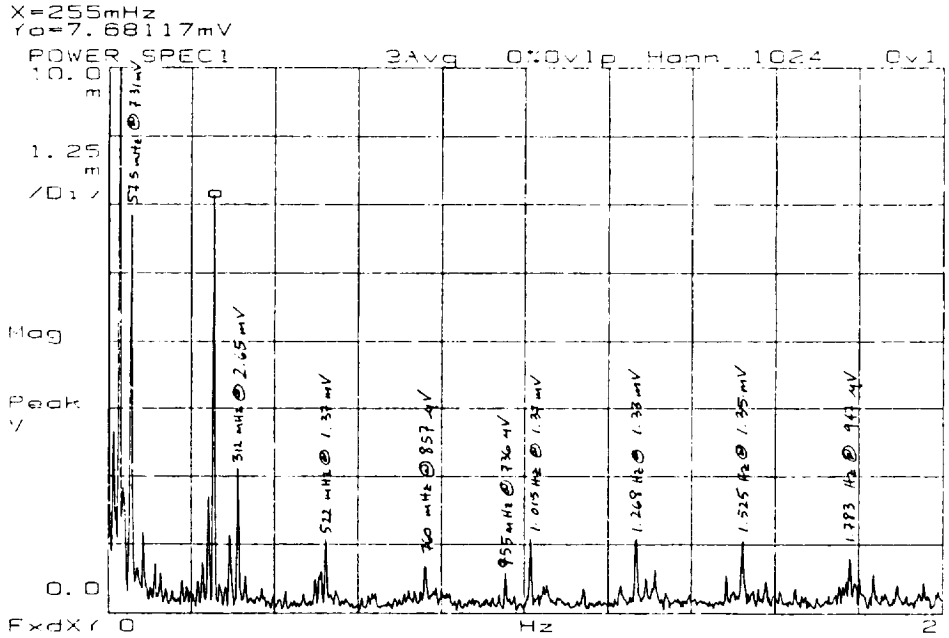

Figure 7: PSD Plot of Azimuth Axis Bearing Disturbances at 10°/sec.

The frequency resolution of the DSA was set at 2.5 mHz allowing frequency separation of the responses of the bearing noise components derived above. This PSD plot shows distinct responses at constant frequencies with a very low noise level. The two spikes at 0.028 Hz and 0.0575 Hz are associated with the 1x and 2x multiples

of the bearing unbalance torques. The spike at 0.255 Hz is associated with either the 1x multiple of an outer race defect, the 1x multiple of a ball defect against the race, or the 2x multiple of a ball defect against a cage. Unfortunately, the geometry of the CRSS bearing results in several defect signatures which are quite closely spaced in frequency, preventing us from determining precisely which phenomena are causing the torque disturbances. In fact, all three defects may contribute to the response at 0.255 Hz shown in the PSD plot. Harmonics of this spike exist at 0.522 Hz and 0.760 Hz as well. This test data gives excellent agreement with the predicted bearing noise component frequencies and also demonstrates the very low frequency nature of the bearing noise.

Critical Process 2: Motor Rotor Housing Installation

The second critical process in the AGA drive module assembly procedure is the installation of the motor rotor housing, which contains the powerful, permanent magnets of the motor. Figure 8 shows the special tooling that was designed and built in order to guide the motor rotors over the drive module stator and prevent the rotor magnets from binding during installation. Close attention to the drive module assembly procedure and tooling design early in the design phase allowed features to be incorporated in the hardware, which in combination with the assembly tooling lowered the risk of the assembly process.

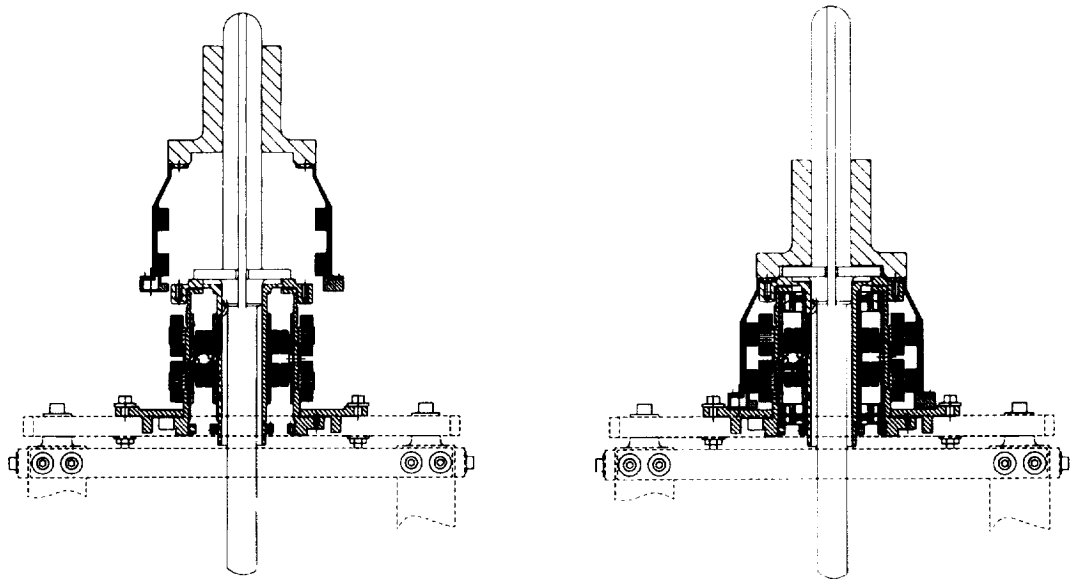

Figure 8: The motor rotors are installed on the drive module using special tooling.

With the integration of the motor rotor housing with the drive module, the assembly of the motors and resolvers was finished. In keeping with our testing philosophy, tests were then performed to prove that the process was successful. The resolvers were tested for accuracy, and the motors were tested for cogging torque and back EMF

voltage, which scales linearly with the torque constant. Additionally, the alignment of the motor zero and resolver zero was verified in order to ensure proper motor commutation. This test uncovered a rotational alignment error in the first drive module, which would have proven very difficult to rectify if it had been found later in the build. Since the error was discovered during the assembly process, the motor rotors were easily rotated to the proper location with little impact to the build schedule. For subsequent builds, a tool was developed to prevent the motor magnetic fields from rotating the rotor housing relative to the rotor before it is bolted down to the rotor.

Critical Process 3: Twist Capsule / RF Coupler Installation & Alignment

In order to transfer electrical signals and power across the gimbal rotating interfaces, each drive module incorporates a wire twist capsule. Additionally, RF signals are transmitted across the rotating interface of the AGA drive module by a quarter wavelength, choke coupled, rotary joint, which is nested within the twist capsule as shown in Figure 3. After installation of the twist capsule and RF coupler onto each drive module, a torque test was performed using the rate table and load cell to measure the twist capsule windup torque.

Although, the precise geometry of the RF coupler choke components is critical to the RF performance of the joint, additional bearings were not used in the twist capsule or RF coupler in order to minimize additional disturbance torques and bearing drag with the drive module. Therefore, to prevent the cantilevered components of the choke from hitting one another due to flexing of rotor shaft during vibration loads, a PTFE sleeve was inserted between relatively robust structural elements of the RF coupler such that the sleeve would take any impact loads before the delicate choke components came into contact. The remaining gap between the rotating components in the region of the sleeve, approximately 0.15 mm (0.006 in.), is small enough that with worst case tolerances, run-out in the RF coupler shaft could cause the components to touch the PTFE. This sliding of the RF coupler rotor and stator on the PTFE sleeve was discovered during the twist capsule windup torque testing of the flight units. Examples of torque traces from aligned and misaligned RF couplers are shown in Figure 9 for the first flight unit. Note the addition of a sinusoidal torque input in the misaligned coupler torque signature, caused by the increase and decrease of pressure on the PTFE sleeve due to runout in the rotor shaft.

Using the torque test as a diagnostic tool, discrepant hardware was either realigned by properly seating the bolted interface between the twist capsule and RF coupler or returned to the vendor for rework. The timing of the torque test in the assembly procedure, immediately after installation of the twist capsule and RF coupler but before wires were trimmed and harnesses installed, allowed the alignment issues to be addressed with minimum disruption to the build schedule.

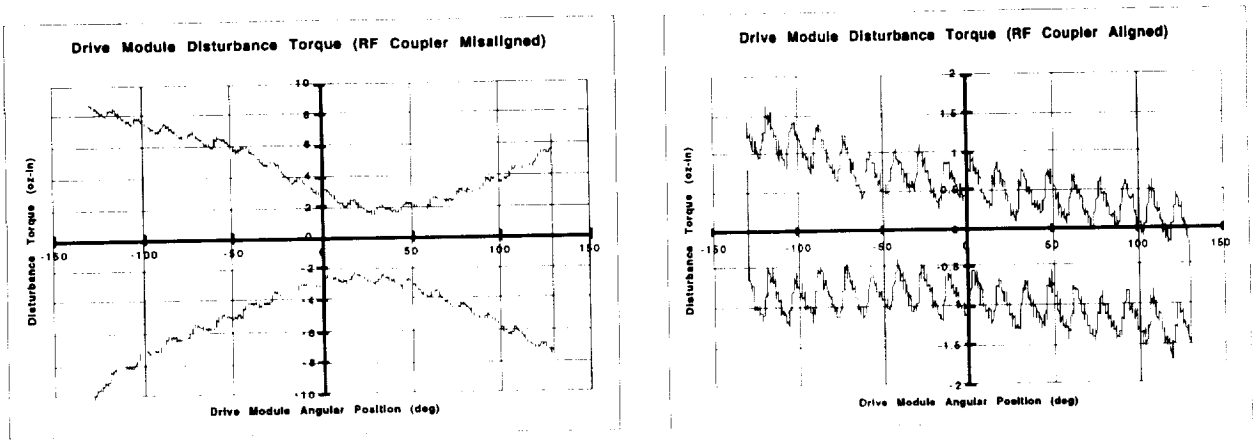

Figure 9: Flight Unit Disturbance Torque Acceptance Test Data. The plot on the left shows elevated torques caused by internal rubbing within a misaligned RF Coupler. The plot on the right shows proper alignment and disturbance torque levels including motor cogging, bearing disturbances and twist capsule windup torque.

AGA Qualification Test Program

After each drive module finished assembly and passed all drive module tests, the two modules (azimuth and elevation) were assembled into the two axis AGA. An aluminum yoke structure holds the two drive modules together in a "T" configuration as shown in Figure 2. Once assembled to the AGA level, a series of baseline functional tests were performed to verify that the unit met its requirements at the assembly level. A commercial, PC based motion controller, incorporating semi-custom servo amplifiers was used to drive the AGA during functional testing. These functional tests were then repeated after the AGA underwent qualification level vibration and thermal vacuum tests in order to verify that its performance was not degraded due to exposure to the launch and space environments. Finally, each drive module was disassembled and inspected to the piece part level, during which time the drive module critical process tests were repeated. The AGA qualification test flow is shown in Figure 10.

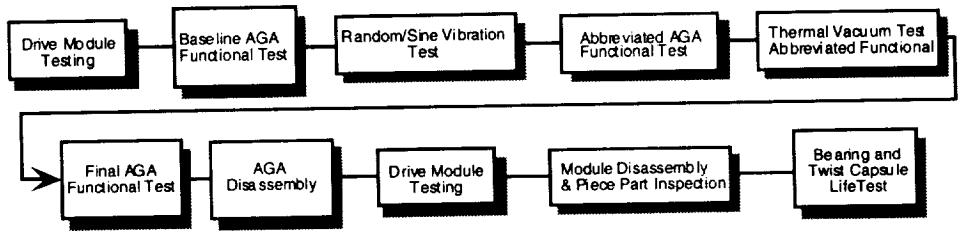

Figure 10: AGA Qualification Test Flow

Random and Sine Vibration Qualification Testing

The random vibration environments for the AGA were derived from a spacecraft level acoustic analysis, while the sine vibration environments were derived from a spacecraft level base shake analysis. Analysis showed, however, that the application of these derived acceleration environments in a fixed base condition was extremely

conservative for both random vibration and sine vibration. Due to lack of rotational degrees of freedom in a fixed and rigid base condition, the gimbal response levels would greatly exceed the spacecraft level results, particularly for the gimbal bearings. To resolve this over-test problem, a subsystem level test concept was implemented. Instead of testing the AGA at a component level (fixed base condition), a subsystem level vibration test was conducted in which the AGA was mounted in its flight configuration on the spacecraft gimbal support structure, allowing additional rotational degrees of freedom at the AGA base. A photograph of the test set-up on the shake table in Lockheed Martin's test facility is shown in Figure 11.

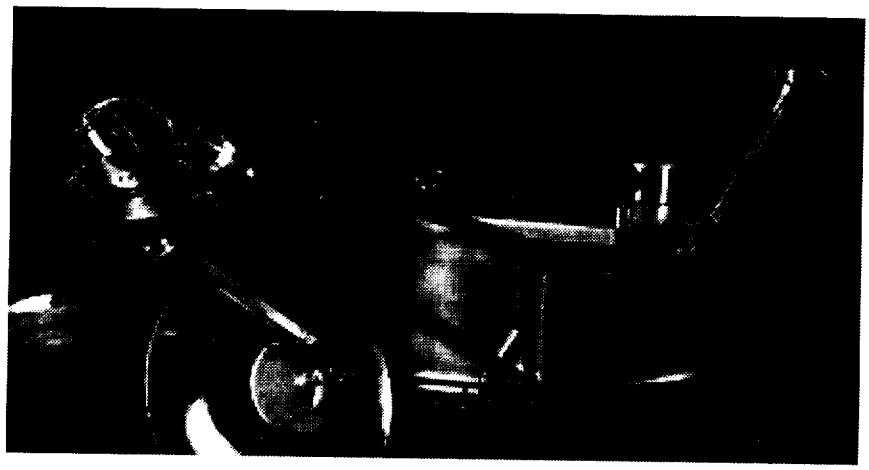

Figure 11: AGA mounted on spacecraft structure on Lockheed Martin's vibration table.

Because of large differences between preliminary and intermediate coupled loads analysis results , as well as the sensitivity of the loads to modeling changes, a serious concern was raised about potential load increases in later analyses. Given these uncertainties, a capability approach based on AGA bearing loads was developed for the first sine vibration frequency band, while the less severe second and the third bands were qualified by the base environment approach. A mechanism analysis determined that the load capability of the bearings was 5560 N (1250 lb), which was reduced to a target test level of 2491 N (560 lb.) after the application of margin and a model uncertainty factor.

The AGA vibration tests were successfully completed with peak response levels measured by accelerometers on the AGA in the three translational directions exceeding the predicted levels from the system level sine and acoustic analyses. The capability approach taken for the vibration testing proved to be fortuitous as the final coupled loads analysis showed greater loads than originally expected. Since the capability levels that the AGA was tested to still exceeded the new predicted levels, no requalification testing was required. This capability approach also allows greater flexibility in using the AGA as a common product for other programs with potentially different vibration environments.

Thermal Vacuum Qualification Testing

The objective of the AGA Qualification Thermal Vacuum Test was to qualify the AGA's design margins for operation when exposed to flight operating and non-operating thermal environments. This was accomplished by demonstrating performance when exposed to these environments and by validating the thermal math model that was used to determine on-orbit AGA temperatures and temperature gradients. The thermal vacuum test was also used to demonstrate performance margins by operating the AGA below the qualification temperature limits and with greater than specified bearing gradients.

The AGA is directly exposed to solar and earth heating and radiates heat directly to space, principally through the antenna. Heating and cooling rates are functions of gimbal surface properties and spacecraft and gimbal orientation. During imaging and wide-band down-link, vehicle and gimbal orientation can change rapidly.

Twelve hour soaks were performed at the hot and cold survival temperatures at the beginning and end of the test. Although not required for operation, in order to show additional margin, abbreviated functional tests were performed at -40°C (40°F), -29°C (-20°F), and -18°C (0°F) as well as the required cold and hot operational temperatures of 4°C (40°F) and 49°C (120°F). Figure 12 shows the motor torque data plotted versus temperature. Note the knee of the curve, where the drag torque dramatically increases at approximately -29°C (-20°F). This increase in torque occurs as the neopentyl ester oil approaches its solidification temperature. The thermal design set point for the bearing temperatures is 4°C (40°F), which provides 33C° (60F°) of margin against a thermal torque increase. The bearing temperature is always maintained above 4°C (40°F) by resistance heaters located on the inner surface of the motor rotor shaft.

Seven total hot / cold cycles were performed to prove the integrity of the AGA design and workmanship, and at the conclusion of the thermal cycling portion of the test, a six hour thermal balance test was performed in order to validate the AGA thermal math model. During the thermal balance test, the external environment was set to -62°C (-80°F), while the AGA rotor was maintained at between 12°C (54°F) and 15°C (58°F) by the AGA heaters. This resulted in a thermal gradient from the inner to outer race thermistors of approximately 6C° (10F°) in the AZ axis and between 3C° (6F°) and 6C° (10F°) in EL axis. By increasing the heater power, the gradient across the bearings in the AZ drive module was increased further to 11C° (20F°). Later analysis using the correlated AGA thermal math model showed that the maximum actual gradient across the bearings (as opposed to the gradient measured with the thermistors) was 4C° (8F°).

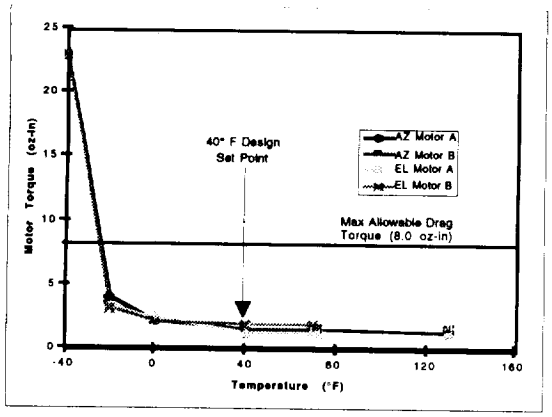

Figure 12: Motor Torque vs. Temperature During T/V Functional Testing.

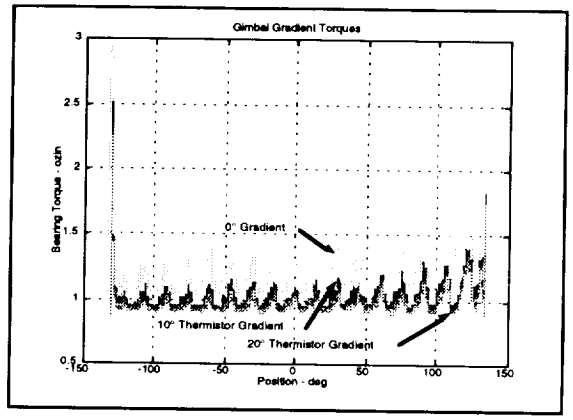

Figure 13: Motor Torque Changes with Bearing Gradients.

The effect of bearing gradients on the drive module drag torque is shown in Figure 13. A reduction of 1.77E-03 N-m (0.25 oz-in) in peak steady-state motor torque is seen for a thermistor gradient of 11C° (20F°) relative to the zero gradient case. This reduction in torque is caused by a reduction in bearing preload due to an increase in the length of the rotor shaft as it is heated relative to the stator. With the exception of slightly lower drag torque, the AGA showed no signs of performance degradation operating with an 4C° (8F°) bearing gradient. The worst case predicted on orbit bearing gradient is 2C° (4F°).

Validation of the AGA thermal design was accomplished by accurately predicting AGA thermal performance under test conditions, then using the model to show requirements compliance under orbital conditions. During the thermal balance test, 16 critical temperatures on the gimbal were measured and compared to thermal math model predictions. Thermal math model assumptions were modified to correlate the test results to model predictions. The correlated thermal math model was able to accurately predict all measured gimbal temperatures within 0.6C°(1F°), and was then used to simulate hot and cold orbit profiles.

Bearing and Twist Capsule Life Testing

Because the AGA would be required to perform numerous different ground track profiles during its operation, the development of a representative life test was a challenge. By analyzing several simulated mission ground track and target profiles, a composite life cycle profile was generated and transformed into gimbal azimuth and elevation angles. This composite life cycle profile was used to generate a life test model which is representative of the actual gimbal slew angles that the AGA will be required to operate over during its on orbit life. This model was then implemented as the basis of the AGA bearing and twist capsule life tests. The development of life test requirements was broken into several steps.

1) Development of ground track and target profiles for the AGA

Mission simulations were performed, which included three separate and distinct simulated ground track and target profiles. This data was in turn converted into azimuth and elevation angles in the respective drive module reference frames.

2) Development of a histogram which describes AGA motion

Histogram plots were generated which described the motion of both the azimuth and the elevation drive modules of the two axis gimbal during the three ground tracks analyzed in 1) above. For simplicity and conservatism, the histograms only considered a change of direction (and not a change of velocity) as an actual gimbal command. The histogram maps the total commanded slew angle versus the total number of commands issuing that slew angle. Figure 14 shows a histogram for which the commands for both axes during all three ground target cases are totaled.

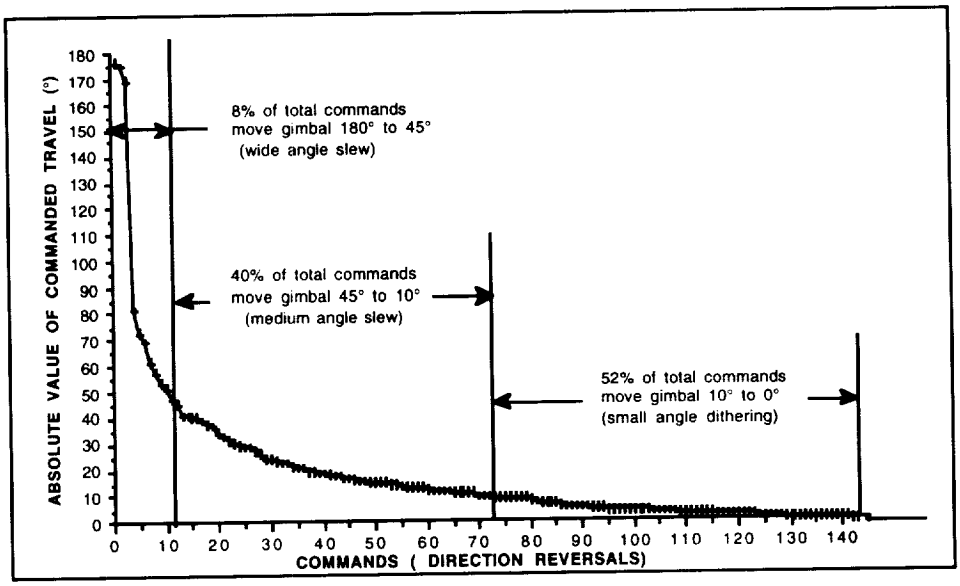

Figure 14: Histogram of combined Az and El axes for 3 combined ground targeting profiles.

3) Combination of ground track/ profiles and histograms into a life model

Given a 7 year mission life, an understanding of the ground track profile times, and the required minutes of imaging per day, we can derive the total number of required composite profiles. Since the life test will be run on only one unit, we required a two times life margin.

(10,220 composite profiles)*(Life Margin of 2) =20,440 composite profiles required for the life test

Once the number of composite profiles was determined, it was necessary to use the histogram information to determine the number of cycles to run at each angular excursion. From Figure 14 we can conclude that 8% of the commands are wide angle slews (45° to 180°), 40% are medium angle slews (10° to 45°), and 52% are small angle dithering (0° to 10°). Since each profile contains 146 commands we can find the total number of cycles.

(146 commands/profiles)*(20,440 profiles) = 2,984,240 commands
= 1,489,200 cycles

Commands can also be defined as a change of direction (c.o.d.) or a direction reversal. In turn, a full cycle is defined as two changes of direction. Knowing the distribution of direction reversals (146 commands) and taking an average angle for each of the three above cases the following life test model was derived:

Average Angle Traveled (°)	% of Total Commands	Change of Direction (c.o.d.)	# of Cycles (c.o.d./2)	Total Cycles
112.5°	8%	12	6	119,136
27.5°	40%	58	29	595,680
5°	52%	76	38	774,384
Totals	100%	146	73	**1,489,200**

4) Life test implementation

The life test utilized the bearings from the azimuth axis of the qualification AGA. These bearings experienced the highest loads during random and sine vibration testing. The bearing life test fixture consisted of flight configuration bearing housings, clamps and resolver housings/spacers. The life test bearings were installed and preloaded using the original procedure. A twist capsule was also mated to the assembly and all circuits were wired in series to a relay to detect an "open" circuit failure during the test. In addition, the RF coupler shaft was intentionally misaligned to obtain the sinusoidal rubbing of the PTFE bumper previously discussed. The magnitude of this friction was conservatively chosen to be twice the allowable specified component friction. The life test was run in a vacuum bell jar at a pressure of 10E-4 torr and at room temperature, since the flight gimbal bearing heaters will control the temperature of the bearings within a range of 4°C (40°F) to 24°C (76°F). The bearing torques were continuously monitored by a load cell and were recorded to a data base. A computer program was written to drive an external motor so that it would repeat the sequence derived above until complete, i.e. 6 cycles of 112.5 °, 29 cycles of 27.5° , 38 cycles of 5°, 6 cycles of 112.5, and so on.

The life test was accelerated. The peak bearing velocities which were used for the three profiles were 63.92°/sec. for 112.5° slews, 64.80°/sec. for 27.5° slews, and 62.83°/sec. for 10° slews. The corresponding average bearing velocities were 45.0°/sec., 45.8°/sec., and 44.4°/sec. respectively. The actual flight bearing velocities are between 0.1°/s and 20°/s. When the ratio of EHD film thickness to surface roughness (λ ratio) is computed we have the following:

Bearing Velocity (°/sec)	5	20	40	60	80
λ ratio	0.016	0.16	0.25	0.33	0.40

Accelerating the life test was considered to be valid for the CRSS application, since bearings with λ ratios below 1.0 are considered to be in similar operational regimes.

The life test was successful and the unit met all requirements when tested after completion. Figures 15 and 16 show pre and post test bearing torque signatures. The post life test bearing torques dropped approximately 1.77E-03 N-m (0.25 in-oz), which is expected due to run-in phenomena. Figure 17 and 18 show pre and post test twist capsule torque signatures. The twist capsule results were more interesting in that the initial torque trace shows the characteristic sinusoidal shape, while the post test torque trace shows a "perfectly" aligned parallelogram shape. Upon disassembly it was noted that the PTFE bumper had flowed to a non rubbing position over the course of the life test, proving that any slight rubbing that would be encountered during the flight builds would be negligible to the AGA performance.

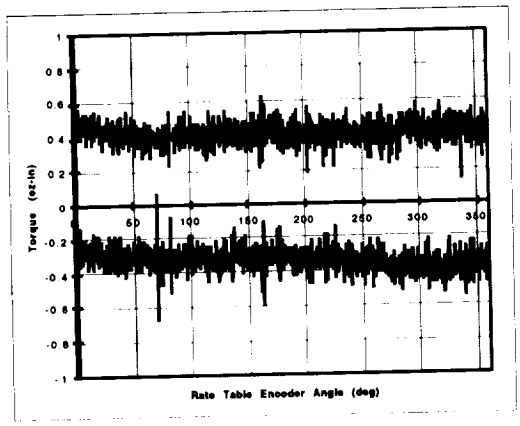

Figure 15: Pre Life Test Bearing Signature @ 1°/sec

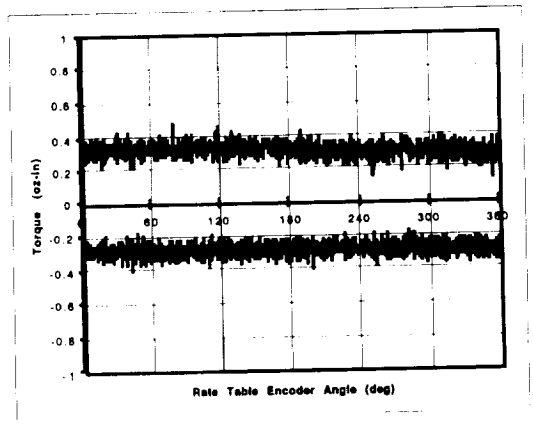

Figure 16: Post Life Test Bearing Torque Torque Signature @ 1°/sec

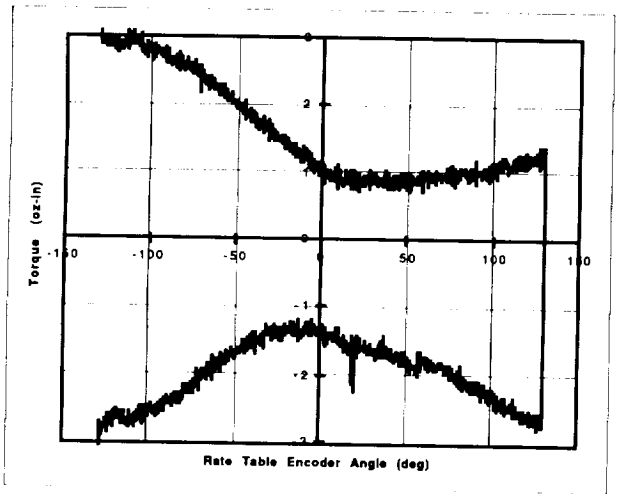

Figure 17: Pre Life Test Twist Capsule Torque Signature

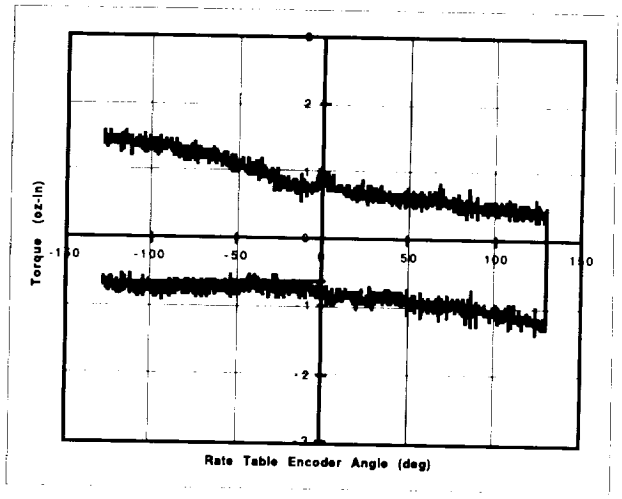

Figure 18: Post Life Test Capsule Torque Signature

Conclusions and Lessons Learned

A low noise Antenna Gimbal Assembly was designed and qualified for space applications. In the course of the development and qualification of the AGA many lessons, intuitive as well as non intuitive, were learned. Some of the more interesting are the following:

• Carefully consider assembly techniques early in the design phase. Many weeks of assembly planning were required before the individual part designs were finalized. Design parts with features to allow easy integration of assembly tooling. Features that should be carefully considered include: extra threaded holes for instruments and tools, through holes for pressing parts apart, precision flat features aligned with critical datums which can be used for optical or mechanical measurements, external scribe marks that convey important hidden internal information such as motor alignments, resolver alignments, and launch lock alignments. Don't forget disassembly! Development of good tooling for disassembly is every bit as important as the assembly tooling. During development you will need to take things apart..... many times.

• Don't try to save money or weight on tools. The aluminum material in many tools had to be replaced with stainless steel because of poor performance and contamination concerns. Soft aluminum tools tended to splinter, chip, and gall during use.

• Test vendor components early and individually. Many problems arose due to the lack of a complete understanding of vendor hardware. Several extensive tolerancing exercises were found to be unjustified when vendor hardware was finally tested. Work with component vendors early in the design phase to develop perceptive tests that gather data which can be used at the next step of integration. Review the vendor

test plans and ensure that the appropriate technology is being used to validate requirements.

• Before finalizing the design, take time to determine the most critical processes required for product success. Develop a comprehensive risk mitigation plan that includes inspection, testing, and appropriate verification for these critical steps. This approach will eliminate many wasted and frustrating hours of trouble shooting, disassembly, and rework.

• Use "off the shelf" products to test for mechanism performance. Since the development of flight like electronic boxes generally lags mechanism design, use of a commercial motion controller can assist in mitigating scheduling conflicts. In addition, closed loop pointing requirements can really only be tested at the sub-system level using the flight electronic boxes. The AGA was tested using a closed loop commercial motion controller where torque current was monitored as a function of velocity and temperature.

Acknowledgments

We deeply appreciate the supreme efforts given by all the individuals involved in the CRSS Gimbal development. Special thanks to Gimbal Team members: Tracey Boissier, Julie Foster, Gary Gerlach, Pio Jimenez, Dave Klinker, Stuart Loewenthal, Ken Oswald, Dan Rezendes and Bill Wenger.

Re-Flight of the Deployable Retrievable Booms

Carlton L. Foster* and Edward E. Litkenhous*

Abstract

The Tethered Satellite System (TSS), a scientific payload which was flown on STS-46 and again on STS-75, included two satellite-mounted Deployable Retrievable Booms (DRBs). The system was launched aboard the Space Shuttle Atlantis in July 1992. However, because of the problems which occurred at the original attempted deployment of the Tethered Satellite, the DRBs were never operated on-orbit during the STS-46 mission. In postflight functional tests, both DRBs failed to relatch properly. This paper discusses the troubleshooting of the anomalies, design changes, and DRB operational constraints incorporated for the STS-75 mission.

Introduction

The DRBs were developed by the Rinaldo Piaggio company, Finale Ligure, Genoa, Italy, under contract to the Italian Space Agency, as part of the joint US-Italian TSS program. These booms were designed to support, deploy, and retrieve probes of the Research on Electrodynamic Tether Effects (RETE) experiment. The RETE was one of the complement of experiments on the TSS intended to study the electromagnetic field around the satellite. Figure 1 illustrates the 1.6 m spherical satellite with both of the 2.4 m DRBs fully extended. The design of this mechanism was described in a paper presented by the developer at the 23rd Aerospace Mechanisms Symposium.

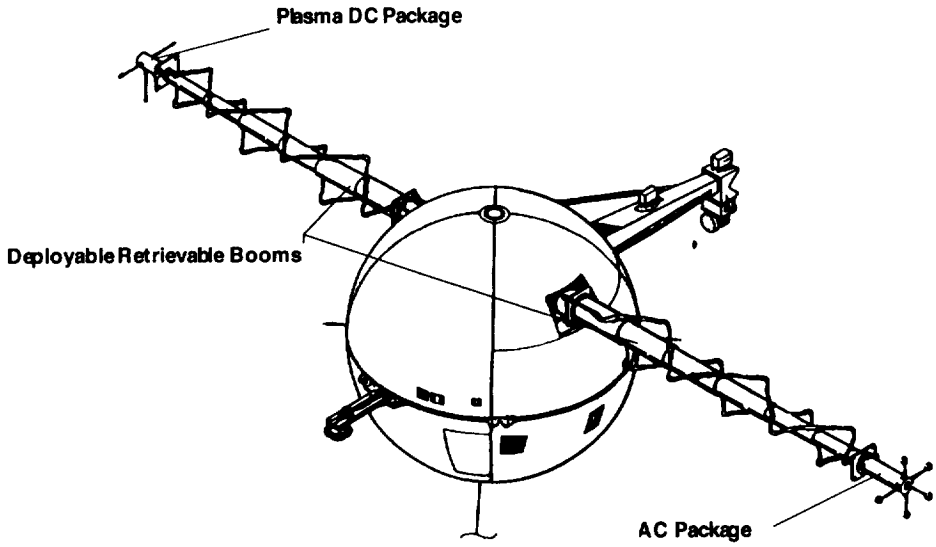

Figure 1. Satellite with DRBs Extended

* NASA Marshall Space Flight Center, Huntsville, AL

Description of Mechanism

The DRB is a telescoping boom consisting of eight concentric Aluminum Alloy tubes (one fixed; seven movable) inside a structural container. Each tube is approximately 400 mm long, and the diameters range from about 120 mm to 40 mm. The containers for the two DRBs are mounted on the Satellite Payload Module Upper Platform, 180 degrees apart. The largest movable tube (No. 1) is connected directly to a recirculating roller screw mechanism, driven by a stepper motor. The remaining movable tubes are deployed and retracted by a system of stainless steel wire ropes and pulleys. All tubes move synchronously (except for a small lag due to cable stretching which results in a characteristic hysteresis in the deployment action). Each movable tube slides on Vespel pads attached to the tube ends on machined flanges. Figure 2 shows a cutaway of the DRB with stowed tubes, and two cross-sections showing the jettison rollers and antijettison latches in the open position.

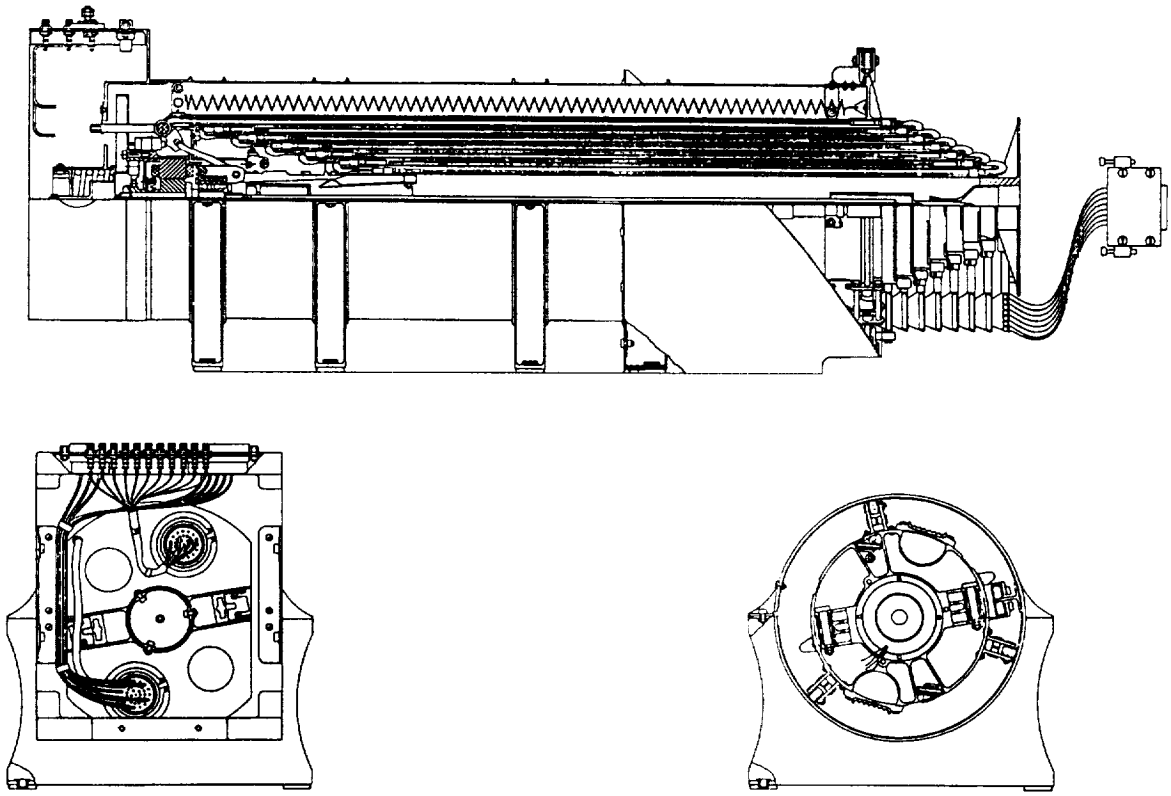

Figure 2. Deployable Retrievable Boom

When fully retracted, the DRBs are restrained against self-deployment by a pair of antideployment latches. The latches are operated by the same actuation as the tube deployment. Two pivoting levers, mounted to a flange on the inboard end of the fixed tube, are moved by the action of two small rollers. These rollers are mounted to the moving nut of the recirculating roller screw mechanism, which is also attached to a flange on the inboard end of tube No. 1. As the tube begins to deploy, the rollers

contact a cam on each lever. A hook near the end of each lever is released from a slot in a machined flange attached to the inboard end of the innermost tube (No. 7). Proper functioning of the latch depends on repeatable hysteresis of the telescoping tubes. The latches are designed to release before tube No. 7 begins to deploy. On retraction, the rollers are clear of the cams before tube No. 7 reaches the latch point, where the hooks snap into the slots and are held in place by leaf springs. Figure 3 shows details of the latch release sequence. Both latching mechanisms are designed to operate simultaneously. The design is redundant; a single latch is sufficient to hold the DRB in place.

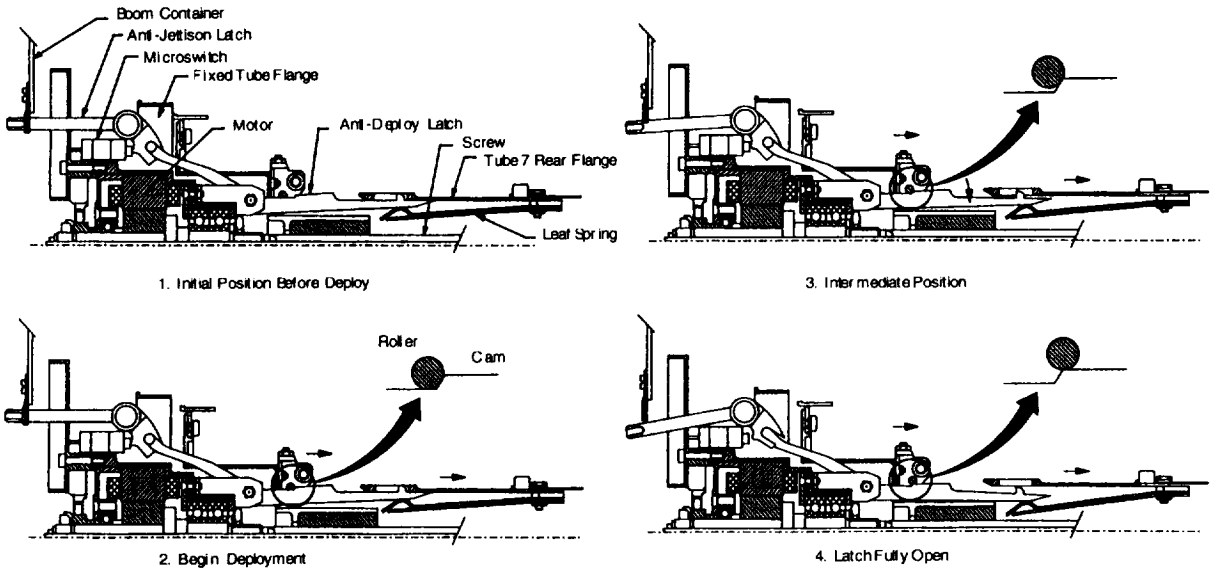

Figure 3. Latch Release Sequence

The fixed tube is attached to the container by a spring-loaded Marman clamp, held closed by a preloaded cable. When unlatched, the boom is jettisonable by firing redundant pyrotechnic cable cutters to release the clamp. The jettison movement follows as a large compression spring separates two electrical connectors, and three tension springs impart a velocity of approximately 0.4 m/s to the jettisonable components. Two sets of Delrin rollers guide the moving parts until separation.

When latched (as for launch, re-entry, and whenever the satellite is in the orbiter cargo bay), jettison is prevented by a pair of antijettison latches. Each antijettison latch is connected by a movable linkage to an antideployment latch. The antijettison feature is designed to operate simultaneously with the antideployment latch. The latching system also includes two pairs of microswitches that indicate latched status, and which also trigger motor power cutoff during boom retraction as the latch hook snaps into the slot. As with the antideployment latches, the antijettison latches are redundant.

Background

During the late 1980's and early 1990's, the qualification test program for the DRB was completed, and the two flight units were manufactured, acceptance-tested, and installed in the satellite. Because of problems during the attempted satellite deployment, the DRBs were not operated during the STS-46 mission.

Three DRB units were manufactured to the same design configuration -- one qualification model (DRB-QM), and two flight models (DRB-A, for deployment of the RETE AC sensors, and DRB-D, for the RETE DC sensors). During postflight functional testing, DRB-A did not relatch, while DRB-D latched following two attempts where the motor stalled momentarily. In preparation for the TSS reflight on STS-75, it was necessary to determine and correct the cause of the anomalous DRB performance.

Although it was known soon after the STS-46 mission that there were DRB anomalies, the investigation, design changes, and reverification activities were not pursued actively for several months. In the US, much of the project attention was directed toward correction of design problems with the Satellite Deployer in preparation for the STS-75 mission. In Italy, the TSS prime contractor, Alenia Spazio, Torino, Italy, was given overall responsibility for TSS performance, including the DRBs. For STS-46, the DRBs were developed under a separate contract, and were provided as "government-furnished equipment" for integration into the satellite.

In addition, the reviews that were conducted before the STS-46 mission focused heavily on safety and interface issues, with emphasis placed on ensuring that the DRBs could be jettisoned. The functional characteristics of the DRBs were highly complex, and few had a thorough understanding of the design.

In some cases, the investigation was hampered because the engineers did not have all the necessary background information from the early DRB development. Certain key personnel, such as skilled technicians who had made delicate adjustments during the original DRB assembly process, were unavailable for the troubleshooting effort. Some of these adjustments were attempted by others during later stages of the investigation and retesting. Several times these attempts were unsuccessful, and the flight hardware suffered some damage as well.

When the causes of the DRB performance problems were eventually identified and understood, the schedule constraints in the few months before the STS-75 launch limited the options of hardware changes that could be implemented.

Investigation Findings

At the beginning of the investigation, there was the presumption that the problem was the result of something simple caused by the STS-46 launch, on-orbit exposure, and re-entry. The DRBs had operated during acceptance testing before integration. It was presumed that, since the DRBs were never powered during the mission, the postflight latching problem must be the result of a change that had occurred after those tests. As the investigation proceeded, it became evident that the problems were numerous, subtle, and had been inherent in the design long before the launch.

Initial Investigation

Examination of both flight units at Piaggio revealed out-of-limit cable tensions. In addition, one broken cable was found on DRB-D. This was attributed to a postflight manual mechanism actuation with an "unknown applied torque." The latching torque for DRB-A was measured at 0.35 N•m; the expected value was approximately 0.18 N•m. These torque measurements were made with the motor unpowered and manually turning the roller screw. The DRB-A was shipped to Alenia for further investigation, while the DRB-D remained at Piaggio for repairs.

Motor Torque

The DRB was powered by a small stepper motor supplied by Sagem. The specified motor stall torque was 0.36 N•m, using constant current power limited to 0.36 A and a stepping frequency of 50 steps per second. This torque was demonstrated by the motor vendor at the component level, but the actual torque output of each motor as installed in the DRB had not been verified. Alenia devised a method to measure the torque by characterizing a flight spare motor. Using recorded voltage and current, a torque versus power curve was developed. Winding temperatures were recorded during the characterization testing, to allow for thermal compensation to the power calculations. The motor parameter measurements provided useful information in troubleshooting the performance anomalies. The DRB-A motor output was found to be approximately 0.20 N•m. This was marginal with a nominal mechanism load of 0.18 N•m, and significantly below the specified 0.36 N•m.

Alenia investigated several possible causes of the motor performance degradation, including effects of controller wave form, motor winding resistance, magnetic permeability of the rotor shaft and magnetic permeability of the ball bearings. None of these could be proven to have affected the motor torque significantly. It was noticed that the motor was much noisier in the DRB than in the motor test fixture. A drawing review showed a loose fit for the rotor and stator mounting pins. Alenia concluded that the motor components were vibrating during operation, resulting in a loss of supplied torque. With tighter pins installed, the motor torque increased to more than 0.30 N•m.

Further motor performance testing showed that, with the motor current increased from 0.36 A to 0.50 A and the stepping rate reduced from 50 to 25 steps per second, the motor stall torque increased to approximately 0.45 N•m. The DRB electronics were changed accordingly. This modification resulted in the maximum achievable performance with the existing motor. The lead time to procure and incorporate a larger motor did not make that a viable option.

Performance Analysis

The analysis of the DRB performance was somewhat conservative in some of the assumptions, and did not correlate well with the values for several parameters measured during the investigation. Apparently, there had not been any specific testing before the STS-46 mission to verify the validity of the analysis. For example, the motor torque shown in the analysis was 0.36 N•m; the actual available torque was significantly less. On the other hand, the nominal mechanism load was calculated to be 0.18 N•m, which coincidentally correlated exactly with the measured torque to operate the DRB-QM. The most significant product of the analysis was a calculated

performance margin of 43% for the worst case predicted load of 0.25 N•m. In the reviews of the DRB before the STS-46 mission, this margin was accepted as adequate. In contrast, the accepted practice for many aerospace mechanisms is specified in MIL-A-83577. Per this document, (not imposed for the DRB) the torque margin should be 100% under worst case environments. Considering the complexity of the DRB moving mechanical interfaces, the 43% margin was inadequate.

Complete Rebuild

Alenia continued the investigation in several areas. Functional testing was performed with a laboratory power supply while awaiting the completion of modifications to the flight DRB electronics. The DRB-A continued to perform erratically, and again did not relatch. When manually actuated, a rough spot was detected, suggesting a problem with the roller screw. Partial disassembly revealed some small notches in the roller recirculation cam of the nut assembly. These were removed, and the DRB-A performed successfully afterwards; however, the erratic performance of the DRBs was never completely explained to everyone's satisfaction. There remained a confidence that, since the DRB had been qualified before the STS-46 mission, the task was "simply" to ensure that the two flight units were correctly assembled and all components met drawing requirements. Considering that efforts to make small adjustments on the assembled mechanisms had been difficult, it was decided that both flight units should be completely disassembled, piece parts inspected and replaced as needed, and each unit was to be reassembled precisely to the design specifications. This was accomplished at Piaggio. Testing at ambient conditions was successful, with measured mechanism loads of 0.18 N•m and motor torques of 0.44 N•m for both units. There was optimism that the DRB problems had been solved. This was not the case.

Repeated Acceptance Testing

In April 1995, the DRBs were shipped to the EuropeanSpace Agency Technology Center (ESTEC) at Noordwijk, the Netherlands, for vibration and thermal vacuum acceptance testing. These tests, required as part of the reverification before delivery to the Kennedy Space Center for final integration into the TSS, were intended to demonstrate that the DRBs met the performance requirements at worst case environmental conditions. The setups were the same as for the original testing. The vibration testing and post-vibration functional tests at ambient were completed without incident, but problems again occurred at the beginning of thermal vacuum testing.

Thermal Vacuum Test

Both units relatched at the cold case of -70°C, but with zero torque margin. The motor stalled before the boom reached the point of latching. As the motor missed steps and torque dropped, the stored energy of the tightly stretched cables caused the roller screw and motor to be rapidly back driven for a few steps. After the cables relaxed slightly, the motor again drove the tubes toward the fully stowed position. This cycle would repeat on its own until the booms eventually latched. This "pumping" action was visible by observing the ends of the almost fully retracted tubes, and was evident on the plotted motor data. It was learned that similar action had occurred in the original acceptance test campaign. Since the booms relatched without having to repeat the command to the motor, the zero margin stalled condition and multiple tries

to relatch were not considered failures. There had been no measurement of motor torque during the original testing, and there was no specific margin requirement. This was taken as an inherent characteristic of the DRB.

The DRB-D failed to unlatch at -70°C; it eventually unlatched at -15°C. The thermal vacuum testing was continued to the hot case of +70°C, and both booms latched and unlatched successfully. On the next cold cycle, both booms latched, but the DRB-D again failed to unlatch. The test was interrupted, and adjustments were made to the roller that releases the antideployment latch, and to the microswitches that indicate latched status. When the test was resumed, the DRB-D apparently functioned properly, but one microswitch indicated "unlatched" when the other three indicated "latched." It was later found that the switch that showed "unlatched" was correct; the others were giving erroneous indications. In addition, the DRB-A failed to latch on the last operational cycle.

Other Problems

It was found afterwards that the DRB-D had probably never latched at any time following the switch adjustments. There had been electrical noise problems with the Electrical Ground Support Equipment, which caused the motor to cut off prematurely. The microswitches had to be bypassed to work around this condition, which compromised the test to some extent. Other problems with the Mechanical Ground Support Equipment forced the testing to be changed from full to partial deployments in the thermal vacuum chamber. It was learned that similar problems had occurred during the original test program, and that the test requirements had been modified to perform only partial deployments.

The most significant finding during the April 1995 test campaign was that there was a short period just before the relatch where the antijettison latch was partially engaged, but that the antideployment latch was still unlatched. Although this was inherent in the latch design, it had never been recognized as a serious problem. Normally this situation existed for only a few seconds before relatch. With the misadjusted microswitches, the motor was being stopped with the DRB in a position which was not latched, but which was also possibly not jettisonable. This was judged to be an unacceptable condition, and the DRBs were shipped back to Alenia for further investigations and modifications.

More Investigation Findings

By this point, the problems with the DRBs were posing a serious threat to the TSS project and the STS-75 reflight mission. The project management appointed a special "Tiger Team" to conduct an independent review of the design and testing of the mechanism. This team worked closely with the Alenia and Piaggio engineers to devise a plan to ensure the DRBs were acceptable for the reflight. Two important modifications were incorporated as a result of the further investigation.

Roller Screw Lubrication

On DRB-D, significant torque spikes started to occur during the re-adjustment of the microswitches. An increased friction in the roller screw assembly was indicated. The

roller screws were lubricated with a MoS_2 dry film lubricant, Microseal. On DRB-A, the motor data traces were very ragged with several high peaks. The nut eventually jammed on the DRB-A roller screw. Both screw assemblies from the flight DRBs were returned to the manufacturer (SKF/Transrol, Chambery, France), along with two others from the DRB-QM and an Engineering Development Unit (EDU). When the DRB screws were inspected, it was found that the Microseal was worn away, and the increased screw-nut friction caused a large reduction in efficiency. A change to wet lubrication was recommended, if cold temperature operation could be demonstrated. The EDU roller screw was lubricated with Brayco 602 grease, resulting in an increase in efficiency from approximately 55% to 80%. This screw was mounted in the DRB-QM for a thermal vacuum and life cycle test at Alenia. The unit worked perfectly at -50°C (worst expected motor temperature), answering concerns about the viscosity at cold temperature. There was no degradation of performance during the life test. The lubrication change was incorporated on both flight model DRBs.

Latch Tip Modification

The cause of the partial engagement of the antijettison latch can be seen in the second view of the relatching sequence shown in Figure 4. Initial contact of the lever on the leaf spring resulted in a complex motion of the latch components. A small modification to the tip of the latch lever, also shown in Figure 4, delayed and reduced this motion, and corrected the problem.

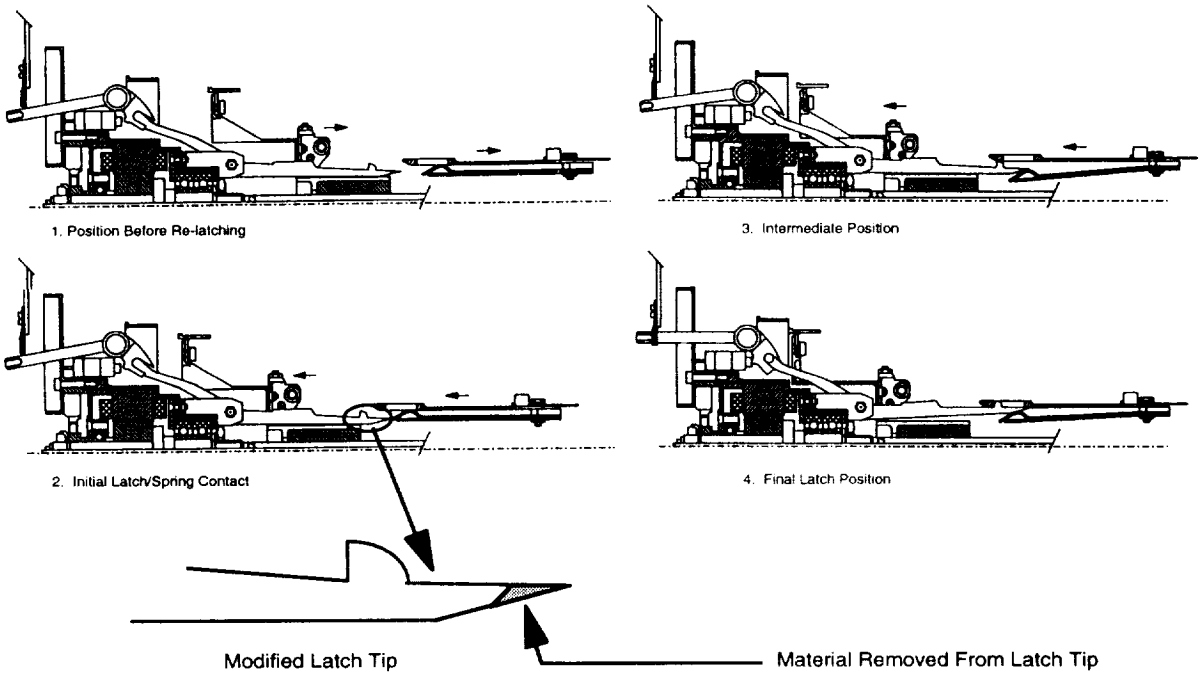

Figure 4. Latching Sequence and Modified Latch Tip

To be sure that the latches and microswitches functioned as intended and were correctly adjusted, the unlatch and relatch movements of both DRBs were mapped and thoroughly evaluated. Figure 5 shows the mapped motion of a typical latch. The line labeled "jettison clearance" represents a 1 mm gap for the antijettison latch pad during retrieval. The line labeled "jettison limit" represents a line-on-line condition, beyond which jettison is prevented. The motion of the latch pad and the hysteresis between deployment and retrieval can be seen. The plot also shows the threshold of switch operation for both the DRB Electronics (DRBE) and Remote Terminal Unit Payload (RTUP) switches. The DRBE switches provided the signal for motor power cutoff, and the RTUP switches provided latch status when the DRBE was unpowered. Knowledge of the measured latch characteristics was later used during the troubleshooting that was required during the next acceptance test campaign.

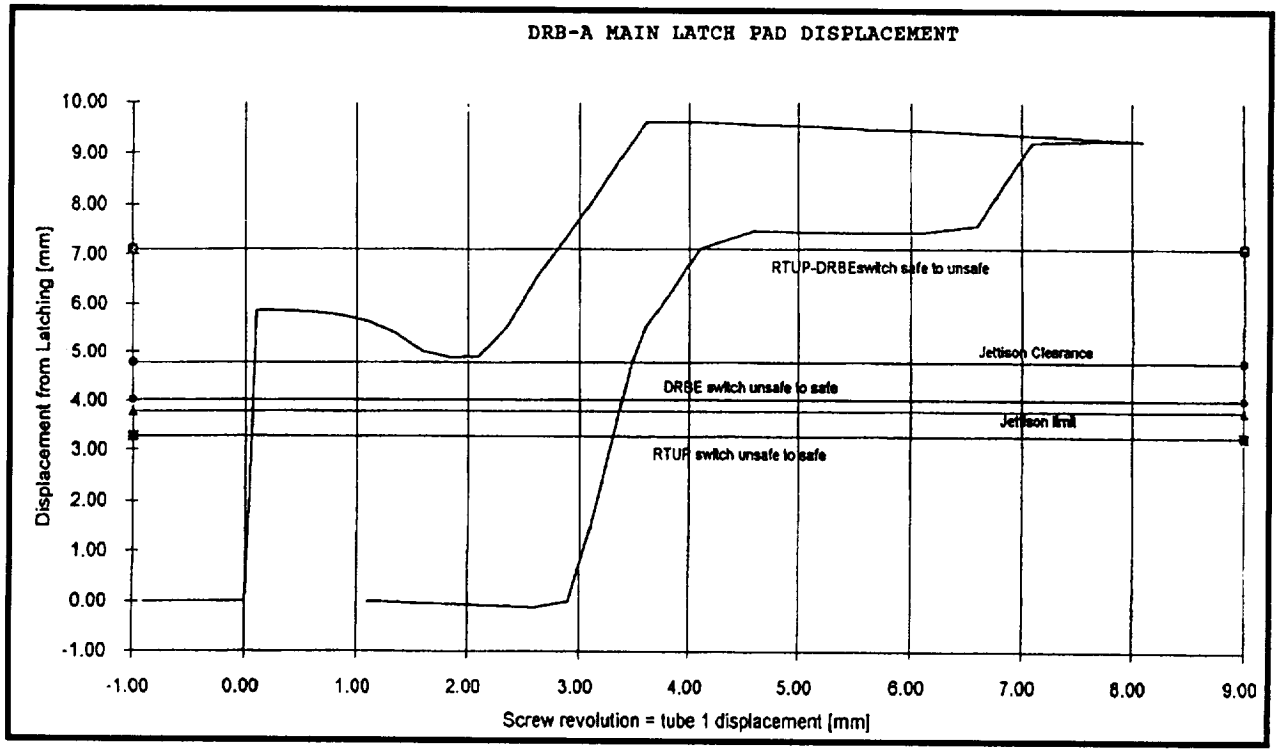

Figure 5. Mapped Latch Motion

Final Acceptance Testing

After all design changes had been implemented, the two flight units were returned to ESTEC in June 1995 for another series of acceptance tests. Again, another case of misadjusted microswitches was found in thermal vacuum. This time it was the encoder switches on DRB-A, which affected the signals for synchronous DRB-A and DRB-D deployment controlled by the DRB electronics. Adjustments were made, vibration testing was repeated, and the unit was returned to the chamber for another thermal vacuum test. The test setup was better instrumented than for the earlier acceptance

tests. Motor data traces were taken for each test run. In addition, the encoder and latch position microswitches were recorded on a strip chart, along with the signal from two accelerometers mounted near the DRB inboard ends. The accelerometers were used to obtain a separate indication of latch actuation. As the hook snaps abruptly into the slot, a shock pulse, detectable by the accelerometers, is carried through the DRB structure. It was planned to monitor data from accelerometers on the TSS to independently confirm successful latch operation if microswitch signals were suspect. Figure 6 shows strip chart and motor data for DRB-D at one cold and one hot case. In addition to the pulse at latching, the accelerometer signals show a distinct structural reaction caused by the backdrive action of the roller screw when the motor stalled. The encoder microswitch signals also show the action of the roller screw at a stalled condition, and at motor power cutoff. The two sets of DRBE and RTUP position switches show simultaneous operation at latching.

In the final thermal vacuum test, at -70°C, DRB-A failed to latch. DRB-D latched with zero margin after multiple stall cycles as observed in earlier testing. DRB-D also failed to unlatch on the first command, but unlatched easily when recommanded. The same problems were found at +70°C. These further illustrated the complexity of the DRB design. Of the three supposedly identical units, the DRB-QM operated properly at both + and -70°C, the DRB-A failed to latch at the same conditions, but unlatched OK, and the DRB-D exhibited difficulty in unlatching but never failed to latch.

An intensive effort was made to experimentally find a combination of temperatures and operating procedures within which the DRBs would perform adequately. The specified range of + and -70°C was beyond the expected worst case on-orbit temperature. The test was amended to perform latch and unlatch cycles at + and -50°C, and at -30°C. It was found that the DRB performance was repeatable, and was much improved at milder temperatures. Relatching was also better assured when the DRBs were retracted to an almost stowed position, and allowed to stabilize before final latching. Sufficient data were obtained to define the operational constraints that were eventually implemented via a waiver. The final recommended operational range was -25°C to +40°C, with a temperature stabiliation period prior to relatch. Within these constraints, the DRBs had demonstrated repeatable satisfactory performance with measured motor torque margin of 31% or better. These operational aspects were easily incorporated in the mission planning, with no impact to the mission timeline. On this basis, the DRBs were accepted for STS-75, the Tethered Satellite Reflight Mission, TSS-1R.

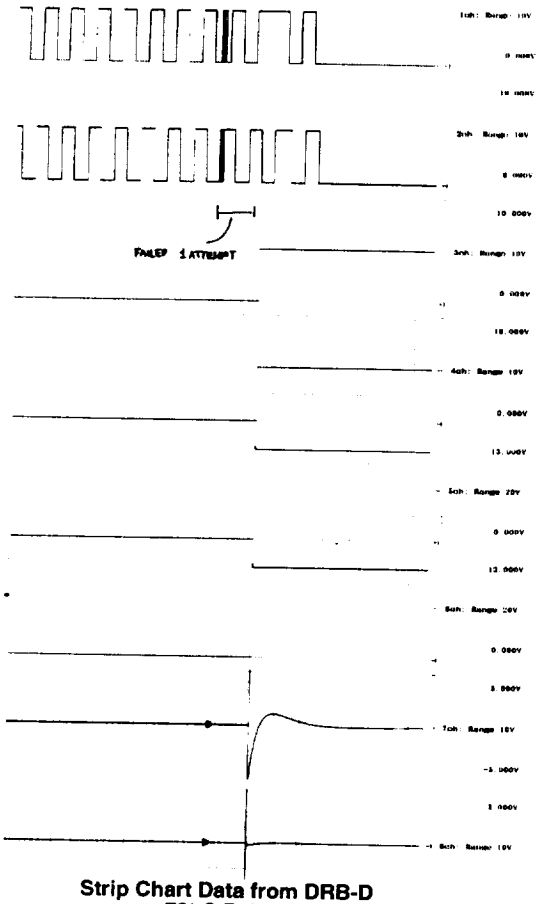

Strip Chart Data from DRB-D
-70° C Relatch

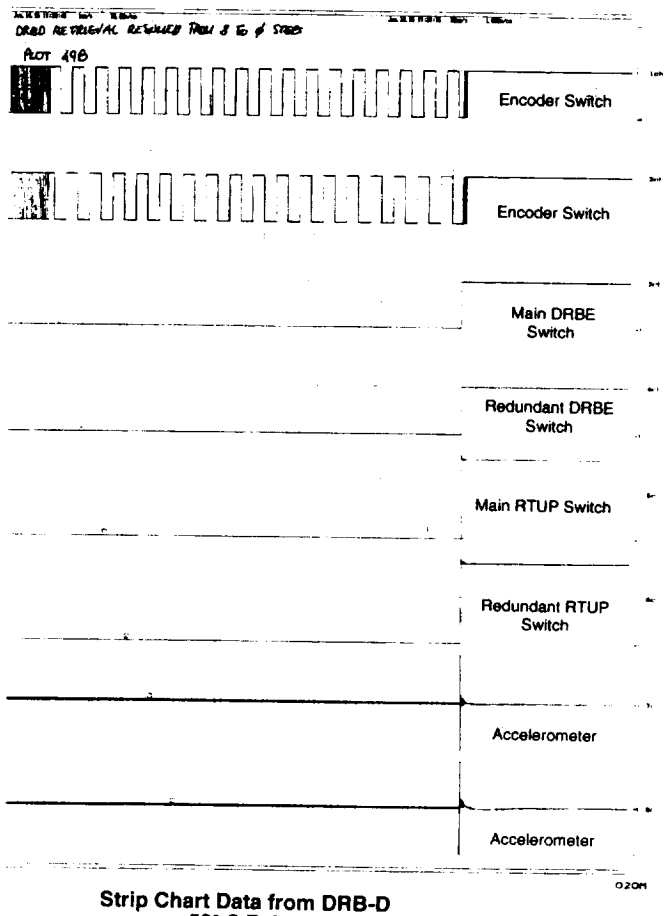

Strip Chart Data from DRB-D
+ 50° C Relatch

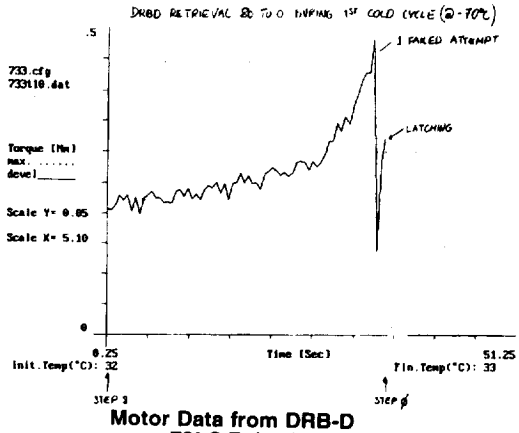

Motor Data from DRB-D
-70° C Relatch

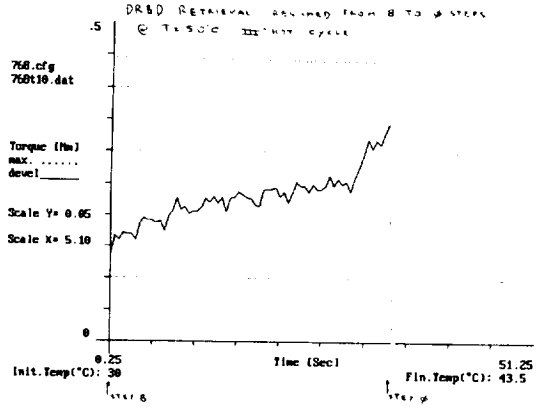

Motor Data from DRB-D
+ 50°C Relatch

Figure 6. DRB Test Data

Landing with DRBs Unlatched

From some of the early reviews of the DRB design, it had been established that the boom must be latched for both launch and landing. The requirement was actually that the DRBs must be safe for all mission phases. The mission rules for STS-46 had been written to require a positive indication of latched DRBs before the satellite was brought within 2.4 km of the orbiter. If the booms could not be latched, they were to be jettisoned. No changes to the jettison features or procedures for the DRBs were recommended. However, from the attention given to the whole relatching activity as a result of the performance problems, it was determined that, when retracted but not latched, the booms were actually not a hazard to the orbiter during re-entry and landing. A very detailed and conservative analysis showed that the DRBs would not move enough to touch the orbiter, and thus would not cause any damage. This assessment was agreed to by the Payload Safety Review Panel. The mission rules for STS-75 were not changed, but the managers had this information and had the option of waiving the rule to jettison in that situation. In the actual sequence of events which occurred during the deployment of the Tethered Satellite, the tether failed at approximately 19.7 km length, and the satellite was lost. The DRBs were thus never operated during the STS-75 mission.

Lessons Learned

Design Margins
Large force and torque margins should always be used, especially if the weight penalty is small. This is particularly important when the complexity of the mechanism makes precise performance analysis impractical or impossible.

Lubrication
It is important to understand the characteristics of candidate lubricants when making a selection. When using off-the-shelf components, it is best to choose materials and lubricants for which there is a large experience base. Thoroughly test any changes or new applications.

Test, Test, Test
Thermal vacuum, random vibration, and life cycle testing will uncover problems.

Completely Identify Causes for Performance Problems
Use care when troubleshooting, to ensure that the problems are properly and completely identified. Incomplete understanding of problems can delay or prevent identifying correct solutions. This results in inappropriate actions, making the situation worse.

Use Caution When Making On-The-Spot Adjustments
For mechanisms which require complicated adjustments during assembly, it is very risky to make even a small change to any element. If the circumstances make such changes necessary, be sure the right tools, fixtures, procedures, and personnel are used. Repeat testing after the changes are completed.

Requirements Should Be Justified
A great deal of effort can be expended attempting to meet unnecessary requirements.

Conclusion

The lessons learned probably sound very familiar. The same things have been written many times about other mechanisms. The challenge is to remember and apply the knowledge.

In the case of the DRBs, problems were identified, addressed and understood. Through the cooperative efforts of a team of individuals from several companies and agencies in the US and Europe, usable solutions were found and implemented for use in the STS-75 mission. However, events did not allow on-orbit execution of these solutions, which is always the "final verification test. "

References

1. Becchi, P. and Dell'Amico, S.: Design and Testing of a Deployable, Retrievable Boom for Space Applications. Proceedings of the 23rd Aerospace Mechanisms Symposium, May 1989. (NASA Conference Publication 3032).
2. Comparetto, V.: DRB Mechanism Analysis. Report No. DRB-RP-RPT-276, dated 17 February 1989.
3. Ciancetta, E.: DRB Stepper Motor Meeting Minutes. Document No. TS-MI-AI-1510, dated 8 November 1994.
4. Tosi, M.: Recirculation Roller Screw Meeting Minutes. Document No. TS-MI-AI-1542, dated 23 May 1995.
5. Allasio, A.: DRBs Testing after Re-Assembly and Readiness for ESTEC Re-Acceptance Tests. Project Correspondence Ref. No. SIEL/AA/95-0784, dated 9 June 1995.
6. Bechtel, T. and Calvert, J.: TSS DRB Safety Team Final Report. September 1995.
7. Minutes of PSRP Safety Technical Interchange Meetings for TSS-1R, dated 16 and 29 January 1996.

TSS-1R Failure Mode Evaluation

Jason A. Vaughn*, Matthew B. McCollum* and Rachel R. Kamenetzky*

Abstract

Soon after the break of the tether during the Tethered Satellite System (TSS-1R) mission in February, 1996, a Tiger Team was assembled at the George C. Marshall Space Flight Center to determine the tether failure mode. One possible failure scenario was the Kevlar' strength member of the tether failed because of degradation due to electrical discharge or electrical arcing. During the next several weeks, extensive electrical discharge testing in low vacuum and plasma environments was conducted in an attempt to reproduce the electrical activity recorded by on-board science instruments during the mission. The results of these tests are presented in this paper.

Introduction

The TSS system, or "satellite on a string," was developed to gather information on the space environment and tether dynamics. TSS-1R consisted of three basic elements; the Deployer System, the satellite, and Shuttle-mounted equipment. The Deployer System was designed to release the satellite, deploy it to a safe distance from the Orbiter, and provide control of the satellite during deployment. Deployer equipment included the Tether Reel Assembly (Reel), Satellite Support Assembly, Deployment Boom (Boom), Lower Tether Control Mechanism (LTCM), Lower Tether Cutter (LTC), Upper Tether Control Mechanism, Upper Tether Cutter, Docking Ring, and Command and Data Management System. The satellite was a 1.6 m diameter sphere weighing 521 kg and served as a remote platform for four science instruments. The tether, 2.54 mm in diameter, provided mechanical and electrical connection between the satellite and the reel. The tether consisted of a NOMEX' core, a 10 wire, 34 AWG copper conductor wrapped around the core in helical fashion, a clear Fluorinated Ethylene-Propylene (FEP) insulation over the conductor, a KEVLAR' strength member, and a NOMEX' outer braid [1]. The TSS-1R payload, which flew in February 1996 on STS-75, consisted of the satellite deployer, the satellite, 3 scientific experiments mounted in the payload bay: Shuttle Electrodynamic Tether System (SETS), Shuttle Potential and Return Electron Experiment (SPREE), Deployer Core Equipment (DCORE), 4 satellite mounted experiments: Research on Electrodynamics Tether Effects, Research on Orbital Plasma Electrodynamics, Satellite Core Instruments (SCORE), Tether Magnetic Field Experiment, and an aft flight deck camera: Tether Optical Phenomena Experiment [2].

History

The TSS-1R mission was the second flight of the TSS hardware that had originally flown on Space Transportation System (STS) mission STS-46. During STS-46, the satellite deployment was stopped at 256 m instead of the planned 20 km because of mechanical interference in the level wind mechanism. After STS-46 numerous

* NASA Marshall Space Flight Center, Huntsville, AL

modifications and refurbishments were made to TSS hardware. Some modifications were required to resolve TSS-1 flight anomalies and some modifications were made as a result of comprehensive reflight studies. Nearly every major sub-system was modified and/or refurbished. However, in the course of the failure investigation, it was discovered none of the design changes to the TSS system contributed to the tether failure [3].

Mission Objectives

The primary goal of TSS-1R was to characterize the electrodynamics and dynamics of long tethered systems deployed in space [3]. Mission objectives required to meet this goal included: 1)characterization of the TSS-1R system current-voltage response and demonstration of electrical power generation; 2)characterization of the satellite's high voltage plasma sheath, current collection, and current loop closure; 3)verification of basic dynamics and control law; and 4)demonstration of the effects of neutral gas on the plasma sheath and current collection process [3].

As the tether is deployed, an electromotive force (EMF) is induced on the tether as it moves through the earth's magnetic field [4]. The maximum value of this EMF when the satellite is fully deployed (tether length is greater than 20 km at this point) was estimated to be -6,000 Volts [3]. Electron guns mounted in the Orbiter payload bay were used to complete the electrical circuit between Orbiter and space plasma. Once the Orbiter to space plasma electrical circuit was completed, current would flow through the satellite-tether-Orbiter-space plasma circuit driven by the EMF on the tether. The DCORE experiment allowed variation of the satellite potential by controlling the current flow between the satellite and Orbiter resulting from the tether EMF. SETS provided measurements of tether voltage and tether current. SPREE measured ion and electron distributions to determine the Orbiter's potential (with respect to the space plasma). SCORE, mounted on the satellite, measured tether current using the Satellite Ammeter (SA). Because it contained its own electrical power, data handling system, and telemetry, tracking and command transmitter/receiver system, the satellite could provide data to ground stations even after tether separation [4].

Failure Description

STS-75 launched on February 22, 1996 at a Greenwich Mean Time (GMT) of day 53, 20 hours, 18 minutes (53/20:18) or 2:18 P.M. CST. Deployment of the satellite began at 56/20:46 GMT. At 57/1:26:02 with 19.7 km of tether deployed, the tether was put into an open circuit configuration and science operations were passive (i.e., tether to Orbiter circuits were open and no current was flowing through the tether) [3]. At this point, the EMF on the tether, as measured by SETS, was -3500 Vdc relative to the Orbiter. At 57/1:29:26, telemetry data indicated that the tether had been severed. Later review of science telemetry data showed that at the 57/1:29:17 mark, 9 seconds before tether separation, the tether EMF measured by SETS changed sharply from -3500 Vdc to -200 Vdc and tether current measured by the SA jumped to 0.9 A. The science instruments were in a passive mode, i.e., switches in SETS and DCORE were open so that no current could intentionally flow to the Orbiter, and SETS measured no current flow. This gave a preliminary indication that the tether conductor was "shorted" to the Orbiter. Because the tether voltage was still relatively high (-50 to -200 Vdc), this

also indicated that tether conductor was arcing to the Orbiter (a high impedance current path) instead of shorting to the Orbiter through metal-to-metal contact (a low impedance current path). The nearly 1 A of current continues to flow intermittently for 9 s before tether separation and continues for 77 s after the tether fails [3]. This indicates that the current is flowing directly to the space plasma from the end of the tether still attached to the satellite.

Test Objective

Using the current and voltage data from SETS and SCORE, the measured deployment rate of the tether at the time of failure, and the length of the tether left after separation, it was possible to determine that the arcing started in the LTCM [3]. The objective of the test program was to determine if a tether could discharge at the same voltage and current levels as recorded on-orbit. The test program would also determine what conditions (high vacuum, low vacuum, and plasma) were necessary to initiate and sustain a discharge. Finally, the test program would also determine if the high voltage on the conductor was enough to breakdown the FEP insulation of the tether and cause a discharge or whether a flaw in the insulation was necessary for discharge initiation.

Test Hardware and Procedure

Tests designed to reproduce the electrical discharge measured by flight sensors onboard TSS-1R were set-up in a diffusion pumped, 1 m x 2 m plasma chamber. The plasma chamber was capable of an ultimate pressure of $1x10^{-7}$ Torr, but most of these tests were run in low vacuum at 10^{-3} Torr. Figure 1 shows the test set-up used during this investigation. The tether sample was connected to a home made, high voltage, high current vacuum feed-through rated at 12 kV and 3 A. The design of this feed-through matured during the course of the testing because power levels were higher than anticipated. The ground plane was placed on an axial translational feed-through and grounded to the chamber wall outside the chamber. Most tests were conducted with the ground plane 0.64 cm from the outside of the tether, but a few tests were conducted with the ground plane 1.91 cm from the tether. These locations were chosen because actual flight ground planes were located these distances relative to the tether. The first location was the entrance slot into the LTCM, and the second the lid to the LTCM.

The plasma source which is not shown in Figure 1 was a simple hollow cathode source capable of producing a low temperature diffuse argon plasma. The hollow cathode plasma source was chosen because it could produce a relatively uniform plasma over the area of interest. Typical electron temperatures (Te) and plasma densities (np) during these tests were on the order of Te=0.8 and $np=1x10^{6}$ cm^{-3}. The emissive and langmuir probes shown in Figure 1 were used to characterize the plasma prior to initiating the tests. Only a few plasma tests were done because on-board flight data indicated the discharge was initiated inside the LTCM were the space plasma did not exist.

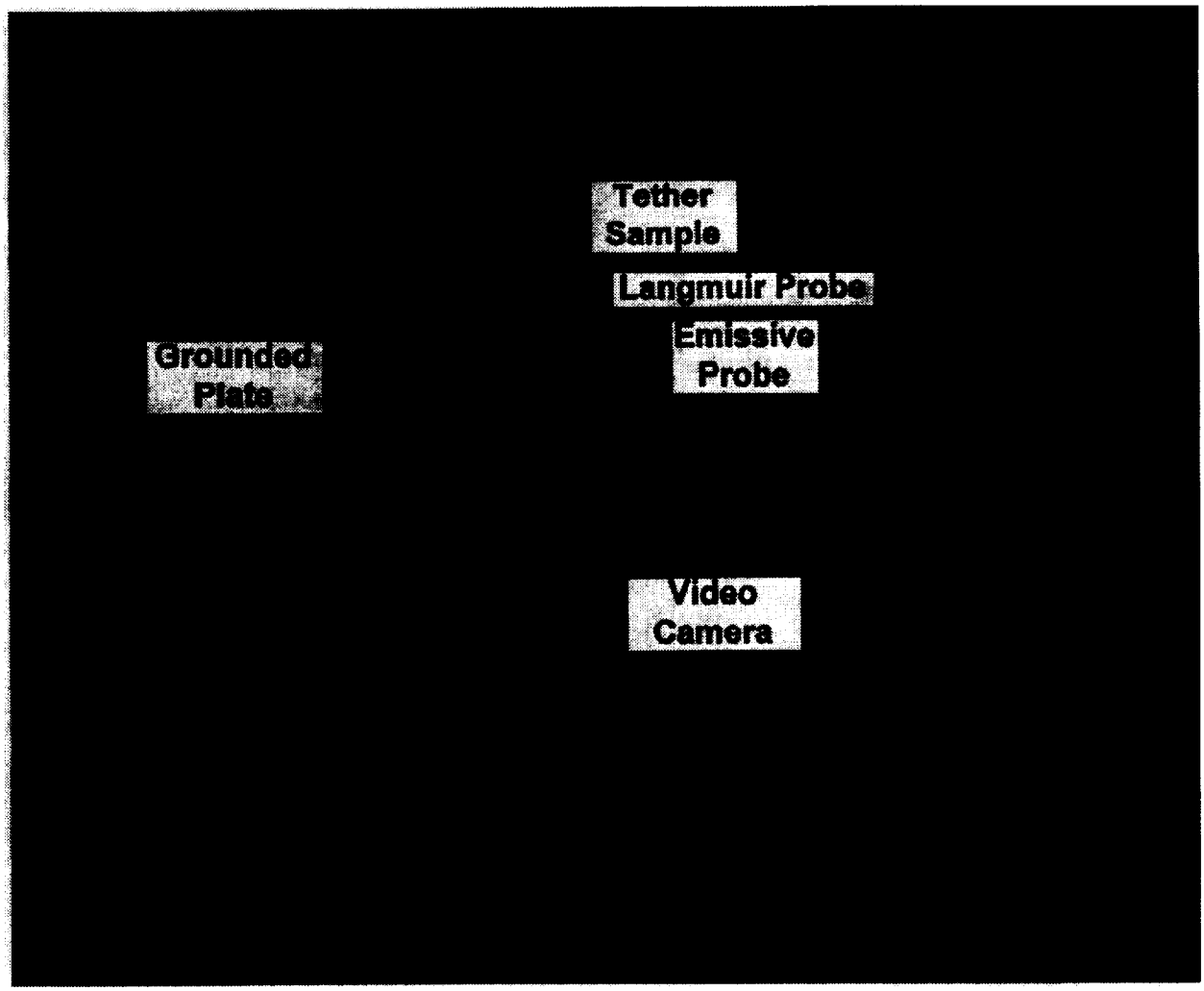

Figure 1. TSS-1R Vacuum Chamber Test

Video images of the discharge tests were taped using a high speed, light sensitive video camera. The camera was placed outside the chamber looking in through an optical view port towards the tether. The speed of the camera was sufficient to tape all discharge events. Several stunning video clips were obtained showing the magnitude of the discharge event.

Because the tether samples used in the tests were only 51 cm long compared to the entire actual flight tether length of 21.2 km, a load resistance had to be incorporated into the tests to simulate the resistance of the entire tether. Figure 2 shows the electrical wiring diagram for the tests. The 2289 W load represents the entire resistance of 21.2 km of tether. Because of the high power involved in these experiments, 300 W high powered resistors were wired in a combination of both parallel and series to develop the necessary resistance. The power supply used during these experiments had a maximum voltage of - 8000 V and a maximum current

of 0.7 A. The power supply was a current limiting supply which meant that for given voltage the current was limited to a specific level. In order to maximize the current during a discharge, the voltage had to be increased rapidly once the discharge was initiated at -3500 V. Data for each test were measured using a computer and data logger. At 2-second intervals the tether voltage (V_t), the power supply voltage (V_p), and tether current were recorded using a computer and data logger. V_t and V_p were measured using a high voltage probe with a high internal impedance and a 1000:1 voltage divider.

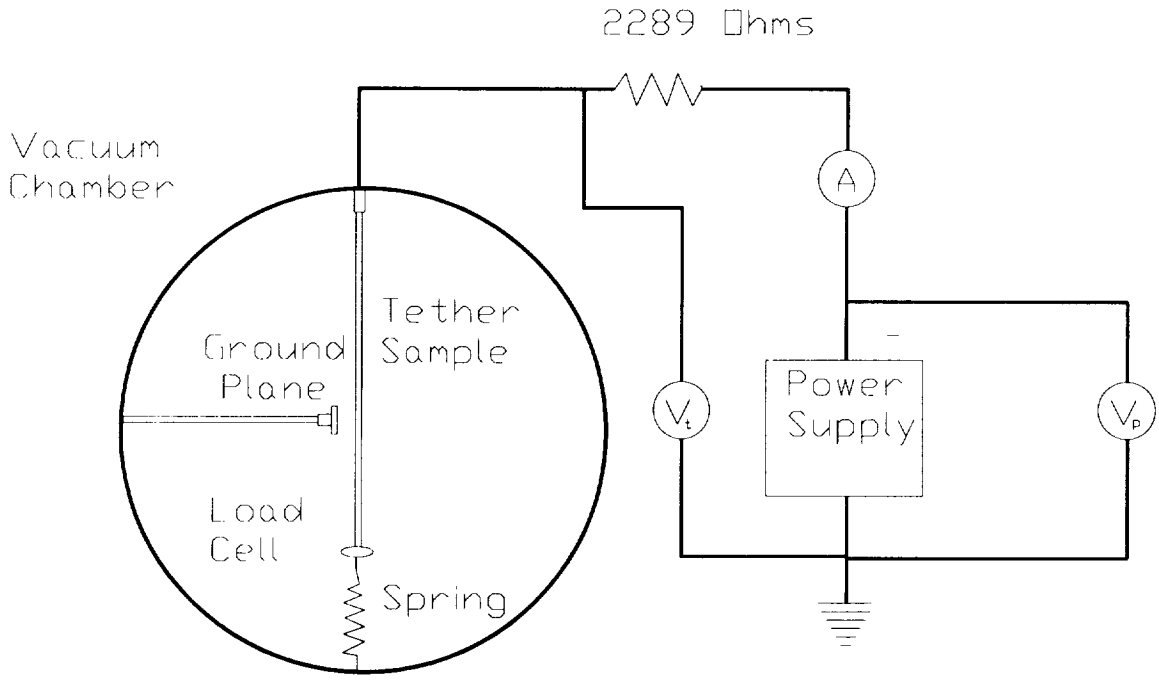

Figure 2. TSS-1R Electrical Test Schematic

At the start of the failure, the TSS-1R tether was loaded with a constant 67 N in tension. In order to increase the fidelity of the simulation, the actual test sample was loaded in a similar manner. A spring and a load cell were connected to the tether sample and the bottom of the chamber (Figure 2), to simulate as close to actual flight tension conditions as possible. The spring was connected to the chamber with a mechanical adjustment to set the tension. The load cell had a maximum load capacity of 111 N, and it was calibrated before each test. The load cell output was recorded at the same time as the tether current and voltage characteristics mentioned above.

Every test was started by cutting a 51-cm length of tether from stock which was cut from the actual 256-m flight tether flown on TSS-1 in 1992. Next a specific defect was made to the tether according to an overall test matrix developed for the investigation. Initially, the tether was exposed to all environments without any defect. Because the good tether did not discharge when biased to the power supply limit of -8000 V, all

efforts concentrated on tethers with some defect. The types of defects considered in these tests were pinholes ranging in size from 0.013 cm to 0.13 cm in diameter and debris imbedded in the tether conductor or insulation. Pinholes were placed into the tether using a blunt wire attached to a soldering iron. This method proved to be the most effective way of producing a hole which could be verified through a 100X microscope. Several other methods were tried including using a needle to penetrate the insulation, but the insulation seemed to heal itself making it difficult to be certain a pinhole actually existed. Later, fine drill bits were used to create very fine pinholes to determine the smallest pinhole which would create a discharge.

The tether was inserted into the chamber and the spring and load cell mechanism were connected to the tether. The correct load on the tether was set, and the chamber was pumped to $1x10^{-3}$ Torr. Higher vacuum levels (i.e., 10^{-7} to 10^{-4} Torr) were tried initially, but the tether would not discharge. Once the correct vacuum level was reached, the computer and data logger were started and the tether voltage was set at -3500 V. The tether would start discharging after waiting for a period of tens of seconds once the correct voltage was set. At the initiation of the discharge, the voltage on the power supply was increased to maximize the total amount of charge available. Typical tests lasted on the order of tens of seconds with discharge voltages of -150 to -200 V and discharge currents of 0.55 to 0.65 A observed. The test was usually concluded when the strength of the tether had deteriorated enough to allow the tension in the tether to initiate the failure. During some of the tests the tether would continue to discharge after the failure.

Experimental Results

The data from the flight sensors onboard TSS-1R [3] indicated the tether shorted to Orbiter ground and initiated an electrical discharge in the LTCM. While inside the LTCM and LTC mechanisms, the tether discharge stopped and reignited several times. When the same spot entered the LEO plasma, the tether maintained a steady discharge until the strength of the tether degraded enough to produce a tensile failure. From start to finish, the entire event lasted for a total of nine seconds. The results of these experimental simulations confirm an electrical discharge of this magnitude caused the flight tether to sever. The tether samples exposed in the vacuum chamber which failed under a tensile load exhibited similar physical characteristics as did the end recovered from TSS-1R. While the test data indicate the electrical discharge was capable of causing the tether to fail, the exact cause that initiated the discharge is unknown. The results from these tests indicate that a small pinhole or silver of debris imbedded into the tether conductor could initiate the discharge.

Figures 3, 4, and 5 show typical test data recorded when a tether with a 0.10-cm-diameter pinhole biased at -3500 V is placed in a $5x10^{-3}$ Torr vacuum. Figure 3 shows the tether potential, (V_t), plotted as a function of time in seconds. Sixteen seconds into the test the tether discharges, dropping most of the initial bias across the 2289 W load. Correspondingly, the tether discharge current increases from zero to 0.3 to 0.6 A as shown in Figure 4. Twenty-four seconds into the test the tether fails under tension as shown in Figure 5. However, the discharge current shown in Figure 4 has not gone to zero at 24 seconds.

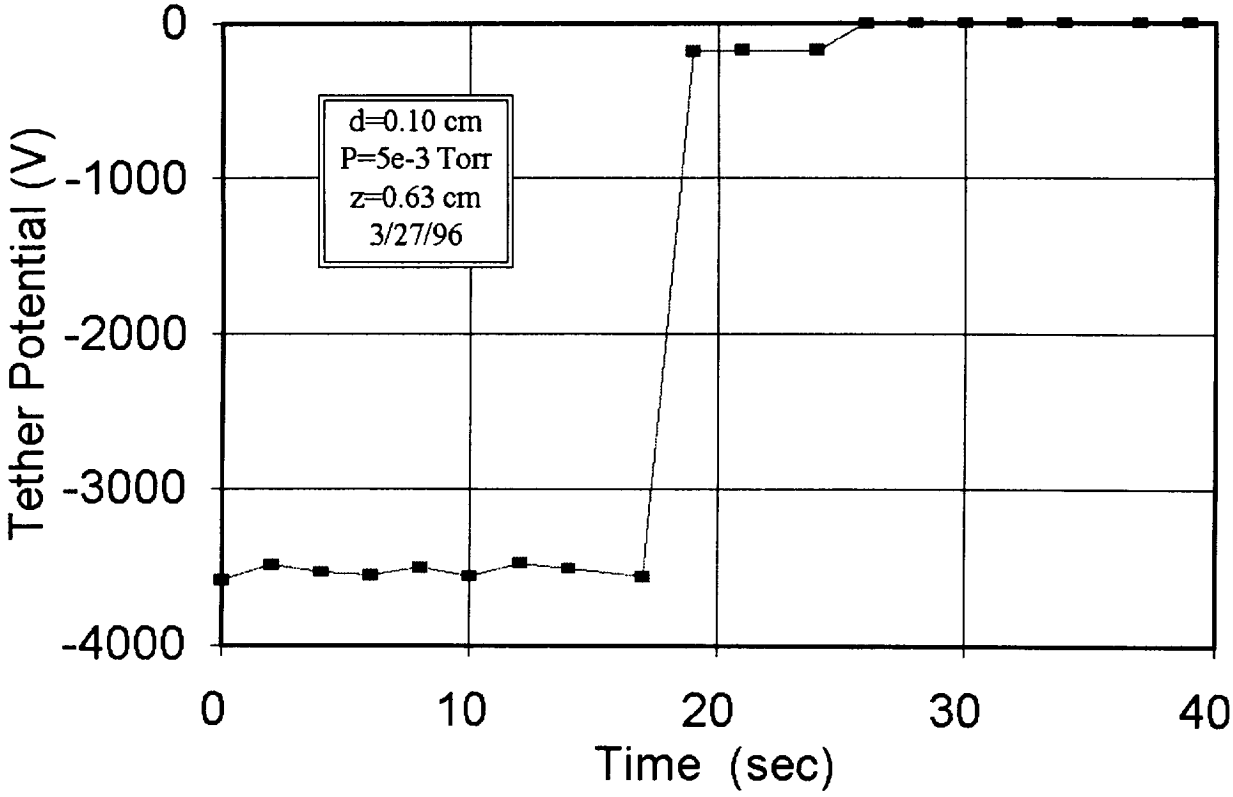

Figure 3. Typical Tether Voltage During Electrical Discharge

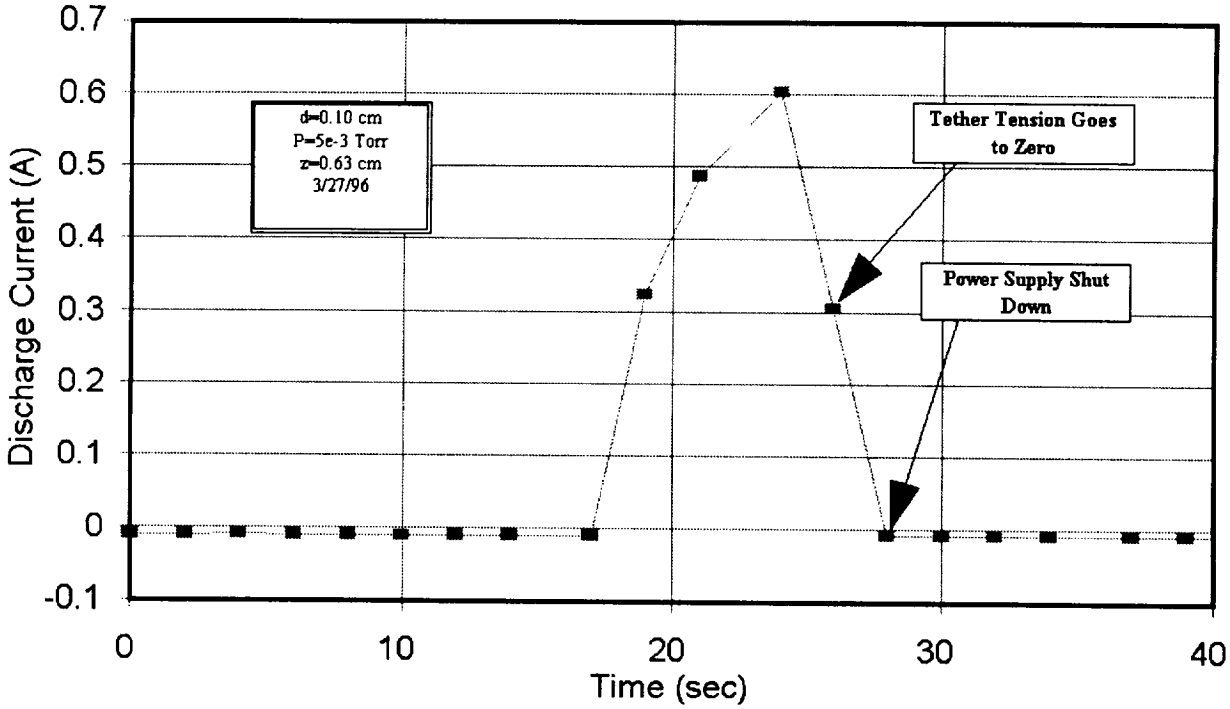

Figure 4. Typical Arc Discharge Current During Discharge

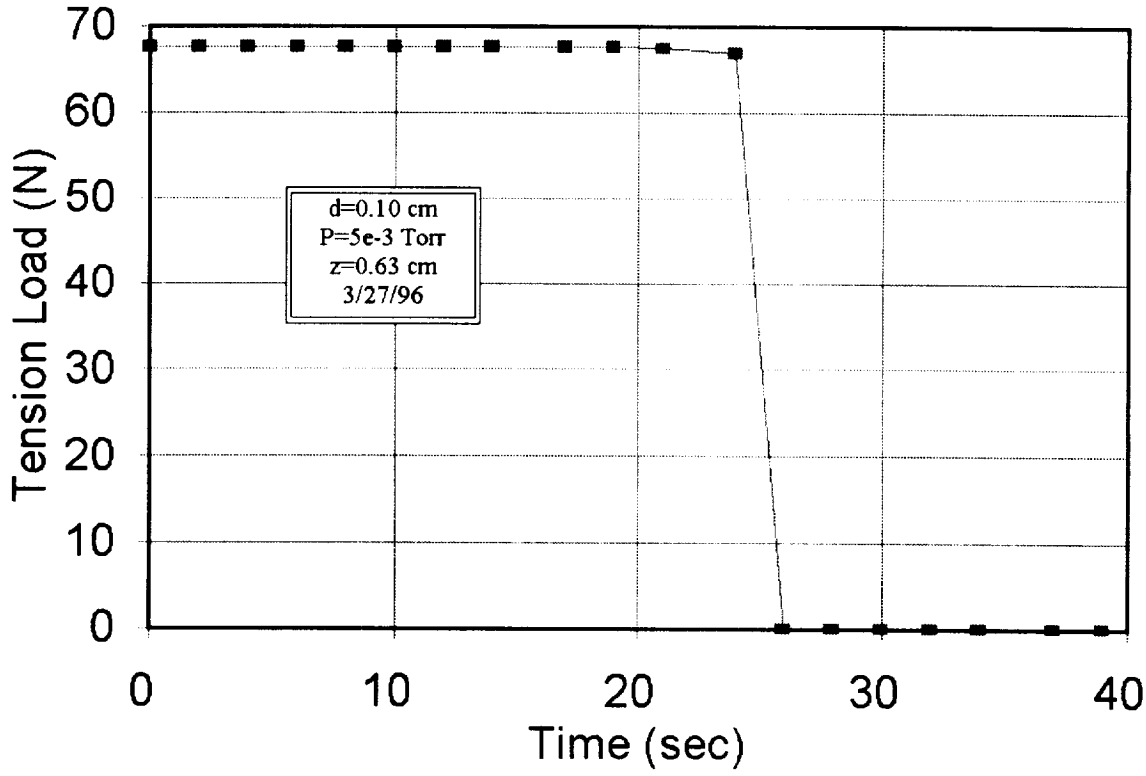

Figure 5. Typical Thether Tension During Discharge

This suggests that the tether continued to discharge to the environment after it was severed because it made its own dense plasma when the small copper wires were exposed to vacuum.

Tests were conducted in a diffuse LEO plasma for two reasons: 1) to determine if a discharge could actually be initiated with a tiny pinhole in a plasma and 2) to determine if the discharge could sustain itself once the tether is severed. Pinholes in dielectric materials exposed to the space plasma have been studied for many years relating back to solar array applications. However, the highest voltage ever considered was -140 V. Because these earlier tests were done at low potentials, the magnitude of current which could be collected through these pinholes at high voltages was not appreciated. Initial tests to expose a pinhole in the TSS-1R tether biased at -3500 V to a diffuse LEO plasma were not successful because the -3500 V could not be applied without a discharge being ignited at a lower potential (~-1500 V to -2000 V). In order to reproduce the conditions experienced by the TSS-1R tether, the plasma source had be turned on and stabilized, turned off, the potential applied to the tether, and the plasma source restarted. Once the plasma was re-established, the tether always discharged immediately causing the tether to fail. However, the length of time

the tether end would discharge after the tether severed was dependent upon the chamber pressure. Figures 6 and 7 show discharge current data taken from two separate plasma tests where the pressure was intentionally left higher in the first figure than the second. The data shown in the first figure continues to discharge for 24 seconds sputtering periodically. The discharge depicted in Figure 6 ran easily, and it had to be shut down at the power supply. Figure 7 shows a similar discharge in a plasma but the ambient pressure was one order of magnitude lower than in Figure 6. The discharge depicted by the data in Figure 7 shows the discharge stops abruptly, and repeated attempts to restart the discharge were not successful. Because of the length of the actual TSS-1R tether, a substantial amount of air was trapped within the hollow center of the tether. After the actual TSS-1R tether severed, the trapped air would escape into the discharge region of the tether and allow it to burn continuously as was observed from actual flight data [3]. Several other studies are presently examining the physics behind these observed phenomena.

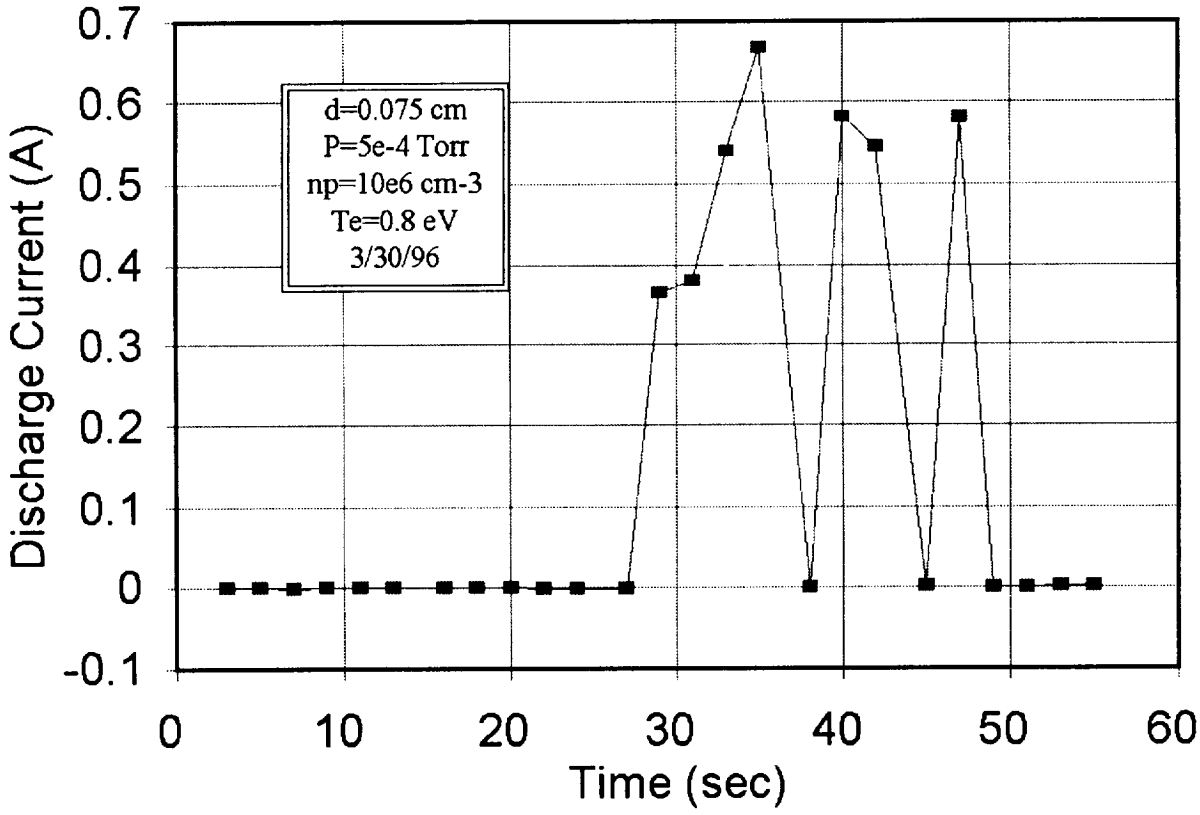

Figure 6. Arc Discharge Current in Plasma (High Pressure)

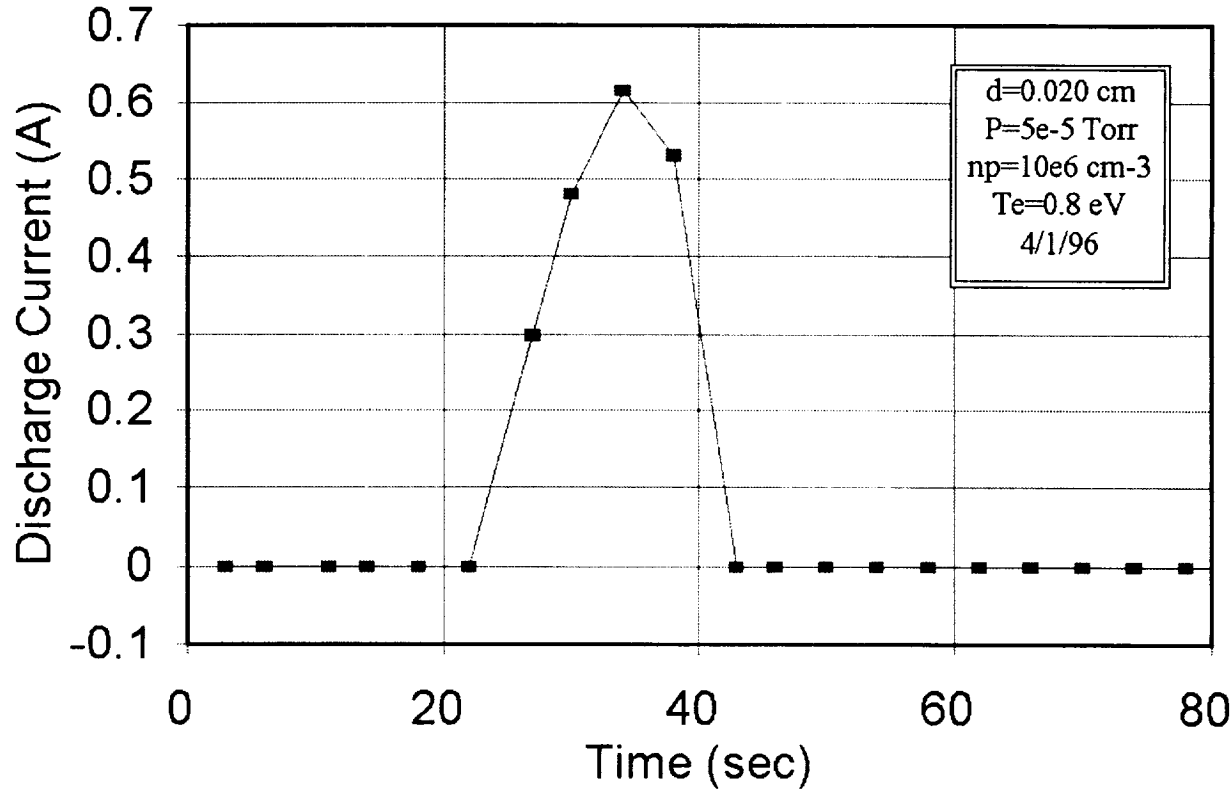

Figure 7. Arc Discharge Current in Plasma (Low Pressure)

Debris in the Tether

During the TSS-1R failure investigation several small metallic slivers were found inside the LTCM causing speculation that these pieces of debris could initiate the discharge. Several tests were done by placing small aluminum slivers into the tether. In one case a sliver made direct contact with the tether conductor, and in the other case the sliver was imbedded in the FEP insulation but not touching the conductor. With the metal particle touching the conductor and the ground plane 0.64 cm from the tether, a discharge was initiated at -3500 V and the tether failed similar to the data shown in Figures 3, 4, and 5. With the metal sliver only in the FEP, a discharge was initiated at -6000 V. Because TSS-1R data indicated the tether had a potential of -3500 V when the tether failed, these results suggest the aluminum sliver would have to be touching the copper conductor.

Static Electricity

After replicating the flight current and voltage data by physically breaching the FEP insulation with either a pinhole or a sliver of debris, other methods were considered which had the potential to breach the insulation without any flaw. Static electricity build up was considered as a possible method which could compromise the FEP insulation. Because both the tether outer NOMEX' layer and the pulleys are dielectrics, static electricity will build up on both the pulley and NOMEX' as the two

separate. Two separate tests were done to determine if enough static potential could be developed to breach the insulation. They were: 1) measure the static potential generated by simulating 19.7 km of tether running over Vespel 3P pulleys at 1 m/sec and 2) measure the maximum electrical potential required to breach the FEP insulation.

A two pulley racetrack was built to simulate the tether running through the deployer mechanism. A 1.5 m tether loop was run at 1 m/sec around the racetrack, and the potential generated on the pulleys was measured using an electrostatic field meter. In all cases the electrostatic field meter was calibrated using a metallic pulley biased from 0 to 5 kV. In order to simulate 19.7 km of tether running over the pulleys the tether was run continuously for 5.5 hours for one single test. Initial measurements were made in a clean room where the relative humidity was 35%, and the potential on the pulley measured was -800 V. A more accurate simulation was to place the racetrack in a low vacuum of 10^{-3} Torr and repeat the test. When the test was run in the vacuum for 5.5 hours the highest potential generated was -1200 V.

The actual potential required to arc through the dielectric was measured at two different facilities using hi-pot testers. One hi-pot tester had a maximum potential of 60 kV and the other a maximum of 40 kV. The tether insulation could not be breached using either machine. However, if a flaw existed in the tether insulation the hi-pot tester would trip at voltages as low as 3 kV.

The results of these two tests suggest the static electricity generated by running the tether over the pulleys was not sufficient to punch through a good piece of tether. However, it should be pointed out that the static electricity build-up is sufficient to attract any kind of debris in the local environment. This fact increases the probability that a debris particle could breach the tether.

Summary

The TSS-1R Mission Failure Board established that the tether failed as a result of arcing and burning of the tether that caused tensile failure of the tether [3]. This position was supported by orbital data and extensive ground testing. Furthermore, the Board stated that the arcing initiated at a breach in the FEP insulation of the tether inside the LTCM. The pressure inside the LTCM, the proximity of the tether to the grounded LTCM box at the entrance pulley, and the high voltage on the tether conductor provided favorable conditions for initiation of arcing [3]. Ground testing in support of the Board investigation supported these positions by determining the proper pressure and ground plane proximity conditions to induce arcing, by determining that arcing would not occur under these conditions unless the FEP insulation had been breached, and by proving that, under favorable conditions, arcing could be initiated and sustained long enough to cause tether failure, and continue after tether separation. These tests were successfully able to replicate arcing currents and voltages recorded on orbit.

References

1. JA-2413, "Tethered Satellite System (TSS-1R) Post Flight (STS-75) Mission Manager Report," George C. Marshall Space Flight Center, August 1996.
2. JA-2422, "Tethered Satellite System (TSS-1R) Post Flight (STS-75) Engineering Performance Report," George C. Marshall Space Flight Center, August 1996.
3. Final Report, TSS-1R Mission Failure Investigation Board, National Aeronautics and Space Administration, 5 May 1996.
4. "Tethered Satellite System (TSS-1R) Data Reference Book," George C. Marshall Space Flight Center, February 1996.

Robotic Materials Handling In Space: Mechanical Design Of The Robot Operated Materials Processing System HitchHiker Experiment

George Voellmer*

Abstract

The Goddard Space Flight Center has developed the Robot Operated Materials Processing System (ROMPS) that flew aboard STS-64 in September, 1994. The ROMPS robot transported pallets containing wafers of different materials from their storage racks to a furnace for thermal processing. A system of tapered guides and compliant springs was designed to deal with the potential misalignments. The robot and all the sample pallets were locked down for launch and landing. The design of the passive lockdown system, and the interplay between it and the alignment system are presented.

Introduction

ROMPS was developed by the National Aeronautics and Space Administration and flew aboard the Space Shuttle "Discovery" on mission STS-64 in September, 1994. The purpose of ROMPS was to investigate the effects of microgravity on several semiconductor manufacturing processes, including crystal growth in thin film semiconductors. The function of the ROMPS robot is to transport pallets containing wafers of different materials from their storage racks to a furnace for thermal processing, and then return them to their racks.

A significant aspect of the ROMPS mechanical design effort was to ensure that the experiment would survive the vibration environment at launch and landing. The robot and all the sample pallets were therefore passively locked down at these times. The challenge lay in allowing for the potential misalignment between the various components that are repeatedly inserted and removed from their launch locks, while keeping the locking mechanism simple and passive. A system of catches, tapered guides, and compliant springs was designed to work within the robot's force and accuracy capabilities.

This paper provides a mechanical design overview of ROMPS, it illustrates the specific steps taken to survive the vibration environment, and it provides a discussion of the robotic object hand-off considerations.

Mechanical Design Overview

As configured for its first flight, ROMPS accommodates 138 material samples. In the September, 1994, Shuttle flight of ROMPS aboard NSTS-64, 9 different types of samples were flown. These particular samples consisted of thin, square wafers ranging from 1 to 1.5 cm on a side.

* NASA Goddard Space Flight Center, Greenbelt, MD

The ROMPS robot picks up a pallet containing a sample wafer and transports it to a halogen bulb furnace, where the material is processed. On its initial space flight, the processing involved rapid heating of the materials to various temperatures. The lack of gravity effects at the time of processing was expected to confer beneficial properties to the materials. The nature of the benefit is different in each of the different types of samples, but it generally results from reducing convective flow within the molten material, or from reducing convective flow of the gases surrounding the material.

The ROMPS experiment, as it attaches to the Space Shuttle (Figure 1), consists of three parts:

1) the Processor can, a full size Get Away Special (GAS) canister with a 127 mm (5 in) extension;

2) the Controller can, a half height canister; and

3) the HitchHiker avionics box.

The Processor can, which houses the robot, the furnaces, and the material samples, is 584 mm (23 in) in diameter and 965 mm (38 in) long. The Controller can is half that height, and it houses the control electronics and computers. The HitchHiker avionics contains the power and data interfaces to the Shuttle.

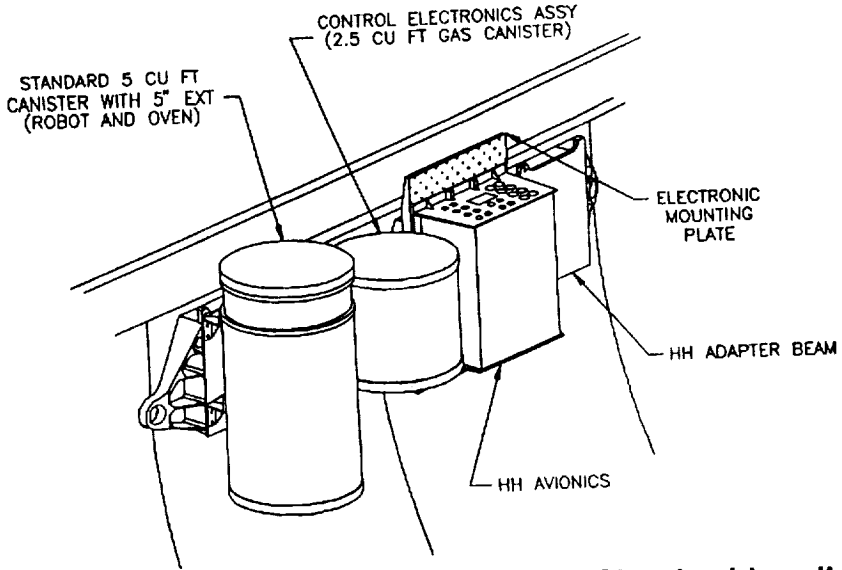

Figure 1. ROMPS As Mounted To The Shuttle sidewall

The ROMPS Robot

The ROMPS robot (Figure 2) is a three axis, cylindrical workspace robot, with a gripper. The Elevation- or Z- axis joint consists of a motor and a ball screw shaft, which together move the carriage arm, and with it the rest of the robot, on linear bearings, up and down along the axis of the can.

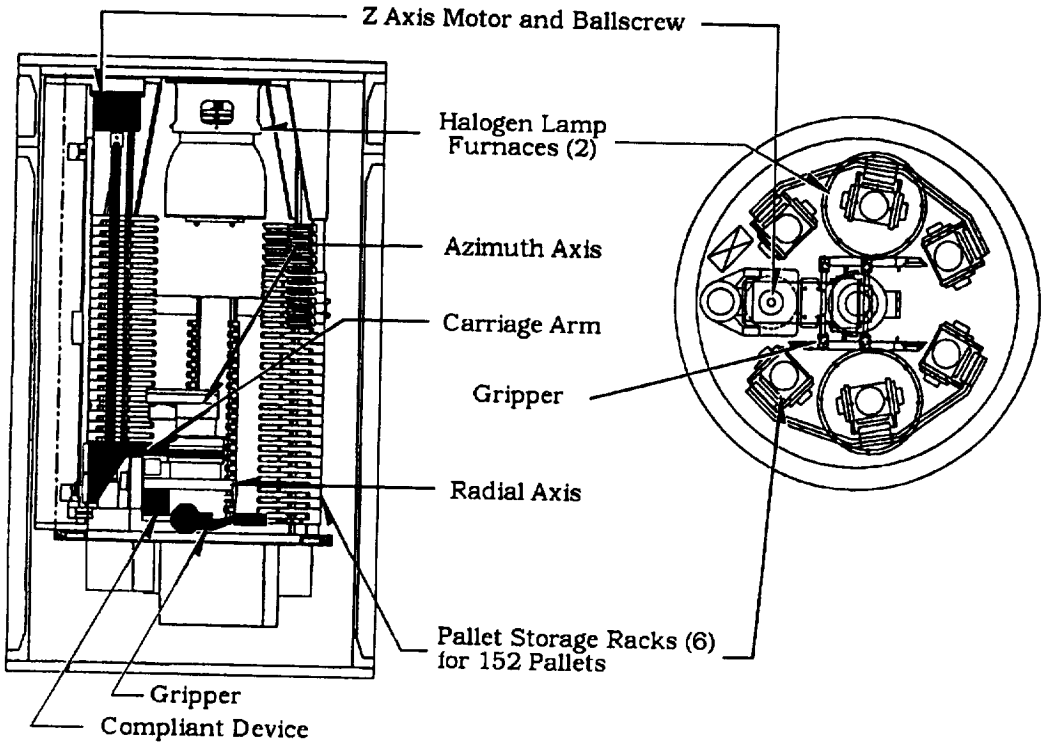

Figure 2. ROMPS Experiment Side And Top View Showing Robot, Furnace, Sample Racks With Samples, And The Location Of The Gripper and the compliant device

The azimuth axis is mounted to the carriage arm. It consists of a motor and a harmonic drive speed reducer, which then forms the base for the radial axis. The azimuth axis is located at the geometric center of the can, so that the robot's radial axis joint is always perpendicular to the GAS can's inner surface.

The radial axis consists of a motor and spur gear set, which drives a ball screw. The ball screw pushes a linear bearing back and forth, radially out towards the can wall.

The gripper (Figure 3) is mounted to this linear bearing via a compliant device. This device provides compliance in the radial axis and elevation axis directions.

The gripper fingers are driven by a hollow motor and a small harmonic drive. An acme screw with left hand threads on one end and right hand threads on the other goes through the hollow motor/harmonic drive assembly, and engages nuts mounted in the fingers. These nuts press against springs in the fingers, moving the fingers. The springs provide compliance for the gripper finger throw axis, as well as the azimuth rotation axis.

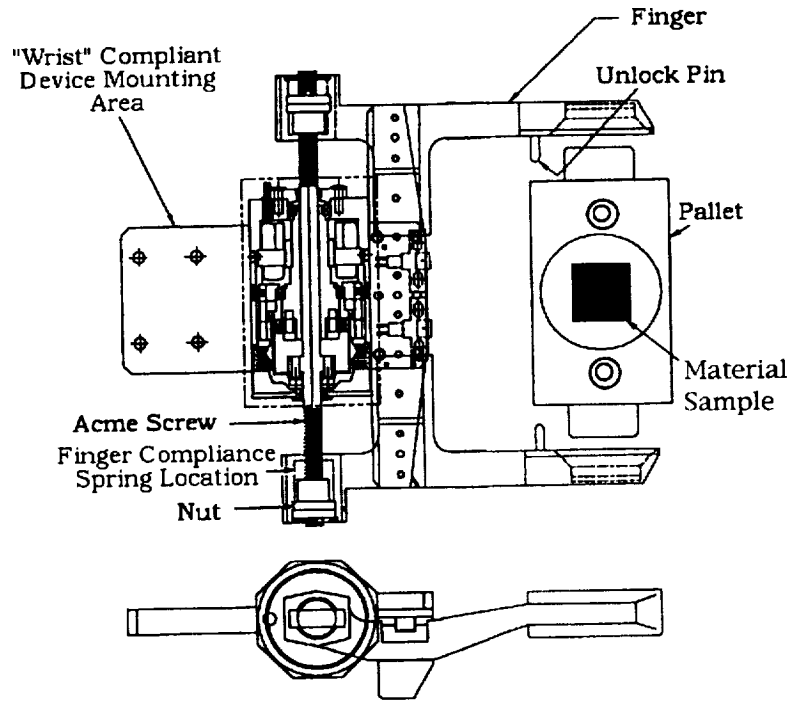

Figure 3. The ROMPS Robot Gripper

ROMPS Operation

In operation, the robot moves into position in front of the pallet in its storage rack by rotating the azimuth joint and moving to the appropriate elevation with the elevation axis drive. During these moves, the radial axis is retracted. Once in position, the radial axis extends, with the gripper fingers open. When the radial axis is in the correct location, the gripper fingers close on the pallet. After a secure grip has been established, the radial axis retracts, pulling the pallet out of its storage rack.

Once free of the rack, the robot moves the pallet into position in front of, and slightly below, one of the furnaces. The radial axis then extends until the pallet is directly below the aperture in the halogen bulb furnace. Two pins extend down from the furnace, which engage two holes in the pallet as the pallet moves up into contact with the base of the furnace, aligning the material sample in the pallet with the focus of the light in the halogen bulb furnace.

An issue of concern was that as the robot grasps the pallets, and when it docks them into the racks and the furnaces, it will always be slightly misaligned. ROMPS accommodates this misalignment by using a passive compliant device and the capture guides built into all the robot interfaces. The capture guides nudge the mating pieces into alignment, and the compliant device provides a controlled amount of "give". This is discussed in detail in the "Object Hand-off" section.

Removal of the sample from the furnace and its return to the storage rack are the reverse of the above sequence.

Before and after all robot operations, the robot gripper is locked to the elevation axis support column by the fingers closing on a launch lock fixture. The fingers simply close to grasp the fixture, and open to release it. This serves to isolate the gripper's compliant device from the launch and landing vibration loads.

The ROMPS robot uses position control; the force is only monitored. When the robot needs to apply a specific force, such as when it is pressing the pallet against the furnace, the robot behaves as though it were moving the pallet past the furnace a certain amount, in this case 3.3 mm (0.13 in). When the pallet contacts the base of the furnace, the compliant device is compressed 3.3 mm (plus or minus the accuracy of the robot). The force is then a function of the compliant device's stiffness in that axis.

Surviving The Vibration Environment

Defining the Vibration Environment

The Space Shuttle vibration environment can be assumed to consist of two components. The first consists of low frequency sinusoidal oscillations, which in the case of ROMPS was determined to be structurally equivalent to a steady gravity loading of 15 G's in any direction. The second component is random "white noise", with a specified spectral energy distribution, or Acceleration Spectral Density (ASD), of 0.022 G^2/Hz between 50 and 800 Hz. From 50 down to 20 Hz and from 800 up to 2000 Hz the slope of the ASD is sloped down to zero logarithmically.

Design Features to Ensure Survival

Hand Analyses as well as Finite Element Analyses were used to verify that the structures all had the required Factors of Safety for the steady 15G loading. The random vibration has the effect of backing out screws, and causing anything relying on a friction hold to "walk" out, in addition to exciting unanticipated structural resonances in the system. Therefore, the robot gripper and all the sample pallets needed to be positively locked down during launch, released once in orbit, and relocked for landing., not using a friction hold.

The Gripper Launch Locks.

The robot axes are stiff and strong enough to survive the launch and landing loads without additional support. This is not true of the robot's gripper: It is attached to the rest of the robot via a compliant device, or spring, as described the previous section. If left unsupported during launch, the gripper would oscillate about this spring, and likely damage the spring. So the gripper needed to be locked down for launch and landing. It was decided to have the fingers grip a launch fixture mounted to the elevation axis support column. This imposed the burden on the fingers of having to hold the load of the gripper during launch and landing, but operationally, it worked very smoothly. The robot was near the ends of travel at startup on all axes, for easy initialization. In the event of position telemetry loss, the robot could be driven to the joint limits and backed off a bit, and it would have a good chance of getting back into the launch locks.

The Pallet Launch Locks.

Figures 4 and 5 show the pallet near the rack. The pallet is essentially a flat tray, and the rack is made up of two rows of tines. The rack resembles two combs, aligned parallel to one another, with the tines facing the same direction. The pallets fit into the

tines of the combs, and are thereby neatly stacked. The sides of the pallets have "fences" which extend downward from the surface of the pallet on the outside of the rack, preventing the pallet from coming out of the rack to the side.

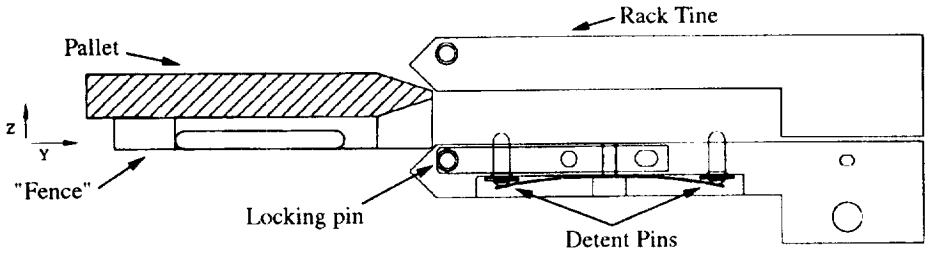

Figure 4. Side View, The Pallet Entering The Rack, Misaligned In +Z

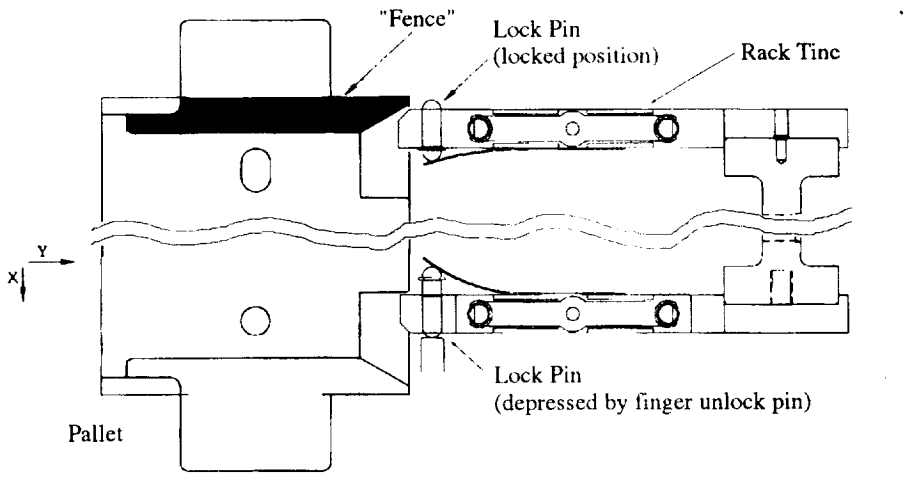

Figure 5. Top View, The Pallet Entering The Rack

Spring-loaded detent pins in the lower rack tines press the pallet up against the upper rack tine with about one pound of force, preventing rattling of the pallets in their rack during launch and landing. A lock pin in each of the tines extends out sideways behind the fence under each pallet, preventing the pallet from coming out of its storage position. An unlock pin in the finger pad (see Figures 3 and 5) presses against the lock pin as the fingers acquire a given pallet, depressing the two lock pins for that pallet, and allowing the pallet to be removed.

This passive method of locking down and releasing the sample pallets proved very reliable during testing and while operating in space, and did not require any additional actuators.

Vibration Test Plan and Outcome of the Test

The experiment was vibrated in all three dimensions to the levels specified earlier, while everything was stowed in its launch locks. A full functional test was subsequently performed, with no anomalies or observed degradation of performance.

The Flight Experience

Mechanically, the experiment operated nominally during the flight. There was one software problem and there were two electrical problems during the flight.

1) Fairly early in the mission, the oven was not shutting off as scheduled. A bug in the operating system of the oven control computer was losing track of the amount of time the oven was engaged. This problem was mitigated during the flight by periodically commanding the computer to reset itself throughout the mission.

2) About 80% through the mission, the robot was found to be hitting its end-of-travel limits unexpectedly during radial motions. After the mission, this was traced back to an intermittent open circuit in one of the radial axis encoder lines, due to a failed splice in the radial axis service loop. The workaround was to reinitialize the encoder counter each time the radial axis moved, so the error from the intermittent dropouts in encoder pulses would not accumulate.

3) The second electrical problem occurred after all the processing was completed and engineering tests were being performed on the robot. The readings on the gripper and wrist strain gauges suddenly went off the scale, causing the overforce protection circuitry to shut down the robot, and about half the temperature sensors went dead. After the flight, this was found to be due to an amplifier integrated circuit that failed. Ironically, this IC was one of the few high-reliability military grade components that had been used in an otherwise commercial grade system. Since the mission had essentially been completed, the force limits were overridden and the robot was commanded to stow itself for landing. The robot operated normally, although with increased risk, since the primary collision and overforce detection system was being bypassed.

Object Hand-off

When an object is being moved from one location to another by an autonomous mechanism, there will always be some uncertainty about exactly where it is located. This can be due to thermal distortions of the structure, backlash in the drive train, manufacturing inaccuracies, limitations on the resolution of the position feedback sensors, accuracy of the control system, or a host of other reasons.

Misalignments are of particular concern when a hand-off of the object is to take place. Vibration during launch and causes anything relying on a friction hold to "walk" out. Therefore, the robot and all the sample pallets need to be positively locked down for launch and landing, not relying on friction. Since the object needs to be locked down securely before and after being moved, as well as during the move (to ensure that the system remain safe to land should the robot fail in mid move), the object cannot shift to accommodate these misalignments.

In order to perform a secure hand-off despite the unavoidable inaccuracies, three things are necessary: 1) a capture range, 2) compliance, and 3) sufficient force.

1) The interfaces need features which will draw the mating objects into alignment, such as tapers or chamfers. The capture range provided by these alignment features must be greater than any possible misalignment.

2) There must be sufficient compliance, or give, specifically built into the system to allow the alignment devices to move the object into alignment.

3) The mating parts must be brought together with enough force to allow the alignment features to deflect the compliant device by the amount of the misalignment.

In the design of the ROMPS robot, a position error budget was developed first, which fixed the required capture range. The force level was then set. Finally, the required stiffness of the compliant device in the various directions where compliance was needed was calculated.

Capture Range

The easiest way to keep the cost of the robot down was to use a position controlled robot, relax the accuracy requirements, and provide a large capture range. This allowed the use of cheaper and simpler control electronics, bearings, other drive train components, and position transducers. Additionally, ground testing of the experiment was much easier: since the misalignment effects of gravity deflecting all the structures and biasing all the backlash is a small percentage of the capture range, it can therefore be neglected, and no gravity off-loading schemes needed to be devised.

The ROMPS robot was be taught the positions of all the interfaces it must reach: hence, the absolute accuracy of the robot is less important than its repeatability. The repeatability of the robot is governed by the controller repeatability, backlash in the drive train, the distortions in the structures due to thermal gradients, thermal expansion coefficient mismatch, and deflections due to loading of the structure. Because of the complexity of the mechanism, many simplifying assumptions were made, and a large margin for error was used.

The controller was designed to give a repeatability of at least 0.76 mm (0.030 in) in all three linear axes, measured at the tool tip.

Drive train components with a total, combined backlash of less than 0.76 mm (0.030 in) per axis were selected.

Thermally matched materials were used in all the pallet storage rack structural members and the robot structural members, and deflections of any part of the experiment with respect to another part due to thermal gradients is less than 0.18 mm (0.007 in), according to the thermal model.

Finally, deflections of the system due to gravity loading were analytically determined to be less than 1.27 mm (0.050 in).

The sum of these errors is 2.97 mm (0.117 in). This is a very conservative number, as the errors are not likely to occur at the same time in the same axis. A target capture range of ±6.35 mm (0.250 in) was chosen for all three axes. This allowed for a

relatively large position error for the robot, given the size of the GAS can (approximately 711 mm (28 in) long x 508 mm (20 in) diameter). At the same time, capture features and a compliant device for a 6.35 mm (0.250 in) capture range did not appear to be too difficult to design for the available space. The only error which will cause a misalignment in an axis in which the robot does not move, such as rotation about the gripper, is the thermal gradient distortion. This misalignment is comparatively small, and easily within the capture range of the interfaces.

Having selected the capture range, it was then necessary to design the interfaces with the appropriate capture features.

The interfaces consist of 1) the pallet fitting into its storage rack, 2) the fingers grabbing a pallet, 3) the pallet fitting against the furnace, and 4) the gripper fingers grabbing the launch locks.

The Pallet/Storage Rack Interface

The transfer of a pallet from the pallet storage racks to the gripper fingers constitutes a hand-off, hence the alignment fixtures need to take into account the potential misalignment of the storage racks, as well as that of the pallet in the gripper, and that of the robot. In the other interfaces, the 6.35 mm (0.250 in) capture range was used as a guideline; here, it was strictly adhered to.

Figures 4 and 5 show the pallet near the rack. The pallet is essentially a flat tray, and the rack is made up of two rows of tines. The rack resembles two combs, aligned parallel to one another, with the tines facing the same direction. The pallets fit into the tines of the combs, and are thereby neatly stacked.

On insertion into its particular set of rack tines, the pallet's largest potential misalignments are in the Z direction (up and down), and in the X axis (left and right). These are the robot's motion directions. Other potential misalignments, such as rotations about Y, are not in the robot's motion directions, and would therefore not be caused by the robot's position error. Rather, misalignment in these directions would be caused by manufacturing and assembly inaccuracies. These can be controlled much tighter than the robot's position inaccuracy, and the potential misalignment here is much smaller. Simply having a loose fit at the interface takes care of these misalignments.

To align the pallet to the rack in the Z direction, the pallet leading edge is chamfered, as well as the top and bottom of the rack tines. The pallet leading edge is only chamfered where the tines can contact it, assuming the worst case misalignment in the y axis. The pallet has a 2.54 mm (0.1 in) chamfer top and bottom, and the rack tines have 4.32 mm (0.17 in) chamfers. These chamfers combine to provide a total capture range, for this axis, of 6.86 mm (0.27 in). The chamfer on the pallet has an angle of 18 deg, and the chamfer on the rack tine has a chamfer of 45 deg. Therefore, if the misalignment is less than the 2.54 mm (0.1 in) capture range of the pallet chamfer, the pallet will enter the rack until the corner where the chamfer on the rack tine starts contacts the 18 deg slope of the pallet chamfer, and the position correction is done by the 18 deg slope. If the misalignment is greater than 2.54 mm (0.1 in), then the leading edge of the pallet will contact the 45 deg slope of the chamfer on the rack tine, and the

correction will be done by the 45 deg slope, until the misalignment becomes less than 2.54 mm (0.1 in). The system then corrects as described earlier.

To align the pallet in the Y direction, the pallet has two "fences" extending down from its bottom surface. When the pallet is in its rack, these fences fall to the outside of the respective rack tine. This prevents the pallet from being moved out sideways, and locates the pallet. There is nominally .76 mm (0.030 in) of play between the pallet and the racks, to prevent binding as the pallet slides in and out of the rack, and to allow for small misalignments in off directions, as discussed earlier. It should be noted that while this play is necessary for the smooth operation of the interface, it contributes directly to the uncertainty in the position of the pallet, and hence to the total capture range required.

Detent spring-loaded pins in the lower rack tines press the pallet up against the upper rack tine with about one pound of force, preventing rattling of the pallets in their rack during launch and landing. A lock pin in each of the tines extends out behind the fence under each pallet, preventing the pallet from coming out of its storage position. An unlock pin in the finger pad presses against the lock pin as the fingers acquire a given pallet, depressing the two lock pins for that pallet, and allowing the pallet to be removed.

As can be seen in Figure 5, the sides of the fences on the pallet are chamfered, and the rack tines are chamfered in this direction as well, although only on the outsides. The fence chamfer is 4.32 mm (0.17 in) deep, and the chamfer on the outside of the rack is 3.81 mm (0.15 in) deep, for a total of 3.81 mm (0.32 in) of capture range.

The Pallet/Finger Interface

The pallet/finger interface, shown in Figures 6 and 7, is the second part of the hand-off of the pallet from the rack to the fingers. The pallets have 2.67 mm (0.105 in) thick, rectangular "ears", or tabs, which extend out from the edges of the pallet. When the pallets are in the rack, the ears extend out the sides.

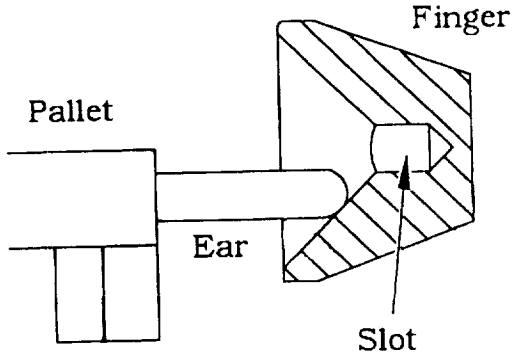

Figure 6. End View (Cross Section) Of The Finger / Pallet Interface, Pallet Misaligned In Z

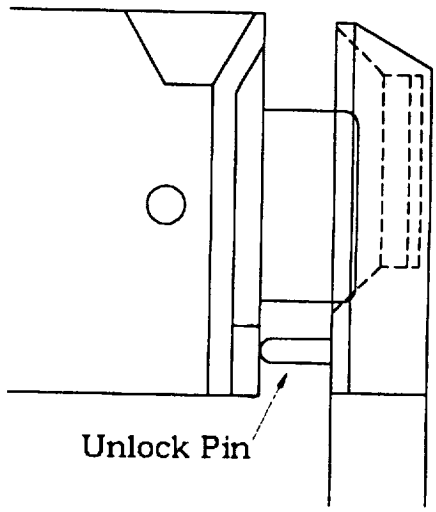

Figure 7. Top View Of The Finger / Pallet Interface

The finger pads each have a slot in their inner faces into which the pallet ears fit, which is 0.51 mm (0.020 in) wider than the pallet ears. The outside edges of the ears are given a full radius, and the bottom of the slot in the finger is V-shaped. Thus when the finger is closed upon the pallet with a force, the ears enter the slots and rattle about until they encounter the bottom of the slot. There, the 45 deg V-shaped bottom centers the ear within the slot. This locates the pallet more repeatably with respect to the finger. If the pallet should encounter a force trying to pry it out of the fingers, however, the ear would tend to spread the fingers until it contacted the side of the slot. At this point, any additional force would not tend to spread the fingers any further, but would be taken up by the finger structure. This feature provides the fail-safe, non-backdriveable grasp of the object necessary for safety in space applications.

As an alignment feature, the slot has a 45 deg chamfer of 6.35 mm (0.250 in) width around it. This fixes the size of the finger pad at

$$2 * 6.35 \text{ mm} + 3.17 \text{ mm} + 2 * .76 \text{ mm (edge thickness)} = 17.4 \text{ mm (0.685 in)}$$

This also fixes the minimum spacing between adjacent pallets in the rack: they had to be far enough apart so that when the finger was at its worst case misalignment up or down, it would not contact the ear of the pallet above or below.

At first, four flat chamfers were put around the slot, which intersected in straight lines radiating out from the slot. Although the chamfer faces are all 45 deg slopes, the line of intersection of two 45 deg slopes is only sloped 35 deg. During testing, the 45 deg slopes were steep enough to pull the pallet into the slot, but if the pallet ear worked its way into the line of intersection of two slopes, which happened every time there was a misalignment in two axes, it would get hung up there.

To overcome this problem, the chamfer had to be curved around the slot. This was done by cutting it with the end of a 45 deg tip end mill. In this way, the slope of the

chamfer is 45 deg at all points. The effect of this is to reduce the capture range from being a rectangle with 6.35 mm (0.25 in) sides to being a circle of 6.35 mm (0.25 in) diameter. Thus, rather than both axes being able to be off by 6.35 mm (0.25 in), the root sum square of the errors could not exceed 6.35 mm (0.25 in).

The Pallet / Furnace Interface

The furnace consists of a halogen bulb in an elliptical reflector. The radiation from the bulb is focused into an aperture in the bottom of the reflector. The sample pallets contain thin, flat films of various materials. These need to be accurately placed in the focus of the beam. The accuracy requirement was given as 0.51 mm (0.020 in) in all three axes.

The bottom of the furnace was made flat, so the Z axis positioning of the sample pallet is accomplished accurately by simply pressing the pallet flat against the bottom of the furnace. The rotational misalignments will be small, and the inherent compliance of the robot together with a positive pressure will ensure flush contact.

For the other two axes, the furnace has two 12.7 mm (0.5 in) diameter pins which extend down on either side of the aperture. These engage two holes in the pallet, on either side of the sample (see Figure 8). One of the holes is round, nominally 0.25 mm (0.010 in) bigger than its pin. The other hole is a slot, with the short axis also 0.25 mm (0.010 in) bigger than the pin. The long axis points toward the other hole and is 2.54 mm (0.1 in) longer than the pin's diameter. This keeps the interface highly repeatable, and prevents it from binding.

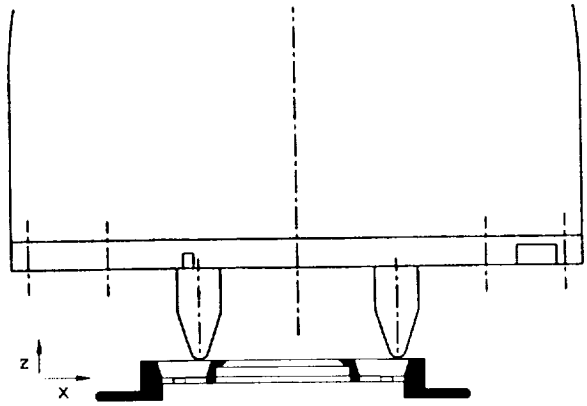

Figure 8. The Pallet Below The Furnace, Misaligned In X

To provide a capture range, the holes in the pallet have a 36 deg countersink which opens up to a diameter of 15.75 mm (0.620 in), and the pins have and rounded tips with a 30 deg taper, for a total capture range of 7.87 mm (0.31 in). The tapered part of the pins is extended away from the base of the oven 12.7 mm (0.5 in). This is because as the robot is moving up in Z to engage a pallet misaligned in X, the robot will comply in Z as force is built up due to the misalignment. The extension ensures that the compliant device is forced to deflect in Z enough to build up sufficient Z force to allow the tapered pin to drive the compliant device over in X.

The Finger / Launch Lock Interface

Since the gripper is mounted to the rest of the robot via a compliant spring, there is a concern that it might oscillate wildly during vibration, stressing the compliant device excessively. For that reason, the gripper will grab a launch lock fixture on the main Elevation axis support post. This relieved any loading from the compliant device during launch and landing. This interface had to be similar to the pallet/finger interface in that the launch lock needs to locate the finger precisely, to prevent rattling, yet large forces must not be able to pry the fingers out of the interface.

This interface was therefore designed in a similar way (see Figure 9). The launch lock fixture is a block of metal with a slot cut into it, which the finger pad fits into. To lock the gripper down, the gripper inserts its fingers into the fixtures and closes them tight. The gripper drive train is a 6.35 mm (0.25 in) diameter, 6.3 threads per cm (16 thread per inch) acme screw, which is a sticking taper and is not backdriveable. The finger cannot be pried out of the fixture, but there is play, to ensure that the pads do not bind in the fixture on their way in or out. This play would allow the gripper to rattle during high vibrations, significantly increasing the contact stresses at the interface, the contact stresses at the finger linear bearings, and the bending stresses in the fingers.

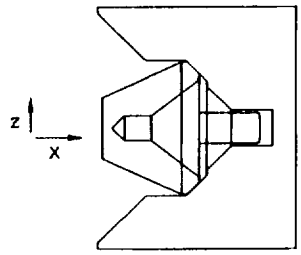

Figure 9. The Gripper Finger In The Launch Lock Fixture

To locate the fingers in the launch lock fixtures, the bottom of the slots in the fixtures have 45 deg slopes which snug up on matching 45 deg chamfers on the top and bottom edges of the finger pads as the fingers close into the fixtures. This locates the fingers in the Z (up and down) direction. Because the grip force is pressing a 45 deg wedge into a 45 deg slot, the normal force at that interface is quite high, and the friction force preventing radial (Y-Axis) motion of the finger pad in the fixture is large enough to prevent rattling in that direction. To prevent a large force from pulling the finger out of the fixture in the radial direction, the Unlock pins in the finger pad (see Figure 3) fit into holes in the launch lock fixture. These holes are chamfered to guide the pin in the radial direction. The holes are 0.76 mm (0.030 in) oversized, to prevent binding.

Working Forces

The working force is the force that the robot is expected to actually use to do its work. It is the average maximum force the robot will need to apply, in a given axis, to perform the task at hand. The maximum force is the force which may be needed to overcome unexpectedly high friction, greater than average misalignment, or some slight binding. The robot's continuous force capacity is the force the robot can exert if the rated voltage is continuously applied to the joint motors, without overheating.

As an initial estimate, a working force level for the robot was set at five pounds in all three axes. Five pounds would be enough to actuate a mechanism or pull a pallet out against its detent springs, it was reasoned, and to provide a comfortably large pressure to ensure proper contact between two mating pieces. Yet five pounds was not such a large force that large motor currents would be needed, or that the motors and drive train would grow heavy and unwieldy. This is of particular concern in a serial-link robot in a gravity field, where the base joints must carry the outboard joint as well as provide a tip force.

As the design progressed, it became apparent that the azimuth joint was only needed to position the gripper, and not to apply any forces. Its maximum force requirement was therefore left as five pounds. The Z axis joint needed to apply a 22 N (5 lb) load to press the pallet against the furnace, and the radial joint needed to apply22 N (5 lb) to push and pull the pallets into and out of their storage racks against the detent springs. These axes' maximum force requirements were therefore multiplied by 5, to get 110 N (25 lb), to ensure a positive torque margin. Additionally, the Z axis needs to lift the rest of the robot up during testing in a gravity field, so an additional 67 N (15 lb) was added to its maximum force requirement for a total of 177 N (40 lb). The robot's joint motors were then selected to provide a continuous force capacity of at least three times the maximum force requirement.

The selection of the grip force was more complicated. The Z and radial axes had working forces of 22 N (5 lb). This would be the force necessary to overcome an average misalignment. The maximum misalignment was assumed to be twice the average misalignment. Assuming a linear compliant device, this set the maximum force level at ten pounds.

Therefore, the gripper fingers squeezing on the pallet ears at the gripper's maximum rated misalignment of 6.35 mm (0.250 in) would have to build up to a ten pound restoring force if the gripper is to deflect the compliant device by 6.35 mm (0.250 in). Figure 10 shows the free body diagram of the finger pads pressing on the pallet ear, providing the restoring force.

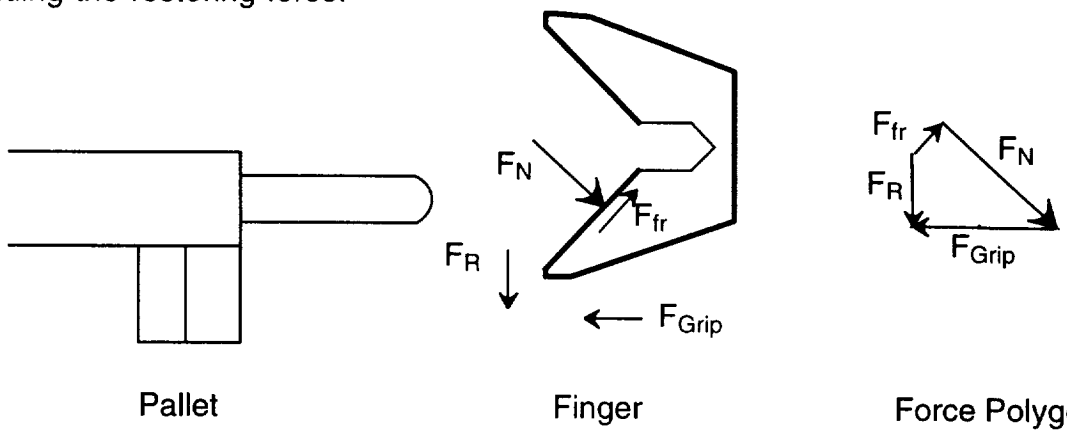

Figure 10. The Free Body Diagram Of The Finger Pad. Forces Shown For The Case When The Fingers Are Contacting The Pallet Ears, And The Fingers Are Too High

The restoring force is then given by

$$F_R = F_N \sin 45° - F_{fr} \sin 45°$$

$$F_R = (F_N - \mu F_N) \sin 45° = (1 - \mu) F_N \sin 45°$$

$$F_R = (1 - \mu) F_{Grip}$$

where

F_R = the restoring force

F_N = the normal force

F_{fr} = the friction force

F_{Grip} = the gripping force

μ = the coefficient of friction between the pallet ear and the finger

A conservative value for μ of 0.38, for two Teflon hardcoat anodized aluminum surfaces, was used to yield a required maximum force of 71 N (16 lb) for the gripper. The gripper drive motor was selected for its inside diameter, to allow the acme screw to pass through the middle. Its continuous force capacity proved to be much higher than what was required.

Compliance

A summary of the compliance requirements is as follows:

For the Z axis: The compliance must handle up to 6.35 mm (0.250 in) misalignment of the pallets entering the rack at 44 N (10 lb) of force. It must also press the pallets against the furnace with a positive force when the robot overtravels the oven's nominal position by 3.3 mm ±2.54 mm (0.130 in ±0.1 in).

For the radial axis: the compliance must also handle up to 6.35 mm (0.250 in) misalignment at 44 N (10 lb) of force, when the pallet is pressed against the alignment pins in the furnace, and when the robot overtravels to ensure that the pallets enter the rack completely.

For the azimuth axis: the compliance must also handle up to 6.35 mm (0.250 in) misalignment at 44 N (10 lb) of force, when the pallet is pressed against the alignment pins in the furnace, and when the robot stores the pallets in the rack.

For the gripper, the compliance must be able to handle an inaccuracy of the gripper fingers closure of up to 0.25 mm (0.010 in), and still ensure a positive grip force. The

compliance must not allow the grip to be opened enough to allow the pallet to be released.

To meet these requirements, two different compliant devices were used: one (Figure 11) at the juncture between the radial axis and the gripper (the robot's "wrist"), and one in the fingers (see Figure 2.4). The compliant device in the robot's wrist consists of two nested, double blade flexures, which allow 6.35 mm (0.250 in) of travel in the Y (radial) and Z directions at a maximum force of 44 N (10 lb). The double blade flexures were used because they each provide compliance in one axis only: they are very stiff in all five other axes. Nesting two of these together, rotated 90 deg with respect to each other, provides a plane of compliance. A spreadsheet program was used to size the blade width and thickness for a given length, spring constant, modulus, and stress level.

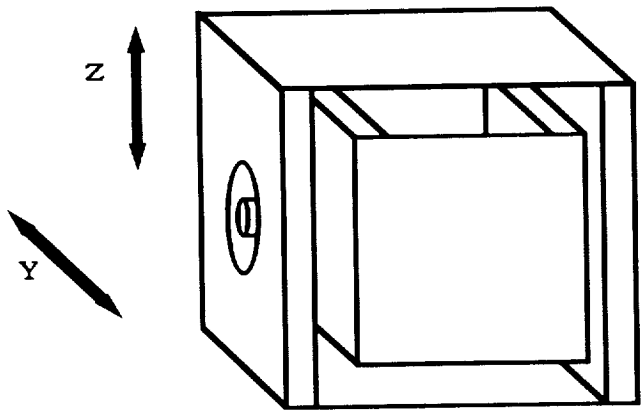

Figure 11. The Wrist Compliant Device

The compliant device for the grip and azimuth directions was simply a spring placed between the nut at the output of the finger drive train acme screw and the finger itself. This spring provides "give" when the gripper grasps a pallet. The accuracy of the gripper finger's positioning was estimated to be 0.51 mm (0.020 in). Since no force control is being used, the only way a positive grip force could be assured without stalling the motor was to command the fingers to close past the point where the pallet would definitely be encountered, and to rely on the compliance to maintain a force close to that desired. The precise force level depends on the position accuracy.

Conclusion

Because of the interplay between capture range, compliance and applied force levels in a materials handling robot, a systematic, logical design process is required. The ground rules must be set: which variables should be accepted as fixed by the problem, and which dependent variables need to be calculated based on those. This is the starting point for all robotics and materials handling mechanism designs. In the ROMPS robot, targets for a) the capture range of the make/break interfaces and b) the joint torques were selected with the goal of minimizing the overall system cost. The required compliant device stiffnesses were then calculated using these values.

3 d.o.f. Robotic Wrist Actuator Redesign

Tom Bonner* and Gabor Tamasi**

Abstract

This paper describes the efforts to redesign, fabricate, assemble and test the wrist actuators on the Automated Tile Processing System (ATPS). The ATPS is a robotic system being developed at Kennedy Space Center to inspect and rewaterproof thermal protection tiles on the space shuttle orbiter prior to launch. The objective of the redesign was to eliminate backlash and provide adequate pitch and yaw actuator force. The wrist actuators have been successfully redesigned, fabricated, tested, and installed. The redesigned wrist actuators meet or exceed all design requirements. The wrist has been reinstalled on the tile processing robot and will be further evaluated during operational testing of the system.

Introduction

The ATPS is designed to decrease the time involved in the tile inspection and rewaterproofing process and minimize human exposure to the toxic waterproofing compound dimethylethoxysilane (DMES). The tile inspection and rewaterproofing systems on the ATPS include a tool plate which is the platform for the vision, inspection, and the DMES injection nozzle mechanism. The tool plate must be manipulated into precise position to align the injector nozzle on each tile for rewaterproofing. Fine positioning is accomplished by a 3 d.o.f. robotic wrist which supports the tool plate providing 90 degrees of pitch and yaw motion and 360 degrees of roll motion. During testing, the actuators driving the pitch and yaw axes of the wrist were found to lack the required force to position the tool plate through the necessary range of motion. The actuators on all three axes also displayed unacceptable backlash. Attempts were made to remedy these problems without a great deal of success. After further testing, decision was made to redesign the wrist actuators.

Original Actuator Design

Description

The original actuators were housed in a cylindrical aluminum housing approximately 16 cm (6.3 in) in diameter and 40.6 cm (16 in) long. The pitch and yaw actuators were composed of direct drive leadscrews driven by brushless DC servo motors as shown in Figure 1. The actuator housings pinned to a bracket on the cylindrical wrist housing. The preloaded lead screw nut threaded into a link that was pinned to the wrist yoke.

* NASA Kennedy Space Center, FL
** PLD Advanced Automation Systems Inc., Rockledge, FL

With the wrist deployed, the pitch and yaw actuators are required to drive the toolplate 45 deg from horizontal in four directions, 90 deg pitch and 90 deg yaw. The original roll actuator was composed of a brushless DC servo motor with a 50:1 planetary gear reduction as shown in Figure 1. The actuator coupled to the wrist roll shaft through spur gears with an additional 1.5:1 reduction for a total 75:1 gear reduction. The roll actuator is required to rotate the toolplate 360 deg regardless of pitch and yaw angle. During initial testing, attempts were made to drive the wrist through its full range of motion with the vision and rewaterproofing toolplate in place. The roll axis performed well, however, unacceptable backlash was observed. When the pitch and yaw axes were displaced, the servos reached current limit while attempting to drive the toolplate back to the horizontal position. The following paragraph describes the analysis and testing that was performed to determine the source of the problems with the wrist actuators.

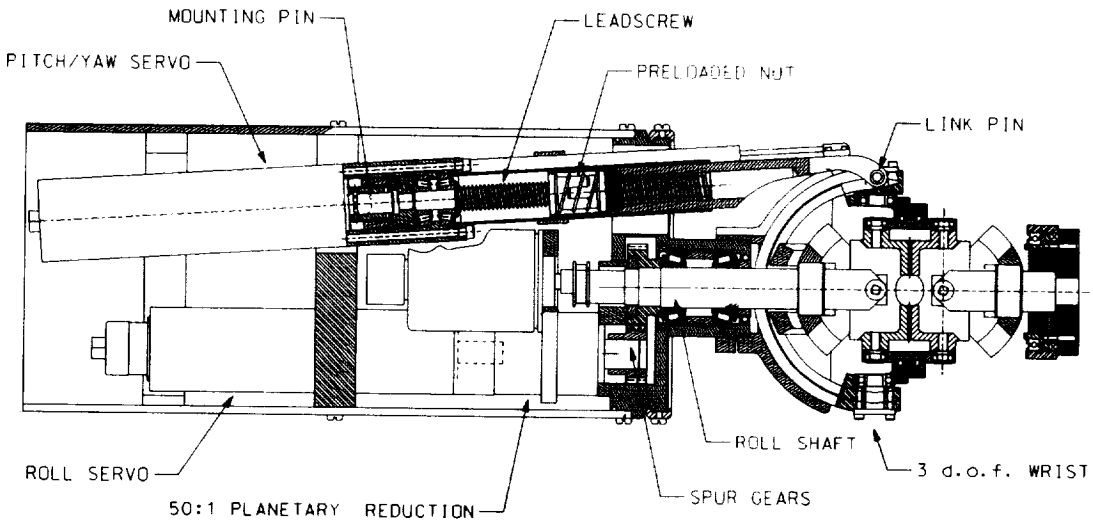

Figure 1. Original Actuator Design

Analysis and Testing

The actuators were removed and load tested to determine their capability. Tests were performed to determine the required pitch/yaw force and roll torque to drive the wrist through its full range of motion. Efforts were also made to locate sources of backlash. The wrist was secured to a test bench with a 267-N (60-lb) load attached with the center of gravity offset 17.8 cm (7 in) from the roll axis to simulate the tool plate. The force required by the pitch and yaw actuators to move the loaded wrist was measured where the actuators pin to the wrist yoke. Measurements were recorded at several angles of displacement (Table 1). The force increased from 979 N (220 lb) at 5 deg to 1779 N (400 lb) at 43 deg on the inner yoke with similar results on the outer yoke.

Table 1. Pitch/Yaw Force Test

Pitch/Yaw Angle (deg)	Required Force (N)	Required Force (lb)
5	979	220
12	1068	240
29	1334	300
43	1779	400

The pitch and yaw actuators were then load tested by placing them in a vertical position and hanging weights from where they pin to the wrist yoke. The weight was increased from approximately 178 N (40 lb) to 645 N (145 lb). The servos began reaching current limit at approximately 578 N (130 lb).

The maximum torque required to rotate the loaded tool plate was measured at the roll input shaft at various angles of pitch and yaw. The torque increased from approximately 12.2 N•m (9 ft•lb) at 7 deg to 40.7 N•m (30 ft•lb) at 48 deg. The backlash in the roll actuator was located in the spur gears coupling the roll input shaft to the planetary reduction on the servo.

The results of the tests clearly show the pitch and yaw actuators to be significantly under powered for this application producing only 578 N (130 lb) maximum force. With a 20% operating margin the actuators would have to produce 2224 N (500 lb) maximum force to drive the pitch and yaw axes to their full 45 deg displacement. The roll actuator provided adequate torque however, backlash found in the spur gears was unacceptable for the precise positioning required and could not be eliminated. The decision was made to redesign the pitch, yaw and roll actuators. The design goals were to meet the force requirements for the pitch and yaw axes and eliminate backlash.

Redesigned Actuators

The greatest challenge of the redesign was selecting the combination of components that would meet the performance requirements and be compact enough to fit in the original housing. The housing was kept in the design because it is the interface between the wrist and its supporting boom.

Pitch/Yaw Actuators

Preloaded ballscrews featuring high efficiency, backlash-free linear motion replaced the original leadscrews on the pitch and yaw axes. The redesigned pitch and yaw actuators are restricted to only linear motion by rigid mounting eliminating the previous pivot mount. The new mounting configuration introduces a transverse loading to the ballscrews that increases with increased pitch/yaw angles. Large enough diameter ballscrews had to be chosen to resist transverse deflection at pitch and yaw angles approaching 45 deg where the transverse load on the ballscrews will be greatest. A

2224-N (500-lb) axial load on the ballscrew produces approximately a 200-N (45-lb) transverse load. A 19-mm (0.75-in)-diameter ballscrew proved to be rigid enough to limit deflection in the fully extended position to within 0.635 mm (0.025 in). Hollow shafts were designed to support the ballnuts allowing the ballscrews to extend and retract through the shaft as the ballnut and shaft rotates. The hollow stainless steel shafts are supported by tapered roller bearings mounted in stainless steel housings fastened to the base of the wrist (Figure 2). The ends of the original actuators were modified into links that pin to the end of the ballscrews on one end and to their original location on the other end. The pins are pressed into the ballscrews and ride on needle bearings pressed into the modified links. Compact, high-torque brushless servo motors with 50:1 cup harmonic drive gearsets were chosen to drive the ballnuts. The harmonic drives provide high efficiency, backlash free operation and concentric mounting making them ideal for this application. The servos were not available off the shelf with integral harmonic drives in the correct size and torque configuration; therefore, motor adapters, housings, and output shafts were fabricated and integrated into compact drive units (Figure 3). The drive units are coupled to the ballnuts using zero backlash polyurethane cable drive chain and sprocket gears (Figure 3, 5). The 48-tooth primary sprocket gear and 64-tooth secondary sprocket gear introduced another 1.33:1 reduction for a total of 67:1 from the servo to the ballnut. The drive units mount to the ballnut shaft housings with adjustable mounts for tensioning the cable drive chains. The pitch and yaw actuators are identical and mounted 90 degrees apart on the base of the wrist (Figure 5).

Roll Actuator

During testing the original roll actuator provided adequate torque; therefore, the original brushless servo on the roll axis was retained. A 100:1 cup harmonic drive gearset was chosen to replace the original 50:1 planetary reduction. The harmonic drive allowed the roll servo output shaft to be concentric with the wrist roll shaft eliminating the spur gears in the original design. An adapter plate and housing were fabricated to mount the harmonic drive to the servo. The adapter plate in the wrist base where the actuator is mounted had to be redesigned to accept the redesigned actuator. The harmonic drive output cup was coupled to the roll shaft using a wedge clamping coupler eliminating the need for keyways or set screws (Figure 2). The coupler wasn't available in a small enough configuration; therefore, a flange and boss were designed for use with the wedge shaped clamping elements which are available as separate units. The harmonic drive output cup is fastened to the flange which is designed to compress the clamping elements between the boss and the roll shaft, securely locking the boss to the shaft.

Absolute Position Measurement

The original linear variable differential transformers (LVDT) were used for position feedback on the pitch and yaw axes. A compact mount was designed to clamp the LVDT's to the armature of the roll servo and also functions as a mount for pitch and yaw travel limit switches, Figure 5. The LVDT plungers are connected to small plates that are fastened to extensions on the end of the ball screws (Figure 5). A small 256-

turn rotary absolute encoder was chosen for the roll axis replacing the bulky belt driven encoder in the original design. The encoder is mounted to the end of the roll servo and driven by a small pinion gear on the end of the shaft (Figure 5). Due to the flammability of the waterproofing chemical, to meet hazard proof requirements, optical travel limit switches were chosen for all three axes.

Improved Serviceability

In the original design, the pitch and yaw actuators were mounted to a circular bracket fastened to the inside of the cylindrical housing and the roll actuator mounted to the wrist base. The pitch and yaw actuators had to be removed with the housing to gain access to the actuators. The redesigned actuators for the three axes are mounted directly to the wrist base allowing the cylindrical housing to be removed separately leaving the actuators fully assembled for inspection and maintenance. A new rear cover plate was designed to secure wire harnesses in cable glands eliminating the pin connectors from the original design. The cable glands lock the wire harnesses firmly to the cover plate and can be easily disconnected to allow for quick removal of the plate and housing. These features significantly improve serviceability of the wrist actuators compared to the previous design.

Testing

There were some problems when the fully assembled wrist actuators were bench tested. Under no-load conditions the pitch and yaw servos were drawing more than the factory-specified continuous current and becoming very hot. The actuators were thoroughly checked for binding and misalignment without any obvious problems found. The problem was discovered to be friction in the harmonic drives caused by packing too much grease into the wave generator bearing. The problem was solved by removing the grease and replacing it with a smaller amount of a less viscous grease. Although the Shell #5 grease originally used in the harmonic drive was specified by the factory, the less viscous Lubriplate grease was used to increase efficiency and should provide sufficient lubrication for the intermittent duty cycle of this application. Another problem discovered during bench testing was slipping of the drive sprocket on the pitch and yaw output shafts. The sprockets are held to the shafts with two set screws that seat on flats machined into the shafts. The set screws worked loose during testing and it became obvious they were not adequate to keep the sprockets from slipping on the shafts. The problem was solved by machining keyways into the shafts and sprockets.

When the actuators were working properly under no-load conditions the housing was installed and the wrist assembly was fastened to the test stand for load testing. A mockup tool plate was fastened in place with enough weight to simulate normal operating conditions. The fully loaded wrist was positioned through its maximum range of pitch and yaw motion while the current draw to the servo motors was monitored. The actuators performed very well, easily moving the loaded tool plate to maximum pitch and yaw angles where the actuators see the greatest resistance. The

current draw to the servo's was well within specification even at maximum load conditions. The roll axis also performed as expected.

Lessons Learned

Using precision components such as harmonic drives and preloaded ballscrews to build robotic manipulators will greatly enhance efficiency and fine positioning capability.

When limited space is available, careful selection of components and paying attention to detail will make the design process much easier.

It is very important when using harmonic drives to choose the correct form and amount of lubrication to fit the application.

Set screws alone are not sufficient to secure sprockets, gears or pulleys to shafts even under moderate torque conditions.

Conclusion

In conclusion, the wrist actuator redesign was a complete success meeting or exceeding all design requirements. The unique aspect of the design is the amount of force developed by the pitch and yaw actuators in such a compact configuration with virtually backlash free operation. The pitch and yaw actuator force was increased by more than four times the original design to more than 2224 N (500 lb). The torque in the roll axis was increased by more than 25% over the original design and backlash eliminated by using a 100:1 harmonic drive gearset, which replaced the less efficient 50:1 planetary gear drive and spur gears. Serviceability was improved by mounting the actuators to the wrist base and designing an easily removable cable bulkhead plate. The success of the design was made possible by combining state of the art components with the painstaking process of designing and fabricating the components necessary to integrate the final assembly into a functional system.

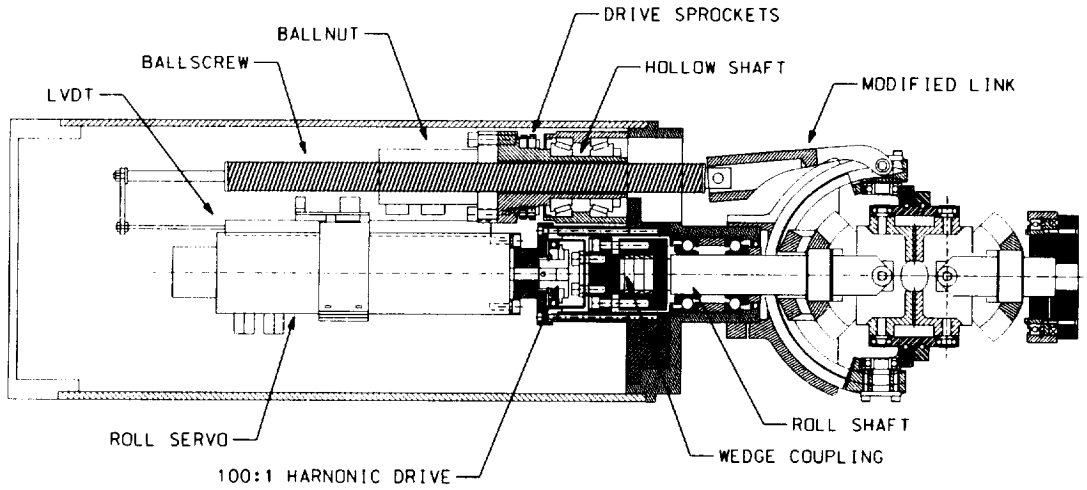

Figure 2. Redesigned Actuators
(shown without pitch/yaw servo drive)

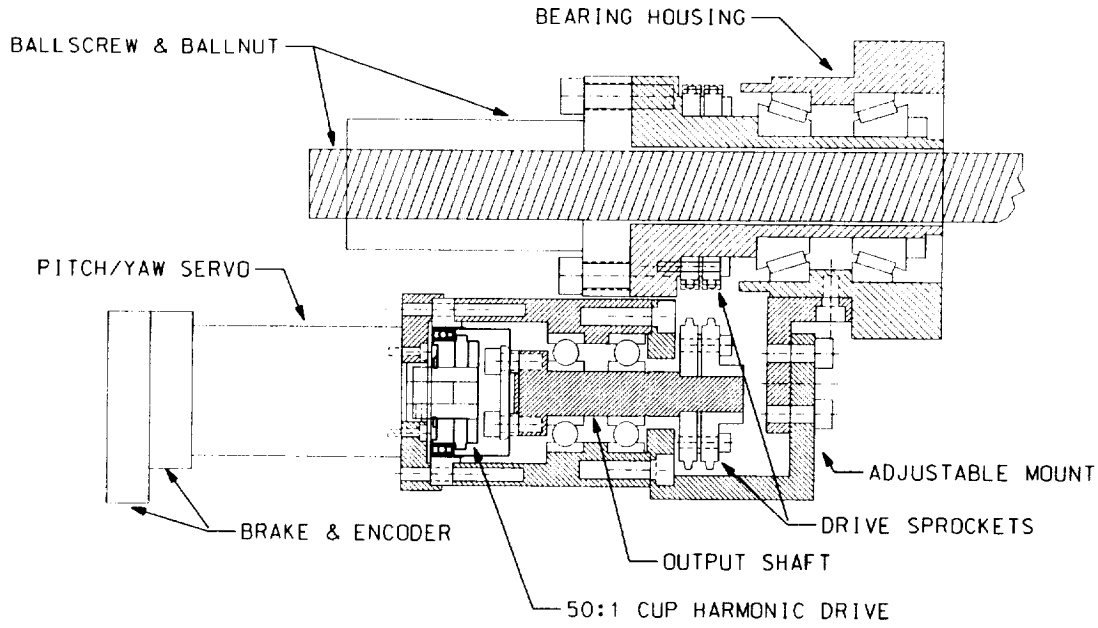

Figure 3. Pitch/Yaw Drive

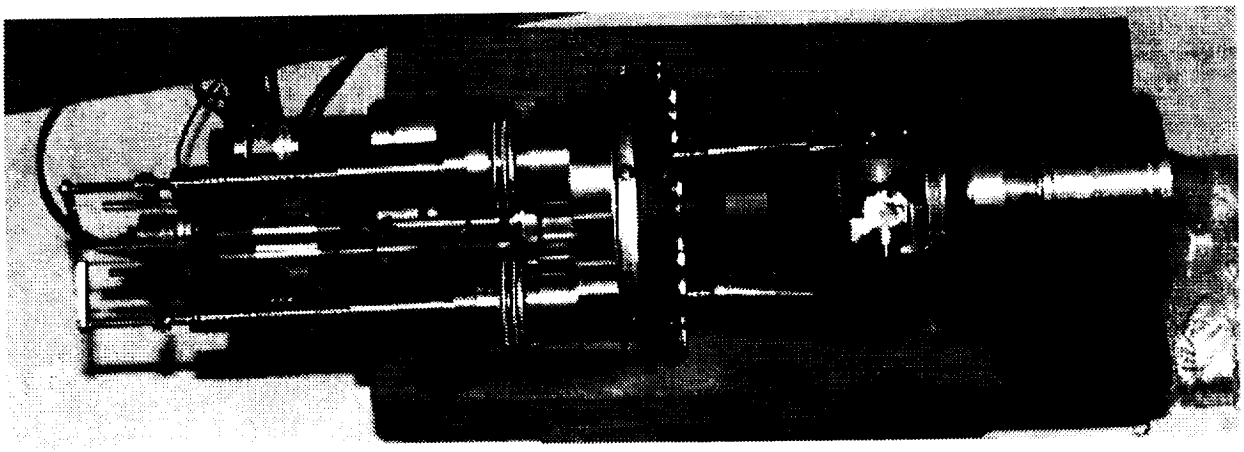

Figure 4.

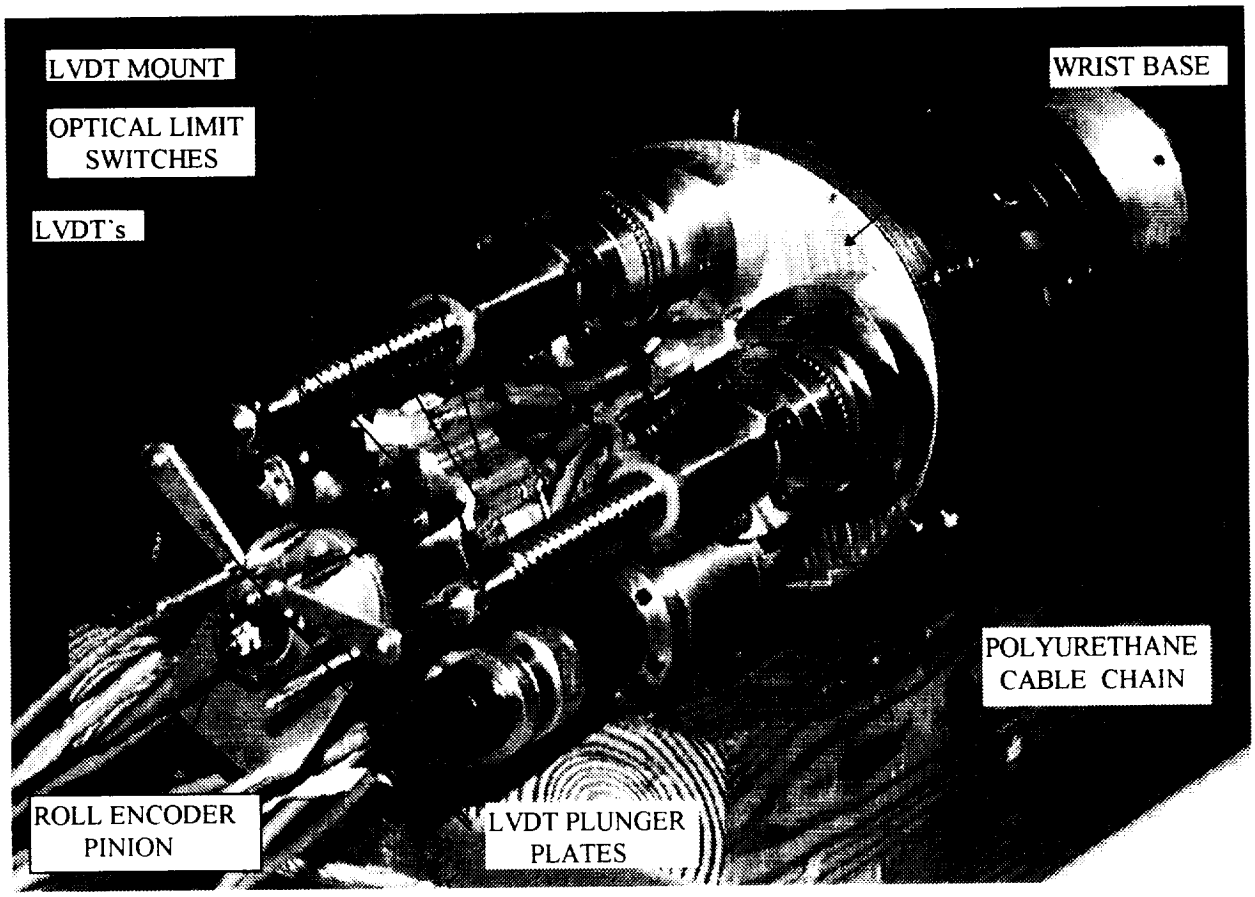

Figure 5.

NASA Space Shuttle Light Weight Seats - The Final Chapter

Steven R. King*

Abstract

This paper completes the lessons learned discussion initiated by the 30th Aerospace Mechanisms Symposium paper titled *NASA Space Shuttle Lightweight Seat.* That paper covered the design, development, test, & evaluation (DDT&E) behind NASA's new Mission Specialist (MS) Light Weight Seat (LWS); however, two additional flight hardware elements of this program remain to be discussed - the Pilot LWS and a Light Weight Recumbent Seat Kit (LW RSK). These two flight elements are the focus of this paper.

Introduction

The Orbiter LWS program is part of a NASA effort geared towards providing sufficient weight and center of gravity margin on future Space Shuttle missions (e.g., Hubble Space Telescope Servicing Mission 2, International Space Station (ISS) assembly flights). NASA directed that the existing orbiter crew seats be redesigned to reduce their weight by some 45%. As previously discussed in the referenced 30th Aerospace Mechanisms Symposium paper, the MS LWSs were successfully completed, achieving a 53% weight savings per seat (i.e., 48.08 kg (106 lb) down to 22.68 kg (50 lb) per seat). These seats are scheduled to make their first flight on STS-82/Orbiter Vehicle (OV)-103 (Discovery) in February 1997.

With MS LWS certification complete, the LWS engineering team began Pilot LWS preliminary design in October 1995. This seat would be a Government Furnished Equipment (GFE) replacement on all OVs for the existing seats used by the orbiter commander and pilot. As with the MS LWS, the project had the goal of providing a quality, high performance (e.g., safer) seat under budget and on time to support first flight on STS-82.

The final flight element of the LWS program is the LW RSK. NASA directed that a new recumbent seating capability be provided which would use the new MS LWSs to achieve a weight saving of up to 62% over the Recumbent Seating System (RSS) built for the Mir docking missions. Physiological research has found that crewmembers returning from long exposures to weightless are under less physical stress and acclimate to the 1G environment much easier when returned laying on their backs (i.e., in a recumbent position). The Mir RSS has been successfully used on the STS-66/OV-104, STS-71/OV-104, and STS-79/OV-104 missions.

The LWS engineering team began LW RSK preliminary design in December 1995. Aligned with the rest of the LWS program, this element had the goal of providing a quality, light weight recumbent seat capability under budget and on time to support (solo kit #7) first flight on STS-84/OV-104 (Atlantis) in May 1997.

* Lockheed Martin Engineering & Sciences, Houston, TX

Pilot Light Weight Seat

Design Approach

Initially the Pilot LWS's design was to have followed a "clean sheet" approach since its first flight was not until STS-88/OV-105 (ISS First Element Launch in December 1997). However due to NASA programmatic needs, the LWS Program accepted the challenge of accelerating Pilot LWS delivery to support STS-82. Flying Pilot LWSs on STS-82 would eliminate some lead ballast used to offset an orbiter forward cg shift. This would in turn increase the flight's propellant margin. Figure 1 shows one of STS-82's Pilot LWSs prior to NASA-Kennedy Space Center (KSC) delivery.

As a result, the Pilot LWS project established the following key ground rules at its start:

- The new seat would maintain all the capabilities of the existing pilot seat. Since the prime goal was to reduce weight, the new seat would not have any added means of absorbing vertical crash loads.
- It would position the crewmember in the same position as the existing pilot seat.
- It would use the motor/drive mechanism and control electronics from the existing pilot seat. This hardware would be refurbished to maintain its flight certification.
- The Pilot LWS would make maximum use of MS LWS hardware to reduce overall project costs and meet the STS-82 schedule commitment. Shared hardware includes the seat back, tilt mechanism, restraint system, and some soft goods. Figure 2 shows the Pilot LWS as configured for the commander's side.
- The Pilot LWS weight savings could be less than 45% as long as the overall orbiter ship set (i.e., two Pilot LWSs and five LWSs) weight savings meets the 45% requirement.
- The floor warpage boundary condition would not apply due to the flight desk's layout and construction.
- The Pilot LWS would not undergo any dynamic testing since no new engineering data would be obtained relative to the MS LWS testing. The Pilot LWS would be subjected to an ultimate static strength certification test equivalent to 20Gs.
- As part of its flight certification, the Pilot LWS would be subjected to the equivalent vibration environment of 100 missions in each of its three axes.

Motor/Drive Mechanism and Control Electronics Trade Study

The above decision to retain and refurbish the existing motor/drive mechanism and control electronics is the result of a comprehensive trade study by Lockheed Martin's Mechanism Control Design Team (MCDT). The study found:

- Refurbishing and using the existing system would result in a significant cost savings plus saving about a year of work.

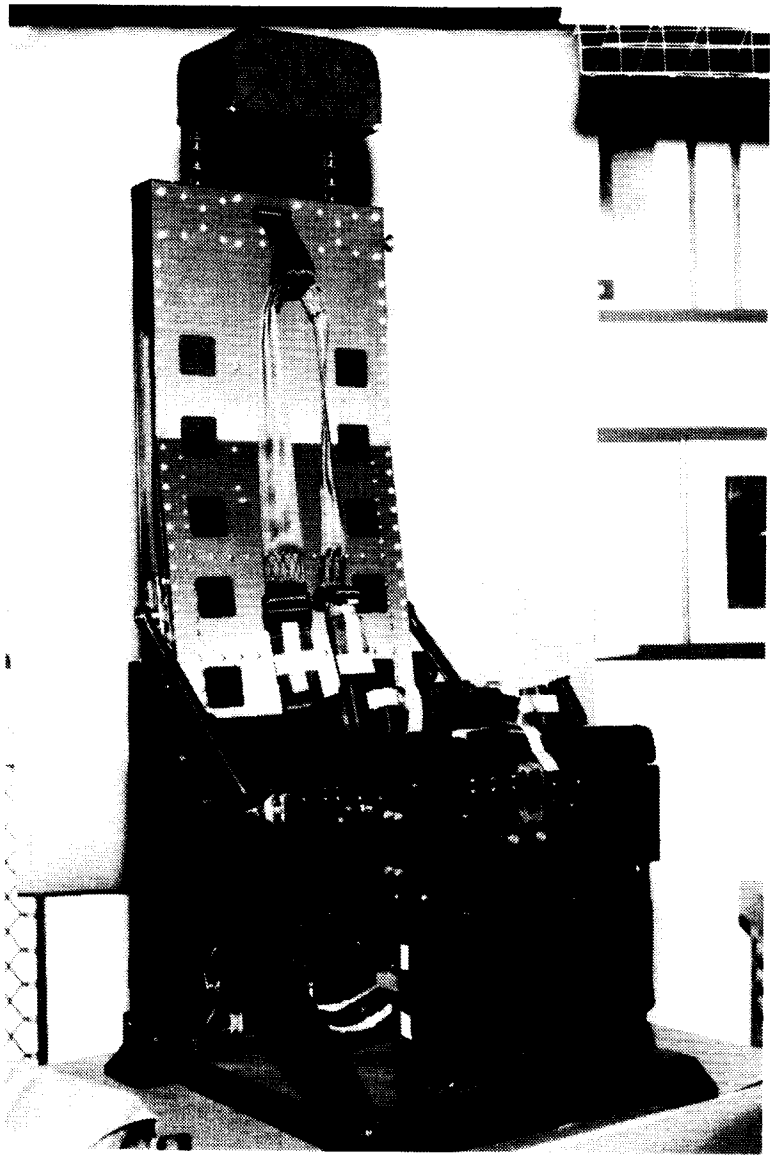

Figure 1. Production Pilot LWS for STS-82

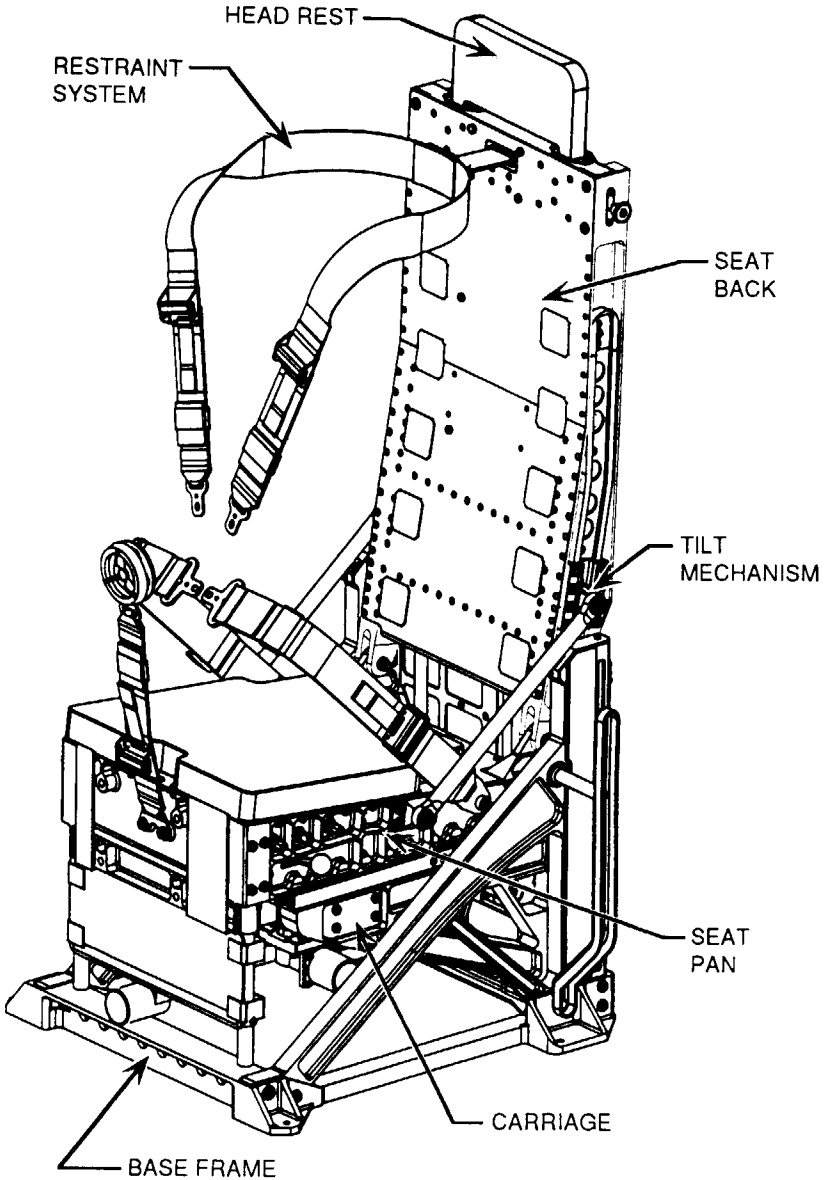

Figure 2. Pilot LWS Major Subassemblies

- The existing system could not be practically reduced in size or weight.

- The system design was basic and not overly complicated which looked fairly optimal for its purpose.

- No change in the seat electrical system or control logic was recommended because of its integration in the orbiter's forward avionics bay. Extensive electrical analysis and re-certification of the electrical systems would have to be performed for any changes.

- Any motor size change would also require electrical analysis and re-certification of the drive mechanism. Therefore, no change in the motor size was recommended.

- Identified a need to reanalyze the existing motor/drive mechanism to certify it for the 20G crash case and to ensure the new seat's reduced global stiffness (i.e., increased flexibility) would not impact performance.

Integrated Product Team (IPT) Lessons Learned

IPT participation was critical to the Pilot LWS project's success. Team representation was essentially the same as for the MS LWS project (e.g., astronaut office, engineering, orbiter project office, manufacturing, sustaining engineering, safety & product assurance). The project used several NASA-Johnson Space Center (JSC) orbiter mockups to conduct engineering studies and crew evaluations. Figure 3 shows the Pilot LWS engineering unit during a formal Crew Station Review (CSR) (April 1996). In addition, the qualification unit was taken to NASA-KSC to perform a fit check on OV-105.

The active involvement of team members (especially crew representatives) with both mockup and flight like hardware contributed to:

- There being only 13 Review Item Dispositions (RIDs) at the Preliminary Design Review (PDR) (December 1995) and one RID at the Critical Design Review (CDR) (May 1996).

- A decision to forego a proposed change to reduce seat vertical travel by 2.54 cm (1.0 in) to save 0.91 to 2.27 kg (2 to 5 lb). This was due to several crew-to-vehicle human factor concerns.

- The successful evaluation of crew equipment interfaces and constraints (e.g., power switches and control knobs with pressurized gloves, Thermal Electrical Liquid Cooling System (TELCS) Unit locating and mounting, commander's side egress handhold, Flight Data File Boxes, and cue cards).

- Successful emergency egress evaluations by NASA-KSC fire and rescue personnel and crewmembers.

- Providing an opportunity during the OV-105 fit check to solve a problem of how to route the Rotational Hand Controller's wiring harness with the Pilot LWS.

Design/Analysis Lessons Learned

Since the project required structural optimization to save weight while maintaining positive structural margins of safety, it was found that the amount of time spent performing analysis almost equaled that of design. Most of the structural analysis involved finite element analysis (FEA) using SDRC's I-DEAS and MSC's NASTRAN software. Once a final design concept was selected, the project used a traditional analysis approach of:

- Creating a global finite element model (FEM).
- Determining load cases.
- Performing load cycles & optimization.
- FEM baselining.
- Structural testing (i.e., planning, performing, FEM correlation, and reporting).
- Documentation.

The Pilot LWS engineering team had to:

- Determine a set of realistic structural boundary conditions between the orbiter flight deck floor and Pilot LWS which could be simulated both in the FEA and through test. This had to take into consideration the 20G floor structure upgrade and its failure modes during a crash. A set of semi-pinned structural constraints with the floor reacting a portion of the base frame's deflection was used through the PDR. However, this approach was felt not to be conservative enough since the floor's behavior (i.e., stiffness) could not be quantified for the crash case. As a result, the base frame was redesigned post-PDR using pinned constraints between the floor and the seat. This change simplified the static test fixture (i.e., the use of adequately stiff I-beams) and facilitated FEM correlation with test data; however, it cost about one month of engineering time and reduced the Pilot LWS weight savings by approximately 2.27 kg (5 lb).
- Analyze the existing motor/drive mechanism for its use in the Pilot LWS and the resulting loads it would be subjected to. Extensive analysis was required to understand the behavior of the 20G capable bearing blocks.
- Prove by analysis that changing the drive mechanism's bearing tracks from stainless steel to titanium (for weight savings) would not violate the mechanism's flight certification (i.e., would not require additional testing).
- Change a pair of the base frame's 7.94 mm (5/16 in) aft-end fasteners from A286 to Custom 455 after they showed signs of shear deformation from the ultimate static test. Where possible, all fasteners were designed to be bearing critical as opposed to shear critical.

Manufacturing Lessons Learned

Several design and manufacturing improvements were identified through the fabrication of a high fidelity engineering unit. These included:

- Being able to visualize opportunities for additional weight savings.
- Time was saved by facing anodized surfaces after metal finish instead of masking them as is normally done for grounding.

Some questions were raised after the manufacture of the Pilot LWS production units regarding the durability of the anodize finish over its service life. The units were not hard anodized due to the project's compacted schedule. Also after manufacturing, a concern over wear particle contamination for the head rest's fiberglass bushings caused the replacement of all bushings with metallic ones. In order to meet manufacturing delivery commitments, the qualification unit did not have flight like metal finish on all surfaces which caused certification electrical bond testing to be performed on a flight unit during its acceptance testing. As with many past GFE projects, fasteners (especially high strength ones) were found to be the pace setter in assembling qualification and flight hardware. Rockwell International's pilot seat-to-floor attachment hole drill template was used to drill the attachment holes in the base frame. This eliminated misalignment concerns since the hole pattern had tight tolerances.

Testing Lessons Learned

Since the existing motor/drive mechanism and control electronics were being refurbished for use in the Pilot LWS design, it was decided that the useful time of these items would be protected by replacing them with structural/mass simulators during all non electrical certification (i.e., static strength and vibration) and acceptance (i.e., vibration) tests. This proved successful but required more test coordination, paperwork, and down time between tests. Certifying the use of the refurbished hardware in the Pilot LWS design for the environments pertaining to life, electromagnetic interference/ electromagnetic compatibility, and acoustics was done by similarity and required no additional testing. During both development and certification testing, several problems were encountered with a 120 VAC three phase power supply used to energize the motor/drive mechanism. These problems centered on one of the power supply's phases failing to energize upon start up which could go undetected.

Two setup problems were observed during static strength testing. Figure 4 shows the Pilot LWS qualification unit at 100% ultimate static load. These were:

- The biting of the seat pan on the lap belt webbing/bracket causing a partial tear through of the webbing at 78% ultimate load. It was determined that the test configuration was putting the webbing in a position which would not be possible during actual use. A piece of Teflon was placed between the seat pan and webbing on the next test run.
- At 85% of ultimate load, a hydraulic actuator used to apply a static load to the test setup bottomed out. This was due to an underestimate of the amount of structural deflection in the entire test setup and elongation of restraint system webbing.

Figure 3. Hands On Design Evaluation

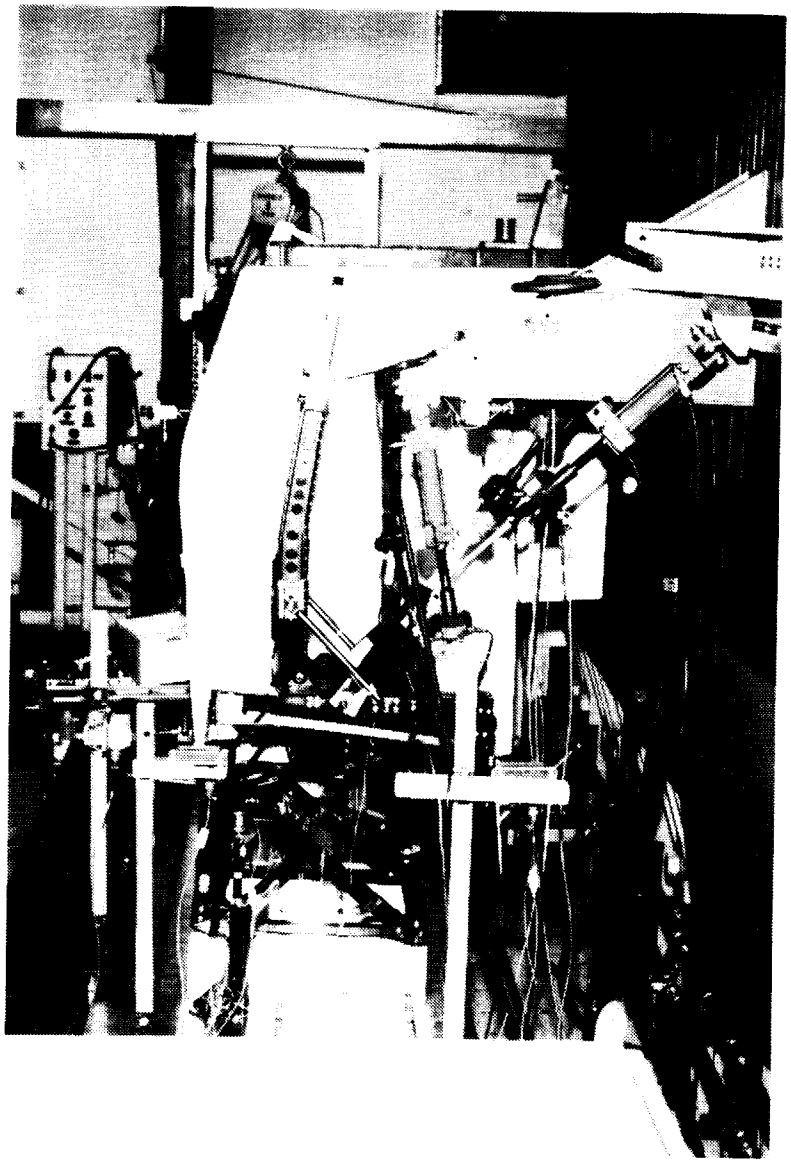

Figure 4. Pilot LWS at 100% Ultimate Static Load

Miscellaneous Lessons Learned

The LWS designers encountered numerous computer related problems as the number and complexity of Pilot LWS computer aided design (CAD) models grew. The project used Unigraphics version 11 CAD software to generate solid models which in turn was used to produce engineering piece-part and assembly drawings. Most of the problems are believed due to workstation and network configuration, and memory allocations. Regardless, these problems resulted in a loss of some productivity due to downtime and slow system response.

The final Pilot LWS design concept selected is 1.34 cm (0.525 in) wider than the existing pilot seat on both its left and right side. As a result, new Flight Data File Boxes for both the commander and pilot were designed to resolve an interference problem. These new boxes are made mostly of Nomex and resulted in an additional 2.27 kg (5 lb) of weight savings per orbiter ship set. The Pilot LWS qualification unit was used to verify its fit through the orbiter's interdeck access hatch during the OV-105 fit check.

Light Weight Recumbent Seat Kit

Design Approach

The LW RSK was originally slated to make its first flight on STS-88; however due to NASA programmatic needs, the LWS Program accepted another challenge of accelerating LW RSK delivery so a solo kit could be flown for the first time on STS-84. The resulting weight savings by flying this kit along with three MS LWSs on STS-84 will allow additional propellant/payload to be flown on the flight.

As a result, the LW RSK project established the following key ground rules at its start:

- The new kit would maintain all the capabilities of the existing Mir RSS (e.g., return from one to three crewmembers). The following designations were assigned: solo kit = kit #6 (Figure 5), dual kit = kit #7 & #8 (Figure 6), and the triple kit = combined solo and dual kits. The kit numbers are based on previously defined orbiter seating locations. Note that kit #7 can be flown by itself to provide a solo capability.
- Crewmembers would be optimally positioned in the orbiter's x-axis (Xo).
- The kit's design would be based on using the MS LWS as is.
- The kit would interface with the MS LWS floor studs and treadmill (i.e., Brownline) fittings.
- The kit would make use of Mir RSS hardware where appropriate.
- The floor warpage boundary condition would not apply.
- The LW RSK would not undergo any dynamic testing; however, it would be subjected to an ultimate static strength certification test equivalent to 20Gs.

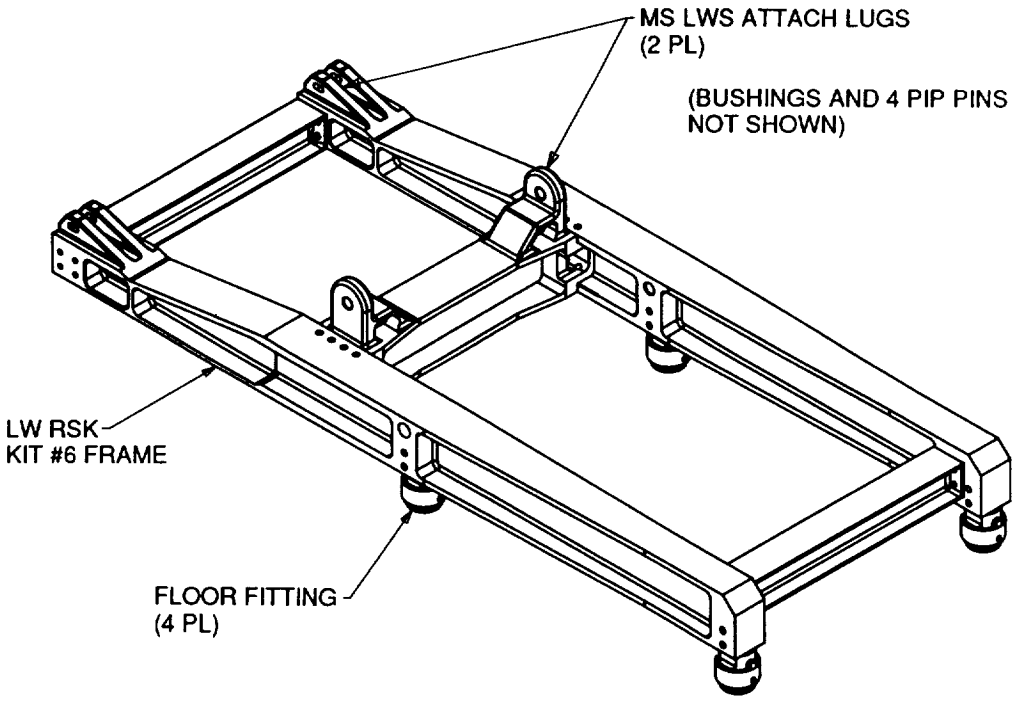

Figure 5. LW RSK Solo Kit (Kit #6)

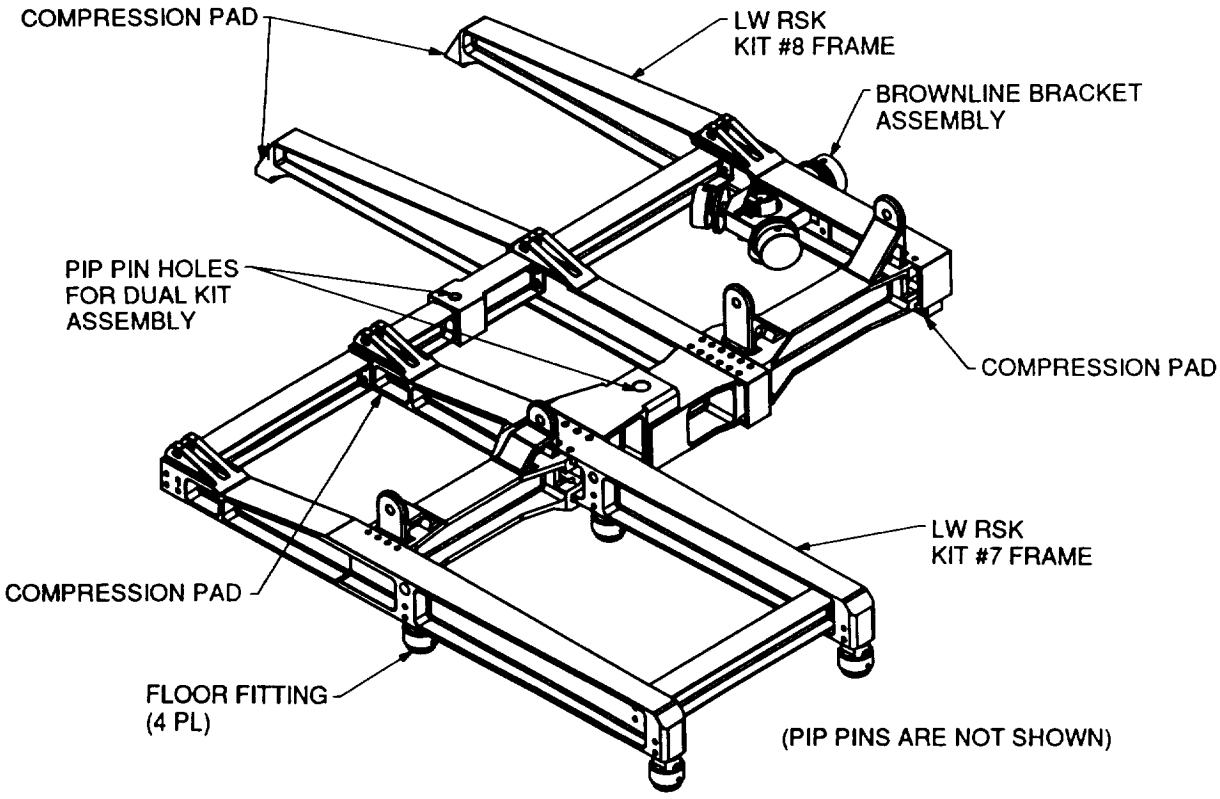

Figure 6. LW RSK Dual Kit (Kit #7 & #8)

- No vibration certification test would be required since the LW RSK is only used during the entry mission phase. The orbiter's vibration environment during entry is considered benign relative to ascent. The kit is disassembled and stowed in foam within a stowage bag during ascent. The LW RSK's pip pins and Brownline Bracket Assembly (BBA) would be required to undergo acceptance vibration testing to prove workmanship.

IPT Lessons Learned

The LW RSK also shares much of the IPT lessons learned of the Pilot LWS in that IPT participation was critical to the LW RSK project's success. Team representation is nearly identical to the Pilot LWS project with the addition of engineering support from the former Mir RSS project. The project also used several NASA-JSC orbiter mockups to conduct engineering studies and crew evaluations. Figure 7 shows the LW RSK qualification unit (dual kit) during a formal CSR (October 1996). In addition, this qualification unit was taken to NASA-KSC to perform a fit check on OV-103.

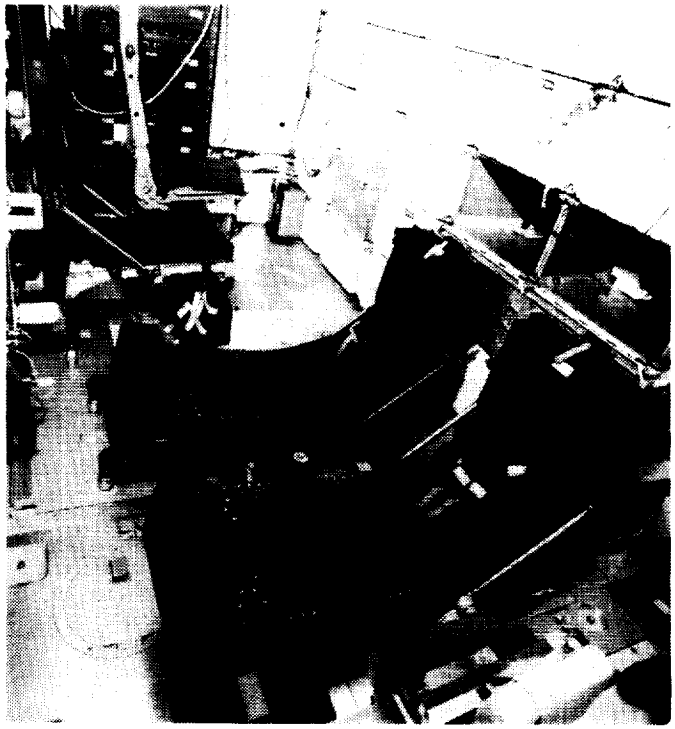

Figure 7. LW RSK Dual Kit with Attached MS LWSs

The active involvement of team members (especially crew representatives) with both mockup and flight like hardware contributed to:

- There being only three RIDs at the PDR (March 1996) and seven RIDs at the CDR (July 1996).

- The generation of a list of up front design "concerns"/assumptions that the entire team could reach consensus on.
- The successful evaluation of crew equipment interfaces and constraints (e.g., BBA, pip pins, oxygen hose routing, TELCS unit mounting).
- Successful emergency egress evaluations by NASA-KSC fire and rescue personnel and crewmembers (Figure 8).

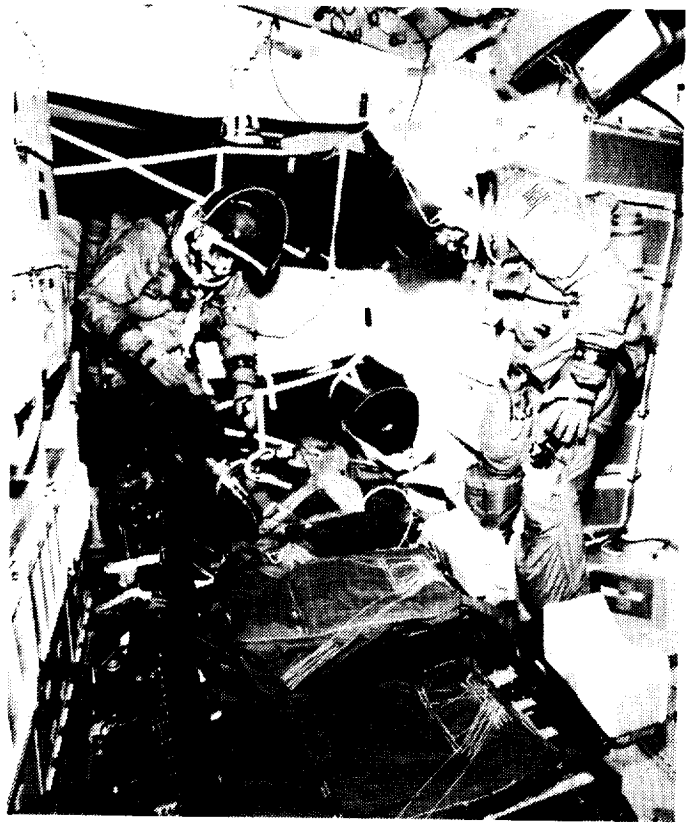

Figure 8. LW RSK Triple Kit Emergency Egress Evaluation

- Demonstrating how the kit could be assembled by one crewmember in 0G.
- Checking stowage scenarios supporting ISS flights (treadmill, stowage bags, etc.).
- Identifying an interference problem between kit #8 and the middeck lockers which was easily solved by changing the end shape of kit #8's port side beam.
- Making kit #6 a different color (blue) from kit #7 (black) to avoid on-orbit crew confusion.

Design/Analysis Lessons Learned

As discussed under Pilot LWS lessons learned, the LW RSK project used the some approach and tools to carryout structural analysis/optimization. The time spent performing analysis also approximately equaled that of design.

The LW RSK engineering team had to:

- Develop a mechanism for kit #8 which transferred only shear loads into the Brownline treadmill fitting while being compliant enough during attachment to compensate for the as-built orbiter differences and on-orbit deflections. The amount of compliance was calculated to be ±4.3 mm (±0.170 in). The resulting mechanism, the BBA (Figure 9), has a lubricated floating aluminum-bronze sleeve which can be locked into position for entry via three knob screws. Each knob screw has a second knob used in a jam nut fashion. The original locking concept used locking setscrews but was eliminated from further consideration since they would have been cumbersome to use onorbit. The Brownline treadmill fitting is allowed to freely translate along its vertical (Zo) axis inside the lubricated BBA sleeve. As a result, the BBA only loads the fitting in shear. Figure 10 shows the BBA attached to the Brownline treadmill fitting in its entry configuration. The BBA has a spring plunger to hold the fitting in the BBA during stowage and initial floor attachment, otherwise the plunger is disengaged. An analysis was performed to ensure the BBA and fitting would stay engaged during the expected landing and rollout low frequency vibrations and during a 20G crash. An early trade study determined it would not be cost effective to convert this Brownline treadmill fitting to a MS LWS spherical floor stud.

- Analyze the failure modes of the orbiter's middeck floor during a crash to determine the feasibility of using compression pads. It was determined that the dual kit would need four compression pads to transfer compressive loads into the floor during a crash. Since the compression pads do not transfer loads during the operational cases, each pad has a 3.2 mm (0.125 in) gap between it and the floor. The crash analysis considered the effects of floor spring rates. In a crash, the orbiter floor would experience some local buckling and crippling as a result of the compression pad loads but no failures (e.g., shear tear out, bearing failure).

- Determine if kit #6 and #7 could be made interchangeable and what weight impact would result. The design of kit #6 and #7 are very similar with their difference coming in a 5.08 cm (2.0 in) offset in where their floor fittings need to be attached to place their seat pans in the same XoZo plane. An interchangeable kit would have meant scaring it so that floor fittings could be mounted in either a kit #6 or kit #7 configuration. The 0.23 kg (0.5 lb) weight of this scaring plus the added maintenance time to reconfigure kits eliminated this concept from further consideration.

- Determine if the MS LWS spherical floor fittings had sufficient tolerance to allow kit #6 and #7 to be attached without regard to as built orbiter differences. No issue was identified since the holes for each seat's floor fittings were drilled with a

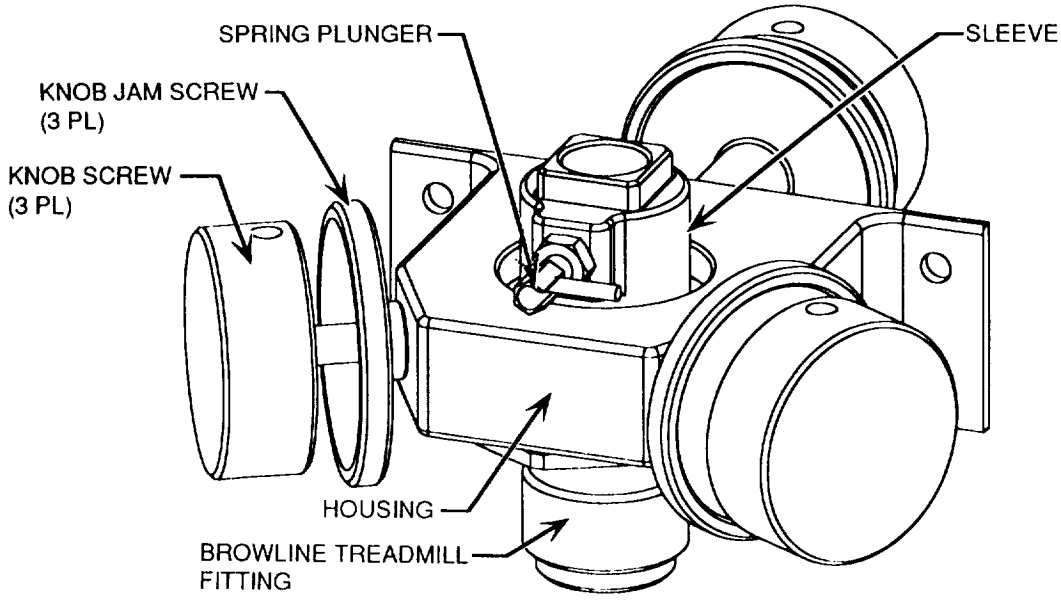

Figure 9. Brownline Bracket Assembly

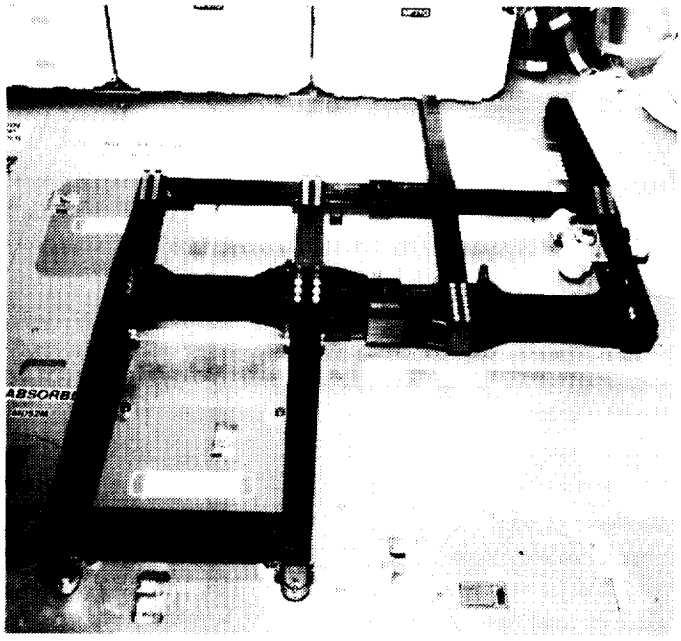

Figure 10. LW RSK Dual Kit Attached to Middeck Floor

template and the floor fitting/stud interface had sufficient margin to overcome the worst case tolerance stackup.

- Analyze the MS LWS to LW RSK interface to determine how to compensate for as built differences (i.e., tolerance stackups) between them. Since the MS LWS had already been designed and built with scarring for use in a recumbent mode, no changes could be applied. Through holes with sufficient strength were provided. The worst case tolerance stackups were also known. A special bushing had to be designed as part of the LW RSK to allow the same pip pin to be used in both upper MS LWS seat back-to-LW RSK locations. This bushing fits in the egress step scar location. It was determined that the kit's lugs (clevis), which provide attachment to the lower MS LWS seat back-to-LW RSK locations, would have to be slotted to compensate for worst case tolerance stackup. However, this resulted in a pip pin with a sloppy fit since the pin's balls could slip through the slot. The pip pin would not pull through since the balls would contact the through hole on the MS LWS's interfacing tang. Sufficient pip pin bearing area is always maintained. In hind sight, the MS LWS's tang should have had the slot as opposed to the kit's clevis. Velcro straps were added to prevent these lower attach pip pins from moving while in place. All LW RSK pip pins are tethered and have parking locations.

- Determine how to modify the MS LWS's launch/entry TELCS unit bracket design so a similar bracket could be designed for use with the MS LWS in the recumbent mode. Evaluations with mockups demonstrated that an elongated version of the launch/entry bracket design would work for the recumbent mode. Since these brackets would have to be exchanged on-orbit, the new brackets would be made a different color from the launch/entry brackets as a crew aid.

Manufacturing Lessons Learned

As discussed under Pilot LWS lessons learned, fasteners (especially high strength ones) were also found to be the pace setter in assembling qualification and flight hardware. The same can be said of flight certified pip pins. Four ball pip pins were selected for use in the LW RSK. In order to meet manufacturing delivery commitments, the qualification unit did not have flight like metal finish on all surfaces causing certification electrical bond testing to be performed on a flight unit during its acceptance testing.

Testing Lessons learned

Two problems were observed during static strength testing. These were:

- At 87% of ultimate load, the test facility's 4,536 kg (10,000 lb) T-slot table (seen in Figure 4 during Pilot LWS testing) on which the dual kit was secured pivoted horizontally causing the load actuator control system to abort the test. Several LW RSK piece-part were either bent or broken as a consequence of the anomaly. It was found that the table was only constrained at the floor to react vertical loads. The test setup generated enough side force to defeat the friction that was holding the table from moving horizontally. The test facility is now using a more detailed pretest checklist to scrutinize test setups.

- At 98.2% of ultimate load, the control system on a load actuator aborted the test when a portion of the BBA's sleeve sheared out. A post test investigation found that the BBA was carrying a moment since the Brownline treadmill fitting's attachment to a load cell was much stiffer than its actual mounting in the orbiter middeck floor. This moment was causing the BBA to carry some vertical (Zo) load and caused the sleeve portion to shear out. When the portion sheared out, stiction between the fitting and BBA was relieved causing the fitting to stoke. This in turn caused a rapid change in actuator stroke which its control system could not compensate for. Throughout this event the BBA and fitting remained engaged. An analysis showed that even without that sleeve portion, the BBA/fitting would have still carried the required amount of shear load through 100% if the test had not aborted. In hind sight, the sleeve could have been designed to carry or negate a moment of this type or the fitting's test mount given a stiffness which better approximated the floor.

Conclusions

Pilot LWS certification testing has been successfully completed and STS-82's production seats (Figure 1) were installed in November 1996. The Pilot LWS configured for the commander weighed in at 51.48 kg (113.5 lb) and 51.26 kg (113 lb) for the pilot side. The baseline pilot seat weighed 78.93 (174 lb). This gives an overall ship set weight savings of 118.12 kg (401.5 lb) which is a 46% (1% better than required). This does not include the additional 2.27 kg (5 lb) weight saving resulting from the new Flight Data File Boxes.

LW RSK certification testing has also been successfully completed and STS-84's flight solo kit (kit #7) has been manufactured. It along with the rest of the LW RSK flight elements are to be delivered to NASA-KSC in February 1997. The triple kit weight savings is ≈60% (i.e., from 77.56 kg (171 lb) down to ≈30.84 kg (≈68 lb)). This value is to be finalized once the triple kit completes acceptance testing.

The events of both the Pilot LWS and LW RSK project could be considered typical of other GFE flight hardware projects based on the author's experience. The paper discussed the benefits of using an IPT approach and the DDT&E lessons learned. These lessons learned communicate the need to define design requirements and perform trade studies early in the project; the practical benefits of using mockups and high fidelity engineering units; the importance of paying attention to details; and the necessity of having project contingency and fall back options.

References

1. Hansen, Chris, et al. "NASA Space Shuttle Lightweight Seat." *30th Aerospace Mechanism Symposium.* NASA CP-3328, NASA Headquarters, Washington, D.C., May 1996: 377-385.

2. JSC-26139, *Program Requirements Document for Mir Mission Recumbent Seat System (RSS) for the Shuttle Orbiter.* NASA-JSC, Houston, Texas, March 1993.

3. JSC-26731, *Program Requirements Document for Lightweight Seats.* NASA-JSC, Houston, Texas, December 1994.

4. JSC-26759, *Lightweight Seat Project Management Plan.* NASA-JSC, Houston, Texas, January 1995.

5. JSC-26811, *Lightweight Seat Project Weight Control Plan.* NASA-JSC, Houston, Texas, October 1994.

6. EA42-95-183, *Lightweight Recumbent Seat Kit (RSK).* NASA-JSC , Houston, Texas, December 1995.

Acknowledgments

The author would like to thank each member of the civil service/contractor Orbiter LWS team for making the Pilot LWS and LW RSK projects a success. Through their dedication, resourcefulness and skill, the Orbiter LWS Program was able to provide NASA with lighter and safer crew seats. NASA's LWS Project Manager was Edgar Castro/ES. Lockheed Martin LWS team members included:

Lynn Bloom	Computer Applications Engineer
Howard Carter	Pilot LWS Test Lead
Todd Colangelo	Mechanical Designer
Monty Carroll	MCDT Lead
Chris Dietz	Pilot LWS Analysis Lead
James Flores	LWS Subsystem Engineer
Randy Gebka	Structures Test Laboratory Lead
Jeff Hagen	Mechanical Designer
Steve King	LWS Project Manager
Mark Landeck	LWS Design Lead
Thang Le	MCDT Mechanical Engineer
Ray Morales	MCDT Electrical Engineer
Bill O'Herren	LW RSK Structural Analysis/Test Lead
Appa Prabhu	Structural Analyst
Doug Prince	Structural Analyst
Allen Reed	Draftsperson
Sonia Ried	LW RSK Design Lead
George Smith	Sustaining Engineering
Scott Staton	Safety & Product Assurance

ION THRUSTER ALIGNMENT MECHANISM (ITAM) FOR ARTEMIS: QUALIFICATION TEST RESULTS AND LESSONS LEARNED

M. Falkner *, C. Schwarzinger *, D. Johnson *

Abstract

A new mechanism for alignment of ion thrusters has been developed and qualified for the European telecommunication satellite ARTEMIS. The pointing range is a 6° halfcone, which is achieved via the two degrees of freedom of the ITAM mechanism. This paper presents the qualification test results of the fully flight representative ITAM Qualification Model (QM) and the lessons learned thereof. The objective is to describe the qualification tests performed on the QM, to outline the test methods, and to discuss the parameters gathered during the campaign. A brief mechanism design description is presented first, followed by a detailed discussion of the environmental, functional and performance tests performed. The lessons learned and possible improvement potentials are presented at the end of this paper.

Introduction

Ion Propulsion is baselined to be used for orbit control (north/south station keeping) of the European geostationary communication satellite ARTEMIS. Two Ion Thrusters are mounted to an Ion Thruster Alignment Mechanism (ITAM) developed by ORS (ÖSTERREICHISCHE RAUMFAHRT- UND SYSTEMTECHNIK GMBH), which will perform the pointing to the center of gravity (CoG) for the north/south station keeping of the satellite during its 10 years mission time.

ORS was founded in 1983 and is the largest aerospace company in Austria. ORS has been and is involved in nearly all European space projects since that time and has made significant contributions in the area of Mechanical Ground Support Equipment, Structures, Mechanisms and Thermal Hardware.

The development history and a detailed technical description have already been presented at the sixth European Space Mechanisms & Tribology Symposium held in Zurich, Switzerland on October 4-6, 1996.

* Österreichische Raumfahrt- und Systemtechnik GmbH (ORS), Vienna, Austria

Mechanism Design Overview

The ITAM supports a platform, where two ion thrusters are mounted, and is able to rotate around two axes. The rotation is controlled by a special control electronics. The main functions of the ITAM are the following:

- To support two types of ion thrusters during launch and in orbit
- To steer the ion thrusters around two axes
- To provide a thermal barrier between the thrusters and the spacecraft

Two ITAM's will be mounted on the ARTEMIS spacecraft, one on the south and one on the north panel, close to the separation plane.

Mechanism Design

The ITAM mechanism (see figure 1 & 2) consists of five main items; the Platform, the Single Point Hinge, the Drive Units, the Strut Units, and the Hold-Down and Release Mechanism (HDRM).

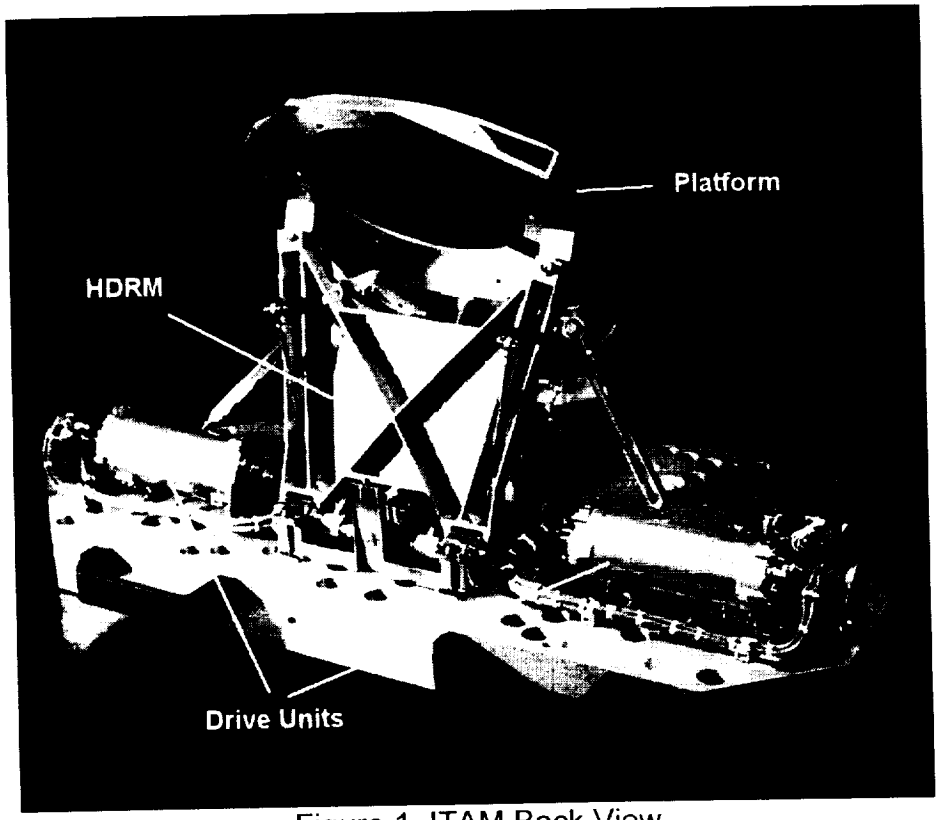

Figure 1 ITAM Back View

Two different Ion Thrusters are mounted to the Platform. The platform has a box-type design and is optimized with respect to mass and stiffness. The Strut Units are made of a titanium alloy and self-lubricating spherical bearing assemblies (rod ends) are directly bolted to the struts.

The Drive Units are operated via permanent magnet disk stepper motors, which drive a preloaded Recirculating Roller Screw via a coupling. The spindle provides a linear motion for the gimbal joints, where the Movable Strut Units are connected to. Both spindle and gimbal joint are supported by preloaded angular contact ball bearings. Redundant limit switches and mechanical end stops indicate the extreme positions of the spindle.

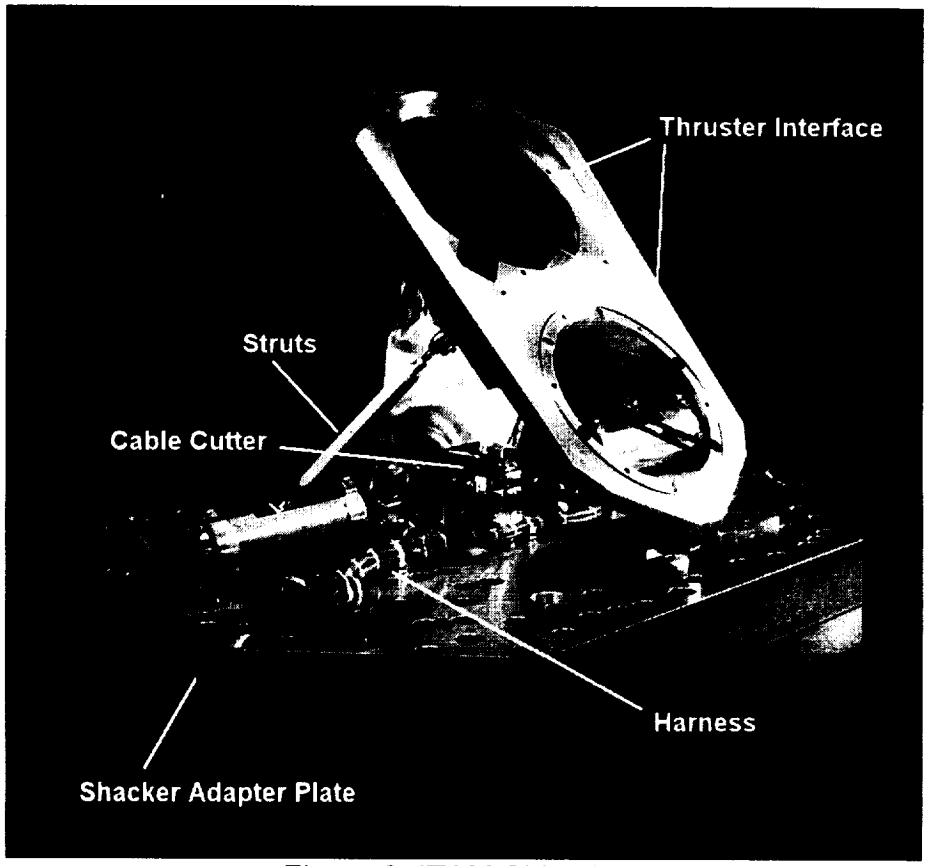

Figure 2 ITAM Side View

The Hold-Down and Release Mechanism has a Ball-Cup interface to the platform which is insensitive against small misalignments. The HDRM is supported by two preloaded duplex angular contact ball bearing pairs. Redundant spring actuators rotate the structure out of the "moving zone" of the platform after release. Redundant limit switches indicate the end position of the HDRM. A redundant pyrotechnic cable cutter releases the HDRM in orbit. The cutter is mounted directly to the S/C panel to avoid introducing

shocks into the mechanism during firing, and therefore protects the acceleration-sensitive ion thrusters.
All tribologically stressed parts are dry lubricated to minimize wear during operation and also to minimize contamination sources. The ball bearings are dry lubricated with ion-plated lead and lead-bronze cages and the roller screw is coated with sputtered Molybdenum Disulfide. The spherical bearings are equipped with self-lubricating reinforced Teflon liners.

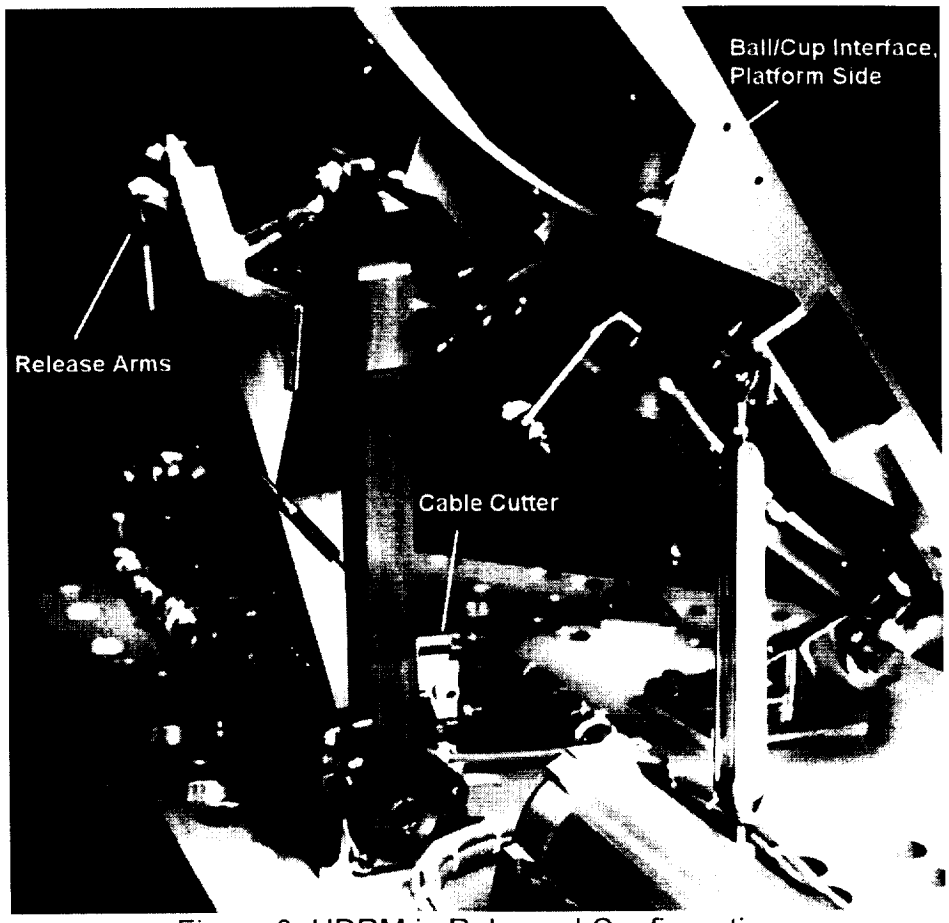

Figure 3 HDRM in Released Configuration

The heat produced by the thrusters during operation will be radiated into space and a small portion will be conducted into the S/C. Thermal barriers inside the mechanism ensure that this heat flux will remain below 5 W.

Kinematics

The requirement on the kinematics is to provide an unambiguous and stabile mobility of the platform by means of two linear drives. The platform is fixed via a ball joint to the spacecraft which provides three rotational degrees of freedom. The Transverse Strut is equipped with two ball joints, one fixed to the platform and one to the spacecraft panel,

and fixes one rotational degree of freedom of the platform. The remaining rotational axes are determined by the center point of the ball joint of the Single Point Hinge and the two pivot points of the Movable Struts, which are fixed on one end to the platform and on the other to the nut of the linear drive. This arrangement with platform, two moving struts and the spacecraft panel forms a four-linkage gear, which becomes stable by means of the other supports of the platform (Single Point Hinge and Transverse Strut).

The special kinematics of the mechanism result in a parallelogram-like shape of the effective alignment range circumscribing the circle defining the 6° halfcone capability of the ITAM. The two symmetrically arranged ITAM allow a spatial deviation of the S/C CoG within a sphere of 340 mm diameter from the nominal position.

Technical Data

Mass:	4.3 kg			
Dimensions:	653 x 288 x 330 mm (length x width x height, stowed)			
Stiffness: (calculated)		Mode 1	Mode 2	Mode 3
	ITAM:	129.1 Hz	219.0 Hz	232.4 Hz
	ITAM + Thrusters:	85.3 Hz	93.8 Hz	109.6 Hz
Alignment Range:	6° halfcone (minimum)			
Speed:	5.4° per minute			
Resolution:	0.003° per motor step			
Power Consumption:	6.8 W average, 19 W peak			

Qualification Test Summary

The ITAM QM successfully passed the qualification test campaign in September, 1996. A summary of the test sequence is shown in the following table:

1 - Electrical Bonding/Isolation	8 - Function Test
2 - HDRM Release Test ambient conditions	9 - Thermal Vacuum Cycling with HDRM release at hot/cold extreme temperatures and Life Test
3 - Performance Test	10 - Performance Test
4 - Physical Properties, mass, cog, moi	11 - Nominal Position of Platform measurement
5 - Function Test	12 - Algorithm Verification measurement
6 - Vibration Test	13 - Electrical Bonding/Isolation
7 - HDRM Release with flight cable cutter	

The qualification test program was designed to demonstrate the integrity and stability of the ITAM design, both during and after exposure to the required environmental test conditions. The test program simulated conditions which are more severe than the mission requirements in order to provide assurance of the design and to detect any design deficiencies.

Physical Properties

The physical properties, mass, cog and MoI, of the ITAM QM were measured without thruster mass dummies installed. For this paper the mass and Moment of Inertia properties are included.

Mass = 4.285 kg

Moment of Inertia about the axes passing through the cog of ITAM:

X-Axis = 0.050 kgm^2	Y-Axis = 0.137 kgm^2	Z-Axis = 0.145 kgm^2

Environmental Tests

Vibration Tests and Thermal Vacuum Cycling Tests will be addressed in the following:

Vibration

Three separate vibration tests were performed, including linear acceleration, sine and random vibration. The Linear Acceleration Test subjected the ITAM to a low frequency sinusoidal vibration in order to envelope the quasi-static loads experienced during launch and transfer orbit. The sinusoidal and random vibration testing demonstrated that the ITAM was able to meet it's design objectives. For all of the vibration testing the ITAM was in the launch configuration, the ion thruster platform was connected to the HDRM via a cable and included mass dummies for both ion thrusters.

The ITAM QM sustained all vibration and linear acceleration loads without degradation or overloading of any structural component, loss of function or permanent deformation, and the ITAM structure is considered to be fully qualified with respect to its mechanical performance. A summary of the vibration test results are given in the following tables.

Natural Frequency

The following table shows the comparison of the measured and predicted natural frequencies of the ITAM. Only the first 4 modes are shown here.

Mode Number	Test Frequency (Hz)	Analysis Frequency (Hz)	Deviation of Test vs. Analysis
1	85.4 / X	82.9 / X	3.0%
2	99.5 / Z 106.2 / Y	91.7 / Z	8.6 % 15.8%
3	127.8 / X	109.6 / X	16.6%
4	135.0 / Z	121.0 / X	11.6%

Maximum Response Accelerations at the ITAM Platform (Interface to the Ion Thrusters)

Sine Vibration

The following table summarizes the maximum measured accelerations at the interfaces of the ITAM and the Ion Thrusters which were measured in the test coordinate system (Y-Axis is perpendicular to the thruster platform) and then transformed in the basic Spacecraft coordinate system as shown in this table. Also shown are the predicted accelerations from the analysis.

	X-excitation (unnotched) Input - 4 g's		Y-excitation (unnotched) Input - 4 g's		Z-excitation (notched) Input - 5.8 g's	
	Test Result	Analysis (at Frequency)	Test Result	Analysis (at Frequency)	Test Result	Analysis (at Frequency)
X-axis	17 g	20.0 g (82.6 Hz)	0.0 g	3.2 g (91.8 Hz)	3.3 g	5.0 g (91.7 Hz)
Y-axis	0.7 g	0.5 g (100 Hz)	1.8 g	5.0 g (91.8 Hz)	3.4 g	6.4 g (91.7 Hz)
Z-axis	2.0 g	2.1 g (100 Hz)	4.9 g	16.0 g (91.8 Hz)	36 g	39.6 g (91.7 Hz)

Random Vibration

This table summarizes the worst case RMS-Accelerations measured at the interface of the ITAM and the Ion Thrusters as measured in the local accelerometer coordinate system (Y-Axis is perpendicular to the ITAM Platform).

	Excitation X -notched RMS acceleration (g's) in PSD value: 0.03007 g^2/Hz	Excitation Y -notched RMS acceleration (g's) in PSD value: 0.017 g^2/Hz	Excitation Z -notched RMS acceleration (g's) in PSD value: 0.03007 g^2/Hz
X axis	35.0	8.0	12.0
Y axis	21.0	37.0	51.5
Z axis	28.0	41.0	35.0

Thermal Vacuum Cycling

The ITAM QM was exposed to a staged thermal vacuum cycling test which included two HDRM release tests, one at each of the minimum and maximum operating temperatures. After the release tests were completed the test item was subjected to 8 qualification level thermal vacuum cycles where the ITAM was operated during each temperature extreme in order to perform a life test while exposed to vacuum conditions at the worst case temperatures.

The ITAM was configured without the thruster mass dummies for this test, however Thruster Heater Dummies were installed to the platform at the thruster interface in order to apply the required heat flux to the platform which simulated the worst case heating condition expected from the ion thrusters. The following table summarizes the thermal vacuum cycling requirements:

Vacuum Conditions	< $1.3*10^{-5}$ mbar
Cycles Required	8
Dwell Time	2 hours minimum
Max Thermal Condition	at Platform (thruster i/f): +210°C at Adapter (S/C i/F): +70°C
Min Thermal Conditions	at Platform (thruster i/f): +70°C at Adapter (S/C i/F): +210°C

Upon completion of the Thermal Vacuum Cycling test the ITAM was inspected and a performance test made. The ITAM performance was nominal and no degradation was evident. However it was seen that the platform was deformed which was detected when the HDRM and platform ball-cup interface could not properly line-up. A post-test failure investigation resulted in the following findings:

During the hot thermal cycles the Dummy Heaters were applying approximately 500 W to the platform vs. an expected heating power of 100 W from the ion thrusters. This resulted in a greatly increased temperature gradient being applied to the platform which consequently also experienced much higher than expected thermal stresses. A post-test dimensional inspection of the platform determined that the platform had been deformed up to 4 mm from it's nominal flatness requirement of 0.1 mm. After consulting with the customer a post test thermal analysis was undertaken which showed that a more realistic maximum temperature which the platform would see in service is 135°C. Consequently the maximum thermal condition for the platform requirement was relaxed to 135°C. Finally, a post test failure analysis as well as delta qualification test for the platform have shown that at 135°C the platform will not experience permanent deformation.

Function & Performance Tests

The main function of the Drive Units is to displace the pivot points of the Movable Struts. An electrical and a mechanical limit stop are located on each end of the moving range of each Drive Unit. The mechanical limit stop has to ensure that no jamming of the motion can occur by moving into the limits, so that a reliable reverse movement is always achievable.

One of the electrical limit switches serves also as a reference switch, in order to avoid the motion direction problems of micro switches. Since micro switches have a large hysteresis in their switching characteristics to avoid chattering, the switch point shifts at different motion directions. To avoid this feature one end switch is used as reference switch so that the reference direction is always the same. An absolute position sensing as well as a special reference strategy could therefore be avoided to synchronize the position counter of the electronics with the mechanism.

The required torque of the Drive Unit is defined by the resistive torque of the Platform motion, the bending moment of the electrical cables and the gas tubes of the thrusters multiplied by the corresponding safety factors. For selecting the stepper motor the internal friction of the bearings and spindle was also considered.
The accuracy of the Drive Unit motion was driven from the overall repeatability accuracy of the platform position of <0.1°. Due to this accuracy requirement and the high motion ratio of the kinematics the Drive Unit has to be backlash free.

During the steady state mode the Drive Units will hold the position stable without external electrical power.

Design Requirements on the Drive Unit

On the Drive Unit all usual flight hardware requirements for mechanisms are applied. This means safety factors for stress and torque, bonding and isolation requirements and PMP (parts, materials & processes) requirements, as for example, outgassing and stress corrosion. Only the verification of the safety factors for torques are verified in the performance test.

Verification of the Drive Unit Function

The function of the ITAM was verified in several steps during the qualification program. The aim was to control the function itself as well as to verify the integrity of the equipment after exposure to several different environmental tests. The function test of the Drive Unit includes a pure movement verification, a verification of proper function of the electrical limit switches and the travel over the entire movement range.

Verification of the Performance

The performance test includes the verification of the repeatability accuracy and the torque, especially the torque margin. For this purpose a control electronics was built, which is called ITAE Simulator (see fig. 4, Ion Thruster Alignment Electronics), to control the qualification model. The simulator includes a power electronics similar to the flight hardware in order to ensure the same performance of the stepper motor.

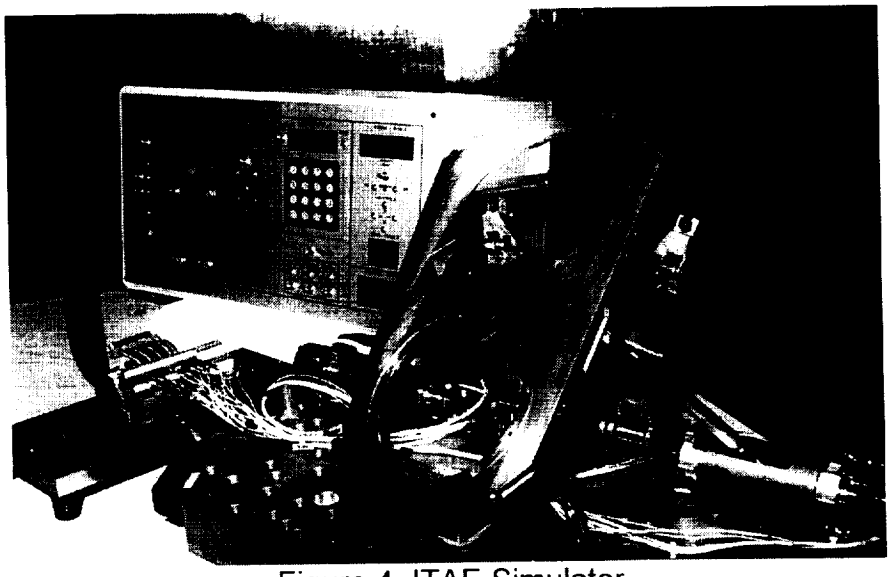

Figure 4 ITAE Simulator

The problem of testing the torque margins is that the electronics, the stepper motor and the spindle, and the strut linkage, builds one integrated system. To separate the motor form the spindle and to measure the torque is not correct because the stepper motor characteristics are angle and speed dependent. That means that only a static torque measurement on the motor will result in the holding torque, which is much higher than the available moving torque. Therefore ORS selected a special measurement method. The idea was to reduce the input current by the safety factor. The output torque at the stepper motor spindle is closely proportional to the input current. The electronics therefore was equipped with a current limiter so that the movement is verified by reduced output torque or the limit current where step losses occurs, which gives the ability to verify the current safety margin.

The verification of the torque margin was performed at the beginning of the qualification test campaign, at the extreme temperature in the thermal vacuum chamber, several times during the life test (which provide a good indication of the degradation process during life), and at the end of the campaign. Figure 5 shows the course of the torque margin during life. Since the current/torque ratio is temperature dependent two margins for both extreme temperature are given.

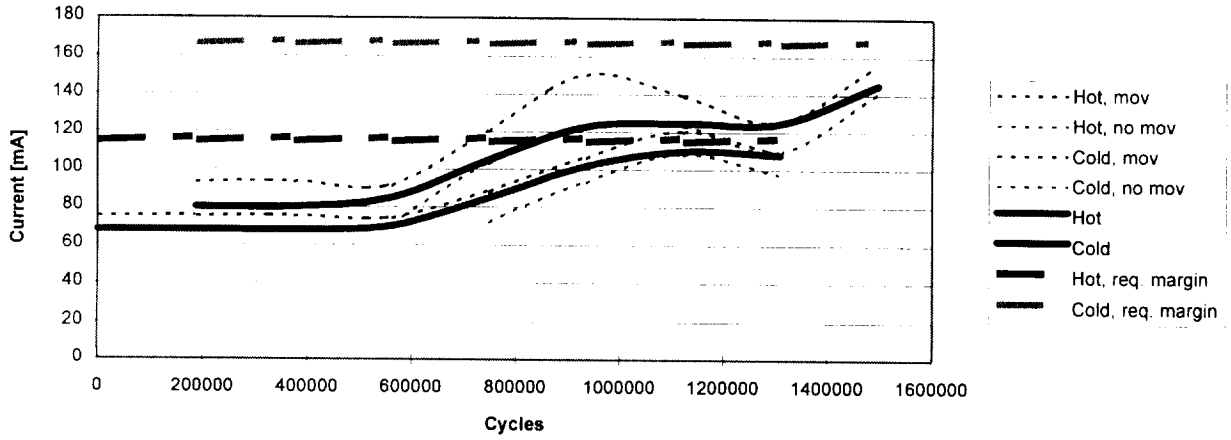

Figure 5 Torque Margin (expressed in amps)

The 1.5 million motor cycles equal a lifetime of 10 years operation in orbit (1 cycle are 4 motor steps, 25 cycles are one spindle revolution, all was driven on 4 mm of the roller screw)

The accuracy was verified at the beginning and the end of the qualification test campaign. For this purpose ORS used a specially developed tool equipped with two cable transducers. By means of the ITAE Simulator the platform was moved to several arbitrary positions. The platform position was recorded (see fig. 6) by means of the transducer voltage output. Afterwards these positions were again approached in the

reversed sequence. The differences of the voltage output at several position were recorded. The result of these tests were that a difference on any position can not be identified by a measurement accuracy of 0.02° for both tests.

Algorithm Verification

The problem of this type of mechanism is that the platform position is not linearly proportional to the input steps. Therefore a repositioning can not be calculated without knowing roughly the absolute position of the mechanism. Therefore a synchronized step counter in the electronics has to be implemented. An algorithm was established to calculate the position of the platform. By means of a 3D measurement device this algorithm was verified. Arbitrary positions of the platform scattered over the entire moving range were approached. The actual position of the thrust interfaces on the platform were measured and the thrust vector was calculated by means of these measurement values. These values were compared with calculated values based on the algorithm. The values were in a high degree of accuracy ($\leq 0.01°$) so that it can be assumed that this algorithm is correct over the entire range.

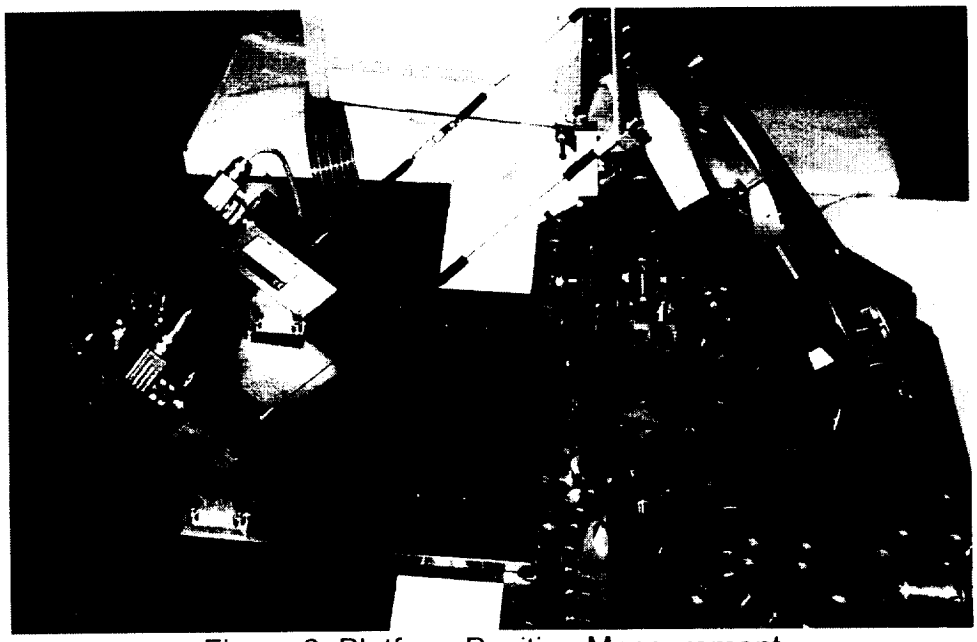

Figure 6 Platform Position Measurement

HDRM Release

This mechanism has the task to support the platform during launch and to release it by means of a pyrotechnic device in orbit. The verification of the mechanism was split in three different tests. First, the function tests, which was performed with a cable cutter simulator and with the original pyrotechnic device, in ambient conditions and vacuum at extreme temperature, second the vibration test, where the capability to support the

platform was verified and third the torque tests, where the torque margins between actuator spring and resistive torque were measured.

The function of the HDRM was tested several times during the environmental testing in order to verify the integrity of the HDRM after exposure to several environmental tests. For these tests a cable cutter simulator was used instead of the original cutter except for the post vibration test release. During the release with the original pyrotechnic cutter accelerometers were applied in order to measure the reaction acceleration of the mechanism.

The torque margins on the actuator springs of the mechanism were tested during the performance tests prior and after the environmental tests (see fig. 7). The results of these tests where that the margins were always inside the expected range (actuation force more than 3 times as the resistive force).

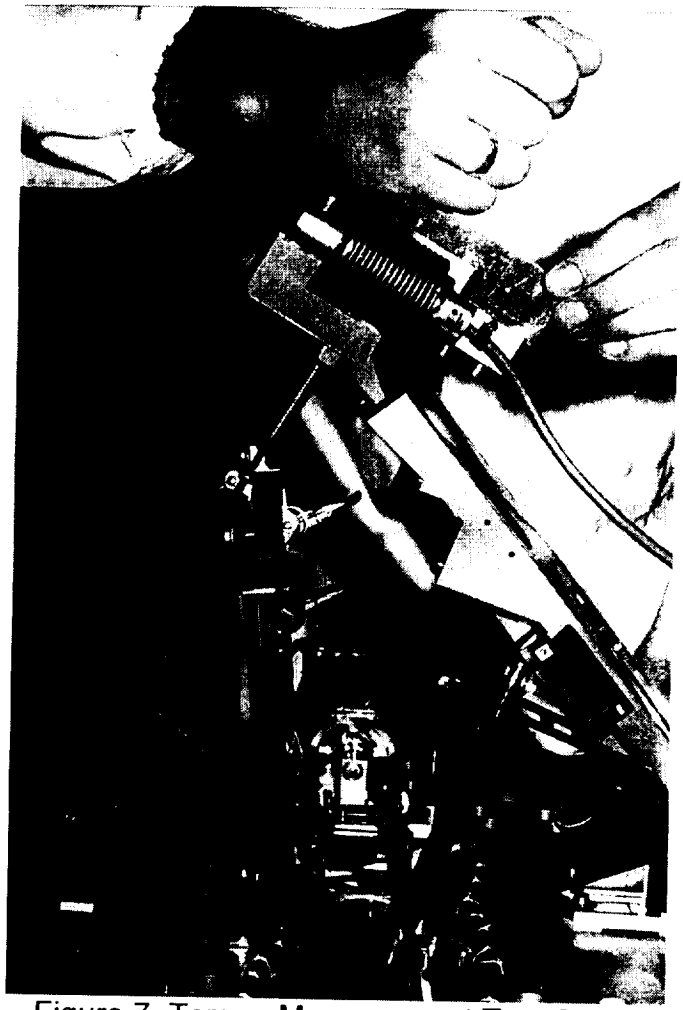

Figure 7 Torque Measurement Test Setup

Lessons Learned & Improvement Potentials

The three main „lessons learned" during the design, development and qualification of the ITAM are explained below.

Drive Unit Roller Screw vs. Lifetime:

The selected MoS_2 lubricated recirculating roller screw exhibited proper performance during the entire qualification test campaign. However, the record indicates an increase of the friction torque, which is mainly related to the roller screw. It can be expected that a further testing would lead to unacceptable margins.

If much higher lifetime requirements are asked for in future applications, it should be carefully considered whether or not the required movement cycles are realistic. If so, another (liquid) lubrication system for the roller screw has to be considered.

Platform Material vs. Thruster I/F Temperature:

The aluminum alloy 7075 T7351 is artificially aged at 160°C. Therefore a temperature near or above that point for a longer period will result in permanent (ambient) loss of strength, which is acceptable for the in-orbit performance of the ITAM. The problem as described before occurred due to high and unevenly distributed power input via heaters, which resulted in high temperature gradients in the platform.

Two things have to be considered for future testing; Care has to be taken to get an even temperature distribution during heat up and steady state qualification tests, and flight hardware must not be exposed to temperatures close to or higher the artificial ageing temperature, because the permanent strength loss is critical with respect to later expected launch loads.

Distributed Design vs. Integration:

Due to severe mass constraints it was decided not to use a common baseframe for the different ITAM components interfacing to the spacecraft structure. This feature increased the effort spent for initial assembly, testing and final integration at several system levels. Also a number of special tools were necessary due to that fact.

Further design developments should carefully consider the advantage of mass reduction compared to the high effort during assembly, integration and testing.

Conclusion

A further development has been started to adapt the existing and qualified ITAM design for other types of Ion Thrusters, and this effort will target on the future use of this mechanism on commercial telecommunication satellites.

The ITAM is considered to be a simple and reliable design and represents principally a general alignment mechanism, which can also be used for small appendages like antennas, mirrors or similar devices which need relocation during in-orbit life.

References

Patent pending PCT/AT 96/00181

M. Falkner, C. Schwarzinger, „The Development of an Ion Thruster Alignment Mechanism (ITAM) for Artemis", Proc. Sixth European Space Mechanisms & Tribology Symposium, Zürich, Switzerland, 4-6 October 1995 (ESA SP-374, August 1995), pp. 137-147

Rotary Mechanism for Contactless Data and Power Transfer in Spacecraft

Gwyn Roberts*, Peter Hadfield*, Martin E. Humphries** , François Bauder+ & Jose M. Gavira Izquierdo++

Abstract

The design, development and testing of a rotary Contactless Transfer Device (CTD) is described. The space-compatible Breadboard Model transfers bi-directional 5 Mbps data using a modulated sub-carrier capacitive technique, and 400 W of power at high efficiency using a rotary transformer. Resonating techniques are used to maximize efficiency. Functional and environmental test results are presented. The advantages of the CTD over slip-rings, especially in high rotational rate or long lifetime applications, is discussed.

Introduction

Conventional techniques for transferring data and electrical power across a rotating interface within spacecraft involve the use of slip-rings or roll-rings. While such devices are well established and adequate for low rates of rotation, their use at high rotational rates introduces many potential problems including friction torque and contact wear resulting in high contact resistance, electrical noise, and the release of debris.

Since rotating joints are frequently mission critical, overcoming the limitations of slip-rings is an issue that is of concern to an increasing number of users. Power and signals are transmitted through rotating or moving interfaces in scanning and pointing mechanisms, solar array deployment mechanisms, robotic joints, remote sensing and other instrumentation. For such users, a *contactless* transmission system would allow higher rotational speeds by the elimination of wear and debris sources, thus allowing high reliability and a long lifetime for a mission. In this paper, we describe the design, development, manufacture and testing of such a space-compatible Breadboard Model (BM) Contactless Transfer Device (CTD).

Applications & Specifications

Following an extensive survey of potential users of a CTD, it was discovered that available technology is already sufficient to adequately meet the majority of the

* IDB Ltd., University of Wales, Bangor, U.K.
** Matra Marconi Space - Space Systems Ltd., Filton, U.K.
+ Mecanex SA, Nyon, Switzerland
++ European Space Agency, Noordwijk, The Netherlands

requirements of solar array deployment mechanisms (SADMs), typically several kW at *very* high efficiency (>99.5%) and one revolution per day. It is possible that it is for this reason that devices such as the rotary-transformer solar-array drive package developed in the late 1960s [1] were not widely adopted. On the other hand, many scanning, pointing, rotating and tracking instruments demand high rotational rates and/or a very long lifetime. Such requirements are only moderately met by current slip-ring or roll-ring technology.

Table 1. Breadboard Model CTD Specifications (2 power & 2 data modules)

PARAMETER	*VALUE*	*NOTES*
Power-Transfer		
Power transfer	>250 W	per module
Input voltage	28 or 50 V DC	
Output voltage	28 or 50 V DC	
Data-Transfer		
Spacecraft to rotating platform:	>5 Mbps digital data	per module
Platform to spacecraft:	>5 Mbps digital data	per module
Mechanical (excluding electronics)		
Outer diameter	182 mm	
Inner diameter	55 mm	to allow access for central axle or pole
Axis length	237 mm	
Mass	<12 kg	without mass-optimisation
Non-operating temp. range	-45 to +90 °C	
Operating temp. range	-25 to +65 °C	
No. of revolutions	5×10^6	FM target > 2×10^6 over 10 years
Rate of rotation	0 to 9500 rpm	limited by bearings only

Generic specifications for this category of applications were therefore used as the baseline for the design of BM CTD (Table 1). Other potential applications include robotic joints and deployment mechanisms.

Design & Manufacture

Technology Selection

An extensive trade-off analysis of many candidate technologies for the transfer of power and data was carried out prior to commencing the detailed design [2].

High inherent reliability was the prime design driver; unless the CTD could exhibit a long lifetime it would offer little advantage over existing technology. It was therefore assigned a high weighting factor. Other aspects addressed during the evaluation process included electromagnetic emission and susceptibility, torque, mass, volume,

power requirements, configurational flexibility, complexity, expansion capability, space approval and development risk.

Data-Transfer—Optical techniques exhibit favorable EMC characteristics, and have been used for data-transfer on earlier ESA contracts for microgravity applications [3,4]. However, their susceptibility to lubricant contamination, and uncertainty about the reliability of optical sources reduced their overall scores in the evaluation process.

The overall winner of the selection process was a capacitive technique. The use of a modulated sub-carrier of a sufficiently high frequency ensures that no interference from the power-transfer system will pass the receiver bandpass filter, and also allows the use of a resonating network to minimize signal loss across the interface.

Power-Transfer—Although microwave, optical and thermal techniques were investigated, it was apparent that only the rotating transformer could operate at a useful efficiency level, hence this technology was selected for use within the CTD.

Design Philosophy

Like the slip-ring/roll-ring units it is designed to replace, the CTD transfers power and data across a rotating interface; however there is a fundamental difference in the way the CTD concept achieves this aim. In a slip-ring based system, each signal or power line to be transferred is allocated one or more *dedicated tracks* within the slip-ring unit. In the case of the CTD on the other hand, signal lines are connected to an electronics module containing multiplexing and modulating electronics; having multiplexed the signal lines, the CTD only requires to provide a *single* channel across the rotating interface (plus one in the reverse direction). Further electronics on the secondary side performs demodulation and demultiplexing functions. Complementary electronics provide bi-directional multi-channel capabilities. It is clear that expanding the capabilities of the CTD are therefore mainly a matter of modifying the electronics rather than the hardware at the rotating interface.

A similar philosophy is employed for the transfer of power across the rotating interface of the CTD. A *single* spacecraft bus is taken across the rotating interface, (the 'ring main' concept), and local regulation is used as required on the secondary side.

The design philosophy has been to minimize the number of components mounted at the rotating interface by mounting the electronic circuitry associated with both data and power-transfer sub-systems remotely. This allows a simple, electrically symmetric interface design, ease of thermal management resulting in high reliability, and improved access to the electronics.

Design Constraints

Crucially, the CTD design has to accommodate a central axle or pole of up to 55 mm diameter, as required by applications such as the Multi-frequency Imaging Microwave

Radiometer (MIMR). The lack of axial access was a problem for many potential systems including fiber optic rotary joints.

Size and mass of the unit were tightly controlled, while EMC and susceptibility to lubricant contamination were critical areas for the design. Furthermore, a modular design was required to ensure configurational flexibility.

Breadboard Model Build Standard

The rotating interface of the BM CTD is flight-representative, though mass and volume optimization have not been carried out, and space-compatible rather than space-qualified bearings have been used. Commercially-rated components have been used for the remotely-mounted electronics in order to allow rapid development.

Multiplexing/demultiplexing techniques are widely used in space applications and the associated technologies are well-established. Furthermore, the specific interface requirements are likely to be very application-specific. For these reasons, the BM does not include multiplexing nor demultiplexing electronics. The data-transfer sub-system may be evaluated using a 5 Mbps signal to represent the composite signal output from a multiplexer, with a second similar signal in the opposite direction to evaluate crosstalk.

The BM CTD described in this paper includes redundant modules for both data and power transfer within the rotating interface.

Detailed Design

The detailed design of the CTD is largely unchanged from that described in [2]. Figure 1 summarises the concepts used in the CTD.

Data-Transfer—The 5 Mbps signal modulates a 100 MHz carrier using Amplitude Shift Keying (ASK). ASK was selected due to the simplicity of the modulation and demodulation techniques; however the transfer bandwidth is sufficient to allow the use of FSK (e.g. for analog video). Within the rotating interface a data-transfer module consists of 4 fixed and 4 rotating capacitance tracks. The air (vacuum) gap between each fixed-rotating pair is around 0.6 mm, giving a nominal capacitance value of around 25 pF. Four pairs of tracks provide bi-directional differential data-transfer capability. A cylindrical arrangement has been selected for ease of assembly and disassembly. A miniature toroidal transformer is used to *resonate* the interface to the carrier frequency. This novel technique minimizes losses across the interface caused by stray capacitance, thus improving interference rejection. After passing across the capacitive interface to the rotating side, the signal is amplified and demodulated using a level detector and shaping filter. A second data-transfer module is used to transfer a baseband signal, (without the resonating network) for comparison of performance.

Power-Transfer—The power-transfer section is essentially a resonant-mode switched-mode power supply. The remotely-located driver circuit on the fixed (primary) side consists of an array of MOSFET switches together with drive-waveform generating circuits. The drive circuits switch at instants when the current level is low, thus minimizing power losses in the drive circuits and reducing the amount of electromagnetic radiation.

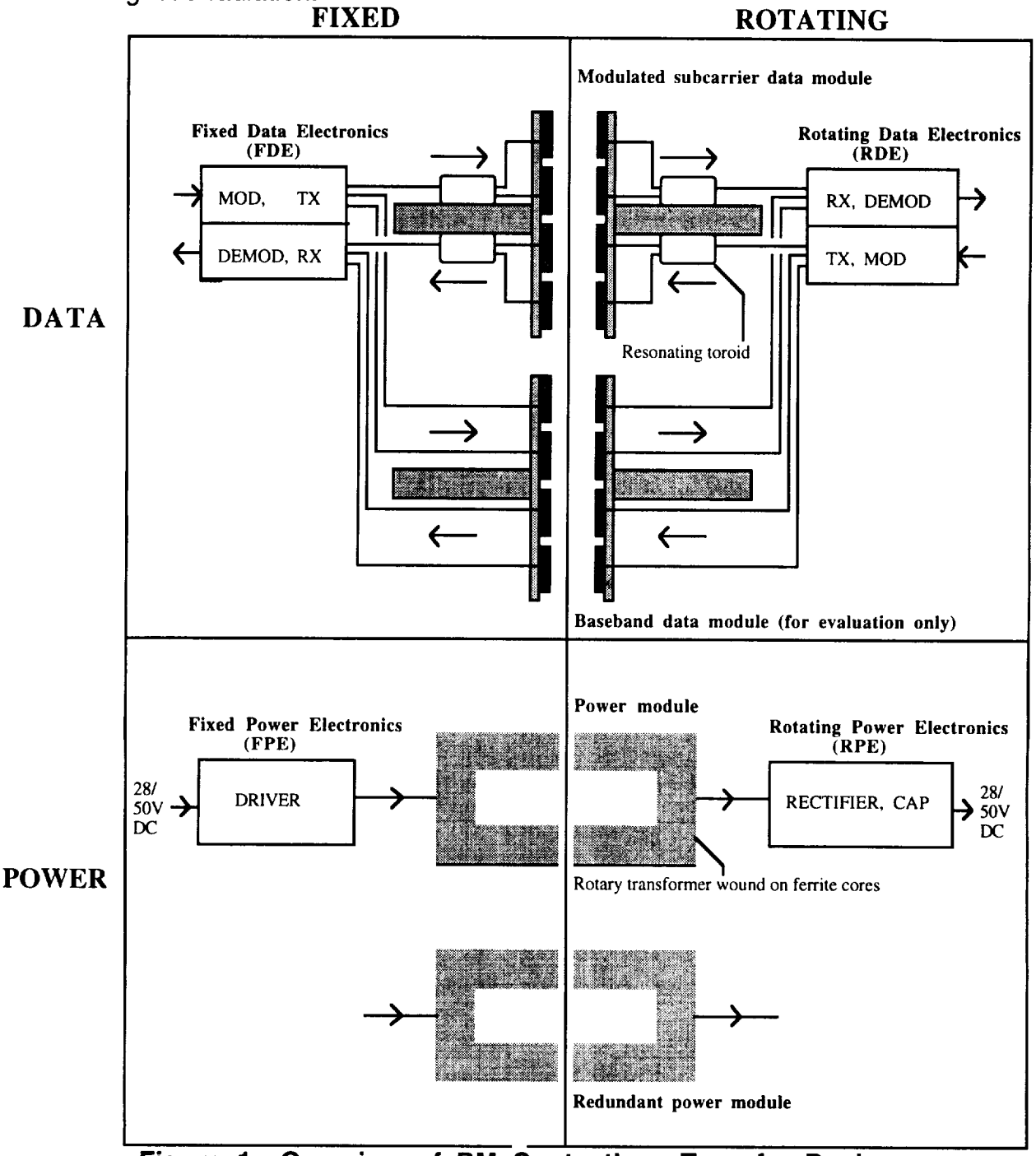

Figure 1 Overview of BM Contactless Transfer Device

Within the rotating interface, a module consists of one fixed and one rotating ring of ferrite cores carrying stranded, heavy-gauge copper wire, to make up the primary and secondary sections respectively of the rotating transformer. Earlier work [3] has shown that by resonating the leakage inductance to the switching frequency, very efficient power transfer may be achieved even though the leakage inductance is very large with this configuration. The remote electronics on the rotating (secondary) side consist of an array of power diodes and a large reservoir capacitor. The power-transfer sub-system operates at a fixed frequency of 25 kHz. Active control of the frequency would compensate for any variation in values of resonant components caused, for example, by ageing; this would however be achieved at the expense of considerable additional complexity. Active control is addressed later in this paper.

The rotating interface of the BM CTD is illustrated in Figure 2. The BM, which includes 2 power modules and 2 data modules, is 237 mm long by 182 mm diameter. The cables exiting towards the top of the photograph are the connections from the rotor to the Rotating Power and Data Electronics. A thin coaxial cable connects to the data-transfer module, while the screened bundles of heavy copper wire are the terminations of the individual windings of the power-transfer transformer, which connects to the Rotating Power Electronics. Identical cables exiting from the side of the BM connect to the Fixed Power and Data Electronics. Other cables visible connect to thermistors used during testing. Each electronic module (not illustrated) is housed in a screened enclosure approximately 145 x 90 x 50 mm. Spacecraft power and data buses connect to those units rather than to the rotating interface directly.

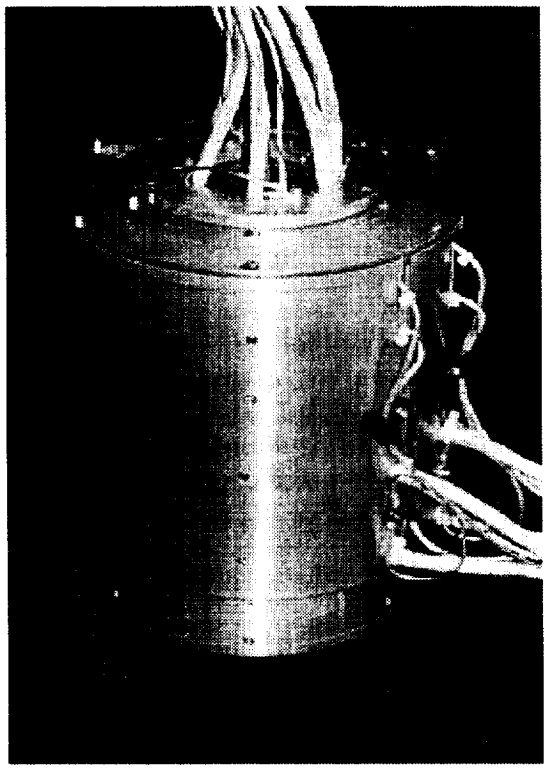

Figure 2 BM CTD Rotating Interface

Evaluation Program

The objectives of the BM test programme were to evaluate the CTD design concept and to demonstrate compliance with the functional requirements. It is anticipated that the results of these tests will allow identification of any areas where design improvements may be implemented prior to fabrication of a Flight Model (FM).

Power Transfer Functional Tests

The power transfer sub-system was evaluated by transferring power from a bench power supply to the Fixed Power Electronics, through the CTD rotating interface, to the Rotating Power Electronics and finally to a 500 W dummy electrical load. Measurement of currents and voltages on the fixed and rotating sides enabled the determination of all necessary performance characteristics.

Of prime concern is the overall DC-DC transfer efficiency - i.e. the ratio of the power delivered into the dummy load to that drawn from the power supply. As illustrated in Figure 3, for a nominal 50 V spacecraft bus, the efficiency exceeds 90% to beyond 300 W. The losses are accounted for by the finite on-resistance of the switching FETs, copper and magnetizing losses within the rotating interface, and losses in the rectifier diodes. This figure is expected to be typical of that obtainable for a CTD, and is considered adequate for instruments in the category being targeted, but not for SADMs.

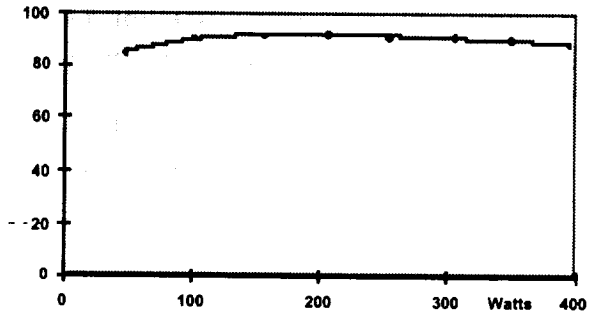

Figure 3 DC-DC transfer efficiency at 56V

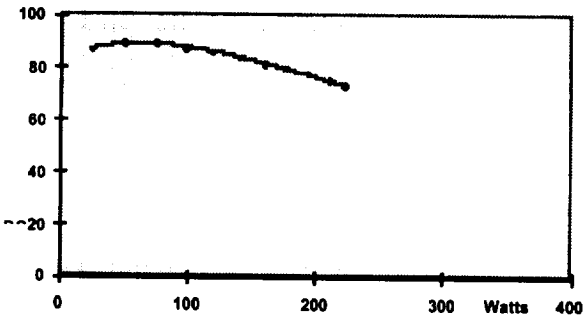

Figure 4 DC-DC Transfer Efficiency At 28V

At a nominal 28V bus voltage, the efficiency is not as high since, for a given power level the current, and therefore the I^2R losses, are higher, as illustrated in Figure 4. Figure 5 further illustrates the effects of variation of input bus voltage, at a nominal power level of 250 W. The reduction of efficiency (upper graph) as the input voltage is reduced is quite marked. The lower graph illustrates the variation of output voltage with input voltage; note that the intention is to utilize local regulation on the rotating side of the interface where necessary.

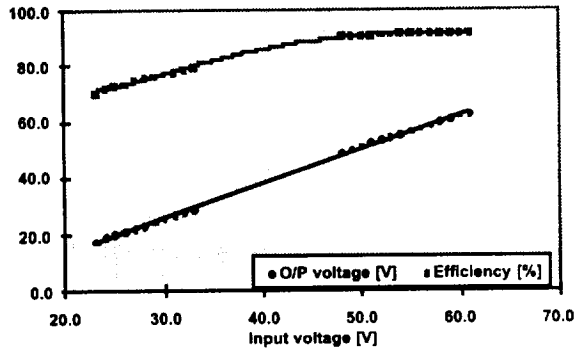

Figure 5 Effect Of Input Voltage On Output Voltage (Bottom) And On Efficiency (Top)

Figures 6 and 7 illustrate the regulation of output voltage at 56V and 28V respectively.

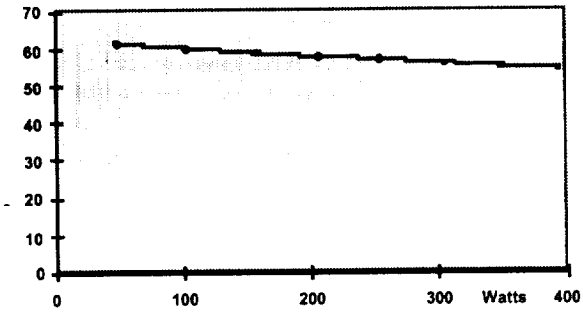

Figure 6 Output Voltage Regulation At 56V

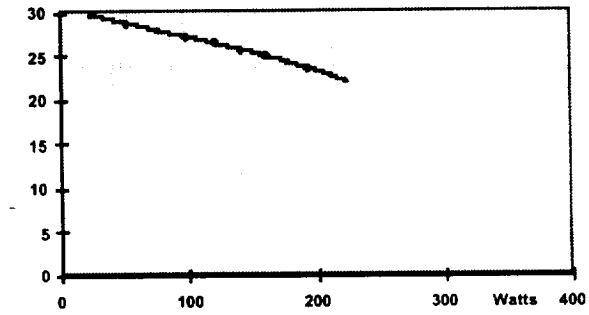

Figure 7 Output Voltage Regulation At 28V

Figure 8 illustrates the output voltage ripple at 28V. As this is directly influenced by the smoothing components within the Rotating Power Electronics module, there is scope to trade off supply cleanliness against volume and mass for specific applications.

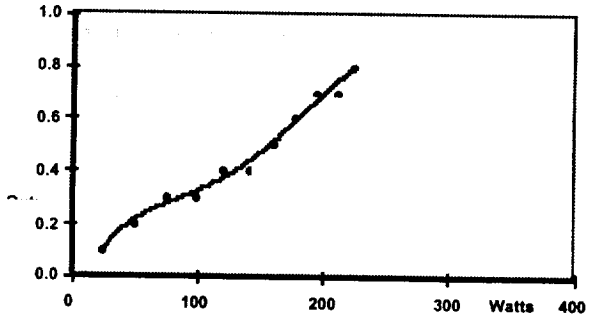

Figure 8 Output Voltage Ripple At 28V

Sensitivity to variations in oscillator frequency is illustrated in Figure 9. A ±10% change of frequency off the nominal 25 kHz resonance causes a reduction in efficiency of <2.5%, and a variation in output voltage of ±1.2V. It is anticipated that these figures are acceptable for the majority of applications, as local regulation is used on the secondary. Note that for a fixed oscillator frequency, variation in value of either the leakage inductance or the capacitor used to resonate it (e.g. ageing) would induce a similar effect. In highly critical applications, active frequency control could be used, though the complexity would increase considerably. The implications of such variations upon EMC emissions should be addressed prior to fabricating a flight model.

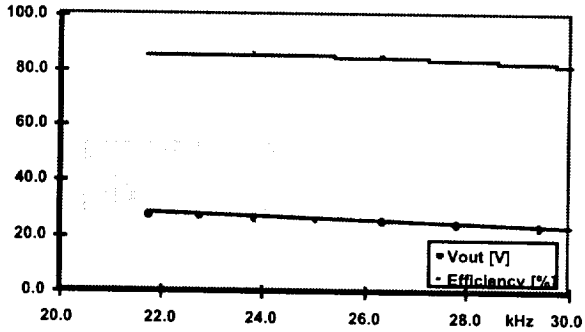

Figure 9 Variation Of Efficiency (Upper) And Output Voltage (Lower) With Frequency

Data transfer functional tests

The prime objective of the tests carried out on the data-transfer sub-system of the CTD were to confirm an acceptably low bit error rate (BER) under all specified conditions. Testing involved applying a 5Mbps Pseudo-Random Binary Signal (PRBS) into the

Fixed Data Electronics, across the rotating interface and into the Rotating Data Electronics. The resulting output bitstream was compared to the original PRBS, and the BER computed. The target maximum BER was 10^{-9}.

Measurements confirmed a *zero BER* under each of the following conditions:

- with the rotor static,
- with the rotor rotated manually in either direction (position independence),
- with the power-transfer system operating at full power (no power-to-data interference),
- with a second 5Mbps signal transferred in the opposite direction (no crosstalk).

Torque measurements

Measurements of torque using a Kistler table yielded a figure of 0.5 Nm. This was due entirely to the preloaded bearings, and was unaffected by the operation of the power-transfer system. Minimization of cogging torque has been an important design driver and has been achieved by careful selection of the numbers of ferrite cores on the fixed and rotating sections. Cogging torque was too low to be measured, and is predicted to be many orders of magnitude lower than the values measured for the BM CTD bearings.

EMC characterisation

The generic EMC specifications for the Polar Platform were used as a baseline for EMC characterization of the rotating interface, remote electronics and interconnecting harnesses of the BM CTD.

In the case of the data-transfer sub-system, of prime concern was evaluation of its immunity to the effects of interference. A conducted susceptibility test successfully demonstrated its immunity to noise on the supply lines. Since both the rotating interface and the remotely-located electronics are metal-cased, the CTD design is very well screened against radiated interference; it was therefore deemed unnecessary to measure radiated susceptibility. The application of a 10 mJ arc discharge to points on the case of the CTD caused temporary disruption of the data transfer followed by immediate return to normal operation, which is acceptable.

Measurements of conducted and radiated emissions from the CTD indicated that further filtering is required for compliance with the standard. However, much of the conducted emissions originate from small DC-DC converters within the electronics modules; these are not flight-representative and are to be replaced by space-qualified units or discrete components in a Flight Model.

Thermal cycling

The rotating interface of the CTD was subjected to repeated thermal cycling in air between -45 and +90°C. Operation of the power-transfer (at full power) and the data-transfer sub-systems was evaluated at a range of temperatures between -25 and

+65°C. No deviation was noted in the performance of either sub-system either during or after thermal cycling. Both the sub-systems were operated at their nominal frequencies during this test; we conclude that operation over temperature is adequate without adaptive frequency control.

Vibration test

Following a low level sine survey from 5-2000 Hz, the CTD was subjected to the sinusoidal vibration profile detailed in Table 2, in both the axial and radial directions followed by random vibration according to the levels shown in Table 3. These values are representative of those within an Arianne launch vehicle.

Table 2. CTD Sinusoidal Vibration Levels

5-18 Hz	11 mm (0-Peak)
18-60 Hz	15g (0-Peak)
60-100 Hz	6g (0-Peak)

Table 3. CTD Random Vibration Levels

Axis	Freq.	Level	Total Level
X or Y axis	20-100 Hz 100-400 Hz 400-2000 Hz	+3 dB/oct 0.25 g^2/Hz -6 dB/oct	12.92
Z axis	20-100 Hz 100-400 Hz 400-2000 Hz	+3 dB/oct 0.25 g^2/Hz -6 dB/oct	12.92

For a brief period immediately after cessation of vibration, torque and BER values were higher than their initial values, due it is believed to a small radial misalignment as a result of damage to a ball inside the bearing assembly. There was no evidence of damage to the power or data modules. Subsequent functional testing at IDB revealed no degradation in performance of power or data-transfer modules as a result of vibration testing.

Summary & Conclusions

A Breadboard Model Contactless Transfer Device based on a modulated sub-carrier capacitive technique for data-transfer and a rotating transformer for power-transfer has been manufactured, and has undergone an extensive environmental test program. This test program, which was unusually rigorous for a BM, has confirmed the selection of these technologies, and has demonstrated the merits of the novel resonating techniques employed in both the power and data transfer sub-systems. An acceptable DC-DC power transfer efficiency of around 90% has been achieved, and robust bi-directional data transfer at 5 Mbps demonstrated.

While the CTD design presented here is aimed primarily at scanning, pointing and tracking mechanisms, the design is readily scaleable both in terms of power and data-handling capacity, and in order to accommodate the constraints of different mechanical envelopes. Furthermore, the concepts may be readily adapted for a planar rather than a rotary interface, thus offering potential applications for robotics or rack assemblies, with minimal or no modification to the electronics.

Further Developments

As a generic device with a wide range of applications, the CTD has been proposed for a technology demonstrator mission for the International Space Station [5]. Further development of the concept to a Qualification Engineering Model (QEM) is expected to commence early in 1997.

Acknowledgements

The CTD project is funded by ESA's Technology Research Program. The authors would like to express their gratitude to all the individuals who have contributed to the project, in particular Aled Williams, John Lawrence, Andrew Wild and Marian Pritchard at IDB, Alwyn Owens of the Univ. of Wales, Bangor and Phil Lane now at UCL, Dr. P-A. Mäusli at Mecanex, Scott Mitchell and Rob Child at MMS.

References

[1] Jessee, R.D., Contract No. NAS5-10459, Westinghouse Electric Corporation, Aerospace Division, Lima, Ohio.

[2] Roberts, G., Owens, A.R., Lane, P.M., Humphries, M.E., Child, R.K., Bauder, F., Gavira, J.M., "A contactless transfer device for power and data", Proc. IEEE 1996 Aerospace Applications Conference, Aspen, Colorado, Feb. 1996, pp333-345.

[3] Owen, R.G., Jones, D.I., Owens, A.R., Roberts, G., Hadfield, P, "The microgravity Isolation Mount - a Columbus facility for improving the microgravity quality of payloads", Proc. International Workshop on Vibration Isolation Technology for Microgravity Science Applications, NASA Lewis Research Center, Cleveland, Ohio, April 1991.

[4] Owens, A.R., Jones, D.I., Owen, R.G., Roberts, G., Robinson, A.A., "Progress in the design of a microgravity facility for in-orbit experiments", Proc. of the 4th European Symposium on Space Mechanisms and Tribology, Cannes, Sept 1989, pp229-234.

[5] Roberts, G., Hadfield, P., Owens, A.R., Bauder, F., Humphries, M.E., Gavira, J.M., "An on-orbit demonstration facility for the contactless transfer of power and data" Proc. First Symposium on the Utilisation of the International Space Station, European Space Operations Centre, Darmstadt, Germany, Sept./Oct. 1996.

☆ U.S. GOVERNMENT PRINTING OFFICE 1997–532-128/60015

REPORT DOCUMENTATION PAGE

Form Approved
OMB No. 0704-0188

1. AGENCY USE ONLY (Leave Blank)	2. REPORT DATE	3. REPORT TYPE AND DATES COVERED
	May 1997	Conference Publication

4. TITLE AND SUBTITLE

31st Aerospace Mechanisms Symposium

5. FUNDING NUMBERS

6. AUTHOR(S)

C.L. Foster and E.A. Boesiger*, Compilers

7. PERFORMING ORGANIZATION NAME(S) AND ADDRESS(ES)

George C. Marshall Space Flight Center
Marshall Space Flight Center, Alabama 35812

8. PERFORMING ORGANIZATON REPORT NUMBERS

M-829

9. SPONSORING/MONITORING AGENCY NAME(S) AND ADDRESS(ES)

National Aeronautics and Space Administration
Washington, DC 20546-0001

10. SPONSORING/MONITORING AGENCY REPORT NUMBER

NASA CP-3350

11. SUPPLEMENTARY NOTES Cosponsors: Lockheed Martin Missiles and Space, Sunnyvale, CA 94088 and the Aerospace Mechanisms Symposium Committee. Conference Coordinator: C.L. Foster, Propulsion Laboratory, Science and Engineering Directorate
*Lockheed Martin Missiles and Space

12a. DISTRIBUTION/AVAILABILITY STATEMENT

Unclassified-Unlimited
Subject Category 15

12b. DISTRIBUTION CODE

13. ABSTRACT *(Maximum 200 words)*

The proceedings of the 31st Aerospace Mechanisms Symposium are reported. NASA Marshall Space Flight Center hosted the proceedings held at the Huntsville Marriott Hotel in Huntsville, Alabama on May 14-16, 1997. The symposium was cosponsored by Lockheed Martin Missiles and Space and the Aerospace Mechanisms Symposium Committee.

14. SUBJECT TERMS

spacecraft components, deployment mechanisms, bearings, tribology

15. NUMBER OF PAGES

403

16. PRICE CODE

A18

17. SECURITY CLASSIFICATION	18. SECURITY CLASSIFICATION OF THIS PAGE	19. SECURITY CLASSIFICATION OF ABSTRACT	20. LIMITATION OF ABSTRACT
Unclassified	Unclassified	Unclassified	